

EFFECT OF NATURAL AND SYNTHETIC ORGANICS  
ON THE PROCESSING OF CERAMICS

BY  
BRETT M. SCHULZ

A THESIS  
SUBMITTED TO THE FACULTY OF  
ALFRED UNIVERSITY

IN PARTIAL FULFILLMENT OF THE REQUIREMENTS  
FOR THE DEGREE OF

DOCTOR OF PHILOSOPHY

IN  
CERAMICS

ALFRED, NEW YORK

SEPTEMBER, 2004

Alfred University theses are copyright protected and may be used for education or personal research only. Reproduction or distribution in part or whole is prohibited without written permission from the author.

EFFECT OF NATURAL AND SYNTHETIC ORGANICS ON THE  
PROCESSING OF CERAMICS

BY

BRETT M. SCHULZ

B.S. ALFRED UNIVERSITY (1994)  
M.S. ALFRED UNIVERSITY (1996)

SIGNATURE OF AUTHOR \_\_\_\_\_ (Signature on file)

APPROVED BY \_\_\_\_\_ (Signature on file)  
WILLIAM M. CARTY, ADVISOR

\_\_\_\_\_  
(Signature on file)  
DAVID A. EARL, ADVISORY COMMITTEE

\_\_\_\_\_  
(Signature on file)  
JAMES R. VARNER, ADVISORY COMMITTEE

\_\_\_\_\_  
(Signature on file)  
REBECCA DeROSA, ADVISORY COMMITTEE

\_\_\_\_\_  
(Signature on file)  
DOREEN EDWARDS, CHAIR, ORAL THESIS DEFENSE

ACCEPTED BY \_\_\_\_\_ (Signature on file)  
ALASTAIR CORMACK, DEAN,  
SCHOOL OF ENGINEERING

## ***Acknowledgements***

I would like to thank my advisor William Carty for his support over the past four years while I have been completing my research for this dissertation. His guidance and support during this process have been invaluable. His energy and enthusiasm for research in materials science is contagious.

I would also like to thank the other faculty members of the School of Engineering that have been involved in my research project; my committee members: David Earl, Rebecca DeRosa, and James Varner, and the other members of the faculty: Doreen Edwards and Caspar McConville who started this project as committee members. Their support has been instrumental in the successful completion of this work.

A graduate thesis is a group effort. While it is impossible to acknowledge everyone involved in helping to complete this work I would like to mention several people. First Hyojin Lee, our laboratory supervisor, thank you for the help with the scanning electron microscope and the shear cell. Also, thank you for taking the time to listen to a few of my more elaborate (sometimes misguided) ideas. Next to Ungsoo Kim it has been a pleasure to work with you once again. The collaborative work discussing ceramic processing, colloidal science, and clay mineralogy have been interesting and enlightening. To Ross Newcomb, Mike Brumback, and Mustaq Ahmed happy hour has not been the same since you graduated.

To the other graduate students and undergraduate students that have passed through Bill Carty's research group it was a pleasure to work with you and good luck with your future endeavors.

I would like to thank my parents for their continued support and advice.

Finally I would like to thank my girlfriend Sara Scheffler. Her support has made this all worth while. Her assistance in the laboratory as my assistant helped me complete this work. Her support outside of the laboratory has made this work worthwhile.

## ***Table of Contents***

### **Chapter 1. Introduction**

Introduction .....	1
--------------------	---

### **Chapter 2. Adsorption of Sodium Poly[acrylic acid] on Alumina and Clay Surfaces**

2.1 Introduction .....	4
2.2 Literature Review .....	4
2.3 Experimental Procedure .....	12
2.4 Results .....	16
2.5 Summary and Conclusions .....	32
2.6 References .....	33

### **Chapter 3. Washing and Beneficiation of Raw Clays to Remove Organic and Inorganic Impurities**

3.1 Introduction .....	35
3.2 Literature Review .....	36
3.3 Experimental Procedure .....	45
3.3.1 Washing and Beneficiation of the Raw Clay .....	45
3.3.2 X-ray Diffraction .....	46
3.3.3 Thermal Analysis .....	48
3.3.4 Specific Surface Area .....	48
3.3.5 Chemical Analysis .....	49
3.3.6 Polymer Adsorption .....	50
3.3.7 FTIR Characterization of Clay .....	50
3.3.8 Commentary on the Selected Clays for This Study .....	51
3.4 Results .....	51
3.4.1 Qualitative Observations .....	51
3.4.2 Verification of pH Active Species in the Supernatant .....	52
3.4.3 X-ray Diffraction .....	54
3.4.4 Thermal Analysis .....	57
3.4.5 Specific Surface Area .....	57
3.4.6 Chemical Analysis .....	58
3.4.7 Polymer Adsorption .....	59
3.4.7.1 TK6 (kaolin clay) .....	60
3.4.7.2 Kingsley (kaolin clay) .....	63
3.4.7.3 Huntingdon (ball clay) .....	64
3.4.7.4 Marquis (ball clay) .....	65

3.4.7.5 M&D (ball clay) .....	67
3.4.7.6 C&C (ball clay) .....	70
3.4.7.7 Polymer Adsorption Summary .....	71
3.4.8 FTIR Characterization of Clay .....	73
3.5 Summary and Conclusions .....	82
3.6 References .....	83
 <b>Chapter 4. Effects of Incremental Additions of Na-PAA to Clay</b>	
4.1 Introduction .....	92
4.2 Literature Review .....	92
4.3 Experimental Procedure .....	93
4.4 Results .....	97
4.5 Summary and Conclusions .....	106
4.6 References .....	107
 <b>Chapter 5. Plasticity of Clays: the Effects of Adding Organic Matter</b>	
5.1 Introduction .....	109
5.2 Literature Review .....	109
5.3 Experimental Procedure .....	128
5.4 Results .....	140
5.5 Summary and Conclusions .....	170
5.6 References .....	172
 <b>Chapter 6. Characterization of Surface Finish from Industry</b>	
6.1 Introduction .....	177
6.2 Options Available to Evaluate Surface Finish .....	177
6.3 Problems with Optical Interferometry .....	179
6.4 Experimental Procedure .....	183
6.5 Results .....	186
6.6 Summary and Conclusions .....	198
6.7 References .....	199
 <b>Chapter 7. Compaction of Granulate</b>	
7.1 Literature Review .....	200
7.2 Blending of Dried Granulate .....	205
7.2.1 Introduction .....	205
7.2.2 Experimental Procedure .....	205
7.2.3 Results .....	210

7.2.4 Summary and Conclusions .....	227
7.3 Mechanics of Granule Deformation .....	228
7.3.1 Introduction .....	228
7.3.2 Relative Humidity Effects .....	228
7.3.2.1 Experimental Procedure .....	228
7.3.2.2 Results .....	229
7.3.2.3 Discussion .....	233
7.3.3 Effect of Granule Size on Compaction - moisture content distribution argument.....	234
7.3.3.1 Experimental Procedure .....	234
7.3.3.2 Results .....	235
7.3.3.3 Discussion .....	239
7.3.4 Summary and Conclusions .....	244
7.4 Alternative Binder Systems for Dry Pressing .....	245
7.4.1 Introduction .....	245
7.4.2 Experimental Procedure .....	245
7.4.3 Organic Selection .....	249
7.4.3.1 Plasticized PVA (pPVA) .....	249
7.4.3.2 Na-Lignosulphonate (Ligno) .....	249
7.4.3.3 pPVA / Veegum™ T .....	250
7.4.3.4 Veegum™ T .....	250
7.4.3.5 Agar .....	251
7.4.3.6 Acrylic Latex Emulsion .....	251
7.4.3.7 Starch .....	252
7.4.3.8 Sugar (Alpha-D(+)-Glucose) .....	252
7.4.3.9 Methyl Cellulose .....	253
7.4.3.10 Carboxymethyl Cellulose .....	253
7.4.3.11 Veegum™ T / Vanzan™ D .....	254
7.4.4 Results .....	254
7.4.4.1 Granule Size Distribution .....	254
7.4.4.2 pPVA .....	257
7.4.4.3 Na-Lignosulphonate (Ligno) .....	260
7.4.4.4 pPVA / Veegum™ T .....	263
7.4.4.5 Veegum™ T .....	266
7.4.4.6 Agar .....	269
7.4.4.7 Acrylic Latex Emulsion .....	272
7.4.4.8 Starch .....	275

7.4.4.9 Sugar (Alpha-D(+)-Glucose) .....	275
7.4.4.10 Methyl Cellulose .....	278
7.4.4.11 Carboxymethyl Cellulose .....	283
7.4.4.12 Veegum™ T / Vanzan™ D .....	284
7.4.4.13 Effects of Replacing pPVA with Veegum™ T .....	289
7.4.4.14 Effects of Vanzan™ D on Veegum™ T Granulate .....	292
7.4.4.15 Comparison of the Binder Systems .....	292
7.4.4.16 Blending of Granulate with Alternative Binder Systems .....	308
7.4.5 Summary and Conclusions .....	315
7.5 References .....	316
<b>Chapter 8. Compaction versus Shear Compaction</b>	
8.1 Introduction .....	326
8.2 Experimental Procedure .....	326
8.2.1 Regression Analysis to Determine Shear P1 .....	328
8.2.2 Plasticity of a Granulated Porcelain Body with Organic Binders .....	329
8.3 Results .....	330
8.3.1 Plasticity of a Granulated Porcelain Body with Organic Binders .....	333
8.4 Summary and Conclusions .....	340
8.5 References .....	341
<b>Chapter 9. Plasticizers for PVA</b>	
9.1 Introduction .....	342
9.2 Literature Review .....	342
9.3 Experimental Procedure .....	342
9.4 Results .....	343
9.5 Summary and Conclusions .....	348
9.6 References .....	349
<b>Chapter 10. Summary and Conclusions</b>	
Summary and Conclusions .....	351
<b>Appendix A. Calibration Curves to Determine the Concentration of Polymer in Solution by Potentiometric Titration</b>	
1.0 Creation of the Calibration Curve .....	358
2.0 Sample Calculation to Determine the Concentration of Polymer in an Unknown Solution .....	358
<b>Appendix B. Calculation of the Free Quartz in a Commercial Clay</b>	
1.0 Chemical Analysis of TK6 .....	362

2.0 Free Quartz from the LOI (Sample Calculation) .....	362
3.0 Free Quartz from the Chemical Analysis (Sample Calculation) .....	363
4.0 Summary .....	364
<b>Appendix C. Chemical Analysis of Organics Used to Affect Plasticity in Clays</b>	
1.0 ICP-AES Rock Analysis .....	365
2.0 ICP-AES Water Analysis .....	366
<b>Appendix D. Calculation to Determine the Surface Tension of Organic Solutions</b>	
1.0 Sessile Drop Method .....	368
2.0 Other Methods of Determining the Surface Tension of Liquids .....	368
3.0 Surface Tension of Liquids .....	369
4.0 Sample Calculation to Determine the Surface Tension from a Sessile Droplet .....	369
<b>Appendix E. Determine the Performance of Blended Granulate in Production at Buffalo China</b>	
1.0 Introduction .....	372
2.0 Experimental Procedure .....	372
3.0 Results .....	372
4.0 Summary and Conclusions .....	378
5.0 References .....	379
<b>Appendix F. Mathematica™ Program Written to Simulate a Droplet Drying in a Spray Dryer</b>	
1.0 List of Variables in the Notebook .....	380
2.0 Series of Equations to Create a “Droplet” with “Particles” .....	382
3.0 Series of Equations to Simulate “Drying” of the “Droplet” .....	384
4.0 Equations to Plot the “Droplet” While “Drying” .....	386
<b>Appendix G. Parameters Associated with the Control of the BE985 Spray Dryer at Alfred University</b>	
1.0 Operational Parameters for the Spray Drier .....	387
<b>Appendix H. Structure of the Organics Used in This Study</b>	
1.0 Organic Structures .....	391
2.0 References .....	394

<b>Appendix I. Images from the Interferometer of the Surface Finish from the Samples Prepared with Alternative Binder Systems</b>	
1.0 Surface Evaluation .....	395
<b>Appendix J. Images from the Interferometer of the Surface Finish from the Samples Prepared Using Blends of Granulate Spray Dried at Alfred University</b>	
1.0 Surface Evaluation .....	419
<b>Appendix K. Regression Method to Determine the Shear P1 Value of the Granulated Porcelain Body</b>	
1.0 Introduction .....	429
2.0 Compaction and Shear Compaction Diagrams .....	429
3.0 Regression Method to Determine the Shear P1 .....	430
4.0 Sample Calculation to Determine the Shear P1 .....	430
<b>Appendix L. Images from the Interferometer of the Surface Finish from the Samples Prepared with Increasing Moisture Content</b>	
1.0 Surface Evaluation .....	431

## **List of Tables**

### **Chapter 2. Adsorption of Sodium Poly[acrylic acid] on Alumina and Clay Surfaces and Clay Surfaces**

2-I.	List of the Polymers Used in the Adsorption Study .....	13
2-II.	Equilibrium pH of a 1 v/o Suspension of the Source Clay Minerals Used in this Study .....	24

### **Chapter 3. Washing and Beneficiation of Raw Clays to Remove Organic and Inorganic Impurities**

3-I.	Typical cec Values for Clay Species and Humic and Fulvic Acids .....	42
3-II.	Inorganic Minerals Identified in Each of the Clay Fractions by X-ray Diffraction on Oriented Slides .....	54
3-III.	Plateau Adsorption Values for the Clays Used in this Study .....	61
3-IV.	Band Assignments for the FTIR Characterization of the Clay Minerals	78

### **Chapter 4. Effects of Incremental Additions of Na-PAA to Clay**

4-I.	Cumulative Concentration of Darvan™ 811 Added as an Incremental Dose to TK6 at pH 6.0±0.2 and pH 9.0±0.2 .....	94
4-II.	Cumulative Concentration of Darvan™ 811 Added as an Incremental Dose to Huntingdon at pH 6.0±0.2 and pH 9.0±0.2 .....	95
4-III.	Chemical Analysis from the Buffer Solutions Used as Eluents for the GPC .....	96
4-IV.	Calibration Equations for the GPC to Relate the Elution Volume (or Time) to the Molecular Weight of the Organic .....	102
4-V.	Results from the Standard Runs and the Statistics for the Standards Relative to the Calibration Curve .....	103
4-VI.	Reported Molecular Weight and the Measured Molecular Weight of Various Na-PAA's used in Chapter 2 .....	105

### **Chapter 5. Plasticity of clays: Effects of Adding Organic Matter**

5-I.	Chemical Analysis for the Lignite (L) and Digested Lignite (DL) from Unimin and the Na-Lignosulphonate (Na-L) from Buffalo China .....	130
5-II.	ICP-AES Chemical Analysis (Rock Analysis) for the Insoluble and Acid Insoluble Fractions of Lignite and Digested Lignite .....	130
5-III.	ICP-AES Chemical Analysis (Water Analysis) for the Soluble Fractions of Lignite and Digested Lignite .....	131

5-IV.	List of the Materials Used to Prepare Solutions to Measure Surface Tension .....	139
5-V.	Moisture Content and Loss on Ignition from the Thermal Analysis of the Lignite and Digested Lignite Fractions .....	142
5-VI.	Models Created Using the Design Expert Software to Predict the Cohesion and Pressure Dependence of the Three Clays in this Study as a Function of Moisture Content .....	144
5-VII.	Minerals Present in the Clays Used to Measure Plasticity .....	149
5-VIII.	Properties of the Clays Used to Measure Plasticity .....	149
5-IX.	Comparison of the Predicted and Actual Cohesion (Coh.) and Pressure Dependence for the TK6 Samples Used to Characterize Plasticity with Salt Additions .....	157
5-X.	Comparison of the Predicted and Actual Cohesion (Coh.) and Pressure Dependence for the TK6 Samples Used to Characterize Plasticity with Lignosulphonate or Lignite Additions .....	164
5-XI.	Comparison of the Predicted and Actual Cohesion (Coh.) and Pressure Dependence for the TK6 Samples Used to Characterize Plasticity with Digested Lignite Additions .....	165

## **Chapter 6. Characterization of Surface Finish from Industry**

6-I.	List of the Number of Samples Characterized for Surface Roughness	183
6-II.	List of the Filters Used for this Study in the MetroPro™ Software .....	186
6-III.	Filters Used to Analyze the Data in the Initial Study .....	186
6-IV.	RMS Roughness Results from the Initial Study .....	188

## **Chapter 7. Compaction of Granulate**

7-I.	Experimental Design Used to Study the Effects of Blended Granulate	206
7-II.	Suspension and Granulate Properties from the Batches Used to Prepare Granulate in This Study .....	215
7-III.	Storage Conditions Used to Regulate the Relative Humidity .....	229
7-IV.	Parameters Used to Model a Drying Droplet in a Spray Dryer .....	235
7-V.	Moisture Content of the Granulate at the Time That It was Prepared by Buffalo China and at the Time of Analysis in This Study .....	238
7-VI.	Binder Systems Investigated as Possible Replacements for pPVA Binder Systems in Dry Pressing .....	246

7-VII.	List of the Granule Blends Selected to Evaluate the Effects of Blending Granulate .....	248
7-VIII.	Mean Particle Size and Standard Distribution from the Granulate Binder Systems in This Study .....	256
 <b>Chapter 8. Compaction versus Shear Compaction</b>		
8-I.	Peak Cohesion Values Determined on the HPASC for Each Binder System in This Study .....	335
 <b>Appendix B. Calculation of the Free Quartz in a Commercial Clay</b>		
B-I.	Chemical Analysis of TK6 Reported by Acme Analytical Laboratories .	362
 <b>Appendix C. Chemical Analysis of Organics Used to Affect Plasticity in Clays</b>		
C-I.	Chemical Analysis for the Samples That were Tested by ICP-AES Rock Analysis .....	365
C-II	Chemical Analysis for the Samples That were Tested by ICP-AES Water Analysis .....	366-7
 <b>Appendix D. Calculation to Determine the Surface Tension of Organic Solutions</b>		
D-I.	List of the Methods Available to Determine the Surface Tension of Liquids .....	368
 <b>Appendix E. Determine the Performance of Blended Granulate in Production at Buffalo China</b>		
E-I.	List of the Samples Provided by Buffalo China for Evaluation of the Surface Finish .....	374
 <b>Appendix G. Parameters Associated with the Control of the BE985 Spray Dryer at Alfred University</b>		
G-I.	Parameters from the Spray Dryer While Preparing the pPVA Granulate for this Study .....	387
G-II.	Parameters from the Spray Dryer While Preparing the Na-Lignosulphonate Granulate for this Study .....	387

G-III.	Parameters from the Spray Dryer While Preparing the pPVA / Veegum™ T Granulate for this Study .....	388
G-IV.	Parameters from the Spray Dryer While Preparing the Veegum™ T Granulate for this Study .....	388
G-V.	Parameters from the Spray Dryer While Preparing the Agar Granulate for this Study .....	388
G-VI.	Parameters from the Spray Dryer While Preparing the Acrylic Latex Granulate for this Study .....	389
G-VII.	Parameters from the Spray Dryer While Preparing the Starch Granulate for this Study .....	389
G-VIII.	Parameters from the Spray Dryer While Preparing the Sugar Granulate for this Study .....	389
G-IX.	Parameters from the Spray Dryer While Preparing the Methyl Cellulose Granulate for this Study .....	390
G-X.	Parameters from the Spray Dryer While Preparing the Carboxymethyl Cellulose Granulate for this Study .....	390
G-XI.	Parameters from the Spray Dryer While Preparing the Veegum™ T / Vanzan™ D Granulate for this Study .....	390

**Appendix J. Images from the Interferometer of the Surface Finish from the Samples Prepared Using Blends of Granulate Prepared at Alfred University**

J-I.	List of the Granule Blends Selected to Evaluate the Effects of Blending Samples with Similar P1 Values .....	419
------	--	-----

**Appendix L. Images from the Interferometer of the Surface Finish from the Samples Prepared with Increasing Moisture Content**

L-I.	List of the Images from the Interferometer and the Measured Roughness and Moisture Content from the Tile Samples .....	431
------	--	-----

## List of Figures

### Chapter 2. Adsorption of Sodium Poly[acrylic acid] on Alumina and Clay surfaces

2-1.	Schematic drawing of a protonated poly[methacrylic acid] where n represents the degree of polymerization.....	10
2-2.	Schematic drawing of a protonated poly[acrylic acid] where n represents the degree of polymerization.....	10
2-3.	Sketch of the kaolinite platelet that was used as a basis for the model for adsorption of Na-PAA on the clay surface.....	12
2-4.	Plot of the effect of the 2L:h ratio on the predicted adsorption levels for kaolinite.....	13
2-5.	Representative titration curve to determine the concentration of the PAA present in the supernatant, shown are the raw data and the first derivative.....	15
2-6.	Initial results from the study investigating the effect of polymer molecular weight on adsorption of Na-PAA on the surface of alumina (APA-0.5) and Huntingdon ball clay at pH 6.....	16
2-7.	Initial results from the study investigating the effect of polymer molecular weight on adsorption of Na-PAA on the surface of alumina (APA-0.5) and Huntingdon ball clay at pH 9.....	17
2-8.	SEM images of Huntingdon ball clay.....	19
2-9.	Viscosity results for the Huntingdon clay as a function of the concentration of Na-PAA in the suspension.....	20
2-10.	Adsorption isotherm for KGa-2, a source clay consisting primarily of kaolinite, at pH 6.....	21
2-11.	Adsorption isotherm for KGa-2, a source clay consisting primarily of kaolinite, at pH 9.....	21
2-12.	Adsorption isotherms for STx-1 a source clay consisting primarily of a calcium montmorillonite, at pH 6.....	22
2-13.	Adsorption isotherm for STx-1, a source clay consisting primarily of calcium montmorillonite, at pH 9.....	22
2-14.	Adsorption isotherm for SWy-2, a source clay consisting primarily of a sodium montmorillonite, at pH 6 on 2.5 v/o suspension.....	23
2-15.	Adsorption isotherm for SWy-2, a source clay consisting primarily of a sodium montmorillonite, at pH 9 on 2.5 v/o suspension.....	23
2-16.	Adsorption isotherm for Tamsil 8 (silica) at pH 6. Negative adsorption values are observed for all additions of PAA.....	26

2-17.	Adsorption isotherm for Tamsil 8 (silica) at pH 9. Negative adsorption values are observed for all additions of PAA.....	26
2-18.	Effect of solids loading on the adsorption of Darvan™ 811 on alumina (APA-0.5) powder.....	27
2-19.	Digital image of the diluted supernatant from the alumina samples at pH 6.0±0.2.....	28
2-20.	Digital image of the diluted supernatant from the Tamsil 8 samples prepared at pH 6.0±0.2.....	28
2-21.	Digital image of the diluted supernatant from the KGa-2 samples prepared at pH 6.0±0.2.....	29
2-22.	Digital image of the diluted supernatant from the KGa-2 samples prepared at pH 9.0±0.2.....	29
2-23.	Digital image of the diluted supernatant from the STx-1 samples prepared at pH 6.0±0.2.....	30
2-24.	Digital image of the diluted supernatant from the STx-1 samples prepared at pH 9.0±0.2.....	30
2-25.	Digital image of the diluted supernatant from the SWy-2 samples prepared at pH 6.0±0.2.....	31
2-26.	Digital image of the diluted supernatant from the SWy-2 samples prepared at pH 9.0±0.2.....	31

### **Chapter 3. Washing and Beneficiation of Raw Clays to Remove Organic and Inorganic Impurities**

3-1.	Schematic showing the relative properties of humic substances and the coloration of solutions prepared from humic substances.....	37
3-2.	Hypothetical structure of humic acid showing the relative concentration and position of the functional groups on the organic molecule.....	38
3-3.	Proposed average structure of Suwannee River fulvic acid.....	39
3-4.	Schematic showing the mechanisms for the formation of humic substances from plant residue.....	40
3-5.	Schematic of the process used to wash and beneficiate the raw clay for this study.....	47
3-6.	Titration curves from a sample of distilled water and a sample of the supernatant from Huntingdon ball clay.....	53
3-7.	X-ray diffraction patterns from oriented slides of TK6 kaolin clay and the clay fractions prepared by washing and beneficiation.....	55

3-8.	X-ray diffraction patterns from oriented slides of Kingsley kaolin clay and the clay fractions prepared by washing and beneficiation.....	55
3-9.	X-ray diffraction patterns from oriented slides of Huntingdon ball clay and the clay fractions prepared by washing and beneficiation.....	56
3-10.	X-ray diffraction patterns from oriented slides of Marquis ball clay and the clay fractions prepared by washing and beneficiation.....	56
3-11.	X-ray diffraction patterns from oriented slides of M&D ball clay and the clay fractions prepared by washing and beneficiation.....	57
3-12.	Loss on ignition (LOI) of the raw clays and clay fractions in this study....	58
3-13.	Specific surface area (SSA) of the raw clay and clay fractions in this study.....	59
3-14.	Amount of free quartz calculated from each raw clay and clay fraction in this study.....	60
3-15.	Adsorption isotherms for TK6 at pH 6.....	62
3-16.	Adsorption isotherms for TK6 at pH 9.....	62
3-17.	Adsorption isotherms for Kingsley kaolin at pH 6.....	63
3-18.	Adsorption isotherms for Kingsley kaolin at pH 9.....	64
3-19.	Adsorption isotherms for Huntingdon ball clay at pH 6.....	65
3-20.	Adsorption isotherms for Huntingdon ball clay at pH 9.....	66
3-21.	Adsorption isotherms for Marquis ball clay at pH 6.....	66
3-22.	Adsorption isotherms for Marquis ball clay at pH 9.....	67
3-23.	Adsorption isotherms for M&D ball clay at pH 6.....	68
3-24.	Adsorption isotherms for M&D ball clay at pH 9.....	69
3-25.	Adsorption isotherms for C&C ball clay at pH 6.....	70
3-26.	Adsorption isotherms for C&C ball clay at pH 9.....	71
3-27.	Relative adsorption of the kaolin clay fractions tested in this study.....	72
3-28.	Relative adsorption of the ball clays tested in this study.....	72
3-29.	Room temperature FTIR spectra from humic acid, dried Darvan™811, and raw Huntingdon.....	73
3-30.	FTIR spectra from raw TK6.....	74
3-31.	FTIR spectra from raw Kingsley.....	75

3-32.	FTIR spectra from the raw Huntingdon.....	75
3-33.	FTIR spectra from coarse Huntingdon.....	76
3-34.	FTIR spectra from the Huntingdon middle fraction.....	76
3-35.	FTIR spectra from raw Marquis.....	77
3-36.	FTIR spectra from raw M&D ball clay.....	77
3-37.	FTIR spectra from humic acid.....	79
3-38.	FTIR spectra from dried Darvan™811.....	80
3-39.	Change in the peak area of the 1850 cm <sup>-1</sup> band and the band between 3755 and 3600 cm <sup>-1</sup> for representative spectra.....	81

#### **Chapter 4. Effects of Incremental Additions of Na-PAA to Clay**

4-1.	Cumulative adsorption results for TK6 at pH 6 and pH 9 after incremental additions of PAA.....	99
4-2.	Cumulative adsorption results for Huntingdon at pH 6 and pH 9 after incremental additions of PAA.....	99
4-3.	Images of the diluted supernatant before titration from the TK6 samples prepared at pH 6.0±0.2.....	100
4-4.	Images of the diluted supernatant before titration from the TK6 samples prepared at pH 9.0±0.2.....	100
4-5.	Images of the diluted supernatant before titration from the Huntingdon samples prepared at pH 6.0±0.2.....	101
4-6.	Images of the diluted supernatant before titration from the Huntingdon samples prepared at pH 9.0±0.2.....	101
4-7.	Calibration curves for the GPC from the standard PAA samples at pH 5 and pH 10.....	104
4-8.	Relative molecular weight results from the GPC for the precipitated material from the titration runs after incremental doses of PAA to Huntingdon ball clay at pH 6.....	105

#### **Chapter 5. Plasticity of Clays: Effects of Adding Organic Matter**

5-1.	Schematic of the double layer of ions surrounding a ceramic particle in an aqueous suspension.....	118
5-2.	Schematics showing how the interactions between structure-making and structure-breaking ions and the particle surface can effect the potential energy at an alumina particle surface, a structure-making surface.....	128

5-3.	Images of the HPASC which was used to characterize plasticity in this study.....	133
5-4.	Representative construction of Mohr's semi circles from TK6 with 14.17% and 22.35% moisture.....	135
5-5.	Schematic showing the construction that was used to measure the sessile drops to determine the surface tension.....	138
5-6.	Digital image of a sessile drop of distilled water on the Teflon™ pedestal.....	140
5-7.	TGA results from the thermal analysis for the lignite fractions.....	143
5-8.	TGA results from the thermal analysis for the digested lignite fractions...	143
5-9.	Viscosity of the TK6 samples prepared with the fractions of lignite.....	144
5-10.	Viscosity of the TK6 samples prepared with the fractions of digested lignite.....	145
5-11.	Results from the HPASC for TK6 and Huntingdon clays.....	145
5-12.	Results from the HPASC for C&C ball clay.....	146
5-13.	Shear rheology map for the three clays used to characterize plasticity...	147
5-14.	Two dimensional schematic of a dilatant system.....	150
5-15.	Hysteresis in the measured stress and the applied load on the HPASC due to a slight misalignment between the load cell and the point load on the test cell.....	151
5-16.	Overall view of the effects of adding salt (NaCl or CaCl <sub>2</sub> •2H <sub>2</sub> O) to samples of TK6 prepared with a target moisture content of 22%.....	152
5-17.	Close up view of the shear rheology map for the samples prepared with NaCl at a target moisture content of 22%.....	153
5-18.	Shear rheology map for the samples prepared with CaCl <sub>2</sub> •2H <sub>2</sub> O at a target moisture content of 22%.....	154
5-19.	Close up view of the shear rheology map for the TK6 samples with added Na-Lignosulphonate at a target moisture content of 22%.....	156
5-20.	Overall view of the shear rheology map for additions of lignite fractions to TK6 with a target moisture content of 22%.....	158
5-21.	Close up view of the shear rheology map for the samples prepared with the insoluble fraction of lignite (LIN) at a target moisture content of 22%.....	159
5-22.	Close up view of the shear rheology map for the samples prepared with the acid insoluble fraction of lignite (LAI) at a target moisture content of 22%.....	159

5-23.	Close up view of the shear rheology map for the samples prepared with the soluble fraction of lignite (LS) at a target moisture content of 22%....	160
5-24.	Overall view of the shear rheology map for the samples prepared with digested lignite fractions at a target moisture content of 22%.....	160
5-25.	Close up view of the shear rheology map for the samples prepared with the insoluble fraction of digested lignite (DLIN) at a target moisture content of 22%.....	161
5-26.	Close up view of the shear rheology map for the samples prepared with the acid insoluble fraction of digested lignite (DLAI) at a target moisture content of 22%.....	161
5-27.	Close up view of the shear rheology map for the samples prepared with the soluble fraction of digested lignite (DLS) at a target moisture content of 22%.....	162
5-28.	Change in the surface tension of solutions prepared with sodium lignosulphonate or Aldrich humic acid.....	167
5-29.	Change in the surface tension of solutions prepared with sodium poly[acrylic acid] or an acrylic latex emulsion.....	168
5-30.	Change in the surface tension of solutions prepared with plasticized PVA or PEG 8000.....	168
5-31.	Change in the surface tension of solutions prepared with calcium chloride or sodium chloride.....	169
5-32.	Change in the surface tension of suspensions prepared with C&C ball clay or TK6 kaolin clay.....	169

## **Chapter 6. Characterization of Surface Finish from Industry**

6-1.	Image of the dry pressed surface from the optical microscope.....	179
6-2.	Image of the glazed surface showing the presence of circular dimples...	181
6-3.	Oblique plot from the optical interferometer showing the thickness of the ink superimposed on the texture of the glazed sample.....	182
6-4.	Schematic of the Michelson interferometer upon which the 5x objective used in this study is based.....	185
6-5.	Peak to valley roughness measured using the optical interferometer for each of the forming methods and surface treatments in this study.....	188
6-6.	RMS roughness measured using the optical interferometer for each of the forming methods and surface treatments in this study.....	189

6-7.	Average roughness measured using the optical interferometer for each of the forming methods and surface treatments in this study.....	189
6-8.	Comparison of the images from the interferometer, SEM, and optical microscope from the green dry pressed surface.....	191
6-9.	Comparison of the images from the interferometer, SEM, and optical microscope from the green jiggered surface.....	192
6-10.	Comparison of the images from the interferometer, SEM, and optical microscope from the green ram pressed surface.....	193
6-11.	Comparison of the images from the interferometer, SEM, and optical microscope from the green pressure cast surface.....	194
6-12.	Comparison of the images from the optical interferometer, SEM, and the optical microscope from the dry pressed and glazed surface.....	195
6-13.	Effect of the area analyzed on the RMS roughness measured using the interferometer for the glazed samples from each forming process and the green dry pressed surface tested in this study.....	197

## **Chapter 7. Compaction of Granulate**

7-1.	Digital image of the surface from a dinnerware sample prepared using a 50-50 blend of pPVA and Ligno granulate.....	207
7-2.	Typical compaction diagram prepared using silicon carbide granulate for demonstration purposes.....	208
7-3.	Pressure at the onset of granule deformation (P1) for the blends prepared using pPVA and Ligno granulate.....	211
7-4.	Pressure at the onset of granule deformation (P1) for blends prepared using pPVA and PEG granulate.....	211
7-5.	Pressure at the onset of granulate deformation (P1) for blends prepared using pPVA and NB granulate.....	212
7-6.	Schematic of compaction in systems with blended granulate.....	214
7-7.	“Compaction diagrams” generated using thin o-rings and steel washers to represent soft and hard granulate.....	215
7-8.	Comparison plot of the P1 values obtained from the blending study.....	216
7-9.	Comparison plot of the compact density obtained from the blending study.....	217
7-10.	Comparison plot of the green strength from the blending study.....	218
7-11.	Contour plot of the RMS roughness as a function of position on the pPVA sample prepared by Buffalo China in the vertical press.....	219

7-12.	Contour plot of the RMS roughness as a function of position on the pPVA sample prepared at Alfred University in the horizontal press.....	220
7-13.	Schematic of the dies installed in the industrial presses used for this study, (A) horizontal press and (B) vertical press.....	221
7-14.	Plot of the roughness results for the pPVA – Ligno blends.....	222
7-15.	Plot of the roughness results for the pPVA – PEG blends.....	222
7-16.	Plot of the roughness results for the pPVA – NB blends.....	223
7-17.	Comparison plot of the lowest RMS roughness reading for each sample as a function of the amount of pPVA granulate in the blend.....	223
7-18.	Correlation plot for the measured P1 value from the blended granulate and the measured RMS roughness from the optical interferometer.....	224
7-19.	Images from the optical microscope of the surface from a 100% PEG sample pressed on the horizontal press at Alfred University.....	225
7-20.	RMS roughness as a function of forming pressure for the samples prepared on the Aeonic press using a hardened steel die.....	227
7-21.	Plot of the pore radius filled as a function of relative humidity of the surrounding environment and the moisture content of the granule samples after three weeks in a humidity controlled environment.....	230
7-22.	Prediction for the moisture content of a compact of assumed spherical particles in a face-centered cubic packing arrangement as a function of particle radius and relative humidity.....	231
7-23.	Plot of the pressure at the onset of granule deformation (P1) as a function of relative humidity for the hydrate granulate.....	231
7-24.	Plot of the pressed density as a function of relative humidity for the hydrated granulate.....	232
7-25.	Plot of the green strength, measured by diametric compression, as a function of relative humidity for the hydrated granulate.....	232
7-26.	Granule size distribution and moisture content distribution for the Ligno granulate.....	236
7-27.	Granule size distribution and moisture content distribution for the pPVA granulate.....	236
7-28.	Granule size distribution and moisture content distribution for the PEG granulate.....	237
7-29.	Granule size distribution and moisture content distribution for the no organic binder (NB) granulate.....	237

7-30.	Comparison plot of the pressure at the onset of granule deformation (P1) for each binder system as a function of the granule diameter.....	240
7-31.	Comparison plot of the pressed density of the pellets prepared for each binder system in this study as a function of granule diameter.....	240
7-32.	Comparison plot of the green strength, measured by diametric compression, for each binder system in this study as a function of granule diameter.....	241
7-33.	Drying time of a virtual droplet as a function of initial droplet radius and solids loading (reported as an area fraction, af).....	241
7-34.	Results from the mathematical model to investigate the spray drying process. The virtual droplet has an initial radius of 200 micrometers and a solid loading of 25 volume percent.....	242
7-35.	Comparison of the granule size distribution obtained from the sieve analysis and the Horiba particle size analyzer for each of the granulate systems supplied by Buffalo China.....	255
7-36.	Plot of the pressure at the onset of granule deformation (P1) as a function of binder concentration for the as-prepared and dried samples with pPVA as a binder.....	258
7-37.	Plot of the compact density as a function of binder concentration for the as-prepared and dried samples with pPVA as a binder.....	258
7-38.	Plot of green strength as a function of binder concentration for the as-prepared and dried samples with pPVA as a binder.....	259
7-39.	Plot of the RMS roughness as a function of binder concentration for samples prepared with pPVA as the binder.....	259
7-40.	Plot of the pressure at the onset of granule deformation (P1) as a function of binder concentration for the as-prepared and dried samples with Na-lignosulphonate as a binder.....	261
7-41.	Plot of the compact density as a function of binder concentration for the as-prepared and dried samples with Na-lignosulphonate as a binder.....	261
7-42.	Plot of green strength as a function of binder concentration for the as-prepared and dried samples with Na-lignosulphonate as a binder.....	262
7-43.	Plot of the RMS roughness as a function of binder concentration for samples prepared with Na-lignosulphonate as the binder.....	262
7-44.	Plot of the pressure at the onset of granule deformation (P1) as a function of binder concentration for the as-prepared and dried samples with a 50-50 mix of pPVA and Veegum™ T as a binder.....	264

7-45.	Plot of the compact density as a function of binder concentration for the as-prepared and dried samples with a 50-50 mix of pPVA and Veegum™ T as a binder.....	264
7-46.	Plot of green strength as a function of binder concentration for the as-prepared and dried samples with a 50-50 mix of pPVA and Veegum™ T as a binder.....	265
7-47.	Plot of the RMS roughness as a function of binder concentration for samples prepared with a 50-50 mix of pPVA and Veegum™ T as the binder.....	265
7-48.	Plot of the pressure at the onset of granule deformation (P1) as a function of binder concentration for the as-prepared and dried samples with Veegum™ T as a binder.....	267
7-49.	Plot of the compact density as a function of binder concentration for the as-prepared and dried samples with Veegum™ T as a binder.....	267
7-50.	Plot of green strength as a function of binder concentration for the as-prepared and dried samples with Veegum™ T as a binder.....	268
7-51.	Plot of the RMS roughness as a function of binder concentration for samples prepared with Veegum™ T as the binder.....	268
7-52.	Plot of the pressure at the onset of granule deformation (P1) as a function of binder concentration for the as-prepared and dried samples with agar as a binder.....	270
7-53.	Plot of the compact density as a function of binder concentration for the as-prepared and dried samples with agar as a binder.....	270
7-54.	Plot of green strength as a function of binder concentration for the as-prepared and dried samples with agar as a binder.....	271
7-55.	Plot of the RMS roughness as a function of binder concentration for samples prepared with agar as the binder.....	271
7-56.	Plot of the pressure at the onset of granule deformation (P1) as a function of binder concentration for the as-prepared and dried samples with acrylic latex as a binder.....	273
7-57.	Plot of the compact density as a function of binder concentration for the as-prepared and dried samples with acrylic latex as a binder.....	273
7-58.	Plot of green strength as a function of binder concentration for the as-prepared and dried samples with acrylic latex as a binder.....	274
7-59.	Plot of the RMS roughness as a function of binder concentration for samples prepared with acrylic latex as the binder.....	274

7-60.	Plot of the pressure at the onset of granule deformation (P1) as a function of binder concentration for the as-prepared and dried samples with starch as a binder.....	276
7-61.	Plot of the compact density as a function of binder concentration for the as-prepared and dried samples with starch as a binder.....	276
7-62.	Plot of green strength as a function of binder concentration for the as-prepared and dried samples with starch as a binder.....	277
7-63.	Plot of the RMS roughness as a function of binder concentration for samples prepared with starch as the binder.....	277
7-64.	Plot of the pressure at the onset of granule deformation (P1) as a function of binder concentration for the as-prepared and dried samples with sugar as a binder.....	279
7-65.	Plot of the compact density as a function of binder concentration for the as-prepared and dried samples with sugar as a binder.....	279
7-66.	Plot of green strength as a function of binder concentration for the as-prepared and dried samples with sugar as a binder.....	280
7-67.	Plot of the RMS roughness as a function of binder concentration for samples prepared with sugar as the binder.....	280
7-68.	Plot of the pressure at the onset of granule deformation (P1) as a function of binder concentration for the as-prepared and dried samples with methyl cellulose as a binder.....	281
7-69.	Plot of the compact density as a function of binder concentration for the as-prepared and dried samples with methyl cellulose as a binder.....	281
7-70.	Plot of green strength as a function of binder concentration for the as-prepared and dried samples with methyl cellulose as a binder.....	282
7-71.	Plot of the RMS roughness as a function of binder concentration for samples prepared with methyl cellulose as the binder.....	282
7-72.	Plot of the pressure at the onset of granule deformation (P1) as a function of binder concentration for the as-prepared and dried samples with carboxymethyl cellulose as a binder.....	285
7-73.	Plot of the compact density as a function of binder concentration for the as-prepared and dried samples with carboxymethyl cellulose as a binder.....	285
7-74.	Plot of green strength as a function of binder concentration for the as-prepared and dried samples with carboxymethyl cellulose as a binder...	286
7-75.	Plot of the RMS roughness as a function of binder concentration for samples prepared with carboxymethyl cellulose as the binder.....	286

7-76.	Image of the dinnerware surface pressed using the 5 wt% agar granulate in the Dorst semi-isostatic die.....	287
7-77.	Plot of the compact density as a function of binder concentration for the as-prepared and dried samples with Veegum™ T and Vanzan™ D as a binder.....	287
7-78.	Plot of green strength as a function of binder concentration for the as-prepared and dried samples with Veegum™ T and Vanzan™ D as a binder.....	288
7-79.	Plot of the RMS roughness as a function of binder concentration for samples prepared with Veegum™ T and Vanzan™ D as the binder.....	288
7-80.	Comparison plot of the pressure at the onset of granule deformation (P1) as a function of binder concentration for the as-prepared samples where pPVA was replaced with Veegum™ T in the binder system.....	290
7-81.	Comparison plot of the compact density as a function of binder concentration for the as-prepared samples where pPVA was replaced with Veegum™ T in the binder system.....	290
7-82.	Comparison plot of green strength as a function of binder concentration for the as-prepared samples where pPVA was replaced with Veegum™ T in the binder system.....	291
7-83.	Comparison plot of the RMS roughness as a function of binder concentration for the as-prepared samples where pPVA was replaced with Veegum™ T in the binder system.....	291
7-84.	Comparison plot of the pressure at the onset of granule deformation (P1) as a function of binder concentration for the as-prepared samples with Veegum™ T or Veegum™ T / Vanzan™ D in the binder system....	293
7-85.	Comparison plot of the compact density as a function of binder concentration for the as-prepared samples with Veegum™ T or Veegum™ T / Vanzan™ D in the binder system.....	293
7-86.	Comparison plot of green strength as a function of binder concentration for the as-prepared samples with Veegum™ T or Veegum™ T / Vanzan™ D in the binder system.....	294
7-87.	Comparison plot of RMS roughness as a function of binder concentration for the as-prepared samples with Veegum™ T or Veegum™ T / Vanzan™ D in the binder system.....	294
7-88.	Summary plot of the fill density from the dried samples of granulate.....	295
7-89.	Summary plot of the pressure at the onset of granule deformation (P1) for the dried samples.....	296
7-90.	Plot of the compact density for the dried samples.....	297
7-91.	Plot of the green strength of the dried samples.....	298

7-92.	Plot of the RMS roughness of the dinnerware samples prepared with a semi-isostatic die on the Dorst press.....	299
7-93.	Plot of the RMS roughness of the tiles prepared with a hardened steel die on the Aeonic press.....	300
7-94.	Image of the dinnerware surface pressed using the 5 wt% agar granulate in the Dorst semi-isostatic die.....	303
7-95.	Images from the optical interferometer of the surface finish of samples prepared with agar as-prepared binder system.....	304-5
7-96.	Images from the optical interferometer of the surface finish of samples prepared with plasticized PVA as a binder system.....	306-7
7-97.	Results from blending granule systems with similar P1 values.....	310
7-98.	Correlation plot of the P1 value from the blended granulate systems versus the normalized P1 value.....	311
7-99.	Correlation plot of the P1 value from the blended granule systems versus moisture content in the granulate.....	311
7-100.	Plot of the RMS roughness as a function of the normalizing factor $P1_{norm}$ .....	312
7-101.	Correlation plot of the RMS roughness as a function of the moisture content in the blended granulate.....	313
7-102.	Plot of the green strength of the dried compacts prepared using blended-granule systems.....	314

## **Chapter 8. Compaction versus Shear Compaction**

8-1.	Digital image of the steam chamber constructed at Alfred University.....	327
8-2.	Comparison of uniaxial compaction curves (black) to shear compaction curves for a sample of dried pPVA granulate.....	329
8-3.	Comparison of the P1 measured in uniaxial (solid symbols) and shear (open symbols) compaction as a function of moisture content.....	330
8-4.	Compact density of the samples prepared by uniaxial compaction.....	331
8-5.	Plot of the green strength of the compacts by uniaxial compaction.....	332
8-6.	Plot of the RMS roughness as a function of moisture content for the Ligno and pPVA granulate.....	332
8-7.	Correlation plot for the RMS roughness and uniaxial P1 value for the Ligno and pPVA granulate samples.....	333
8-8.	Plot of the measured cohesion as a function of moisture content for the binder systems in this study.....	334

8-9.	Plot of the pressure dependence measure using the HPASC for each of the binder systems in this study.....	335
8-10.	Cohesion and moisture content as a function of pressure dependence for the granulate with the lignosulphonate binder system.....	336
8-11.	Cohesion and moisture content as a function of pressure dependence for the granulate with the pPVA binder system.....	337
8-12.	Cohesion and moisture content as a function of pressure dependence for the granulate with the PEG binder system.....	338
8-13.	Cohesion and moisture content as a function of pressure dependence for the granulate with the NB binder system.....	339

### **Chapter 9. Plasticizers for PVA**

9-1.	Results from the DMA for the PVA binder system.....	345
9-2.	Digital images of the organic solutions used to determine $T_g$ .....	346
9-3.	Plot from Chapter 7.4 showing the effect of pPVA concentration on the measured P1 value in uniaxial compaction.....	347

### **Appendix A. Calibration Curves to Determine the Concentration of Polymer in Solution by Potentiometric Titration**

A-1.	Titration curves for Acumer™ 1510 that were used to generate a calibration curve.....	359
A-2.	Calibration curve for Acumer™ 1510.....	359
A-3.	Titration curve from the alumina sample prepared with approximately 0.90 mg/m <sup>2</sup> of PAA used for the sample calculation.....	360

### **Appendix D. Calculation to Determine the Surface Tension of Organic Solutions**

D-1.	Image of the sessile drop used to calculate the surface tension of the 3 wt% PEG 8000 solution.....	370
------	---	-----

### **Appendix E. Determine the Performance of Blended Granulate in Production at Buffalo China**

E-1.	RMS roughness results of the samples provided by Buffalo China for evaluation throughout this project.....	373
E-2.	Plot of the measured RMS surface roughness from the various blends studied in the first industrial trial.....	375
E-3.	Summarized results from the two industrial trials at Buffalo China.....	377

## **Appendix H. Structure of the Organics Used in this Study**

H-1.	Schematic of a fully hydrolyzed poly[vinyl alcohol] (left) where “n” represents the degree of polymerization.....	391
H-2.	Schematic of a simplified lignosulphonate molecule.....	391
H-3.	Schematic of the structure of a dried acrylic latex.....	392
H-4.	Schematic of the structure of a mer of starch.....	392
H-5.	Schematic of the structure of sugar (glucose) the building block for polysaccharides.....	392
H-6.	Schematic of the structure of a mer of methyl cellulose.....	393
H-7.	Schematic of the structure of a mer of sodium carboxymethyl cellulose..	393
H-8.	Schematic of the structure of poly[ethylene glycol].....	393

## **Appendix I. Images from the Interferometer of the Surface Finish from the Samples Prepared with Alternative Binder Systems**

I-1.	Images of the surface finish of the samples prepared using the granulate spray dried using pPVA as a binder system.....	396-7
I-2.	Images of the surface finish of the samples prepared using the granulate spray dried using Na-lignosulphonate as a binder system.....	398-9
I-3.	Images of the surface finish of the samples prepared using the granulate spray dried using pPVA / Veegum™ T (50-50 wt% mixture) as a binder system.....	400-1
I-4.	Images of the surface finish of the samples prepared using the granulate spray dried using Veegum™ T as a binder system.....	402-3
I-5.	Images of the surface finish of the samples prepared using the granulate spray dried using agar as a binder system.....	404-5
I-6.	Images of the surface finish of the samples prepared using the granulate spray dried using an acrylic latex emulsion as a binder system.....	406-7
I-7.	Images of the surface finish of the samples prepared using the granulate spray dried using starch as a binder system.....	408-9
I-8.	Images of the surface finish of the samples prepared using the granulate spray dried using sugar as a binder system.....	410-1
I-9.	Images of the surface finish of the samples prepared using the granulate spray dried using methyl cellulose as a binder system.....	412-3
I-10.	Images of the surface finish of the samples prepared using the granulate spray dried using carboxymethyl cellulose as a binder system	414-5

I-11.	Images of the surface finish of the samples prepared using the granulate spray dried using Veegum™ T / Vanzan™ D (80-20 wt% mixture) as a binder system.....	416-7
I-12.	Images of the surface finish of the samples prepared using the granulate spray dried using pPVA as a binder system at Buffalo China..	418

**Appendix J. Images from the Interferometer of the Surface Finish from the Samples Prepared Using Blends of Granulate Prepared at Alfred University**

J-1.	Image from the optical interferometer of the surface finish of the sample dry pressed in a hardened steel die with an elastomer insert prepared using a 50-50 blend 2 wt% starch and 1 wt% pPVA- Veegum™ T of granulate.....	420
J-2.	Image from the optical interferometer of the surface finish of the sample dry pressed in a hardened steel die with an elastomer insert prepared using a 50-50 blend of 1 wt% Ligno and 0.50 wt% Veegum™ T - Vanzan™ D granulate.....	420
J-3.	Image from the optical interferometer of the surface finish of the sample dry pressed in a hardened steel die with an elastomer insert prepared using a 50-50 blend of 5 wt% acrylic latex and 5 wt % agar granulate....	420
J-4.	Image from the optical interferometer of the surface finish of the sample dry pressed in a hardened steel die with an elastomer insert prepared using a 50-50 blend of 1 wt% sugar and 5 wt% agar granulate.....	421
J-5.	Image from the optical interferometer of the surface finish of the sample dry pressed in a hardened steel die with an elastomer insert prepared using a 50-50 blend of 0.50 wt% agar and 5 wt% acrylic latex granulate	421
J-6.	Image from the optical interferometer of the surface finish of the sample dry pressed in a hardened steel die with an elastomer insert prepared using a 50-50 blend of 2 wt% Veegum™ T and 2 wt% agar granulate...	421
J-7.	Image from the optical interferometer of the surface finish of the sample dry pressed in a hardened steel die with an elastomer insert prepared using a 50-50 blend of 5 wt% agar and 5 wt% starch granulate.....	422
J-8.	Image from the optical interferometer of the surface finish of the sample dry pressed in a hardened steel die with an elastomer insert prepared using a 50-50 blend of 2 wt% agar and 1 wt% pPVA-Veegum™ T granulate.....	422
J-9.	Image from the optical interferometer of the surface finish of the sample dry pressed in a hardened steel die with an elastomer insert prepared using a 50-50 blend of 2 wt% Veegum™ T-Vanzan™ D and 2 wt% Ligno granulate.....	422

J-10.	Image from the optical interferometer of the surface finish of the sample dry pressed in a hardened steel die with an elastomer insert prepared using a 50-50 blend of 2 wt% Veegum™ T-Vanzan™ D and 0.50 wt% starch granulate.....	423
J-11.	Image from the optical interferometer of the surface finish of the sample dry pressed in a hardened steel die with an elastomer insert prepared using a 50-50 blend of 1 wt% sugar and 1 wt% agar granulate.....	423
J-12.	Image from the optical interferometer of the surface finish of the sample dry pressed in a hardened steel die with an elastomer insert prepared using a 50-50 blend of 5 wt% acrylic latex and 5 wt% sugar granulate...	423
J-13.	Image from the optical interferometer of the surface finish of the sample dry pressed in a hardened steel die with an elastomer insert prepared using a 50-50 blend of 1 wt% starch and 0.50 wt% carboxymethyl cellulose granulate.....	424
J-14.	Image from the optical interferometer of the surface finish of the sample dry pressed in a hardened steel die with an elastomer insert prepared using a 50-50 blend of 1 wt% acrylic latex and 1 wt% Veegum™ T granulate.....	424
J-15.	Image from the optical interferometer of the surface finish of the sample dry pressed in a hardened steel die with an elastomer insert prepared using a 50-50 blend of 0.50 wt% methyl cellulose and 0.50 wt% acrylic latex granulate.....	424
J-16.	Image from the optical interferometer of the surface finish of the sample dry pressed in a hardened steel die with an elastomer insert prepared using a 50-50 blend of 0.50 wt% Veegum™ T-Vanzan™ D and 0.50 wt% Ligno granulate.....	425
J-17.	Image from the optical interferometer of the surface finish of the sample dry pressed in a hardened steel die with an elastomer insert prepared using a 50-50 blend of 0.50 wt% sugar and 2 wt% pPVA granulate.....	425
J-18.	Image from the optical interferometer of the surface finish of the sample dry pressed in a hardened steel die with an elastomer insert prepared using a 50-50 blend of 2 wt% Ligno and 2 wt% sugar granulate.....	425
J-19.	Image from the optical interferometer of the surface finish of the sample dry pressed in a hardened steel die with an elastomer insert prepared using a 50-50 blend of 2 wt% starch and 2 wt% Veegum™ T-Vanzan™ D granulate.....	426
J-20.	Image from the optical interferometer of the surface finish of the sample dry pressed in a hardened steel die with an elastomer insert prepared using a 50-50 blend of 1 wt% pPVA-Veegum™ T and 1 wt% Veegum™ T-Vanzan™ D granulate.....	426

J-21.	Image from the optical interferometer of the surface finish of the sample dry pressed in a hardened steel die with an elastomer insert prepared using a 50-50 blend of 5 wt% pPVA and 5 wt% pPVA-Veegum™ T granulate.....	426
J-22.	Image from the optical interferometer of the surface finish of the sample dry pressed in a hardened steel die with an elastomer insert prepared using a 50-50 blend of 5 wt% Ligno and 0.70 wt% methyl cellulose granulate.....	427
J-23.	Image from the optical interferometer of the surface finish of the sample dry pressed in a hardened steel die with an elastomer insert prepared using a 50-50 blend of 5 wt% agar and 5 wt% Ligno granulate.....	427
J-24.	Image from the optical interferometer of the surface finish of the sample dry pressed in a hardened steel die with an elastomer insert prepared using a 25-75 blend of 5 wt% agar and 5 wt% Veegum™ T granulate...	427
J-25.	Image from the optical interferometer of the surface finish of the sample dry pressed in a hardened steel die with an elastomer insert prepared using a 25-75 blend of 0.50 wt% agar and 5 wt% Veegum™ T granulate.....	428
J-26.	Image from the optical interferometer of the surface finish of the sample dry pressed in a hardened steel die with an elastomer insert prepared using a 25-75 blend of 5 wt% agar and 1 wt% pPVA granulate.....	428
J-27.	Image from the optical interferometer of the surface finish of the samples dry pressed in a hardened steel die with an elastomer insert prepared using pPVA granulate spray dried at Buffalo China.....	428

**Appendix K. Regression Method to Determine the Shear P1 Value of the Granulated Porcelain Body**

K-1.	Compaction diagrams from the Instron (uniaxial compaction) and the HPASC (shear compaction) for a sample of dried pPVA granulate.....	429
------	---	-----

**Appendix L. Images from the Interferometer of the Surface Finish from the Samples Prepared with Increasing Moisture Content**

L-1.	Image of the surface finish of the dry pressed sample prepared in a hardened steel die with an elastomer insert using the lignosulphonate binder at a moisture content of 0.00%.....	432
L-2.	Image of the surface finish of the dry pressed sample prepared in a hardened steel die with an elastomer insert using the lignosulphonate binder at a moisture content of 0.88%.....	432

L-3.	Image of the surface finish of the dry pressed sample prepared in a hardened steel die with an elastomer insert using the lignosulphonate binder at a moisture content of 1.16%.....	432
L-4.	Image of the surface finish of the dry pressed sample prepared in a hardened steel die with an elastomer insert using the lignosulphonate binder at a moisture content of 2.12%.....	433
L-5.	Image of the surface finish of the dry pressed sample prepared in a hardened steel die with an elastomer insert using the lignosulphonate binder at a moisture content of 5.69%.....	433
L-6.	Image of the surface finish of the dry pressed sample prepared in a hardened steel die with an elastomer insert using the lignosulphonate binder at a moisture content of 6.86%.....	433
L-7.	Image of the surface finish of the dry pressed sample prepared in a hardened steel die with an elastomer insert using the lignosulphonate binder at a moisture content of 8.56%.....	434
L-8.	Image of the surface finish of the dry pressed sample prepared in a hardened steel die with an elastomer insert using the lignosulphonate binder at a moisture content of 8.59%.....	434
L-9.	Image of the surface finish of the dry pressed sample prepared in a hardened steel die with an elastomer insert using the pPVA binder at a moisture content of 0.00%.....	434
L-10.	Image of the surface finish of the dry pressed sample prepared in a hardened steel die with an elastomer insert using the pPVA binder at a moisture content of 0.28%.....	435
L-11.	Image of the surface finish of the dry pressed sample prepared in a hardened steel die with an elastomer insert using the pPVA binder at a moisture content of 0.99%.....	435
L-12.	Image of the surface finish of the dry pressed sample prepared in a hardened steel die with an elastomer insert using the pPVA binder at a moisture content of 1.39%.....	435
L-13.	Image of the surface finish of the dry pressed sample prepared in a hardened steel die with an elastomer insert using the pPVA binder at a moisture content of 1.94%.....	436
L-14.	Image of the surface finish of the dry pressed sample prepared in a hardened steel die with an elastomer insert using the pPVA binder at a moisture content of 2.69%.....	436
L-15.	Image of the surface finish of the dry pressed sample prepared in a hardened steel die with an elastomer insert using the pPVA binder at a moisture content of 5.52%.....	436

L-16.	Image of the surface finish of the dry pressed sample prepared in a hardened steel die with an elastomer insert using the pPVA binder at a moisture content of 5.68%.....	437
L-17.	Image of the surface finish of the dry pressed sample prepared in a hardened steel die with an elastomer insert using the pPVA binder at a moisture content of 7.10%.....	437
L-18.	Image of the surface finish of the dry pressed sample prepared in a hardened steel die with an elastomer insert using the pPVA binder at a moisture content of 9.92%.....	437
L-19.	Image of the surface finish of the dry pressed sample prepared in a hardened steel die with an elastomer insert using the pPVA binder at a moisture content of 12.16%.....	438

## ***Abstract***

Dry pressing has been shown to be an efficient and cost effective method of manufacturing ceramic ware. Dry pressed parts are typically manufactured with a low moisture content which has the further advantage of eliminating the drying step that is necessary for plastic formed ware, i.e., jiggered or ram pressed. Problems associated with the use of dry pressing in an industrial setting involve the high loss rate during the bisque firing process and the poor surface finish of the green (unfired) ware. It was the goal of this research to improve the surface finish of dry pressed ware to a level that is satisfactory for decorating of the bisque fired ware. The current surface finish of the dry pressed ware resulted in a decoration that was not aesthetically pleasing.

The adsorption of organic additives, specifically dispersants, on the surface of particles is an important aspect of ceramic processing. The interactions between organic additives, specifically sodium poly[acrylic acid] and poly[vinyl alcohol], have been demonstrated to result in phase separation into distinct domains during the spray-drying process. This phase separation leads to a poly[vinyl alcohol]-rich film on the surface of the granulate which will increase the P1 value, the pressure at the onset of granule deformation, of the granulate. This negative interaction between the organics increases the surface roughness of the dry pressed ware.

The presence of naturally-occurring organics, specifically humic acid and fulvic acid, interfered with the adsorption of poly[acrylic acid] on the surface of clay particles. The competitive adsorption between the naturally-occurring organics in clay and poly[acrylic acid] lead to a tertiary blend of organics in solution which will further aggravate the phase separation of the additives. Furthermore the presence of these organics in solution interfered with the titration method used to determine the amount of polymer which adsorbed on the particle surface.

The amount of polymer dispersant which adsorbed on the surface of a kaolinite particle was predicted by a model based upon the mineralogy of the kaolinite platelet. Preliminary adsorption studies with commercial clays found a

significant deviation from the predicted levels. Work with source clay minerals confirmed the model for adsorption. Washing and beneficiation by sedimentation of commercial clays was determined to improve the adsorption levels of poly[acrylic acid] to the predicted levels.

The presence of digested lignite in a commercial clay, added by the supplier to improve plasticity, was found to not significantly effect the plasticity as determine by the HPASC. Instead the presence of sodium chloride, a byproduct of the process used to fraction the organics, was found to change the shear rheology of the clay. The digested lignite was prepared by treating lignite in hot sodium hydroxide. The result was a low molecular weight species that was observed to improve the rheology of a 30 volume percent clay suspension, but there was no significant improvement in the measured cohesion of a commercial kaolin clay.

The roughness of the industrially prepared ware was determined using an optical interferometer to set a baseline for improvements in the surface finish of the dry pressed ware. Two routes were investigated to reduce the measured surface roughness of the dry pressed ware. The first involved the blending of dried granulate with different P1 values. The second involved the study of alternative binder systems to replace plasticized poly[vinyl alcohol] (pPVA) which has been demonstrated to undergo phase separation in the presence of poly[acrylic acid] (PAA) and poly[methacrylic acid] (PMAA) which are commonly used dispersants in the ceramic industry.

Blending of dried granulate was determined to significantly improve the surface finish of the ware. The role of moisture content, controlled by the relative humidity, and granule size were determined. Moisture content was observed to have a significant role in compaction and storage of dried granulate at 90% relative humidity was observed to restore the attributes (P1, compact density, and green strength) of the granulate to those of the as-received material. Granule size was observed to be insignificant provided that the extreme fines, sub-230 mesh, were not tested.

A reduction in the granule size distribution was observed to significantly reduce the measured RMS roughness of dry pressed ware. Granulate prepared at Alfred University had a significantly smaller mean diameter relative to the industrially prepared granulate. The result was an overall reduction in the depth of the features between compacted granules at the sample surface. This led to a significant reduction in the surface roughness of the dry pressed ware.

Alternative binders to replace a plasticized poly[vinyl alcohol] were observed to show improvements in the surface finish of the ware dry pressed in a semi-isostatic die. Blends of granulate prepared with alternative binders, selected on a basis of a normalized P1 value, were not observed to have a significant reduce the measured P1 value. Instead the change in the P1 value of the blended granulate was observed to be strongly correlated to the moisture content of the granulate. The measured RMS roughness was observed to slightly decrease with an increase in the moisture content of the granulate.

The combination of shear and uniaxial pressure were observed to significantly decrease the P1 value of the granulate. The role of moisture content during uniaxial compaction was again observed. Above 3 wt% moisture plateaus were observed in the uniaxial P1 value, the compact density, green strength, and the RMS roughness. The P1 value in shear was observed to be nearly independent of moisture content and more than an order of magnitude lower than the uniaxial P1 value.

The effects of organic binders on the plasticity of a granulated porcelain body were determined using the HPASC as a function of moisture content. Relative to the granulate with no organic binder system the addition of a plasticized poly[vinyl alcohol] and poly[ethylene glycol] were observed to decrease the maximum cohesion of the body and increase the pressure dependence at the maximum cohesion. The addition of lignosulphonate was observed to significantly increase the maximum cohesion, as well as increase the area under the curve in the shear rheology map, of the body and decrease the pressure dependence of the system. Based upon the criteria set forth in this thesis the addition of plasticized poly[vinyl alcohol] or poly[ethylene glycol] were

determined to be detrimental to the plasticity of the clay body while the addition of lignosulphonate was observed to be beneficial to the plasticity. These changes in plasticity were related to the adsorption of lignosulphonate and the change in the surface tension of the water in the samples due to the organic additives.

The results from a dynamic mechanical analyzer to determine the glass-transition temperature, indicated that the plasticizer used in this study, supplied by Buffalo China from their process line, is not an effective plasticizer for poly[vinyl alcohol]. Concentrated solutions of the two organics were observed to phase separate into distinct domains. Furthermore two peaks were observed in the  $\tan \delta$ , the ratio of the loss modulus to the storage modulus, curves from the dynamic mechanical analyzer. Each peak corresponded to a glass transition temperature of an organic component in the test film, prepared using a glass fiber cloth as a substrate. An effective plasticizer would result in a shift of the glass-transition temperature of the organic. No shift was observed in the glass-transition temperature of the poly[vinyl alcohol] indicating that there was no associated complex between the organics. Comparison with a poly[vinyl alcohol] and glycerin mixture showed that glycerin is an effective plasticizer for poly[vinyl alcohol] resulting in the glass-transition temperature shifting to lower temperatures.

In summary the most important aspect to improving the surface finish of dry pressed ware, i.e. facilitating compaction, is the selection of the organic additives. Additives which are observed to have a negative interaction, i.e. to phase separate into distinct domains, will result in an organic rich film at the surface of the granule thus increasing the P1 value of the granulate. The presence of water in the granulate can counteract this effect by plasticizing the organic. A suitable moisture content of the granulate is crucial to compaction. With little moisture, the binder will be hard and difficult to deform. Excess moisture results in poor flowability and the pressed part sticking to the die. The use of a binder which created an organic gelatin was observed to significantly improve the compaction of blended granule systems since the water which was

trapped in the gelatin structure was available to plasticize the second organic binder. The highest green strength observed in this study resulted from a 50-50 weight percent blend of an agar binder system and a lignosulphonate binder system. Excessive amount of an organic which creates a gelatin will result in a reduction in the flowability of the granulate and sticking of the ware to the membrane surface after compaction.

## **1. Introduction**

The adsorption of organics on the surface of ceramic particulate is an aspect of ceramic processing which is often ignored. Polymeric surfactants, specifically dispersants, are assumed to adsorb to the particle surface creating a steric or electrosteric barrier to agglomeration. The interaction between the particle surface and the dispersant are assumed to result in strong adsorption; little attention is given to the charged nature of the particle surface or the polyelectrolyte, a polymeric additive with an ionizable species on each monomeric building block.

Less attention is given to interactions between the organic species that are commonly used in the processing of ceramics, e.g., dispersants, binders, plasticizers, thickeners, anti-foams, etc. For the purposes of this thesis the interactions of organic additives will be classified into three groups: 1) no interaction, 2) a negative interaction, and 3) a positive interaction. A negative interaction is observed when the additives phase separate into distinct domains. A positive interaction is observed when the additives form an associated complex, e.g., by hydrogen bonding, to form a new "hybrid" organic species. In the case of no interaction the organic additives remain in a homogeneous solution, but no associated complex is formed, i.e., each polymeric additive retains its individual attributes.

This thesis investigates the adsorption of poly[acrylic acid] on the surface of various ceramic substrates, including alumina, crystalline silica, and various silicate minerals. The affinity of the poly[acrylic acid] dispersant for the powder surface was quantified using a potentiometric titration technique to determine the concentration of polymer remaining in the supernatant of the suspension after adsorption. The interactions between polymeric additives and the resulting consequences for the deformation of spray-dried granulate were determined by generating compaction diagrams and relating the P1 value, the pressure at the onset of granule deformation, to the measured surface roughness. The primary goal of this research was to reduce the measured surface roughness of dry-pressed dinnerware from an industrial process.

The remainder of this thesis is divided into nine chapters:

Chapter 2 reports the results of an adsorption study investigating the effects of polymer molecular weight on the adsorption plateau value for an alumina and a ball clay substrate. The affinity of Darvan™ 811, a sodium poly[acrylic acid] with a molecular weight of approximately 3500 Daltons, for silica and well characterized silicate minerals (purchased from the Source Clay repository) was also determined.

Chapter 3 investigates the effects of a washing and beneficiation process to remove organic and inorganic impurities from commercial kaolinitic clays. The adsorption plateau value for the beneficiated clay fractions was determined using the potentiometric titration technique from Chapter 2.

Chapter 4 investigates the effects of competitive adsorption between naturally-occurring organics, present in commercial kaolinitic clays, and Darvan™ 811. Incremental doses of Darvan™ 811 were added to the kaolinitic clays to gradually remove the adsorbed natural organics from the clay surface. The molecular weight of the naturally occurring organics which were removed from the kaolinite surface due to competitive adsorption was determined using gel permeation chromatography.

Chapter 5 studies the effects of naturally-occurring organics on the plasticity of a relatively non-plastic commercial kaolin clay.

Chapter 6 reports the results from a baseline study to characterize the surface roughness of commercially manufactured dinnerware from industrial dry pressing, jiggering, ram pressing, and pressure-casting operations.

Chapter 7 summarizes the studies to improve the surface roughness of the dry-pressed dinnerware. The benefits of blending samples of dried granulate prepared with different organic binder systems is reported in Chapter 7.2. The effects of moisture content and granule size on deformation are reported in Chapter 7.3. Alternative binder systems to replace a plasticized poly[vinyl alcohol] binder system are investigated in Chapter 7.4.

Chapter 8 reports the results from a study to investigate the benefits of applying shear during the compaction process as opposed to applying only a uniaxial load. The effects of moisture content on the compaction of a granulated porcelain body in uniaxial and shear compaction were investigated. The plasticity of a granulated porcelain body prepared with various organic binder systems is also reported.

Chapter 9 investigates the plasticizer supplied by Buffalo China for this research. The change in the glass-transition temperature as plasticizer is added to a sample of poly[vinyl alcohol] was determined by dynamic mechanical analysis.

Chapter 10 is an overall summary and conclusions.

## **2. Adsorption of Sodium Poly[acrylic acid] on Alumina and Clay Surfaces**

### **2.1 Introduction**

It is proposed that the phase separation of polymeric additives used in the spray drying process results in the poor surface finish of dry-pressed dinnerware manufactured using a semi-isostatic press. Polymeric additives are used to control the rheology of the clay-water system, the deformation of the dried granulate, and the properties of the pressed green body. Polymeric dispersants are used to control the particle – particle interactions in the clay-water system by either steric (the polymer acts as a physical barrier to flocculation) or electrosteric (a charged polymer, a polyelectrolyte, is used to create both an electrostatic and a physical barrier to flocculation) repulsion. It is traditionally assumed that the dispersant exhibits strong chemisorption on the surface of the particle to create electrosteric repulsion between the particles.

When other polymeric additives, i.e., binders, plasticizers, anti-foaming agents, etc., are added to the system to either control the rheological properties or the properties of the green body later in the process, the additives can interact in one of three ways: 1) there can be no interaction between the additives, 2) a positive interaction where an associated complex is formed by hydrogen or van der Waals bonding and 3) a negative interaction, where the additives phase separate into distinct domains. Since the dispersant is strongly adsorbed to the surface of the particulate, a negative interaction will result in the other additives migrating to the surface to minimize the interaction between the two phases. To understand the affinity of dispersants for the surface of the particulate, adsorption studies using sodium poly[acrylic acid] (Na-PAA) dispersants of various molecular weight have been performed using alumina and ball clay as an adsorbent.

### **2.2 Literature Review**

The driving force for adsorption of polymers on the surface of particles is not clearly understood. It is accepted that polymer adsorption results in a reduction in Gibb's free energy (G) of the system.<sup>1,2</sup> An overly simplified way to

understand the reduction in free energy is to consider a polymer in solution exchanging places with adsorbed monomeric species (including ions or lower molecular weight species) on the surface of a particle. The polymer in solution has three degrees of translational freedom of the system, and energy is required, in the form of enthalpy (H), to adsorb the polymer on the particle surface. By exchanging the polymer with a group of monomeric species, equal to the number of adsorption sites between the polymer and the particle surface, the entropy (S) of the system is increased since each of the monomeric species will have three degrees of translational freedom. Thus the Gibbs free energy is reduced since:

$$\Delta G = \Delta H - T\Delta S \quad (1)$$

Therefore, in this simplified model for adsorption, the free energy of the system is reduced by replacing monomeric species on the particle surface with a polymeric species and there should be a driving force for the adsorption of larger molecular weight polymers on the particle surface.

This simplified description for polymer adsorption has proven accurate for non-ionic polymeric additives, e.g., PVA. Koopal investigated the adsorption of PVA on the surface of silver iodide, a hydrophobic surface, and oxidized carbon black, a hydrophilic surface.<sup>3</sup> Koopal identified several criteria that need to be considered when studying the adsorption of polymers on a surface. These are:

- the absorbance on (nonporous) adsorbents usually increases with time over extended periods
- from an ordinary polymer sample preferential adsorption of the larger molecules over smaller ones occurs, the extent of which depends on the adsorption conditions
- due to this preference, the molecular weight dependence of adsorption cannot be directly obtained from isotherms of various samples differing in molecular weight
- the adsorbent content (i.e., the surface area to volume ratio, S/V) may affect the amount of polymer adsorbed per unit area
- desorption upon dilution is seldom achieved, but the addition of competitive adsorbates or a change in the solvent power can induce (partial) desorption, so that it is not clear if equilibrium has been obtained.

- Koopal<sup>3</sup>

The concentration of PVA remaining in the supernatant after equilibration for various periods of time was determined using a spectrophotometric technique. The results indicate that initially the lower molecular weight fractions in a sample

of PVA (polydispersity of the samples was 2.41, 3.49, and 5.83) adsorb and with time the adsorbed species are replaced by a higher molecular weight chain of PVA. These results are explained by the diffusion rate and reformation of the higher molecular weight species. This adsorption behavior is typical for weak adsorption; PVA is a non-ionic polymeric additive.

Adsorption of polyelectrolytes, e.g., PAA, show a different behavior compared to non-ionic surfactants. Ramachandran and Somasundaran investigated the adsorption of sodium poly[styrene sulphonate],  $M_w$  of 4,000 and 1,200,000, on the surface of hematite.<sup>4</sup> The concentration of polymer adsorbed was determined using a depletion technique and the molecular weights of the species remaining in the supernatant were characterized using size exclusion chromatography (SEC). They determined that in the absence of an electrolyte the lower molecular weight additive adsorbed more quickly and at a higher surface coverage (measured in  $\text{mg}/\text{m}^2$ ) compared to the 1,200,000 molecular weight sample. In conditions where competitive adsorption was a factor, i.e., samples where both molecular weights were added, the lower molecular weight sample was preferentially adsorbed on the surface. The adsorption plateau was observed to be consistent with the individual adsorption isotherms. Upon the addition of an electrolyte to the system, 0.1 M NaCl, the adsorption isotherms are shifted to a higher concentration of adsorbed polyelectrolyte. Furthermore the 1,200,000 molecular weight polymer is observed to be preferentially adsorbed and, with time, the higher molecular weight polymer will replace the lower molecular weight polymer on the surface of the particle. This was explained by a change in the conformation of the polymer in the salt solution, i.e., the presence of dissolved cations resulted in a coiled conformation.

De Laat and van den Heuvel investigated the competitive adsorption of poly[acrylic acid] (PAA) on the surface of  $\text{BaTiO}_3$ .<sup>5</sup> Their study investigated the competitive and displacive adsorption of poly[vinyl alcohol] (PVA) and PAA using SEC, calibrated with poly[ethylene oxide] standards, to determine the concentration and molecular weight of the polymeric species remaining in the supernatant after equilibration. Their results indicate that both PVA and PAA

adsorb on the surface of BaTiO<sub>3</sub> and that a plateau is reached after the surface is covered, corresponding to 0.19 mg/m<sup>2</sup> for the PVA and 0.40 mg/m<sup>2</sup> for the PAA, no equilibration time was indicated. Upon adsorption from solution there was no apparent change in the molecular weight distribution of the PVA sample. The PAA sample showed a preferential adsorption for the high molecular weight fractions, when insufficient polymer was available to cover the surface, and an intermediate molecular weight from the distribution when excess polymer was present in solution. Adsorption of PVA and NH<sub>4</sub>-PAA, added simultaneously, showed that when insufficient PAA was present PVA, added at a concentration above the surface saturation limit, adsorbed on the BaTiO<sub>3</sub> surface. As the concentration of the PAA was increased and the PVA concentration held constant in the solution, the amount of PVA adsorbed decreased as the concentration of PAA adsorbed increased. Once the surface was saturated with PAA, no PVA was adsorbed from solution. When the PVA was allowed to adsorb prior to the addition of PAA it was observed that the PVA was not displaced from the BaTiO<sub>3</sub> surface and an adsorption isotherm was generated for PAA in the presence of a PVA covered surface.

De Laat and van den Heuvel investigated the molecular weight fractionation of PAA salts, the cationic species on the polymer chain were not identified, on a BaTiO<sub>3</sub> surface.<sup>6</sup> Their results indicate that for low molecular weight PAA samples there was preferential adsorption of an intermediate molecular weight species. For PAA samples that only have molecular weight fractions above this critical size, the molecular weight was not indicated since it was only a relative measure determined using the PEO standards, the lower molecular weight fractions were preferentially adsorbed. They indicated that initially adsorption was dictated by the diffusion rate of the polymer fractions to the positively charged surface of the particle. As the surface of the particle was covered with the negatively charged polymer an electrostatic barrier was created preventing further adsorption. They indicated that longer polymer chains had a greater charge, i.e., more functional groups on the chain, and this resulted in a greater electrostatic barrier to adsorption. As previously discussed there is a thermodynamic driving force to adsorb the longest polymer chains from solution

and therefore the shorter polymer chains were replaced by the intermediate length chains, the electrostatic barrier was too great to allow adsorption of the longest polymer chains. The addition of an electrolyte to the system resulted in the preferential adsorption of the longest chains from solution. As the concentration of electrolyte, a 10,000 Dalton PAA salt in the presence of  $\text{KNO}_3$  was used in this study, was increased the longest chains were preferentially adsorbed leaving the shortest chains in solution. In the presence of a 0.2 M  $\text{KNO}_3$  solution the longest chains of PAA were removed from solution shifting the chromatogram to the lower molecular weight fractions. This change in the fraction that was preferentially adsorbed was explained by the cations shielding the negative charges on the adsorbed polymer chains. This allowed the longer chains to adsorb on the surface thus further reducing the free energy of the system.

De Laat, van der Heuvel, and Bohmer studied the kinetics of PAA adsorption on  $\text{BaTiO}_3$ .<sup>7</sup> Adsorption experiments were performed over a period of 15 minutes to several weeks. Two PAA molecular weights, determined using PEO references, were tested in this study, 10,400 and 47,600; the 10,400 Dalton sample fell near the critical molecular weight indicated in the article mentioned previously and the 47,600 Dalton sample had a higher molecular weight than the critical size. Initially the lower molecular weight fraction was observed to adsorb on the surface, but with increasing equilibration time up to 24 days the higher molecular weight fractions were observed to displace the lower molecular species. The effect was enhanced in the presence of 0.03 M  $\text{KNO}_3$ , where after 24 days the higher molecular weight fractions were completely adsorbed on the surface and the only species remaining in solution were of lower molecular weight. The 47,600 Dalton sample showed a similar behavior, but the effects were less dramatic with the chromatograms showing a shift to adsorption of the higher molecular weights. The presence of  $\text{KNO}_3$  in solution was observed to enhance the adsorption of PAA on the surface of  $\text{BaTiO}_3$  due to changes in the conformation of the polymer.

Ceserano and Aksay investigated the adsorption of poly[methacrylic acid] (PMAA) on the surface of submicrometer alumina.<sup>8</sup> Adsorption isotherms were generated using a potentiometric titration technique which determined the concentration of polymer remaining in the supernatant after adsorption from solution. Higher concentrations of polymer were added until the surface was fully covered. The effects of pH on the concentration of adsorbed polymer were also determined. Their results indicated that more PMAA is adsorbed as the pH is reduced due to a change in the conformation.

As the pH of an aqueous solution of PMAA is adjusted the conformation of the polymer changes as the functional groups on the polymer chain are protonated or deprotonated. The structure of PMAA is shown schematically in Figure 2-1. Above pH 9.5 the functional groups are de-protonated resulting in a fully open, or dissociated, conformation due to the negative charge on the functional groups. As the pH is decreased the functional groups gradually become protonated and at an approximate pH of 3 the functional groups are fully protonated. The result is a coiled conformation for the polymer chain since there is no net charge on the polymer; the polymer is more hydrophobic when fully protonated. Due to the change in conformation of the polymer chain, more organic is necessary at lower pH values to fully cover the particle surface, all polymer concentrations are normalized for the particle surface area on a  $\text{mg}/\text{m}^2$  basis. The addition of soluble salts to the polymer solution serves to satisfy the negative charge on the functional groups of the polymer chain. These electrolytes therefore change the conformation of the polymer and compress the dissociation curve to higher pH values; the polymer is fully dissociated at a pH of 9.5, but in the presence of salts the polymer's functional groups are associated with a cation at a higher pH. Furthermore the addition of divalent or trivalent cations to the polymer solution can result in the precipitation of the polymer from solution since these species will chelate the organic.<sup>9-13</sup>

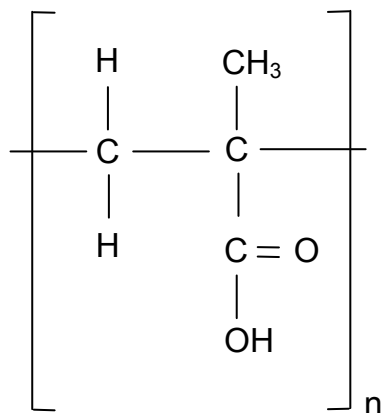


Figure 2-1. Schematic drawing of a protonated poly[methacrylic acid] where n represents the degree of polymerization.

Cesarano and Aksay investigated the benefits of using polyelectrolytes to stabilize highly concentrated suspensions of alumina.<sup>14</sup> The polyelectrolytes selected for the study were PMAA and poly[acrylic acid] (PAA), the structure of PAA is shown in Figure 2-2. The effects of polyelectrolyte additions were studied as a function of pH, solids loading, and molecular weight. The results indicated that PMAA and PAA were both effective dispersants for processing of alumina suspensions and that both additives behave in a similar manner in aqueous solutions.

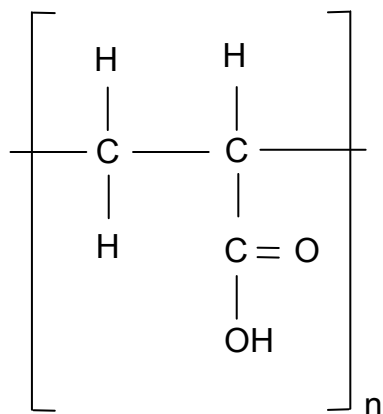


Figure 2-2. Schematic drawing of a protonated poly[acrylic acid] where n represents the degree of polymerization. The sodium salt of PAA was used in this study, i.e., the proton on the carboxylic acid group is replaced by a sodium ion.

PMAA and PAA are well known dispersants for alumina.<sup>8,14</sup> The isoelectric point, the pH at which there is no net charge on the particle surface, of alumina is approximately 9.0 to 9.5. This corresponds to the pH where PMAA and PAA are fully dissociated. Therefore the pH where alumina is flocculated, resulting in high viscosity, is also the pH where the organic dispersant is most effective at covering the particle surface. Thus the adsorption of the negatively charged polymer on the alumina surface results in a negative charge on the particle surface creating an electrostatic barrier to aggregation.

As the pH is adjusted away from the isoelectric point (iep) charges develop on the particle surface due to protonation and deprotonation of active sites on the surface. Above pH 9.5 the alumina particle has a net negative surface charge and there is little affinity between the negative polymer and the negative particle surface, i.e., there is little adsorption. Below pH 9.5 the alumina particle has a net positive charge and there is an electrostatic attraction between the polymer and the particle surface.<sup>15</sup>

Carty proposed a model for the adsorption of PAA or PMAA on the surface of a kaolinite platelet.<sup>16</sup> The model considered the mineralogy of the kaolinite platelet, which consists of a gibbsite layer, considered to be alumina-like, and a silica-like layer, shown schematically in Figure 2-3. Since the isoelectric point of silica is approximately 2-2.5 the silica-like surface is negatively charged across most of the pH range, therefore little adsorption of PMAA or PAA, which has a negative charge when dissociated, will occur on the silica-like surface. Therefore adsorption can only occur on the alumina-like basal plane and, possibly, the platelet edge. By measuring the dimensions of clay platelets, using a scanning electron microscope, it was determined that the ratio of the point-to-point distance for the basal plane to the platelet thickness, referred to as  $2L:h$ , was approximately 10:1.

Based upon these dimensions the expected adsorption on the only the alumina-like basal plane would be approximately 41% of that expected for alumina, normalized for the surface area on a  $\text{mg}/\text{m}^2$  basis. For the alumina-like basal plane plus the platelet edge the predicted adsorption level would be

approximately 59% of the alumina adsorption. The predicted adsorption level on the kaolinite platelet as a function of the 2L:h ratio is plotted in Figure 2-4, slight deviations from the average 2L:h ratio will result in fluctuations in the measured adsorption plateau.

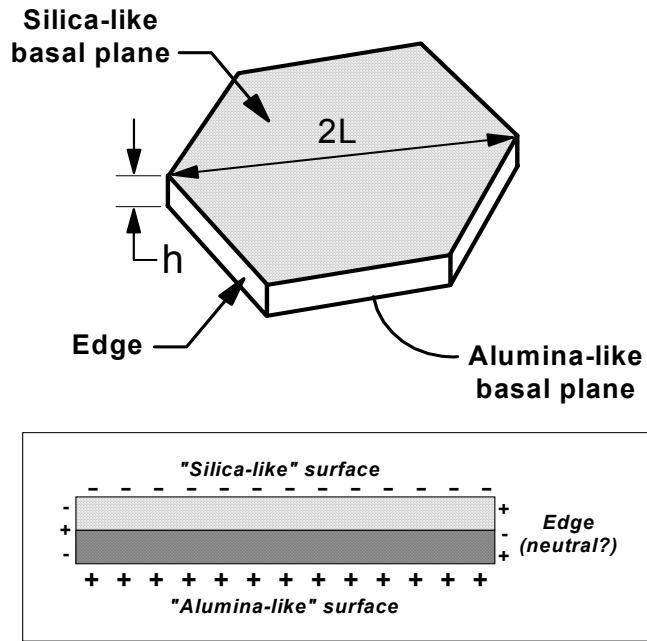


Figure 2-3. Sketch of the kaolinite platelet that was used as a basis for the model for adsorption of Na-PAA on the clay surface. Polymer is assumed to adsorb on the alumina-like basal plane and possibly the platelet edge. Based upon the 2L:h ratio of the platelet the amount of polymer adsorbed on the clay surface can be predicted as a percentage of the polymer adsorbed on an alumina surface, normalized on a  $\text{mg}/\text{m}^2$  basis to account for the difference in specific surface area (adapted from Carty<sup>16</sup>).

### 2.3 Experimental Procedure

Seven Na-PAA dispersants of different molecular weight were evaluated to determine their affinity for the surface of alumina (APA-0.5, Ceralox, Tucson, AZ), and clay (Huntingdon ball clay, United Clays, Brentwood, TN). The dispersants that were evaluated are listed in Table 2-I, along with the molecular

weight and polydispersity, a measure of the distribution of molecular weight of the polymeric chain.

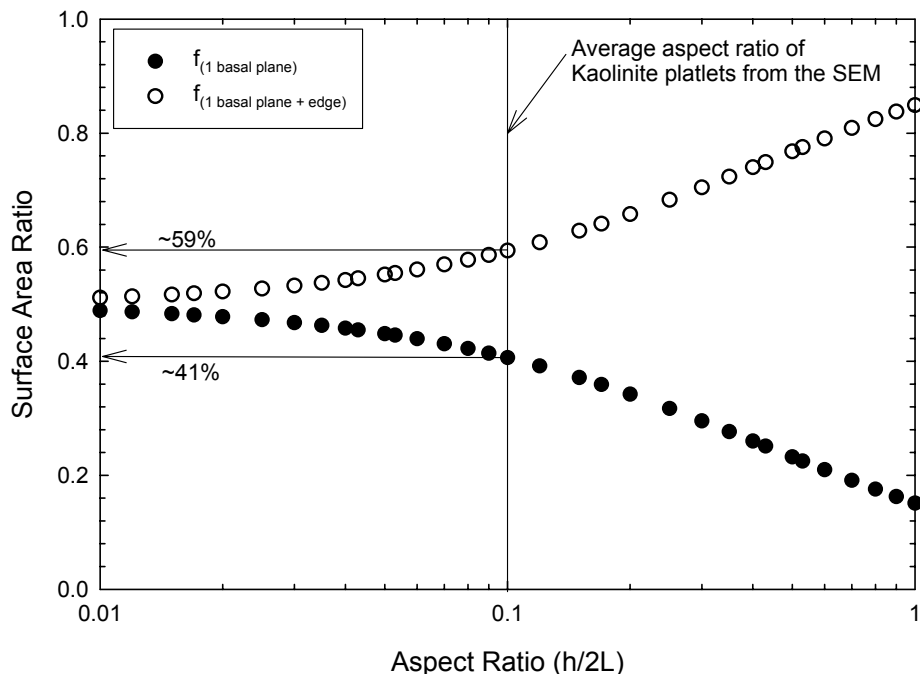


Figure 2-4. Plot of the effect of the 2L:h ratio on the predicted adsorption levels for kaolinite. Plotted is the predicted adsorption level for the alumina-like basal plane and the alumina-like basal plane with the edge (adapted from Carty<sup>16</sup>).

Table 2-1. List of the Polymers Used in the Adsorption Study.

Polymer	Molecular Weight (Daltons)	Polydispersity Index*	Solids Concentration
Acumer™ 1010 †	2000	1.27 – 1.30	0.44
Acumer™ 1510 †	55000	1.27 – 1.30	0.27
Acumer™ 9400 †	3600	1.27 – 1.30	0.42
Acusol™ 410 N †	10000	1.27 – 1.30	0.40
Acusol™ 445 N †	4500	1.27 – 1.30	0.45
Acusol™ 448 N †	3200	1.27 – 1.30	0.46
Darvan™ 811 ‡	~ 3500	1.50	0.43

\* The polydispersity index is a measure of the distribution of the polymer molecular weight, measured as the ratio of Mw/Mn, the molecular weight average and the molecular number average respectively.

† Rohm and Haas, Philadelphia, PA

‡ R.T. Vanderbilt, Norwalk, CT

Suspensions were prepared at 15 volume percent (v/o) solids and increasing amounts of polymer, based upon the surface area of the powder, were added to the samples. Two sets of samples were prepared one at pH 9.0 and the other at pH 6.0, to determine the effects of pH on the adsorption of the polymer. The pH was adjusted to within  $\pm 0.2$  of the target value. These pH values were selected since pH 9 is near the iep of alumina and pH 6 is near the expected iep of kaolinite, kaolinite iep is determined based upon the mineralogy and the iep of alumina (9-9.5) and silica (2-3). Recent evidence has indicated that the iep of kaolinite is closer to 7-7.5.<sup>17</sup> The samples were agitated on a shaker table for a period of 24 hours prior to centrifuging the samples. The supernatant was removed from the samples and 40 mL of the supernatant was diluted, using distilled water, to a volume of 85 mL. The pH of the supernatant was adjusted above 10.5 so that the polymer was fully dissociated. The samples were titrated using 0.25 M HCl to determine the amount of polymer remaining in the supernatant. The volume of HCl necessary to saturate the active sites on the polymer chain was determined as the volume of titrant between the two inflection points. The inflection points in the curve were determined using the first derivative of the titration curve, shown in Figure 2-5. The concentration of polymer remaining in solution was determined using a calibration curve. The calibration curve for Acumer™ 1510 and a sample calculation to determine the concentration of polymer in solution are shown in Appendix A.

To validate the proposed model for polymer adsorption on the surface of kaolinite, clay samples from the Source Clays Repository [The Source Clays Repository, The Clay Minerals Society, Purdue University, West Lafayette, IN] were purchased for evaluation. Three samples were purchased: 1) KGa-2 (a poorly-crystallized-Georgia kaolin which is nearly pure), 2) STx-1 (a Ca-montmorillonite which was predicted to be non-swelling), and 3) SWy-2 (a Na-montmorillonite which was predicted to swell in an aqueous suspension). Data on the mineralogy and properties of the Source Clay Minerals has been summarized and reported by the Clay Mineralogy Society.<sup>18</sup> Samples were prepared using the above procedure with the exception of the SWy-2 clay. Since

the SWy-2 swelled in aqueous suspensions only a 2.5 v/o solids suspension could be prepared with confidence that all the powder was fully wetted. Furthermore suspensions prepared above 2.5 v/o gelled so that they were nearly solid. Adsorption isotherms were also generated using a silica sample (Tamsil 8, United Clays, Brentwood, TN) at pH  $9.0 \pm 0.2$  and  $6.0 \pm 0.2$  using the procedure previously described. Only Darvan™ 811 was used to generate adsorption isotherms for the source clay samples and Tamsil 8.

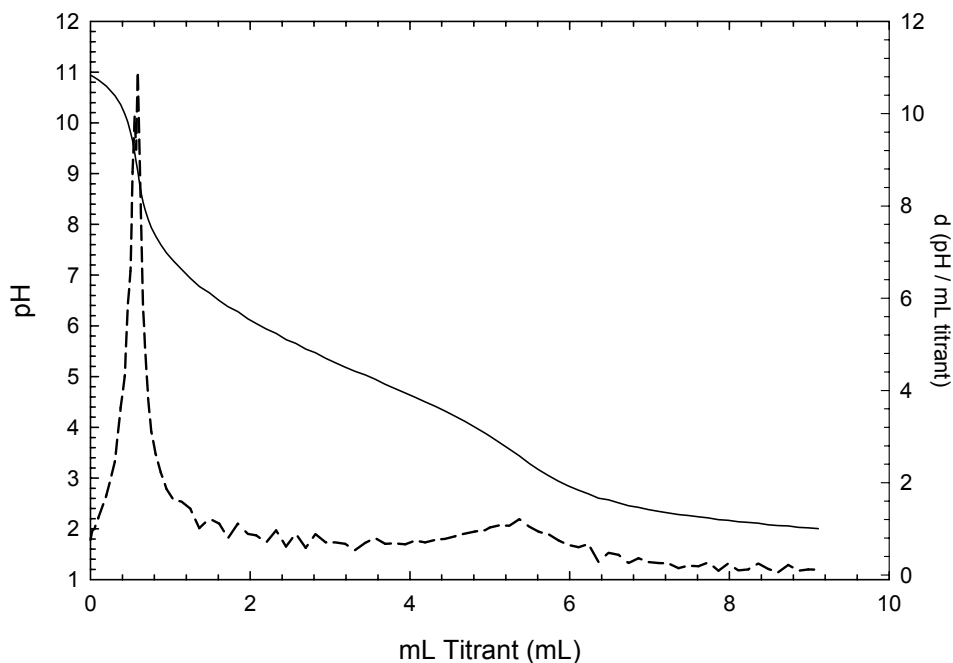


Figure 2-5. Representative titration curve to determine the concentration of the PAA present in the supernatant, shown are the raw data (solid line) and the first derivative (dashed line). The milliliters of titrant (0.25 M HCl) between the two inflection points was converted to the concentration of polymer using a calibration curve.

To determine the effect of solids loading on adsorption, samples were prepared using APA-0.5 alumina with a target Darvan™ 811 concentration of  $0.4 \text{ mg/m}^2$ . Suspensions were prepared from 2.5 v/o up to 35 v/o at a pH of  $9.0 \pm 0.2$  and  $6.0 \pm 0.2$ . The samples were allowed to equilibrate for a period of 24 hours prior to centrifuging the samples to test the supernatant for polymer concentration with the exception of one sample at 2.5 v/o which was left to

equilibrate for 2 weeks. The effects of equilibration time on adsorption were previously determined by Kim and a plateau was observed in the adsorption level after 6 hours, the shortest time tested.<sup>19</sup> Samples were left to equilibrate for up to 9 days.

## 2.4 Results

The adsorption isotherms for alumina with each of the dispersants investigated can be observed in Figures 6 (pH 6) and Figure 2-7 (pH 9). The adsorption for each of the polymers at pH 9 on the surface of the alumina showed a plateau between 0.32 and 0.45 mg/m<sup>2</sup> adsorbed. At pH 9 the polymer chain is greater than 95% dissociated and can efficiently cover the surface of the powder. The adsorption plateaus at pH 9 were in good agreement with the previous work of Cesarano et al.<sup>8</sup>

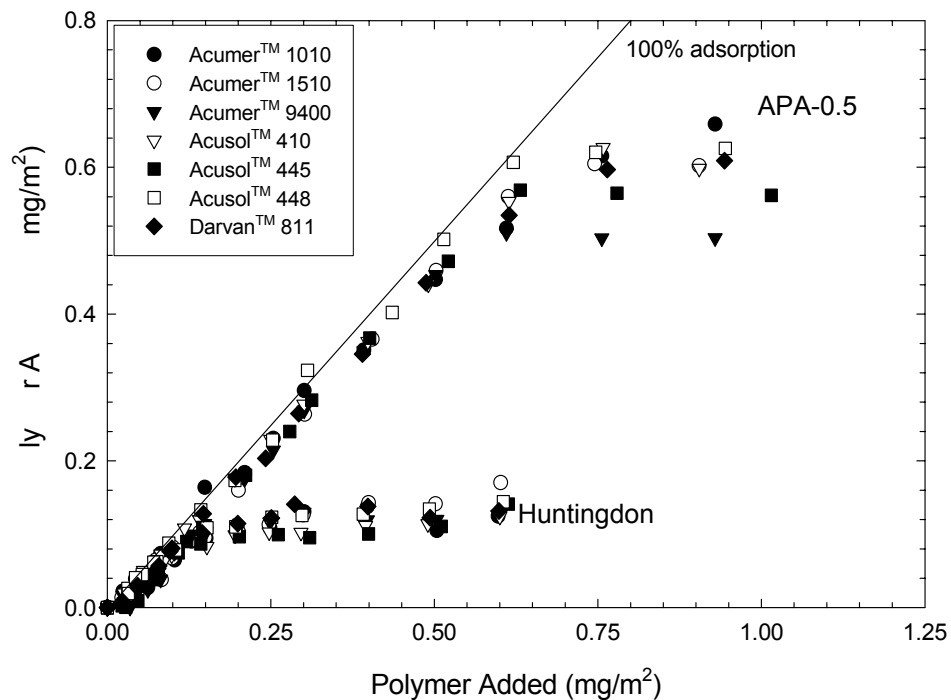


Figure 2-6. Initial results from the study investigating the effect of polymer molecular weight on adsorption of Na-PAA on the surface of alumina (APA-0.5) and Huntingdon ball clay at pH 6. The adsorption levels for the ball clay are significantly below the predicted level.

When the pH was reduced to 6 the polymer was no longer fully dissociated, the polymer chain takes a coiled conformation that is not as efficient at covering the surface of the particle. The adsorption isotherms showed that more polymer was adsorbed to the surface of the particle. The adsorption plateau at pH 6 occurred between 0.5 and 0.67 mg/m<sup>2</sup> for the polymers studied. The concentration of polymer adsorbed on the surface of the particle varied slightly with each polymer, but the general trend remained the same. The adsorption plateaus at pH 6 were in good agreement with the previous work of Cesarano et al.<sup>8</sup>

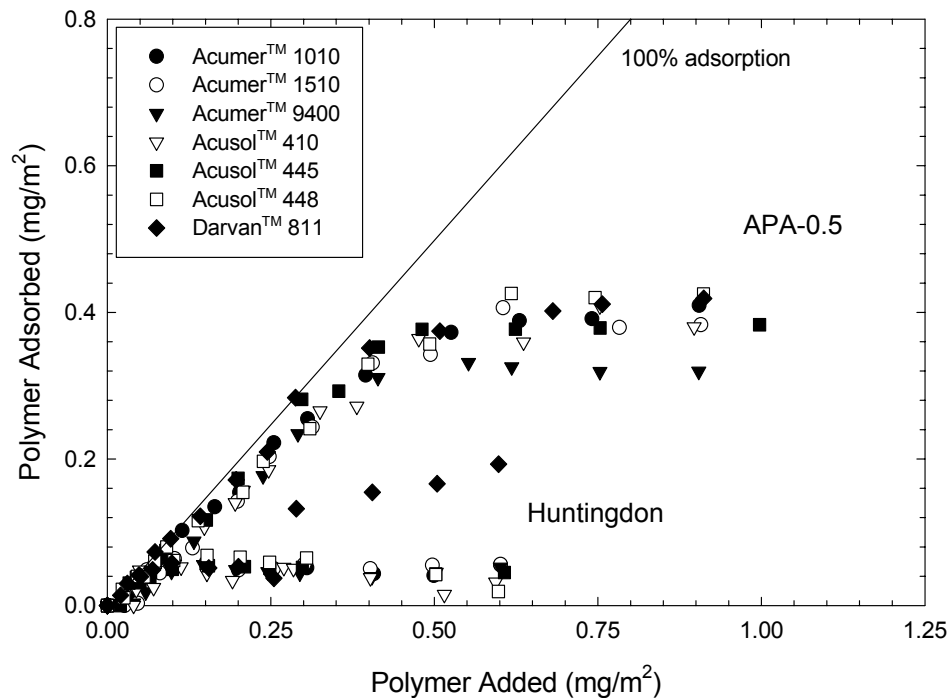


Figure 2-7. Initial results from the study investigating the effect of polymer molecular weight on adsorption of Na-PAA on the surface of alumina (APA-0.5) and Huntingdon ball clay at pH 9. The adsorption levels for the ball clay are initially below the predicted level.

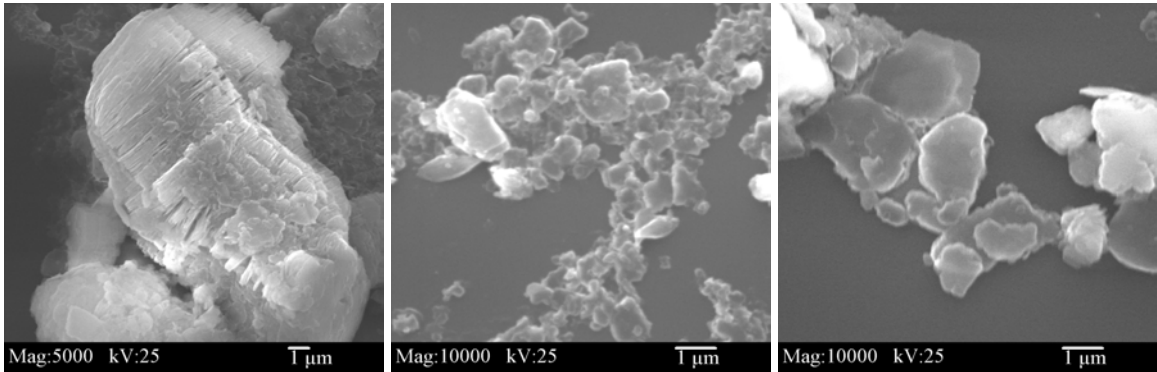
The process was repeated using Huntingdon clay as the adsorbate. Since the clay sample contained alkali and alkaline earth ions, organic impurities, and a variety of clay species, the adsorption isotherms do not reach a clear plateau value. The results from the Huntingdon clay can be observed in Figures 6 (pH 6)

and Figure 2-7 (pH 9), for the seven polymers that were tested; the data has been plotted with the results from the APA-0.5 for easy comparison. At pH 9 a plateau was observed between 0.05 and 0.07 mg/m<sup>2</sup>. When the pH was reduced to 6 the amount of polymer adsorbed on the surface of the particulate increased. The adsorption plateau at pH 6 was observed between 0.1 and 0.14 mg/m<sup>2</sup> adsorbed.

The supernatant collected from the Huntingdon samples was observed to be very dark in color at pH 9 and at pH 6 the coloration of the supernatant was observed to darken with increasing additions of PAA. At pH 9 the organic species that are naturally present in soils are soluble; the solubility of natural organic species will be discussed in Chapter 3. Furthermore, it was believed that the addition of higher amounts of polymer to the suspension force species from the surface of the kaolinite particles, which remain in the supernatant after centrifuging the sample. These species were simultaneously titrated with the PAA in solution to change the surface charge, increasing the amount of acid necessary to reduce the pH of the supernatant. Since more acid was used in the titration, the calculated amount of polymer on the surface of the particle was decreased since a differential technique was used, i.e., the amount of polymer adsorbed was determined as the difference between the amount added and the amount detected in the supernatant. Upon titration to a pH of 2 a dark precipitate was formed and the solution above the precipitate was nearly colorless.

There are two arguments against the adsorption model proposed by Carty.<sup>16</sup> The first is that clay booklets, face to face agglomerated kaolinite platelets, can have an aspect ratio such that 41% of the surface area corresponds to the platelet edge, i.e., a 2L:h ratio of 2.31:1. SEM images, Figure 2-8, show that the booklets break down in aqueous suspensions to form individual platelets. Addition of a dispersant or adjusting the pH away from the iep aids in the breakdown of the clay booklets. Therefore the 2L:h ratio of 10:1 more closely reflects the aspect ratio of the kaolinite platelets in an aqueous suspension. The second argument is that the adsorption on only the platelet edge would correspond to 18% of the adsorption measured on alumina

particulate, i.e., the difference between the predicted adsorption levels in the model is 18% corresponding to adsorption on only the platelet edge. The initial adsorption levels for the Huntingdon clay is approximately 18% of the adsorption measured on the alumina surface. The viscosity results, Figure 2-9, for Huntingdon show that the minimum viscosity occurs at approximately  $0.2 \text{ mg/m}^2$ , which is approximately 41% of the surface coverage necessary to achieve the minimum viscosity in an alumina (APA-0.5) suspension. Suspensions were prepared at 30 v/o for the Huntingdon and 35 v/o for the alumina, the pH of the viscosity suspensions was not adjusted prior to measuring the viscosity.



Raw Huntingdon booklet

Raw Huntingdon Clay  
pH 6,  $0.00 \text{ mg/m}^2$  PAA

Raw Huntingdon Clay  
pH 6,  $0.33 \text{ mg/m}^2$  PAA

Figure 2-8. SEM images of Huntingdon ball clay. Shown are the as-received powder that was not suspended in water (left), the clay suspended in water at pH  $6.0 \pm 0.2$  with  $0.00 \text{ mg/m}^2$  of Darvan™ 811 (center), and the clay suspended in water at pH  $6.0 \pm 0.2$  with  $0.33 \text{ mg/m}^2$  of Darvan™ 811 (right). A clay booklet is observed in the as-received powder that was not suspended in water. Suspending the clay in water eliminates the booklets and only individual clay platelets are observed.

The adsorption isotherm for the source clay samples is shown in Figures 10 and 11 (KGa-2, pH 6 and 9 respectively), Figures 12 and 13 (STx-1, pH 6 and 9 respectively), and Figures 14 and 15 (SWy-2, pH 6 and 9 respectively). The iep of the source clay samples was estimated by adding a small quantity of the sample to distilled water to create a 1 v/o suspension. The pH of the suspension approached the iep as the surface reached equilibration with the water. The measured equilibrium pH is reported in Table 2-II. The equilibrium pH of the

suspensions is an indication of the interactions between the water and the particle surface. The KGa-2 clay was observed to have a low pH due to either adsorption of minerals on the alumina-like surface, e.g., 2:1-layer silicates, or adsorption of an organic species; the supernatant of the KGa-2 suspensions that were prepared for adsorption were light in color indicating that little organic material was present in the supernatant. The two montmorillonite clays are observed to have a higher equilibrium pH due to a cation exchange phenomenon. The calcium or sodium on the clay surface was replaced by a proton from solution on the negative basal planes of the 2:1-layer silicates. The removal of the proton from solution increased the pH of the suspension. The pH of a solution is defined as negative logarithm of the concentration of protons in solution.

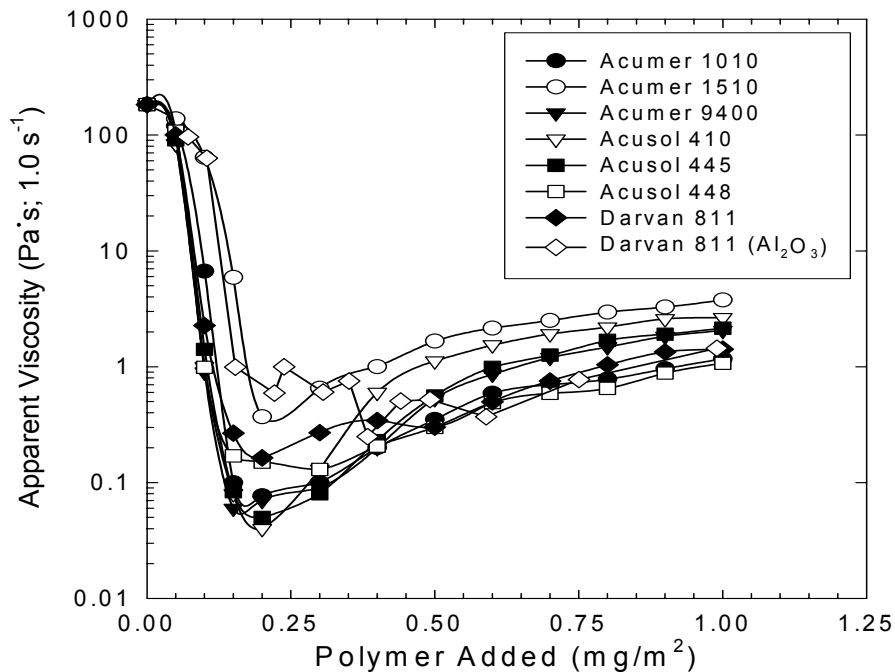


Figure 2-9. Viscosity results for the Huntingdon clay as a function of the concentration of Na-PAA in the suspension. Results are also shown for APA-0.5 with Darvan™ 811 additions. A minimum is observed in the viscosity of the APA-0.5 at approximately 0.38 mg/m<sup>2</sup>. The minimum for the clay suspensions is observed at approximately 0.2 mg/m<sup>2</sup>, 52% of that observed for the alumina system. Clay suspensions were prepared at 30 v/o while the alumina suspensions were prepared at 35 v/o, pH of the suspensions was not adjusted.

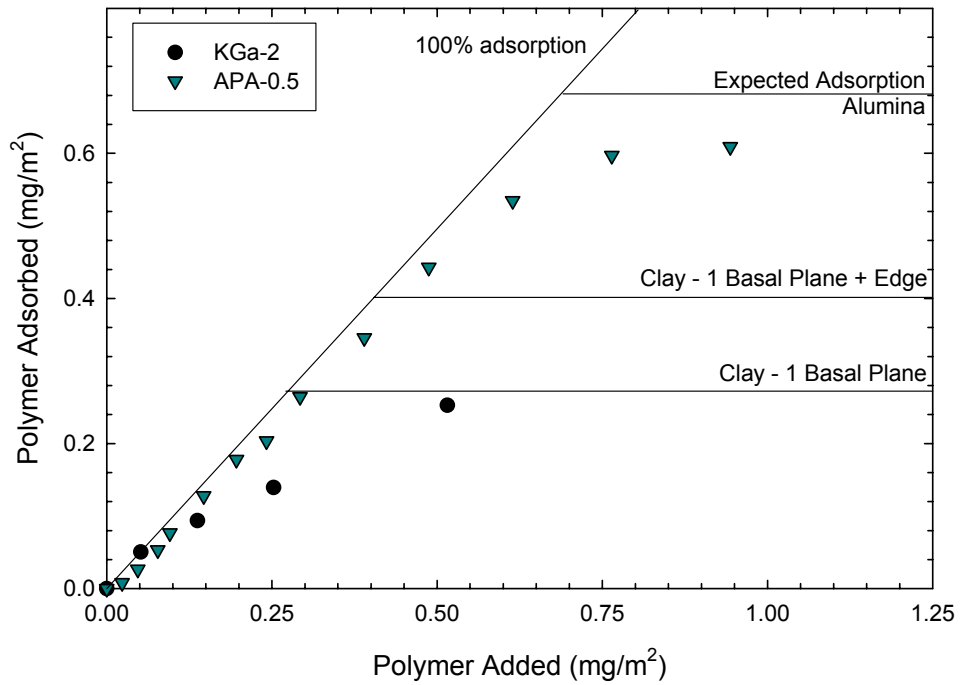


Figure 2-10. Adsorption isotherm for KGa-2, a source clay consisting primarily of kaolinite, at pH 6. The plateau value for adsorption on the kaolinite is observed to approach the value predicted from the model for adsorption on the alumina-like basal plane.

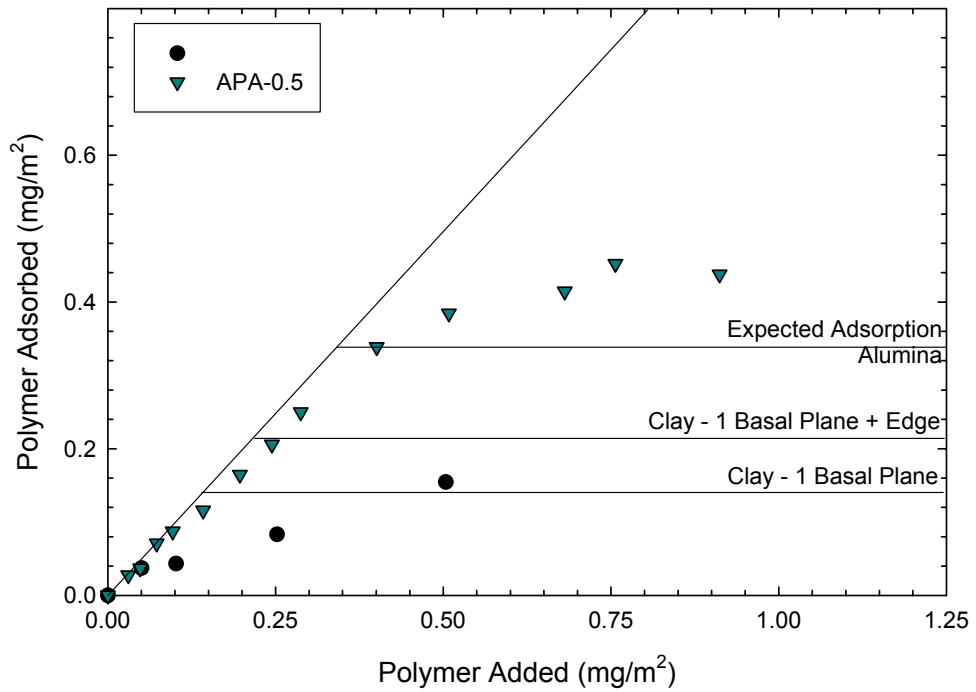


Figure 2-11. Adsorption isotherm for KGa-2, a source clay consisting primarily of kaolinite, at pH 9. The plateau value for adsorption is observed to approach the value predicted from the model for adsorption on the alumina-like basal plane.

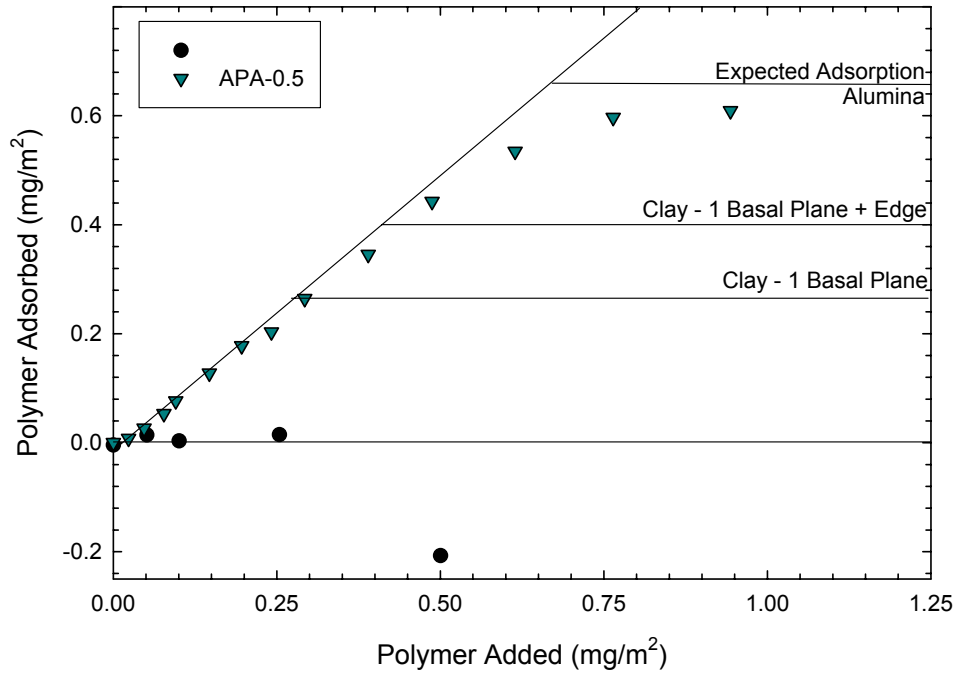


Figure 2-12. Adsorption isotherms for STx-1 a source clay consisting primarily of a calcium montmorillonite, at pH 6. Adsorption is observed to be negligible or negative due to the low affinity of the PAA for the 2:1-layer silicate.

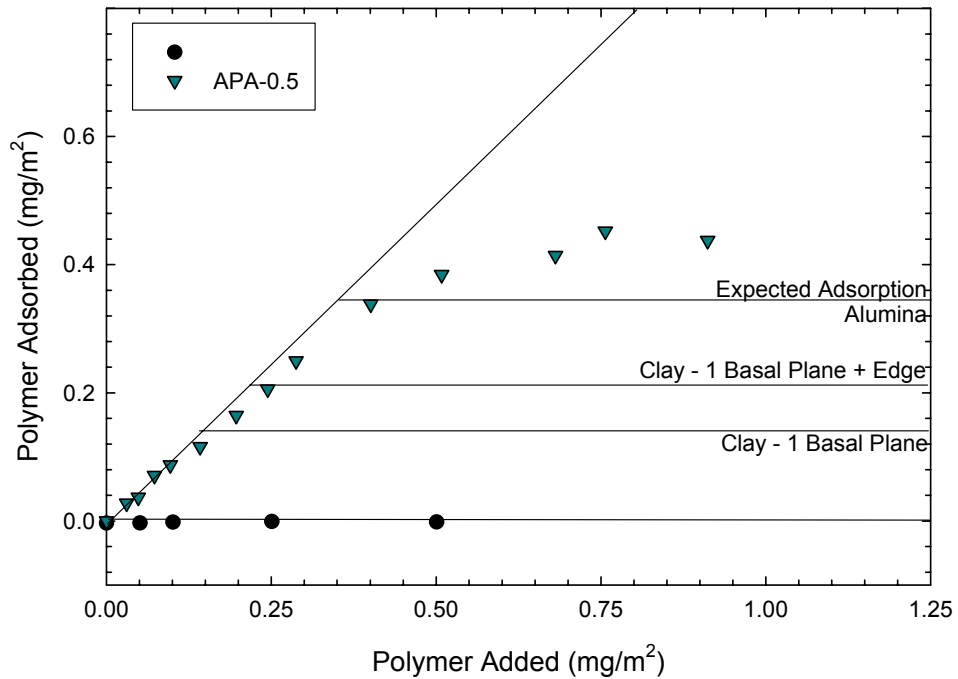


Figure 2-13. Adsorption isotherm for STx-1, a source clay consisting primarily of calcium montmorillonite, at pH 9. Adsorption on the montmorillonite surface is observed to be slightly negative due to the low affinity of the negatively charged PAA for the 2:1-layer silicate.

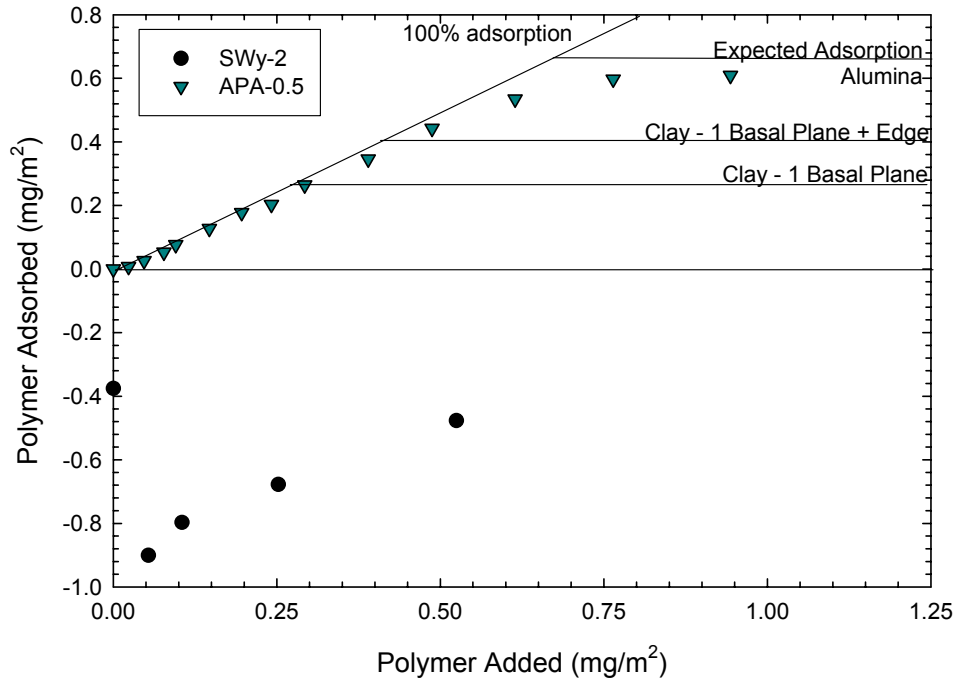


Figure 2-14. Adsorption isotherm for SWy-2, a source clay consisting primarily of a sodium montmorillonite, at pH 6 on 2.5 v/o suspension. Negative adsorption levels are measured on the montmorillonite surface due to the delamination of the swellable mineral.

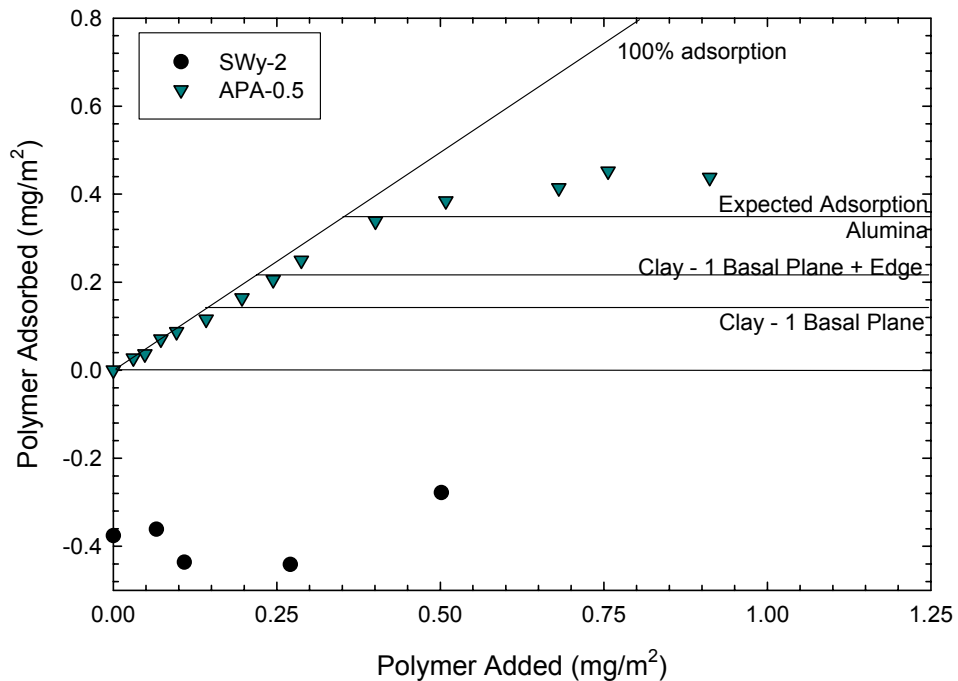


Figure 2-15. Adsorption isotherm for SWy-2, a source clay consisting primarily of a sodium montmorillonite, at pH 9 on 2.5 v/o suspension. Negative adsorption levels are measured for the montmorillonite surface due to the delamination of the swellable mineral.

Table 2-II. Equilibrium pH of a 1 v/o Suspension of the Source Clay Minerals Used in this Study.

Clay Sample	Equilibrium pH
KGa-2	3.56
STx-1	7.35
SWy-2	9.37

Only small quantities of Darvan™ 811 were observed to adsorb on the surface of the STx-1 sample. The STx-1 is a Ca-montmorillonite which is a 2:1-layer silicate, i.e., an alumina-like layer sandwiched between two silica-like layers. Therefore the two basal planes are silica-like in nature while the edge is a combination of silica-like and alumina-like sites. According to the model proposed by Carty, PAA would have little affinity for the basal surfaces of a 2:1-layer silicate and may only adsorb on the edge of the platelet.

The adsorption isotherms for the SWy-2 are unclear. The swellable nature of the Na-montmorillonite resulted in very fine particulate as the clay delaminated in suspension. This resulted in a very high viscosity for the 2.5 v/o suspension that was used for adsorption. This combination of factors hindered the settling of the particles during the centrifuging process. Titration of the supernatant, which contained significant quantities of particulate, resulted in a gel due to flocculation of the particulate; at pH 2 after titration the edge has a slight positive charge (due to the alumina-like sites) and the faces were both negatively charged or net neutral resulting in edge to face agglomeration. All adsorption levels for the SWy-2 were observed to be negative indicating that more “organic” was detected in solution than was originally added to the suspension. The presence of pH-active sites on the clay surface further confounded the titration technique since a differential method was used to determine the concentration of polymer remaining in suspension.

The adsorption isotherms for the Tamsil 8 silica powder are shown in Figure 2-16 (pH 6) and Figure 2-17 (pH 9). The results showed that no adsorption of Darvan™ 811 occurred on the silica surface. The silica surface has a negative charge at the pH values used to generate adsorption isotherms.

Therefore the negative particle surface and negative polymer chain electrostatically repelled each other due to the like charges and PAA does not adsorb on silica surfaces. All adsorption levels were observed to be negative, indicating that more “polymer” was detected in the supernatant than was originally added to the suspension, and the amount of material detected in the supernatant increases with increasing addition of PAA. Some species present in the Tamsil 8, whether a salt or an organic, remained in the supernatant and was titrated while determining the concentration of polymer remaining in solution.

The effects of alumina (APA-0.5) solids loading on the adsorption of Darvan™ 811 at pH 6 and 9 are shown in Figure 2-18. At pH 6 adsorption of PAA was observed to be independent of solids loading and the average concentration of polymer adsorbed on the alumina surface was approximately  $0.62 \text{ mg/m}^2$ , very close to the value indicated by Cesarano et al. At pH 9 a different behavior was observed, adsorption was a function of solids loading. Initially low concentrations of polymer adsorb on the alumina surface and, above 15 v/o alumina, a plateau was observed at approximately  $0.29 \text{ mg/m}^2$ . This difference in adsorption behavior was an artifact of the surface charge on the alumina. At pH 6 the surface was positively charged and there was an electrostatic driving force for adsorption, i.e., the particle was positively charged and the polymer is negatively charged. At pH 9, close to the iep of alumina, the particle surface had no net charge. The negatively charged polymer was not electrostatically attracted to the particle surface. Therefore the particle and the polymer need to be in close proximity for adsorption to occur. At some critical distance, which is not known, the polymer and the particle surface will be obscured from each other and adsorption will not occur. Above a critical solids loading, determined to be approximately 15 v/o in this study, there is sufficient alumina in the system that the polymer is always near to a particle surface thus facilitating adsorption.

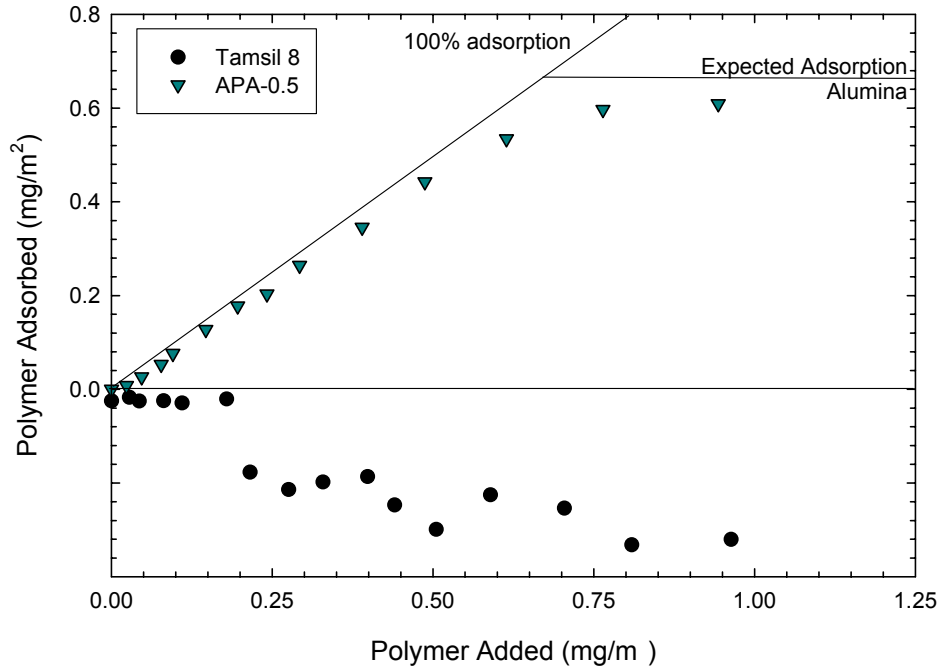


Figure 2-16. Adsorption isotherm for Tamsil 8 (silica) at pH 6. Negative adsorption values are observed for all additions of PAA.

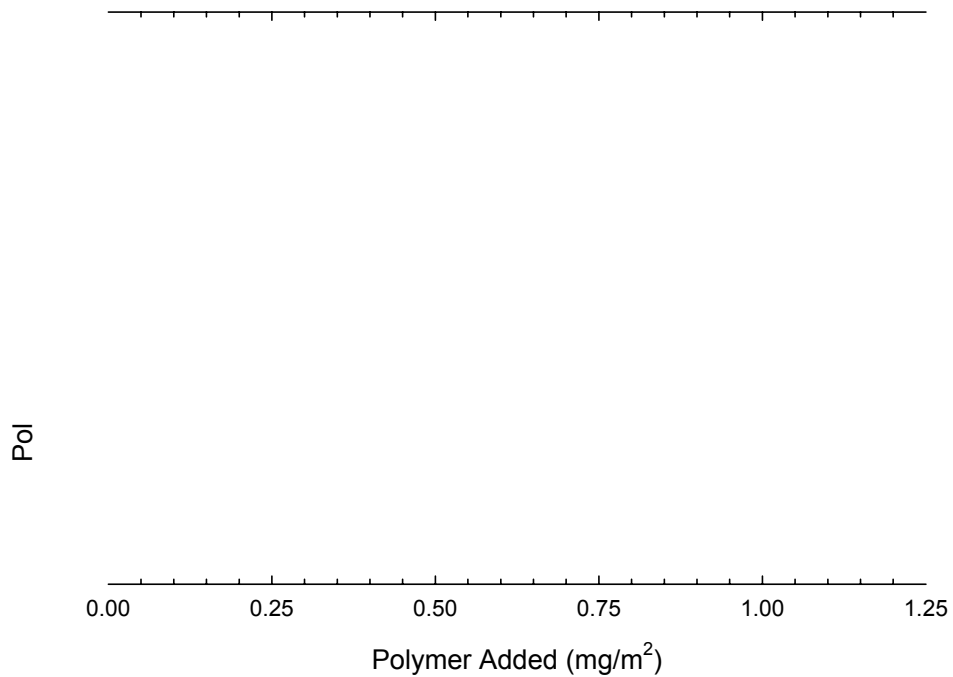


Figure 2-17. Adsorption isotherm for Tamsil 8 (silica) at pH 9. Negative adsorption values are observed for all additions of PAA.

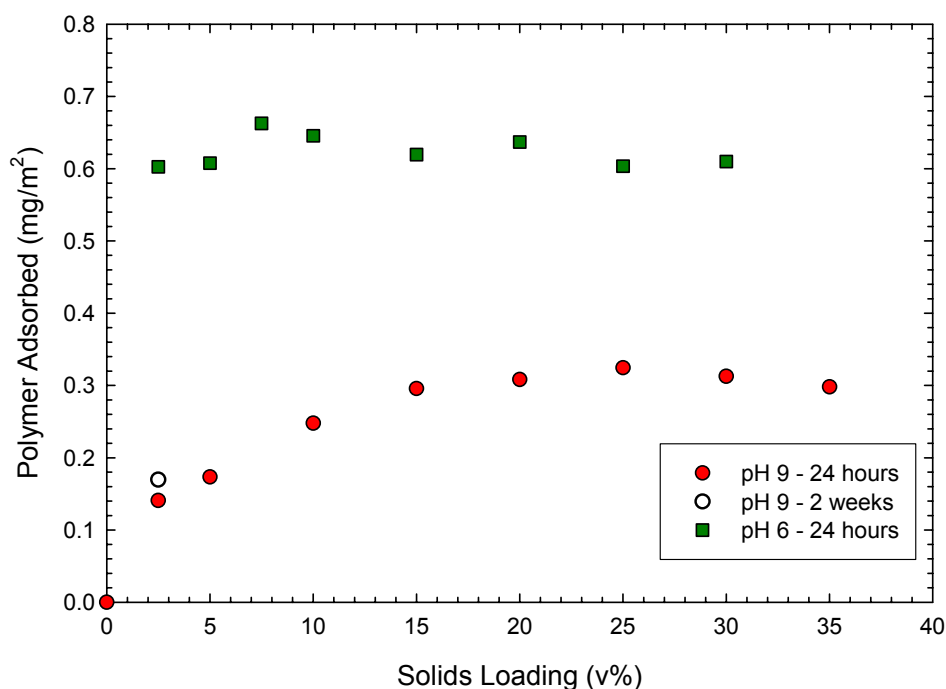


Figure 2-18. Effect of solids loading on the adsorption of Darvan™ 811 on alumina (APA-0.5) powder. Adsorption levels increase with solids loading at pH 9 due to weak adsorption, i.e., there is no electrostatic attraction between the particle surface and the polymer. A plateau is observed at 15 v/o. At pH 6 adsorption is independent of solids loading due to the electrostatic attraction between the alumina surface and the polymer, i.e., strong adsorption.

Digital images were taken of the diluted supernatant, prepared for titration, from the alumina, Tamsil 8, and the source clay samples. These images were taken to document the change in the coloration of the supernatant. No apparent change in the coloration was observed with the exception of the SWy-2 source clay sample which appears green due to the fine particulate remaining in suspension after centrifuging the samples; the as-received sample of SWy-2 from the Source Clay Repository was green. The images of the supernatant are shown in Figure 2-19 (APA-0.5, pH 6), Figure 2-20 (Tamsil 8, pH 6), Figure 2-21 (KGa-2, pH 6), Figure 2-22 (KGa-2, pH 9), Figure 2-23 (STx-1, pH 6), Figure 2-24 (STx-1, pH 9), Figure 2-25 (SWy-2, pH 6), and Figure 2-26 (SWy-2, pH 9).



Figure 2-19. Digital image of the diluted supernatant from the alumina samples at pH  $6.0 \pm 0.2$ . No coloration of the supernatant is observed.

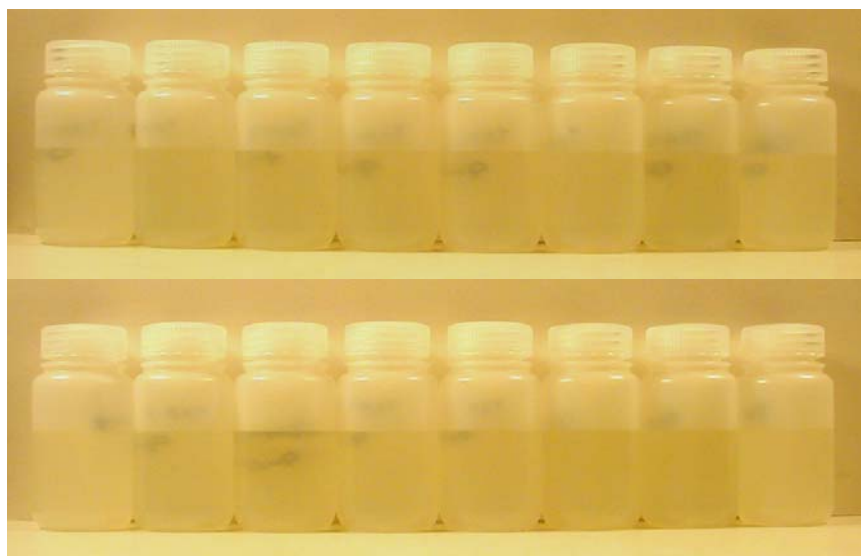


Figure 2-20. Digital image of the diluted supernatant from the Tamsil 8 samples prepared at pH  $6.0 \pm 0.2$ . The concentration of PAA in the samples increases from left to right and from top to bottom. No coloration of the supernatant is observed.



Figure 2-21. Digital image of the diluted supernatant from the KGa-2 samples prepared at  $\text{pH } 6.0 \pm 0.2$ . The concentration of PAA increase from left to right. No coloration of the supernatant is observed.



Figure 2-22. Digital image of the diluted supernatant from the KGa-2 samples prepared at  $\text{pH } 9.0 \pm 0.2$ . The concentration of PAA increases from left to right. No coloration of the supernatant is observed.



Figure 2-23. Digital image of the diluted supernatant from the STx-1 samples prepared at  $\text{pH } 6.0 \pm 0.2$ . The concentration of PAA increases from left to right. No coloration of the supernatant is observed.



Figure 2-24. Digital image of the diluted supernatant from the STx-1 samples prepared at  $\text{pH } 9.0 \pm 0.2$ . The concentration of PAA increases from left to right. No coloration of the supernatant is observed.



Figure 2-25. Digital image of the diluted supernatant from the SWy-2 samples prepared at pH  $6.0\pm 0.2$ . The concentration of PAA increases from left to right. The supernatant appears opaque at high concentration of PAA due to the presence of fine particles remaining in suspension after centrifuging.



Figure 2-26. Digital image of the diluted supernatant from the SWy-2 samples prepared at pH  $9.0\pm 0.2$ . The concentration of PAA increases from left to right. The supernatant appears opaque at high concentration of PAA due to the presence of fine particles remaining in suspension after centrifuging.

## **2.5 Summary and Conclusions**

The adsorption plateau for Na-PAA on an alumina surface has been demonstrated to fall near the plateau values from the work of Cesarano et al. Adsorption of Na-PAA on the surface of a kaolinitic clay, Huntingdon ball clay, has been demonstrated to deviate significantly from the predicted values proposed by Carty. These predicted values were determined using a model for adsorption based upon the mineralogy of kaolinite, the primary mineral in kaolinitic clays. Adsorption of Na-PAA's on alumina and a kaolinitic clay has been demonstrated to be independent of molecular weight within the range tested, i.e., up to 55,000 Daltons.

Adsorption isotherms generated using source clays demonstrate that the model proposed by Carty was accurate for kaolinite. The adsorption isotherms for KGa-2, a nearly pure kaolinite, fell near the predicted levels from the model at pH 6 and 9. Adsorption on STx-1, a non-swelling Ca-montmorillonite, was found to be negligible due to the mineralogy of montmorillonite (a 2:1-layer silicate). Adsorption on SWy-2, a swelling Na-montmorillonite, was unclear due to the very fine particles that remain in suspension after centrifuging the sample. Negative adsorption levels were measured on the surface of the silica powder.

Therefore adsorption of an anionic polyelectrolyte, at the pH values used in this study, occurs only on the alumina-like basal plane and possibly the edge of the kaolinite platelet. Furthermore adsorption of Na-PAA could only occur on the edge of 2:1-layer silicates, specifically montmorillonite, due to the silica-like basal planes on the surface. Deviations from the proposed adsorption levels in the commercial clays were caused by the presence of a dark material in the supernatant at either pH 9 or with higher additions of Na-PAA.

## 2.6 References

1. C.A.J. Hoeve, "Theory of Polymer Adsorption at Interfaces," pp. 1-10 in *Polymers at Interfaces*. Edited by M.J. Schick. Interscience Publishers, New York, New York, 1971.
2. "Adsorption," pp. 551-567 in *Encyclopedia of Polymer Science and Technology*, Vol. 1. Edited by H.F. Mark, N.G. Gaylord, and N.M. Bikales. Interscience Publishers, New York, New York, 1967.
3. L.K. Koopal, "The Effect of Polymer Polydispersity on the Adsorption Isotherm," *J. Colloid Interface Sci.*, **83** [1] 116-29 (1981).
4. R. Ramachandran and P. Somadundaran, "Competitive Adsorption of Polyelectrolytes: A Size Exclusion Chromatographic Study," *J. Colloid Interface Sci.*, **120** [1] 184-88 (1987).
5. A.W.M. de Laat and G.L.T. van den Heuvel, "Competitive and Displacement Adsorption of Polyvinyl Alcohol and the Ammonium Salt of a Polyacrylic Acid on BaTiO<sub>3</sub>," *Colloids Surf., A*, **70** [2] 179-87 (1993).
6. A.W.M. de Laat and G.L.T. van den Heuvel, "Molecular Weight Fractionation in the Adsorption of Polyacrylic Acid Salts onto BaTiO<sub>3</sub>," *Colloids Surf., A*, **98** [1-2] 53-9 (1995).
7. A.W.M. de Laat, G.L.T. van den Heuvel, and M.R. Bohmer, "Kinetic Aspects in the Adsorption of Polyacrylic Acid Salts onto BaTiO<sub>3</sub>," *Colloids Surf., A*, **98** [1-2] 61-71 (1995).
8. J. Cesarano III and I.A. Aksay, "Stability of Aqueous  $\alpha$ -Al<sub>2</sub>O<sub>3</sub> Suspension with Poly(methacrylic acid) Polyelectrolyte," *J. Am. Ceram. Soc.*, **71** [4] 250-5 (1988).
9. C. De Stefano, A. Gianguzza, D. Piazzese, and S. Sammartano, "Quantitative Parameters for the Sequestering Capacity of Polyacrylates Towards Alkaline Earth Metal Ions," *Talanta*, **61** [2] 181-94 (2003).
10. C. Geffroy, J. Persello, A. Foissy, P. Lixon, F. Tournilhac and B. Cabane, "Molar Mass Selectivity in the Adsorption of Polyacrylates on Calcite," *Colloids Surf., A*, **162** [1-3] 107-21 (2000).
11. J.S. Duca and A.J. Hopfinger, "Molecular Modeling of Polymers 18. Molecular Dynamics Simulation of Poly(acrylic acid) Copolymer Analogs. Capture of Calcium Ions as a Function of Monomer Structure, Sequence, and Flexibility," *Comput. Theor. Polym. Sci.*, **9** [3-4] 227-44 (1999).
12. K. Ogawara, S. Kawazoe, T. Tamura, S. Kawauchi, M. Satoh, and J. Komiyama, "Divalent Counterion Binding on Na-poly( $\alpha$ -hydroxyacrylate)," *Polymer*, **39** [2] 437-40 (1998).
13. B.M. Schulz, "Characterization of Gypsum Mold Materials"; M.S. Thesis. Alfred University, Alfred, New York, 1996.

14. J. Cesarano III and I.A. Aksay, "Processing of Highly Concentrated Aqueous  $\alpha$ -Alumina Suspensions Stabilized with Polyelectrolytes," *J. Am. Ceram. Soc.*, **71** [12] 1062-67 (1988).
15. "Colloidal Properties of Alumina," pp. 111-15 in *Alumina as a Ceramic Material*. Edited by W.H. Gitzen. The American Ceramic Society, Westerville, Ohio, 1970.
16. W.M. Carty, "The Colloidal Nature of Kaolinite," *Am. Ceram. Soc. Bull.*, **78** [8] 72-6 (1999).
17. M.T. Brumbach, "Surface Charge, Rheology, and Variability of Kaolinitic Clays"; M.S. Thesis. Alfred University, Alfred, New York, 2002.
18. "Clay Minerals Society Source Clays," *Clays Clay Miner.*, **49** [5] 371-452 (2001).
19. U. Kim, "Role of Polymer Compatibility in Ceramic Processing"; Ph.D. Thesis. Alfred University, Alfred, New York, 2002.

### **3. Washing and Beneficiation of Raw Clays to Remove Organic and Inorganic Impurities**

#### **3.1 Introduction**

Polymeric dispersants are commonly used in industry to control the rheology of colloidal particle systems. This work focuses on the adsorption of Na-PAA, specifically Darvan™ 811, on the surface of commercially available kaolinitic clays. The concentration of adsorbed polymer was predicted based upon on the work of Cesarano and Aksay<sup>1</sup> with alumina and a model based upon the mineralogy of kaolinite,<sup>2</sup> the primary mineral in kaolinitic clays. The effects of impurity minerals and naturally-occurring-organic species were determined by performing a washing and beneficiation process.

It was the purpose of this study to determine the effects of mineral and organic impurities present in commercial clays (termed “raw” to signify the fact that the clay has not been altered) on the adsorption of Na-PAA. The results of this study were used to validate the proposed model for polymeric adsorption on a kaolinite surface.

Previous work, reported in Chapter 2, studying the adsorption of various molecular weight Na-PAA polymers on the surface of alumina, APA-0.5, and Huntingdon ball clay found a significant deviation between the predicted and actual adsorption levels on the surface of ball clay. The model for adsorption on clay surfaces assumed that adsorption of the polymer occurred on the alumina-like basal plane of the kaolinite platelet with possible adsorption on the platelet edge. Depending on the dimensions of the clay platelet, i.e., the 2L:h ratio, the amount of polymer adsorbed was predicted as a percentage of the polymer that would adsorb on an alumina surface, on a mg/m<sup>2</sup> basis to normalize for the difference in specific surface area. Since the affinity of the dispersant for the edge of the clay platelet is unknown, two predictions have been made for polymer adsorption; one for adsorption only on the alumina-like basal plane and the other which considers adsorption on the alumina-like basal plane and the platelet edge.

Adsorption studies using silica and well characterized source clays, purchased from the Clay Minerals Society, provided some insight into the effects of inorganic impurities. Darvan™ 811 was observed to not adsorb on the surface of silica or 2:1-layer silicates, specifically montmorillonite. Work with KGa-2, a nearly-pure kaolinite source clay, was observed to verify the proposed model by Carty for adsorption on kaolinite.

### **3.2 Literature Review**

Kelly developed a method to determine the organic matter response in clays.<sup>3-5</sup> The method involved determining the concentration of organic matter present in the clay by dissolution of the organic material in an alkali solution, specifically NaOH, NaCO<sub>3</sub>, and sodium silicate (all solutions were 0.25 N). The concentration of organic species in the supernatant was determined photometrically by the absorbance between wavelengths of 366 and 600 (unspecified units). Based upon Kelly's results NaCO<sub>3</sub> was most effective at extracting organic material from the clays tested. Based upon this conclusion a broader test with 20 clay samples was performed using 0.25 N NaCO<sub>3</sub> as the extractant. By repeatedly treating the clay sample with the digestant solution more organic material could be removed from the clay. A hydrogen peroxide treatment was found to be more effective than NaCO<sub>3</sub> at removing organics from the clay. A correlation was found between the concentration of organic removed from the clay and the total concentration of organic prior to treatment, determined by LOI.

While the organics present in clay are commonly referred to as lignite this is not an accurate description. The organic material in clays are humic substances consisting of humin, humic acid, and fulvic acid; while other humic substances have been found it has been determined that they are actually subgroups of these three categories. Other non-humic substances in clays consist of tannins, carbohydrates, waxes, resins, and fats; all by-products from the decomposition of plant and animal remains.<sup>6-12</sup> Humic substances are formed by the microbial action on plant (lignite) and animal residue. These materials are differentiated by their solubility in aqueous conditions; see Figure

3-1 for a schematic illustration of the properties of humic substances. Humin is an insoluble material that has a black appearance and a high molecular weight, greater than 300,000 Daltons. Solutions of humic acid have a gray to brown appearance. Humic acid is soluble in alkali conditions. Fulvic acids have a yellow to golden appearance in solution and are soluble at all pH values. Humic acids and fulvic acids are primarily differentiated by their solubility, humic acid will precipitate from solution at a pH less than 2.5. Further distinctions between humic and fulvic acid involve the relative amounts of carbon and oxygen in the structure; humic acids have a higher carbon content while fulvic acids have a higher oxygen content. These properties can be extrapolated to state that fulvic acids have more functional groups in their structure, accounting for the difference in molecular weight.<sup>6,9,13-20</sup> These are only general rules used to distinguish between humic and fulvic acids; a schematic illustration of the structure of humic acid is shown in Figure 3-2 and fulvic acid is shown in Figure 3-3.<sup>6</sup>

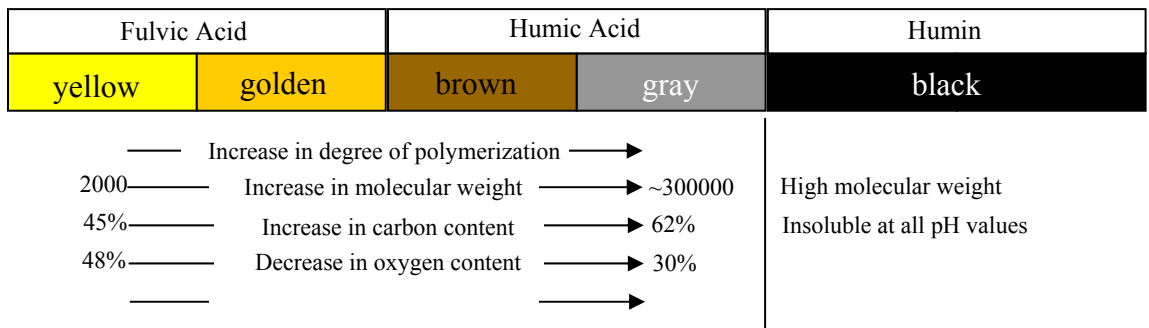


Figure 3-1. Schematic showing the relative properties of humic substances and the coloration of solutions prepared from humic substances (adapted from Stevenson<sup>6</sup>).

Lignite can be decomposed in the laboratory by treatment with either hydrogen peroxide or heated 1N sodium hydroxide.<sup>6</sup> Both of these methods serve to breakdown the lignite structure into lower molecular weight species. The presence of sodium ions in solution can also serve to increase the solubility of naturally-occurring organics.<sup>4,5</sup>



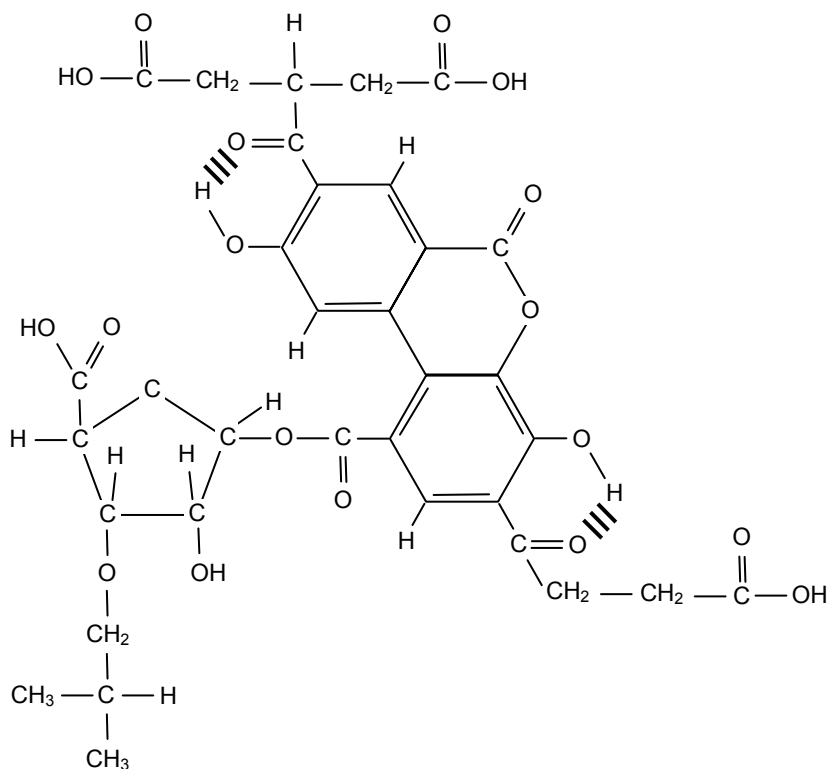


Figure 3-3. Proposed average structure of Suwannee River fulvic acid (adapted from Stevenson<sup>6</sup>).

Humic substances are formed by microbial action on organics present within the soil. These organics can be from plant residue (lignite, cellulose, and carbohydrates) or animal residue (tannins, fats, waxes, etc.). Four pathways are generally accepted for the formation of humic substances from plant residues, shown schematically in Figure 3-4.<sup>6</sup> The structure of the principle organics is complex consisting of aromatic carbon rings and linear hydrocarbon chains. Microorganisms serve to transform the plant residues into useful building blocks for humic substances. These building blocks consist of smaller, simpler organic structure such as sugars, amino compounds, polyphenols, and other decomposition products. The nature of these decomposition products is dependent on the chemical nature of the starting material, e.g., humic substances from a coniferous forest would differ from humic substances from a hardwood forest. The building blocks are then combined by mesomeric free radials in various combinations resulting in a covalent bond between the two mesomeric species. This process continues to form a modified lignin with a high

molecular weight. The lignin (assuming that humic substances represent modified lignins) is then converted to a humic substance through the loss of  $\text{OCH}_3$  groups, resulting in the exposure of phenolic  $\text{OH}$  groups, and the oxidation of the terminal side chains to form  $\text{COOH}$  groups. Bacteria are apparently responsible for the demethylation of lignin without the degradation of the polymer. Animal residues would form humic substances in a similar manner, but the building blocks would differ.<sup>6,21,22</sup>

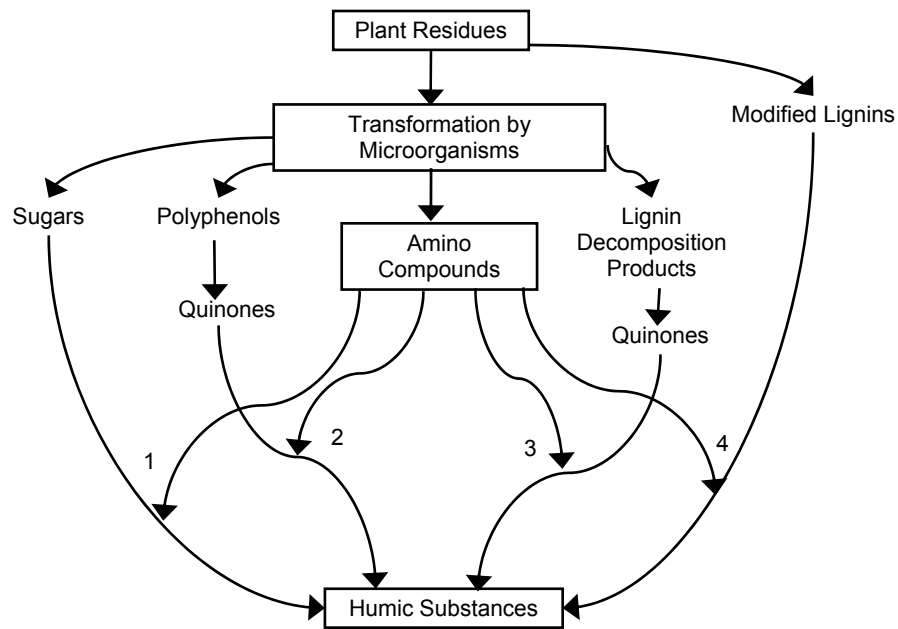


Figure 3-4. Schematic showing the mechanisms for the formation of humic substances from plant residue. Four possible pathways are illustrated: 1) reducing sugars, 2 and 3) by reacting quinines, and 4) through modified lignins (adapted from Stevenson<sup>6</sup>).

The solubility of humic substances can be related back to their structure. Both humic and fulvic acid can contain carboxylic acid ( $-\text{COOH}$ ), alcoholic ( $-\text{OH}$ ), ketonic ( $>\text{C}=\text{O}$ ), and amine ( $-\text{NH}_2$ ) groups. These groups can be protonated or deprotonated as a function of  $\text{pH}$ , similar in behavior to PMAA and PAA. While the exact  $\text{pH}$  at which these reactions occur differ from PMAA and PAA, due to the bonding environment, the presence of these species in solution can interfere

with a titration technique to determine the concentration of polymer remaining in solution after adsorption.<sup>6,8,13,15,20,23-30</sup>

There are two ways to consider the presence of humic substances in aqueous solutions.<sup>6,31-38</sup> The first is to consider the humic substance a soluble organic that changes conformation and solubility as a function of pH so that the humic substances can be fractionated. The second is to consider the humic substance as a colloidal particle, i.e., a very fine particle, that is insoluble and which still has pH active sites on the surface. At low pH these colloids have no net charge allowing aggregation and sedimentation of the higher molecular weight species. At high pH the colloids have a net negative charge that prevents aggregation (enhances dispersion) and thus the dispersed species will not settle in a centrifugal field. Both theories on humic substances allow for adsorption on particle surfaces.<sup>6,9,19,33,39-79</sup> The colloidal theory predicts a change in the “molecular weight” of the humic substances as a function of pH, i.e., the aggregated cluster will be composed of many colloidal particles thus increasing the measured molecular weight at low pH. For the remainder of this thesis the term “soluble humic substance” will be taken to include the colloidal aspects of humic substances.

Soluble humic substances are known to have a cation exchange capacity (cec). The presence of the deprotonated functional groups in the humic substances allows cations to bond to the humic structure and preferential bonding with higher valence cations.<sup>6,23,27,29,35-37,39,41,45-49,51,60,66,67,73,78,80-91</sup> While monovalent cations will bond to the functional groups, the humic species will remain soluble in aqueous solutions, provided that the pH allows dissolution. Chelation with higher valence cations will decrease the solubility of humic substances. Once the functional groups are saturated with chelated ions the result is an insoluble species. The cation exchange capacity of humic substances has been determined to range from 485-870 cmole<sub>e</sub>/kg for humic acids and values up 1400 cmole<sub>e</sub>/kg for fulvic acids.<sup>6</sup> The values are significantly higher than typical cec values for clays, shown in Table 3-I.

The interactions between humic substances and dissolved cations have been documented in numerous studies. Most of these studies investigate the ability of humic substances to chelate toxic substances, e.g., mercury and heavy metal cations, from water. These studies are of interest since removal of these species from water prevents the toxic substances from entering the ecosystem.

Table 3-I. Typical cec Values for Clay Species and Humic and Fulvic Acids.<sup>6</sup>

<b>Material</b>	<b>CEC (cmole<sub>c</sub>/kg)</b>
Kaolinite	3-5
Illite	30-40
Montmorillonite	80-150
Vermiculite	100-150
Humic Acid	485-870
Fulvic Acid	Up to 1400

Humic substances are known to adsorb on the surface of clays. Several theories have been proposed for the mechanism of adsorption, in addition to the theories already discussed in Chapter 2:<sup>6</sup>

- 1) physical adsorption (van der Waals forces)
- 2) electrostatic attraction or chemical adsorption
- 3) hydrogen bonding
- 4) coordination complexes (chelation)

While strictly speaking the last two categories are subgroups of the first two categories they will be discussed separately. Van der Waals forces occur through an induced dipole and result in weak bonds between materials. These forces play a significant role in the adsorption of nonionic or nonpolar species, when working with humic and fulvic acids van der Waals interactions play only a minor role below a pH of 9.5, the iep of alumina. Below this pH the surface of the particle is charged and the humic substance has a net negative charge due to deprotonation of the functional groups. Due to the charged nature of the particle and organic species electrostatic attraction plays a more significant role in

adsorption. Hydrogen bonding occurs between two electronegative atoms through bonding with a single  $H^+$  ion, resulting in a slightly stronger bond than is achieved by van der Waals forces. Coordination complexes form between a higher valence metal ion (which is positively charged) and a negative organic species and a negative clay surface. The metal ion serves as a bridge between the two negative species, e.g., a silica-like surface on the clay particle and a deprotonated functional group.

Humic substances have also been identified to specifically adsorb to the surface of alumina, selected as a model substrate for adsorption on clay surfaces.<sup>79</sup> Humic substances were isolated from various water systems, i.e., river and lakes, in Australia and fractionated by their solubility and affinity for the packing material in various columns, e.g., XAD 8. XAD resins are ion exchange resins of various polarity to extract organics from solution. Specific adsorption of the humic substances on the surface of alumina particles was identified by a shift in the iep of the alumina suspension as well as a reduction in yield stress of a 30 v/o alumina suspension. Fulvic acids were identified to affect the greatest shift in the iep of alumina suspensions. This was related to the concentration of functional groups, which were negatively charged, on the fulvic acid species. Silica was also studied as a possible adsorbent for humic substances, but preliminary tests indicated that the silica surface would not be appropriate due to the net negative charge on the silica surface above a pH of 2.0-2.5, the iep of silica.

The protonation and deprotonation of the humic substances result from pH active functional groups in the humic molecule.<sup>6,13,20,84,92,93</sup> Numerous studies have investigated these pH active sites by potentiometric titration of humic substances. Some sites on humic substances, particularly fulvic acid, have been shown to have pKa values as low as 0.5, i.e., these sites are not protonated until a pH of 0.5. Santos et al. have shown that the method of potentiometric titration has limitations when applied to humic substances, including hysteresis in the titration curve.<sup>94</sup> This hysteresis can be caused by variations in the titration method, e.g., “back” titration with acid instead of “direct” titration with base,

variations in the equilibration times between titrant addition, or different calibration procedures.

Nuclear magnetic resonance, NMR, is a technique used to investigate the nature and concentration of functional groups in humic substances.<sup>95-100</sup> The combination of NMR (or NMA, nuclear microprobe analysis) and XPS has proven to be useful in probing the concentration of function groups and the binding energies of humate-metal complexes. Both <sup>13</sup>C and <sup>1</sup>H NMR have been demonstrated to be useful in characterizing the structure of humic substances and in some cases N 1s spectra have been used to identify the presence of amine groups in humic structures.

Clays have been characterized by Fourier transform infrared (FTIR) spectroscopy to study the effects of ionic substitution on the vibrational frequency as adsorption bands.<sup>101-106</sup> Marel and Beutelspacher compiled a series of FTIR spectra for clay minerals from various sources.<sup>101</sup> Small variations are observed in the spectra from the same clay mineral from different sources. The small shifts are due to ionic substitution in the clay structure.

Humic substances are commonly characterized by FTIR, as are many organic materials.<sup>23,70,87,100,107</sup> Studies involving FTIR typically investigate the effects of binding cations to the functional groups on the humic substances. Differences are observed between humic and fulvic acids as well as differences in the spectra of humic substances from various sources. Furthermore evidence of the binding mechanism between humic substances and particulate can be determined by DRIFT. Wiszniowski determined that the binding of humic substances on the surface of TiO<sub>2</sub> is pH dependent with the carboxylate groups being responsible for adsorption in the acidic region.<sup>70</sup> He also concluded that in the acidic region there are free carboxylic acid groups on the humic structure indicating that the humic molecule extends into the solution surrounding the TiO<sub>2</sub> particle.

Yang and Wang studied humic substances using FT-Raman spectroscopy.<sup>108</sup> They prepared samples of humic substances for characterization as well as samples that were treated in boiling acid. Based

upon the collected spectra they deduced that humic substances are built from low molecular weight species consisting of structurally disordered carbon networks.

### **3.3 Experimental Procedure**

#### *3.3.1 Washing and Beneficiation of the Raw Clay*

Preparation of clay samples at high pH resulted in a negatively charged clay surface (both alumina-like and silica-like surfaces were negative above a pH of 9.5) and a deprotonated (negative) functional group on the organic species. Therefore an electrostatic repulsion existed between the organic species and the particle surface. This allowed the organic species to be partially desorbed from the particle surface. Inorganic impurities in kaolinite clays can also be removed from the kaolinite surface using this process due to the similar charges on all the clay surfaces.

Fifty pound samples of raw clay were dispersed in fifty liters of distilled water to create an approximately twenty volume percent suspension. The pH of the suspension was adjusted between 9.5 and 10.5, using 10N NaOH, to disperse the clay and dissolve soluble organics present on the clay surface. The system was mixed for 45 minutes using a high intensity mixer (SHAR Inc., Fort Wayne, IN).

After 45 minutes the mixer was turned off and the suspension was allowed to settle for a period of ninety minutes, the resulting sediment was dried for characterization as the coarse fraction of the clay. Due to the similar density of the materials present in kaolinitic clays segregation occurred primarily by particle size. The material remaining in suspension was decanted off and allowed to settle for an additional ten days. After ten days the material still remaining in suspension was decanted off and dried for characterization as the fine fraction of the raw clay. The settled material was again suspended in fifty liters of distilled water with the pH adjusted between 9.5 and 10.5. This suspension was allowed to settle for an additional ten days. The material remaining in suspension was discarded and the settled material was dried as the middle fraction, assumed to

be beneficiated kaolinite, for characterization. A schematic of the process is shown in Figure 3-5.

This process was used to wash and beneficiate two commercial kaolin clays, TK6 (Dry Branch Kaolin Co., Dry Branch, GA) and Kingsley (Kentucky-Tennessee Clay Co., Nashville, TN), and four commercial ball clays, Huntingdon (United Clays, Brentwood, TN), Marquis (United Clays, Brentwood, TN), M&D (Kentucky-Tennessee Clay Co., Nashville, TN), and C&C (H.C. Spinks Clay Company, Paris, TN). The raw clay and each fraction of the beneficiated clay was characterized by X-ray diffraction on oriented slides, thermal analysis (DTA/TGA), specific surface area (multipoint BET by N<sub>2</sub> adsorption), chemical analysis (inductively coupled plasma), and for polymer adsorption levels (using a titration technique). Data for the composition and chemical analysis of C&C ball clay were taken from the thesis of Caughel.<sup>109</sup>

After the beneficiation process sufficient impurity species (both organic and inorganic) remained in the clay fractions to cause deviations from the predicted adsorption levels. A process of repeated washing was used to further beneficiate the clay fractions for testing of polymer adsorption levels. A sample of the clay fraction was suspended in distilled water at a pH of 9.5 and placed on a shaker table. The suspension was mixed for 24 hours followed by centrifuging the suspension. The material remaining in suspension was discarded and the sediment was resuspended in distilled water. This process was repeated until the supernatant was clear after centrifuging. The clay was then dried and the specific surface area was measured prior to determining the adsorption levels.

### *3.3.2 X-ray Diffraction*

The minerals present in the raw clay and each clay fraction were identified by their d-spacing using oriented slides prepared using the Millipore Filter Transfer technique. Swellable minerals, i.e., smectites, were further identified by ethylene glycol solvation of the oriented slides. More information on the identification of clay minerals by X-ray diffraction on oriented slides can be found in Moore and Reynolds.<sup>110</sup>

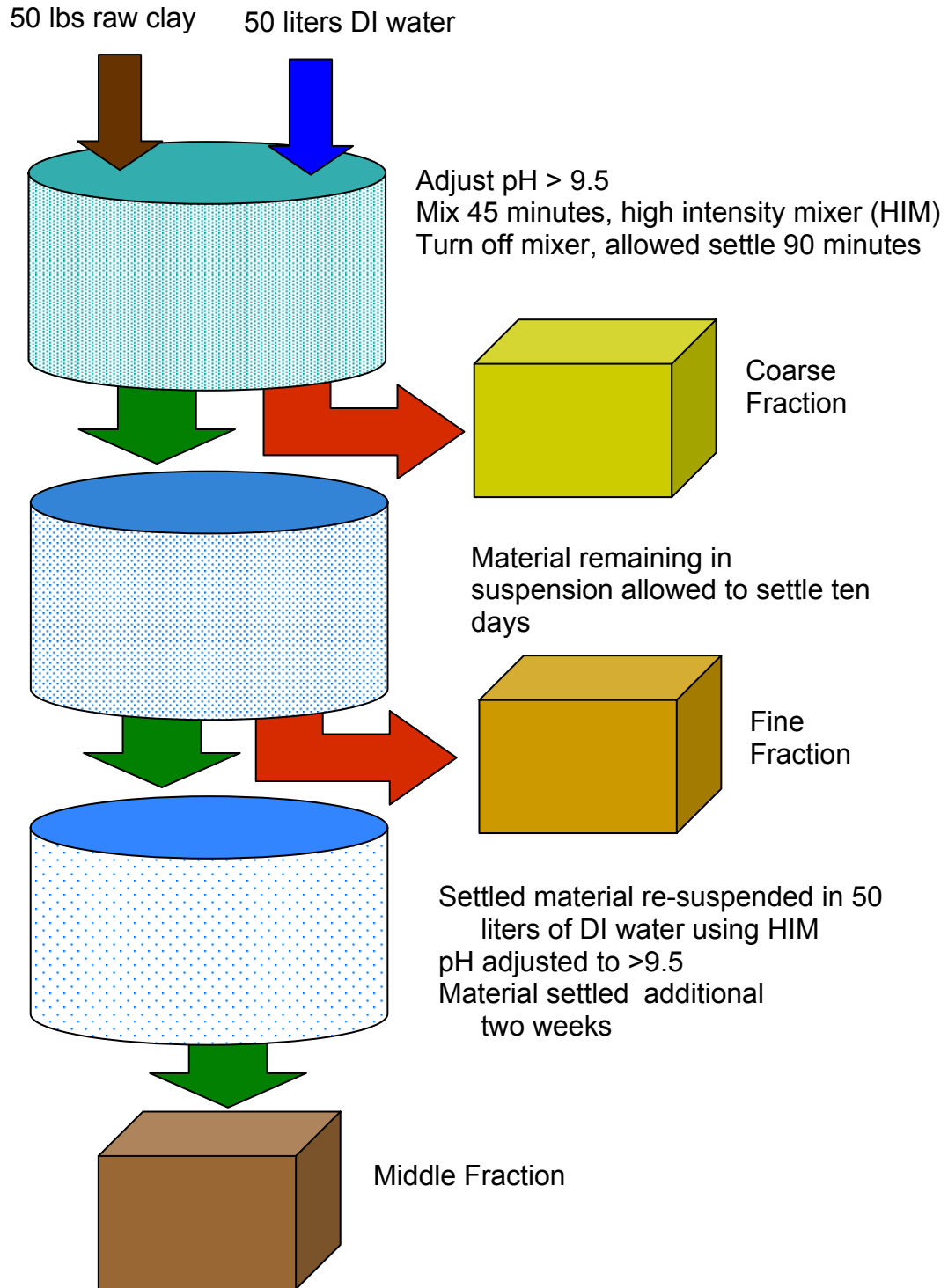


Figure 3-5. Schematic of the process used to wash and beneficiate the raw clay for this study. Due to the volume fraction of the clay suspension, “capture” during sedimentation occurred resulting in fine species within the coarser clay fractions.

### 3.3.3 Thermal Analysis

Differential thermal analysis and thermogravimetric analysis were performed using a simultaneous DSC-TGA (SDT 2960, TA Instruments, New Castle, DE). Loss on ignition (LOI) was determined by the difference in sample weight between the temperatures of 150°C and 850°C. These temperatures were selected so that all of the physical water was removed from the system and the high temperature weight would fall within the high temperature plateau of the test. The LOI was compared to the theoretical LOI for pure kaolinite, calculated as 13.94%, due to the dehydration of the lattice water in the structure. Deviations from the theoretical LOI were the result of impurity species in the raw clay. The presence of quartz or 2:1-layer silicates (e.g., smectite, illite, chlorite) lower the LOI of the clay sample. The presence of organic species in the clay increases the LOI. The amount of free quartz, assuming that only quartz and kaolinite are present in the clay fraction, was determined by the deviation in the LOI from the theoretical loss for pure kaolinite.

The free quartz determined from the LOI was calculated using two equations and two unknowns. The equations used were:

$$f_{\text{quartz}} + f_{\text{kaolinite}} = 1 \quad (2)$$

$$f_{\text{quartz}} * \text{LOI}_{\text{quartz}} + f_{\text{kaolinite}} * \text{LOI}_{\text{kaolinite}} = \text{LOI}_{\text{meas.}} \quad (3)$$

Where  $f_{\text{quartz}}$  and  $f_{\text{kaolinite}}$  were the fraction of quartz and kaolinite respectively and  $\text{LOI}_{\text{meas.}}$  was the measured LOI of the clay sample. Since the theoretical LOI of kaolinite was 13.94% and the LOI of quartz was 0%, rearranging and combining these two equations to solve for the fraction of quartz yielded the equation:

$$f_{\text{quartz}} = 1 - (\text{LOI}_{\text{meas.}}/13.94) \quad (4)$$

A sample calculation to determine the amount of free silica in a commercial clay, based upon the LOI, is shown in Appendix B.

### 3.3.4 Specific Surface Area

The specific surface area (SSA) of the samples was determined via nitrogen adsorption (Gemini 2375, Micromeritics Instruments Corp., Norcross,

GA) on the raw clay and dried fractions prepared by washing and beneficiation. Samples were outgassed for one hour prior to analysis (FlowPrep 060, Micromeritics Instruments Corp., Norcross GA). The SSA was determined using six relative pressures between 0.05 and 0.30, of N<sub>2</sub> gas. A best-fit regression was then performed using the BET method to determine the specific surface area of the powder.

### 3.3.5 Chemical Analysis

Chemical analysis was performed using inductively coupled plasma atomic emission spectroscopy (ICP-AES) at an external laboratory (Acme Analytical Laboratories Ltd., Vancouver, British Columbia, Canada). The chemical analysis was used to determine the amount of free quartz in the system, assuming that the raw clay contained only pure kaolinite with a quartz impurity. Chemical analysis was not performed on the Kingsley clay or the beneficiated fractions from this clay.

The calculation to determine the amount of quartz in the clay using the chemical analysis was slightly more involved. The data provided from the ICP rock analysis of the clay samples is reported as the weight percent of oxides present. The stoichiometry of kaolinite is Al<sub>2</sub>O<sub>3</sub>•2SiO<sub>2</sub>•2H<sub>2</sub>O, or one mole of alumina, two moles of silica, and two moles of lattice water. During ICP the lattice water was evaporated and the result was metakaolin (Al<sub>2</sub>O<sub>3</sub>•2SiO<sub>2</sub>). Therefore for every mole of alumina present in the clay there should have been two moles of silica and any excess silica was assumed to be free quartz. By converting the weight percent data from the ICP to moles the amount of free quartz was determined by taking two times the number of moles of alumina and subtracting the result from the total number of moles of silica. If there was a remainder after subtracting that value was the number of moles of free quartz in the clay sample. The presence of 2:1-layer silicates or other silicate minerals invalidated this method of determining the amount of free quartz present in the clay. A sample calculation to determine the amount of free silica in a commercial clay, based upon the chemical analysis, is shown in Appendix B.

### 3.3.6 Polymer Adsorption

The concentration of polymer remaining in the supernatant after adsorption was determined using a potentiometric technique described in Chapter 2. The described technique was varied to assure that no particulate material remained in the supernatant by increasing the centrifuge time as necessary. Due to the presence of a high concentration of swellable material in the fine fraction of some clays it was necessary to dilute a smaller volume of supernatant; corrections were made in the calculations to compensate for these changes.

### 3.3.7 FTIR Characterization of Clay

Fourier transform infrared spectroscopy, FTIR, (Nexus 870 FTIR E.S.P., ThermoNicolet, Waltham, MA) is useful technique to probe the structure and ionic substitution in clays. Changes in ionic substitution result in a shift in the vibrational frequency of some bands in the collected spectra. Furthermore the presence, and degradation, of organic species in the clay could be determined by collecting a series of spectra at various temperatures. An environmental chamber (Nexus Smart Collector, Spectra Tech, Shelton, CT) was connected to the FTIR so that spectra could be collected *in-situ* at elevated temperatures. At each temperature 400 scans were collected to increase the signal to noise ratio of the spectra. The resolution during the data collection was set at 4  $\text{cm}^{-1}$ . Spectra were collected at room temperature, 125°C, 200°C, 350°C, 500°C, 550°C, 650°C, and after the sample had cooled from its thermal cycle. The samples were allowed to equilibrate for 20 minutes prior to collecting the spectra at each temperature. The environmental chamber was purged with atmospheric air that had been purified using a water trap and a CO<sub>2</sub> filter. The result was a purge gas rich in nitrogen and oxygen. Spectra were collected for each raw clay sample as well as some of the clay fractions from the beneficiation process. For comparison spectra were also collected from a sample of dried Darvan™ 811 and a sample of humic acid as a function of temperature.

Samples for FTIR were prepared by carefully loading a ground clay sample into the crucible of the environmental chamber. While KBr pellets are

customary for performing FTIR analysis of solid samples there are two flaws with this method when performing this type of characterization. First the KBr needs to be stored at an elevated temperature, approximately 50°C, to prevent the KBr salt from absorbing moisture from the air (KBr is hygroscopic and will absorb enough water to form a fluid if the sample is improperly stored). At these temperatures ionic substitution in the clay structure, due to diffusion, can occur thus substituting  $K^+$  for the ions in the clay, thus changing the IR spectra of the clay sample.<sup>111</sup> Second, samples were run in the environmental chamber up to 650°C and at these temperatures the KBr could either sublime or attack the chamber.<sup>112</sup>

### *3.3.8 Commentary on the Selected Clays for this Study*

Kaolin deposits tend to be heterogeneous materials, comprised of more than one mineral, and typically have lower concentrations of free silica (quartz) and organic impurities. Ball clays are also heterogeneous materials and typically have higher concentrations of quartz and organic impurities. Ball clays typically have a significantly higher specific surface area relative to kaolin clays due to extensive weathering in stream beds. These clays were selected to provide a broad spectrum of impurities for analysis using the titration technique.

## **3.4 Results**

### *3.4.1 Qualitative Observations*

Suspensions prepared with kaolin clays were observed to have a much lighter supernatant after centrifuging. This is assumed to be due to the presence of primarily fulvic acid in the raw clay, which creates a light yellow solution, as opposed to humic acid which results in a dark brown solution. Fulvic acid is a water soluble organic species at all pH values with a low molecular weight, low carbon content, and relatively high oxygen content. Samples prepared with ball clays tended to have a much darker supernatant indicating the presence of humic acid in solution. Humic acid is a water soluble organic species at high pH due to its higher molecular weight and higher carbon content. Insoluble organic matter can also be present in the raw clay in the form of humin. Since humin is

insoluble at all solution pH values it will not be discussed in reference to the titration results.<sup>6</sup> The presence of humin in the clay must still be considered during firing since it can result in defects such as black core, but that is a topic outside of this thesis.

Raw clays that contained a high concentration of swellable clay minerals were problematic in the washing and beneficiation process. Most noticeable was M&D, which contained a large quantity of smectite as well as a high concentration of divalent cations. This combination of factors resulted in a system that did not settle over the ten day period in this study. Therefore the suspension was further diluted to decrease the particle-particle interactions and reduce the cation concentration followed by high intensity mixing. The beneficiation process was then repeated to segregate the minerals present in the raw clay by sedimentation.

During the beneficiation process the swellable minerals were concentrated into the fine fraction from the raw clay. It was observed that suspensions prepared using the fine clay fraction were often of higher viscosity even when completely dispersed and resulted in a thicker settled layer after centrifuging the sample. The soluble organic species that were present in the raw clay were also concentrated in the fine fraction since the majority of the water from the washing process served as a carrier for the fine fraction. This water was removed, by evaporation, to isolate the fine fraction. During the drying process the soluble organics precipitated within the consolidated layer of the dried clay.

#### *3.4.2 Verification of pH Active Species in Supernatant*

Prior to commencing an in depth study to determine the effects of removing impurity species it was necessary to verify that pH active species were present in the supernatant from the clay suspensions. A 15 v/o Huntingdon suspension was prepared at high pH, greater than 9.5, without addition of polymeric dispersant. The system was placed on a shaker table for seven days to reach equilibrium; the pH was checked daily and maintained above 9.5. The suspension was then centrifuged and the supernatant, which was very dark, was removed and titrated using the technique described in Chapter 2. The titration

curve from the supernatant was compared to that of distilled water with an initial pH above 10.5. The resulting curves are shown in Figure 3-6. While both curves show two inflection points, more HCl was necessary to titrate the supernatant sample relative to distilled water. This corresponded to a concentration of 0.134 milligrams of PAA in the supernatant; this was determined using the calibration curve for Darvan™ 811. Based upon the specific surface area of the Huntington ball clay this was equivalent to a surface coverage of 0.041 mg/m<sup>2</sup>. This indicated that a pH active species was present in the supernatant of the clay suspension without any addition of PAA. A dark brown precipitate was formed upon titration of the supernatant from the Huntington sample to a pH of 2; based upon the precipitation of the material in an acidic solution this material was presumed to be humic acid.

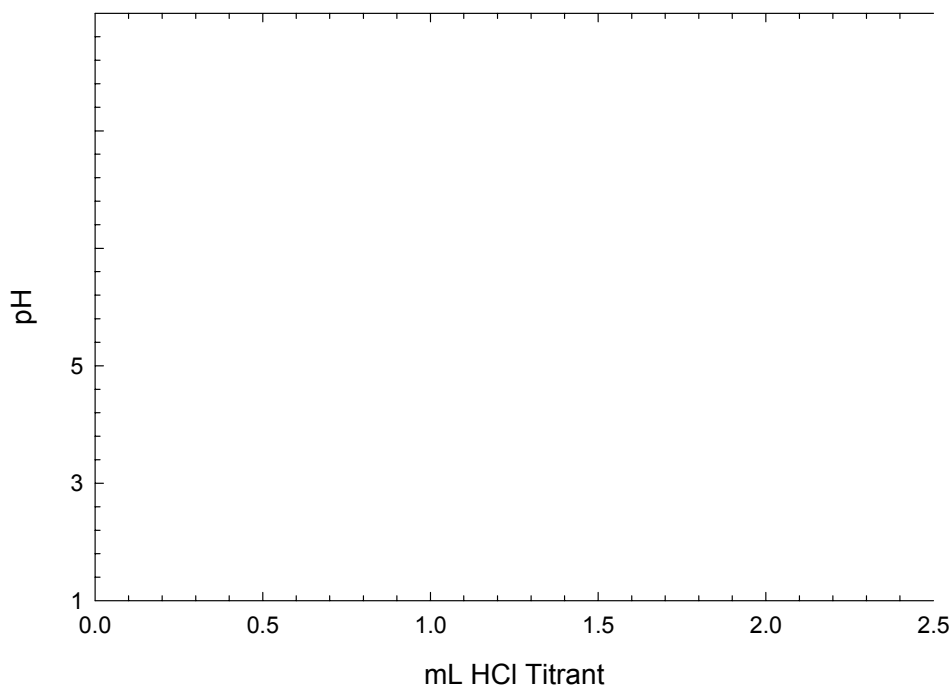


Figure 3-6. Titration curves from a sample of distilled water and a sample of the supernatant from Huntington ball clay. The supernatant sample appeared black prior to titration. The concentration of PAA detected in the supernatant sample is significantly higher than that detected in the distilled water sample. The amount of 0.25 M HCl between the inflection points was converted to an equivalent concentration of Na-PAA in solution. The supernatant sample was determined to have a concentration equivalent to 0.041 mg/m<sup>2</sup> of PAA in solution, based upon the specific surface area of the Huntington ball clay.

### 3.4.3 X-ray Diffraction

The inorganic minerals identified in each of the clay fractions from the beneficiation process are listed in Table 3-II; the results from C&C ball clay are taken from the thesis of Caughel.<sup>109</sup> The most prevalent mineral in each fraction, determined from the relative intensities of each peak, is listed first. The diffraction patterns for the raw clay and each clay fraction can be observed in Figure 3-7 (TK6), Figure 3-8 (Kingsley), Figure 3-9 (Huntingdon), Figure 3-10 (Marquis), and Figure 3-11 (M&D). Impurity minerals were present in each of the raw clays tested in this study. All of the clays tested, with the exception of TK6, contain a quartz impurity. Huntingdon and Marquis clays contained a 14Å mineral, which indicates an unnamed 2:1-layer silicate. TK6 contained a mixed-layer clay that swelled to approximately 34Å during the solvation process.

Table 3-II. Inorganic Minerals Identified in Each of the Clay Fractions by X-ray Diffraction on Oriented Slides.

	<b>Coarse Fraction</b>	<b>Middle Fraction</b>	<b>Fine Fraction</b>
<b>TK6</b>	Kaolinite	Kaolinite Smectite	Smectite Kaolinite Mixed-layer clay
<b>Kingsley</b>	Kaolinite Quartz	Kaolinite	Smectite Kaolinite
<b>Huntingdon</b>	Kaolinite Quartz Illite	Kaolinite 14Å mineral	Kaolinite 14Å mineral
<b>Marquis</b>	Quartz Kaolinite Illite	Kaolinite 14Å mineral	Kaolinite 14Å mineral
<b>M&amp;D</b>	Quartz	Quartz Kaolinite	Kaolinite Chlorite/Smectite
<b>C&amp;C*</b>	Quartz Kaolinite Illite	Quartz Kaolinite Illite	Kaolinite

\* Data taken from the thesis of Caughel<sup>109</sup>

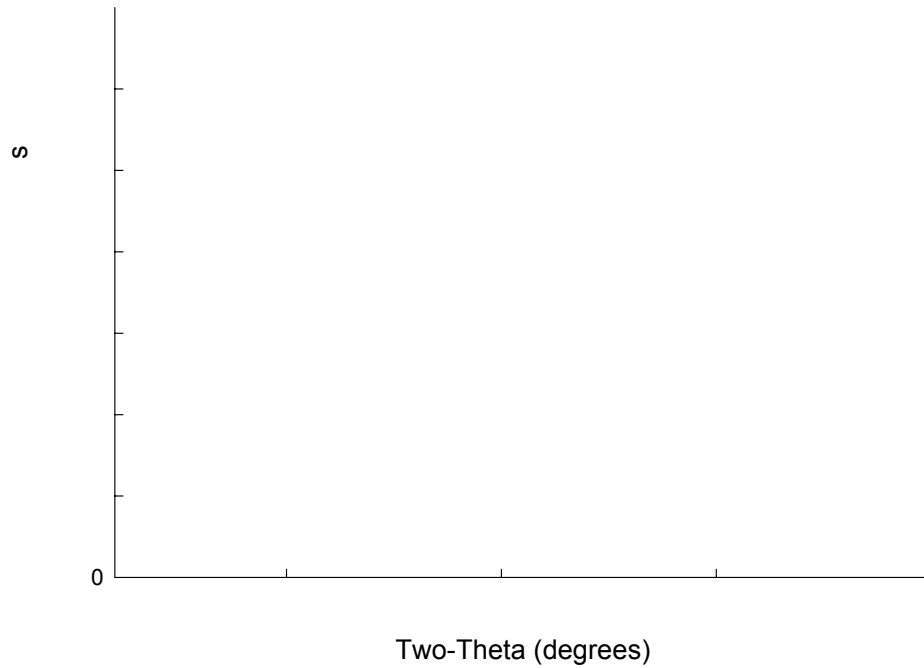


Figure 3-7. X-ray diffraction patterns from oriented slides of TK6 kaolin clay and the clay fractions prepared by washing and beneficiation. TK6 is observed to contain primarily kaolinite with a smectite impurity.

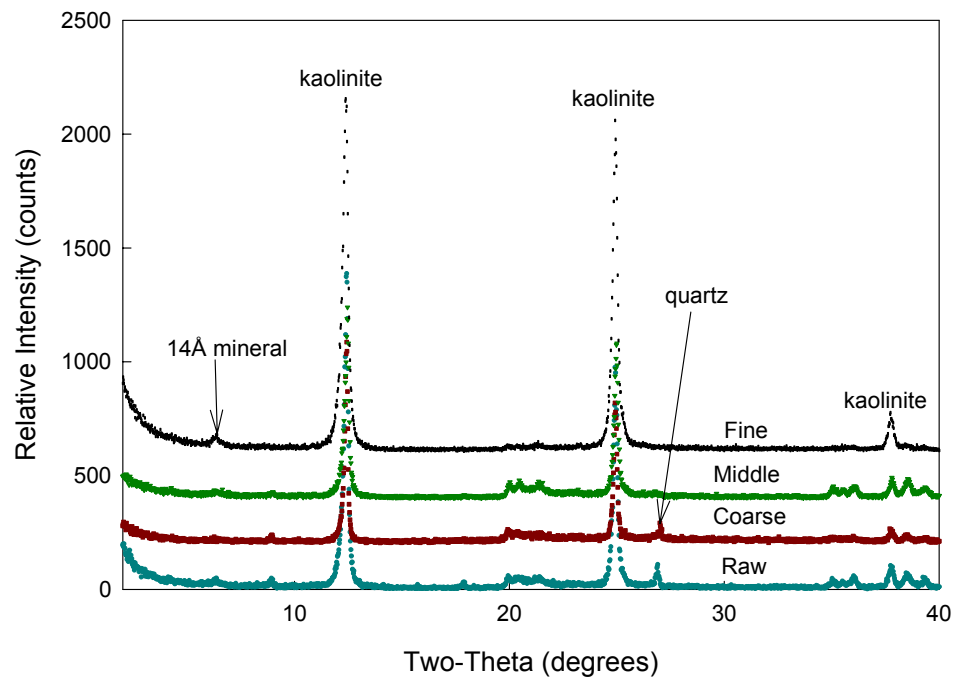


Figure 3-8. X-ray diffraction patterns from oriented slides of Kingsley kaolin clay and the clay fractions prepared by washing and beneficiation. Kingsley is observed to contain primarily kaolinite with quartz and 2:1-layer silicate impurities.

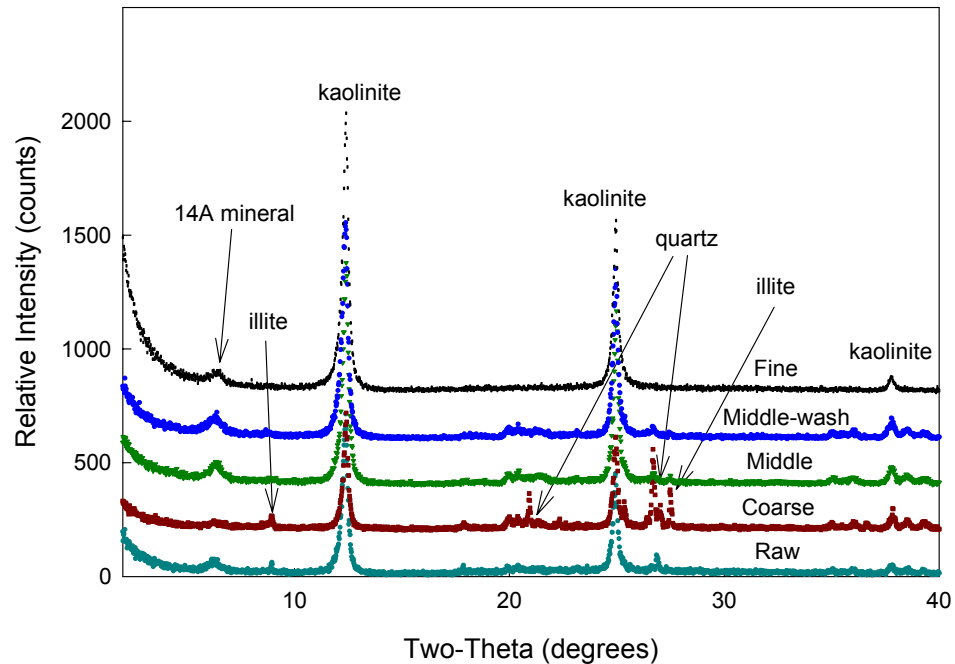


Figure 3-9. X-ray diffraction patterns from oriented slides of Huntingdon ball clay and the clay fractions prepared by washing and beneficiation. Huntingdon is observed to contain impurities of quartz and 2:1-layer silicates (illite and a 14Å mineral). Successive washing of the middle clay fraction is observed to have little effect on the mineral species present.

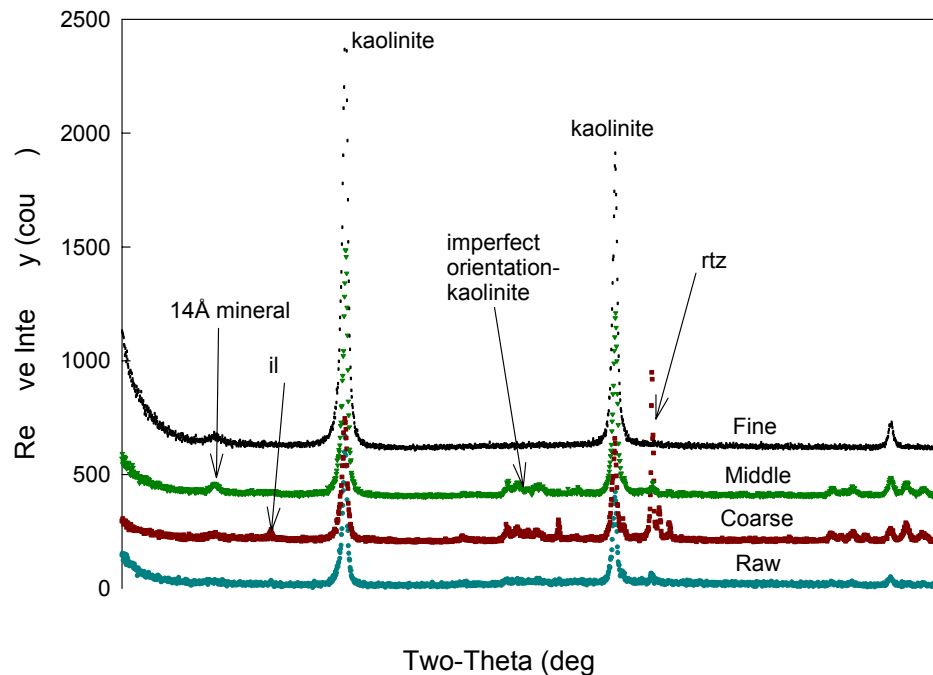


Figure 3-10. X-ray diffraction patterns from oriented slides of Marquis ball clay and the clay fractions prepared by washing and beneficiation. Imperfect orientation of the kaolinite platelets can be observed in the diffraction patterns. Marquis is observed to contain a quartz impurity as well as 2:1-layer silicates (i.e., illite and a 14Å mineral).

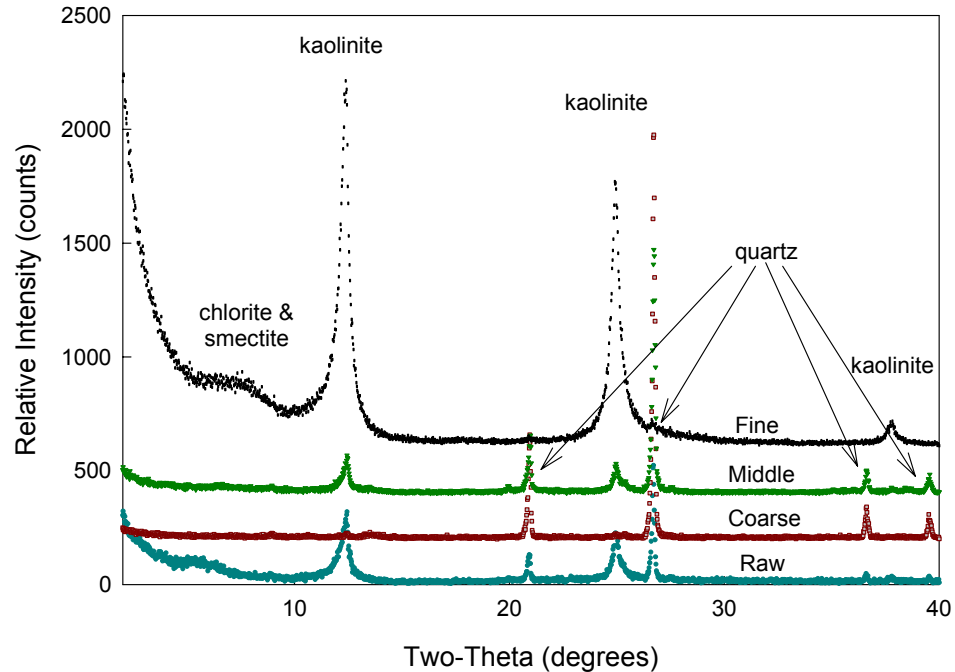


Figure 3-11. X-ray diffraction patterns from oriented slides of M&D ball clay and the clay fractions prepared by washing and beneficiation. The coarse and middle fractions are observed to contain mostly quartz while the fine fraction is primarily kaolinite with a 2:1-layer silicate impurity.

#### 3.4.4 Thermal Analysis

The summarized results from the LOI are presented in Figure 3-12. Also shown is the theoretical LOI for kaolinite, 13.94%. Deviations from this value were the result of impurity species in the clay. Due to the heterogeneous nature of the raw clay, it was difficult to determine which species was present in the clay solely from the LOI. It was also difficult to determine the quantity of each species present in the clay fraction since swellable minerals had a variable LOI depending on their thermal history and the storage of the clay samples prior to testing. None of the LOI values exceeded the theoretical limit for kaolinite. The LOI from the beneficiated clay fractions was observed to increase in the finer clay fractions indicating a decrease in the amount of free quartz and a possible increase in the amount of organic present in the fraction.

#### 3.4.5 Specific Surface Area

The SSA of the raw clay as well as each clay fraction is shown in Figure 3-13. The SSA of the fine fraction was significantly higher than that of the coarser

fractions. The fine fraction of the raw clay was primarily composed of 2:1-layer silicates, i.e., minerals that consisted of an alumina-like layer sandwiched between two silica-like layers, which typically have a higher SSA.

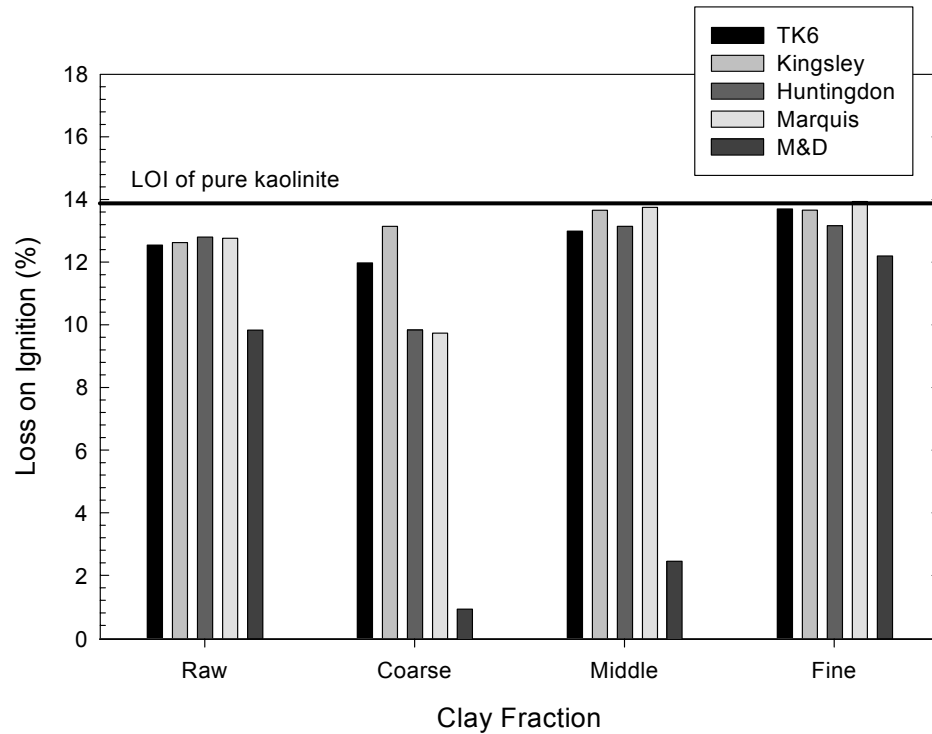


Figure 3-12. Loss on ignition (LOI) of the raw clays and clay fractions in this study. The LOI is observed to increase with the finer clay fractions indicating the presence of less quartz and possibly more organic species in the finer fractions of the beneficiated clay.

### 3.4.6 Chemical Analysis

The amount of free quartz calculated from the chemical analysis as well as the amount of free quartz determined from the LOI is shown in Figure 3-14 for each of the clay fractions tested. The free quartz from the raw clay was concentrated in the coarse and middle fractions of the beneficiated clay. The amount of free quartz was determined by assuming that only kaolinite and free quartz are present in the clay. Any deviation from the stoichiometry for kaolinite in the chemical analysis was assumed to be the result of free quartz in the clay. The presence of 2:1-layer silicates invalidates this assumption and the result was

that there appears to be free quartz in the fine fraction of the beneficiated clay. Analysis of the results from X-ray diffraction indicated that there was no free quartz present in the fine fraction of any clay tested in this study.

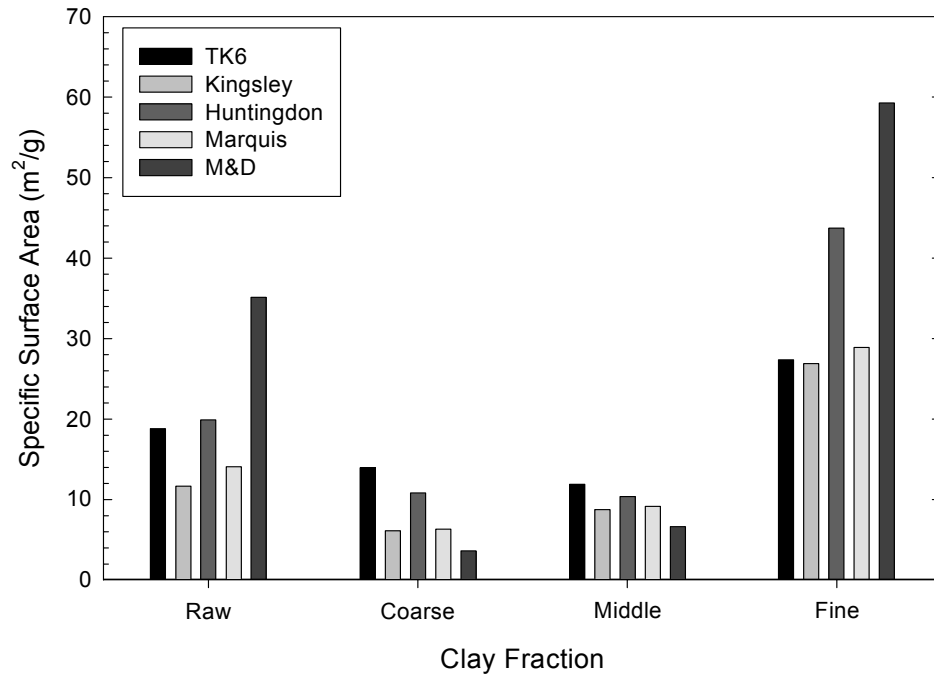


Figure 3-13. Specific surface area (SSA) of the raw clay and clay fractions in this study. The SSA increases for the finer clay fractions due to segregation by sedimentation.

### 3.4.7 Polymer Adsorption

The adsorption results will be discussed for each clay individually followed by an overall discussion of the results from the washing and beneficiation process used in this study. The plateau adsorption results are summarized in Table 3-III.

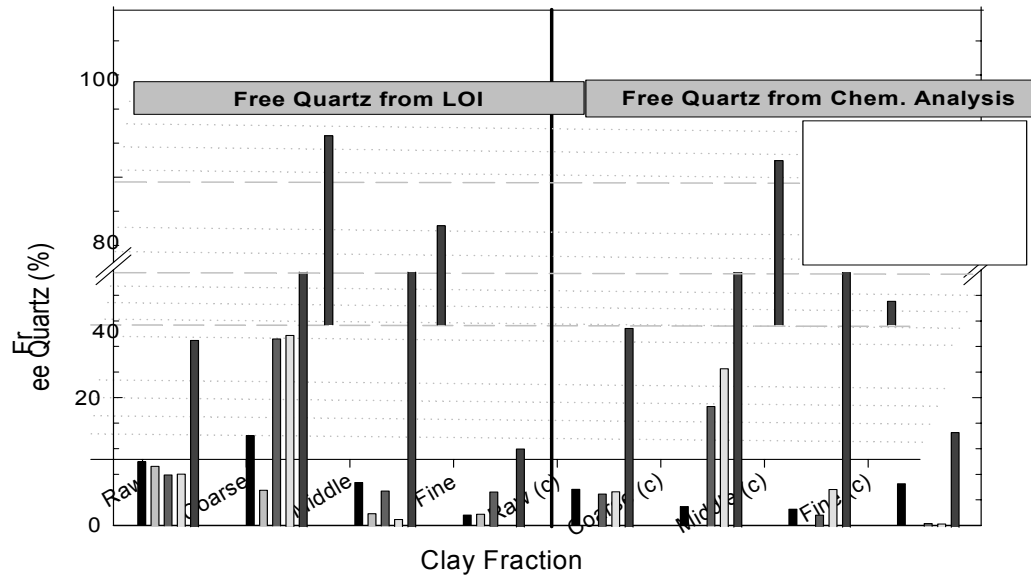


Figure 3-14. Amount of free quartz calculated from each raw clay and clay fraction in this study. The free quartz was calculated from the LOI and chemical analysis (by ICP). The calculated amount of free quartz assumes that only kaolinite and quartz are present in the sample. The presence of 2:1-layer silicates in the clay fractions causes a discrepancy in the actual amount of free quartz present.

### 3.4.7.1 TK6 (kaolin clay)

Dispersant was added at levels that were predicted to be within the plateau region of the adsorption isotherm. The adsorption isotherms for TK6 were observed in Figure 3-15 (pH 6) and Figure 3-16 (pH 9). The adsorption was tested on the coarse fraction at pH 6. The concentration of polymer adsorbed falls significantly below the predicted level for all of the clay fractions tested. The suspensions remained light yellow with increasing supernatant from the clay polymer additions indicating that only fulvic acid was present in the raw clay. The results showed that there was a slight increase in the concentration of polymer adsorbed on the coarse fraction, relative to the raw clay. The middle and fine fractions of the beneficiated clay have lower adsorption levels than the raw clay due to the presence of high surface area 2:1-layer silicates in the fine clay fraction.

Table 3-III. Plateau Adsorption Values for the Clays Used in this Study.

Powder	Fraction	Adsorption Plateau (mg/m <sup>2</sup> )	
		pH 6.0±0.2	pH 9.0±0.2
APA-0.5 (alumina)	N/A	0.603±0.009	0.411±0.009
TK6 (kaolin clay)	As received	0.138±0.019	0.124±0.07
	Coarse	0.170±0.000	N/A
	Middle	0.047±0.003	0.045±0.006
	Fine	0.089±0.007	0.039±0.01
Kingsley (kaolin clay)	As received	0.180±0.012	0.151±0.017
	Coarse	0.190±0.022	0.147±0.018
	Middle	0.115±0.014	0.098±0.011
	Middle - wash	0.153±0.021	0.114±0.022
	Fine	0.153±0.021	0.102±0.009
Huntingdon (ball clay)	As received	0.080±0.011	0.166±0.024
	Middle	0.103±0.021	0.148±0.029
	Middle - wash	0.180±0.049	0.163±0.005
Marquis (ball clay)	As received	0.124±0.009	0.096±0.009
	Middle	0.145±0.010	0.053±0.010
	Middle - wash	0.211±0.045	0.154±0.008
M&D (ball clay)	As received	0.110±0.012	0.095±0.005
	Coarse	-0.035±0.037	-0.023±0.050
	Middle	0.107±0.015	0.088±0.007
	Middle – wash	0.129±0.021	0.097±0.016
	Fine	0.136±0.013	0.012±0.010
	Fine - wash	0.309	0.216±0.007
C&C (ball clay)	As received	0.076±0.014	0.040±0.025
	As rec. - wash	0.092±0.003	0.108±0.011
	Coarse	0.000±0.023	-0.012±0.013
	Middle	0.107±0.005	-0.026±0.044
	Fine	0.139±0.003	0.105±0.011

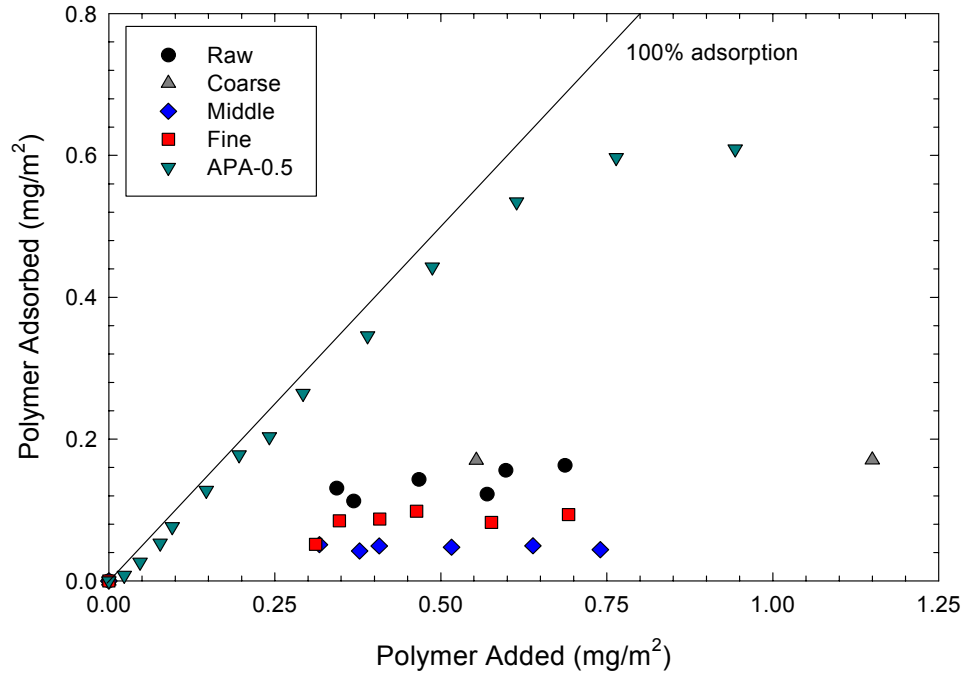


Figure 3-15. Adsorption isotherms for TK6 at pH 6. The process of washing and beneficiating the clay has little effect on the adsorption level of Na-PAA on the clay surface. The coarse clay fraction shows slightly higher adsorption levels after segregation. Adsorption levels were determined by preparing suspensions within the plateau region of the adsorption isotherm.

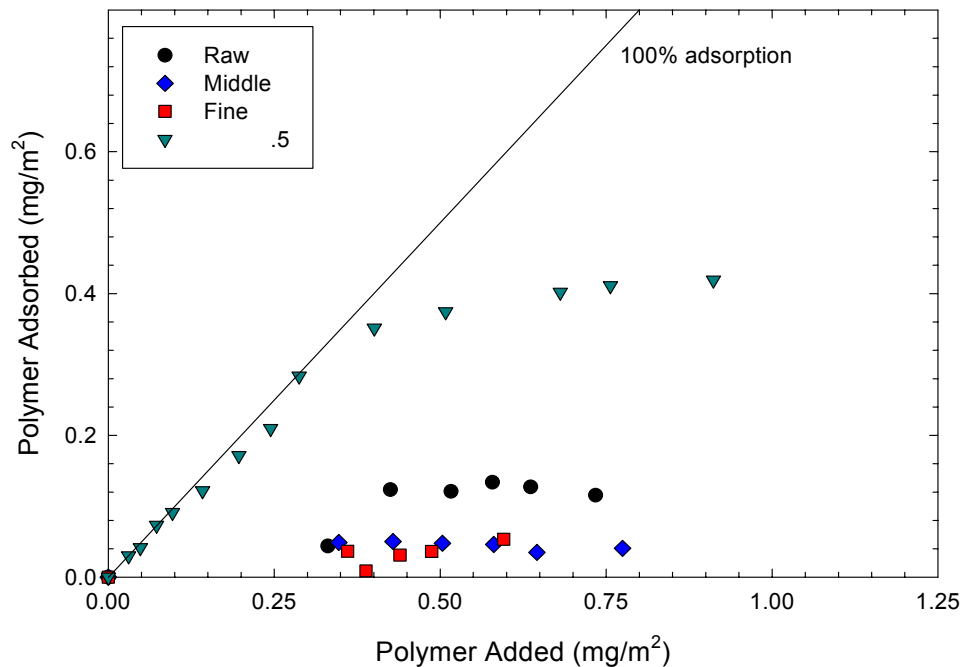


Figure 3-16. Adsorption isotherms for TK6 at pH 9. The adsorption levels for the middle and fine fractions fall below the adsorption level for the raw clay. The coarse fraction was not tested at pH 9. Adsorption levels were determined by preparing suspensions within the plateau region of the adsorption isotherm.

### 3.4.7.2 Kingsley (kaolin clay)

The entire adsorption isotherm was prepared for the Kingsley clay. The adsorption isotherms are shown in Figure 3-17 (pH 6) and Figure 3-18 (pH 9). The concentration of adsorbed polymer fell significantly below the predicted levels from the model of the kaolinite platelet. The highest adsorption levels were observed for the raw clay; the same level was reached for the coarse fraction of Kingsley, which consisted primarily of kaolinite. Successive washings of the middle fraction were observed to increase the concentration of adsorbed polymer on the surface of the clay platelet at pH 6, but little effect was observed at pH 9.

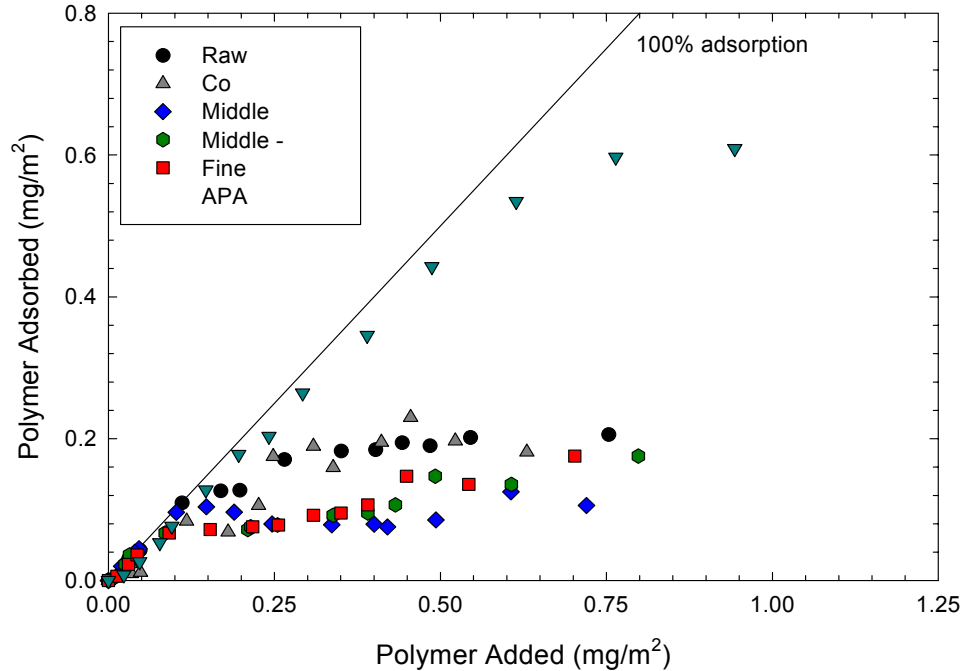


Figure 3-17. Adsorption isotherms for Kingsley kaolin at pH 6. The coarse fraction of the segregated clay has approximately the same adsorption level as the raw clay. The middle and fine fractions have lower adsorption plateaus due to impurity minerals that are present in the clay. Successive washing of the middle fraction is observed to have no significant effect on the adsorption level.

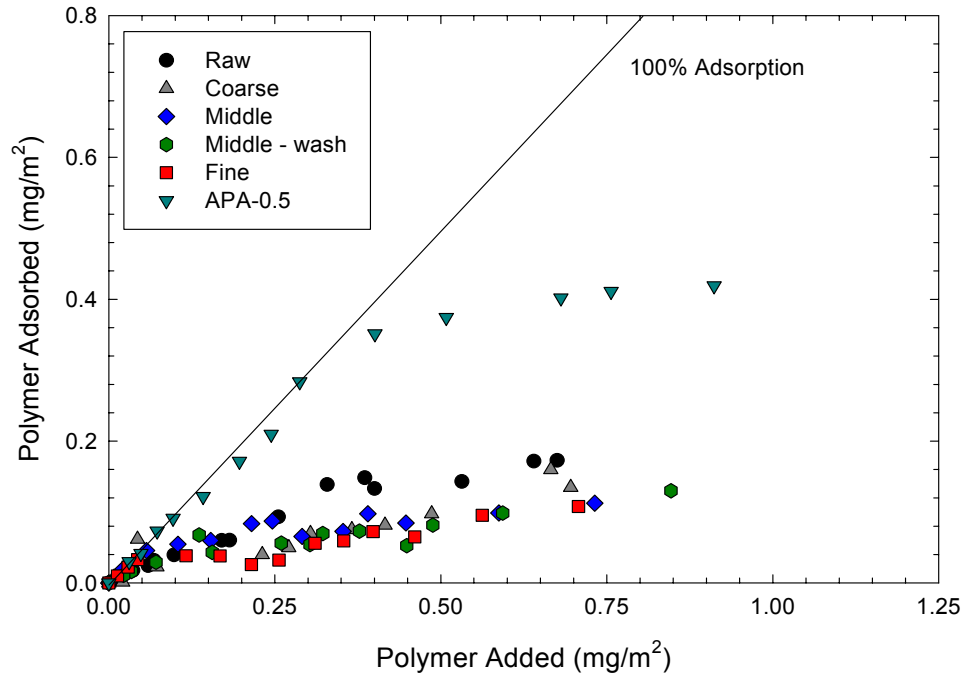


Figure 3-18. Adsorption isotherms for Kingsley kaolin at pH 9. The coarse fraction and raw clay have approximately the same adsorption plateau value while the middle and finer fractions from the segregated clay have lower adsorption plateaus due to impurity minerals in the clay. Successive washing of the middle fraction is observed to have no significant effect of the adsorption levels.

#### 3.4.7.3 Huntingdon (ball clay)

The adsorption isotherms for Huntingdon are shown in Figure 3-19 (pH 6) and Figure 3-20 (pH 9). Only the raw clay and middle fraction were tested for the Huntingdon ball clay. There was little difference in the adsorption isotherms for the raw clay and the middle fraction at pH 6. After successive washings of the middle fraction the plateau value was observed to significantly increase due to the removal of impurity species prior to determining the adsorption plateau. The adsorption level was observed to approach that predicted by the model of the kaolinite platelet. Typical adsorption of the polymer on the clay was observed in all of the isotherms at pH 9 and all of the samples are observed to reach approximately the same plateau value with little benefit of successive washing of the middle fraction. This was due to the soluble organics remaining in the supernatant from all of the suspensions that were prepared after centrifuging. The detected concentration of organic in the supernatant with no polymer addition was taken as a “background” concentration and subtracted from the

result prior to analysis. In all cases at pH 9 the adsorption level was observed to approach that predicted by the model of the kaolinite platelet.

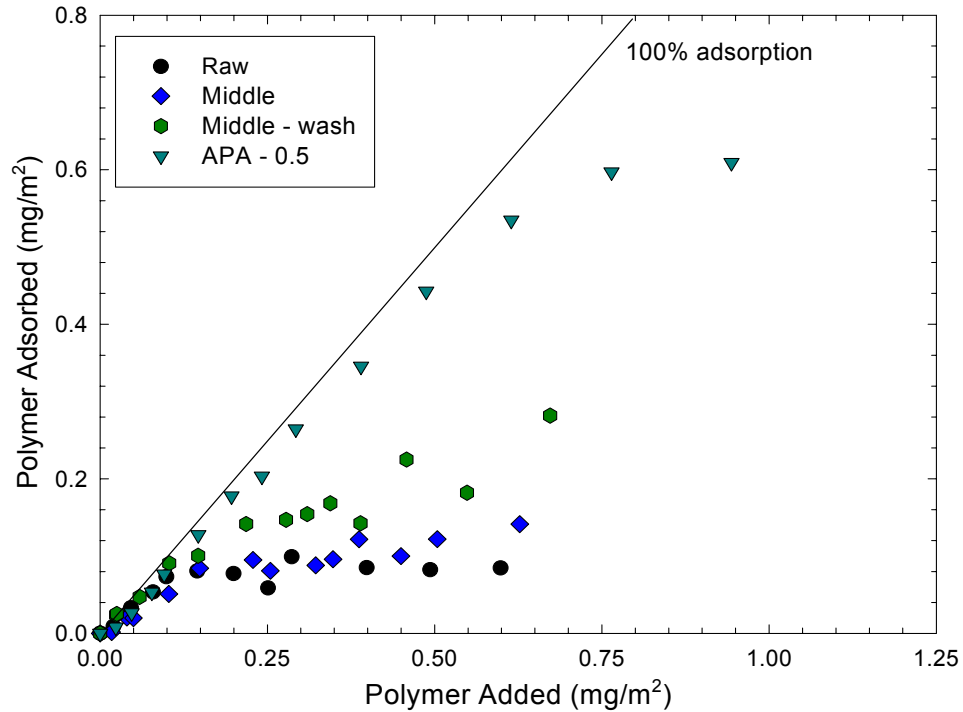


Figure 3-19. Adsorption isotherms for Huntingdon ball clay at pH 6. Only the raw clay and middle fraction were tested for adsorption. The adsorption plateau values initially fall significantly below the predicted level. After repeated washing of the middle fraction water the plateau value approaches the predicted value.

#### 3.4.7.4 Marquis (ball clay)

The adsorption isotherms for Marquis are shown in Figure 3-21 (pH 6) and Figure 3-22 (pH 9). At pH 6 typical adsorption was evident in the isotherms, but the plateau value falls significantly below the predicted level. With successive washings the plateau value was observed to approach the predicted level from the model. At pH 9 typical adsorption was evident in the isotherms. The plateau value for the middle fraction of the beneficiated clay was observed to approach the predicted level from the model at high additions of polymer. With successive washings the predicted level was approached at lower polymer additions relative to the as-prepared middle clay fraction. A dark supernatant was not evident in the Marquis samples after centrifuging.

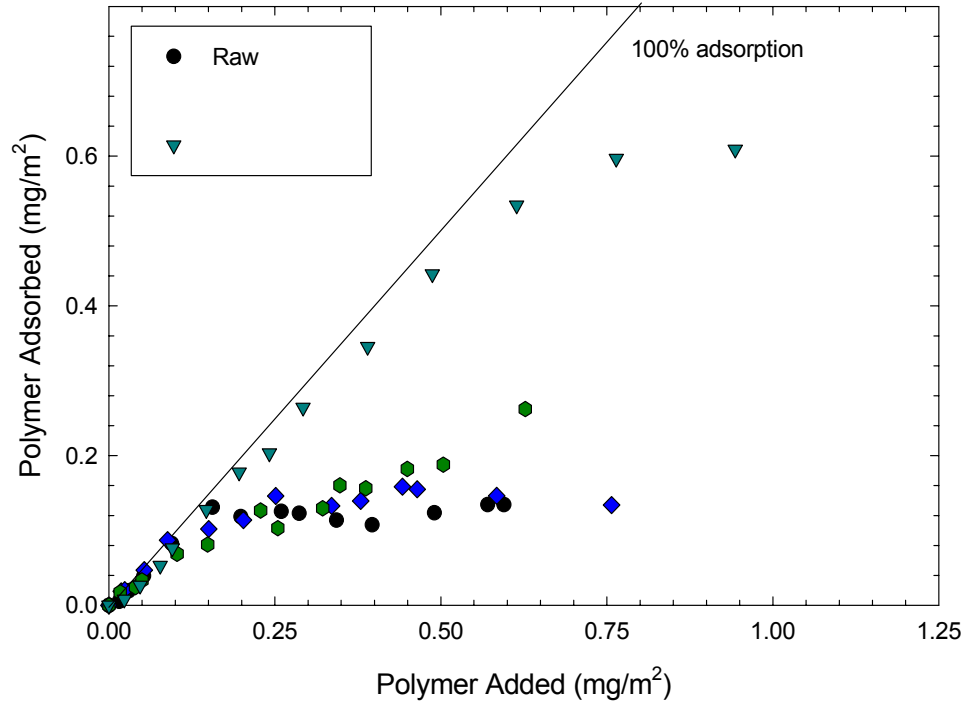


Figure 3-20. Adsorption isotherms for Huntington ball clay at pH 9. Only the raw and middle fractions were tested to determine the adsorption levels. All of the clay fractions reach approximately the same plateau value. The concentration of organic species present with no PAA addition was taken as a background.

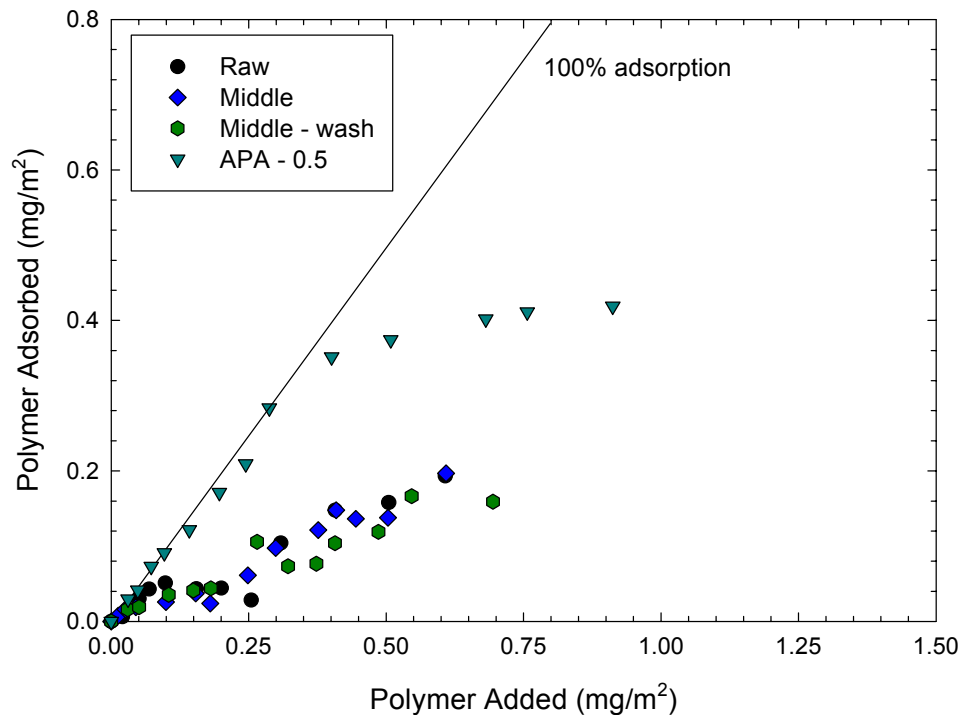


Figure 3-21. Adsorption isotherms for Marquis ball clay at pH 6. Only the raw clay and middle fraction were tested. There is an increase in the concentration of polymer adsorbed on the clay surface after successive washing of the middle fraction of the beneficiated clay.

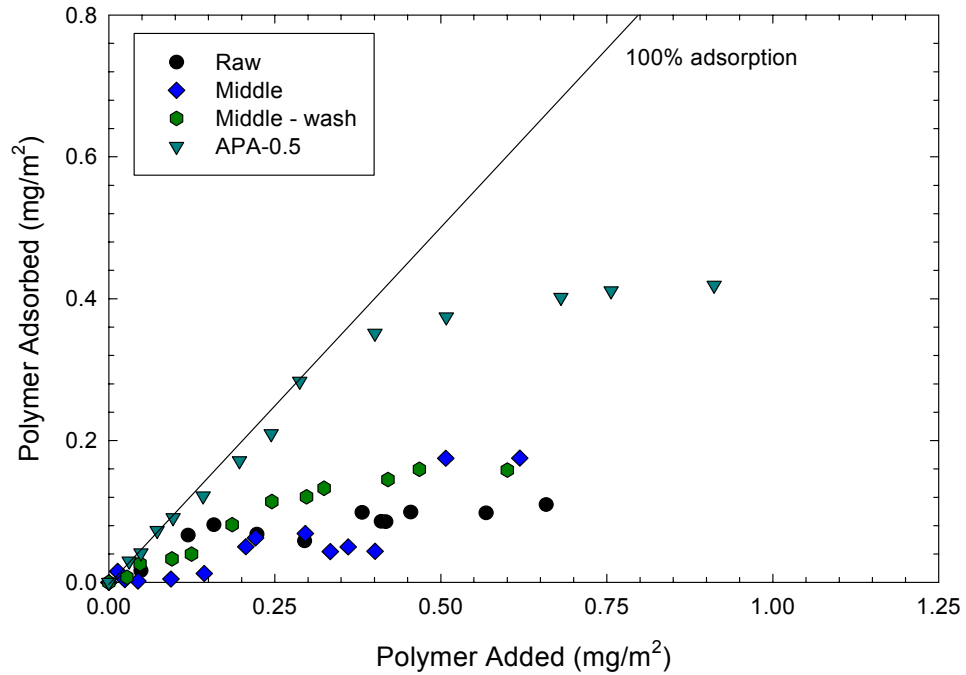


Figure 3-22. Adsorption isotherms for Marquis ball clay at pH 9. Only the raw clay and middle fraction were tested. The adsorption plateau value is observed to increase after beneficiation of the raw clay. Successive washing of the middle fraction results in the plateau value being reached at lower polymer additions.

#### 3.4.7.5 M&D (ball clay)

The adsorption isotherms for M&D can be observed in Figure 3-23 (pH 6) and Figure 3-24 (pH 9). The isotherms for each fraction of the beneficiated clay are plotted. The raw M&D ball clay had a relatively high specific surface area, compared to other commercial clays, as well as a high concentration of soluble divalent cations. The high surface area was the result of a high concentration of fine, swellable 2:1-layer silicates that hinder gravimetric settling. The divalent cations further confounded the problem by exceeding the critical coagulation concentration and causing particle-particle interactions, i.e., a network was created between the clay particles hindering gravimetric settling.

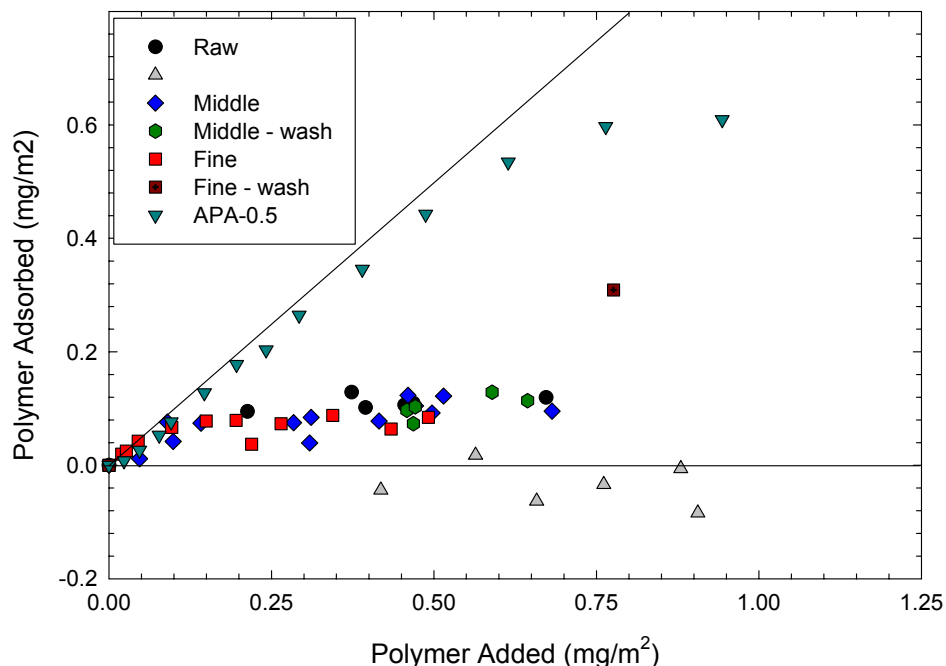


Figure 3-23. Adsorption isotherms for M&D ball clay at pH 6. The coarse fraction of the clay resulted in a negative concentration of polymer in the supernatant, i.e., more polymer is detected than was originally added to the suspension. This is due to soluble organic species in the supernatant and the low affinity of Na-PAA for the surface of quartz, the primary mineral in the coarse fraction. The adsorption plateau values are all below that predicted by the model. When the fine fraction is subjected to successive washing the adsorption plateau reaches the value predicted by the model since the concentration of impurity minerals and organic species have been reduced in the clay fraction.

The coarse and middle fractions from the beneficiated clay had quartz as the primary mineral. The resulting isotherms from the coarse fraction at pH 6 and 9 show negative adsorption, i.e., more organic was detected in the supernatant than was originally added to the suspension. This was the result of soluble organic species being removed from the powder surface. These species were then detected during titration as unadsorbed Na-PAA. The middle fraction also showed very low adsorption levels and successive washing of the fraction did not result in a significant increase in the concentration of adsorbed polymer, due to the high concentration of quartz in the middle fraction.

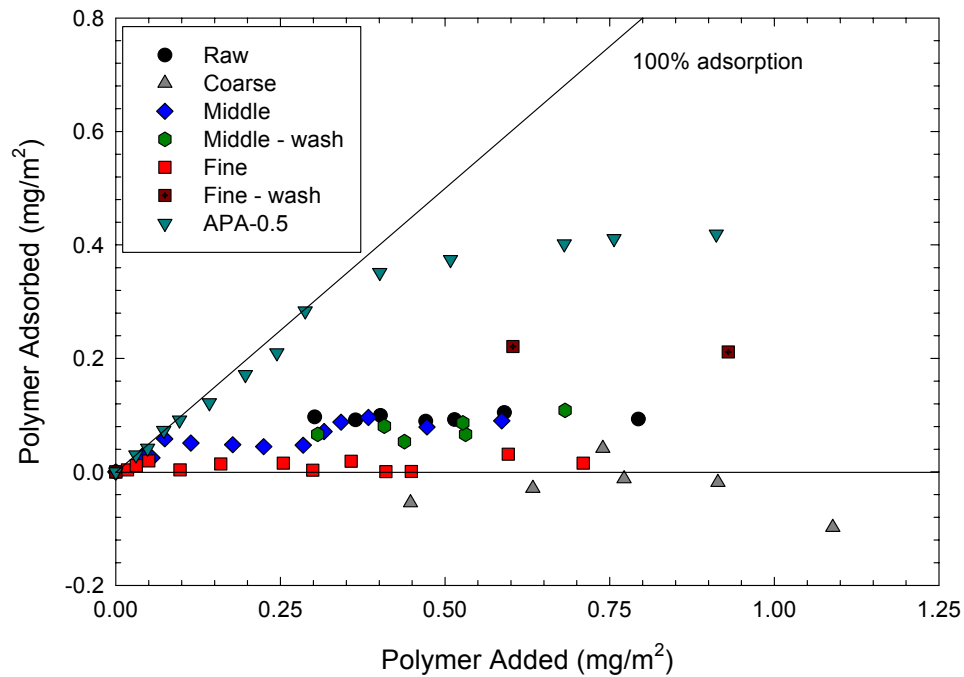


Figure 3-24. Adsorption isotherms for M&D ball clay at pH 9. Negative concentrations of adsorbed polymer are again determined for the coarse fraction of the clay. All of the fractions tested have adsorption levels significantly below that predicted by the model. The fine fraction was subjected to successive washing to remove impurities and the adsorption plateau approaches the level predicted by the model since the concentration of impurity minerals and organic species have been reduced in the clay.

The concentration of polymer adsorbed on the fine fraction was initially very low due to the presence of high surface area, swellable 2:1-layer silicates and a high concentration of soluble organics that remained in the fine fraction of the clay. Successive washing of the fine fraction served to remove some of these species from the clay; the 2:1-layer silicates remained in suspension after centrifuging and were removed when the supernatant was decanted from the sample, as indicated by the change in SSA. Before washing the fine fraction SSA was 51.77 m<sup>2</sup>/g and after washing the SSA was reduced to 27.40 m<sup>2</sup>/g. After successive washing the adsorption plateau approached the levels predicted by the model for the kaolinite platelet for the suspensions prepared using the fine clay fraction at pH 6 and 9.

### 3.4.7.6 C&C (ball clay)

The adsorption isotherms for C&C can be observed in Figure 3-25 (pH 6) and Figure 3-26 (pH 9). The concentration of polymer detected with no PAA addition was negative in all cases indicating that a pH active species was present in solution with no initial addition of dispersant. These species were released from the surface of the clay or clay fractions in an aqueous suspension. With increasing addition of PAA polymer was adsorbed on the particle surface with the exception of the coarse fraction. The adsorption level for the coarse fraction in all cases was negative, again indicating that a pH active species was released from the particle surface. The highest adsorption plateaus were observed for the fine fraction of the C&C ball clay, a similar plateau level was observed at pH 9 for the raw clay which was washed at high pH prior to performing the adsorption tests.

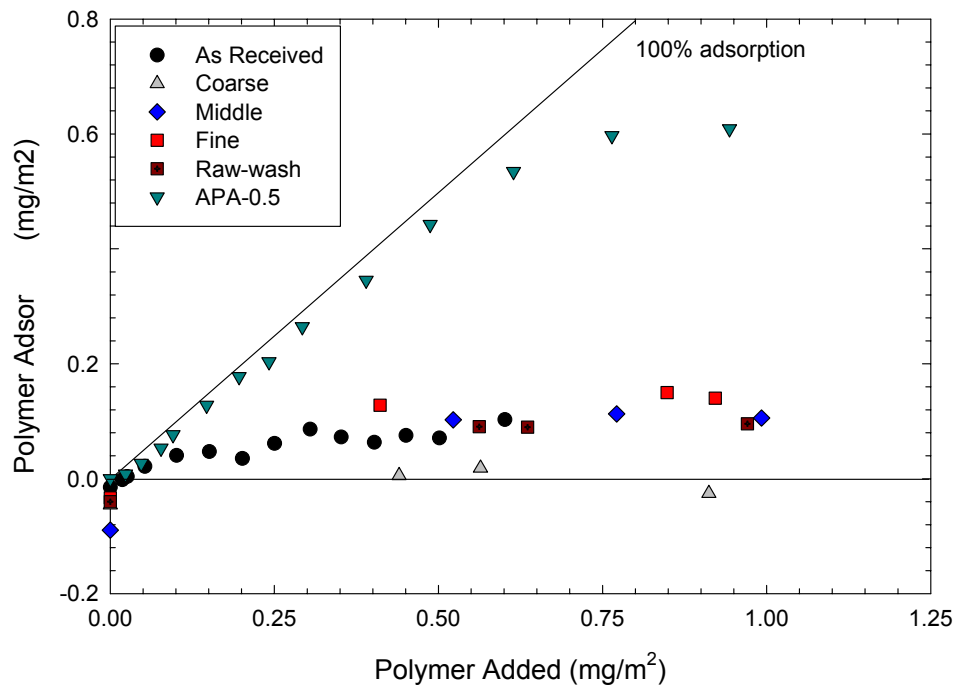


Figure 3-25. Adsorption isotherms for C&C ball clay at pH 6. Negative adsorption is observed for all samples with no added PAA. Beneficiation of the fine fraction is observed to result in the highest adsorption levels at pH 6. The coarse fraction, assumed to be primarily quartz, shows low adsorption levels. The adsorption levels are not observed to approach the predicted levels possibly due to the high concentrations of quartz present in the raw clay. Fractions were not subjected to successive washings.

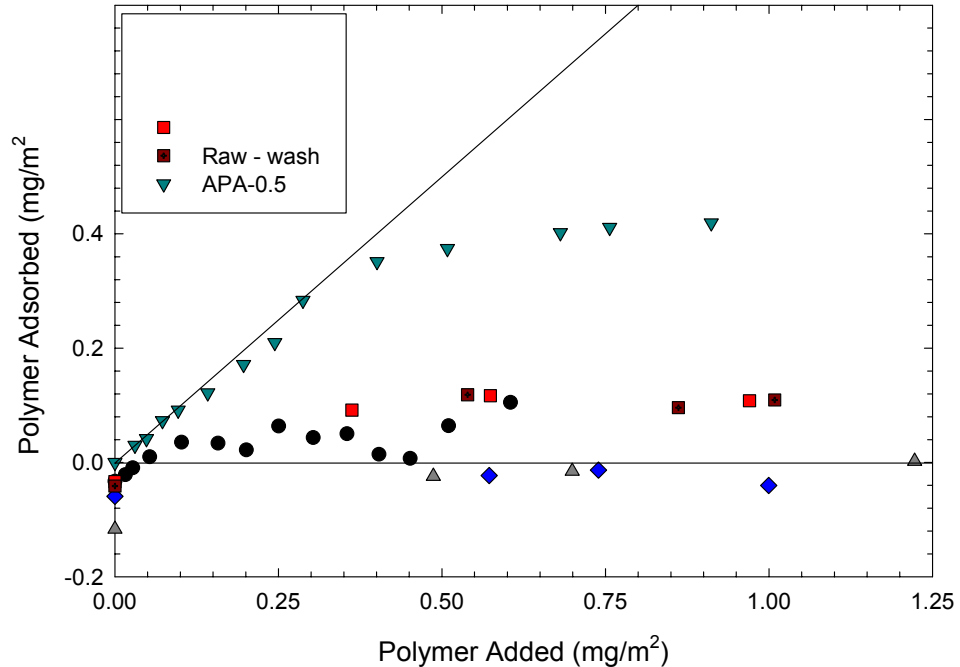


Figure 3-26. Adsorption isotherms for C&C ball clay at pH 9. All samples have negative adsorption levels with no added PAA. The coarse and middle fractions are observed to have negative adsorption for all additions of PAA. The fine fraction and the washed sample of raw clay have the highest adsorption levels. The adsorption levels are not observed to approach the predicted levels possibly due to the high concentrations of quartz present in the raw clay. Fractions were not subjected to successive washings.

#### 3.4.7.7 Polymer Adsorption Summary

To demonstrate the effects of the washing and beneficiation process the relative adsorption of each clay fraction, calculated as the concentration of polymer adsorbed after treatment divided by the concentration adsorbed on the untreated (or raw) clay surface, is shown in Figure 3-27 (kaolin clays studied) and Figure 3-28 (ball clays studied with the exception of C&C). After treatment the amount of polymer adsorbed on the clay surface was observed to increase for the fractions that contain primarily kaolinite, i.e., the coarse fraction for the kaolin clays and the middle (Huntingdon and Marquis) or fine (M&D and C&C) fractions for the ball clays. With washing and beneficiation of the raw clay the adsorption levels on the kaolinite fractions approached the level predicted by the model of the kaolinite platelet.

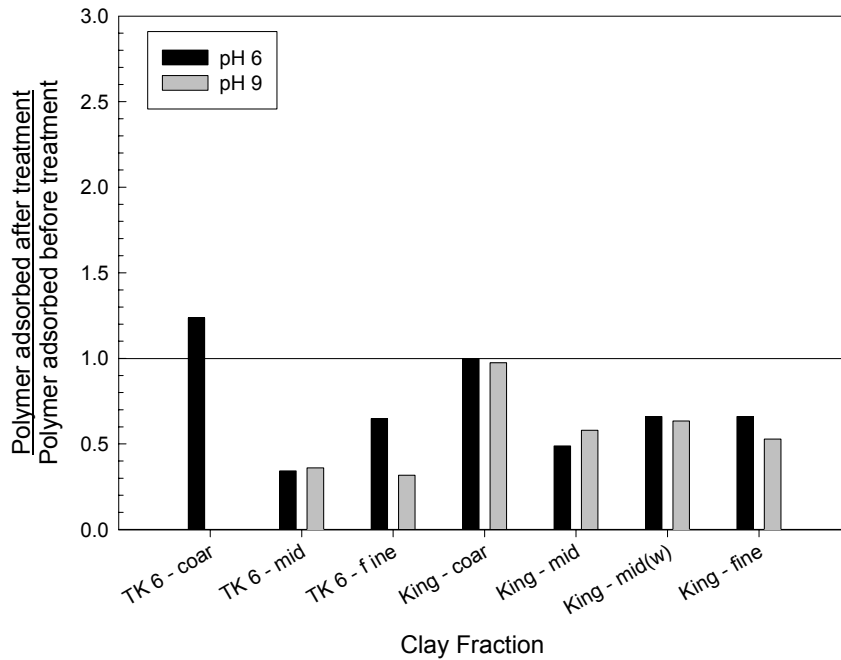


Figure 3-27. Relative adsorption of the kaolin clay fractions tested in this study. The relative adsorption for the coarse fractions of the kaolin clays are either equivalent to or increased by the beneficiation of the raw clay. The finer fractions of the kaolin clays are comprised of impurity minerals and the relative adsorption is lower.

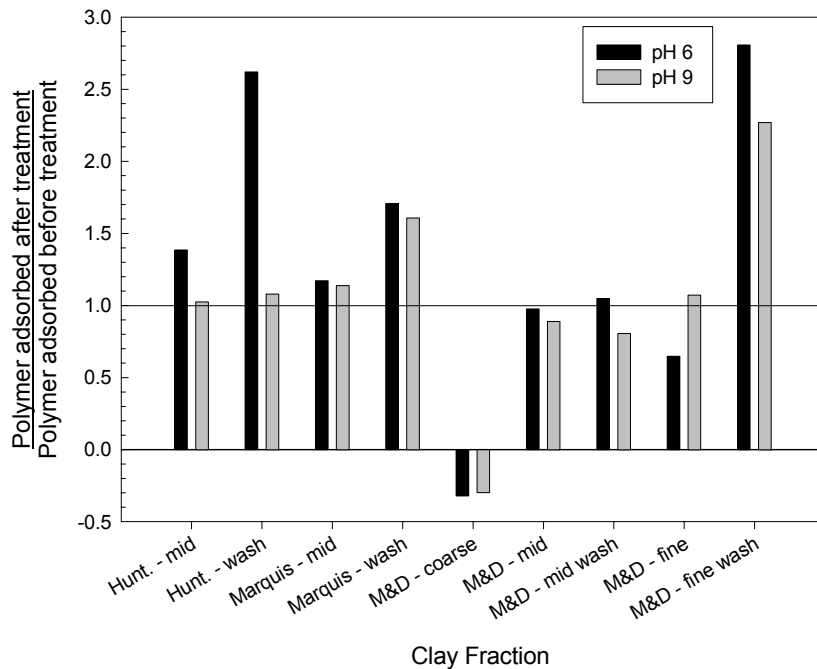


Figure 3-28. Relative adsorption of the ball clays tested in this study. The adsorption of the Na-PAA on the finer fractions is enhanced by segregation of the raw clay. Depending on the particle size of the kaolinite in the raw clay successive washing of either the middle or fine fractions of the clay can significantly enhance the concentration of polymer adsorbed. Not shown are the results for C&C.

### 3.4.8 FTIR Characterization of Clay

Room temperature spectra are shown for samples for Huntingdon ball clay, dried Darvan™811, and humic acid [Humic Acid, sodium salt, Aldrich, Milwaukee, WI] in Figure 3-29; the curves have been offset to allow easy comparison of the spectra. Similarities were observed in the spectra from humic acid and Darvan™ 811 indicating that there were similar bonding arrangements and functional groups in the samples. These groups are proposed to be carboxylic acid groups which typically have a vibrational frequency at  $1822\text{ cm}^{-1}$ , assigned to the C=O stretching vibration in carboxylic acid groups.<sup>104</sup> Furthermore similar vibrational bands were observed in the Huntingdon ball clay sample, although there were several vibrational bands which were overlapped making identification difficult.

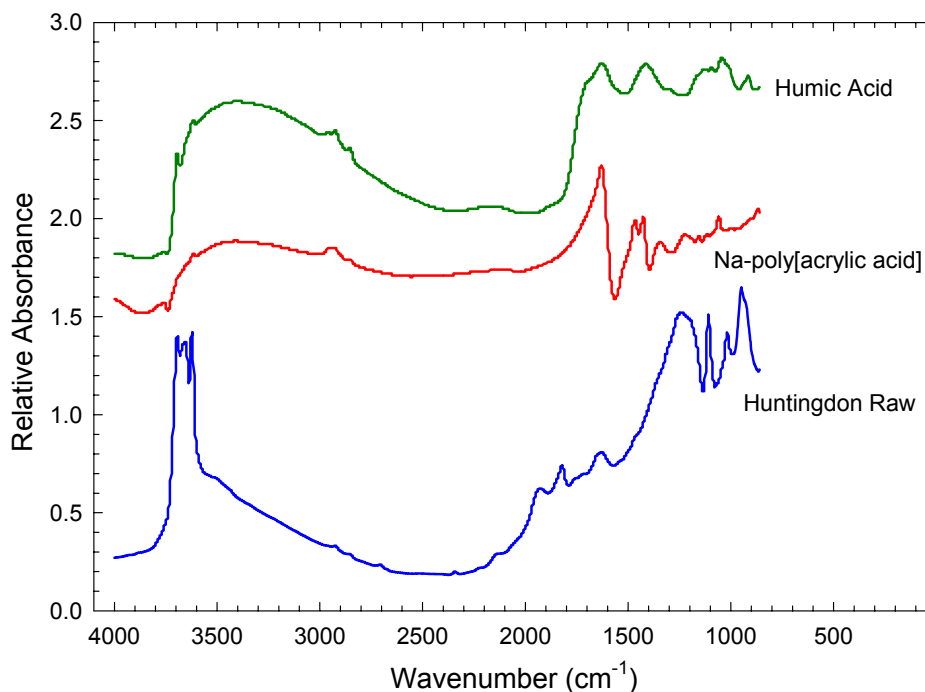


Figure 3-29. Room temperature FTIR spectra from humic acid, dried Darvan™ 811, and raw Huntingdon. Similarities are observed in all three spectra. The Huntingdon sample is observed to have the clearest adsorption bands. Both humic acid and PAA have a broad adsorption band at high wavenumbers due to physical water.

The results from the FTIR analysis using the environmental chamber are shown in Figure 3-30 (TK6), Figure 3-31 (Kingsley), Figure 3-32 (raw

Huntingdon), Figure 3-33 (Huntingdon, coarse fraction), Figure 3-34 (Huntingdon, middle fraction). Figure 3-35 (Marquis), and Figure 3-36 (M&D). The curves have been offset to allow easy comparison of the spectra. In each case vibrational bands were observed to change in intensity with temperature. Some bands were observed to decrease in intensity at low temperature (between 100 and 300°C), these bands were associated with the presence of organics or physical water in the clay. Bands associated with the lattice water in kaolinite were observed to decrease in intensity above 550°C. A small band was observed at approximately 2675  $\text{cm}^{-1}$  which initially grew in intensity with temperature, followed by the loss of the band above 550°C. This small band was assigned to a carbonate vibration. The increase in the intensity of the bands was initially due to the desorption of the carboxylic acid group from the clay surface followed by combustion at elevated temperatures.<sup>104</sup> For a complete assignment of the pertinent bands in the FTIR spectra see Table 3-IV.

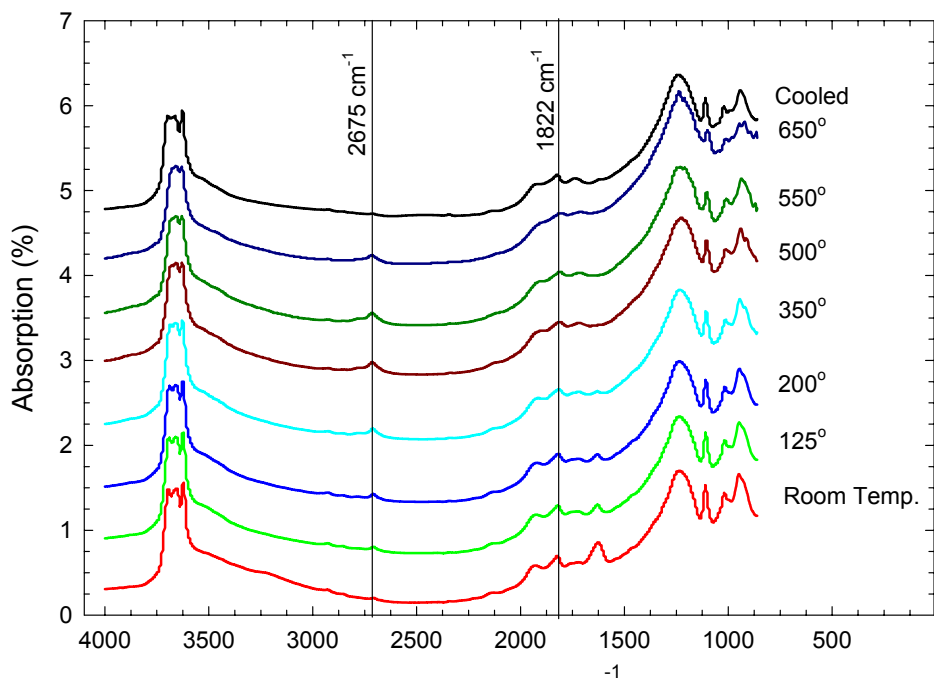


Figure 3-30. FTIR spectra from raw TK6. With thermal treatment the clay is observed to dehydroxylate (lose lattice water) and the adsorption at 1822  $\text{cm}^{-1}$  (C=O stretch in carboxylic acid) is observed to be reduced. An adsorption band appears at  $\sim 2675 \text{ cm}^{-1}$  at higher temperatures followed by its gradual extinction.

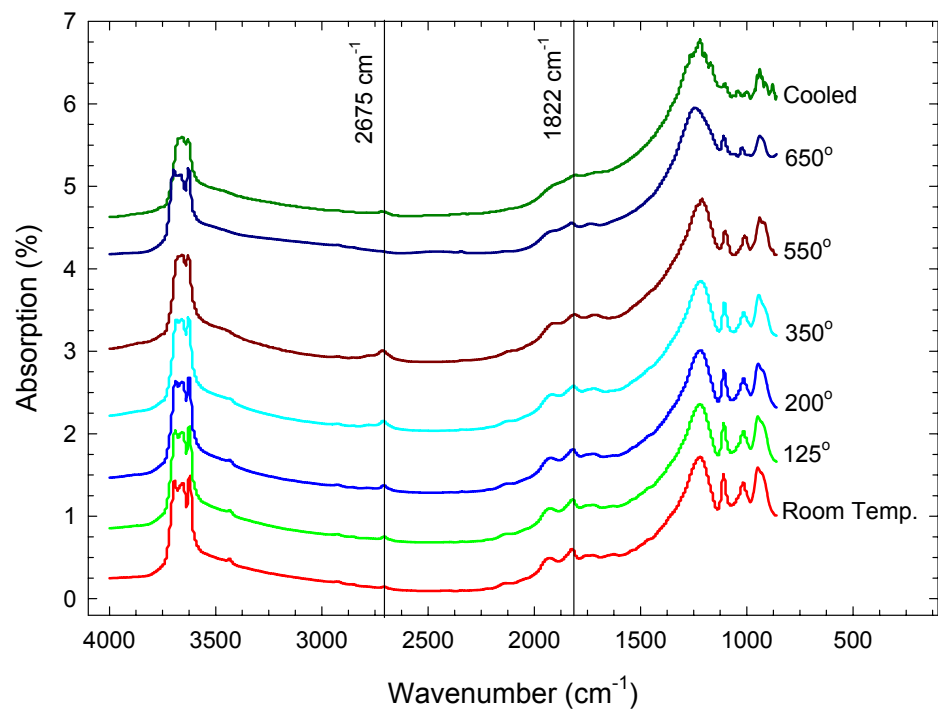


Figure 3-31. FTIR spectra from raw Kingsley. With thermal treatment the clay is observed to dehydroxylate and the adsorption at 1822 cm<sup>-1</sup> (C=O stretch in carboxylic acid) is observed to be reduced. An adsorption band appears at ~2675 cm<sup>-1</sup> at higher temperatures followed by its gradual extinction.

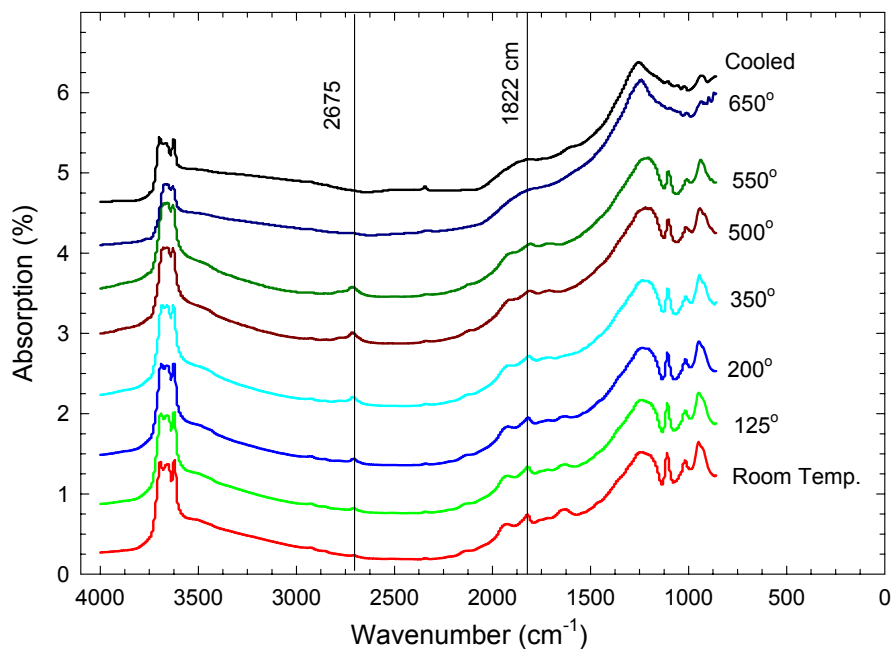


Figure 3-32. FTIR spectra from the raw Huntingdon. With thermal treatment the clay is observed to dehydroxylate (lose lattice water) and the adsorption at 1850 cm<sup>-1</sup> (C=O stretch in carboxylic acid) is observed to be reduced. An adsorption band appears at ~2675 cm<sup>-1</sup> at higher temperatures followed by its gradual extinction.

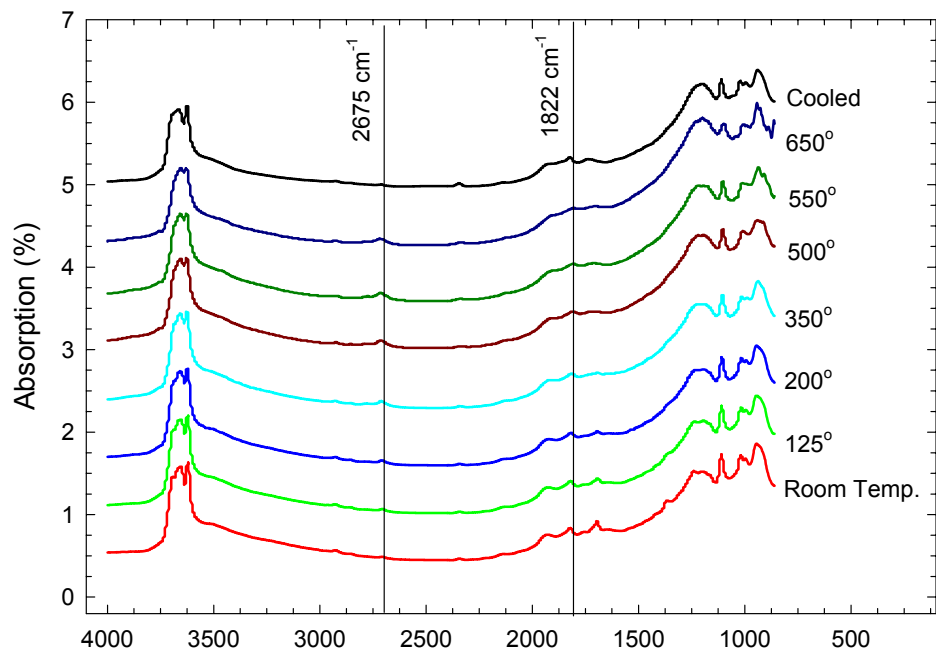


Figure 3-33. FTIR spectra from coarse Huntingdon. With thermal treatment the clay is observed to dehydroxylate and the adsorption at  $1850\text{ cm}^{-1}$  (C=O stretch in carboxylic acid) is observed to be reduced.

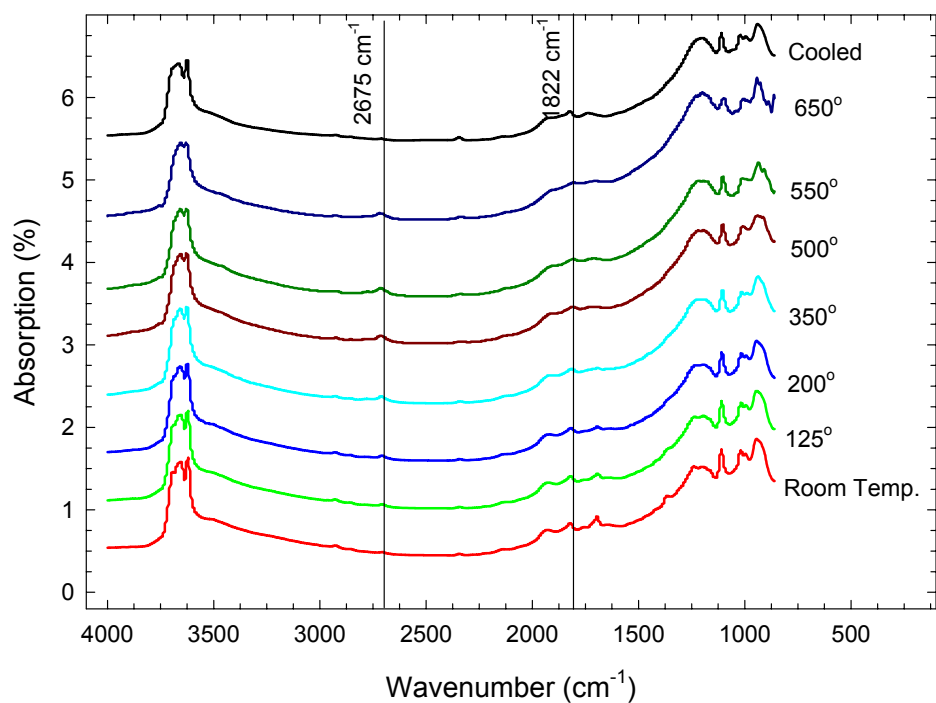


Figure 3-34. FTIR spectra from the Huntingdon middle fraction. With thermal treatment the clay is observed to dehydroxylate (lose lattice water) and the adsorption at  $1850\text{ cm}^{-1}$  (C=O stretch in carboxylic acid) is observed to be reduced. An adsorption band appears at  $\sim 2675\text{ cm}^{-1}$  at higher temperatures followed by its gradual extinction.

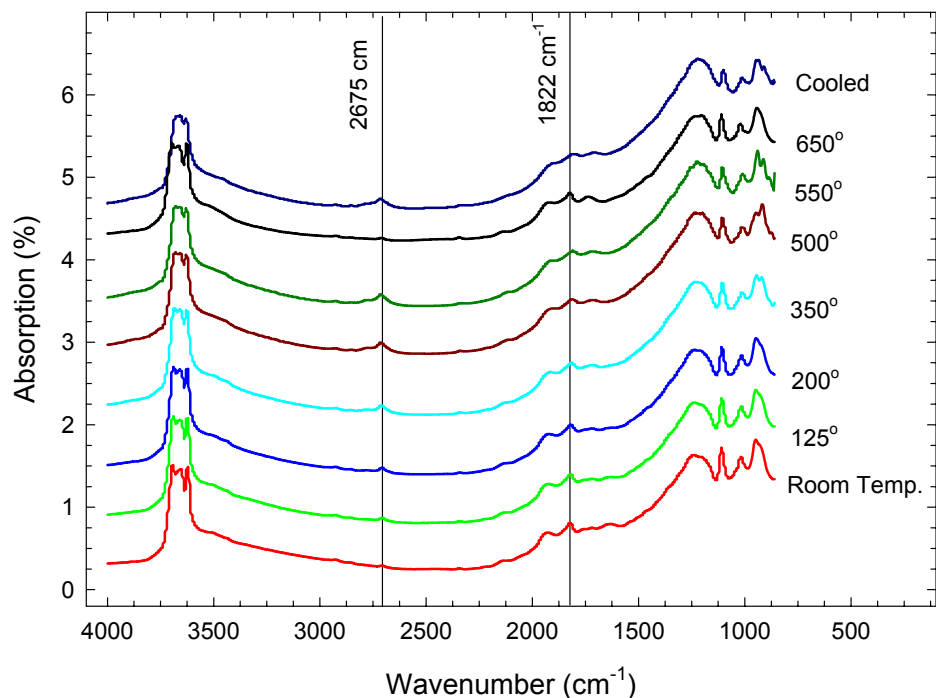


Figure 3-35. FTIR spectra from raw Marquis. With thermal treatment the clay is observed to dehydroxylate and the adsorption at 1850  $\text{cm}^{-1}$  (C=O stretch in carboxylic acid) is observed to be reduced. An adsorption band appears at  $\sim 2675 \text{ cm}^{-1}$  at higher temperatures.

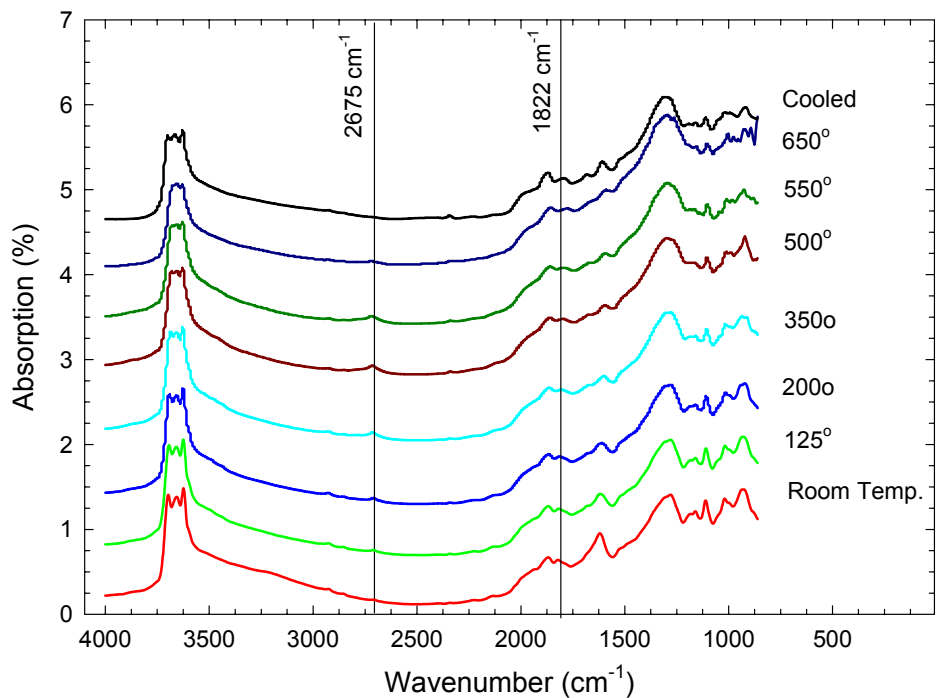


Figure 3-36. FTIR spectra from raw M&D ball clay. With thermal treatment the clay is observed to dehydroxylate and the adsorption at 1850  $\text{cm}^{-1}$  (C=O stretch in carboxylic acid) is observed to be reduced. An adsorption band appears at  $\sim 2675 \text{ cm}^{-1}$  at higher temperatures followed by its gradual extinction.

Table 3-IV. Band Assignments for the FTIR Characterization of the Clay Minerals.

Band (cm <sup>-1</sup> )	Assignment & Reference	Band (cm <sup>-1</sup> )	Assignment & Reference
3750	H <sub>2</sub> O vapor <sup>101</sup>	1760	C=O in COOH <sup>104</sup>
3690-3625	M <sub>3</sub> O-H vib. Clay <sup>102,103,105</sup>	1720	asym C=O in COOH <sup>104</sup>
3505	SiO-H vib. <sup>102</sup>	1680	OH bend, <sup>101</sup> asym C=O in COOH <sup>104</sup>
3440	Molecular H <sub>2</sub> O <sup>101,102</sup>	1650	OH vib., <sup>101</sup> H-OH, <sup>102</sup> C=C <sup>104</sup>
3400	O-H vib. <sup>101,103</sup>	1620	OH vib. <sup>101,103</sup>
3345	O-H vib. <sup>101,103</sup>	1540	COO-M <sup>104</sup>
3220	Absorbed H <sub>2</sub> O <sup>101</sup>	1495	COO-M <sup>104</sup>
3035	C-H stretch <sup>103</sup>	1460	CH <sub>2</sub> deform. <sup>103</sup>
2940	C-H asym stretch <sup>102,103</sup>	1415	CH <sub>2</sub> deform. <sup>102,103</sup>
2845	C-H asym stretch <sup>104</sup>	1360	N/A
2675	O-H in COOH <sup>104</sup>	1280	CH <sub>2</sub> wag <sup>102,103</sup>
2510	N/A	1230	CH <sub>2</sub> wag <sup>102,103</sup>
2470	N/A	1190	Si-O-Si <sup>102</sup>
2450	N/A	1160	Si-O, <sup>103</sup> R-OH in quartz <sup>103</sup>
2390	HA vibration	1120	Si-O, <sup>103</sup> R-OH in clay <sup>103</sup>
2340	CO <sub>2</sub>	1090	Si-O-Si, <sup>102</sup> Si-O, <sup>103</sup> R-OH in clay <sup>103</sup>
2235	N/A	1050	Si-O, <sup>103</sup> R-OH in clay <sup>103</sup>
2100	Al-O-H	1030	Si-O-Si, <sup>102</sup> Si-O, <sup>103</sup> R-OH in clay <sup>103</sup>
2045	Al-O-H	1000	Si-O, <sup>103</sup> R-OH in clay <sup>103</sup>
1930	Al-O-H	940	Si-OH, <sup>102</sup> Si-O, <sup>103</sup> R-OH in clay <sup>103</sup>
1870	Si-O-Si <sup>102</sup>	920	Si-O, <sup>103</sup> R-OH in clay, <sup>103</sup> AlAlOH smectite <sup>106</sup>
1825	C=O in COOH <sup>104</sup>	885	Si-CH <sub>3</sub> , <sup>102</sup> Si-O, <sup>103</sup> AlFeOH in smectite <sup>106</sup>
Vib. = vibration frequency Aro. = aromatic Deform. Deformation M = metal cation (including H <sup>+</sup> )		HA = humic acid Asym. = asymmetrical R = cation (not H <sup>+</sup> ) N/A = no relevant assignment found	

The FTIR results from the two organics are shown in Figure 3-37 (Aldrich humic acid) and Figure 3-38 (Darvan™ 811). Broad adsorption bands were apparent in the room temperature spectra from both organics due to physical water in the samples. With thermal treatment the broad adsorption band was reduced in intensity and a new band appeared at approximately  $2950\text{ cm}^{-1}$ . This band disappears in the humic acid sample while it grows in intensity in the PAA.

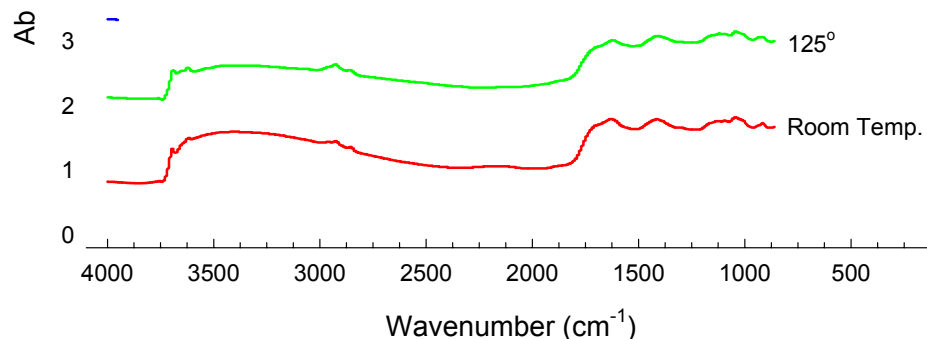


Figure 3-37. FTIR spectra from humic acid. The adsorption bands are observed to initially sharpen into distinct peaks followed by the decomposition of the humic acid at  $500^{\circ}\text{C}$ . The cooled spectrum is observed to be nearly flat. Band at  $\sim 2950\text{ cm}^{-1}$  is assigned to C-H stretch.

To summarize the FTIR results from the characterization of the clay and the effects of the thermal treatment on the change in the FTIR spectra, two bands were selected for comparison before and after the thermal treatment. The band at  $1822\text{ cm}^{-1}$  was assigned to the C=O stretching vibration in the carboxylic acid group. The band between  $3755$  and  $3600\text{ cm}^{-1}$  was assigned to chemical water present in the sample, this was taken to include: 1)  $\text{OH}^-$  vibrations in clay or humic substances and 2)  $\text{OR}^-$  vibrations in carboxylic acid groups (where R represents a monovalent cation). The change in the intensity of these bands was

determined using the software package [OMNIC v.6.0, ThermoNicolet, Waltham, MA] to measure the area under the curve and the reduction in the area was calculated. This calculation was performed for the Darvan™ 811 (PAA), humic acid, TK6, Kingsley, Huntingdon raw, Huntingdon coarse, Huntingdon middle, and M&D samples. The results are plotted in Figure 3-39.

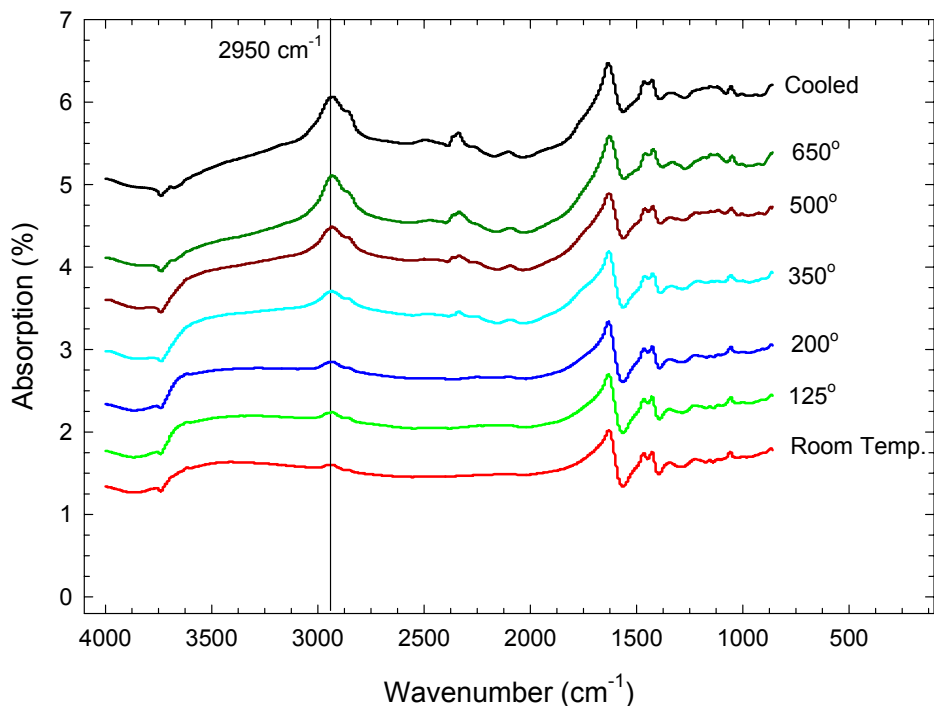


Figure 3-38. FTIR spectra from dried Darvan™811. The adsorption bands are observed gradually weakened due to decomposition of the PAA above 350°C. Band at ~2950 cm<sup>-1</sup> is assigned to C-H stretch which grows in intensity at elevated temperatures due to the thermal degradation of the carboxylic acid groups.

Complete dehydroxylation of the clays or burn out of the organics was not achieved during the thermal treatment in the environment chamber. This may in part be due to the design of the chamber or the thermal cycle used. The Darvan™ 811 sample did not have an apparent band at 1822 cm<sup>-1</sup> and therefore no change in peak area was calculated. The PAA and humic acid both showed a significant reduction in the peak area during the thermal treatment indicating a significant loss in the amount of sample present, as previously indicated the

cooled band for the humic acid is nearly a flat line. The clay samples showed a range for the reduction in peak area of each band. This may be due to different bonding environments (due to chelation, etc) or adsorption between the organics and the clay surface.

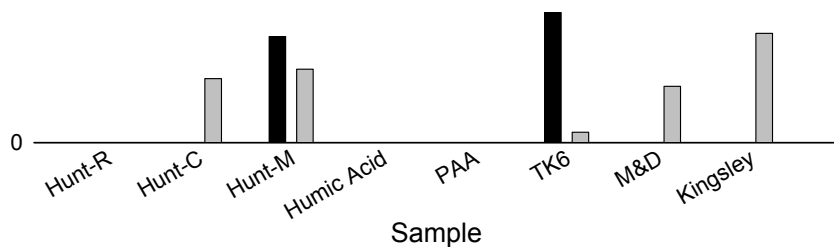


Figure 3-39. Change in the peak area of the  $1850\text{ cm}^{-1}$  band and the band between  $3755$  and  $3600\text{ cm}^{-1}$ , see text for band assignments, for representative spectra.

### **3.5 Summary and Conclusions**

Impurity species present in raw clay interfere with the accurate determination of the adsorption isotherm by a titration technique. Deviations from the predicted behavior, based upon a model of the kaolinite platelet, are the result of soluble organics and impurity minerals, e.g., quartz and 2:1-layer silicates, in the raw clay. While washing and beneficiation of the raw clays is not feasible in an industrial process, washing at high pH, greater than 9.5, and beneficiation by sedimentation can remove these species and allow the accurate determination of the adsorption level on clay platelets. Complete elimination of the organics present in clay is difficult to achieve, but a process of repeatedly washing the clay improved the adsorption results. The current study has demonstrated the accuracy of the model for adsorption based upon the mineralogy of the kaolinite platelet. Slight deviations from the predicted levels are the result of minor variations in the dimensions of the clay platelet, i.e., 2L:h.

Characterization of clays and organics by FTIR in an environmental chamber showed that the decomposition of the organics and kaolinite (i.e., the degradation of kaolinite to metakaolin) can be monitored as a function of temperature. Complete decomposition was not achieved due to either the thermal schedule, insufficient dwell time at temperature, or insufficient oxygen for complete combustion of the organics.

### 3.6 References

1. J. Cesarano III and I.A. Aksay, "Stability of Aqueous  $\alpha$ -Al<sub>2</sub>O<sub>3</sub> Suspension with Poly(methacrylic acid) Polyelectrolyte," *J. Am. Ceram. Soc.*, **71** [4] 250-5 (1988).
2. W.M. Carty, "The Colloidal Nature of Kaolinite," *Am. Ceram. Soc. Bull.*, **78** [8] 72-6 (1999).
3. W.J. Kelly, "Sampling Procedures for Raw Materials," *Ceram. Eng. Sci. Proc.*, **16** [3] 98-101 (1995).
4. W.J. Kelly, "Procedure for Determining the Response of Organic Matter in Ball Clays to Alkaline Digestion," *Ceram. Eng. Sci. Proc.*, **18** [2] 216-27 (1997).
5. W.J. Kelly, "Determining the Response of Organic Matter in Ball Clay," *Am. Ceram. Soc. Bull.*, **77** [2] 57-61 (1998).
6. F.J. Stevenson, *Humus Chemistry: Genesis, Composition, Reactions*, 2<sup>nd</sup> ed. John Wiley & Sons, New York, New York, 1994.
7. M.J. Stentiford, "Role of Organic Substances in Ball Clays," *Ceram. Inf.*, **17** [198] 563-4 (1982).
8. S. Boulton, R. Jugdaohsingh, K. White, B. Smith, and J. Powell, "Evidence that Polysaccharide and Humic and Fulvic Acids are Co-extracted during Analysis but Have Different Roles in the Chemistry of Natural Waters," *Appl. Geochem.*, **16** [9-10] 1261-267 (2001).
9. M.N. Jones and N.D. Bryan, "Colloidal Properties of Humic Substances," *Adv. Colloid Interface Chem.*, **78** [1] 1-48 (1998).
10. V.I. Esteves and A.C. Duarte, "Thermogravimetric Properties of Aquatic Humic Substances," *Mar. Chem.*, **63** [3-4] 225-33 (1999).
11. I. Fernandez, A. Cabaneiro, and T. Carballas, "Thermal Resistance to High Temperatures of Different Organic Fractions from Soils under Pine Forests," *Geoderma*, **104** [3-4] 281-98 (2001).
12. G.M.K. Abotsi and K. Osseo-Asare, "Surface Chemistry of Carbonaceous Gold Ores I. Characterization of the Carbonaceous Matter and Adsorption Behavior in Aurocyanide Solution," *Int. J. Miner. Process.*, **18** [3-4] 217-36 (1986).
13. J.A. Leenheer, R.L. Wershaw, G.K. Brown, and M.M. Reddy, "Characterization and Diagenesis of Strong-acid Carboxyl Groups in Humic Substances," *Appl. Geochem.*, **18** [3] 471-82 (2003).
14. C. Lin, S.H. Liu, and O.J. Hao, "Effect of Functional Groups of Humic Substances on UF Performance," *Water Res.*, **35** [10] 2395-402 (2001).

15. M.M. de Souza Sierra, K. Arrend, A.N. Fernandes, M. Giovanela and B. Szpoganica, "Application of Potentiometry to Characterize Acid and Basic Sites in Humic Substances – Testing the BEST7 Program with a Weak-acid Mixture," *Anal. Chim. Acta*, **445** [1] 89-98 (2001).
16. A.G. Zavarzina, V.V. Demin, T.I. Nifant'eva, V.M. Shkinev, T.V. Danilova, and B.Y. Spivakov, "Extraction of Humic Acids and Their Fractions in Poly(ethylene glycol)-based Aqueous Biphasic Systems," *Anal. Chim. Acta*, **452** [1] 95-103 (2002).
17. P. Warwick, A. Hall, V. Pashley, and N. Bryan, "Investigation of the Permeability of Humic Molecules Using Zeta Potential Measurements," *Chemosphere*, **45** [3] 303-7 (2001).
18. G. Wang, S. Hsieh, and C. Hong, "Destruction of Humic Acid in Water by UV Light – Catalyzed Oxidation with Hydrogen Peroxide," *Water Res.*, **34** [15] 3882-887 (2000).
19. Y. Cho and W. Choi, "Visible Light-Induced Reactions of Humic Acids on TiO<sub>2</sub>," *J. Photochem. Photobiol. A: Chem.*, **148** [1-3] 129-35 (2002).
20. J.C. Masini, G. Abate, E.C. Lima, L.C. Hahn, M.S. Nakamura, J. Lichtig, and H.R. Nagatomy, "Comparison of Methodologies for Determination of Carboxylic and Phenolic Groups in Humic Acids," *Anal. Chim. Acta*, **364** [1-2] 223-33 (1998).
21. A. Cozzolino and A. Piccolo, "Polymerization of Dissolved Humic Substances Catalyzed by Peroxidase. Effects of pH and Humic Composition," *Org. Geochem.*, **13** [3] 281-94 (2002).
22. G.G. Hevia, D.E. Buschiazzo, E.N. Hepper, A.M. Urioste, and E.L. Anton, "Organic Matter in Size Fractions of Soils of the Semiarid Argentina. Effects of Climate, Soil Texture and Management," *Geoderma*, **1999** [3-4] 1-13 (2003).
23. V.P. Evangelou, M. Marsi, and M.A. Chappell, "Potentiometric-Spectroscopic Evaluation of Metal-ion Complexes by Humic Fractions Extracted from Corn Tissue," *Spectrochim. Acta, A*, **58** [10] 2159-75 (2002).
24. R.D. Porasso, J.C. Benegas, M.A.G.T. van den Hoop, and S. Paoletti, "Analysis of Potentiometric Titrations of Heterogeneous Natural Polyelectrolytes in Terms of Counterion Condensation Theory: Application to Humic Acid," *Biophys. Chem.*, **86** [1] 59-69 (2000).
25. S.B. Ceppi, M.I. Velasco, and C.P. De Pauli, "Differential Scanning Potentiometry: Surface Charge Development and Apparent Dissociation Constants of Natural Humic Acid," *Talanta*, **50** [5] 1057-63 (1999).
26. J.D. Ritchie and E.M. Perdue, "Proton-binding Study of Standard and Reference Fulvic Acids, Humic Acids, and Natural Organic Matter," *Geochim. Cosmochim. Acta*, **67** [1] 85-96 (2003).

27. G. Abate and J.C. Masini, "Acid-Base and Complexation Properties of a Sedimentary Humic Acid. A Study on the Barra Bonita Reservoir of Tiete River, Sao Paulo State, Brazil," *J. Braz. Chem. Soc.*, **12** [1] 109-16 (2001).
28. Z. Struyk and G. Sposito, "Redox Properties of Standard Humic Substances," *Geoderma*, **102** [3-4] 329-46 (2001).
29. P. Lubal, D. Siroky, D. Fetsch, and J. Havel, "The Acidobasic and Complexation Properties of Humic Acids. Study of Complexation of Czech Humic Acids with Metal Ions," *Talanta*, **47** [2] 401-12 (1998).
30. J. Riggle and R. von Wandruszka, "Conductometric Characterization of Dissolved Humic Materials," *Talanta*, **57** [3] 519-26 (2002).
31. T.J. Manning, T. Bennett, and D. Milton, "Aggregation Studies of Humic Acid using Multiangle Laser Light Scattering," *Sci. Total Environ.*, **257** [2-3] 171-76 (2000).
32. J.P. Pinheiro, A.M. Mota, M.L.S. Simoes Goncalves, and H.P. van Leeuwen, "The pH Effect in the Diffusion Coefficient of Humic Matter: Influence in Speciation Studies using Voltammetric Techniques," *Colloids Surf., A*, **137** [1-3] 165-70 (1998).
33. S. Wold and T.E. Eriksen, "Diffusion of Lignosulphonate Colloids in Compacted Bentonite," *Appl. Clay Sci.*, **23** [1-4] 43-50 (2003).
34. M.J. Head and W.J. Zhou, "Evaluation of NaOH Leaching Techniques to Extract Humic Acids from Palaeosols," *Nucl. Instrum. Methods Phys. Res. B*, **172** [1-4] 434-39 (2000).
35. Y. Wang, C. Combe, and M.M. Clark, "The Effects of pH and Calcium on the Diffusion Coefficient of Humic Acid," *J. Membr. Sci.*, **183** [1] 49-60 (2001).
36. S. Jansen, M. Paciolla, E. Ghabbour, G. Davies, and J.M. Varnum, "The Role of Metal Complexation in the Solubility and Stability of Humic Acid," *Mater. Sci. Eng. C*, **4** [3] 181-87 (1996).
37. N.A. Wall and G.R. Choppin, "Humic Acids Coagulation: Influence of Divalent Cations," *Appl. Geochem.*, **18** [10] 1573-582 (2003).
38. A. Cozzolino, P. Conte, and P. Piccolo, "Conformational Changes of Humic Substances Induced by Some Hydroxy-, Keto-, and Sulfonic Acids," *Soil Biol. Biochem.*, **33** [4-5] 563-571 (2001).
39. J. Wu, L.J. West, and D.I. Stewart, "Effect of Humic Substances on Cu(II) Solubility in Kaolin-Sand Soil," *J. Hazard. Mater.*, **94** [3] 223-38 (2002).
40. C.P. Schulthess and C.P. Huang, "Humic and Fulvic Acid Adsorption by Silicon and Aluminum Oxide Surface on Clay Minerals," *Soil Sci. Soc. Am. J.*, **55** 34-42 (1991).

41. E. Pefferkorn, E. Ringenboch, and F. Elfarissi, "Aluminum Ions at Polyelectrolyte Interfaces. I. Mechanism of Polyacrylic Acid / Aluminum Oxide and Humic Acid / Kaolinite Complex Formation," *Colloid Polym. Sci.*, **279** [7] 629-37 (2001).
42. A.W.P. Vermeer and L.K. Koopal, "Adsorption of Humic Acid to Mineral Particle. 2. Polydispersity Effects with Polyelectrolyte Adsorption," *Langmuir*, **14** [15] 4219-216 (1998).
43. L.K. Koopal, Y. Yang, A.J. Minnard, P.L.M. Theunissen, and W.H. Van Riemsdijk, "Chemical Immobilisation of Humic Acid on Silica," *Colloids Surf. A*, **141** [3] 385-95 (1998).
44. A. Liu, R.C. Wu, E. Eschenazi, and K. Papadopoulos, "AFM on Humic Acid Adsorption on Mica," *Colloids Surf. A*, **174** [1-2] 245-52 (2000).
45. M. Arias, M.T. Barral, and J.C. Mejuto, "Enhancement of Copper and Cadmium Adsorption of Kaolin by the Presence of Humic Acids," *Chemosphere*, **48** [10] 1081-1088 (2002).
46. R.A. Akbour, J. Douch, M. Hamdani, and P. Schmitz, "Transport of Kaolinite Colloids through Quartz Sand: Influence of Humic Acid, Ca<sup>2+</sup>, and Trace Metals," *J. Colloid Interface Sci.*, **253** [1] 1-8 (2002).
47. C. Wu, C. Lin, H. Ma, and T. His, "Effect of Fulvic Acid on the Sorption of Cu and Pb onto  $\gamma$ -Al<sub>2</sub>O<sub>3</sub>," *Water Res.*, **37** [4] 743-52 (2003).
48. Z. Wu, Z. Gu, X. Wang, L. Evans, and H. Guo, "Effects of Organic Acids on Adsorption of Lead onto Montmorillonite, Goethite, and Humic Acid," *Environ. Pollut.*, **121** [3] 469-75 (2003).
49. J. Boily and J.B. Fein, "Proton Binding to Humic Acids and Sorption of Pb(II) and Humic Acid to the Corundum Surface," *Chem. Geol.*, **168** [3-4] 239-253, (2000).
50. J.B. Fein, J. Boily, K. Güclü, and E. Kaulback, "Experimental Study of Humic Acid Adsorption onto Bacteria and Al-oxide Mineral Surfaces," *Chem. Geol.*, **162** [1] 33-45 (1999).
51. K. Vermöhlen, H. Lewandowski, H. Narred, and M.J. Schwuger, "Adsorption of Polyelectrolytes onto Oxides – the Influence of Ionic Strength, Molar Mass, and Ca<sup>2+</sup> Ions," *Colloids Surf., A*, **163** [1] 45-53 (2000).
52. K. Au, A.C. Penisson, S. Yang, and C.R. O'Melia, "Natural Organic Matter at Oxide / Water Interfaces: Complexation and Conformation," *Geochim. Cosmochim. Acta*, **63** [19-20] 2903-917 (1999).
53. Z. Sokolowska and S. Sokolowski, "Influence of Humic Acid on Surface Fractal Dimension of Kaolin: Analysis of Mercury Porosimetry and Water Vapor Adsorption Data," *Geoderma*, **88** [3-4] 233-249 (1999),
54. Y. Shen, "Sorption of Humic Acid to Soil: The Role of Soil Mineral Composition," *Chemosphere*, **38** [11] 2489-499 (1999).

55. A. Violante, M. Arienzo, F. Sannino, C. Colombo, A. Piccolo, and L. Gianfreda, "Formation and Characterization of OH-Al-Humate-Montmorillonite Complexes," *Org. Geochem.*, **30** [6] 461-68 (1999).
56. S.M. Shevchenko and G.E. Bailey, "Non-bonded Organo-mineral Interactions and Sorption of Organic Compounds on Soil Surface: a Model Approach," *J. Mol. Struct. (Thermochem.)*, **422** [1-3] 259-270 (1998).
57. S.M. Shevchenko and G.E. Bailey, "Modeling Sorption of Soil Organic Matter on Mineral Surface: Wood-Derived Polymers on Mica," *SupraMol. Sci.*, **5** [1-2] 143-57 (1998).
58. S.J. Marshall, W.A. House, N.J. Russell, and G.F. White, "Comparative Adsorption of Natural and Commercially Available Humic Acids to River Sediments," *Colloids Surf., A*, **144** [1-3] 144-37 (1998).
59. K. Hayase and H. Tsubota, "Sedimentary Humic Acid and Fulvic Acid as Surface Active Substances," *Geochim. Cosmochim. Acta*, **47** [5] 947-52 (1983).
60. D.I. Drever and L.L. Stillings, "The Role of Organic Acids in Mineral Weathering," *Colloids Surf., A*, **120** [1-3] 167-81 (1997).
61. C. Jouany, "Surface Free Energy Components of Clay-Synthetic Humic Acid Complexes from Contact-Angle Measurements," *Clays Clay Miner.*, **39** [1] 43-9 (1991).
62. N.C. Lockhart, "Electrical Conductivity and the Surface Characteristics of Kaolinite Clay and Clay-Humic Acid Complexes," *Clays Clay Miner.*, **29** [6] 423-8 (1981).
63. H. Vali and R. Hesse, "The Microstructure of Dilute Clay and Humic Acid Suspensions Revealed by Freeze-Fracture Electron Microscopy: Discussion," *Clays Clay Miner.*, **40** [5] 620-3 (1992).
64. G. Farkas and N. Katona, "Fluidizing Effect of Humic Compounds in Kaolinic Slurries," *Interceram*, **40** [3] 175-8 (1991).
65. R. Lapasin and E. Lucchini, "Influence of Some Industrial Deflocculating Agents on the Rheologic Characteristics of a Slick for Earthenware," *Ceram. Inf.*, **17** [197] 478-80 (1982).
66. E. Tombacz, M. Gilde, I. A'braham, and F. Szanto, "Effect of Electrolyte Concentration on the Interaction of Humic Acid and Humate with Montmorillonite," *Appl. Clay Sci.*, **3** [1] 31-52 (1988).
67. F. Elfarissi and E. Pefferkorn, "Kaolinite / Humic Acid Interaction in the Presence of Aluminum Ion," *Colloids Surf., A*, **168** [1] 1-12 (2000).
68. M.M. Bob and H.W. Walker, "Effect of Natural Organic Coatings on the Polymer-Induced Coagulation of Colloidal Particles," *Colloids Surf., A*, **177** [2-3] 215-22 (2001).

69. W. Huang, P. Peng, Z. Yu, and J. Fu, "Effects of Organic Matter Heterogeneity on Sorption and Desorption of Organic Contaminants by Soils and Sediments," *Appl. Geochem.*, **18** [7] 955-72 (2003).
70. J. Wiszniowski, D. Robert, J. Surmacz-Gorska, K. Miksch, and J. Weber, "Photocatalytic Decomposition of Humic Acids on TiO<sub>2</sub>, Part I: Discussion of Adsorption and Mechanism," *J. Photochem. Photobiol. A*, **152** [1-3] 267-73 (2002).
71. T. Juhna, M. Klavins, and L. Eglite, "Sorption of Humic Substances on Aquifer Material at Artificial Recharge of Groundwater," *Chemosphere*, **51** [9] 861-8 (2003).
72. J. Cases, J. Mielczarski, E. Mielczarska, L.J. Michot, and F. Villieras, "Ionic Surfactants Adsorption on Heterogeneous Surfaces," *C. R. Geosci.*, **334** [9] 675-88 (2002).
73. P. Reiller, V. Moulin, F. Casanova, and C. Dautel, "Retention Behavior of Humic Substances onto Mineral Surfaces and Consequences upon Thorium (IV) Mobility: Case of Iron Oxides," *Appl. Geochem.*, **17** [12] 1551-62 (2002).
74. J. Duan, F. Wilson, N. Graham, and J.H. Tay, "Adsorption of Humic Acid by Powdered Activated Carbon in Saline Water Conditions," *Desalination*, **151** [1] 53-66 (2003).
75. M. Bob and H.W. Walker, "Enhanced Adsorption of Natural Organic Matter on Calcium Carbonate Particles Through Surface Charge Modification," *Colloids Surf., A*, **191** [1-2] 17-25 (2001).
76. H. Katsumata, S. Kaneco, R. Matsuno, K. Itoh, K. Masuyama, T. Suzuki, K. Funasaka, and K. Ohta, "Removal of Organic Polyelectrolytes and Their Metal Complexes by Adsorption onto Xonotlite," *Chemosphere*, **52** [5] 909-15 (2003).
77. X. Zhang and R. Bai, "Adsorption Behavior of Humic Acid onto Polypyrrole-Coated Nylon 6,6 Granules," *J. Mater. Chem.*, **12** [9] 2733-9 (2002).
78. E.K. Kim and H.W. Walker, "Effect of Cationic Polymer Additives on the Adsorption of Humic Acid onto Iron Oxide Particles," *Colloids Surf., A*, **194** [1-3] 123-31 (2001).
79. P.J. Harbour, "Particle-Particle Interactions in Concentrated Colloidal Suspensions in the Presence of Natural Organic Matter"; Ph.D. Thesis. The University of Melbourne, Victoria, Australia, 2002.
80. S. Kam and J. Gregory, "The Interaction of Humic Substances with Cationic Polyelectrolytes," *Water Res.*, **35** [15] 3557-66 (2001).
81. Y. Takahashi, Y. Minal, S. Ambe, Y. Makide, and F. Ambe, "Comparison of Adsorption Behavior of Multiple Inorganic Ions on Kaolinite and Silica in the Presence of Humic Acid Using the Multitracer Technique," *Geochim. Cosmochim. Acta*, **63** [6] 815-36 (1999).

82. F. Elfarissi L. Nabzar, E. Ringenbach, and E. Pefferkorn, "Polyelectrolytic Nature of Humic Substances-Aluminum Ion Complexes, Interfacial Characteristics and Effects on Colloid Stability," *Colloids Surf., A*, **131** [1-3] 281-94 (1998).
83. S.H. Sutherland and S.E. Cabaniss, "Aluminum Binding to Humic Substances Determined by High Performance Cation Exchange Chromatography," *Geochim. Cosmochim. Acta*, **61** [1] 1-9 (1997).
84. P. Buurman, B. van Lagen, and A. Piccolo, "Increase in Stability Against Thermal Oxidation of Soil Humic Substances as a Result of Self Association," *Org. Geochem.*, **33** [3] 367-81 (2002).
85. J.E. Gregor, C.J. Nokes, and E. Fenton, "Optimising Natural Organic Matter Removal from Low Turbidity Waters by Controlled pH Adjustment of Aluminum Coagulation," *Water Res.*, **31** [12] 2949-58 (1997).
86. C. Donisa, R. Mocanu, and E. Steinnes, "Distribution of Some Major and Minor Elements Between Fulvic and Humic Acid Fractions in Natural Soils," *Geoderma*, **111** [1-2] 75-84 (2003).
87. K.M. Elkins and D.J. Nelson, "Spectroscopic Approaches to the Study of the Interaction of Aluminum with Humic Substances," *Coord. Chem. Rev.*, **228** [2] 205-25 (2002).
88. A.G.S. Prado and C. Airoidi, "Humic Acid-Divalent Cation Interactions," *Thermochim. Acta*, **405** [2] 287-92 (2003).
89. P.A.W. van Hees, E. Tipping, and U.S. Lundstrom, "Aluminum Speciation in Forest Soil Solution – Modelling the Contribution of Low Molecular Weight Organic Acids," *Sci. Total Environ.*, **278** [1-3] 215-29 (2001).
90. M.D. Paciolla, S. Kolla, and S.A. Jansen, "The Reduction of Dissolved Iron Species by Humic Acid and Subsequent Production of Reactive Oxygen Species," *Adv. Environ. Res.*, **7** [1] 169-78 (2002).
91. M.A.G.T. van den Hoop, R.D. Porasso, and J.C. Benegas, "Complexation of Heavy Metals by Humic Acids: Analysis of Voltammetric Data by Polyelectrolyte Theory," *Colloids Surf., A*, **203** [1-3] 105-16 (2002).
92. L.H. Mikkelsen, "Applications and Limitation of the Colloid Titration Method for Measuring Activated Sludge Surface Charges," *Water Res.*, **37** [10] 2458-66 (2003).
93. A.L.R. Merce, I.H.Z. Spir, M. Jose, O. Salmon, R.A. Giannoni, and A.S. Mangrich, "Model Compounds of Humic Acid and Oxovanadium Cations. Potentiometric Titration and EPR Spectroscopy Studies," *J. Braz. Chem. Soc.*, **10** [6] 463-8 (1999).
94. E.B.H. Santos, V.I. Esteves, J.P.C. Rodrigues, and A.C. Duarte, "Humic Substance's Proton-Binding Equilibria: Assessment of Errors and Limitation of Potentiometric Data," *Anal. Chim. Acta*, **392** [2-3] 333-41 (1999).

95. F. Mercier, V. Moulin, M.J. Giuttet, N. Barre, M. Gauteir-Soyer, P. Trocellier, and P. Toulhoat, "Applications of New Surface Analysis Techniques (NMA and XPS) to Humic Substances," *Org. Geochem.*, **33** [3] 247-55 (2002).
96. F. Monteil, E.B. Brouwer, S. Masset, Y. Deslandes, and J. Dumonceau, "Combination of X-ray Photoelectron and Solid-State  $^{13}\text{C}$  Nuclear Magnetic Resonance Spectroscopy in the Structural Characterisation of Humic Acids," *Anal. Chim. Acta*, **42** [2] 243-55 (2000).
97. D.A.N. Ussiri and C.E. Johnson, "Characterization of Organic Matter in a Northern Hardwood Forest Soil by  $^{13}\text{C}$  NMR Spectroscopy and Chemical Methods," *Geoderma*, **111** [1-2] 123-49 (2003).
98. C. Keeler and G.E. Maciel, " $^{13}\text{C}$  NMR Spectral Editing of Humic Material," *J. Mol. Struct.*, **550-551** 297-305 (2000).
99. S.A. Jansen, M. Malaty, S. Swabara, E. Johnson, E. Ghabbour, G. Davies, and J.M. Varnum, "Structural Modeling in Humic Acids," *Mater. Sci. Eng. C*, **4** [3] 175-9 (1996).
100. G. Ricca, F. Severini, G. DiSilvestro, C.M. Yuan, and F. Adani, "Derivatization and Structural Studies by Spectroscopic Methods of Humic Acids from Leonardite," *Geoderma*, **98** [3-4] 115-25 (2000).
101. H.W. van der Marel and H. Beutelspacher, *Atlas of Infrared Spectroscopy of Clay Minerals and Their Admixtures*. Elsevier Scientific Publishing, New York, New York, 1974.
102. C.A. Capozzi, "Processing, Structure, and Properties of Organically Modified Silicates"; Ph.D. Thesis. Alfred University, Alfred, New York, 1992.
103. V. Lorprayoon, "Infrared Spectra of Thiophenes and Related Compounds Absorbed on Montmorillonites"; Ph.D. Thesis. Alfred University, Alfred, New York, 1981.
104. D. Lee, "Thin Film Coatings on Glasses or Ceramics and Structural Determination by Drift Spectroscopy"; Ph.D. Thesis. Alfred University, Alfred, New York, 1998.
105. S. Petit, "Crystal Chemistry of Talcs: a NIR and MIR Spectroscopic Approach," Presentation at the 2003 Clay Minerals Society Meeting Workshop, Athens, Georgia, June 7, 2003 (unpublished).
106. J. Madojeva and P. Komadel, "Information Available from Infrared Spectra of the Fine Fractions of Bentonites," Presentation at the 2003 Clay Minerals Society Meeting Workshop, Athens, Georgia, June 7, 2003 (unpublished).
107. J. Chen, B. Gu, E.J. LeBoeuf, H. Pan, and Sheng Dai, "Spectroscopic Characterization of the Structural and Functional Properties of Natural Organic Matter Fractions," *Chemosphere*, **48** [1] 59-68 (2002).

108. Y. Yang and T. Wang, "Fourier Transform Raman Spectroscopic Characterization of Humic Substances," *Vib. Spectrosc.*, **14** [1] 105-12 (1997).
109. C.M. Caughel, "Characterization of Clay Raw Materials"; M.S. Thesis. Alfred University, Alfred, New York, 2002.
110. D.M. Moore and R.C. Reynolds, Jr., *X-ray diffraction and the Identification and Analysis of Clay Minerals*; Oxford University Press, New York, New York, 1997.
111. P. Komadel, "Chemical Treatments of Smectites," 2003 Jackson Award Presentation, Clay Minerals Society, Athens, Georgia, June 9, 2003 (unpublished).
112. *Handbook of Chemistry and Physics*, 72<sup>nd</sup> ed.; p. 4-84. Edited by D.R. Lide. The Chemical Rubber Company, Boca Raton, Florida, 1991.

## **4. Effects of Incremental Additions of Na-PAA to Clay**

### **4.1 Introduction**

In the previous two chapters the competitive adsorption between Na-PAA (specifically Darvan™ 811) and humic substances was discussed. In this chapter the effects of incremental additions of Na-PAA, Darvan™ 811, to clays to gradually displace the humic substances from the clay surface are investigated. It was hypothesized that by gradually adding PAA to a clay slurry, there would be change in the molecular weight of the humic substances displaced from the clay surface, with the most hydrophilic species being the first removed and the most hydrophobic the last fraction removed.

### **4.2 Literature Review**

Chromatography, including liquid chromatography, size exclusion chromatography, and gel permeation chromatography, is an effective means of characterizing the molecular weight of organic species in solution. Numerous studies have investigated the molecular weight of humic substances in solution by chromatography.<sup>1-15</sup> The consensus of these studies was that humic acid is a higher molecular weight species relative to fulvic acid and that the molecular weight of these species depended on their source, the extraction technique, and the eluent that was used to characterize the molecular weight. These factors can change the conformation of the humic substances in solution and thus vary the measured molecular weight.

A fully dissociated organic molecule will have a more open conformation compared to a partially dissociated or fully protonated molecule. The open conformation will prevent the molecule from entering the smaller pore structure in the column of the chromatograph. Therefore the dissociated molecules appear to have a higher molecular weight relative to a partially dissociated molecule since it will pass through the detector more quickly. Due to the lack of standard humic substances for calibration of the chromatograph, only relative molecular weights for humic substances can be reported.

Janos prepared a review on the use of separation methods, i.e., chromatography, in the chemistry of humic substances.<sup>15</sup> A standardized method of fractioning humic substances has been developed by the International Humic Substances Society; this process involves fractioning the humic substances by their solubility as a function of pH. Another procedure for isolating humic substances, typically from water samples, involves the use of XAD sorbents, columns packed with different XAD resins that have various degrees of hydrophobicity; use of a gradient eluent can enhance the fraction process with XAD resins. Janos concludes that chromatography methods are effective for characterizing humic substances as well as providing information about their properties and composition. Structural data for humic substances has been generated by GC-MS (gas chromatography-mass spectrometry) and rapid progress in LC-MS (liquid chromatography-mass spectrometry) instrumentation has made it possible to study the properties of humic substances at the molecular level.

#### **4.3 Experimental Procedure**

To investigate the effects of incrementally adding Na-PAA to TK6 kaolin clay and Huntingdon ball clay 15 v/o suspensions were prepared for adsorption. Four samples were prepared at both pH  $6.0 \pm 0.2$  and pH  $9.0 \pm 0.2$  for each clay. Initially the samples were prepared without PAA, centrifuged, and the supernatant was tested using the titration method previously described in Chapter 2. The sediment was resuspended with distilled water and dosed with a small addition of PAA followed by readjusting the pH to the target value. The target concentrations of PAA are listed in Table 4-I for the TK6 samples and Table 4-II for the Huntingdon samples in this study. Images of the diluted supernatant before titration were taken to show the change in the color of the solution due to the addition of Darvan™ 811.

Table 4-I. Cumulative Concentration of Darvan™ 811 Added as an Incremental Dose to TK6 at pH 6.0±0.2 and pH 9.0±0.2.

Addition	pH 6.0±0.2		pH 9.0±0.2	
	Target grams	Target mg/m <sup>2</sup>	Target grams	Target mg/m <sup>2</sup>
0	0.00	0.00	0.00	0.00
1	0.37	0.17	0.13	0.06
2	0.43	0.20	0.17	0.08
3	0.50	0.23	0.22	0.10
4	0.56	0.26	0.26	0.12
5	0.59	0.27	0.28	0.13
6	0.61	0.28	0.30	0.14
7	0.63	0.29	0.33	0.15
8	0.69	0.32	0.37	0.17
9	0.78	0.36	0.41	0.19
10	0.85	0.39	0.43	0.20
11	0.87	0.40	0.46	0.21
12	0.89	0.41	0.48	0.22
13	0.91	0.42	0.54	0.25
14	0.95	0.44	0.61	0.28
15	1.52	0.70	1.08	0.50

This process was repeated until it was expected, based upon the adsorption model for kaolinite platelets, that the surface of the clay particles would be saturated with PAA. To determine the change in the molecular weight of the organics displaced from the surface gel permeation chromatography (GPC) was used. The instrument used for this study was a Waters HPLC pump (Waters 1515 Isocratic HPLC Pump, Waters Corp., Milford, MA) equipped with poly[hydroxymethacrylate] packed columns (Shodex-OH pak KB-G, KB-802, KB-804 and KB-806M columns, Showa Denko KK, Tokyo, Japan) and a refractive index detector (Waters 2410 refractive index detector, Waters Corp., Milford, MA). Data was collected using the Breeze GPC software (Breeze v.3.20, Waters Corp., Milford, MA). The system was calibrated using Na-PAA narrow standards (Waters Corp., Milford, MA). The eluent was passed through the guard column

(KB-G) followed by the KB-802, KB-804, and finally the KB-806M columns, in this manner the maximum separation as a function of molecular weight was achieved. A flow rate of 1 mL/min and an internal temperature of 30°C was used for the eluent in all of the studies. Using these test parameters the total flow time through the GPC system was approximately 33 minutes. As an eluent two systems were tested: 1) a 10 wt% pH 5 buffer solution and 2) a 10 wt% pH 10 buffer solution; no change in the pH of the buffer solution was measured after dilution with distilled water. The chemical analysis of the buffer solutions, taken from the manufactures' MSDS sheets, is listed in Table 4-III. These two systems were selected in an attempt to change the conformation of the PAA standards and thus vary the elution time.

Table 4-II. Cumulative Concentration of Darvan™ 811 Added as an Incremental Dose to Huntingdon at pH 6.0±0.2 and pH 9.0±0.2.

Addition	pH 6.0±0.2		pH 9.0±0.2	
	Target grams	Target mg/m <sup>2</sup>	Target grams	Target mg/m <sup>2</sup>
0	0.00	0.00	0.00	0.00
1	0.32	0.17	0.11	0.06
2	0.38	0.20	0.15	0.08
3	0.44	0.23	0.19	0.10
4	0.50	0.26	0.23	0.12
5	0.52	0.27	0.25	0.13
6	0.54	0.28	0.27	0.14
7	0.55	0.29	0.29	0.15
8	0.61	0.32	0.32	0.17
9	0.69	0.36	0.36	0.19
10	0.75	0.39	0.38	0.20
11	0.76	0.40	0.40	0.21
12	0.78	0.41	0.42	0.22
13	0.80	0.42	0.48	0.25
14	0.84	0.44	0.54	0.28
15	1.34	0.70	0.96	0.50

Table 4-III. Chemical Analysis from the Buffer Solutions Used as Eluents for the GPC.

<b>pH 5 Buffer Solution*</b>	
<b>Chemical</b>	<b>Concentration</b>
Citric Acid	<3%
Sodium Hydroxide	<1%
Water	Balance
<b>pH 10 Buffer Solution**</b>	
<b>Chemical</b>	<b>Concentration</b>
Di-sodium ethylene diamine tetraacetate dihydrate	1.0%
Potassium Carbonate	0.6%
Potassium Borate	0.4%
Potassium Hydroxide	0.2%
Cl Acid blue 9, disodium salt	0.02%
Water	97.78%

\* Acros Organics, Fair Lawn, NJ

\*\* Fisher Scientific, Pittsburgh, PA

The GPC operates by passing a carrier fluid, an eluent, through a series of columns. Within these columns was a gradually smaller and smaller pore structure that served to trap lower molecular weight species. Thus the higher molecular weight species, which were not trapped in the columns, pass rapidly through the system and were analyzed first at the detector. With time the lower molecular weight species passed from the column and were detected. The result was a plot of the signal as a function of time, which was related back to molecular weight through the use of known standards.

To verify that the GPC was giving accurate results several industrial PAA's, those used in Chapter 2, were tested in the GPC and the results compared to the manufacturer's stated molecular weight.

The precipitated material was prepared by dissolving the samples in the pH 10 eluent so as to obtain a roughly 1 wt% solution of organic; approximately 0.1 g of organic was dissolved in 10 mL of eluent. The samples were filtered

through a 0.45  $\mu\text{m}$  filter [0.45  $\mu\text{m}$  Nylon Fisherbrand Syringe Filter, Fisher Scientific, Pittsburgh, PA] and de-aired using an aspirator vacuum pump [Brinkman Model B-169 Vacuum Aspirator, Sibata Scientific Technology Ltd., Tokyo, Japan]. The samples were subsequently stored in a cool, dark place to prevent degradation of the samples by UV light prior to testing the samples with the GPC. Samples were stored for a period of not more than 5 days to minimize degradation of the organic. Standards and known samples of PAA were prepared in a similar fashion, i.e., a 1 wt% solution of the polymer in the proper eluent.

Samples were run using the above procedure and the molecular weight of the organic present in the samples was initially calculated using the pH 5 calibration curve. While this procedure is unorthodox it was used in an attempt to achieve the maximum separation between the peaks in the chromatograph. Since no humic acid molecular weight standards are available as a reference, only relative molecular weights can be reported. The molecular weight of the humic substances in each sample was calculated using both the pH 5 and pH 10 calibration equations. A peak associated with the unadsorbed Darvan™ 811 in the sample was used as a reference to calculate the percent error in the measured molecular weight. The reported molecular weights for the humic substances were relative to the molecular weight of the Na-PAA narrow standards under the test circumstances used in this study. No effort has been made to characterize the structure of the humic substances in this research as this is outside the subject matter of this thesis.

#### **4.4 Results**

The results from the adsorption portion of the study indicate that organics are displaced from the clay surface with each subsequent addition of PAA, i.e., in most cases a negative adsorption level is calculated from the titration data. The results from the adsorption on TK6 are shown in Figure 4-1. The results from the adsorption on Huntingdon are shown in Figure 4-2. Preferential adsorption of the humic substances may be preventing the complete displacement at the surface due to the more hydrophobic nature (relative to PAA) of the humic substances.

PAA gradually replace the more hydrophobic humic substances since it satisfied more of the charge sites on the powder surface, i.e., it reduces the free energy of the system as discussed in Chapter 2.

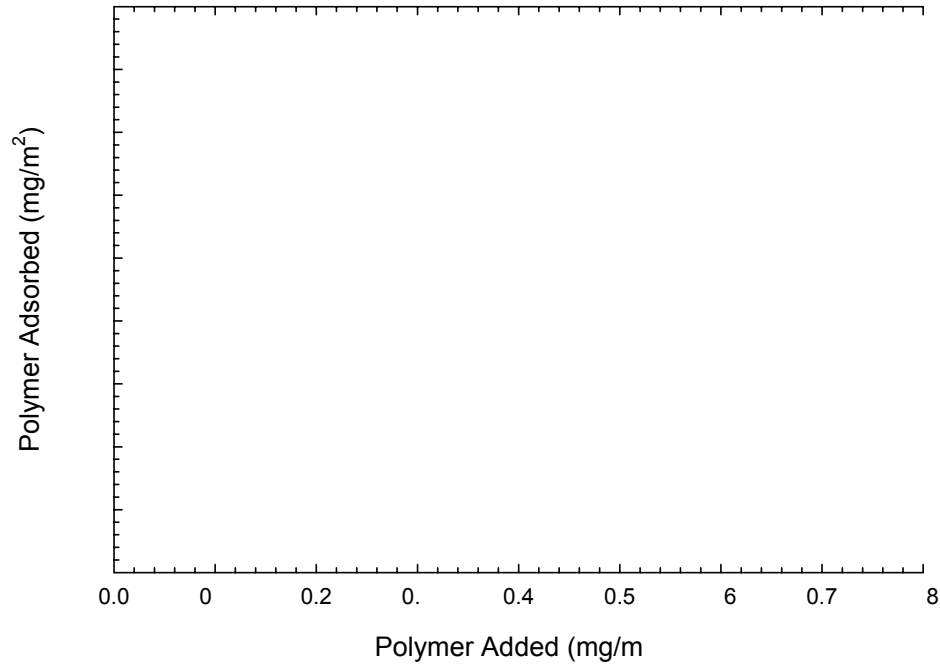


Figure 4-1. Cumulative adsorption results for TK6 at pH 6 (open symbols) and pH 9 (closed symbols) after incremental additions of PAA. Incremental additions of PAA to TK6 result in a negative adsorption isotherm as organics are displaced from the surface of the commercial clay.

With each addition of PAA to the suspension more organic was removed from the surface of the clay resulting in a negative adsorption value. It was observed at both pH 6 and 9 that larger additions of PAA result in more organic being removed from the clay surface. With smaller additions of PAA lesser quantities of organic in the clay were removed, corresponding to the plateaus observed in Figures 1 and 2. After titrating the supernatant samples the liquid above the precipitated material was decanted and the precipitate was dried at 50°C. A precipitate was only formed after titrating the Huntingdon samples; the species present in the TK6 clay remained dissolved after titration. The images from the diluted TK6 supernatant samples are shown in Figure 4-3 (pH 6) and Figure 4-4 (pH 9); there was no visible change in the supernatant after titration.

The images from the diluted Huntington supernatant samples before titration are shown in Figure 4-5 (pH 6) and Figure 4-6 (pH 9); after titration a dark precipitate was formed.

A calibration curve was fit to the standard PAA runs so that the molecular weight of the unknown samples could be determined. For the pH 5 eluent a linear regression best fit the data while the pH 10 eluent was best fit by a quadratic regression. The calibration equations for both the pH 5 and pH 10 eluents are listed in Table 4-IV along with the statistics for the curve fit. The statistics from each standard run relative to the calibration curve are listed in Table 4-V. The data from the standard runs and the calibration curves are plotted in Figure 4-7.

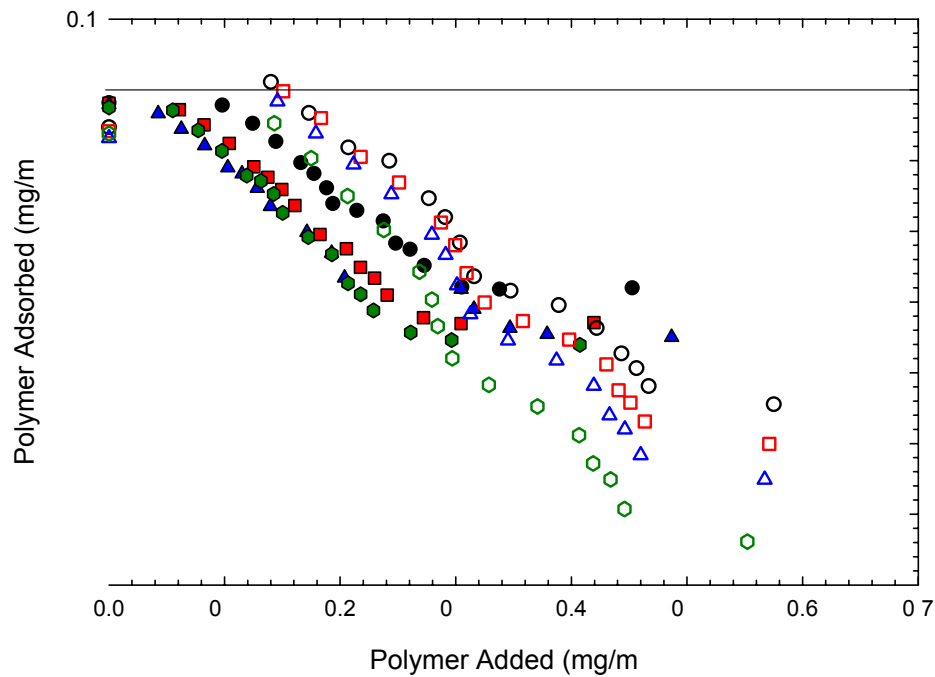


Figure 4-2. Cumulative adsorption results for Huntington at pH 6 (open symbols) and pH 9 (closed symbols) after incremental additions of PAA. Incremental additions of PAA to TK6 result in a negative adsorption isotherm as organics are displaced from the surface of the commercial clay.

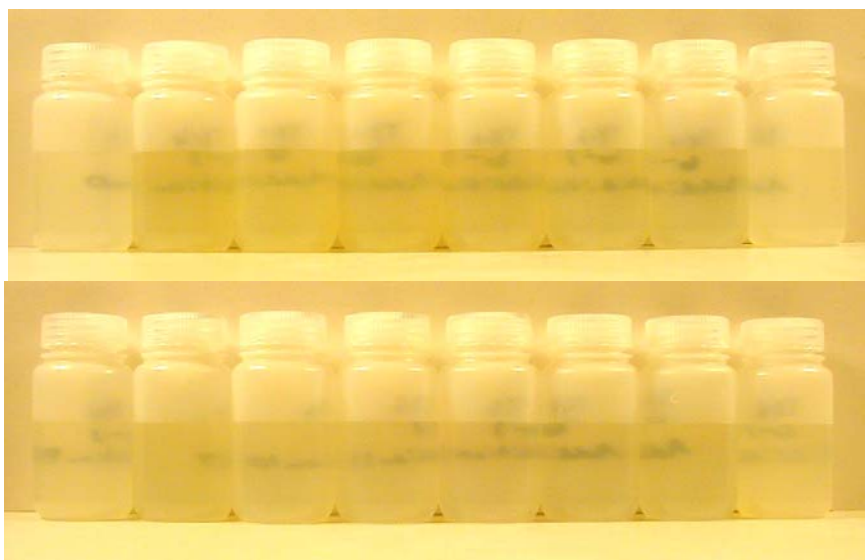


Figure 4-3. Images of the diluted supernatant before titration from the TK6 samples prepared at  $\text{pH } 6.0 \pm 0.2$ . Samples number 0 through 7 are shown in the top image while samples number 8 through 15 are shown in the bottom image. Incremental additions of Darvan™ 811 are observed to change the coloration of the supernatant. Target concentrations of Darvan™ 811 are listed in Table 4-I.

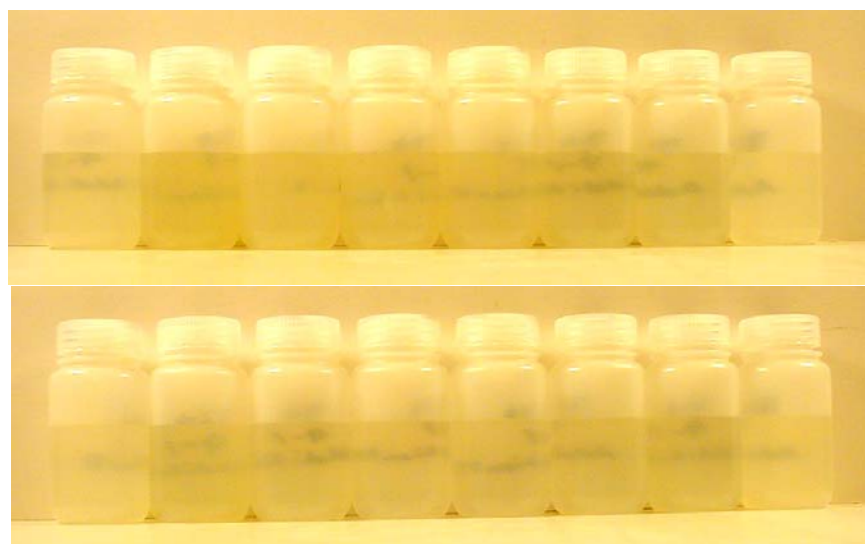


Figure 4-4. Images of the diluted supernatant before titration from the TK6 samples prepared at  $\text{pH } 9.0 \pm 0.2$ . Samples number 0 through 7 are shown in the top image while samples number 8 through 15 are shown in the bottom image. Incremental additions of Darvan™ 811 are observed to change the coloration of the supernatant. Target concentrations of Darvan™ 811 are listed in Table 4-I.

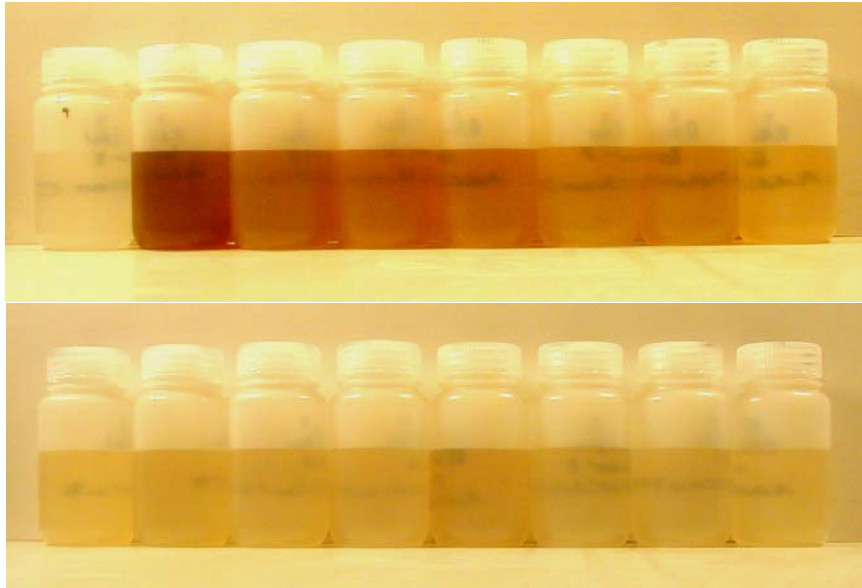


Figure 4-5. Images of the diluted supernatant before titration from the Huntingdon samples prepared at  $\text{pH } 6.0 \pm 0.2$ . Samples number 0 through 7 are shown in the top image while samples number 8 through 15 are shown in the bottom image. Incremental additions of Darvan™ 811 are observed to change the coloration of the supernatant. Target concentrations of Darvan™ 811 are listed in Table 4-II.

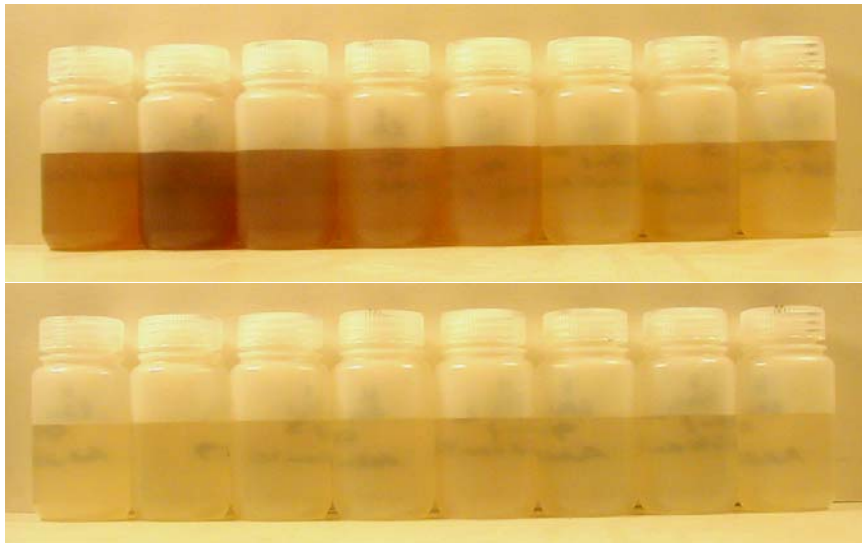


Figure 4-6. Images of the diluted supernatant before titration from the Huntingdon samples prepared at  $\text{pH } 9.0 \pm 0.2$ . Samples number 0 through 7 are shown in the top image while samples number 8 through 15 are shown in the bottom image. Incremental additions of Darvan™ 811 are observed to change the coloration of the supernatant. Target concentrations of Darvan™ 811 are listed in Table 4-II.

Table 4-IV. Calibration Equations for the GPC to Relate the Elution Volume (or Time) to the Molecular Weight of the Organic.

pH	Calibration Equation	R <sup>2</sup>	Std. Error
5	$\log(\text{MW})=13.1 - 0.413*V$	0.985	0.166
10	$\log(\text{MW})=0.236+1.03*V-0.0411*V^2$	0.989	0.122

Using these calibration curves samples of industrial PAA, those used in Chapter 2, were tested to verify that accurate molecular weights were measured using the GPC. The results are listed in Table 4-VI along with the calculated error, based upon reported value from the manufacturer, in the molecular weight. There was some error in the measured molecular weights of the polymers, primarily at the intermediate molecular weights where there is a poor fit in the calibration curve. At the lower molecular weights, between 28,000 and 3,000 Daltons, there is less error in the measured molecular weight; this was the region of interest since the molecular weight of Darvan™ 811 and the unknown humic substances were expect to fall within this range of molecular weights.

Since there was little difference in the trend of the adsorption results at pH 6 and pH 9 (differences were expected in the concentration of polymer adsorbed due to changes in the polymer conformation) only the GPC results from one set of pH 6 data will be reported. The results from the GPC analysis indicated that there was little variation in the molecular weight of the species displaced from the surface of the Huntingdon clay as a function of PAA addition at pH 6, Figure 4-8. A linear regression through the pH 10 data resulted in a slope of -290.2 with a R<sup>2</sup> value of 21.99, i.e., a very poor fit to the data. An average value model, i.e., a model where “y” was independent of “x,” resulted in a R<sup>2</sup> value of 32.86, still a very poor fit, but it was an improvement over the linear regression.

Table 4-V. Results from the Standard Runs and the Statistics for the Standards Relative to the Calibration Curve.

<b>pH 5 eluent</b>			
<b>Standard MW (Daltons)</b>	<b>Elution Volume (mL)</b>	<b>Predicted MW (Daltons)</b>	<b>Error (%)</b>
1100000	16.826	1323467	-16.88
782200	17.476	712987	9.71
222300	18.042	416333	-46.61
115000	20.200	53388	115.40
62900	20.426	43043	46.13
28000	21.060	23559	18.85
16000	21.610	13959	14.62
7500	22.247	7611	-1.46
2925	23.000	3718	-21.32
900	23.846	1662	-45.84
192*	26.152	185	3.72
192*	26.156	185	4.03
192*	26.173	182	5.72
<b>pH 10 eluent</b>			
<b>Standard MW (Daltons)</b>	<b>Elution Volume (mL)</b>	<b>Predicted MW (Daltons)</b>	<b>Error (%)</b>
1100000	16.826	897467	22.57
782200	17.158	678609	15.27
222300	17.857	351998	-36.85
115000	18.633	152298	-24.49
62900	19.608	45242	39.03
28000	19.967	27679	1.16
16000	20.395	14894	7.42
7500	20.929	6559	14.35
2925	21.478	2667	9.67
900	21.963	1149	-21.66

\* Molecular weight of citric acid which was present in the as-received buffer solution.

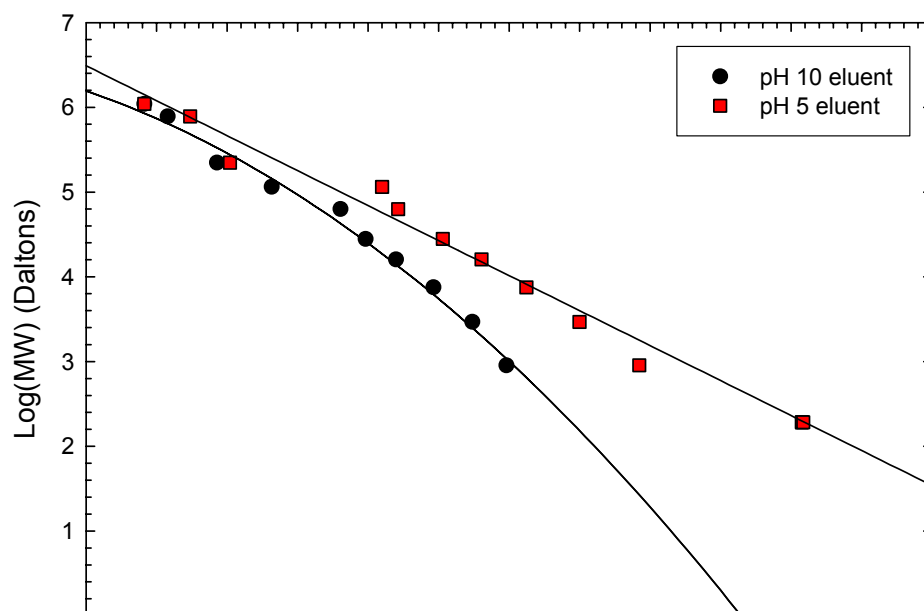


Figure 4-7. Calibration curves for the GPC from the standard PAA samples at pH 5 and pH 10. Also plotted are the best fit regression models, from the GPC software, used to convert eluent volume into molecular weight for the unknown samples.

Table 4-VI. Reported Molecular Weight and the Measured Molecular Weight of Various Na-PAA's Used in Chapter 2.

Sample	Reported MW (Daltons)	pH 5 eluent		pH 10 eluent	
		Measured MW (Daltons)	Residual (%)	Measured MW (Daltons)	Residual (%)
Acumer™ 1010	2000	N/A	N/A	1391	30.45
Acumer™ 1510	55000	42327	23.04	55172	-0.31
Acumer™ 9400	3600	N/A	N/A	2005	44.31
Acusol™ 410	10000	N/A	N/A	7864	21.36
Acusol™ 445	4500	N/A	N/A	5030	-11.78
Acusol™ 448	3200	N/A	N/A	1065	66.72
Darvan™ 811	~3500	3546	-1.31	2277	34.94

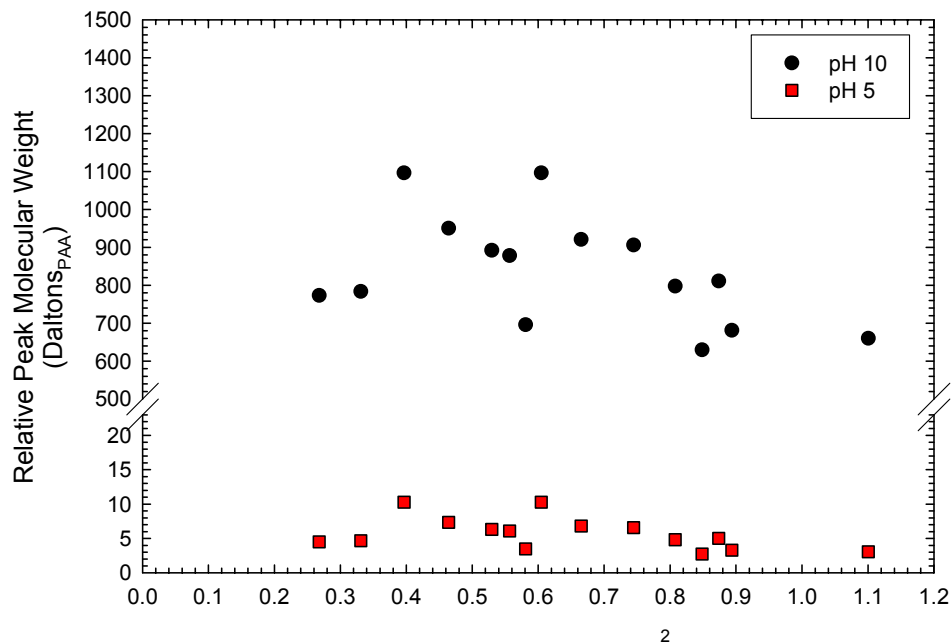


Figure 4-8. Relative molecular weight results from the GPC for the precipitated material from the titration runs after incremental doses of PAA to Huntington ball clay at pH 6. Samples were prepared using the pH 10 eluent and the molecular weight was calculated using the pH 5 and pH 10 calibration equations. Little variation is observed in the measured molecular weight of the precipitated organic.

Upon talking to the supplier of Huntington clay it was learned that Unimin (the supplier) adds organic material to the mined clay in an attempt to increase the plasticity of the clay. The organic material that is added to the clay was identified as digested lignite. As mentioned in Chapter 3 there are two methods of manufacturing digested lignite: 1) react the lignite with hydrogen peroxide and 2) react the material with heated sodium hydroxide. Both of these methods decompose the organic breaking it down into smaller molecules that are precursors for humic substances. The generation of humic substances from these precursors takes time and microbial action to recombine the low molecular weight species into high molecular weight humic substances.

#### ***4.5 Summary and Conclusions***

PAA did displace the organics adsorbed on the surface of kaolinitic clays. The organic additives used by Unimin to improve plasticity of the Huntingdon clay were displaced from the particle surface and characterization of the molecular weight revealed that there was little variation in the molecular weight of these species. The driving force for this displacement, as discussed in Chapter 2, involved the difference in molecular weight and the number of functional groups on the organic that adsorb to sites on the particle surface. The higher molecular weight PAA displaces the digested lignite, but due to the more hydrophobic nature of the digested lignite the displacement was a slow process requiring several treatments.

#### 4.6 References

1. N.A. Wall and G.C. Choppin, "Humic Acids Coagulation: Influence of Divalent Cations," *Appl. Geochem.*, **18** [10] 1573-82 (2003).
2. A. Cozzolino, P. Conte, and A. Piccolo, "Conformational Changes of Humic Substances Induced by Some Hydroxy-, Keto-, and Sulfonic Acids," *Soil Biol. Biochem.*, **33** [4-5] 563-71 (2001).
3. H. Katsumata, S. Kaneco, R. Matsumo, K. Itoh, K. Masuyama, T. Suzuki, K. Funasaka, and K. Ohta, "Removal of Organic Polyelectrolytes and Their Metal Complexes by Adsorption onto Xonotlite," *Chemosphere*, **52** [5] 909-15 (2003).
4. S.H. Sutherland and S.E. Cabaniss, "Aluminum Binding to Humic Substances Determined by High Performance Cation Exchange Chromatography," *Geochim. Cosmochim. Acta*, **61** [1] 1-9 (1997).
5. D.A.N. Ussiri and C.E. Johnson, "Characterization of Organic Matter in a Northern Hardwood Forest by <sup>13</sup>C NMR Spectroscopy and Chemical Methods," *Geoderma*, **111** [1-2] 123-49 (2003).
6. M. Benedetti, J.F. Ranville, M. Ponthieu, and J.P. Pinheiro, "Field-flow Fractionation Characterization and Binding Properties of Particulate and Colloidal Organic Matter from the Rio Amazon and Rio Negro," *Org. Geochem.*, **33** [3] 269-79 (2002).
7. U. Shou, C.A. Maurice, "Considerations in the Use of High-Pressure Size Exclusion Chromatography (HPSEC) for Determining Molecular Weights of Aquatic Humic Substances," *Water Res.*, **34** [14] 3505-24 (2000).
8. R.R. Engebretson and R. von Wandruszka, "The Effect of Molecular Size on Humic Acid Associations," *Org. Geochem.*, **26** [11-12] 759-67 (1997).
9. H.A. Walker and M.M. Bob, "Stability of Particle Flocs upon Addition of Natural Organic Matter under Quiescent Conditions," *Water Res.*, **35** [4] 875-82 (2001).
10. E. O'Loughlin and Y. Chin, "Effect of Detector Wavelength on the Determination of the Molecular Weight of Humic Substances by High-Pressure Size Exclusion Chromatography," *Water Res.*, **35** [1] 333-8 (2001).
11. V.I. Esteves and A.C. Duarte, "Thermogravimetric Properties of Aquatic Humic Substances," *Mar. Chem.*, **63** [3-4] 225-33 (1999).
12. N.M. Jones and N.D. Bryan, "Colloidal Properties of Humic Substances," *Adv. Colloid Interface Sci.*, **78** [1] 1-48 (1998).
13. S. Boulton, R. Jugdaohsingh, K. White, B. Smith, and J. Powell, "Evidence that Polysaccharide and Humic and Fulvic Acids are Co-extracted During Analysis But Have Different Roles in the Chemistry of Natural Waters," *Appl. Geochem.*, **16** [9-10] 1261-7 (2001).

14. A. Cozzolino and A. Piccolo, "Polymerization of Dissolved Humic Substances Catalyzed by Peroxidase. Effects of pH and Humic Composition," *Org. Geochem.*, **33** [3] 281-94 (2002).
15. P. Janos, "Separation Methods in the Chemistry of Humic Substances," *J. Chromatogr. A*, **983** [1-2] 1-18 (2003).

## **5. Plasticity of Clays: Effects of Adding Organic Matter**

### **5.1 Introduction**

During the course of this research it was learned that organic additives are occasionally added by suppliers in an attempt to improve the plasticity of clays. One such clay, Huntingdon ball clay, was used in this research to generate adsorption isotherms. The presence of organic material interfered with the accurate determination of the adsorption plateau value. Based upon this information it was decided to investigate the effects of adding organic material to a clay which exhibited relatively poor plasticity. The change in rheology of a 30 v/o suspension and a plastic mass, i.e., moisture content between 12 and 30 wt%, as a function of the concentration of organic was determined using two parallel-plate rheometers.

### **5.2 Literature Review**

The plasticity of clays has been a topic of much discussion for nearly a century. The term plasticity is often confused with workability and other terms such as stickiness, adhesion, cohesion, yield value, and mobility which are used to describe this property of clays.<sup>1-3</sup> Plasticity is defined as the ability of a material to permanently deform under a pressure greater than the yield pressure and to maintain the deformed shape after the pressure has been removed. As with metals there are two parts to the deformation of a clay: 1) the elastic region and 2) the plastic region. At pressures less than the yield pressure the material deforms in an elastic manner and no permanent deformation is observed upon removing the pressure. Once the yield pressure is exceeded a permanent deformation is observed and upon removing the external pressure there is some elastic recovery in stiff materials, e.g., metals. In the case of particle systems there is little or no elastic recovery.

Plasticity has been characterized using potter's methods where the effects of bentonite additions on the plasticity of clay, thrown by hand on a potter's wheel, were determined.<sup>4</sup> Based upon the results additions of bentonite between 5 and 10% were observed to improve the ability of the potter to throw a thin walled vase. Furthermore it was stated that the plasticity of the bentonite doped

clays was similar to the plasticity liked by the potter. This result was used to validate the colloidal theory of plasticity.

The colloidal theory for plasticity stated that plasticity was caused by the enveloping film of colloidal material which surround clay grains.<sup>5-8</sup> This colloidal material can be crystalline or amorphous and organic or inorganic in nature. Soil mechanics define a colloid as any particle which has at least one dimension less than one micrometer in size. A better definition of a colloid for ceramists would be any particle system that does not settle under a gravitational force due to Brownian motion. This definition takes into consideration the dimensions of the particles in the colloid as well as the density of material.

By changing the pH of the system or the species that are present in a clay Bole proposed that one can affect the plasticity of the system. Furthermore to show how ineffective the “touch” method, as used by potters, of characterizing plasticity can be Bole arranged an experiment where potters were invited to evaluate the plasticity of five clays. Two blindfolded tests were performed, on separate occasions, followed by a third test where the observers were unrestricted in their evaluation. The results from the potters were compared to the results from two standard tests, the dye adsorption test and the Atterburg test. Significant variations in plasticity were found between observations taken at different times and with observers. The results from the standard tests were in agreement with each other, but there were significant deviations from the opinions of the potters. Based upon the results Bole concluded that the touch method of determining plasticity was not sensitive enough to differentiate between clays.

Some of the other theories for the plasticity of clays involve the surface tension of the pore fluid between the clay particles (stretched membrane theories), particle size and shape effects, and the water of hydration of the clay platelets.

Norton stated that the stretched membrane surrounding the clay particles during drying exerted a hydrostatic force which drew the particles into contact. The surface tension of the wetting liquid prevented evaporation from the smallest

pores and water was preferentially removed from the larger pores.<sup>8</sup> While this did have consequences for drying of ceramic ware, Norton instead focused on the “plasticity” of the system; plasticity was defined as the ability of a clay mass to retain its shape after an external pressure caused deformation. As indirect proof of his theory he stated that the yield point of a clay mass should increase as water was removed from the system and this effect was directly observed in the casting of ceramic ware. The leathery cast on the surface of a gypsum mold has a much higher yield value compared to the casting slip. Slowly drying the ware further increased the yield point as the particles were drawn into closer contact by the surface tension of the water. Furthermore as direct proof of the stretched membrane theory Norton placed a quantity of a non-plastic powder, flint, into a rubber balloon. The balloon was then evacuated so that the atmospheric pressure would exert a consolidating force similar to surface tension exerted by water. After evacuation the balloon could be deformed and it would retain its shape, similar to a plastic clay mass. During the subsequent discussion A.L. Johnson pointed out that stretched membrane theory neglected the change in plasticity that was experimentally observed due to cation exchange at the clay surface.

Schwartz examined the effects of surface tension of the yield value of clay masses prepared in water, surface tension of 73 dynes/cm, and a 1% solution of Santomerse D, an organic surfactant that reduced the surface tension to 33 dynes/cm.<sup>9</sup> The addition of the organic surfactant to the clay systems was observed to reduce the yield point of the clay mass. Furthermore the presence of Santomerse D reduced the strength, maximum deformation, and workability of the clay. These results were confirmed in a separate study by Kingery and Francl where a series of organic solutions were studied to vary to surface tension from 71.0 dynes/cm (water) to 16.0 dynes/cm.<sup>10</sup>

Plasticity chiefly involves the amount of water that is present in the body at the time that it is tested.<sup>11</sup> Clays can have water requirements from 15 to 27%. A highly plastic clay is able to withstand a large distortion without cracking and easily deform under an external pressure. Many of the tests that are reported in

the literature involve the use of tension to determine the plasticity of clays. Stress-strain curves were developed for the body either in compression,<sup>12-17</sup> torsion,<sup>18,19</sup> or in direct tension.<sup>17,20-23</sup> In all tests there was an initial pressure that must be exerted, the yield stress, to induce flow of the sample. Once the yield stress was exceeded plastic deformation of the sample was observed and there was little change in the stress required to induce a large strain, i.e.,  $d\sigma/d\epsilon$  decreased in the stress-strain curve. Most of these tests failed to replicate the loads used in industry to form ceramic ware, e.g., ram pressing or jiggering. Furthermore they failed to consider the high shear that is present in these forming processes.

Other tests that have been used to characterize the plasticity of clays involve the use of penetrometers with various geometries. Relationships between the amount of penetration in a given time were then related back to the plasticity by monitoring the penetration as a function of time. The results were then plotted as  $\log(\text{penetration distance})$  versus time and the resulting slope was the plasticity.<sup>24,25</sup>

Compressive tests on clays have also been used to characterize plasticity.<sup>26</sup> Stress-strain diagrams were generated by placing the clay specimen between two parallel plates. A load was then applied and the stress-strain was traced on a smoked glass plate. Stresses up to 10 psi were tested in the study.

Whittaker determined the effects of particle size on the plasticity of kaolinite and established the empirical formula:<sup>27</sup>

$$\text{Log}(S) = A \cdot P + B \quad (5)$$

where S was the surface available for 100 g of clay, P was the product of the yield and the strain at optimum plasticity, and A and B were empirical constants. This relationship was determined by testing several clays with different mean particle sizes and particle size distributions. The plasticity of the clays was determined at various moisture contents by testing the samples in torque and measuring the angle of twist in the body.

Triaxial tests are commonly used to evaluate soils to determine their deformation under a constrained load.<sup>28</sup> Samples are tested under a condition where the principle stresses  $\sigma_{22} = \sigma_{33}$ . The third principle stress,  $\sigma_{11}$ , is then varied to study the failure of the soil under a given stress state. Tests are performed where  $\sigma_{11}$  is in either compression or tension. In order to fully understand the deformation of the soil a series of tests must be performed where  $\sigma_{22}$ , and therefore  $\sigma_{33}$ , are varied. This process of testing soils is time consuming, but results in a clearly defined failure envelope for the soil. A series of Mohr's circles could be constructed to understand the failure of the soil for each stress state.<sup>28,29</sup>

Jenke developed a shear cell for testing soils and other materials to understand their flow.<sup>29</sup> The cell consisted of a constrained bottom ring and top ring that could be dragged. Samples were compacted into the cell when the top and bottom rings were aligned. By sliding the top ring over the bottom ring a shear plane was created when the sample failed. By compacting the samples under various loads prior to the test, as well as maintaining various loads on the top portion of the cell during the test, a series of Mohr's semicircles could be constructed to give an understanding of the failure envelope for the sample. Jenke's test using the shear cell was considerably faster than the triaxial test, but there were problems with obtaining a uniformly compacted sample. Under low consolidating loads, prior to testing, the sample would compact at the leading edge of the bottom ring under shear. This resulted in a non-uniform packing of the material in the cell, thus changing the test parameters and invalidating the test.

Carty developed a high pressure annular shear cell (HPASC) to characterize the shear rheology of powder systems.<sup>30,31</sup> The HPASC is a high-pressure parallel-plate rheometer. The test cell is designed with an annular (donut) shape. The bottom portion of the cell is rotated while the top portion is held stationary by two load cells, placed across the diameter of the test cell. The torque transmitted through the sample, i.e., the torque necessary to prevent the top portion of the cell from rotating, is measured using these two load cells. A

normal load is applied to the cell through a hydraulic, dead-weight system at the top of the cell. The pressure at the top of the cell is monitored using a load cell. Since the bottom portion of the cell rotates and the top is stationary significant shear is applied to the sample. The torque measured at the top portion of the cell is converted to a shear stress using the equation:<sup>32</sup>

$$\tau_{12}(R) = \left( \frac{M}{2\pi R^3} \right) \left[ 3 + \frac{d \ln M}{d \ln \dot{\gamma}_R} \right] \quad (6)$$

For Newtonian fluids the term  $d \ln M / d \ln \dot{\gamma}_R$  equals one and the resulting shear stress is:<sup>32</sup>

$$\tau_{12}(R) = \left( \frac{2M}{\pi R^3} \right) \quad (7)$$

where M is the torque and R is the radius. By varying the normal load on the cell a series of Mohr's circles could be constructed. The center of the Mohr's circle was located along the x-axis, where "x" was equal to the normal stress, and the measured shear stress defines the radius of the circle.

Novak used the HPASC to measure the plasticity of pseudo-boehmite powders used in the catalyst industry.<sup>33</sup> The results from the HPASC were correlated to the shear behavior of the same powders in a piston extruder mounted in an Instron testing machine. A good correlation between the results from the HPASC and the piston extruder was found. The HPASC was determined to be a useful tool to characterize the rheology of extrudable, and non-extrudable, systems.

Lee used the HPASC to characterize the plasticity of clay and clay systems.<sup>34</sup> The results from the HPASC were explained by the degree of pore saturation (DPS) in the sample. In all the samples tested by Lee a maximum was observed in the measured cohesion with increasing moisture content. This maximum was related to the point where the DPS=1, i.e., the pores in the sample were completely filled with water. Upon exceeding the maximum in the curve,

excess water was present in the pores,  $DPS > 1$ , and the cohesion rapidly decreased. When insufficient water was present to saturate the pores, i.e.,  $DPS < 1$ , the cohesion was again lower and a higher pressure dependence, related to the internal friction within the sample, was observed. Kaolin clays were observed to have a higher pressure dependence compared to ball clays, but less water was necessary to reach the maximum in cohesion in a shear rheology map, a plot of the cohesion versus pressure dependence. Ball clays were observed to have a broader curve in the shear rheology map and mixtures of kaolin and ball clay, at a 2:1 ratio, were observed to fall between the curves for the two constituent clays. A whiteware composition (consisting of 30% ball clay, 14% kaolin, 23% quartz, and 33% feldspar) was observed to have the highest cohesion and a very broad curve. The amount of moisture necessary to reach the maximum cohesion was reduced relative to the clays tested due to the presence of non-plastics in the body. Aging in a ball clay-water system was found to be related to the dissolution of raw materials, i.e., an increase in the cation concentration, rather than growth of an organic. Aging was found to significantly reduce the peak cohesion value and increase the pressure dependence to slightly higher values.

Leone studied the effects of specific surface area, determined by nitrogen adsorption of ball clays on the shear rheology determined using the HPASC.<sup>35</sup> Specific surface area is inversely related to particle size. The results of that study showed that there was a significant correlation between the pressure dependence of the sample and the specific surface area of the clay. No relationship was found between the cohesion of the samples and the specific surface area. Finer clays, with higher specific surface area, were observed to have a higher pressure dependence.

Kupinski studied the effects of moisture content, addition of dispersants, and salt additions on the shear rheology, measured using the HPASC, of clays and whiteware batches.<sup>36</sup> While no effect of the salt additions was found in Kupinski's research, industrial experience and other research demonstrates that additions of salt (particularly in excess of the critical coagulation concentration)

have a significant effect of the shear behavior of clay-based and alumina systems. The addition of PAA was observed to reduce the pressure dependence and with no significant change in the cohesion of the sample.

Salts are known coagulants for colloidal particle systems. The addition of salts in excess of the critical coagulation concentration (CCC), defined by the Schulze-Hardy rules, are observed to result in a significant increase in the viscosity of the sample for the same solids loading.<sup>37,38</sup> DLVO theory states that the presence of salt in the liquid phase of a suspension will compress the double layer surrounding the particles thus reducing the electrostatic barrier to coagulation; a schematic of the double layer is shown in Figure 5-1.<sup>37-39</sup> Particles will therefore approach each other and reside in the primary minimum in the potential energy diagram, thus increasing the interparticle separation and allowing more particle-particle interactions and an observed increase in the viscosity of the system.

Numerous authors have observed a decrease in viscosity of particle systems with the addition of salts; this behavior is contrary to the predictions from DLVO theory. Two theories have been proposed to explain the decrease in viscosity with the addition of salts; note that these are not salts which exhibit specific adsorption on the powder surface, but rather salts which act as indifferent electrolytes. The first theory involves the water of hydration surrounding the ion in solution. The second theory involves what are referred to as structure-making and structure-breaking ions in solution.

Pashley investigated the effects of hydration forces between two mica surfaces in the presence of alkali cations.<sup>40</sup> A correlation was observed between double layer theory and hydration forces with the surface cation exchange properties of mica, determined by measuring the forces between freshly cleaved mica surfaces. Based upon the results it was decided that a short-range repulsive “hydration” force existed between the mica surfaces due to the adsorption of hydrated cations. Cation exchange at the surface was a function of pH and the concentration of the cation present in solution surrounding the particle surface; by increasing the concentration of the cation in solution an

increase in the physisorption (as opposed to chemisorption) of that species was affected on the mica surface. By preventing the desorption of the hydrated species as the two surfaces approach there was an additional repulsive force, termed a “secondary hydration.” By decreasing the pH of the system, i.e., increasing the concentration of  $H^+$  in solution, the  $H^+$  ions replaced the hydrated metal ions on the surface thus eliminating the hydration barrier as the two mica surfaces approach the primary minimum in the potential energy curve. Furthermore  $Li^+$  and  $Na^+$  ions had an increased tendency to desorb as the surfaces approach due to their greater hydration, i.e.,  $K^+$  and  $Cs^+$  were more effective at creating the “secondary hydration” repulsive force between the mica surfaces. Pashley concluded that short-range repulsive hydration forces between mica surfaces were due to the presence of adsorbed hydrated cations on the mica surface. Thus the secondary hydration model proposed by Pashley and Israelachvili predicted that ionic binding to a colloidal surface should increase as the hydration enthalpy of said ion decreases due to the barrier to adsorption presented by a tightly held hydration shell.<sup>40-43</sup>

Velamakanni et al. used the presence of these hydration forces to efficiently pack particles during pressure consolidation, i.e., pressure casting of the samples.<sup>44</sup> It was proposed that the presence of short-range (<5 nm) repulsive hydration forces between particles had a lubricating effect allowing particle rearrangement during consolidation. By preparing coagulated alumina suspensions, dispersed at pH 4 and coagulated with  $NH_4Cl$ , an initial decrease in packing density was observed with low-concentration salt additions, relative to the disperse system at pH 4 with no salt. Higher concentrations of salt were observed to increase the packing density of the pressure cast samples. The reported packing density of the coagulated systems, even at levels approaching the CCC, was always shown to be less than that of the dispersed systems; no indication of casting rates was reported in the study. Overall the dispersed and coagulated systems had a significantly higher packing density compared to the flocculated system prepared at pH 9 with no additions.

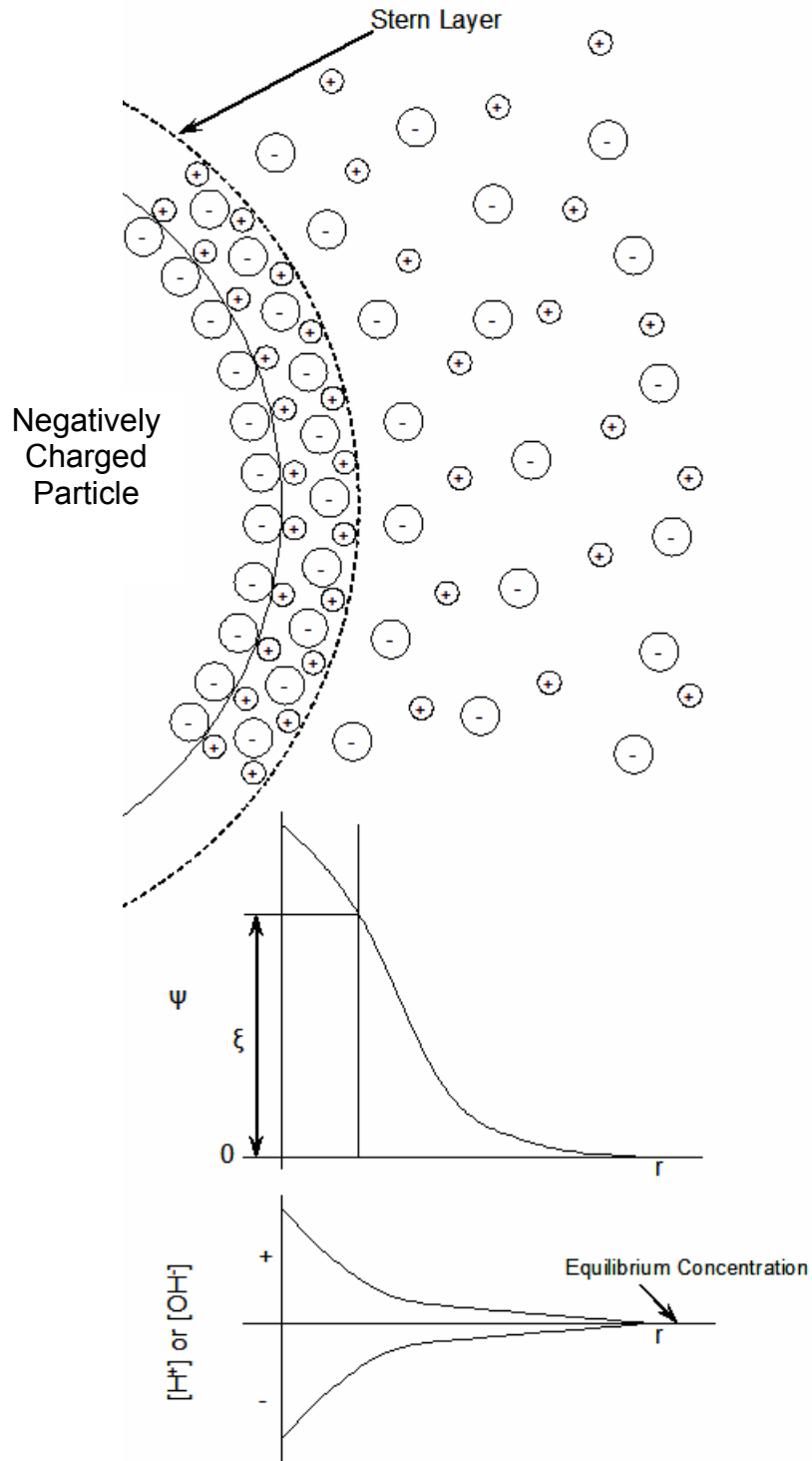


Figure 5-1. Schematic of the double layer of ions surrounding a ceramic particle in an aqueous suspension. A negative charge is assumed on the particle surface. Counterions are attracted close to the particle surface to compensate for the surface charge. At distances far from the particle surface no net charge is observed in the suspension. Schematics for the zeta potential and the ionic concentration are also shown.

Velamakanni et al. investigated the effect of interparticle forces on the rheology of pressure-consolidated alumina particle systems, prepared by pressure filtration at 14.6 MPa.<sup>45</sup> The pH was varied from 3 to 9 for suspensions prepared without salt. The ionic strength of the pH 4 suspensions was varied from 0.1 to 2.0 M  $\text{NH}_4\text{Cl}$ . The addition of an indifferent electrolyte to a dispersed suspension was observed to result in a very-short-range repulsive potential. The consolidated samples were tested under uniaxial compression to induce flow. An increase in the measured peak stress under uniaxial compression was observed above a pH of 4; under pH 4 the measured peak stress was reported as 0 MPa. Above pH 4.2 the peak stress was observed to plateau at approximately 1.5 MPa; all samples contained 0.1 M  $\text{NH}_4\text{Cl}$ . At pH 4 higher additions of salt were observed to increase the peak stress to induce flow; at 0.1 M the peak stress was measured at approximately 0.9 MPa, and above 0.5 M the peak stress plateaued at approximately 0.35 MPa. The changes in the peak stress to induce flow of the saturated compact were related to DLVO theory. Flocculated systems were observed to be strongly aggregated while the particles in dispersed systems were observed to repel each other. In the coagulated state the particles reside in a shallow hydration minimum at a small separation distance resulting in a weakly bonded network of particles in the compact. Dispersed systems were able to pack to a high density due to the repulsive forces allowing rearrangement even when the particles approach under the consolidating pressure.

Chang et al. showed that equivalent relative densities could be achieved using dispersed slurries, pH 4 with no added salt, and coagulated slurries, pH 4 with  $\text{NH}_4\text{Cl}$  additions, by increasing the consolidation pressure in a pressure filtration apparatus.<sup>46</sup> At a pressure of less than 1 MPa the dispersed and coagulated systems were determined to have equivalent relative densities. Flocculated slurries, prepared at pH 9 with no additions, consistently had a much lower relative density compared to the dispersed and coagulated systems. The behavior of the coagulated systems was related back to the short-range repulsive forces between particles in the coagulated systems allowing particle rearrangement. The dispersed systems were observed to be relatively insensitive to the consolidating pressure, i.e., there was only a small increase in

the compact density with increasing pressure. The relative density was observed to increase from 0.45 at 0.001 MPa to 0.55 at approximately 1 MPa compared to the coagulated system which increased from 0.39 at 0.002 MPa to 0.60 at 1 MPa.

Yanez et al. tested the shear modulus and yield stress of attractive alumina particle networks as a function of volume fraction (from 0.1 to 0.5), pH (2, 4, 5, 6, and 9), and salt additions (0.25 M to 2.5 M  $\text{NH}_4\text{Cl}$ ).<sup>47</sup> Based upon the results two types of rheological behavior were identified. The first behavior was for particle systems with a low surface charge density, i.e., close to the iep. Close to the iep the behavior of the particle systems in water were predicted by DLVO theory to model the attractive/repulsive interaction between the particles. For systems with a high surface charge density DLVO theory could not predict the particle interactions. The attractive network created by adding salt to a dispersed system was shown to be much weaker compared to the attractive network close to the iep. The results for the coagulated systems at pH 2 and 4 was a potential well preventing the particles from approaching; at some critical separation a repulsive force between the particles prevented a strong attraction between the particles. When the potential well was sufficiently deep the particles remain trapped at a finite separation distance and the particles cannot escape the potential well due to Brownian motion. This type of behavior in coagulated systems was referred to by the authors as a non-DLVO short-range repulsive force that prevented strong attractive networks.

Franks et al. used this short-range repulsion between alumina particles in coagulated systems to create a “brittle-to-plastic” transition.<sup>48</sup> Alumina systems were prepared at pH 12, which was termed dispersed, and coagulated with 0.5 M  $\text{Li}^+$ ,  $\text{Cs}^+$ , or tetraethylammonium ( $\text{TEA}^+$ ) all salts were chlorides. Uniaxial compression tests were performed on samples prepared by pressure consolidation (filtration) of an aqueous suspension at various pressures. Relative to flocculated samples prepared at pH 9 there was an overall increase in the relative density of the sample for a given consolidation pressure. Furthermore the samples prepared with the  $\text{TEA}^+$  salt were observed to have the highest

relative density, followed by the  $\text{Cs}^+$  and the  $\text{Li}^+$  samples which had the lowest density of the salt coagulated samples. With increasing consolidation pressure, up to 40 MPa, the relative density of the samples was observed to converge, but the salt-coagulated samples maintain a higher relative density compared to the flocculated system. Upon testing the consolidated samples in uniaxial compression two types of behavior were observed, termed brittle and plastic. The brittle behavior was observed for samples with a peak stress  $>5.5$  MPa, from an engineering stress-strain curve, and the samples were observed to crack at applied strains  $\leq 0.20$ . Plastic behavior was observed at peak stresses  $<5.5$  MPa, and no cracks were observed during the loading of the samples. Brittle behavior was typically observed at the high consolidation pressures. With increasing ion radius, i.e.,  $\text{Li}^+$ ,  $\text{Cs}^+$  to  $\text{TEA}^+$ , the transition from a plastic compact to a brittle compact was observed to occur at a lower consolidation pressure. Based upon these results Franks et al. proposed a model where the larger cations separate the hydrated particle surface (particle separation is determined by the cation size and ability to penetrate the hydrated layer of the particle). As the consolidation pressure was increased the water of hydration was squeezed from between the particle surfaces so that only the cations separated the particle surfaces. At high consolidation pressures the cations were squeezed from between the particle surfaces and replaced by  $\text{H}^+$  ions. In this manner the surfaces were maintained at a neutral charge (each negative site on the particle surface was compensated by a cation or a  $\text{H}^+$  ion) and the surfaces could approach into adhesive contact.

Franks and Lange investigated the effects of  $\text{NH}_4\text{Cl}$  additions to dispersed alumina slurries and found that a “plastic-to-brittle” transition existed as a function of the consolidating pressure and the pH of the system.<sup>49,50</sup> Previous work, cited above, used pH 12 slurries. Similar results were found working with alumina slurries at pH 4, 5, and 6. The relative density of flocculated systems at pH 9 was found to be independent of the concentration of  $\text{NH}_4\text{Cl}$ . Dispersed systems at pH 4, 5, and 6 were observed to have a decrease in the relative density with increasing salt concentration, and the more dispersed the slurry, i.e., the lower the pH, the higher the relative density of the compact. The flocculated and coagulated compacts all exhibited a plastic-to-brittle transition as the relative

density, or the consolidation pressure, increased. This was due to the particles forming a tighter-packed system that prevented rearrangement of the particles under the uniaxial pressure. Conversely, dispersed systems, which had a narrow range of relative density despite the range of consolidation pressures used to prepare the samples, were all observed to display a brittle failure under a uniaxial pressure due to the dense packing of the particles in the starting compact. It was observed that a decrease in the pH of the initial slurry, resulting in a more dispersed system, shifted the plastic-to-brittle transition of the coagulated systems to higher consolidation pressures.

Franks and Lange expanded the study to also include the effects of particle size and morphology on the mechanical behavior of saturated, consolidated alumina powder compacts prepared by pressure filtration.<sup>51</sup> Five samples of alumina with various particle sizes and morphology were tested in a flocculated state, pH 9, and in a coagulated state, dispersed at pH 4 and coagulated with  $\text{NH}_4\text{Cl}$ . The coagulated samples had a weakly attractive particle network while the flocculated samples had a strongly attractive network. In all cases the dispersed samples at pH 4 with no salt packed to a higher relative density than the flocculated samples. Higher relative densities were achieved using larger particle sizes, within the range tested of 0.23 to 2.0 micrometers mean diameter. Furthermore the spherical powders packed to a lower relative density than the blocky particles. For each powder morphology tested the plastic-to-brittle transition, as defined in their earlier study, in the flocculated system was shifted to a higher consolidating pressure with an increase in particle size. The spherical powders were observed to transition from a plastic to a brittle compact at lower relative densities compared to the blocky powder. The coagulated systems were observed to transition from a plastic to a brittle material at a higher consolidation pressure as the particle size increases. The spherical powders were again observed to transition at higher consolidation pressures relative to the blocky powder. The dispersed systems were all observed to crack under a uniaxial load with the measured peak stress increasing with decreasing mean particle diameter.

Franks and Lange compared the plastic flow of coagulated alumina compacts to the plastic flow of clay; a sample of prepared potter's clay with a solids fraction 0.566 was used in their study.<sup>52</sup> Samples of alumina were prepared by pressure filtration of a 0.2 solids fraction alumina suspension that was coagulated with  $\text{NH}_4\text{Cl}$ ,  $\text{LiCl}$ ,  $\text{NaCl}$ ,  $\text{KCl}$ ,  $\text{CsCl}$  or  $\text{TEACl}$ . The results from the coagulated systems were compared to flocculated compacts at pH 9 with no addition. The compacts were loaded under uniaxial compression and deformed until a constant flow stress was observed; this was done to prevent artifacts associated with breaking down the attractive network between particles. The stress necessary to induce flow upon reloading the samples was then measured. Higher flow stresses were observed for compacts prepared at higher consolidation pressures and, as cited previously, a plastic-to-brittle transition occurs at high consolidation pressures. The deformation of clay (which exhibited classical plastic deformation, i.e., the sample deformed by bulging in the center of the cylinder upon uniaxial loading,) was observed to be intermediate between a pH 4 coagulated system consolidated at 10 MPa (which deformed at the lower platen) and a pH 5 coagulated system consolidated at 100 MPa (which exhibited brittle failure). Further consolidation of the clay in a filter press, up to 10 MPa, was observed to increase the flow stress of the sample. Samples were prepared at pH 12 and coagulated with 0.5 M monovalent chloride salts ( $\text{LiCl}$ ,  $\text{NaCl}$ ,  $\text{KCl}$ , and  $\text{CsCl}$ ). This was done to control the magnitude of the attractive potential between the alumina particles. The  $\text{LiCl}$  resulted in a highly attractive network, i.e., a deep potential well, which increased the flow stress of the alumina compact; although a greater strain was necessary to reach the peak flow stress. The addition of 0.5 M  $\text{CsCl}$  resulted in the weakest attractive network, i.e., the shallowest potential well, which resulted in the lowest flow stress.  $\text{NaCl}$  and  $\text{KCl}$  were found to be intermediate, and the trend followed the ionic radii of the cations.

Berube and de Bruyn investigated adsorption at the interface between rutile and aqueous solutions containing an electrolyte to model the electrochemical double layer.<sup>53</sup> The effects of both anions and cations were studied. It was determined that the results were significantly different than

previously obtained results for mercury and silver iodide adsorbents. They determined that specific adsorption of cations decreased in the order  $\text{Li}^+ > \text{Na}^+ > \text{Cs}^+$ , and for anions, specific adsorption decreased in the order  $\text{Cl}^- \approx \text{ClO}_4^- \approx \text{NO}_3^- > \text{I}^-$ . Based upon their work a model of the double layer surrounding a  $\text{TiO}_2$  particle was developed which took into account the “ordering effect” of the hydroxylated surface on the hydrogen bonding of liquid molecules. The hydroxylated surface has a “structure-promoting” role on the potential-determining ions,  $\text{OH}^-$  and  $\text{H}_3\text{O}^+$ . Furthermore the adsorption of inorganic ions in the double layer was related to their disrupting or promoting influence on the structural order in the surface region. Therefore a structure-promoting surface, i.e., a hydrophilic surface, will attract structure-promoting ions and a structure-disrupting surface will attract structure-disrupting ions. Based upon their theory the differences in the adsorption isotherms (for electrolytes) between the  $\text{TiO}_2$  surface and the previous results for mercury and AgI were explained.

Johnson et al. studied the binding for monovalent cations and anions on alpha alumina using electroacoustic measurements.<sup>54</sup> For the salts studied they determined that  $\text{NaNO}_3$ ,  $\text{KNO}_3$ ,  $\text{CsNO}_3$ ,  $\text{KBr}$ ,  $\text{KCl}$ , and  $\text{KI}$  are all indifferent electrolytes for the alumina surface while  $\text{LiNO}_3$  resulted in a significant change in the yield stress behavior for alumina, i.e.,  $\text{LiNO}_3$  specifically adsorbed on the alumina surface. For tests performed using 1 M solutions of the above salts it was determined that monovalent cations bind to the negatively charged alumina surface in the sequence  $\text{Li}^+ > \text{Na}^+ > \text{K}^+ \approx \text{Cs}^+$ . The anions tested were observed to bind to the alumina surface to an almost identical extent for the concentration and the pH range tested. The cation sequence was consistent with the structure-making structure-breaking model proposed by Berube and de Bruyn. This sequence for binding on the alumina surface was inconsistent with the secondary hydration theory. The hydration enthalpy for the cations became less negative as the cation radius increases, indicating that the smaller cations were more easily hydrated. Therefore the cations with the greatest affinity for their hydration shells also exhibited the greatest association with the charged alumina surface. The anions used in their study all had similar hydration enthalpies. In a second article the shear yield stress was shown to follow the same sequence for the

cations studied showing that the strength of the interparticle network decreases with increasing cation radius.<sup>55</sup>

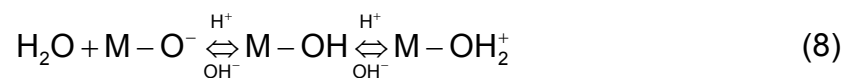
Franks et al. investigated the effects of various anions on the interparticle strength of alumina and zirconia suspensions.<sup>56</sup> The sodium salts of  $\text{IO}_3^-$ ,  $\text{BrO}_3^-$ ,  $\text{Cl}^-$ ,  $\text{NO}_3^-$ , and  $\text{ClO}_4^-$  were studied. The shear yield strength of the alumina suspensions confirmed the previously referenced series for the cation species and the series  $\text{IO}_3^- > \text{BrO}_3^- > \text{Cl}^- \approx \text{Br}^- \approx \text{NO}_3^- \approx \text{I}^- > \text{ClO}_4^-$  for the anion species. The structure-maker anions,  $\text{IO}_3^-$  and  $\text{BrO}_3^-$ , produced the strongest network of particles and the structure-breaker anions,  $\text{ClO}_4^-$ ,  $\text{NO}_3^-$ , and  $\text{Cl}^-$ , produced the weakest attractive network. A theory was proposed where structure-breaker ions were effective at creating a short-range repulsive barrier with a shallow attractive well which was related to the size of the ionic species; larger ions had a shallower well. Furthermore the structure-maker ions created a short-range repulsive barrier to aggregation, but simultaneously created a deep attractive well which was related to the size of the ionic species; larger ions create a deep narrow well. In both cases there was a barrier to strong aggregation of the particles, but in the case of the structure-maker ions the deep well prevented the particles from easily escaping the potential energy well. A schematic of the energy wells proposed by Franks et al. for the interactions is shown in Figure 5-2.

Ruckenstein and Manciu used a simplified Poisson-Boltzmann formalism to account for the interactions between electrolyte ions and colloidal particles that were not included in the mean potential.<sup>57</sup> This method was used to calculate the force between two parallel plates. They demonstrated that the short-range interactions between the ions and plates affect the double layer at large separations by modifying the surface potential and surface charge density. Specifically they included the change in the hydration free energy of the structure-making structure-breaking ions. By considering long-range van der Waals interactions between the ions and the system, ion-dispersion interactions, an attractive force between the plates was generated in their model. By considering the ion-dispersion interactions in traditional double layer theory they

calculated a “double layer attraction” at very large separations, although they state that these forces do not affect the stability of colloidal systems.

From the previous discussion it can be stated that the particle-particle interactions in aqueous systems are of crucial importance in controlling the rheology of the particle system. Evanko et al. studied the effects of aqueous solution chemistry on the surface charge, viscosity, and stability of concentrated alumina (specifically a high-surface-area pseudo-boehmite) dispersions.<sup>58</sup> The surface charge on the alumina powder was determined by potentiometric titration using NaOH as a titrant. It was determined that by increasing the concentration of the dissolved electrolyte there was a corresponding increase in the surface charge of the alumina, measured between 0.1 and 10 wt% solids, but at particular pH values below the point of zero net proton charge (PZNPC) the surface charge decreased with increasing solids loading. It was proposed that this phenomenon was due to overlap of the diffuse layer surrounding the particles at high solids loading. Therefore the surface charge data obtained at low solids loading may not be representative of more concentrated suspensions. Other conclusions included that the viscosity was greatest near the PZNPC and that viscosity increased with increasing solids content. Furthermore suspensions near the PZNPC had the lowest stability while suspensions prepared at pH values away from the PZNPC had higher stability. Addition of an electrolyte to suspensions near the PZNPC resulted in a reduction in the measured viscosity while at pH values away from the PZNPC the viscosity was higher relative to suspensions with no electrolyte.

Johnson et al. summarized the relationships between the surface chemistry and rheology of concentrated mineral suspensions.<sup>59</sup> Van der Waals forces create an attractive potential between particles resulting in agglomeration. In an aqueous suspension the particles develop a surface charge which is related to the pH of the system by the relationship:



Addition of acid results in a positive charge on the particle surface and addition of base results in a negative surface charge. To compensate for this surface

charge an electrical double layer is created surrounding the particle. The strongly associated surface water surrounding the particle results in a short-range repulsive force between two particles as they approach; this effect is enhanced by a surface which possesses a strong hydrogen bonding ability. Results from Pashley for mica surfaces in the presence of salt solutions, cited previously, confirms this once a critical salt concentration was exceeded for each cation. The structure-inducing behavior of each ionic species is closely related to the hydration enthalpy of that species and structure-making ions adsorb more strongly to the structure-making surface than do the structure-breaking ions (and vice versa). The combination of a structure-making surface with a structure-breaking ion will generate a repulsive force with greater range, but of weaker strength, than the combination of a structure-making ion and structure-making surface. A particle with a high surface charge is most likely to show an interaction with either structure-making or structure-breaking ions resulting in a repulsive force between the particles and a reduction in viscosity. The adsorption of a polymer on the surface of a particle can result in either a steric (physical) barrier or an electrostatic (charged, physical) barrier. These barriers prevent the particles from approaching and agglomerating in the primary (and secondary) potential energy well. The addition of an electrolyte to a mineral suspension typically reduces the measured zeta potential, the charge on the Stern layer (the interface between the strongly held layer of ions and the diffuse layer of ions). Specific adsorption of species, ion or polymer, on the surface of particles results in a shift in the isoelectric point of the particle. This results in a change in the surface chemistry of the particle and possible aggregation at a pH away from the point of zero charge of the particle.

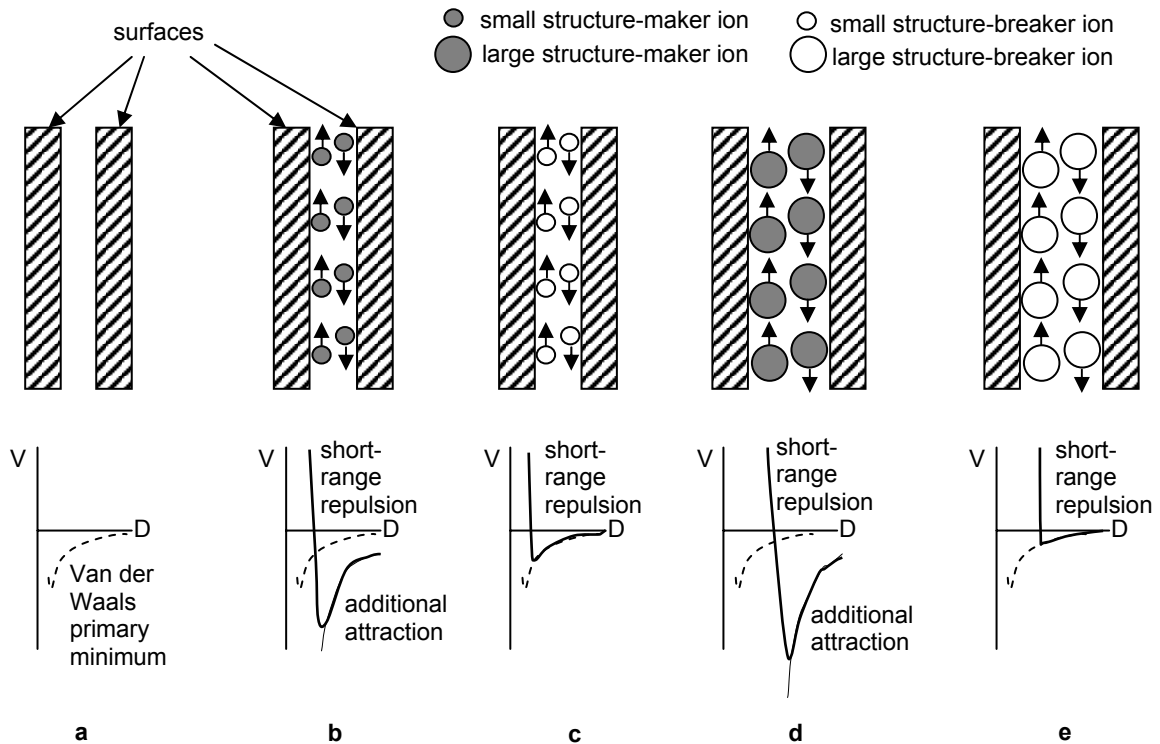


Figure 5-2. Schematics showing how the interactions between structure-making and structure-breaking ions and the particle surface can effect the potential energy at an alumina particle surface, a structure-making surface. Shown are the condition where (a) at the iep there is no surface charge and van der Waals only exists and the particles reside in the primary minimum resulting in strong agglomeration and (b-e) where there is a high surface charge and a high electrolyte concentration resulting in complete neutralization of the surface charge. The effect of ion size and type on the short-range repulsion is shown schematically, repulsion due to diffuse double layer is assumed to be negligible. Schematics are based upon a proposed theory by Franks et al. (adapted from Franks et al.<sup>56</sup>).

### 5.3 Experimental Procedure

The organics used in this study were lignite (L), digested lignite (DL), and sodium lignosulphonate (Na-L). The lignosulphonate was supplied by Buffalo China and was used in the as-received condition. The lignite and digested lignite were supplied by Unimin and were the materials that are dope into the mined Huntingdon clay to improve the plasticity (the lignite is reacted to create the digested lignite). Based upon the pH, greater than 12.5, and the chemical analysis listed in Table 5-1 it is proposed that this material was generated by reacting the lignite in hot sodium hydroxide; the complete chemical analysis from

each organic is listed in Appendix C. The samples of lignite and digested lignite were fractioned by their solubility as a function of pH into an insoluble fraction (IN), an acid-insoluble fraction (AI), and a soluble fraction (S). Fractioning of the organic additives followed the procedure set forth by the International Humic Substances Society as discussed in the next paragraph. The fractioned organics will therefore be described by the source organic and the fraction, e.g., the lignite, insoluble fraction will be referred to as LIN whereas the digested-lignite, insoluble fraction will be referred to as DLIN, *et cetera*.

The organics from Unimin were fractioned by adding the as-received organic to distilled water and increasing the pH to above 10.5 using concentrated (~10N) NaOH. The pH was maintained above 10.5 for a period of seven days at which point the material was centrifuged and the sediment was taken as the insoluble material. The supernatant was decanted and acidified using 6N HCl to a pH of less than 2 to precipitate any acid-insoluble material. After agitating for 24 hours the material was again centrifuged resulting in the acid-insoluble fraction. The supernatant was dried as the soluble fraction of the organic. The result of this fractioning process is the formation of NaCl in solution. Each fraction of organic was characterized for chemical analysis and by thermogravimetric analysis.

Chemical analysis was performed at an outside laboratory [Acme Analytical Laboratories Ltd., Vancouver, British Columbia, Canada] on each of the organic fractions prepared in this study. The insoluble and acid-insoluble fractions were tested using inductively coupled plasma-atomic emission spectroscopy (ICP-AES) rock analysis and a test for the organic carbon and sulphur content. The soluble (S) fractions were tested using ICP-AES water analysis. The rock analysis reports the detected ions present as an oxide while the water analysis reports the concentration of the ions present in their ionized form. The results are reported in Table 5-II for the rock analysis and Table 5-III for the water analysis samples.

During the process of preparing the lignite for fractioning, inorganic material was observed in the sample. A sample of the lignite was characterized

by X-ray diffraction on a randomly-oriented slide to determine what inorganic minerals were present. It was assumed that the inorganic impurities in the lignite samples would also be present in the digested lignite. These inorganic impurities were concentrated into the insoluble fraction by centrifuging the samples. Thermal analysis (DTA/TGA) was performed on each of the organic fractions from the lignite and digested lignite to determine the fraction of combustible material present in the sample. The heating rate for the organic fractions was 5K / minute up to 1000°C. The LOI of the organic fractions was determined using the process described in Chapter 3. The moisture content of the organic fractions was determined by the weight loss between room temperature and 110°C, based upon the dry weight of the sample at 110°C. The LOI was calculated based upon the weight of the sample at 150°C.

Table 5-I. Chemical Analysis for the Lignite (L) and Digested Lignite (DL) from Unimin and the Na-lignosulphonate (Na-L) from Buffalo China.

Sample	Na <sub>2</sub> O (wt%)	K <sub>2</sub> O (wt%)	MgO (wt%)	CaO (wt%)	Al <sub>2</sub> O <sub>3</sub> (wt%)	Fe <sub>2</sub> O <sub>3</sub> (wt%)	SiO <sub>2</sub> (wt%)	TiO <sub>2</sub> (wt%)	Tot/C (wt%)	Tot/S (wt%)	LOI (wt%)
L	0.09	0.34	0.25	0.58	10.62	1.38	31.01	1.42	31.53	0.66	54
DL	10.54	0.27	0.23	0.55	8.88	1.06	15.08	1.13	32.21	0.54	62
Sample	Na <sup>+</sup> (at%)	K <sup>+</sup> (at%)	Mg <sup>2+</sup> (at%)	Ca <sup>2+</sup> (at%)	Al <sup>3+</sup> (at%)	Fe <sup>3+</sup> (at%)	Si <sup>4+</sup> (at%)	Ti <sup>4+</sup> (at%)	Li <sup>+</sup> (at%)		
Na-L	8.32	0.25	0.08	0.74	0.01	0.13	0.12	0.00	0.00		

Table 5-II. ICP-AES Chemical Analysis (Rock Analysis) for the Insoluble and Acid-insoluble Fractions of Lignite and Digested Lignite.

Sample	Na <sub>2</sub> O (wt%)	K <sub>2</sub> O (wt%)	MgO (wt%)	CaO (wt%)	Al <sub>2</sub> O <sub>3</sub> (wt%)	Fe <sub>2</sub> O <sub>3</sub> (wt%)	SiO <sub>2</sub> (wt%)	TiO <sub>2</sub> (wt%)	Tot/C (wt%)	Tot/S (wt%)	LOI (wt%)
LIN	1.12	0.32	0.18	0.35	0.36	1.07	46.12	1.56	23.69	0.45	39.3
LAI	1.45	0.08	0.13	0.41	3.86	1.44	5.35	0.91	48.65	0.83	86.0
DLIN	3.02	0.46	0.17	0.08	15.80	0.76	35.54	1.95	22.71	0.37	41.6
DLAI	6.77	0.02	0.03	0.13	0.81	0.55	1.10	0.63	49.24	0.58	95

Table 5-III. ICP-AES Chemical Analysis (Water Analysis) for the Soluble Fractions of Lignite and Digested Lignite; Concentrations have been Normalized for the Amount of Water Present in the Organic.

Sample	Na <sup>+</sup> (at%)	K <sup>+</sup> (at%)	Mg <sup>2+</sup> (at%)	Ca <sup>2+</sup> (at%)	Al <sup>3+</sup> (at%)	Fe <sup>3+</sup> (at%)	Si <sup>4+</sup> (at%)	Ti <sup>4+</sup> (at%)	Li <sup>+</sup> (at%)
LS	37.38	0.04	1.33	4.27	1.11	1.74	0.01	0.00	0.00
DLS	33.17	0.02	0.38	1.47	1.13	1.30	0.02	0.00	0.00

Samples of the fraction lignite and digested lignite were added to 30 v/o TK6 suspensions. The suspensions were adjusted between pH 6.0 and 6.5 to aid in dissolving the dried organic additives. Samples of Huntingdon and C&C ball clays were also prepared at 30 v/o solids for comparison with a target pH between 6.0 and 6.5. The samples were allowed to equilibrate for 24 hours prior to measuring the rheology using a stress-controlled rheometer [AR 2000 Stress-Controlled Rheometer, TA Instruments, New Castle, DE] to determine if the organic additives had any significant effect on the rheology. A 40 mm parallel-plate geometry was used at 25°C, controlled using a Peltier plate, and a gap of 1 mm between the plates. The suspensions were initially sheared at 150 s<sup>-1</sup> prior to collecting data. Data was recorded, using the software [Rheology Advantage Instrument Control AR v.4.1.0, TA Instruments, New Castle, DE], from a shear rate of 150 to 0.001 s<sup>-1</sup> at 10 points per logarithmic decade. Five runs were averaged for each sample. Log-log plots were prepared of the apparent viscosity versus shear rate and a linear regression (on a log-log plot) was calculated in Excel [Microsoft Excel v.2000, Microsoft Corporation, Mountain View, CA]. The intercept on the log-log plot was calculated and the viscosity was reported at 1.0 s<sup>-1</sup>.

Three clays were selected to characterize the plasticity: 1) Huntingdon ball clay (which is sold by the manufacturer with digested lignite to improve the plasticity of the clay), 2) C&C ball clay (which is a highly plastic clay), and 3) TK6 kaolin clay (which was selected as a clay to have poor plasticity). Samples were prepared using a Brabender prep-mixer [C.W. Brabender Instruments Inc., South Hackensack, NJ] which is designed as a small-scale sigma mixer. Dried powder,

approximately 200 grams, was poured into the mixing chamber and water was slowly added as the material was folded by the sigma blades in the mixer. Once all of the water had been added the mixer was run approximately 20 minutes. The inhomogeneous mixture was removed from the mixer and gradually reloaded while the mixer was running. The mixer was then run for another period of approximately 20 minutes. The nearly homogenous material was then removed from the mixer and allowed to age for 48 hours in a sealed polypropylene container.

Samples of C&C ball clay were also prepared on a Muller Mixer [Laboratory Simpson Mixer, National Engineering Co., Chicago, IL] to determine if there was any significant difference in mixing between the two methods. The Muller mixer is effective for larger samples, approximately 3000 grams of dry powder. Enough water was added to the batch to prepare the sample with the lowest moisture content. After mixing for 20 minutes a 500 gram sample was removed and water was added so as to reach the next moisture content, care was taken to compensate for the material removed. This process was repeated until enough water had been added to create a sample with enough moisture to exceed the peak in the shear rheology diagram.

The HPASC is a high-pressure, parallel-plate rheometer; see Figure 5-3 for images of the apparatus. The sample cell is designed with an annular shape and a rectangular cross section. Machined inserts, Figure 5-3c, (designed with teeth to grip the sample) are used in the top and bottom portion of the cell to prevent the sample from slipping at the interface between the cell and the sample. The bottom portion of the cell is rotated at approximately 0.53 rpm and the top portion of the cell is held stationary. Two load cells, Figure 5-3b, are mounted horizontally and the torque transmitted through the sample (measured as the load necessary to keep the top portion stationary) was monitored. This load was converted into a shear stress using the equation:<sup>32</sup>

$$\tau_{12}(R) = \left( \frac{M}{2\pi R^3} \right) \left[ 3 + \frac{d \ln M}{d \ln \dot{\gamma}_R} \right] \quad (9)$$

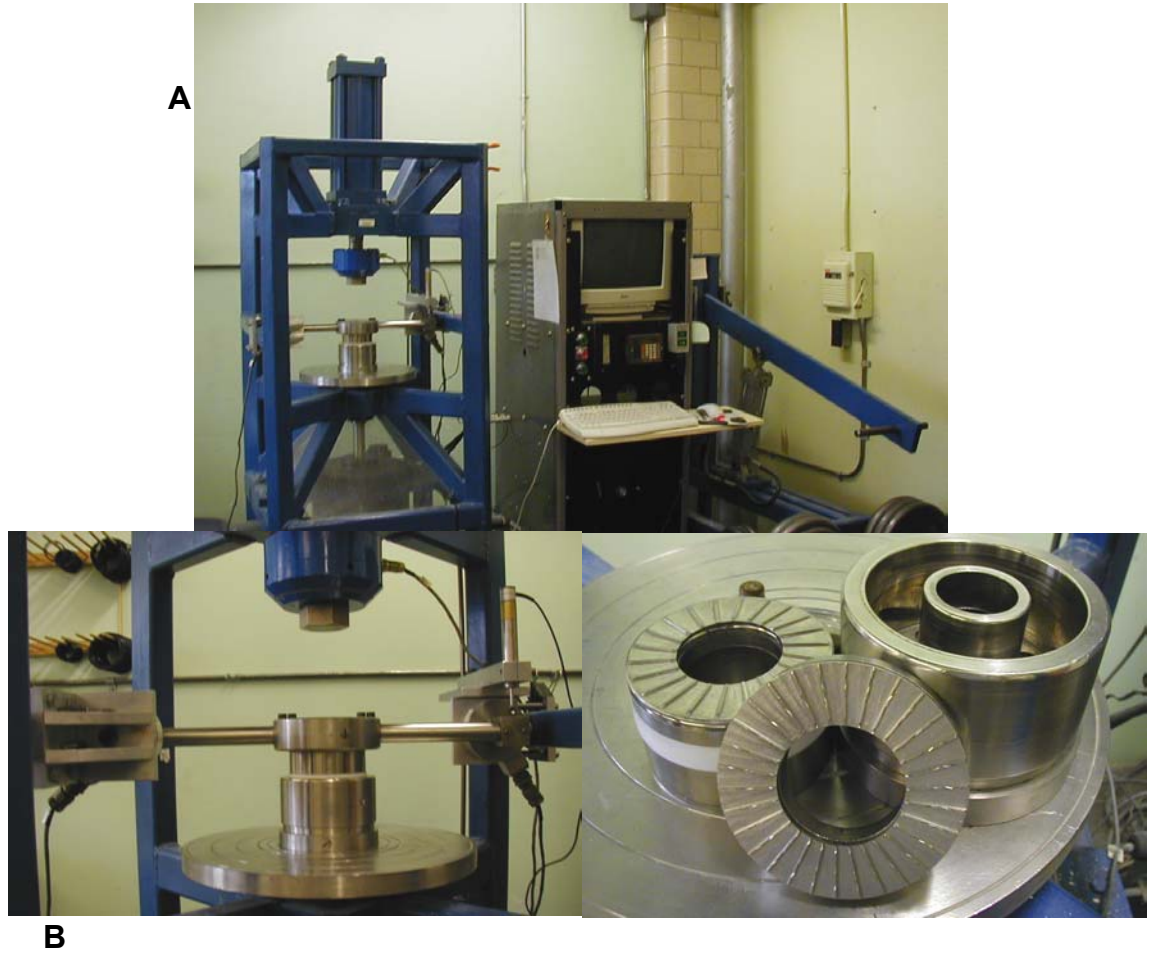


Figure 5-3. Images of the HPASC which was used to characterize plasticity in this study. Shown are A) an overall image (top) showing the dead weight system, the data acquisition system, and the test frame, B) a close up of the test frame (bottom left) showing the assembled cell, and the load cells, and C) a close up of the cell and it's inserts (bottom right).

For Newtonian fluids the term  $d \ln M / d \ln \dot{\gamma}_R$  equals one and the resulting shear stress is:<sup>32</sup>

$$\tau_{12}(R) = \left( \frac{2M}{\pi R^3} \right) \quad (10)$$

where M is the torque and R is the radius. The outer radius of the cell was used so that the maximum shear stress is calculated. A consolidating pressure was applied through a dead-weight system pushing on a hydraulic cylinder. This load was transmitted to the top of the sample cell, pushing on a stainless steel ball to provide a point load. The resulting pressure, calculated as the load divided by

the area of the sample cell, was monitored using a load cell. A seal was created at the top and bottom insert using o-rings to prevent the loss of sample or expression of water during the test, i.e., this was an undrained test. To prevent trapped air from interfering with the test a small vent was machined into the side of the cell, during the initial loading of the sample the vent was open and once the sample was consolidated the vent was sealed using a set screw pushing on a small ball bearing.

Data was collected using an Excel macro every three seconds. Prior to collecting data the sample was equilibrated under the lowest consolidating pressure for a period of 4.25 minutes, corresponding to approximately 2.25 revolutions of the bottom cell. Data was collected for two minutes, approximately 1 revolution, and the consolidating pressure was increased using the dead-weight system. After the initial equilibration the sample was equilibrated for two minutes, followed by two minutes of collecting data. This process was followed until either the maximum load was reached or some outside variable (typically observed as a friction effect or the expression of water from the samples) interfered with the test.

The data from the shear cell was analyzed using the Mohr-Coulomb failure law:<sup>28</sup>

$$\tau_{ff} = c + \sigma_{ff} \tan \phi \quad (11)$$

which is the equation for a straight line, where  $\tau_{ff}$  is the shear stress at failure and  $\sigma_{ff}$  is the normal stress at failure. The y-intercept “c” is taken as the cohesion of the sample and  $\tan \phi$  is the angle from the horizontal, a measure of the internal friction of the sample. Mohr developed a graphical means of analyzing the stress state within a body under shear. Based upon the assumption that the maximum shear stress in the sample was measured under a given consolidating load a series of Mohr’s semi circles were plotted with the consolidating pressure on the x-axis and the measured shear stress defining the radius of the circle. Each datum pair, i.e., consolidating load and measured shear stress, collected by the macro was used in a linear regression. For each consolidating load on the dead-weight system there were 40 data points in the

linear regression, i.e., there were forty repeat experiments for each consolidating load. Data not falling on a straight line were removed from the analysis. At low consolidating loads the sample may have been in an elastic state, reversible deformation, rather than a plastic state, permanent deformation. At higher consolidating loads friction effects due to loss of sample around the o-ring may have resulted in an increase in the measured shear stress; this problem typically occurred in samples with low moisture content. A set of Mohr's semi-circles are shown in Figure 5-4 for TK6 at two different moisture contents.

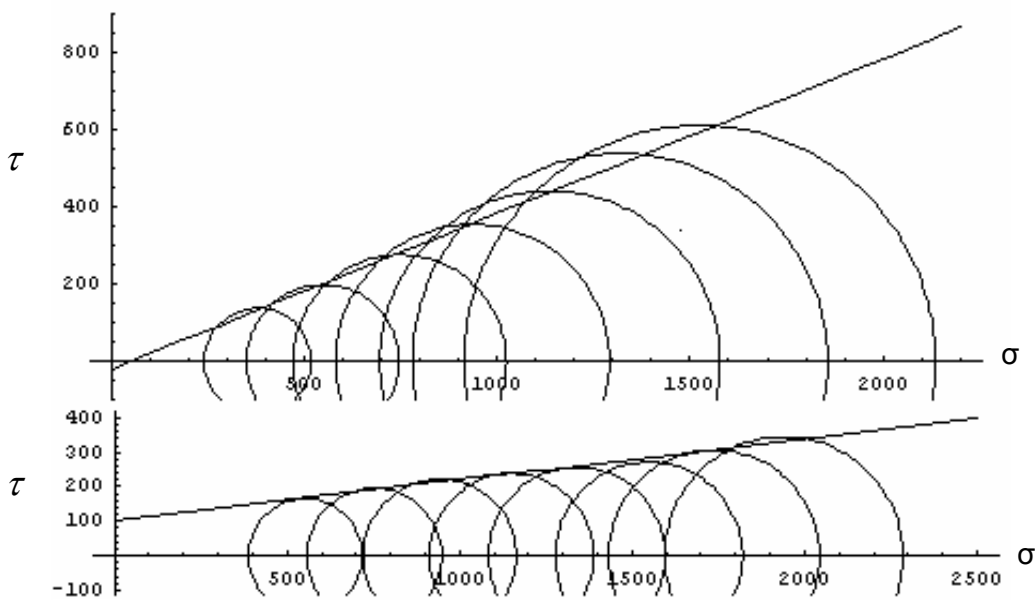


Figure 5-4. Representative construction of Mohr's semi circles from TK6 with 14.17% (top) and 22.35% moisture (bottom). The pressure dependence (the slope of the linear regression) and the cohesion (the y-intercept of the linear regression) were calculated in Excel using 40 repeat experiments at each normal load. Plots were generated using Mathematica™ software [Mathematica™ for Students v.4.1.1.0, Wolfram Research, Inc., Champaign, IL].

Based upon the linear regression a slope and an intercept were determined along with a 95% confidence interval for each term in the regression. For the purposes of analyzing the data the slope from the regression was called the pressure dependence, a measure of the internal friction, of the sample and the intercept was called the cohesion of the sample. As a general rule for plastic bodies the cohesion passes through a maximum with increasing moisture

content and the pressure dependence decreases with increasing moisture content.

Models were created using Design Expert [Design Expert v.6.0.4, Stat-Ease Inc., Minneapolis, MN] and the regression package in Excel software. These models were used to predict the cohesion and pressure dependence as a function of moisture content for the clays used in this study. The models could not accurately predict the cohesion behavior since there was a discontinuity in the data; based upon past experience it is known that the cohesion exhibits a sharp peak at the maximum that could not be predicted by the models.

Due to the formation of significant quantities of NaCl in the organic additives the effect of salt additions on the plasticity of the samples was characterized. Two salts were selected for this study: 1) NaCl, which was the species created in the organics and 2) CaCl<sub>2</sub> (added as CaCl<sub>2</sub>•2H<sub>2</sub>O), since this material is commonly used in industry as a coagulant. The salts were added to TK6 clay as a saturated solution and the target moisture content was 22%. The samples were prepared using the Brabender mixer and the process previously described.

Each organic additive was mixed, on a mg/m<sup>2</sup> basis, into a 200 g sample of TK6 and the plasticity was measured using the HPASC. Samples were prepared with a target moisture content of 22% using the Brabender mixer. To determine if the additives were having a significant effect on the plasticity of the clay the predicted results from the models were compared to the test results from the samples with salt or organic additions. Large deviations in predicted cohesion or pressure dependence relative to the measured values were taken as a significant effect.

As mentioned in the literature review, Norton theorized that the surface tension of the wetting liquid has an important role in the plasticity of clays. Work by Schwartz and Kingery et al., cited previously, indicated that there was a reduction in the yield point of the clay mass. The greater the reduction in the surface tension of the liquid, relative to water, the lower the measured yield point

of the clay mass. Additives to increase the surface tension of water were not investigated in these cited studies.

The surface tension of organic solutions was determined using a sessile drop method developed by Dorsey<sup>60</sup> and modified by Padday.<sup>61,62</sup> The technique involves placing a drop of the solution on a non-wetting surface. The dimensions of the droplet are measured as shown in Figure 5-5. The dimensions of the droplet were used to calculate a factor,  $f$ , using the equation:

$$f = \frac{(r_{45} - h_{45})}{r_{90}} - 0.4142 \quad (12)$$

which calculates the “flatness” of the droplet. The terms  $r_{45}$  and  $r_{90}$  are the radii at the 45° tangent and the vertical tangent respectively. The term  $h_{45}$  is the distance from the top to the droplet to the 45° tangent radius. This factor is then used to calculate the surface tension using the equation:

$$\gamma = g(\rho_{\text{lig}} - \rho_{\text{air}})r_{90}^2 \left[ \frac{0.05200}{f} - 0.12268 + 0.0481 * f \right] \quad (13)$$

where  $\gamma$  is the surface tension of the solution,  $\rho_{\text{lig}}$  is the density of the solution, and  $\rho_{\text{air}}$  is the density of air. The term “ $g$ ” is the acceleration due to gravity. Evaporation of the liquid will slightly alter the measured surface tension since evaporation will alter the structure of the water at the surface of the droplet.

The high surface tension of water is the result of the structured water at the interface between air and water.<sup>63,64</sup> Hydrogen bonding and van der Waals forces caused the water molecules to be highly ordered at the interface. Salts are known to slightly increase the surface tension of water since they aid in the structuring of the water at the interface. The measured surface tension of salt solutions increases with the concentration of salt. Organic additives typically reduce the measured surface tension of solutions. Organics which are highly hydrophobic, water hating, will migrate to the interface since the air surrounding the droplet is hydrophobic in nature. The organics at the interface disrupt the structured water thus reducing the measured surface tension of the solution.

Small additions of hydrophobic organics will dramatically reduce the surface tension and once the interface is saturated with organic no further reduction is observed. Organics which are more hydrophilic, water loving, will remain in the bulk of the solution and will have little effect on the measured surface tension of the solution.

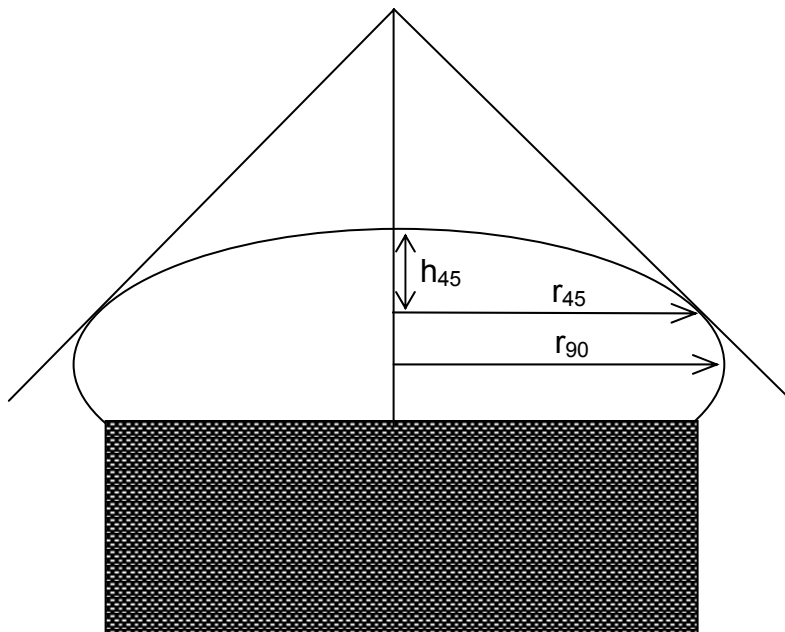


Figure 5-5. Schematic showing the construction that was used to measure the sessile drops to determine the surface tension.

Solutions were prepared with increasing concentrations of organic, salt, or clay from 0.05 wt% up to 5 wt% in distilled water, the materials tested are listed in Table 5-IV; selection of additives for these experiments was based upon the research in the remainder of this thesis. The surface tension of the distilled water as well as a sample of deionized water that had been stored in a container with a CO<sub>2</sub> filter was also determined. Carbon dioxide will dissolve in water to form carbonic acid changing the pH from 7 to approximately 5. The distilled water to prepare the solutions for this study had a pH of about 5.5 while the deionized water with the CO<sub>2</sub> filter had a pH of about 6.8.

A Teflon™ pedestal with a diameter of 2.86 cm was used as the non-wetting surface in this study. The pedestal was machined such that the two ends were parallel. The pedestal was placed on a flat surface and the organic solution was carefully placed on the Teflon™ surface. A digital camera was used to capture the shape of the resulting drop taking care that the camera lens and the top edge of the Teflon™ were at the same height. A digital image of a sessile drop on the Teflon™ base is shown in Figure 5-6. The resulting images were projected on a board and the dimensions of the droplet were measured. A small grid was projected simultaneously with the image to aid in measuring the droplet. The diameter of the Teflon™ pedestal in the image was used to determine the magnification.

Table 5-IV. List of the Materials Used to Prepare Solutions to Measure Surface Tension.

<b>Material</b>	<b>Concentration Range (wt%)</b>
Deion. Water, CO <sub>2</sub> filter (pH ~6.8)	N/A
Dist. Water, pH ~5.5	N/A
Na-Lignosulphonate	0.10, 1.50, 3.00, 4.00, 5.00
Humic Acid	0.05, 1.00, 2.50, 3.00, 5.00
Na-PAA (Darvan™811)	0.05, 1.50, 3.00, 4.00, 5.00
Acrylic Latex emulsion	0.05, 1.00, 2.50, 4.00, 5.00
Plasticized PVA	0.05, 1.50, 3.00, 4.00
PEG 8000	0.05, 1.50, 3.00, 4.00, 5.00
CaCl <sub>2</sub>	0.25, 2.10, 4.25
KCl	0.20, 1.50, 2.70, 5.75
C&C	0.05, 1.00, 2.00, 3.00, 5.00
TK6	0.05, 1.00, 2.50, 3.00, 5.00



Figure 5-6. Digital image of a sessile drop of distilled water on the Teflon™ pedestal. Diameter of the Teflon™ pedestal is 2.86 cm which was used to determine the magnification of the image.

To accurately calculate the surface tension of the solutions the density of the solution and the density of the surrounding air needed to be calculated. The temperature and the relative humidity of the air were monitored during the process of taking the digital images of the sessile drops. Psychrometric charts were used to estimate the amount of water present in the air, reported as the kilograms of water per kilogram of dry air, at each temperature and relative humidity. The density of water and dry air were determined using the CRC Handbook for each temperature and the rule of mixtures was used to calculate the density of the moist air. The density of the starch and sugar were determined using a Helium pycnometer. The density of the other dry organic additives could not be determined using the pycnometer, therefore solutions were prepared at 25 wt% organic and a small flask, volume of 25 mL, and an analytical balance were used to determine the density of solution. The rule of mixtures was used to calculate the density of the organic; a sample of calculation to determine the density of the air, the density of the liquid, and surface tension of the organic solution is shown in Appendix D.

#### **5.4 Results**

Based upon the chemical analysis reported in Table 5-II and 5-III the concentration of sodium in the samples was observed to increase with treatment to fraction the organic samples. Furthermore the concentration of sodium in the digested-lignite samples, supplied from industry, was observed to be much higher compared to the lignite samples, leading to the conclusion that the digested lignite was prepared using hot sodium hydroxide.

X-ray diffraction indicated the presence of quartz, kaolinite, and montmorillonite in the lignite sample. No effort was made to remove these species from the organic prior to preparing the samples for characterization of the rheology and plasticity. These minerals remained in the digested-lignite sample provided by Unimin and it was assumed that the minerals are added to the mined Huntingdon clay simultaneously with the digested lignite.

The results from the thermal analysis of the organic fractions are shown in Figure 5-7 (lignite fractions) and Figure 5-8 (digested-lignite fractions). The thermal cycle for the insoluble fraction of the digested lignite was terminated early. The thermal gravimetric results from the insoluble fraction for lignite and the as-received digested-lignite sample show that significant quantities of non-combustible material were present in these fractions. The LOI results are listed in Table 5-V for each of the fractions tested. The acid-insoluble fractions both contained considerable amounts of physical water which evaporated prior to reaching 100°C; the LAI fraction contained 16.85 wt% water and the DLAI sample contained 58.52 wt% water. These samples were not thoroughly dried to prevent degrading the organic, the concentration of organic reported in the following figures has been adjusted to compensate for the water present in the organic fractions. The soluble fractions both have very low LOI values. Above 800°C a significant weight loss is observed as the sodium chloride first melts, the reported melting point for sodium chloride is 801°C, and then gradually evaporates.

Upon adding lignite or digested-lignite fractions to 30 v/o suspensions of TK6 clay there was a significant change in the rheology of the systems. The results are plotted in Figure 5-9 (lignite) and Figure 5-10 (digested lignite) as a function of the concentration (in mg/m<sup>2</sup>) of organic added to the suspension, also shown in the figures is the viscosity of 30 v/o Huntingdon and C&C ball clay suspensions with no organic additions. Similar effects are observed upon addition of fractioned lignite or digested to 30 v/o TK6 suspensions. The addition of the insoluble fractions (IN) was observed to reduce the measured viscosity of the samples until a plateau was reached at a minimum viscosity. The addition of

the acid-insoluble fractions (AI) initially decreases the measured viscosity followed by an increase as the concentration of sodium exceeded the CCC and coagulated the suspension. The samples prepared with the soluble organic fractions all have a high viscosity due to the concentration of sodium present in the system coagulating the suspension (even at the lowest addition level). Compared to the ball clay samples the viscosity of the TK6 sample with no organic additive is observed to have a much lower viscosity due to particle size effects. Fluctuations in the viscosity of the TK6 sample with no addition are due to slight variations in the pH of the system.

Table 5-V. Moisture Content and Loss on Ignition from the Thermal Analysis of the Lignite and Digested-lignite Fractions.

<b>Organic Fraction</b>	<b>Moisture Content (wt%)</b>	<b>LOI (wt%, dwb)</b>
Lignite as rec.	2.05	46.48
Lig. Acid-insoluble	16.85	84.18
Lig. Soluble*	11.11	19.85
Dig. Lig. (as rec.)	3.89	57.63
DL Insoluble	3.15	29.99
DL Acid-insoluble	58.52	89.00
DL Soluble*	7.68	19.18

\* Samples were dried at 110°C prior to the thermal cycle

The results from the HPASC for each of the commercial clays are shown in Figure 5-11 (TK6 and Huntingdon) and Figure 5-12 (C&C). Based upon statistical analysis aging time (2 days versus 14 days) is observed to result in a significant variation in the cohesion of the samples; there was a small increase in the intercept in the cohesion model with longer aging. Aging of the C&C sample was not observed to significantly affect the pressure dependence. The mixer used to prepare the samples was not observed to cause a significant variation in the cohesion or pressure dependence. The models from Design Expert have been plotted in each of the figures. Again, the models cannot accurately predict

the cohesion near the peak value due to a known discontinuity in the data. The models from Design Expert for each clay are shown in Table 5-VI.

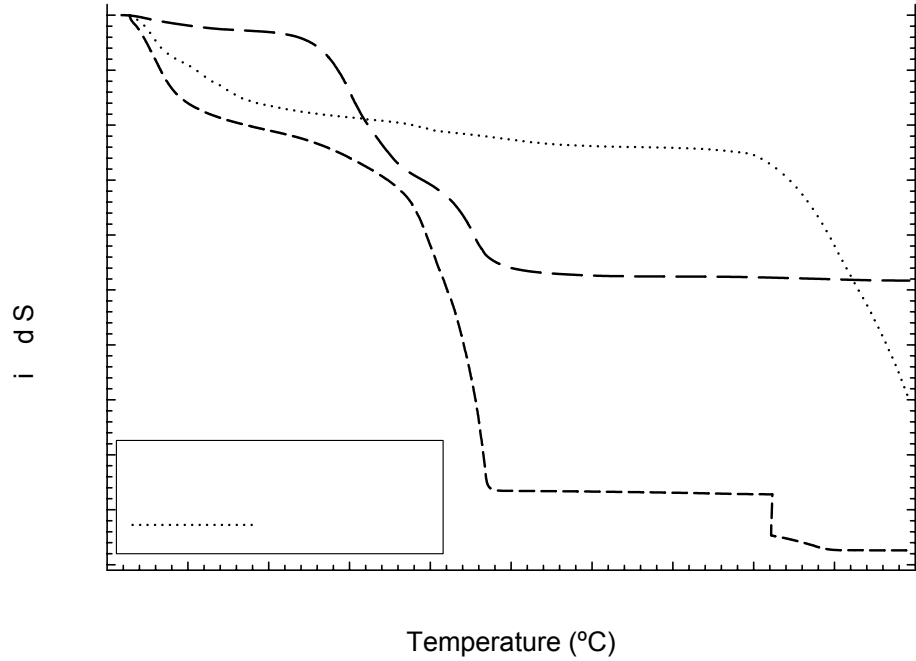


Figure 5-7. TGA results from the thermal analysis for the lignite fractions.

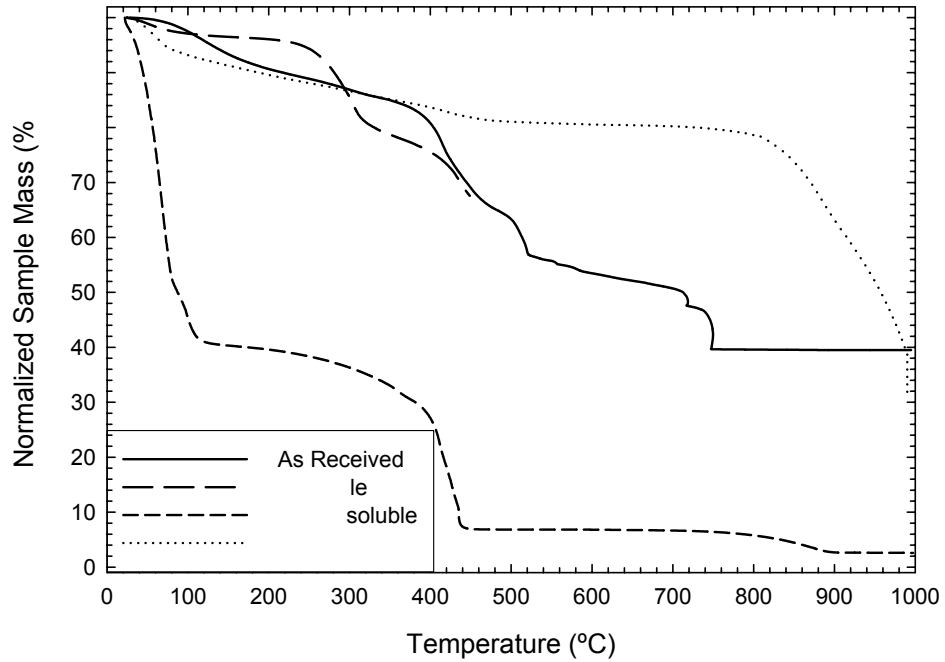


Figure 5-8. TGA results from the thermal analysis for the digested-lignite fractions.

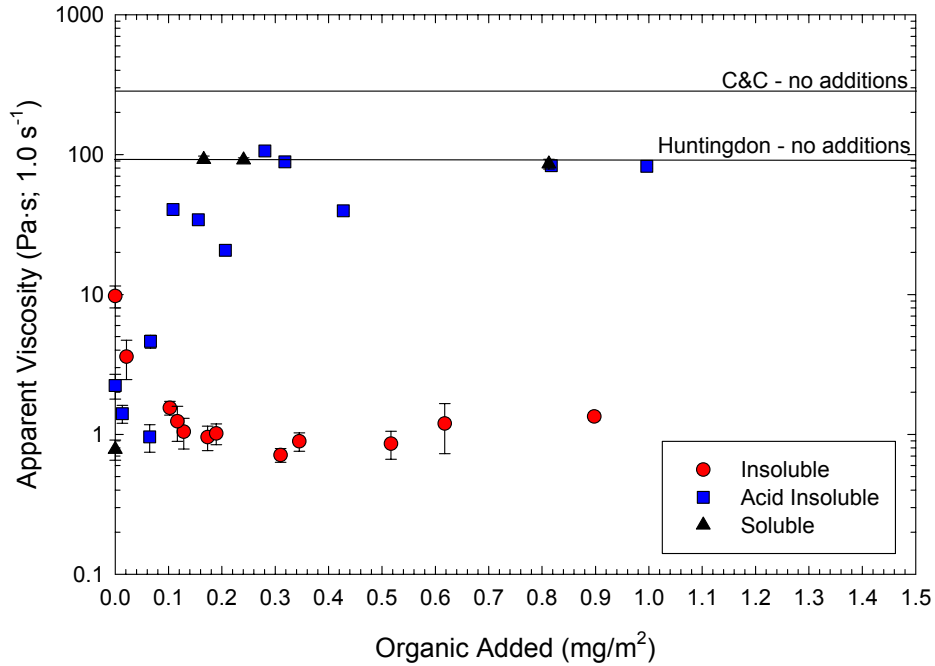


Figure 5-9. Viscosity of the TK6 samples prepared with the fractions of lignite. The insoluble fraction is observed to significantly reduce the measured viscosity. Additions of the acid-insoluble fraction are observed to initially reduce the viscosity, but with higher additions the samples are coagulated due to the presence of NaCl. The soluble fractions are all observed to be coagulated.

Table 5-VI. Models Created Using the Design Expert Software to Predict the Cohesion and Pressure Dependence of the Three Clays in this Study as a Function of Moisture Content.

Clay	R <sup>2</sup>	Model Equation	
TK6	0.950	Cohesion	$Coh = -7710.13 + 675.96*MC - 14.62*MC^2$
	0.995	Press. Dep.	$1/(P.D.)^{0.5} = -37.52 + 6.99*MC - 0.41*MC^2 + 0.008*MC^3$
C&C	0.861	Cohesion aged 2 days	$Coh_2 = 2642.74 - 620.15*MC + 42.18*MC^2 - 0.86*MC^3$
		Cohesion aged 14 days	$Coh_{14} = 2673.86 - 620.15*MC + 42.18*MC^2 - 0.86*MC^3$
	0.985	Press. Dep.	$Log_{10}(P.D.) = -10.72 + 1.68*MC - 0.09*MC^2 + 0.001*MC^3$
Huntingdon	0.965	Cohesion	$Coh = 3955.35 - 528.12*MC + 23.03*MC^2 - 0.32*MC^3$
	0.996	Press. Dep.	$P.D. = -7.48 + 1.06*MC - 0.05*MC^2 + 0.0006*MC^3$

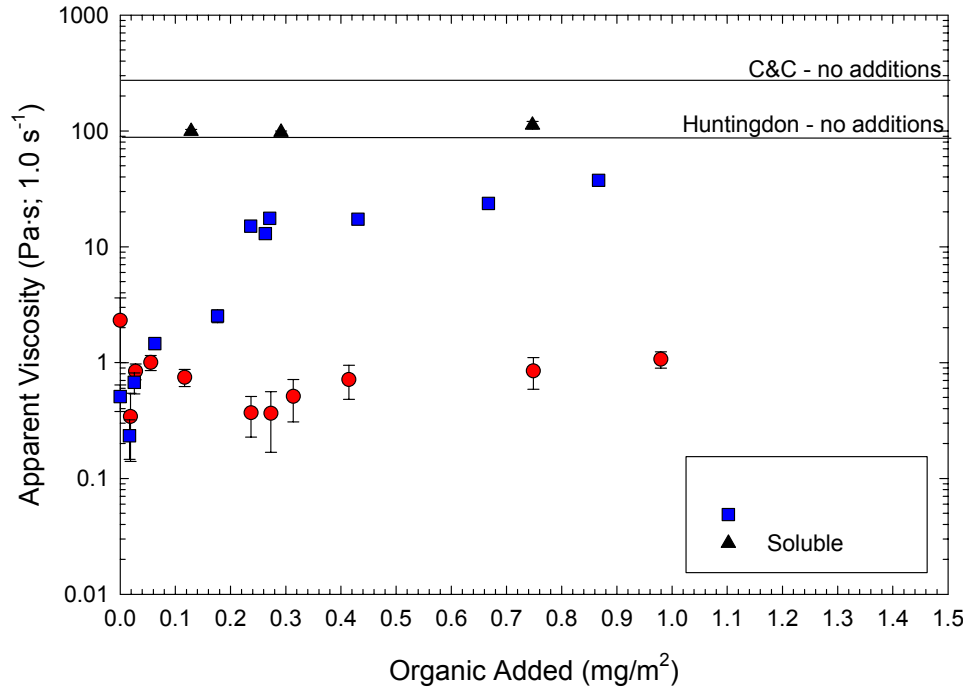


Figure 5-10. Viscosity of the TK6 samples prepared with the fractions of digested lignite. The insoluble fraction is observed to significantly reduce the measured viscosity. Additions of the acid-insoluble fraction are observed to initially reduce the viscosity, but with higher additions the samples are coagulated due to the presence of NaCl. The soluble fractions are all observed to be coagulated.

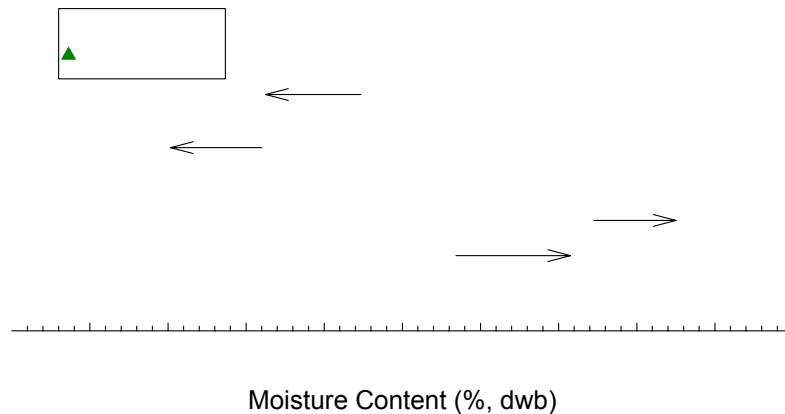


Figure 5-11. Results from the HPASC for TK6 and Huntingdon clays. Also plotted are the models from Design Expert to predict cohesion and pressure dependence as a function of the moisture content. Cohesion results are plotted as closed symbols and pressure dependence is plotted as open symbols.

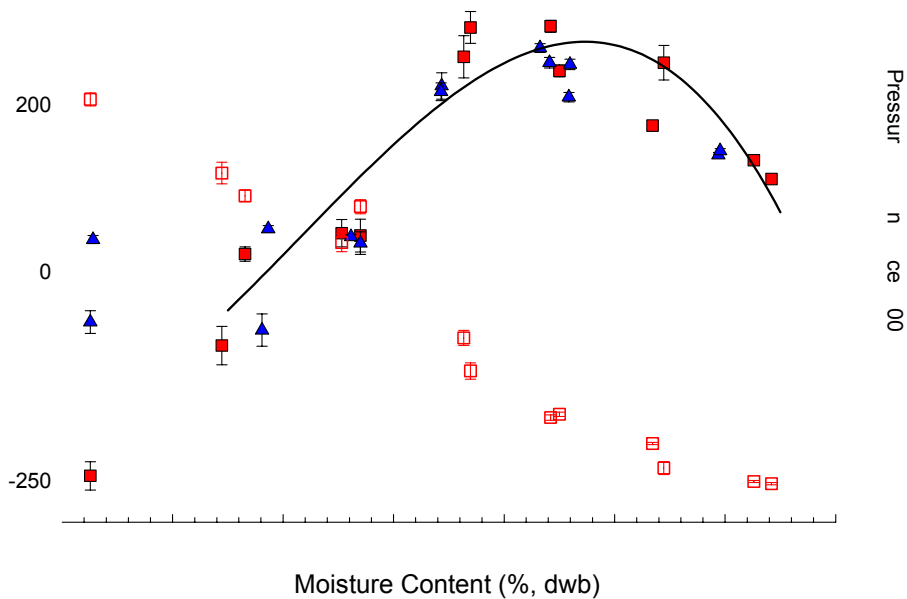


Figure 5-12. Results from the HPASC for C&C ball clay. Also plotted are the models from Design Expert to predict cohesion and pressure dependence as a function of the moisture content. Cohesion results are plotted as closed symbols and pressure dependence is plotted as open symbols. No significant effect of mixer type was observed, but a significant effect of aging time was observed, not shown.

The results from the HPASC were plotted in a shear rheology map (cohesion as a function of pressure dependence) in Figure 5-13; moisture content of the samples is reported in the figure. As observed by Lee<sup>34</sup> an increase in the amount of water added to the clay sample initially increased the cohesion of the clay as the particles were wetted. A maximum was observed in the cohesion when the DPS approached a value of one, i.e., the pores in the clay sample are saturated with water. Once excess water was added,  $DPS > 1$ , the cohesion of the clay was observed to decrease as the sample became more fluid. An increase in the moisture content of the samples is observed to decrease the pressure dependence since the water acted as a lubricating film reducing the internal friction between the particles.

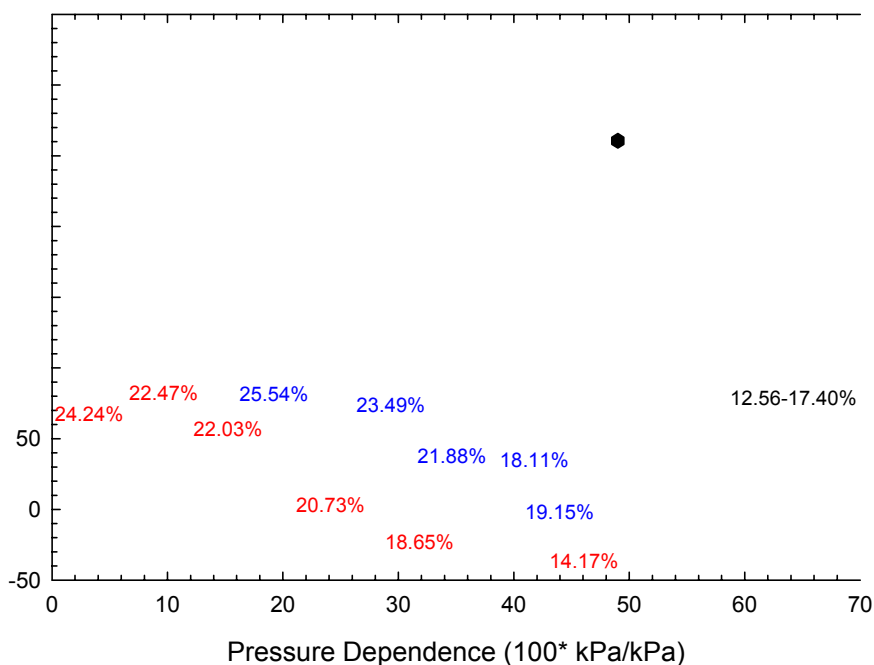


Figure 5-13. Shear rheology map for the three clays used to characterize plasticity. Moisture content for each sample is shown in the figure. Peak cohesion has been indicated by a vertical line for each clay.

The TK6 was observed to have a maximum in the shear rheology map near a moisture content of 22%. The maximum in the shear rheology map for the C&C ball clay was observed to be near a moisture content of 20%. No peak in the shear rheology map was observed for the Huntingdon ball clay, although it is proposed that the maximum cohesion was between 25.54 and 29.05% moisture. Comparison of the results from the HPASC on the shear rheology map indicate that the TK6 and Huntingdon have a lower maximum cohesion compared to the C&C. Furthermore the maximum cohesion for the TK6 and Huntingdon clays was observed at a lower pressure dependence relative to the C&C clay. The amount of water necessary to achieve the maximum cohesion was greatest for the Huntingdon. Based upon the results for the TK6 clay it was decided to prepare all future TK6 samples with a target moisture content of 22%, near the peak cohesion value for TK6 clay.

These results can be related back to the mineralogy and particle size of the clays; see Table 5-VII for the mineralogy and Table 5-VIII for the measured properties of the clays. The results from the adsorption study, Chapter 3,

indicate that the kaolinite fraction in TK6 is significantly coarser compared to the ball clays; during the segregation process in Chapter 3 the kaolinite fraction of the TK6 settled during the first 45 minutes after turning off the high-shear mixer. The kaolinite fraction for the Huntingdon clay was observed to be the middle fraction while the fine fraction of the C&C was observed to be primarily kaolinite. The C&C ball clay contains a significant amount of free quartz, determined from both the chemical analysis and the LOI of a clay sample. The presence of free quartz, a non-plastic material, will reduce the water necessary to achieve a maximum in the cohesion curve. This happens for two reasons: 1) the size of the free quartz in commercial clays tends to be large relative to the kaolinite particles and 2) the quartz particles tend to be blocky in shape compared to the hexagonal platelets that are typical of kaolinite (and many other clay) particles. The C&C has a higher specific surface area compared to the Huntingdon resulting in the higher cohesion, but the amount of water necessary to reach said maximum is reduced by the high quantities of free quartz (approximately 30%) in the C&C.

It is important to note that at the lower moisture contents a negative cohesion was sometimes calculated from the linear regression of the data. Theoretically it is impossible to have a negative cohesion. There are two possible reasons for the presence of a negative cohesion: 1) frictional effects, due to material leaking around the o-rings, augmenting the torque transmitted to the load cell and 2) there is a dilatant transition at the high normal loads. Frictional effects were observed to degrade the o-rings in the top portion of the sample cell. The gradual degradation of the o-rings allowed the test material to flow between the top insert and the cell wall which created more drag and increased the measured torque resulting in a higher calculated shear stress. Dilatant, or shear thickening, rheology is associated with the test specimen expanding to allow flow, shown schematically using a two dimensional array of spheres in Figure 5-14. The presence of non-plastic, blocky minerals, e.g., quartz, in the clay sample can interfere with the alignment of the clay platelets. For the system to flow past one of these regions, or for the quartz grains to roll, the system must slightly expand. Most likely a combination of these two effects at high normal loads caused the negative cohesion value. Both of these effects

result in a higher calculated shear stress. When the linear regression was performed these data points shift the regression to a higher slope value and a lower (negative) cohesion value.

Table 5-VII. Minerals Present in the Clays Used to Measure Plasticity.

<b>TK6</b>	
Mineral	Concentration (wt%)
Kaolinite	87.34
Quartz	7.1
Illite	0.9
Smectite	3.7
Chlorite	0.9
<b>C&amp;C</b>	
Mineral	Concentration (wt%)
Kaolinite	66.1
Quartz	30.0
Illite	3.9
<b>Huntingdon</b>	
Mineral	Concentration (wt%)
Kaolinite	93.2
Quartz	5.3
Illite	1.3
Chlorite	0.2

Table 5-VIII. Properties of the Clays Used to Measure Plasticity.

<b>Property</b>	<b>Units</b>	<b>TK6</b>	<b>C&amp;C</b>	<b>Huntingdon</b>
Specific Surface Area	m <sup>2</sup> /g	23.46	23.90	20.67
Mean Particle Size*	µm	0.10	0.09	0.11
LOI (TGA)	%	13.2	9.3	13.4

\* Equivalent spherical diameter calculated from the specific surface area assuming spherical particles

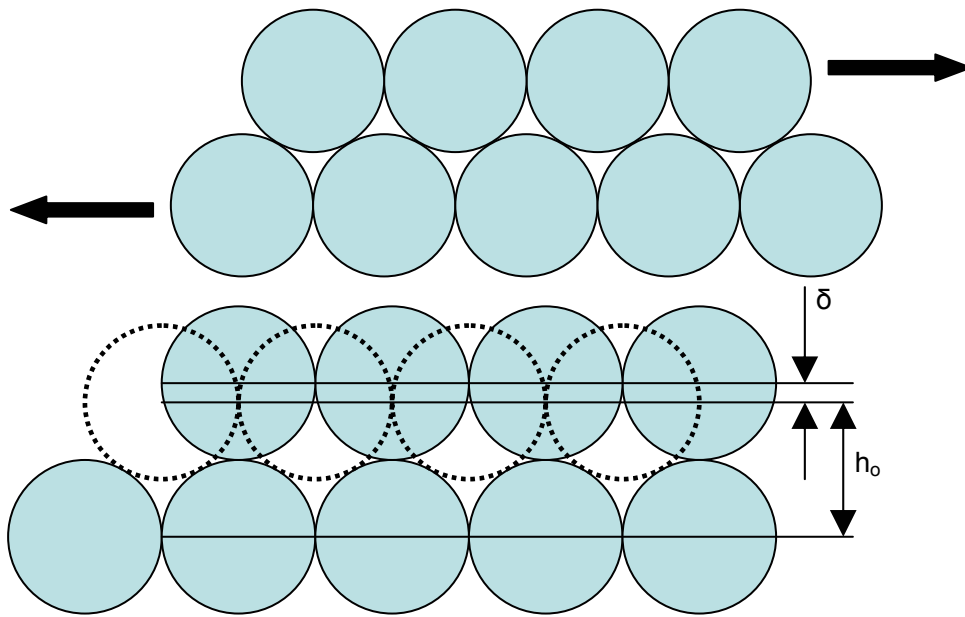


Figure 5-14. Two dimensional schematic of a dilatant system. The spheres represent particles that are tightly packed (top) under shear and the system must expand by a distance  $\delta$  to allow the particles to slide past one another or “flow.”

Furthermore it was noticed that during the course of the test the normal and shear stress would undergo a hysteresis for a set load on the dead-weight system. This hysteresis, shown in Figure 5-15, is a systematic error caused by a slight misalignment between the load cell and the center of the test cell. The steel ball which serves as a point load on the test cell was slightly misaligned and as the test cell rotated the point load moved off center. When the point load was off center the normal load applied to the sample was resolved into two forces: a vertical force, which was monitored by the load cell, and a horizontal force which was not recorded. When the point load was directly centered under the load cell all of load from the dead-weight system was applied to the sample. Prior to commencing this thesis the HPASC was renovated and the misalignment between the load cell the test cell were virtually eliminated, but a small systematic error still remained.

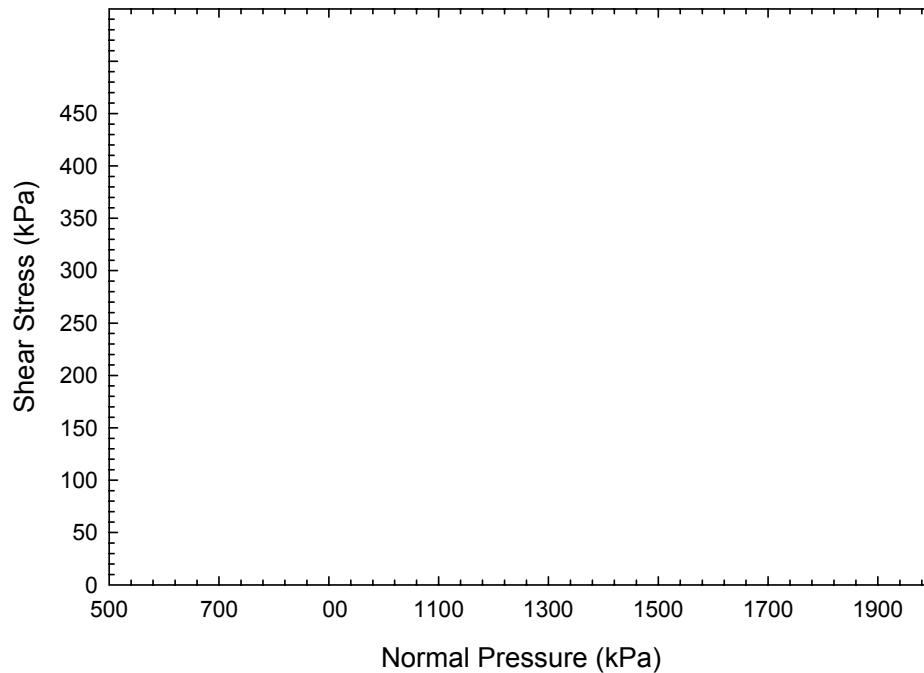


Figure 5-15. Hysteresis in the measured stress and the applied load on the HPASC due to a slight misalignment between the load cell and the point load on the test cell. The misalignment causes the applied load from the dead weight system to be resolved in to a normal load, which is monitored by the load cell, and a horizontal load. Data is plotted for TK6 clay samples at 20.53% moisture content, also plotted is the average and standard deviation of the shear stress.

The results of the salt additions to TK6, prepared at a target moisture content of 22%, are shown in Figure 5-16 (overall effects), Figure 5-17 (NaCl only), and Figure 5-18 (CaCl<sub>2</sub>•2H<sub>2</sub>O only). The predicted cohesion and pressure dependence, calculated from the models reported in Table 5-VI, is compared to the measured values from the samples prepared with NaCl or CaCl<sub>2</sub>•2H<sub>2</sub>O in Table 5-IX.

Overall the addition of salt was observed to reduce the measured cohesion of the sample. The smallest addition of NaCl to TK6 was observed to reduce the pressure dependence and cohesion of the sample and, with increasing concentration, the pressure dependence was observed to increase. Once the CCC of the salt was exceeded the pressure dependence of the sample decreased with no significant change in the cohesion. The smallest addition of CaCl<sub>2</sub>•2H<sub>2</sub>O was observed to slightly reduce the cohesion of the sample with no

significant effect on the measured pressure dependence. Higher additions of  $\text{CaCl}_2 \cdot 2\text{H}_2\text{O}$  were observed to significantly increase the pressure dependence with no significant effect on the measured cohesion. At the highest additions of  $\text{CaCl}_2 \cdot 2\text{H}_2\text{O}$  a significant increase in the cohesion was observed, relative to the samples without salt, along with a significant reduction in the pressure dependence. This effect was most noticeable at the highest addition of  $\text{CaCl}_2 \cdot 2\text{H}_2\text{O}$  at 16.59% moisture shown in Figure 5-16.

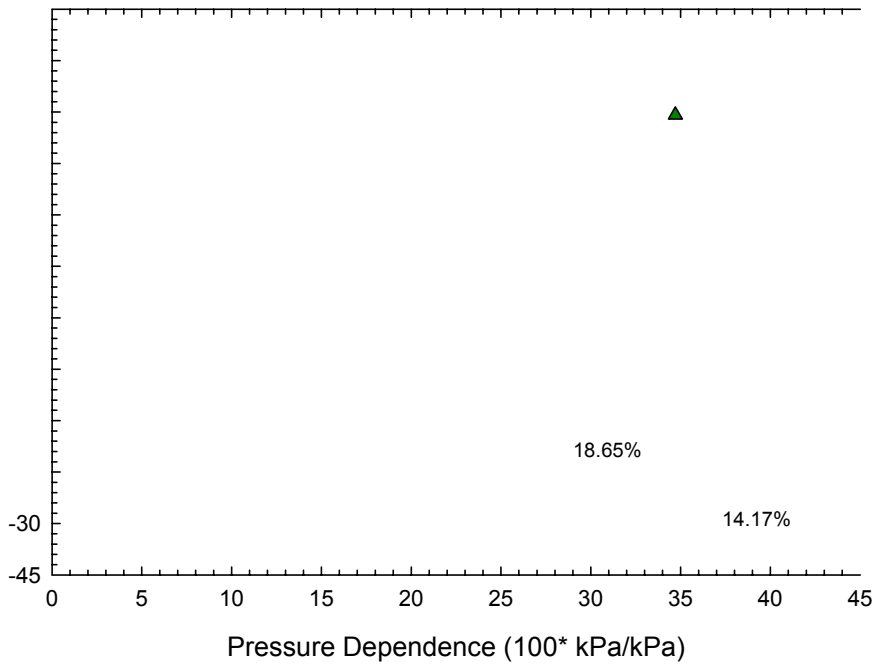


Figure 5-16. Overall view of the effects of adding salt ( $\text{NaCl}$  or  $\text{CaCl}_2 \cdot 2\text{H}_2\text{O}$ ) to samples of TK6 prepared with a target moisture content of 22%. Note the sample prepared with a concentrated solution of  $\text{CaCl}_2 \cdot 2\text{H}_2\text{O}$ .

As mentioned previously salts are known coagulants for colloidal ceramic suspensions or pastes. When a ceramic particle is placed in an aqueous medium it develops a surface charge depending on the pH of the medium. Upon adding powder to water the pH is naturally driven to the iep (the point of no net charge on the particle surface) of the ceramic powder, e.g., alumina goes to a pH of 9.0-9.5 when added to deionized water. In the presence of an indifferent electrolyte, both  $\text{NaCl}$  and  $\text{CaCl}_2$  are indifferent electrolytes for clay; the iep is equivalent to the point of zero charge on the particle surface. By adjusting the

pH of the suspension the surface charge is changed as the surface becomes protonated or deprotonated (addition of acid protonates the surface resulting in a net positive charge while addition of base deprotonates the surface resulting in a net negative charge).

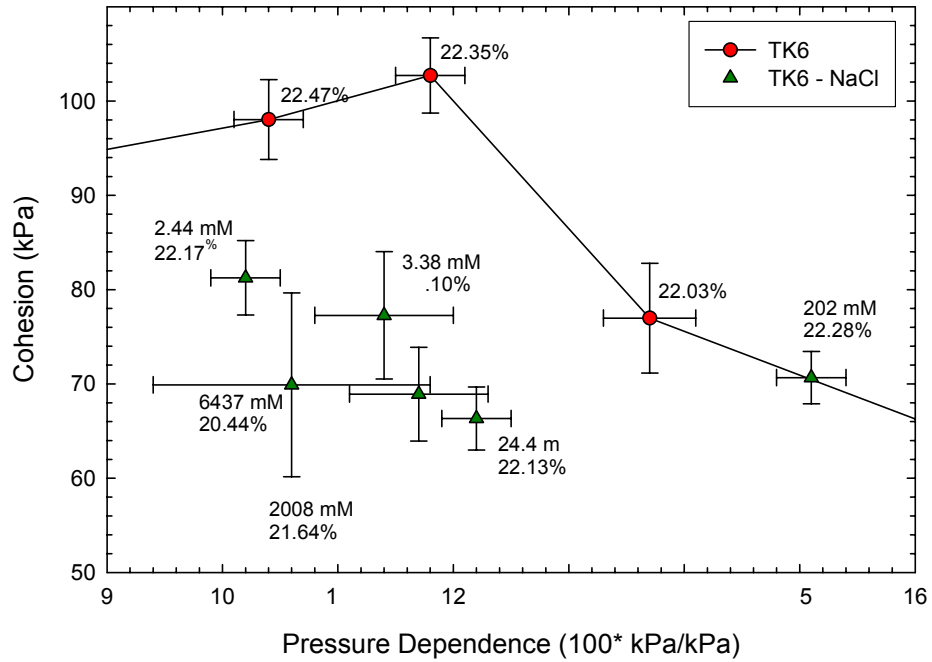


Figure 5-17. Close up view of the shear rheology map for the samples prepared with NaCl at a target moisture content of 22%. Additions of NaCl are observed to overall reduce the cohesion of the sample. Pressure dependence initially increases with salt addition, but above the CCC for NaCl the pressure dependence is observed to decrease.

The particle in suspension has a double layer of ions that compensate for the charge on the particle surface, shown schematically in Figure 5-1. When the particle is placed in motion by an electric field the diffuse layer of ions is stripped away and a net charge remains at the Stern layer. This net charge is the zeta potential and is a function of pH. When the zeta potential is sufficiently high (either positive or negative) electrostatic repulsion occurs between particles due to like surface charges and a dispersed system results. At the iep of the system there is no repulsion between the particles and a flocculated system results.

For the purposes of this discussion a flocculated system will be defined as a system at the isoelectric point where strong agglomeration occurs due to no net charge on the particle surface. A dispersed system is therefore a system where there is sufficient charge on the particle surface to result in electrostatic repulsion, either by adjusting the pH of the system or by the addition of a polyelectrolyte (a dispersant). A coagulated system is induced by adding a material, e.g., an acid, a base, or a salt, to a previously dispersed suspension so as to compress the double layer by compensating the charges on the particle surface.

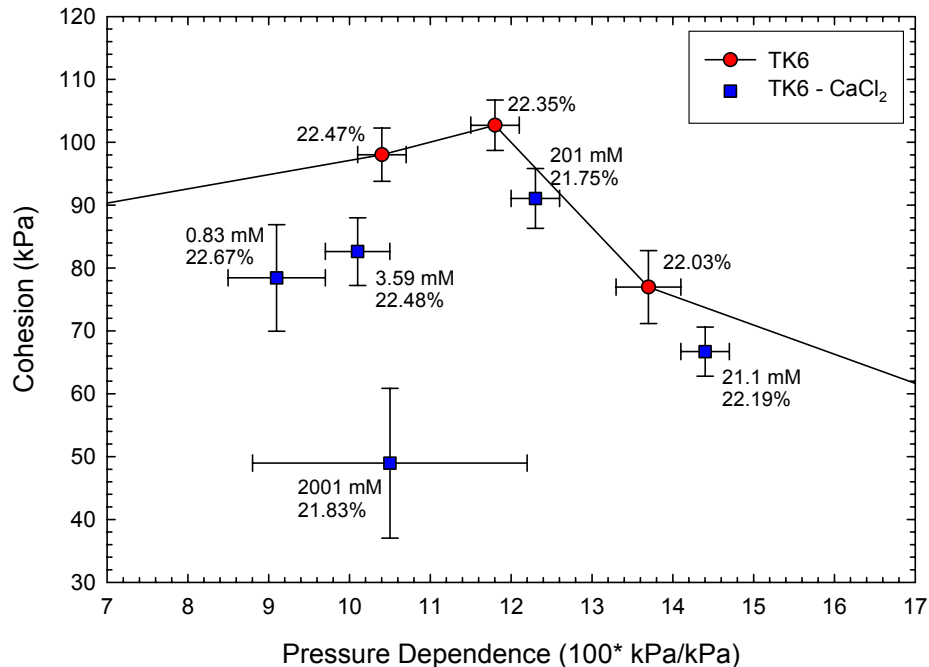


Figure 5-18. Shear rheology map for the samples prepared with  $\text{CaCl}_2 \cdot 2\text{H}_2\text{O}$  at a target moisture content of 22%. Additions of  $\text{CaCl}_2 \cdot 2\text{H}_2\text{O}$  are observed to overall reduce the cohesion of the sample. Pressure dependence initially increases with salt addition.

The addition of salt to a dispersed system compensates, i.e., balances, the charge on the particle surface compressing the double layer. This effect is dependent upon the charge on the ion balancing the surface charge, i.e., monovalent ions are less effective than divalent ions which are less effective than trivalent ions. Based upon the Schulze-Hardy rules CCC's have been determined for various electrolytes, these rules have been confirmed by previous

research by Sundlof,<sup>65</sup> Rossington,<sup>66</sup> and Schuckers.<sup>67</sup> The systems tested in these studies were 35 v/o alumina suspensions, 30 v/o clay suspensions, and a plastic body with a porcelain composition respectively.

A transition was observed in the pressure dependence of the samples with increasing additions of salt. Little change was observed in the cohesion of the samples with addition of salt. Below the CCC an increase was observed in the pressure dependence of the samples with increasing concentration of salt. Above the CCC the pressure dependence was observed to decrease, significantly higher error was observed above the CCC. The transition for the NaCl samples was observed to occur at approximately 200 mM which is similar to the values predicted by the Schulze-Hardy rules. The transition for the  $\text{CaCl}_2 \cdot 2\text{H}_2\text{O}$  samples occurred at approximately 21.2 mM which is slightly higher than the predicted values from the Schulze-Hardy rules. This deviation was caused by the high surface charge on the clay platelets which increased the CCC of the particle system.

The results from the Na-lignosulphonate additions to TK6 with a target moisture content of 22% are shown in Figure 5-19. The moisture content was difficult to control due to evaporation during the mixing process. Due to the dominant role of moisture content in the measured properties of the plastic body, i.e., cohesion and pressure dependence, the data was broken down into three groups. The first group had a moisture content of approximately 21.6% (dotted circles), the second group had a moisture content of approximately 22.05% (solid circles), and the third group had a moisture content of approximately 22.42% (dashed circles). The predicted cohesion and pressure dependence, calculated from the models reported in Table 5-VI, for the lignosulphonate samples is reported in Table 5-X. These results were compared to the measured values for the samples prepared with NaCl or  $\text{CaCl}_2 \cdot 2\text{H}_2\text{O}$  in Table 5-IX.

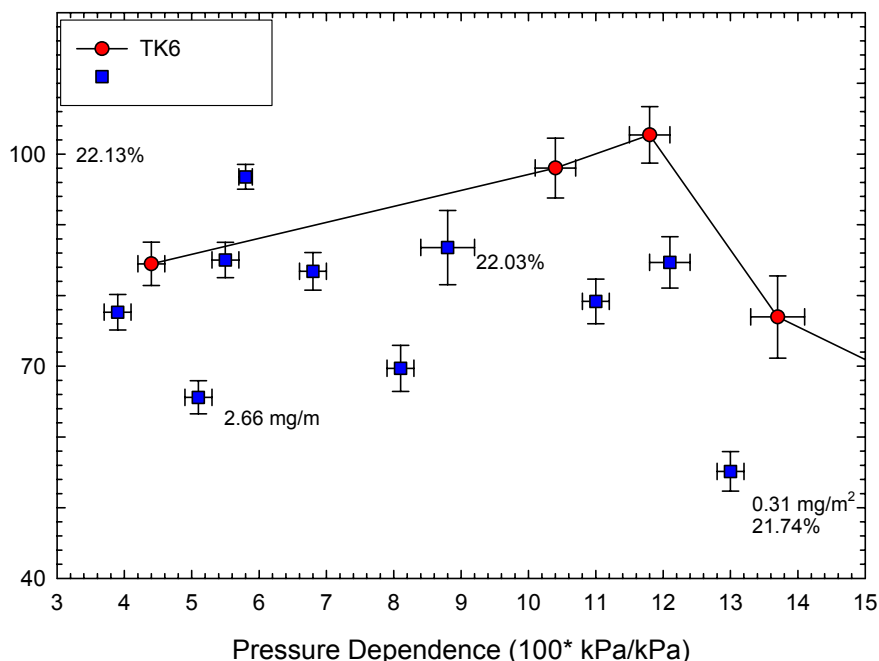


Figure 5-19. Close up view of the shear rheology map for the TK6 samples with added Na-Lignosulphonate at a target moisture content of 22%. Three sets of data are presented at various moisture contents (see text for details).

The dotted circles have a moisture content below the peak cohesion value of the TK6 without additives. Little variation is observed in the cohesion value, but it is observed that with increasing concentration of lignosulphonate the sample undergoes a significant reduction in the pressure dependence. Lignosulphonate is an effective dispersant for the clay-based systems and with increasing additions the organic molecule provides an electrosteric barrier, a charged physical barrier, to particle-particle interactions. A similar trend is observed for the samples in solid circles. There is a small increase in the measured cohesion of the sample relative to the TK6 without additives. With increasing additions of lignosulphonate the pressure dependence is observed to be significantly reduced. The samples in dashed circles all have a moisture content greater than that of the peak cohesion value in the TK6 samples without additives. Only low concentrations of lignosulphonate were added to these samples, but it can be observed that there is an overall decrease in the measured cohesion, relative to the samples with no additives. Furthermore there

is an observed decrease in the pressure dependence with an increase in the concentration of lignosulphonate.

Table 5-IX. Comparison of the Predicted and Actual Cohesion (Coh.) and Pressure Dependence for the TK6 Samples Used to Characterize Plasticity with Salt Additions.

Moisture Content, % (mM added)	Predicted		Actual		Error	
	Coh. (kPa)	P.D. (100* kPa/kPa)	Coh. (kPa)	P.D. (100* kPa/kPa)	Coh. (%)	P.D. (%)
<b>NaCl</b>						
22.10 (3.4)	86.31	13.2	77.27±6.74	11.4±0.6	-11.69	-16.2
22.17 (2.4)	88.97	12.8	81.25±3.95	10.2±0.3	-9.50	-25.6
22.13 (24.4)	87.47	13.1	66.33±3.34	12.2±0.3	-31.86	-7.0
22.28 (202)	92.86	12.1	70.66±2.78	15.1±0.3	-31.41	19.6
21.64 (2008)	65.81	16.3	68.92±4.97	11.7±0.6	4.51	-39.7
<b>CaCl<sub>2</sub>•2H<sub>2</sub>O</b>						
22.67 (0.8)	103.29	10.0	78.42±8.48	9.1±0.6	-31.71	-9.9
22.48 (3.6)	98.89	11.0	83.61±5.38	10.1±0.4	-19.70	-9.0
22.19 (21.1)	89.71	12.7	66.72±3.91	14.4±0.3	-34.46	11.9
21.75 (201)	71.11	15.7	91.06±4.77	12.3±0.3	21.91	-26.5
21.83 (2001)	74.83	15.0	48.95±11.9	10.5±1.7	-52.85	-43.0

The effects of the lignite fractions on the plasticity of TK6 at a target moisture content of 22% are shown in Figure 5-20 (overall effects), Figure 5-21 (LIN), Figure 5-22 (LAI), and Figure 5-23 (LS). The results from the lignite fractions show no clear trend in the data. Therefore it was concluded that these materials have no significant effect of the plasticity of TK6. The LIN fraction was demonstrated in Figure 5-7 to have an effect on the viscosity of a 30 v/o suspension of TK6, where the additions were shown to reduce the viscosity of the suspension. Overall any changes that were observed in the plasticity of the samples were likely due to the presence of sodium chloride which was created during fractioning of the organics. A comparison of the predicted cohesion and pressured dependence to the measured values is reported in Table 5-X.

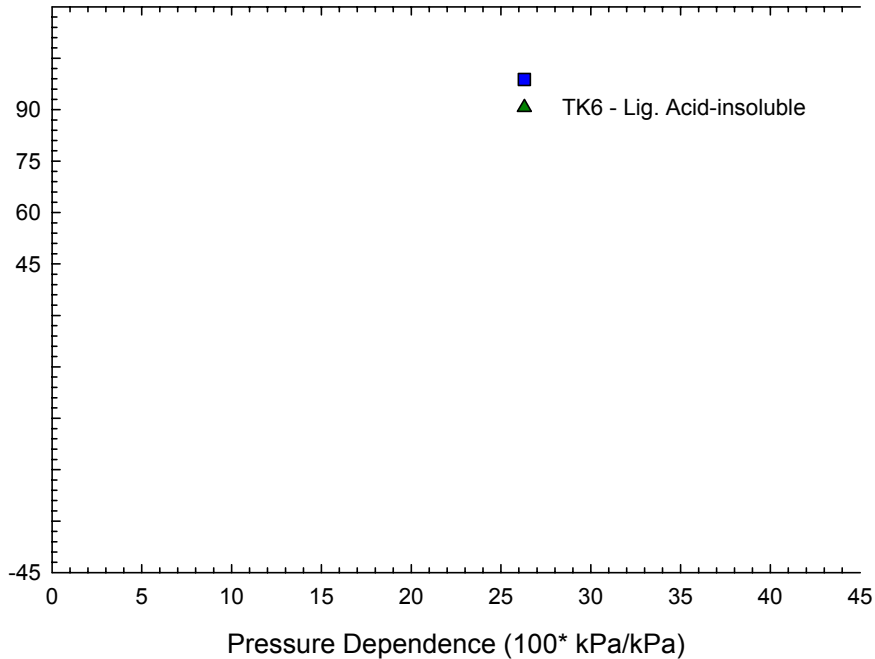
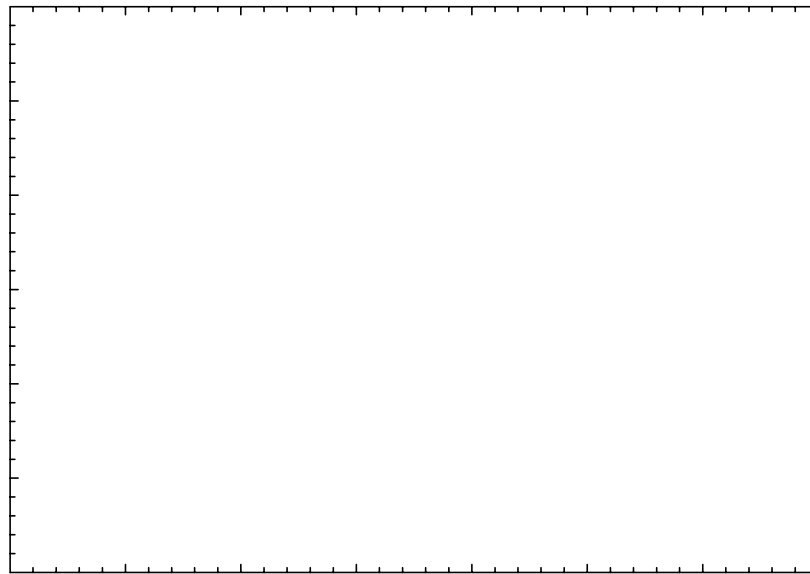


Figure 5-20. Overall view of the shear rheology map for additions of lignite fractions to TK6 with a target moisture content of 22%

The effects of the digested-lignite fractions on the plasticity of TK6 at a target moisture content of 22% are shown in Figure 5-24 (overall effects), Figure 5-25 (DLIN), Figure 5-26 (DLAI), and Figure 5-27 (DLS). The results from the DLIN fraction were broken down into two sets of data; one with a moisture content of approximately 21.85% (dotted circles, Figure 5-25) and the second with an approximate moisture content of 22.3% (solid circles, Figure 5-25). At a moisture content of 21.85%, below the peak cohesion value, the pressure dependence was observed to increase while there no significant change in the cohesion from the TK6 sample without additives. At 22.3% moisture a similar trend was observed where the pressure dependence of the samples decreased and the cohesion increased with increasing addition of the insoluble lignite fraction.



Pressure Dependence (100\* kPa/kPa)

Figure 5-21. Close up view of the shear rheology map for the samples prepared with the insoluble fraction of lignite (LIN) at a target moisture content of 22%. No clear trend is observed in the data.

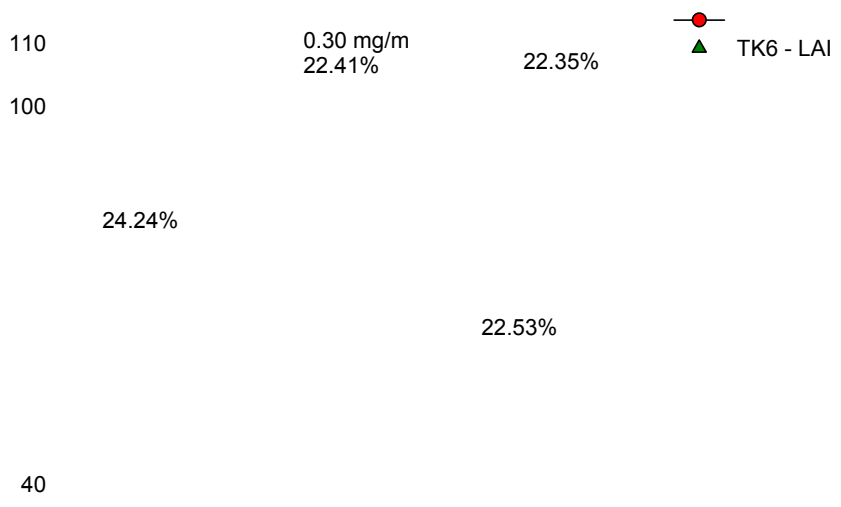


Figure 5-22. Close up view of the shear rheology map for the samples prepared with the acid-insoluble fraction of lignite (LAI) at a target moisture content of 22%. No clear trend is observed in the data.

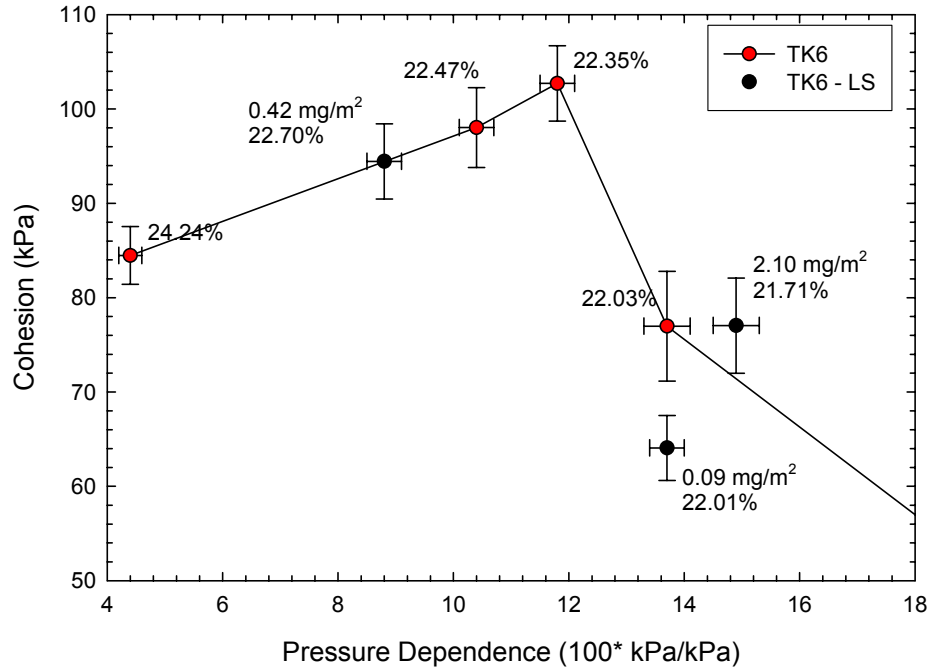


Figure 5-23. Close up view of the shear rheology map for the samples prepared with the soluble fraction of lignite (LS) at a target moisture content of 22%. No clear trend is observed in the data.

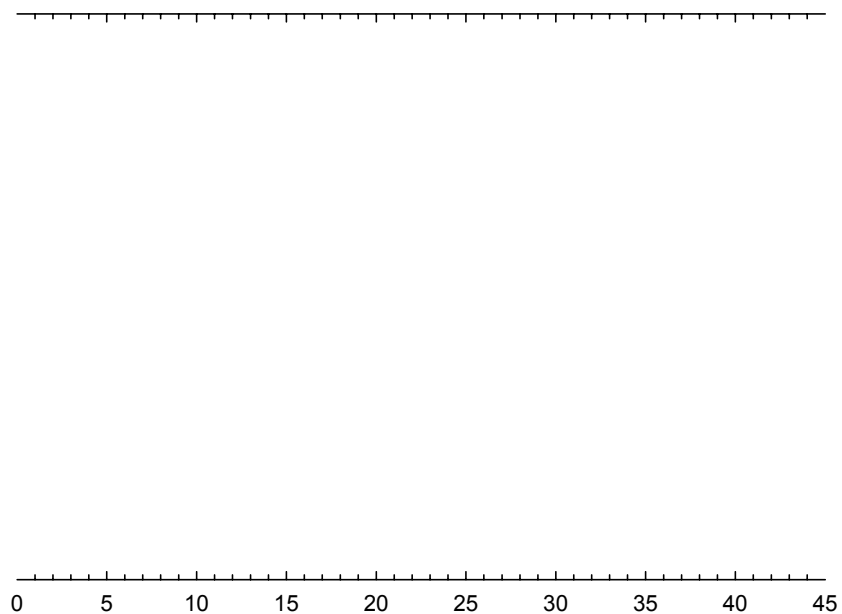


Figure 5-24. Overall view of the shear rheology map for the samples prepared with digested-lignite (DL) fractions at a target moisture content of 22%.

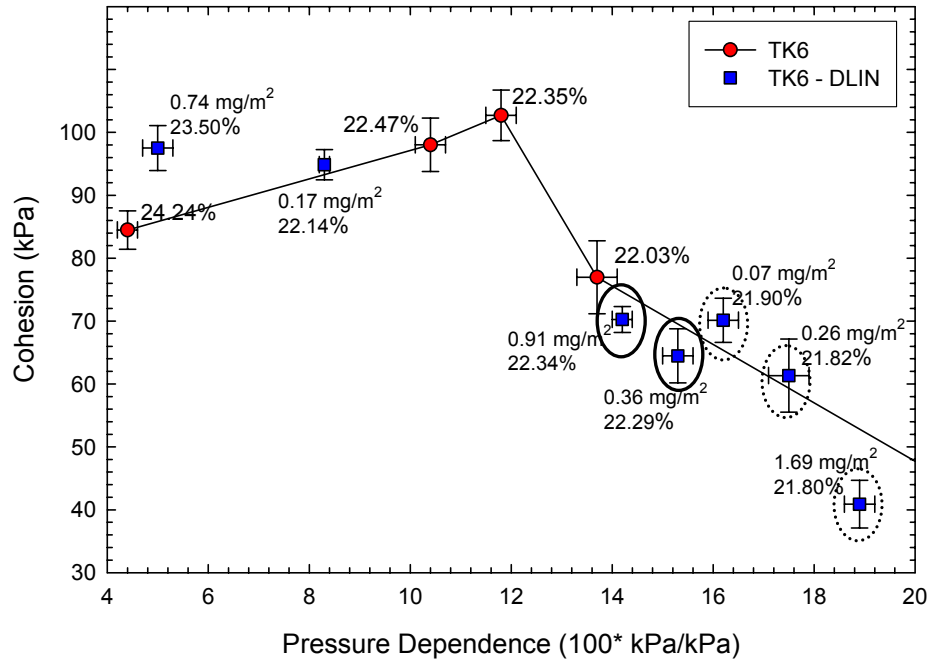


Figure 5-25. Close up view of the shear rheology map for the samples prepared with the insoluble fraction of digested lignite (DLIN) at a target moisture content of 22%. Two sets of data are observed, see text for details.

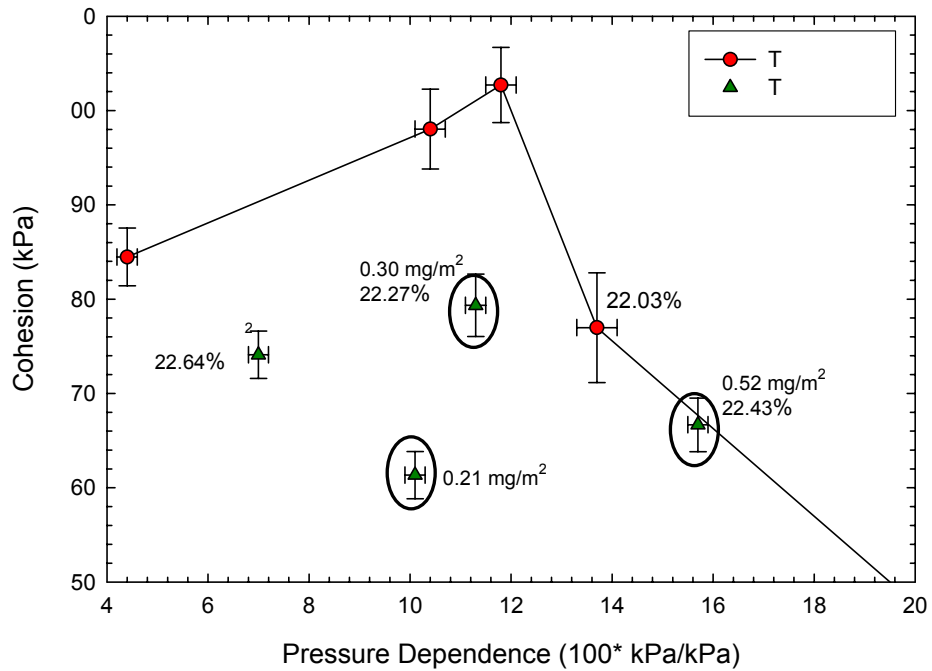


Figure 5-26. Close up view of the shear rheology map for the samples prepared with the acid-insoluble fraction of digested lignite (DLAI) at a target moisture content of 22%. Additions of DLAI are observed to increase the pressure dependence of the samples and reduce the cohesion.

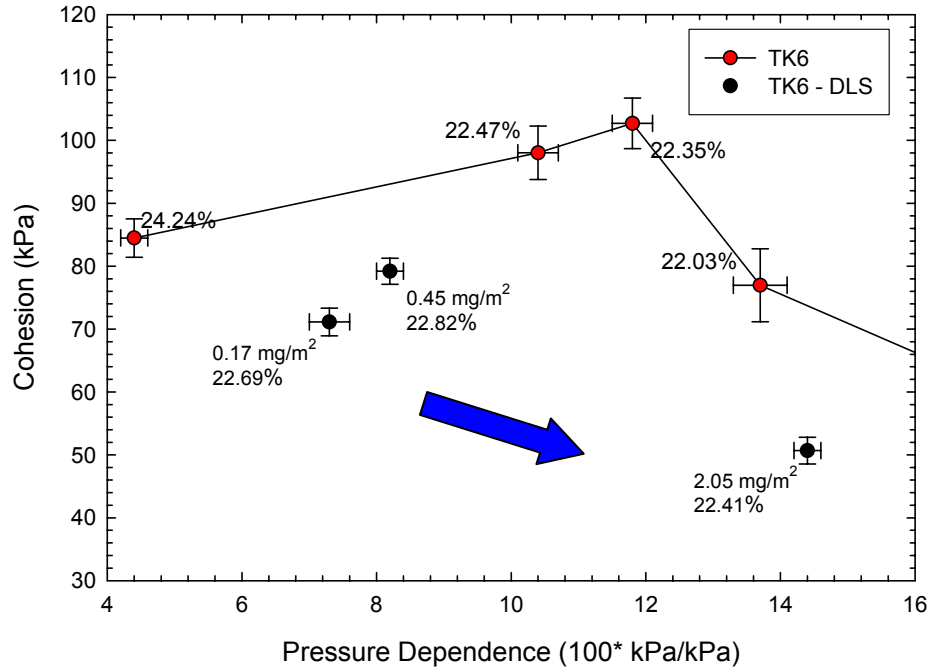


Figure 5-27. Close up view of the shear rheology map for the samples prepared with the soluble fraction of digested lignite (DLS) at a target moisture content of 22%. Additions of DLS are observed to increase the pressure dependence of the samples while decreasing the cohesion.

Additions of DLAI were observed to reduce the cohesion and increase the pressure dependence. Additions of DLS were observed to significantly reduce the cohesion of the sample and with increasing additions the pressure dependence was observed to increase. A comparison of the predicted cohesion and pressure dependence from the models in Table 5-VI to the measured cohesion and pressure dependence for the samples prepared with digested lignite are shown in Table 5-XI.

The error reported in Table 5-IX, 5-X, and 5-XI was calculated based upon the actual value. Therefore a negative error indicated that the predicted value was greater than the actual value. With increasing salt concentration a 30% reduction in the cohesion of the clay mass was observed. At the highest concentrations, 2 M and 6.44 M, sufficient salt was added to change the structure of the water. In one liter of water there are 27.8 moles of water ions, either OH<sup>-</sup> or H<sup>+</sup>. Therefore a 2 M solution of NaCl will have 1 salt ion, either a cation or

anion, for every 13.9 water ions. At 6.44 M there are 4.31 water ions for every salt ion. For calcium chloride the number of ions present in solution increases since there are three ions per molecule of salt. Since the highest concentrations of salt resulted in structured water those results were not been included in Table 5-IX.

The results for lignosulphonate, Table 5-X, are separated into two groups: group one has a moisture content below the peak in the shear rheology diagram for TK6 while group two has a moisture content near the peak in the shear rheology diagram. Both groups of samples had a significant reduction in the pressure dependence relative to the predicted value. The highest addition of lignosulphonate, at a moisture content of 21.55%, resulted in a 335.6% decrease in the pressure dependence of the plastic mass. Similar reductions in the pressure dependence were observed near the peak in the shear rheology diagram. Initially the cohesion of the samples was observed to decrease relative to the TK6 prediction, but with higher additions of lignosulphonate the cohesion was observed to increase. At the highest addition, at a moisture content of 21.55%, a 20.97% increase in the cohesion is observed. At 22% moisture lignosulphonate was observed to increase the cohesion of the clay and decrease the pressure dependence. Lignosulphonate is an effective dispersant for clay and the reduction in the pressure dependence with addition of lignosulphonate is due to the electrosteric barrier between the particles. This barrier resulted in a decrease in the particle-particle interactions thus reducing the internal friction.

Additions of fractioned lignite had an unclear effect on the cohesion and pressure dependence. Overall the addition the insoluble or acid-insoluble fractions of the lignite were observed to reduce the cohesion of the clay relative to the predicted value. There was a variable effect on the pressure dependence of samples with higher additions of these fractions. The addition of the soluble fraction of lignite was observed to initially decrease the cohesion of the clay. Higher additions were observed to increase the cohesion. Little effect was observed on the pressure dependence of the samples.

Table 5-X. Comparison of the Predicted and Actual Cohesion (Coh.) and Pressure Dependence for the TK6 Samples Used to Characterize Plasticity with Na-lignosulphonate or Lignite Additions.

Moisture Content, % (mg/m <sup>2</sup> added)	Predicted		Actual		Error	
	Coh. (kPa)	P.D. (100* kPa/kPa)	Coh. (kPa)	P.D. (100* kPa/kPa)	Coh. (%)	P.D. (%)
<b>Na-lignosulphonate</b>						
21.74 (0.31)	70.63	15.6	55.13±2.80	13.0±0.2	-28.13	-20.3
21.81 (0.50)	73.91	15.2	79.16±3.17	11.0±0.2	6.64	-37.7
21.53 (1.31)	60.34	17.1	69.70±3.26	8.1±0.2	13.42	-111.5
21.55 (1.80)	61.35	17.0	77.62±2.52	3.9±0.2	20.97	-335.6
22.43 (0.09)	97.51	11.3	83.42±2.64	6.8±0.2	-16.89	-65.9
22.42 (0.21)	97.23	11.3	96.77±1.75	5.8±0.1	-0.47	-95.5
22.13 (0.77)	87.47	13.1	85.02±2.49	5.5±0.2	-2.88	-137.4
<b>Lignite - insoluble fraction</b>						
22.44 (0.09)	97.80	11.2	92.74±3.34	8.5±0.3	-5.45	-32.1
22.28 (0.24)	92.85	12.1	63.36±3.87	14.3±0.3	-46.56	15.1
22.52 (0.35)	99.93	10.8	77.37±3.45	10.7±0.3	-29.17	-0.8
21.97 (0.14)	81.00	14.1	64.22±3.65	14.6±0.3	-26.13	3.6
21.65 (0.59)	66.33	16.3	59.74±3.34	17.3±0.3	-10.98	6.0
22.89 (0.91)	106.64	8.9	68.50±1.78	6.9±0.1	-55.68	-29.4
23.39 (1.70)	106.88	6.9	88.54±2.73	4.9±0.2	-20.72	-39.9
<b>Lignite - acid-insoluble fraction</b>						
22.59 (0.10)	101.61	10.4	89.29±3.20	8.2±0.2	-13.80	-27.0
22.54 (0.21)	100.43	10.7	43.31±4.44	16.6±0.3	-131.86	35.7
22.41 (0.30)	96.94	11.4	102.2±4.85	10.0±0.4	5.15	-13.9
22.53 (0.50)	100.18	10.7	73.31±3.26	13.5±0.2	-36.65	20.5
<b>Lignite - soluble fraction</b>						
22.01 (0.09)	82.68	13.8	64.06±3.44	13.7±0.3	-29.07	-0.9
22.70 (0.42)	103.86	9.8	94.44±3.98	8.8±0.3	-9.98	-11.9
21.71 (2.10)	69.20	15.8	77.04±5.05	14.9±0.4	10.17	-6.3

Table 5-XI. Comparison of the Predicted and Actual Cohesion (Coh.) and Pressure Dependence for the TK6 Samples Used to Characterize Plasticity with Digested-lignite Additions.

Moisture Content, % (mg/m <sup>2</sup> added)	Predicted		Actual		Error	
	Coh. (kPa)	P.D. (100* kPa/kPa)	Coh. (kPa)	P.D. (100* kPa/kPa)	Coh. (%)	P.D. (%)
<b>Digested Lignite - insoluble fraction</b>						
21.90 (0.07)	77.97	14.5	70.12±3.51	16.2±0.3	-11.20	10.2
21.82 (0.26)	74.37	15.1	61.33±5.82	17.5±0.4	-21.25	13.8
21.80 (1.69)	73.45	15.2	40.90±3.79	18.9±0.3	-79.58	19.5
22.14 (0.17)	87.85	13.0	94.85±2.40	8.3±0.1	7.39	-56.6
22.29 (0.36)	93.19	12.1	64.47±4.29	15.3±0.3	-44.56	21.0
22.34 (0.91)	94.81	11.8	70.26±2.06	14.2±0.2	-34.94	16.9
23.50 (0.74)	105.55	6.5	97.51±3.57	5.0±0.3	-8.24	-29.2
<b>Digested Lignite - acid-insoluble fraction</b>						
22.64 (0.06)	102.69	10.2	74.10±2.50	7.0±0.2	-38.58	-45.0
22.35 (0.12)	95.12	11.7	61.34±2.51	10.1±0.2	-55.07	-16.2
22.27 (0.18)	92.52	12.2	79.34±3.31	11.3±0.2	-16.60	-8.0
22.43 (0.30)	97.51	11.3	66.67±2.84	15.7±0.2	-46.26	28.1
<b>Digested Lignite - soluble</b>						
22.69 (0.17)	83.51	13.7	50.69±2.12	14.4±0.2	-104.55	31.3
22.82 (0.45)	103.68	9.9	79.19±2.07	8.2±0.2	-33.58	-12.9
22.41 (2.05)	105.78	9.3	71.12±2.21	7.3±0.3	-36.29	-56.1

The addition of the insoluble fraction of the digested lignite was observed to significantly reduce the cohesion of the clay relative to the predicted level. Simultaneously an increase in the pressure dependence was observed with increasing addition of the insoluble fraction. The addition of the acid-insoluble fraction of digested lignite was observed to reduce the cohesion of the clay. Initially a significant decrease was observed in the pressure dependence, but with higher additions the pressure dependence was observed to increase. The addition of the soluble fraction of digested lignite was observed to significantly reduce the cohesion of the clay and decrease the pressure dependence.

The change in the surface tension affected by adding organics, salts, or clay to distilled water are shown in Figure 5-28 (Na-lignosulphonate and humic acid), Figure 5-29 (Na-PAA and acrylic latex emulsion), Figure 5-30 (pPVA and PEG 8000), Figure 5-31 ( $\text{CaCl}_2$  and KCl), and Figure 5-32 (C&C and TK6). No significant difference was measured in the surface tension between the distilled water at pH 5.5 and deionized water stored with a carbon dioxide filter. The surface tension of the distilled water has been plotted as a line in each of the figures to represent the average of the measured values; the standard deviation of the measured values is indicated by the band. Additions of lignosulphonate, pPVA, PEG, and an acrylic emulsion were all observed to reduce the surface tension of the solutions. Additions of salt, humic acid, and Na-PAA were not observed to significantly effect the measured surface tension. Preparation of suspensions with clay was observed to increase the surface tension. Adding insoluble materials, e.g., clay, to a suspension is known to increase the surface tension of the system; this effect is used in the spray drying process to break up the stream of suspension into spherical droplets which rapidly dry in the heated chamber. The addition of hydrophilic organics, e.g., PAA, did not significantly effect the surface tension since these materials remained in the bulk of the solution. Hydrophobic organics, e.g., PVA or PEG, migrated to the surface of the droplet reducing the surface tension of the solution. The smallest additions of PVA or PEG were observed to significantly reduce the surface tension of the solution from 83 dynes/cm (the average value measured for the distilled water used to prepare the solutions in this study) to approximately 68 dynes/cm for PEG solutions and approximately 50 dynes/cm for the pPVA system. The smallest addition in the prepared solutions was sufficient to saturate the interface and minimize the surface tension.

Based upon the work cited in the literature review an increase in the surface tension of the wetting liquid was expected to increase the plasticity of the clay.<sup>8-10</sup> Materials which were observed to increase the surface tension of the liquid, e.g. salts, were observed to decrease the peak cohesion of the clay and, below the CCC, increase the pressure dependence. This combination of effects has been defined, for the purposes of this research, as a system which exhibits

“poor” plasticity. Additives which were observed to decrease the surface tension of distilled water, e.g., Na-Lignosulphonate, were observed increase the peak cohesion and reduce the pressure dependence of the clay at a target moisture content of 22%. This combination of effects has been defined as a system which exhibits “good” plasticity.

Based upon the results reported in Chapter 4 no comparison can be made between the additions of lignite or digested-lignite fractions and the Aldrich humic acid. The digested lignite which was added by the supplied to Huntingdon clay was not a humic substance, but rather the precursor of a humic substance. The addition of Aldrich humic acid was observed to have no significant effect on the surface tension of distilled water. Additions of Aldrich humic acid to the clay samples to characterize plasticity was cost prohibitive; furthermore humic acid has been classified by OSHA as a hazardous material.

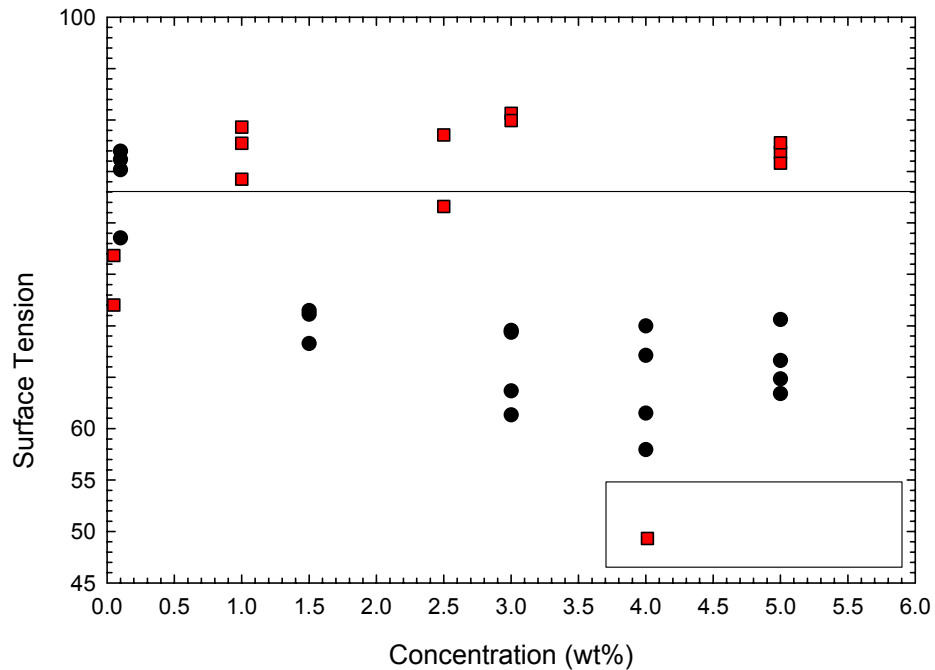


Figure 5-28. Change in the surface tension of solutions prepared with sodium lignosulphonate or Aldrich humic acid. Lignosulphonate is observed to reduce the surface tension while humic acid is observed to have little effect on the surface tension.

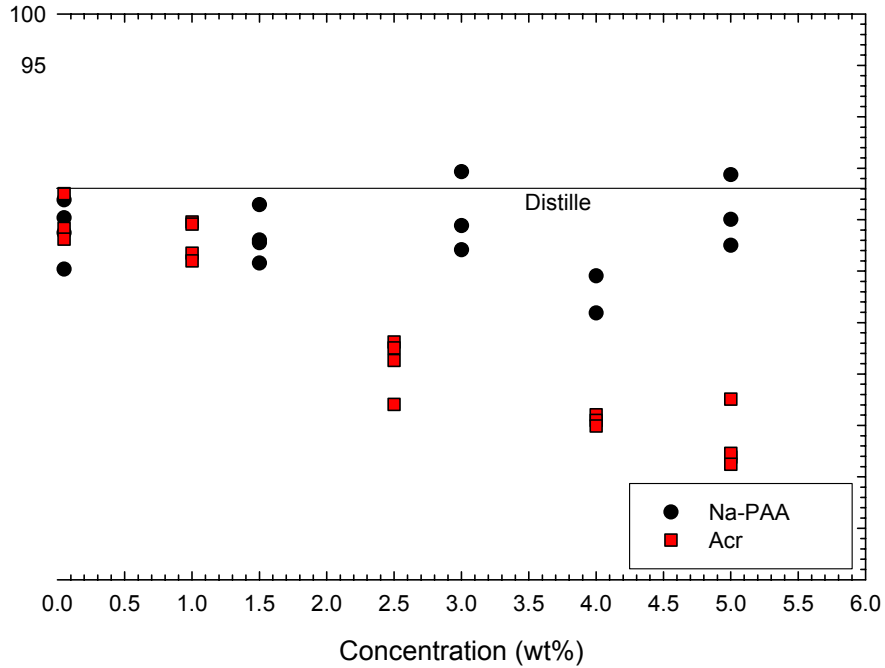


Figure 5-29. Change in the surface tension of solutions prepared with sodium poly[acrylic acid] or an acrylic latex emulsion. Na-PAA is observed to have little effect on the surface tension while the emulsion is observed to reduce the surface tension.

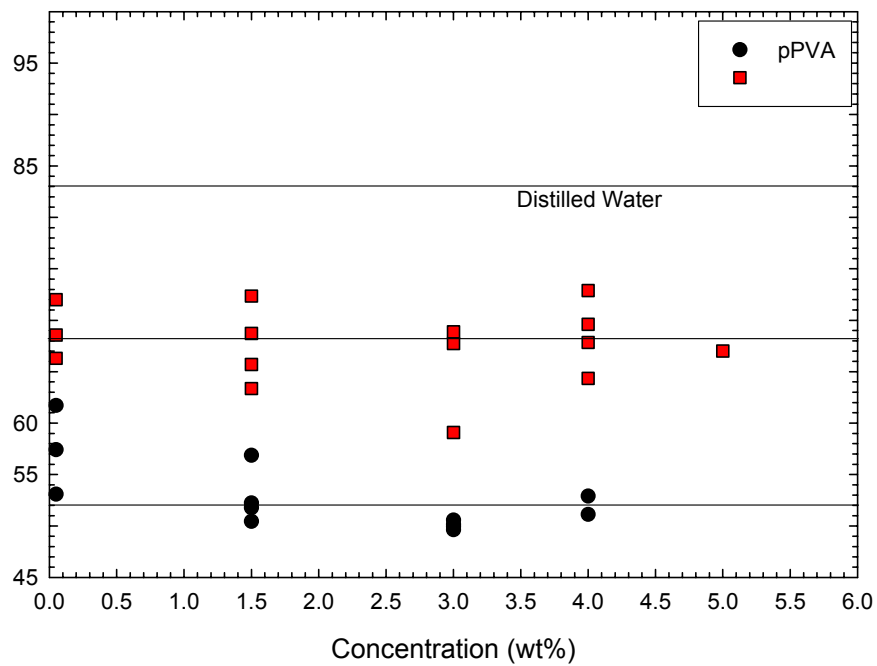


Figure 5-30. Change in the surface tension of solutions prepared with a plasticized PVA or PEG 8000. Both organics are observed to reduce the surface tension at the smallest addition level.

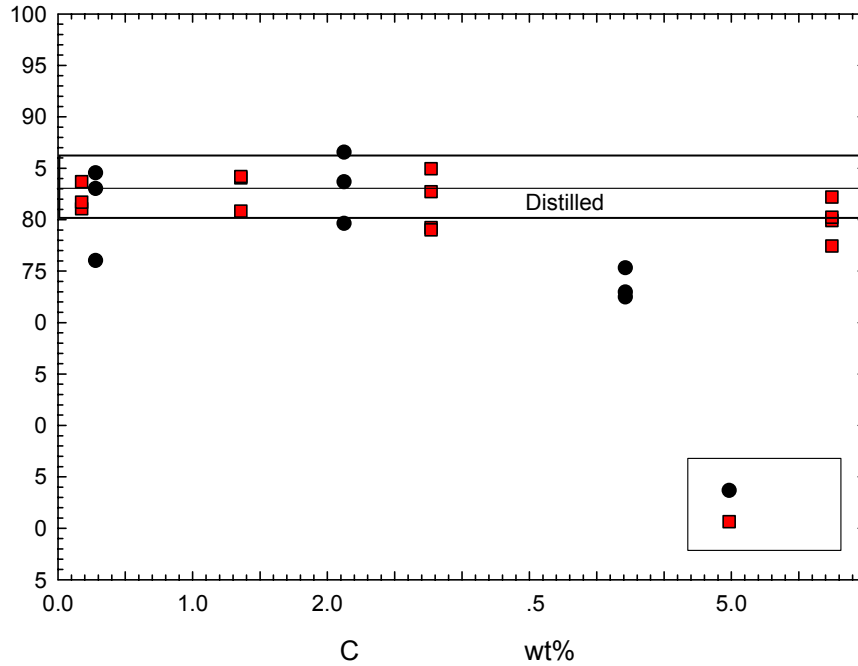


Figure 5-31. Change in the surface tension of solutions prepared with calcium chloride or sodium chloride. Additions of salt are not observed to significantly effect the surface tension.

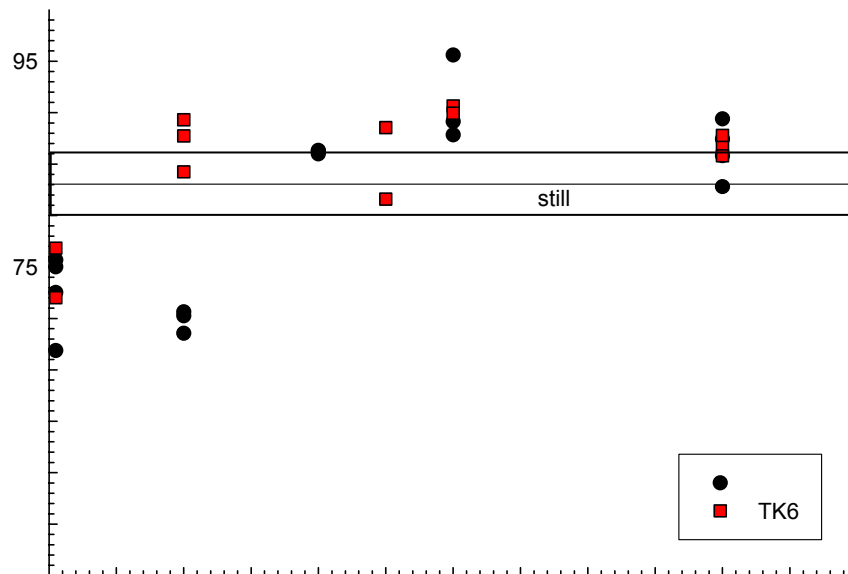


Figure 5-32. Change in the surface tension of suspensions prepared with C&C ball clay or TK6 kaolin clay. Additions of clay to form a suspension are observed to slightly increase the surface tension.

## **5.5 Summary and Conclusions**

The viscosity of 30 v/o TK6 suspensions was observed to decrease with the addition of the insoluble lignite or insoluble digested-lignite fractions. No increase was observed in the viscosity at higher additions of these additives. The addition of the acid-insoluble fraction of lignite or digested lignite was observed to initially decrease the viscosity, but at higher addition levels the viscosity increased due to coagulation which was a result of the high concentration of NaCl created during fractioning the organics. The addition of the soluble fractions of lignite or digested lignite resulted in a significant increase in the viscosity of the TK6 suspensions due to the high concentration of NaCl in solution.

C&C ball clay was observed to have the lowest moisture requirement to reach a maximum in the cohesion. This was due to the high concentration of non-plastic materials, specifically quartz, in the clay. TK6 was observed to pass through a maximum in cohesion at a lower moisture content compared to Huntingdon ball clay. Huntingdon ball clay is a fine clay compared to TK6. The maximum cohesion value for the Huntingdon and TK6 clays were similar in magnitude and occur at a similar pressure dependence. The maximum cohesion value for the C&C clay was greater in magnitude than that of the other clays in this study and was observed to occur at a higher pressure dependence.

Changes in the shear rheology of plastic masses prepared with added salts, specifically NaCl and  $\text{CaCl}_2 \cdot 2\text{H}_2\text{O}$ , showed changes in the plasticity of the samples. Additions of salt, even at the lowest levels tested, were observed to primarily reduce the cohesion of the samples. Additions of salt below the CCC were observed to increase the pressure dependence of the sample and above the CCC the pressure dependence was observed to decrease. These results may be explained by either a hydration repulsive force between the particles or the structure-making structure-breaking theories for the interactions between minerals and indifferent electrolytes. This non-DLVO behavior is primarily observed in systems of particles with a high surface charge such as kaolinite or systems at a pH far from the iep.

The addition of sodium lignosulphonate was observed to enhance the plasticity of clay. With increasing addition of the organic an increase was observed in the cohesion of the samples with a corresponding decrease in the pressure dependence. While additions of fractioned lignite and digested lignite were observed to affect the viscosity of 30 v/o suspensions of TK6, no beneficial effect was observed on the plasticity of the samples.

Salts, which were observed to either slightly increase or have no significant effect upon the surface tension of distilled of water, were observed to reduce the measured cohesion, up to a 30% reduction at the CCC, and increase the pressure dependence, up to 20% at the CCC, of TK6 samples prepared at a target moisture content of 22%. Additives which were observed to decrease the surface tension of distilled water, e.g., Na-lignosulphonate, were observed to increase the measured cohesion up to 20% with a simultaneous decrease of more than 300% in the pressure dependence of the clay.

## 5.6 References

1. E.C. Bingham, "Plasticity as a Means for Control of Properties," *J. Am. Ceram. Soc.*, **7** [6] 430-6 (1924).
2. G.L. Barna, "Plasticity of Clay Minerals," *Am. Ceram. Soc. Bull.*, **46** [11] 1091-3 (1967).
3. R.E. Wilson and F.P. Hall, "The Measurement of the Plasticity of Clay Slips," *J. Am. Ceram. Soc.*, **5** [12] 916-27 (1922).
4. P.E. Cox, "A Study of Plasticity by Practical Potter's Methods," *J. Am. Ceram. Soc.*, **7** [3] 151-3 (1924).
5. G.A. Bole, "Mechanism of Plasticity from Colloidal Standpoint," *J. Am. Ceram. Soc.*, **5** [8] 469-77 (1922).
6. E.C. Bloor, "Plasticity in Theory and Practice," *Trans. Br. Ceram. Soc.*, **58** 429-53 (1959).
7. E.A. Hauser and A.L. Johnson, "Plasticity of Clays," *J. Am. Ceram. Soc.*, **25** [9] 223-7 (1942).
8. F.H. Norton, "Fundamental Study of Clay: VIII, a New Theory for the Plasticity of Clay-Water Masses," *J. Am. Ceram. Soc.*, **31** [8] 236-41 (1948).
9. B. Schwartz, "Fundamental Study of Clay: XII a Note on the Effect of the Surface Tension of Water on the Plasticity of Clay," *J. Am. Ceram. Soc.*, **35** [2] 41-3 (1952).
10. W.D. Kingery and J. Francl, "Fundamental Study of Clay: XIII, Drying Behavior and Plastic Properties," *J. Am. Ceram. Soc.*, **37** [12] 596-602 (1954).
11. J.W. Whittemore, "Water of Plasticity," *Am. Ceram. Soc. Bull.*, **21** [11] 268-9 (1942).
12. S.J. McDowell, "Notes on a Method for Determination of Workability of Plastic Clays," *J. Am. Ceram. Soc.*, **11** [2] 99-102 (1928).
13. G. Huiras and H.W. Hennicke, "Compression-Test Measuring of Plasticity," *Ceram. Forum Int.*, **65** [5] 127-33 (1988).
14. R.L. Peek, Jr., "Parallel Plate Plastometry," *J. Rheol.*, **3** [3] 345-72 (1932).
15. H.W. Hennicke and H. Segerer, "On the Use of a Roller Machine as a Plasticity Tester," *Ceram. Forum Int.*, **62** [1] 15-20 (1985).
16. F.P. Hall, "The Plasticity of Clays," *J. Am. Ceram. Soc.*, **5** [6] 346-54 1922.
17. S.R. Hind, "The Plasticity of Clay. Part I. Mechanical Methods of Measurement," *Trans. Br. Ceram. Soc.*, **29** 177-207 (1930).
18. R.P. Graham and J.D. Sullivan, "Improved Machine Shows Different Forms of Failure of Clay Bodies in Torsion," *Am. Ceram. Soc. Bull.*, **18** [3] 97-100 (1939).

19. C.W. Parmelee and R.D. Rudd, "Further Developments on Torsional Apparatus for Measuring Plasticity," *J. Am. Ceram. Soc.*, **12** [8] 552-5 (1929).
20. H.M. Macey, "Experiments on Plasticity. Parts I and II," *Trans. Br. Ceram. Soc.*, **43** 5-28 (1943-44).
21. H.M. Macey, "Experiments on Plasticity. Part III – Some Experiments with Alternating Stresses," *Trans. Br. Ceram. Soc.*, **47** 183-90 (1948).
22. H.M. Macey, "Experiments on Plasticity. Part V – The Behavior of Clays in the Tensional Experiment with Particular Reference to the "Local Elongation" or "Necking"," *Trans. Br. Ceram. Soc.*, **47** 291-326 (1948).
23. H.M. Macey, "Experiments on Plasticity. Part VI – The Phenomenon of "Backlash"," *Trans. Br. Ceram. Soc.*, **47** 259-67 (1948).
24. F.A. Kirkpatrick and W.B. Orange, "Tests of Clays and Limes by the Bureau of Standards Plasticimeter," *J. Am. Ceram. Soc.*, **1** [3] 170-84 (1918).
25. J.W. Whittemore, "Mechanical Method for the Measurement of the Plasticity of Clays and Mixtures of Clays," *J. Am. Ceram. Soc.*, **18** [11] 352-9 (1935).
26. R. Russell and C.F. Hanks, "Stress-Strain Characteristics of Plastic Clay Masses," *J. Am. Ceram. Soc.*, **25** [1] 16-28 (1942).
27. H. Whittaker, "Effect of Particle Size on Plasticity of Kaolinite," *J. Am. Ceram. Soc.*, **22** [1] 16-23 (1939).
28. *Soil Mechanics*. Edited by T.W. Lambe and R.V. Whitman. John Wiley and Sons, New York, New York, 1969.
29. A.M. Jenike, "Storage and Flow of Solids," Bulletin Number 123, Utah Engineering Experiment Station, University of Utah, Salt Lake City, Utah, March, 1970.
30. W.M. Carty and C. Lee, "The Characterization of Plasticity," pp. 89-101 in *Science of Whitewares*. Edited by V.E. Henkes, G.Y. Onoda, and W.M. Carty. The American Ceramic Society, Westerville, Ohio, 1996.
31. W.M. Carty, K.R. Rossington, and D. Shuckers, "Plasticity Revisited," pp. 225-36 in *Science of Whitewares II*. Edited by W.M. Carty and C.W. Sinton. The American Ceramic Society, Westerville, Ohio, 2000.
32. C.W. Macosko, *Rheology – Principles, Measurements, and Applications*; pp. 217-20. VCH Publishers, New York, New York, 1994.
33. P.A. Nowak, "Correlation of Extrusion Behavior with High Pressure Shear Rheometry"; M.S. Thesis. Alfred University, Alfred, New York, 1995.
34. C. Lee, "The Characterization of Plasticity in Clay-based Systems"; M.S. Thesis. Alfred University, Alfred, New York, 1995.
35. L. Leone, "Plastic Properties of Commercial Clays"; B.S. Thesis. Alfred University, Alfred, New York, 1995.

36. P.T. Kupiniski, "The Effects of Water Chemistry on Clay-based Suspension and Plastic Body Rheology"; M.S. Thesis. Alfred University, Alfred, New York, 2000.
37. D.J. Shaw, *Introduction to Colloid and Surface Chemistry*, 4<sup>th</sup> ed.; pp. 210-43. Butterworth – Heinemann, Boston, Massachusetts, 1991.
38. R.J. Hunter, *Introduction to Modern Colloid Science*; pp. 277-8. Oxford Science Publications, New York, New York, 1993.
39. E. Verwey and J.Th.G. Overbeek, *Theory of the Stability of Lyophobic Colloids*. Elsevier, Amsterdam, 1948.
40. R.M. Pashley, "DLVO and Hydration Forces Between Mica Surfaces in Li<sup>+</sup>, Na<sup>+</sup>, K<sup>+</sup>, and Cs<sup>+</sup>, Electrolyte Solutions: A Correlation of Double-layer and Hydration Forces with Surface Cation Exchange Properties," *J. Colloid Interface Sci.*, **83** [2] 531-46 (1981).
41. R.M. Pashley, "Hydration Forces Between Mica Surfaces in Electrolyte Solutions," *Adv. Colloid Interface Sci.*, **16** [1] 57-62 (1982).
42. J.N. Israelachvili, "Forces Between Surfaces in Liquids," *Adv. Colloid Interface Sci.*, **16** [1] 31-47 (1982).
43. R.M. Pashley and J.N. Israelachvili, "Measurement of the Hydrophobic Interaction Between Two Hydrophobic Surfaces in Aqueous Electrolyte Solutions," *J. Colloid Interface Sci.*, **98** [2] 500-14 (1984).
44. B.V. Velmakanni, J.C. Chang, F.F. Lange, and D.S. Pearson, "New Method for Efficient Colloidal Particle Packing via Modulation of Repulsive Lubricating Hydration Forces," *Langmuir*, **6** [7] 1323-5 (1990).
45. B.V. Velmakanni, F.F. Lange, F.W. Zok, and D.S. Pearson, "Influence of Interparticle Forces on the Rheological Behavior of Pressure-Consolidated Alumina Particle Slurries," *J. Am. Ceram. Soc.*, **77** [1] 216-20 (1994).
46. J.C. Chang, F.F. Lange, and D.S. Pearson, "Pressure Sensitivity for Particle Packing of Aqueous Al<sub>2</sub>O<sub>3</sub> Slurries vs Interparticle Potential," *J. Am. Ceram. Soc.*, **77** [3] 1357-60 (1994).
47. J.A. Yanez, T. Shikata, F.F. Lange, and D.S. Pearson, "Shear Modulus and Yield Stress Measurements of Attractive Alumina Particle Networks in Aqueous Slurries," *J. Am. Ceram. Soc.*, **79** [1] 2917-24 (1996).
48. G.V. Franks, M. Colic, M.L. Fisher, and F.F. Lange, "Plastic-to-Brittle Transition of Consolidated Bodies: Effect of Counterion Size," *J. Colloid Interface Sci.*, **193** [1] 96-103 (1997).
49. G.V. Franks and F.F. Lange, "Plastic-to-Brittle Transition of Saturated, Alumina Powder Compacts," *J. Am. Ceram. Soc.*, **79** [12] 3161-8 (1996).
50. G.V. Franks and F.F. Lange, "Plastic Flow of Saturated, Consolidated Alumina Powder Compacts: Particle Size and Binary Mixtures," *J. Am. Ceram. Soc.*, **82** [6] 1595-7 (1999).

51. G.V. Franks and F.F. Lange, "Mechanical Behavior of Saturated, Consolidated, Alumina Powder Compacts: Effect of Particle Size and Morphology on the Plastic-to-Brittle Transition," *Colloids Surf., A*, **146** [1-3] 5-17 (1999).
52. G.V. Franks and F.F. Lange, "Plastic Clay-like Flow Stress of Saturated Advanced Ceramic Powder Compacts," *J. Eur. Ceram. Soc.*, **21** [7] 893-9 (2001).
53. Y.G. Berube and P.L. Bruyn, "Adsorption at the Rutile-Solution Interface II. Model of the Electrochemical Double Layer," *J. Colloid Interface Sci.*, **28** [1] 92-105 (1968).
54. S.B. Johnson, P.J. Scales, and T.W. Healy, "The Binding of Monovalent Electrolyte Ions on  $\alpha$ -Alumina. I. Electroacoustic Studies at High Electrolyte Concentrations," *Langmuir*, **15** [8] 2836-43 (1999).
55. S.B. Johnson, G.V. Franks, P.J. Scales, and T.W. Healy, "The Binding of Monovalent Electrolyte Ions on  $\alpha$ -Alumina. II. The Shear Yield Stress of Concentrated Suspensions," *Langmuir*, **15** [8] 2844-53 (1999).
56. G.V. Franks, S.B. Johnson, P.J. Scales, D.V. Boger, and T.W. Healy, "Ion-Specific Strength of Attractive Particle Networks," *Langmuir*, **15** [13] 4411-20 (1999).
57. E. Ruckenstein and M. Manciu, "Specific Ion Effects via Ion Hydration: II. Double layer Interactions," *Adv. Colloid Interface Sci.*, **105** [1-3] 177-200 (2003).
58. C.R. Evanko, R.F. Delisio, D.A. Dzonbak, and J.W. Novak, "Influence of Aqueous Solution Chemistry on the Surface Charge, Viscosity, and Stability of Concentrated Alumina Dispersions in Water," *Colloids Surf., A*, **125** [2-3] 95-107 (1997).
59. S.B. Johnson, G.V. Franks, P.J. Scales, D.V. Boger, and T.W. Healy, "Surface Chemistry – Rheology Relationships in Concentrated Mineral Suspensions," *Int. J. Miner. Process.*, **58** [1-4] 267-304 (2000).
60. N.E. Dorsey, "A New Equation for the Determination of Surface Tension from the Form of a Sessile Drop or Bubble," *J. Wash. Acad. Sci.*, **18** [19] 505-9 (1928).
61. J.F. Padday, "Surface Tension. Part I. The Theory of Surface Tension," pp. 39-99 in *Surface and Colloid Science*. Edited by E. Matijevic. Wiley Interscience, New York, New York, 1969.
62. J.F. Padday, "Surface Tension. Part II. The Measurement of Surface Tension," pp. 101-49 in *Surface and Colloid Science*. Edited by E. Matijevic. Wiley Interscience, New York, New York, 1969.
63. J.E. Glass, "Adsorption Characteristics of Water-Soluble Polymer at Aqueous-Organic Liquid Interfaces," *J. Polym. Sci., C*, **34**, 141-57 (1971).

64. W.M. Carty, "Processing of Ceramic Fibers from Particle Suspensions"; Ph.D. Thesis. University of Washington, Seattle, Washington, 1992.
65. B.R. Sundlof, "Aqueous Processing of Alumina and Phase Behavior of Polymeric Additives"; Ph.D. Thesis. Alfred University, Alfred, New York, 1999.
66. K.R. Rossington, "Colloidal Behavior of Clay in Whiteware Suspensions"; Ph.D. Thesis. Alfred University, Alfred, New York, 2000.
67. D.S. Schuckers, "The Effect of  $[Ca^{2+}]$  on Plasticity in a Whiteware Body"; B.S. Thesis. Alfred University, Alfred, New York, 1999.

## **6. Characterization of Surface Finish from Industry**

### **6.1 Introduction**

To quantify changes in the surface finish of dry-pressed ware and to set a baseline for the other forming processes used in the dinnerware industry, a preliminary study to quantitatively characterize the surface roughness of dinnerware from four different forming operations was performed. The forming methods selected from Buffalo China's industrial process were: 1) dry pressing, 2) jiggering, 3) ram pressing and 4) pressure casting. Samples were taken from the industrial process at each step where the surface was modified, i.e., the green surface, the bisque fired surface, the vibratory processes surface, and the fired glazed surface. These results were used as a baseline for future changes in the measured roughness of dinnerware samples prepared at Alfred University.

### **6.2 Options Available to Evaluate Surface Finish**

Several options are available for characterizing the surface finish or roughness of materials, e.g., optical interferometry, stylus-type profilometer, atomic force microscopy, and optical or scanning electron microscopy. Since it was the goal of this study to quantitatively measure the surface roughness of the surface, semi-quantitative methods such as optical (OM) or scanning electron microscopy (SEM) were not suited to this study. The soft nature of the green surface would be damaged by dragging a stylus across the surface and no roughness data would be collected, instead the surface would be scratched by the stylus tip. While atomic force microscopy (AFM) would be suited to this study the lateral and vertical resolution would by far exceed the needs of this work and the time necessary to collect data from a large area on the surface made AFM a poor choice for this research. Based upon an estimated 15 minutes to analyze a 150  $\mu\text{m}$  by 150  $\mu\text{m}$  area it would take approximately 17.28 hours to analyzed the same area per scan in the optical interferometer; a typical scan to collect data using the interferometer would take 17 seconds to scan 150 micrometers in the z-direction. Therefore the optical interferometer was selected to quantitatively measure the surface roughness. A comparison between the data collected from the optical interferometer and that collected from the SEM and optical

microscope has been performed. Further information on the operation of the optical interferometer will be presented in the experimental procedure section.

Older stylus-type profilometers cannot resolve the surface roughness of a curved sample; the curvature of the surface obscures the roughness data. To eliminate this problem the scan length needs to be reduced so that the curvature is minimized. Newer stylus-type profilometers are computer controlled and the curvature of the sample can be removed using the software package. Dragging a sharp tip, usually made of diamond or silicon nitride, across the surface and measuring the deflection of the arm collects the data. The result is a two-dimensional measurement of the surface roughness. More sophisticated instruments that are computer controlled can generate a three-dimensional image of the surface by collecting a series of line scans. The measurement is a contact process resulting in damage to the surface of soft materials. Stylus-type profilometers can suffer from tip artifacts since the profilometer cannot resolve features smaller than the tip.

AFM uses the deflection of a tip attached to a cantilever to contour the surface of a material. In this manner a three-dimensional image of the surface can be generated. While AFM has the ability to measure sub-angstrom vertical deflections and the lateral resolution is sub-nanometer, the time necessary to scan large areas makes AFM inefficient, especially when this level of resolution is not necessary. AFM also suffers from tip artifacts when measuring the surface. This problem can be reduced by proper selection of the tip for characterizing the surface.

Microscopy is traditionally used to evaluate the surface finish of materials. The use of OM or the SEM gives a semi-quantitative measure of the surface roughness. Typically the roughness is evaluated by creating shadows on the surface, either by light or the electron beam, and the absence of information is used to gauge the quality of the surface. An example of this semi-quantitative method to determine the surface roughness is shown in Figure 6-1. Shown is an OM image of a green dry-pressed sample surface manufactured in industry using spray-dried granules. Having the incident light nearly parallel to the surface of

the sample creates the shadowing observed in the image. The texture of the surface can be observed and semi-quantitatively estimated, which may meet the requirements in a production setting. Since there is no reference for the surface roughness and information is missing from the image, it is impossible to quantitatively measure the roughness of the sample.

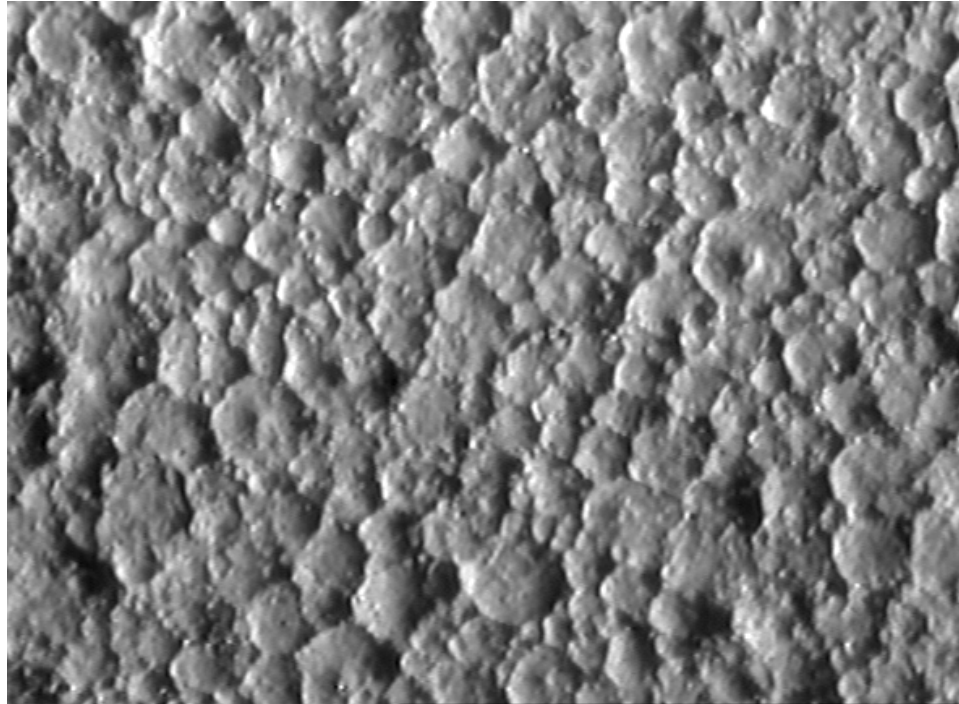


Figure 6-1. Image of the dry-pressed surface from the optical microscope. The light source was placed on the right of the sample with the incident beam nearly parallel to the surface to create shadows on the surface. The shadows are a semi-quantitative indication of the surface roughness.

### ***6.3 Problems with Optical Interferometry***

This technique uses visible “white” light to analyze the surface roughness of a sample. Ideally the light is reflected off the external surface and an interference pattern is generated when the light is recombined with light reflected from a reference mirror. When materials that are optically clear, i.e., transparent to visible light, are analyzed the light from the source can penetrate the surface

and detect interfaces within the material. This type of effect has been observed when working with glazed samples.

The surface of the fired samples contains transparent grains that are penetrated by the light from the interferometer. The result, when using the extended scan option which will be described in the experimental procedure section, is either a large spike of noise or the detection of a deep valley in the surface of the sample. The spike of noise is the result of the scan in the z-direction not detecting the bottom surface of the transparent grain. Typically this would result in a “hole” in the data, an area where no valid information is collected. The interferometer uses a mathematical algorithm called frequency domain analysis (FDA) to convert the interference pattern (frequency data) to a three-dimensional image of the surface. With the FDA set to low the software cannot resolve the lack of data and instead interprets the absence of a signal as noise. The deep valleys that are detected in the surface of the sample result from the light reflecting from the bottom surface of the transparent grains.

For this study glazed samples were prepared using a clear, gloss glaze, representative of the process used in industry, that is transparent to the incident light, hence the name “clear.” The analysis of the glazed samples showed the presence of small circular dimples in the three-dimensional image of the glaze. A semi-quantitative comparison, made using the SEM, did not show the presence of surface roughness in the glazed samples. The optical microscope with reflected light, the same arrangement used by the interferometer, was used to analyze the surface. Small spherical bubbles below the surface of the glaze were observed in the optical microscope, determined to be sub-surface by initially focusing on the surface of the glaze and then focusing on the bubbles. The interferometer was able to detect this interface between the two phases beneath the surface of the glaze. Since the light was focused on the concave surface of the bubbles the interferometer interpreted this high intensity reflection as the external surface of the glaze. A contour plot from one of the glazed samples that shows the presence of bubbles is shown in Figure 6-2.

The presence of these erroneous signals can be reduced in three ways:

- 1) the extended scan length can be increased to start the scan closer to the sample
- 2) the data can be filtered prior to analysis; this will be discussed in the experimental procedure
- 3) the surface of the sample can be coated to mask the internal surfaces

By extending the scan length to collect data well below the surface of the sample, the signal-to-noise ratio can be increased. This reduces the amount of noise present in the collected data, but cannot eliminate all of the noise or the detection of the interfaces within the sample. The consequence of increasing the scan length is longer data collection times; 11 seconds of scan time are required for every 100  $\mu\text{m}$  of scan length in the z-direction.

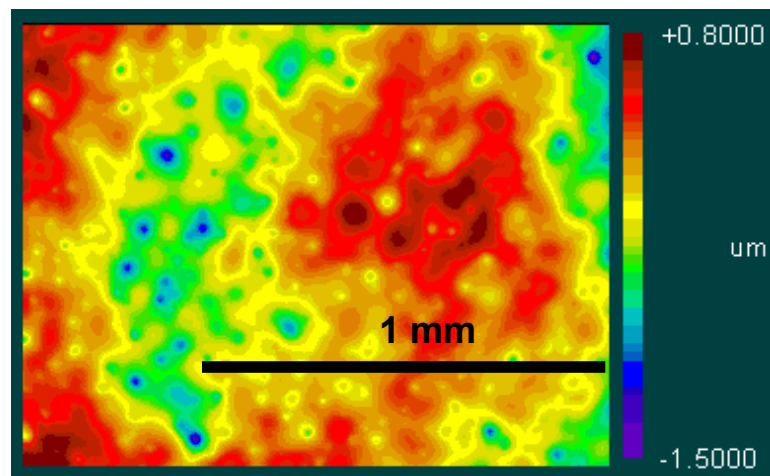


Figure 6-2. Image of the glazed surface showing the presence of circular dimples. These depressions in the surface were determined to be subsurface and are recorded by the interferometer due to the incident light penetrating the clear glaze.

There are several methods of coating the surface to be analyzed. A metallic coating can be sputtered onto the surface. Unfortunately, to have a coating thick enough to prevent the transmission of all light would be time consuming and expensive to create. A coating can be painted onto the surface, but due to the sensitivity of the instrument the texture in the coating will be

measured. This method has been attempted, Figure 6-3, using a black permanent marker. It can be observed that while the coating did block out the subsurface interfaces, the texture of the coating is superimposed onto the surface of the sample.

Focusing the instrument is extremely important. The intensity of the light reflected from the surface is a maximum when the instrument is focused on the surface of the sample. The interferometer measures the intensity reflected from the surface of the sample. The brightness of the light source is adjusted so that the intensity of the reflected light is sufficient for detection; there is a preset range of intensity that will generate repeatable results using the interferometer. If the intensity of the light saturates the detector, data will not be collected from some regions of the surface due to glaring. Therefore focusing the instrument is one of the most important parts of properly operating the optical interferometer.

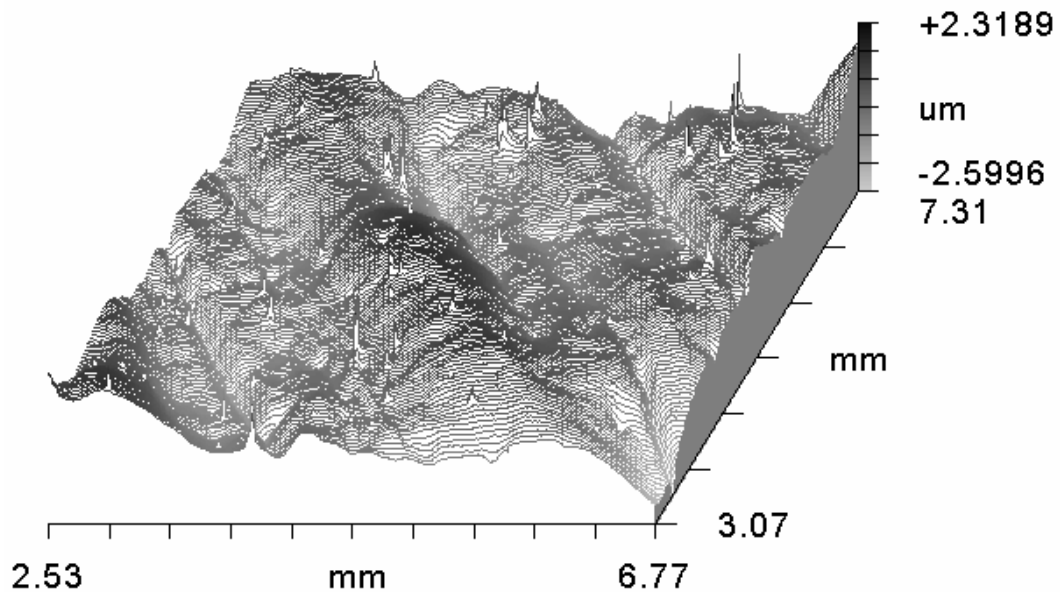


Figure 6-3. Oblique plot from the optical interferometer showing the thickness of the ink superimposed on the texture of the glazed sample. The ink lines run from front, right to back, left in the image. Small spikes of noise can be observed on the surface of the sample, this image was prepared using the unfiltered data.

## 6.4 Experimental Procedure

Prior to any experimental activity it was necessary to quantify the surface roughness of each forming process used by Buffalo China to manufacture dinnerware. These processes were: 1) dry pressing, 2) ram pressing, 3) jiggering, and 4) pressure casting. Samples were collected from each forming process for characterization. The surface finish was quantified using an optical interferometer [NewView model 5032, Zygo Corporation, Middlefield, CT]. Some of these samples were kept in the green state for characterization while others were processed according to Buffalo China's standard firing cycle. The firing process at Buffalo China entailed a bisque firing step at 1290°C followed by vibratory processing of the bisque ware; the dinnerware was passed through a vibrating bed of milling media. The vibratory processing of the ware improved the tactile quality of the surface finish, i.e., the surface of the vibratory processed plate feels significantly smoother relative to the unprocessed ware. The ware was then decorated and coated with glaze and fired to form a thin glass film on the surface. Table 6-I outlines the number of samples that were characterized at each stage of the firing process and from each forming process. Details on the forming and firing of porcelain ceramics can be reviewed in Reed,<sup>1</sup> Norton,<sup>2</sup> and Rahaman.<sup>3</sup> Information on the phase evolution of a porcelain body during firing can be found in several references.<sup>4-9</sup>

Table 6-I. List of the Number of Samples Characterized for Surface Roughness.

Forming Process	Number of samples analyzed for surface roughness			
	Green	Bisque Fired	Vibratory Processed	Glazed
Dry Pressing	20	24	24	23
Ram Pressing	14	24	24	23
Jiggering	18	24	24	23
Pressure Casting	5	8	7	8

The optical interferometer uses a white light source which is passed through a beam splitter (a partially silvered mirror). Half of the light intensity is then reflected from the sample surface while the other half is reflected from a reference mirror. The light is then recombined at the partially silvered mirror and an interference pattern is created depending on whether the light is in or out of phase. The head of the instrument travels in the “z” direction to collect an image of the surface. The result, for a perfectly smooth surface, is a series of bright or dark images as the two reflected beams are in and out of phase. For a rough surface a series of bright and dark bands are created that travel across the surface. A schematic of the interferometer (based upon the Michelson interferometer) is shown in Figure 6-4.

For this work a 5x Michelson objective was used. This objective resulted in the analysis of an area of 1.44 mm by 1.08 mm for each scan (each corresponding to 76,800 data points, a 320 by 240 grid of pixels or data points). A stitching application was used to take a series of images with a 25% overlap between each image. For this initial study a series of 48 images (a 6 by 8 grid) was studied for statistically significant results. This resulted in the analysis of a 6.85 mm by 6.76 mm area and 2.27 million data points, on each unglazed sample. The extended scan option, which allows for the quantitative characterization of very rough surfaces (up to 7.3 mm of scan length), was used for the unglazed samples. Due to the glossy finish of the glazed samples the extended scan could not be used and two smaller areas were analyzed on the surface each corresponding to 2.52 mm by 2.70 mm (a 2 by 3 grid, 336,000 data points). The instrument settings used in this study resulted in a lateral resolution of 4.5  $\mu\text{m}$  and a vertical resolution of better than 20 nm.

Filters were used to eliminate noise from the analysis. Noise was considered to be high frequency data that was superimposed upon the surface features. The various filtering options available in the software [MetroPro v.7.4.3, Zygo Corporation, Middlefield, CT] are listed in Table 6-II. The filters used to analyze the data in this study are listed in Table 6-III. While filtering the data was beneficial to remove unwanted noise, which artificially inflates the measured

roughness, it was possible to over-filter the data. Therefore only minimal filtering was used to analyze the results.

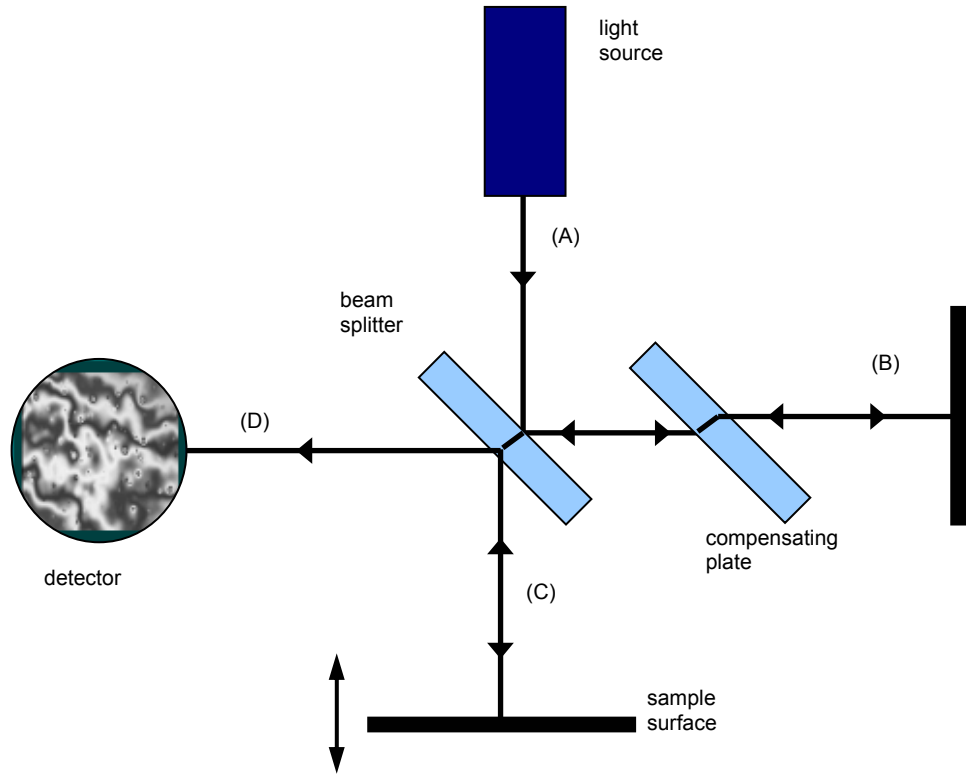


Figure 6-4. Schematic of the Michelson interferometer upon which the 5x objective used in this study is based. The incident light (A) passes through a beam splitter, with half reflected (B) from a fixed, reference mirror and half reflected (C) from a position adjustable mirror (the sample). The light is recombined at the beam splitter to create an interference pattern depending on the path length difference traveled by the two beams (D). Bright and dark fields are observed at the detector due to constructive and destructive interference. The interferometer scans the head of the instrument through the z-direction to create the interference pattern, as opposed to moving the sample. Shown in the detector is an interference pattern from a glazed surface, notice the bright and dark bands that constitute a change in vertical position, corresponding to the roughness, of the surface.

Table 6-II. List of the Filters Used for this Study in the MetroPro™ Software.

<b>Filter</b>	<b>Effect on the roughness measurement</b>
Off	No filter of the data
Low Pass	Data above a set frequency is rejected
<b>Filter Method</b>	<b>Resulting Effect on the filtered data point</b>
Median	Applies the “middle” value of all valid data points to the central data point
FFT Auto	Fast Fourier Transform – automatic. A Fourier transform is applied to the data points and the filter window size is not used. The frequency settings for the Fourier transform are automatically selected. This algorithm should only be used as a starting point for selecting the frequency settings.
FFT Fixed	A Fast Fourier Transform that uses fixed frequency, settings determined by the operator, for the frequency cutoffs.

Table 6-III. Filters Used to Analyze the Data in the Initial Study.

<b>Surface</b>	<b>Filter</b>	<b>Area Analyzed</b>
<b>Green</b>	Low pass, median, window 5	6.85 mm by 6.76 mm
<b>Bisque Fired</b>	Low pass, FFT Fixed, freq. 15 1/mm	6.85 mm by 6.76 mm
<b>Vibratory Processed</b>	Low pass, FFT Fixed, freq. 15 1/mm	6.85 mm by 6.76 mm
<b>Glazed</b>	None	2.52 mm by 2.70 mm (2 each)

## 6.5 Results

Three roughness results were reported by the interferometer. The peak to valley roughness (PV) was a worst-case statistic that measures the distance from the highest point to the lowest point on the surface. Since only two points were considered for the measurement, it was not representative of the overall surface roughness.

The root-mean-square roughness (RMS) was determined as the standard deviation of all the measured data points on the surface. The formula to calculate the RMS roughness was:

$$\text{RMS} = \left( \frac{y_1^2 + y_2^2 + y_3^2 + \dots + y_N^2}{N} \right)^{1/2} \quad (14)$$

where each  $y_i$  is the deviation from the reference plane, determined by the software, for the  $i^{\text{th}}$  data point and  $N$  is the total number of data points. Based upon equation 14 the RMS roughness was an area-weighted statistic.

The average roughness ( $R_a$ ) was determined to be the average deviation from the reference plane. The formula to calculate the average roughness was:

$$R_a = \left( \frac{y_1 + y_2 + y_3 + \dots + y_N}{N} \right) \quad (15)$$

where each  $y_i$  is the deviation from the reference plane for the  $i^{\text{th}}$  data point and  $N$  is the total number of data points. Based upon equation 15 the average roughness was also an area-weighted statistic.

The results from the characterization of the surface finish from each forming process are shown in Figure 6-5 (PV roughness), Figure 6-6 (RMS roughness) and Figure 6-7 (average roughness). The results are also reported in Table 6-IV for the RMS roughness. All of the results showed similar trends. The dry-pressed surface had the highest roughness of the four forming techniques. There was an increase in the measured roughness when the ware was bisque fired; it is proposed that this increase was due to the effects of sintering (firing) at a free surface.

Vibratory processing of the sample was observed to slightly decrease the measured roughness. The vibratory process involved passing the bisque fired ware through a bed of abrasive media which was vibrated. The media removed features that protruded from the ware's surface as the ware passed through the bed. This process resulted in a noticeable difference in the tactile quality of the surface, i.e., the surface felt significantly smoother to the touch.

Table 6-IV. RMS Roughness Results from the Initial Study.

	Green	Bisque Fired	Vibratory Processed	Glazed
Dry-pressed	8.54 ± 0.61	9.10 ± 0.79	8.51 ± 1.03	0.40 ± 0.12
Pressure Cast	4.61 ± 0.71	5.24 ± 1.10	5.36 ± 0.86	0.35 ± 0.08
Ram Pressed	3.23 ± 0.39	3.74 ± 0.58	3.41 ± 0.59	0.31 ± 0.08
Jiggered	3.04 ± 0.75	3.47 ± 0.84	3.40 ± 0.67	0.32 ± 0.09

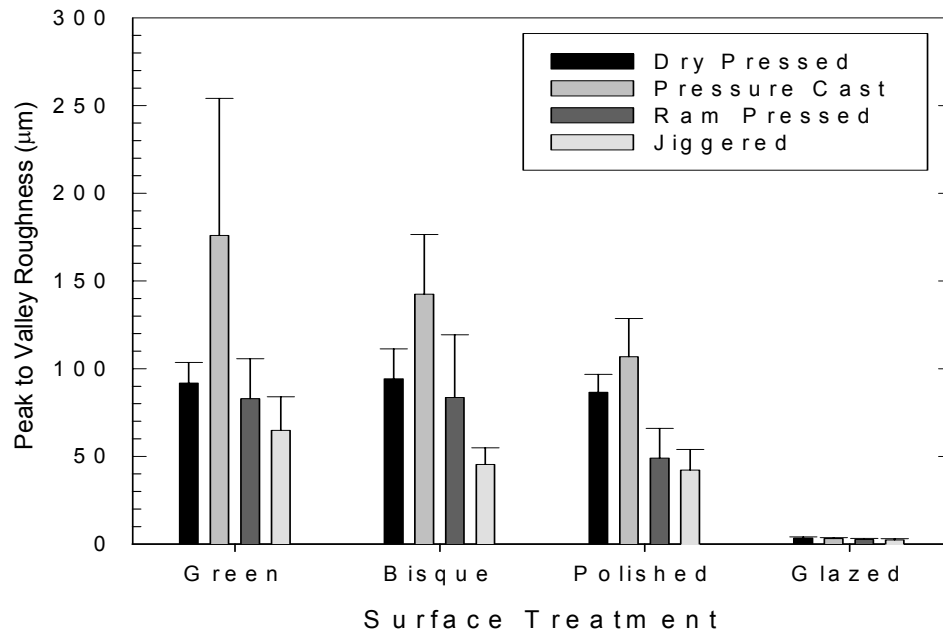


Figure 6-5. Peak to valley roughness measured using the optical interferometer for each of the forming methods and surface treatments in this study. There is a large amount of variation, as evidenced by the large error, in the peak to valley roughness results since the measurement is a worse case statistic and aberrations on the surface inflate the peak to valley distance.

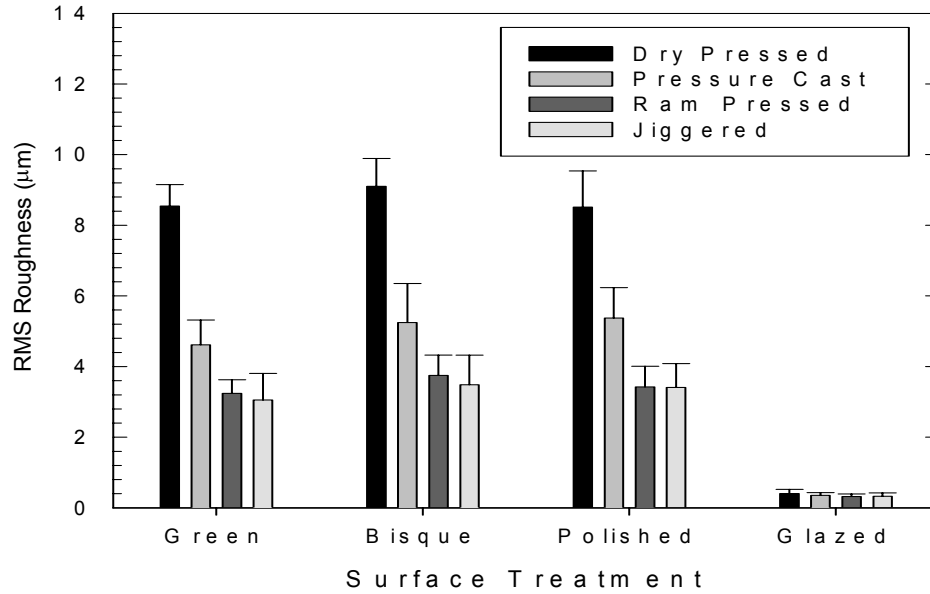


Figure 6-6. RMS roughness measured using the optical interferometer for each of the forming methods and surface treatments in this study. The roughness from the plastic forming methods is statistically similar for each of the treatments tested while the dry-pressed surface is more than twice as rough. The roughness of the pressure-cast ware is significantly higher than that from the plastic forming processes, but is still lower than that of the dry-pressed ware.

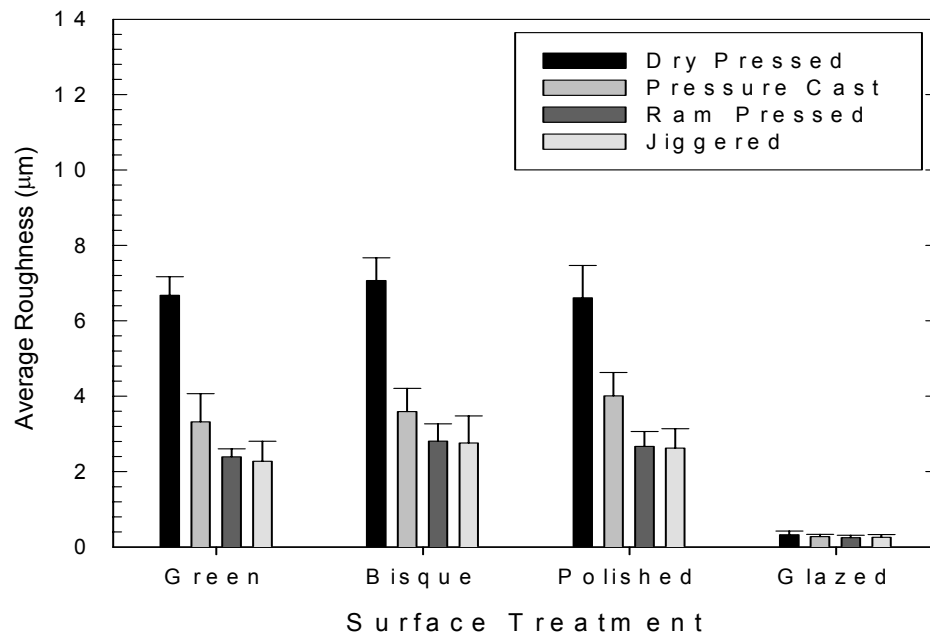


Figure 6-7. Average roughness measured using the optical interferometer for each of the forming methods and surface treatments in this study. The roughness from the plastic forming techniques and the pressure-cast ware is observed to be statistically similar while the roughness from the dry pressing process is more than twice that of the other techniques.

Once the surface was glazed and fired no significant difference was observed between the measured roughness from the various forming processes. While the roughness of the ware was no longer significantly different, the problems associated with a poor finish from the dry-pressed ware were not solved. There was still a problem associated with decorating the bisque fired ware prior to glazing. The poor surface finish ruined the aesthetic quality of the applied decoration and the dry-pressed surface was visible through the transparent glaze, thus destroying the overall aesthetic quality of the ware. While an opaque glaze would solve the problems associated with the visible surface under the glaze, other problems have been documented with the use of an opacified glaze.<sup>10</sup>

Images from the surface were recorded using the optical interferometer, the interference pattern was converted to a contour plot of the surface using frequency domain analysis. Frequency domain analysis is a mathematical algorithm that is an integral part of the software package, it is this algorithm that converts the interference pattern (frequency data) into roughness data. The surface was also analyzed using the semi-quantitative methods of SEM and optical microscopy. Both of these techniques were referred to as semi-quantitative, since the analyzed features rely on the absence of data, e.g., shadows created by the light source in the optical microscope.

The images from the surface can be observed in Figure 6-8 (green, dry-pressed surface), Figure 6-9 (green, jiggered surface), Figure 6-10 (green, ram pressed surface), Figure 6-11 (green, pressure-cast surface), and Figure 6-12 (glazed surface of the dry-pressed ware). To assure that representative images

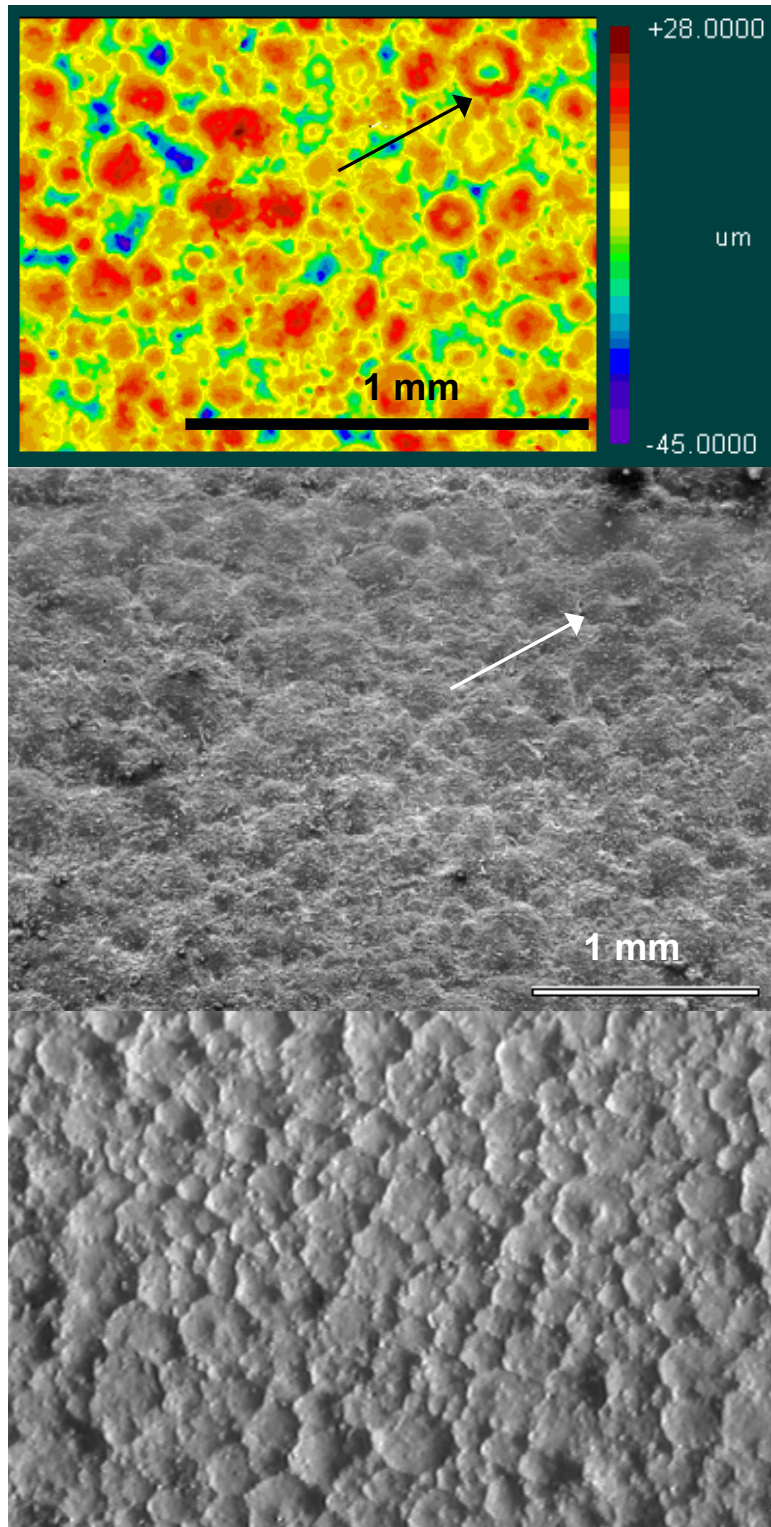


Figure 6-8. Comparison of the images from the interferometer (top), SEM (middle), and optical microscope (bottom) from the green dry-pressed surface. An arrow has been placed in the top two images to reference an irregularly shaped granule observed in each image.

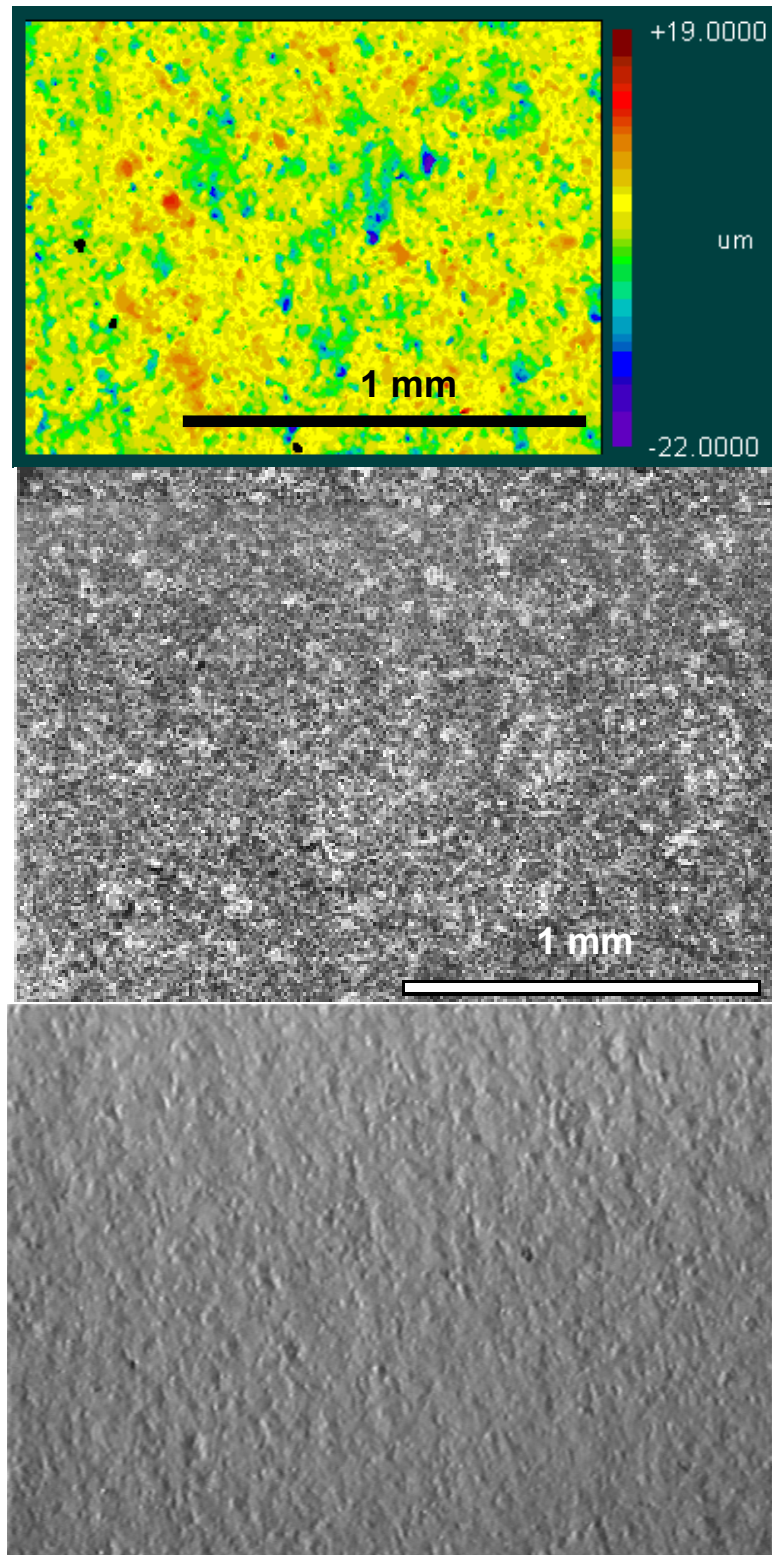


Figure 6-9. Comparison of the images from the interferometer (top), SEM (middle), and optical microscope (bottom) from the green jiggered surface. Large scale texture, with an approximate periodicity of 400 micrometers, on the surface is observed in the image from the interferometer.

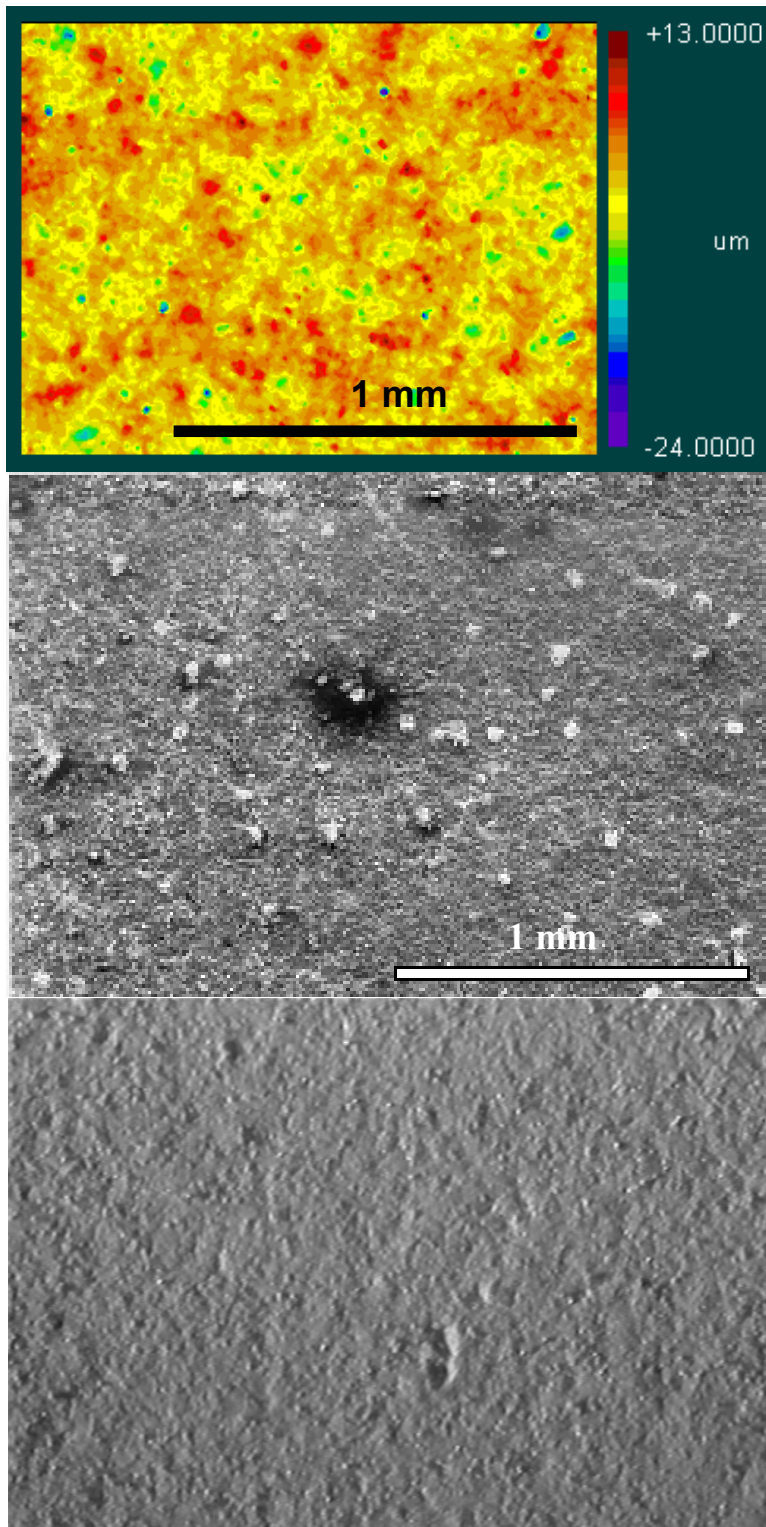


Figure 6-10. Comparison of the images from the interferometer (top), SEM (middle), and optical microscope (bottom) from the green ram-pressed surface. A surface defect is observed in the image from the optical microscope that would result in higher peak to valley roughness measurement.

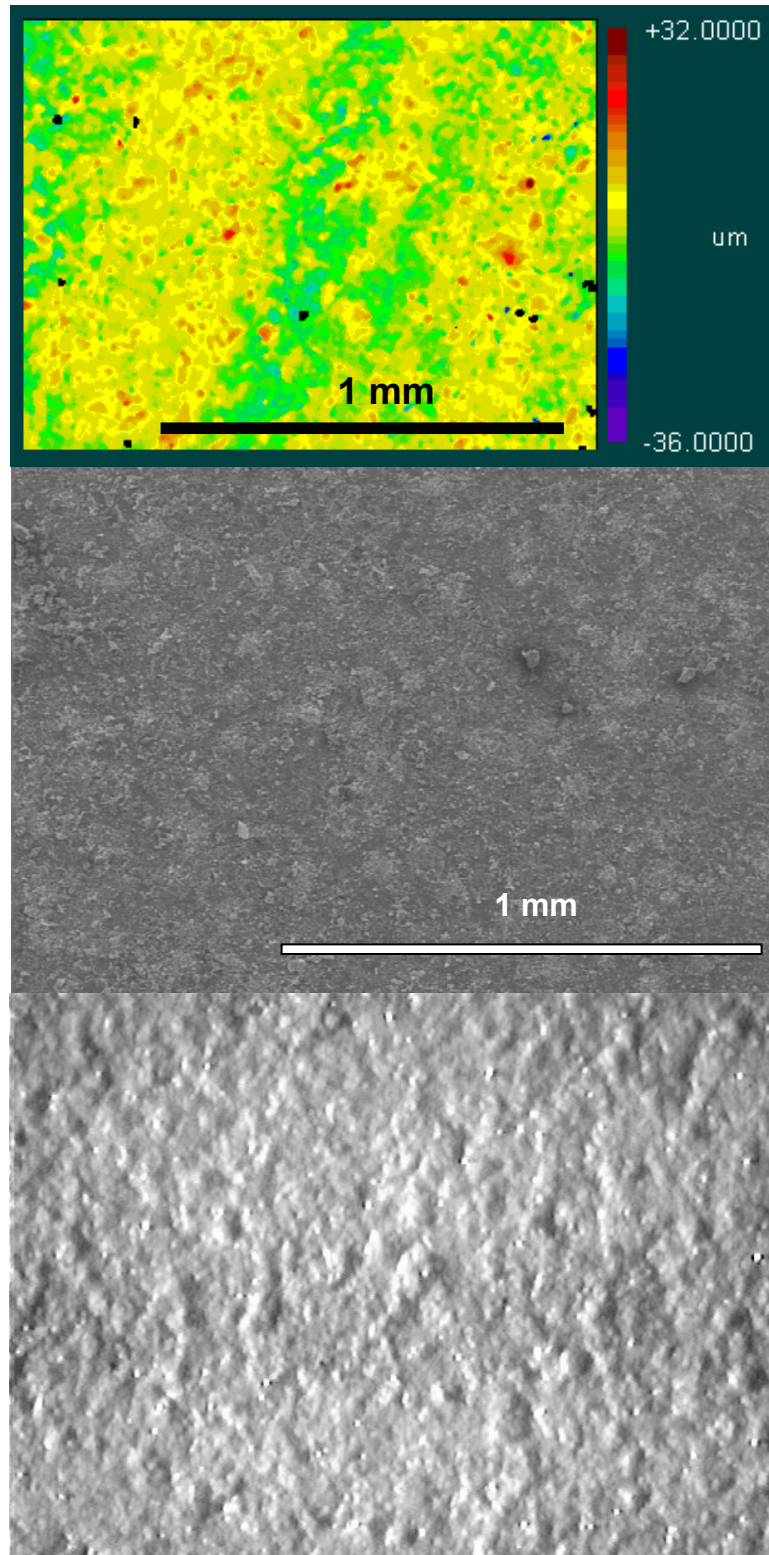


Figure 6-11. Comparison of the images from the interferometer (top), SEM (middle), and optical microscope (bottom) from the green pressure-cast surface. Long range periodicity is observable in the image from the interferometer. More texture is visible in the image from the optical microscope.

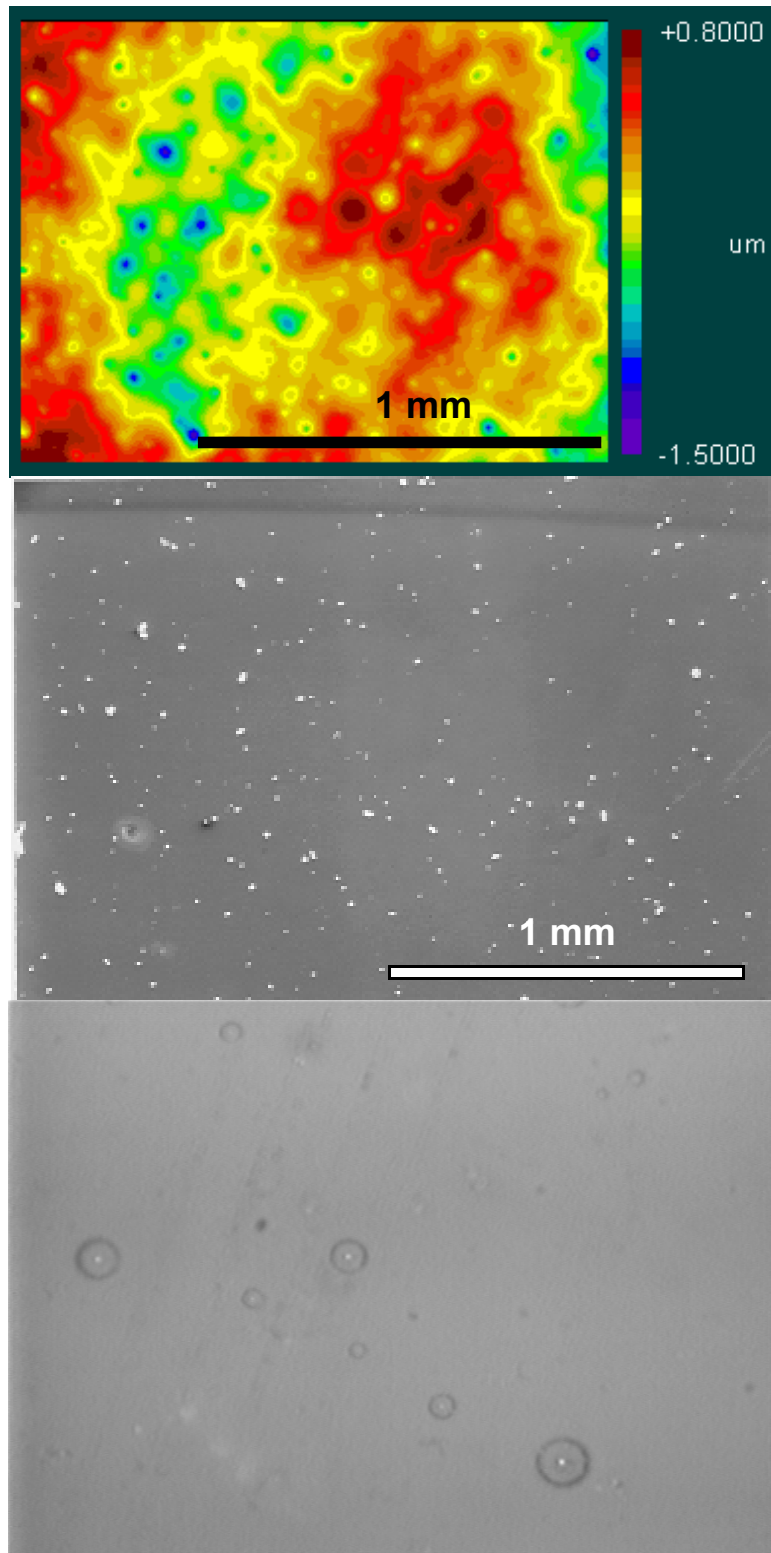


Figure 6-12. Comparison of the images from the optical interferometer (top), SEM (middle), and the optical microscope (bottom) from the dry-pressed and glazed surface. The image from the optical microscope shows the presence of subsurface bubbles in the glaze film that are recorded by the interferometer as the external surface, artificially inflating the measured roughness.

were being generated by the optical interferometer, a feature was selected and analyzed using both the optical interferometer and the SEM. Arrows are shown to mark features in the images of the dry-pressed surface from the interferometer and the SEM. No discernable features were available on the other surfaces to serve as a reference.

The images from the interferometer of the glazed surface showed a series of bright, spherical depressions, randomly located on the surface. Evaluation of the glazed surface in the optical microscope indicated that these depressions were actually sub-surface bubbles trapped in the glassy film of the glaze, Figure 6-12-bottom. These sub-surface features focused the reflected light and were evaluated by the interferometer to be the external surface of the glaze. No special effort was made to eliminate these features from the measured roughness, i.e., no filtering was applied to the glazed surface to remove these features, as that might have suppressed features in the real surface.

For the remainder of this thesis only the RMS surface roughness will be plotted as it is representative of the whole area analyzed. To determine the size of the area that needed to be analyzed to obtain a representative measurement of the roughness a large area on the surface of the glazed samples and the green dry-pressed surface was measured. Using the masking feature in the software smaller areas were analyzed within the larger area. The RMS roughness was recorded as a function of the area analyzed (reported as  $\text{mm}^2$  rather than a width by a length). The results, Figure 6-13, indicated that a plateau was observed in the measured RMS roughness for the green ware at approximately  $14 \text{ mm}^2$ . This area is significantly less than that measured for the unglazed samples, but greater than that measured for the glazed surfaces. The roughness reading for the glazed surface was not observed to plateau. The change in the measured roughness was due to the long-range roughness, typically referred to as the waviness, of the surface. By analyzing only a small region of the surface this waviness was not considered. The optical interferometer considered the waviness, roughness, and “noise” as being superimposed upon the same surface. As mentioned previously, filters in the

software were used to block these features from consideration when determining the surface roughness.

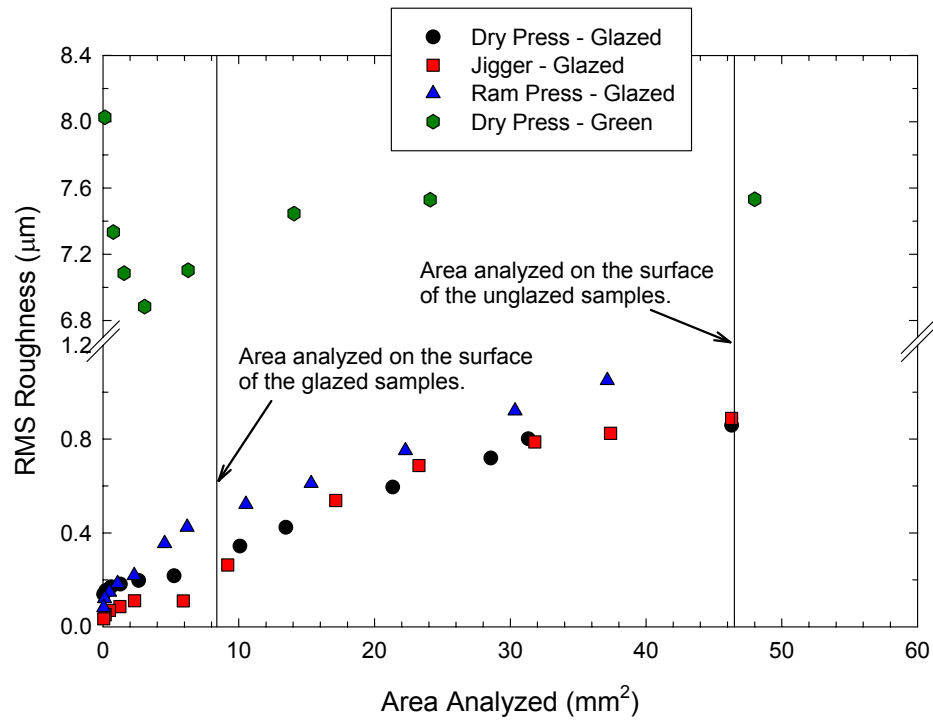


Figure 6-13. Effect of the area analyzed on the RMS roughness measured using the interferometer for the glazed samples from each forming process and the green dry-pressed surface tested in this study.

## **6.6 Summary and Conclusions**

The roughness of the dry-pressed ware was determined to be significantly higher than that of the other forming processes. The ware manufactured by plastic-forming processes, i.e., ram pressing and jiggering, was determined to be identical from a statistical evaluation. The roughness of the pressure-cast ware was determined to be intermediate between the plastic-formed ware and the dry-pressed ware.

The roughness of the ware was observed to increase upon firing of the green ware. When the ware was vibratory processed the roughness was observed to slightly decrease. The roughness of the glazed ware was observed to be statistically equivalent for each of the forming techniques evaluated in this study. The measured roughness of the glazed ware was significantly lower than that of the unglazed ware. Glazing of the ware was not an acceptable method of solving the roughness problem. While the ware was smooth, the problems associated with the roughness of the dry-pressed surface were not solved, i.e., the dry-pressed ware still could not be decorated and the poor surface finish of the pressed ware was visible through the clear gloss glaze.

Based upon the results from the initial quantification of the surface roughness it was determined that the RMS roughness of the dry-pressed surface needed to be less than that of the pressure-cast surface, i.e., less than 4.60 micrometers. This would allow for decoration of the ware and the appearance of an aesthetically pleasing surface under the glaze.

## 6.7 References

1. J.S. Reed, *Principle of Ceramics Processing*, 2<sup>nd</sup> ed.; Ch. 21-26. Wiley Interscience Publications, New York, New York, 1995.
2. F.H. Norton, *Fine Ceramics: Technology and Applications*; Ch. 9,10. Robert E. Krieger Publishing, Malabar, Florida, 1987.
3. M.N. Rahaman, *Ceramic Processing and Sintering*; Ch. 6. Marcel Dekker, New York, New York, 1995.
4. S.T. Lundin, "Microstructure of Porcelain," in *Microstructure of Ceramic Materials, Misc. Publ. – Natl. Bur. Stand.*, **257**, 93-106 (1964).
5. W.M. Carty and U. Senapati, "Porcelain – Raw Materials, Processing, Phase Separation, and Mechanical Behavior," *J. Am. Ceram. Soc.*, **81** [1] 3-20 (1998).
6. W.M. Carty, "Observations on the Glass Phase Composition of Porcelains," *Ceram. Eng. Sci. Proc.*, **23** [2] 79-94 (2002).
7. W.M. Carty, "Glass Phase Composition in Porcelains and Correlation with Pyroplastic Deformation," *Ceram. Eng. Sci. Proc.*, **24** [2] 108-32 (2003).
8. D. Seymour, "Phase Evolution in Electrical Porcelains during Firing"; M.S. Thesis. Alfred University, Alfred, New York, 2000.
9. R. Hennauer and T. Juttner, "Glass Phase Evolution in Porcelain during Firing"; B.S. Thesis. Alfred University, Alfred, New York 2001.
10. R.J. Castilone, "An Investigation into the Metal-Marking Behavior of Glazes"; M.S. Thesis. Alfred University, Alfred, New York, 1995.

## **7. Compaction of Granulate**

### **7.1 Literature Review**

Spray-dried granulate is prepared to improve the flowability of fine powders that are used in the ceramic industry.<sup>1-17</sup> Fine powders are necessary to reduce the sintering temperature of ceramic ware. Fine powders are easily agglomerated in air resulting in poor flowability. Processing of the powders is necessary to eliminate the agglomerates. Typical processing involves mixing the powder in water under high shear to break the agglomerates into individual particles. Organic dispersants are added to improve the rheology of the powder-water system since adjusting the pH on an industrial scale is impractical.

Other organics, e.g., binders, plasticizers, lubricants, etc., are added to the powder-water system to impart the attributes necessary for the subsequent processing steps, e.g., dry pressing, firing, etc.<sup>1,18-44</sup> The interactions between organic additives, specifically dispersants and poly[vinyl alcohol] (PVA) binder systems, was investigated by Kim.<sup>45</sup> The interactions of the organics were classified into three categories: 1) no interaction where a homogeneous organic solution results, 2) a positive interaction where an associated complex is formed between the organic additives, and 3) a negative interaction where the additives phase separate into distinct domains. Kim demonstrated that during the drying process, e.g., in a spray dryer, mixtures of PMAA with PVA and mixtures of PAA with PVA will phase separate into distinct domains. Since the dispersant (PMAA or PAA) is adsorbed on the surface of the powder the result is a PVA-rich film coating the exterior of the granule. This situation is referred to as a case-hardened granulate which is difficult to deform under a uniaxial pressure, i.e., during compaction. Furthermore the adsorption of a polymeric additive on the surface of a ceramic particle will served to enhance the phase separation of immiscible mixtures of organics.<sup>46-49</sup>

The spray-drying process involves the atomization of a homogeneous suspension into a spray dryer at an elevated temperature; typical temperatures in industry are around 600°C. The high surface tension of the suspension results in nearly spherical droplets. The surface area-to-volume ratio of the droplet results

in the rapid loss of water due to evaporation resulting in a dried, nearly spherical, homogeneous granule of ceramic powder with organic additives; as mentioned previously phase separation of the organics will result in an inhomogeneous distribution of the organic additives. The granule has a much larger diameter compared to the starting particulate thus improving the flowability of the feed for a pressing operation. The improved flowability of the granulate results in improved die fill and a more uniform density in the pressed part.<sup>50</sup>

During compaction a pressure is applied to the ceramic granulate to cause deformation. Poor compaction results in residual intergranular porosity which may not be removed during the sintering process. The large residual pores will serve to weaken the fired ceramic since they may be large enough to act as a critical flaw.<sup>51-63</sup> To improve compaction it is important to properly select a binder system that will easily deform under pressure.

Compaction is typically characterized in an Instron testing machine using a hardened steel die in under a uniaxial load.<sup>54,64-97</sup> The data from the Instron (typically load versus displacement) is converted to a plot of percent theoretical density versus log(pressure). The resulting plot consists of three regions named I, II, and III. In region I the granulate settles into tight packing with little change in the percent theoretical density of the compact. In region II there is a significant increase in the density of the compact with an increase in pressure as the granulate is deformed. In region III there is little change in the compact density with an increase in pressure, densification occurs by either filling the intragranular porosity or fracturing the particulate. In region III elastic energy is stored within the compact due to overly high pressures and deformation of the test machine can occur, i.e., deflection of the crosshead. The inflection points between these regions are used to describe the behavior of the granulate and binder systems during compaction. The inflection point between region I and II is typically referred to as P1 and is described as the pressure at the onset of granule deformation. The second inflection point is between regions II and III and is referred to as P2, the pressure at the onset of elastic energy storage.

Compaction of granulate prepared from a flocculated suspension has been demonstrated to result in a reduction in the measured P1 value, i.e., deformation starts at a lower pressure.<sup>98,99</sup> The granulate prepared from flocculated systems is initially of lower density since the particles become agglomerated during the spray-drying process, the particles come into contact and stick together. The porous granulate is easily deformed under pressure since the granulate is friable and easily crushed under pressure.

Addition of a salt to the suspension for spray drying has also been demonstrated to enhance the deformation of granulate.<sup>100</sup> The addition of a salt, even below the CCC, will result in a transition from a dispersed to a coagulated system as water is evaporated in the spray dryer. Evaporation of the water will increase the relative concentration of the salt in solution and eventually the CCC of the salt will be exceeded as water is removed. Once again this will result in an agglomerated, albeit weakly agglomerated, system that is friable and easily crushed under pressure.

The compaction of granulated feed materials has been a topic of much research. Uniaxial compaction and isostatic compaction have been researched to correlate the different stress states to the deformation.<sup>101-103</sup> Compaction diagrams were prepared by loading a series of samples to different pressures and measuring the density of the resulting compacts. The samples prepared using an isostatic system were observed to reach a higher relative density for a set consolidation pressure compared to uniaxial compaction. This difference in the density was attributed to shear between the granulate during consolidation in the isostatic press. During these studies the presence of physical moisture in the granulate was determined to have a significant role in the deformation and hardness of the granulate. Automation of this process in an Instron has facilitated the generation of uniaxial compaction curves.

Walker investigated the use of poly[ethylene glycol] (PEG) organics as a binder system for dry pressing spray-dried alumina.<sup>104,105</sup> Two molecular weights were used in the study, an 8000 and a 20,000 Dalton. The 20,000 Dalton PEG (PEG 20M) material consists of two 8000 Dalton chains which are joined using a

4000 Dalton di-epoxide group chain. PEG organics were demonstrated to have a low P1 value, the pressure at the onset of granule deformation, resulting in good deformation and compacts with a high relative density.

Barnes investigated the effects of alumina type, dispersant type, and binder type and concentration on the rheology and compaction of spray-dried granulate.<sup>106</sup> Four alumina powders were investigated A16sg, Premalox-10, A152sg, and A152gr; the Premalox-10 alumina is indicated by Barnes as hard to disperse. Three binder systems were tested in the study: 1) PEG 20M, 2) PEG 20M with hydroxyethyl cellulose (HEC) in a 2.33:1 ratio, and 3) an acrylic latex emulsion. The A16sg with the PEG 20M-HEC binder system was observed to have the highest green density and green strength of the alumina powders tested. The A16sg samples prepared with the PEG 20M organic were observed to have the lowest strengths of the binders tested. The coarser alumina powders, including the aggregated Premalox-10, were also observed to be weaker and of lower density relative to the A16sg.

Density gradients are commonly observed during the compaction of granulate.<sup>52,107-116</sup> These gradients are due to problems with transmitting the load through the granulate bed or die-wall friction. Near the punch face a high-density region is typically observed while in the center of the compact there exists a low-density region. This density gradient can result in warping or cracking of the compact during sintering. Density gradients have also been related to segregation during die fill. Larger granules tend to roll to the edges of the die while finer granules remain packed in the center. This segregation causes different compaction to occur in the center of the compact compared to the edges.

By measuring P1 for a series of binder systems or binder concentrations it is possible to compare the properties of the binder systems and select a system that easily deforms. While deformation is important to forming a high-density compact the ability to handle said compact after forming is also important. Binders are added to ceramic systems to impart green strength to the compact after pressing. The green strength of compacts can be compared by performing

a diametral compression test.<sup>117-119</sup> A circular compact is loaded across the diameter while sitting on edge. This results in a tensile force normal to the loading diameter that causes failure of the compact.

The strength of the pressed compacts is related to the size of the granule. Larger granules will have larger residual pores in the compact, thus weakening the compact.<sup>55,76,79,83,121,124-127</sup> At some critical granule size compaction is hindered due to poor rearrangement of the granulate; the fine granulate (or individual particles) compact poorly. Therefore there is an optimum granule diameter to facilitate compaction.

Moisture content is known to have a significant effect on the compaction of granulate. Physical moisture within the granulate is known to serve as a plasticizer for many organics. Plasticizers interfere with the crystalline nature of the organics, i.e., the alignment of the polymer chains, reducing the glass-transition temperature of the organic. Above the glass-transition temperature the polymer is observed to be soft and rubbery (therefore easily deformed) while below the glass-transition temperature the polymer is considered hard and brittle (therefore hard to deform). Organics can be used as plasticizers, e.g., glycerin or a low-molecular-weight poly[ethylene glycol] (PEG) are well-known plasticizers for PVA, to reduce the glass-transition temperature of organic binders.

## **7.2 Blending of Dried Granulate**

### *7.2.1 Introduction*

In an attempt to improve the surface finish of dry-pressed ware, blends of dried, industrial granulate, supplied by Buffalo China, were prepared. Binary blends were selected so that there would be a difference in the P1 values of the selected components, each blends contained the plasticized PVA granulate as one of the constituents. The resulting blends were evaluated for P1, compact density, and green strength. Dinnerware samples were pressed on an industrial, horizontal, semi-isostatic, dry press using the blends of dried granulate for evaluation of the surface roughness using the optical interferometer.

### *7.2.2 Experimental Procedure*

The first attempt to reduce the surface roughness involved blending of granulate with different P1 values. P1 is referred to as the pressure at the onset of granule deformation in the compaction diagram. Buffalo China has in the past experienced superior surface finish while changing granulate binder systems.<sup>128</sup> It was proposed that the superior finish was the result of two different binder systems blending in the feed system for Buffalo China's press. A statistical experimental design was prepared to study the effects of blending granulate. A D-optimal mixing design was used to study the effects of binary blends of granulate with different binder systems. Seven blends were evaluated in ten experiments with repeat experiments for the unblended samples and the 50-50 wt% mixture. The blends were selected so as to reflect the design of Buffalo China's spray dryer which has six nozzles for atomizing the suspension to form granulate; the blends used in the study are shown in Table 7-I.

Granulate was prepared by Buffalo China in their industrial spray dryer in 3000-pound batches. Four binder systems were selected for evaluation in the initial trial: 1) Buffalo China's standard dry-pressing batch consisting of a plasticized PVA (pPVA), 2) a sodium-lignosulphonate binder (Ligno), 3) a poly[ethylene glycol] (PEG) binder with a molecular weight of 8000, and 4) no organic binder (NB). The binder systems were selected in an attempt to find

alternatives with a lower P1 value compared to pPVA. Ligno has in the past been demonstrated to have very low P1 values.<sup>129</sup> PEG 8000 is a waxy material that has a low P1 value that has been used in other studies as a binder for dry pressing.<sup>104,106</sup> European tile manufacturers work with granulate that has no organic binder system and continue to press tiles that measure up to one square meter in size with a thickness of 1.5 cm.

Table 7-I. Experimental Design Used to Study the Effects of Blended Granulate.

Run Number	pPVA Granulate	Other Granulate
1	0.00	1.00
2	1.00	0.00
3	0.50	0.50
4	0.17	0.83
5	0.83	0.17
6	0.67	0.33
7	0.00	1.00
8	1.00	0.00
9	0.50	0.50
10	0.33	0.67

Blends of granulate were prepared by tumbling the constituents together. Figure 7-1 is an optical microscopy image of a dry-pressed sample prepared using a 50-50 blend of the pPVA with Ligno. The Ligno was dyed blue, using food coloring, prior to spray drying so that a homogeneous blend of granulate could be observed. During the spray-drying process the blue food coloring degraded to a green color. Figure 7-1 shows a uniform distribution of the pPVA (beige) granulate within the Ligno (green) granulate. All binder systems and granulate blends were characterized for P1, compact density, and green strength. Samples were prepared using the blended granulate and pressed using an industrial, semi-isostatic, horizontal press [PI550G, Dorst Maschinen und Anlagen-Bau, Kochel, W. Germany, loaned by Lenox China] for evaluation of the surface finish using the optical interferometer.



Figure 7-1. Digital image of the surface from a dinnerware sample prepared using a 50-50 blend of pPVA and Ligno granulate. The Ligno granulate was dyed blue, using food coloring, prior to spray drying. The blue color degraded to a green color during the spray drying process. A uniform distribution of the pPVA and Ligno granulate can be observed in this image.

Compaction diagrams were generated using the dried granulate that was stored at 110°C for a period of 16 hours. Compaction diagrams were generated using an Instron Universal Testing Machine [Model 8562, Instron Corporation, Canton, MA]. Pellets were prepared by pouring approximately 2 grams of granulate into a 19.05-mm-diameter hardened steel die lubricated with a thin layer of oleic acid [Fisher Scientific, Fair Lawn, NJ]. The crosshead speed was set at 3 mm/minute up to a maximum load of 3650 kilograms force. The position of the crosshead and load on the samples were recorded at ten data points per second. Using the initial and final dimensions of the die, i.e., before and after compaction, the data from the Instron was converted to percent theoretical density versus Log(pressure). Figure 7-2 is an example of a compaction diagram where the P1 value has been marked using a graphical method. P2 is also indicated in Figure 7-2, this is the pressure at the onset of elastic energy storage in the compact. Release of this energy results in defects in the pressed part,

therefore the samples in this study were not pressed above P2. To analyze the data the second derivative of the density versus Log(pressure) data was calculated and the P1 value was taken as the maximum in the second derivative versus Log(pressure) plot. Five pellets were prepared using the dried granulate for each blend. After compaction the pellets were weighed and placed in a dryer at 110°C for 16 hours prior to determining the density and green strength.

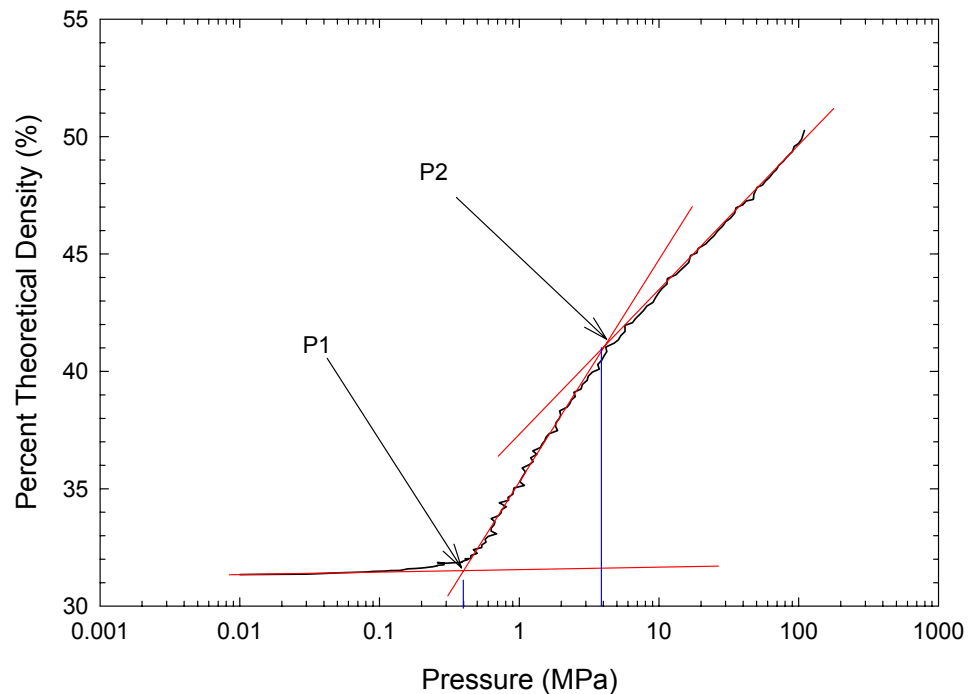


Figure 7-2. Typical compaction diagram prepared using silicon carbide granulate for demonstration purposes. Marked on the diagram using a graphical method are P1 and P2, the pressure at the onset of granule deformation and the pressure at the onset of elastic energy storage respectively.

The compact density was determined by measuring the dried dimensions of the pellets from the compaction study, using a vernier caliper accurate to 0.01 mm, and dried weight, using an analytical balance accurate to 0.0001 grams. The density was calculated by assuming that the geometry of the pellet could be approximated by a right circular cylinder. In cases where the pellet stuck to the die, no correction was made to the calculated density. The compact density is the average of five samples in the dried state.

The green strength of the compacts was measured using a diametral compression test [Quantachrome Crush Strength Analyzer, Quantachrome Instruments, Boynton Beach, FL]. The dried pellets were set on edge and a load was applied across the diameter of the pellet. Tensile forces were generated across the diameter of the pellet and a green strength was calculated using the formula:

$$\text{Green Strength} = \left( \frac{2 * L}{\pi * t * d} \right) \quad (16)$$

where L is the load at failure, t is the pellet thickness, and d is the pellet diameter. The green strength is the average of five samples in the dried state.

The dinnerware samples were pressed using the Dorst semi-isostatic press. The die in the press was oriented horizontally, so that the granulate was fed by a vacuum system. The granulate was pulled into the die cavity by a vacuum and hydraulic pressure was used to inflate an elastomer membrane which compacted the granulate. The pressure on the membrane was approximately 300 bar (30 MPa), but during the initial loading the pressure peaks at nearly 350 bar. Twenty-eight samples were pressed and fourteen were selected at random for evaluation of the surface roughness in the green state on the optical interferometer. A five-by-five grid of images (each 1.44 mm by 1.08 mm with a 25% overlap) was collected for a total area analyzed of 5.77 mm by 4.33 mm and 1.23 million data points.

As another reference point for evaluating the surface finish of dry-pressed ware samples were prepared in a hardened steel die using the unblended, as-received granulate prepared by Buffalo China. While hardened steel dies are not typical for pressing of ceramic bodies, mainly due to the down time associated with cleaning the die approximately every third pressed part, hardened steel dies typically result in superior surface finish. The high hardness of the steel die readily deforms the granulate, but the flow of fine particles between the punches and the die wall gradually causes the punches to stick in the die. An elastomer membrane, used in semi-isostatic and isostatic presses, is a compliant unit that

will deform around the granulate. Samples were pressed using an Aeonic press [HD-80/6.7, Aeonic Press Company, Easton, PA] at pressures in the range of 5,000 to 10,000 psi. These pressures were all greater than that in the Dorst press.

### *7.2.3 Results*

The compaction results for P1 are shown in Figure 7-3 (pPVA-Ligno blends), Figure 7-4 (pPVA-PEG blends), and Figure 7-5 (pPVA-NB blends). In all cases a change was observed in the measured P1 value of the blended granulate, i.e., blending of the granulate results in a hybrid P1 value. The blended systems were observed to have intermediate values relative to the unblended systems. This shift in the P1 value was related to the percolation threshold of the blended system. When the blends are comprised of nearly 100% of a single binder system, the resulting P1 value is near to that of the unblended granulate. The primary constituent in the blend acts as a support creating a three dimensional network in which the minority constituent is shielded. Upon applying a load the primary constituent supports the load thus the measured P1 value is near to that of the unblended granulate. In the intermediate region the P1 value falls between the two extremes of the unblended granulate. In this region neither of the constituents can create a network to support the load. The harder granulate pushes on the softer granulate causing deformation and better compaction. A schematic illustration of this is shown in Figure 7-6 for a 50-50 blend of hard and soft granulate. This type of behavior is most clearly seen in Figure 7-4 for the pPVA-PEG blends. The other systems shows a slightly different behavior where the P1 value continues to decrease as more pPVA granulate is substituted in the blend, this is an artifact of blending two hard granules, i.e., the second granulate is harder than the pPVA granulate. While the pPVA-NB blends were observed to have the lowest P1 values, dinnerware manufactured in an industrial process at Buffalo China were observed to have insufficient strength to survive the forming and ejection process. Data from the industrial trials at Buffalo China is presented in Appendix E.

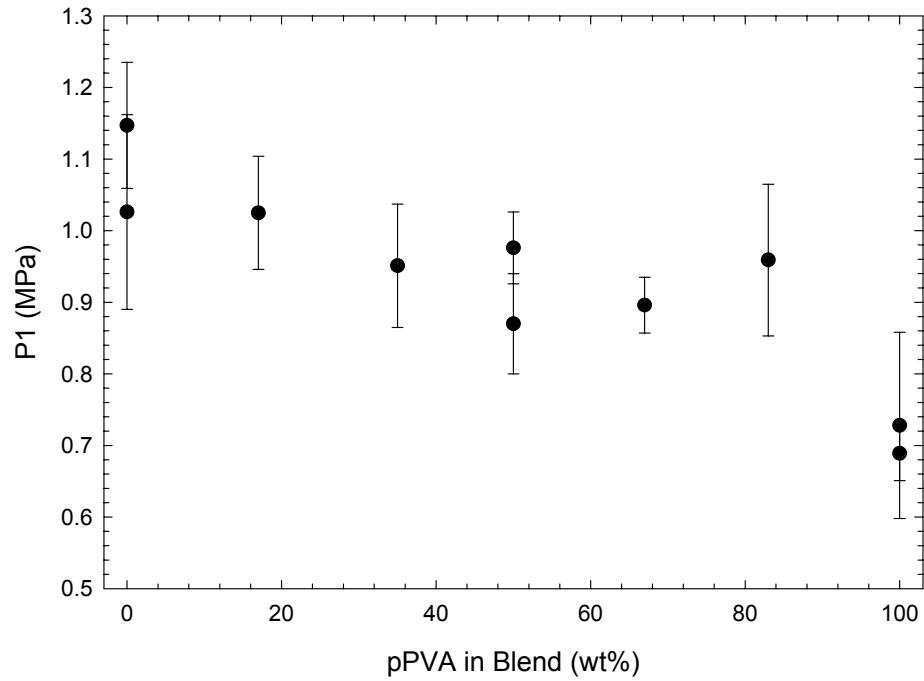


Figure 7-3. Pressure at the onset of granule deformation (P1) for the blends prepared using pPVA and Ligno granulate. The P1 value of unblended Ligno granulate is observed to be higher than that of pPVA granulate.

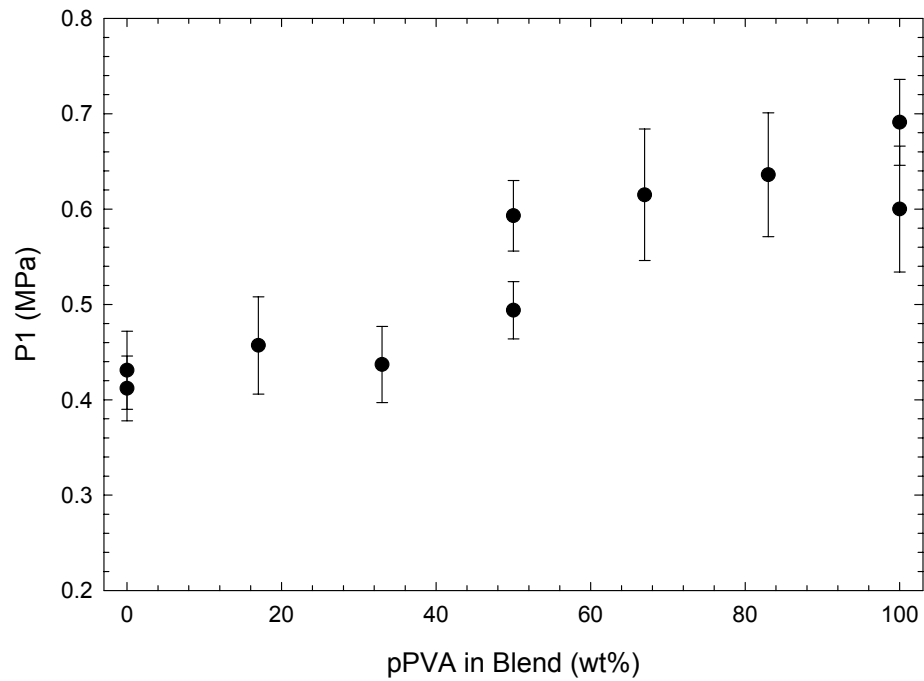


Figure 7-4. Pressure at the onset of granule deformation (P1) for blends prepared using pPVA and PEG granulate. P1 of unblended PEG granulate is lower than that of pPVA granulate.

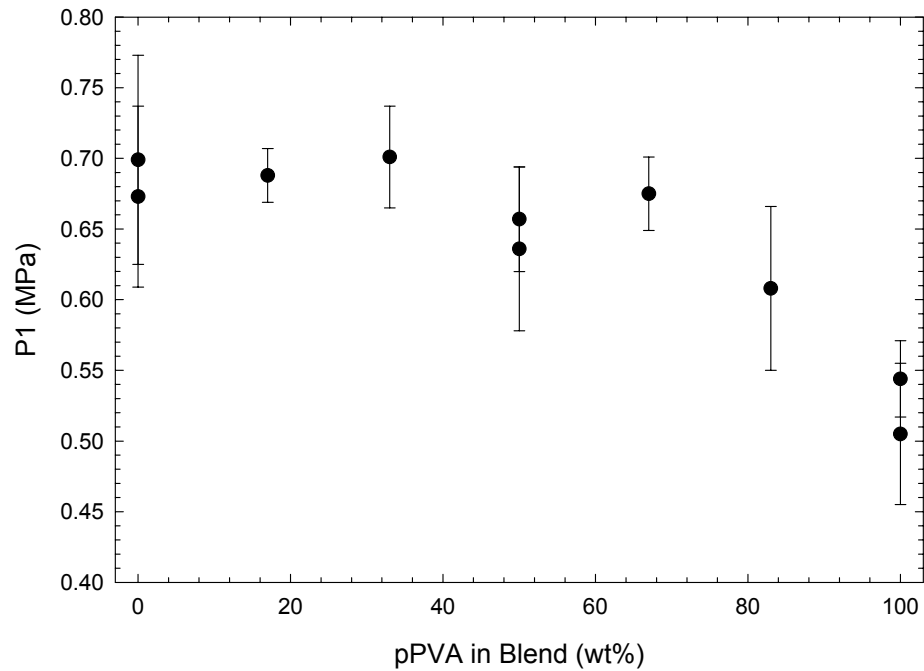


Figure 7-5. Pressure at the onset of granulate deformation (P1) for blends prepared using pPVA and NB granulate. P1 of unblended NB granulate is higher than that of pPVA granulate.

To validate this model for compaction a Lexan™ die was constructed. A thin slot was left open in the center of the die thus creating a two dimensional die. The die was placed into the Instron and compaction diagrams were generated using neoprene o-rings of various thickness, solid steel washers, and solid rubber disks to simulate soft, hard, and intermediate granulate respectively. The loading rate was maintained the same as used for the hardened steel die, i.e., 3 mm/minute, to a maximum load of approximately 23 kilograms force. Compaction diagrams were generated by measuring the projected area, i.e., an areal density, of the neoprene o-rings and disks and the steel washers, example compaction diagrams are shown in Figure 7-7.

Noise is observed in the compaction diagrams from these pseudo-systems due to the neoprene sticking on the surface of the Lexan™ die; no lubricants were used in this study. The washers and solid neoprene disks were taken to have an areal density equivalent to their projected, solid area. The o-

rings were considered completely deformable with an areal density equivalent to that of the neoprene. Blends of hard and soft “granulate” were run in the simulated die and compaction diagrams were generated. Movies were taken of the deformation process and, despite problems with the neoprene sticking and not transferring the load through the body, the softer granulate were observed to be deformed by the harder granulate. In “blends” where the harder “granulate” were able to create a network, the load was observed to be supported by the harder “granulate,” leaving the softer “granulate” undeformed. Overall the soft “granulate” was observed to deform around the hard “granulate” facilitating the compaction and rearrangement of the “granulate” under a normal load.

A comparison of the P1 results from the blended granulate study can be observed in Figure 7-8. The pPVA-Ligno blends were observed to overall have higher P1 values than the pPVA granulate. This result was contrary to the goal of blending the granulate. It was the goal to develop a blended system with a lower P1 value when compared to the pPVA granulate. It was theorized that the Ligno granulate, which initially had the highest P1 value out of the binder systems studied, formed a more dense granule on drying. Lignosulphonate is also known to serve as a dispersant, thus increasing the repulsion between the particles in the suspension. This allowed further rearrangement of the particles upon drying, resulting in a densely packed granule with a high P1 value. This hypothesis was ratified by the viscosity data collected by Buffalo China prior to spray drying (Table 7-II). The lignosulphonate system was observed to have a very low viscosity for roughly the same specific gravity as the pPVA system, i.e., there was more repulsion between the particles in suspension prior to spray drying. The pPVA-PEG blends showed an increase in the measured P1 value as pPVA granulate was added in the blend. The pPVA-NB blends showed a slight decrease in the measured P1 value as pPVA granulate was added to the blend. This small shift in the measured P1 value was within experimental error.

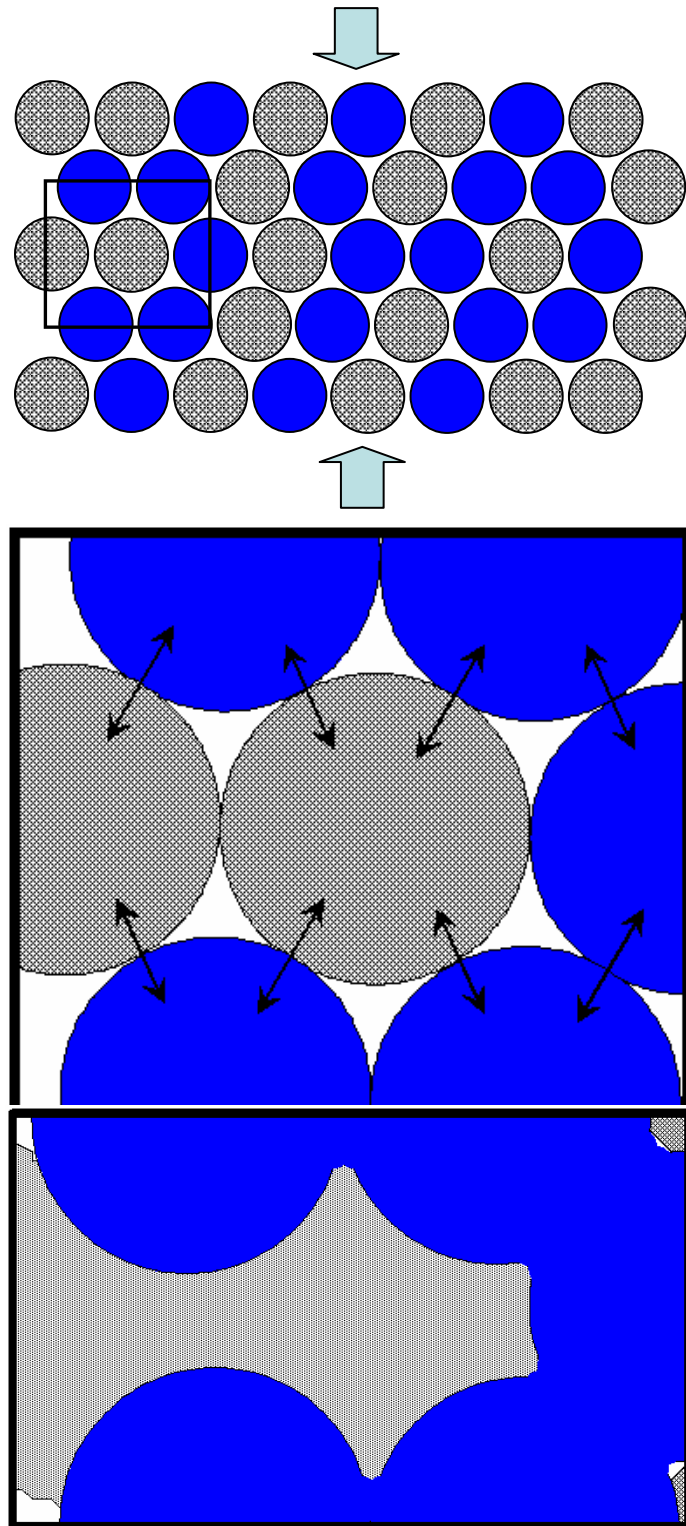


Figure 7-6. Schematic illustration of compaction in systems with blended granulate. The textured circles represent soft granules while the solid are hard granules. During compaction the hard granule remain relatively undeformed while the soft granules fill in voids between the hard granules.

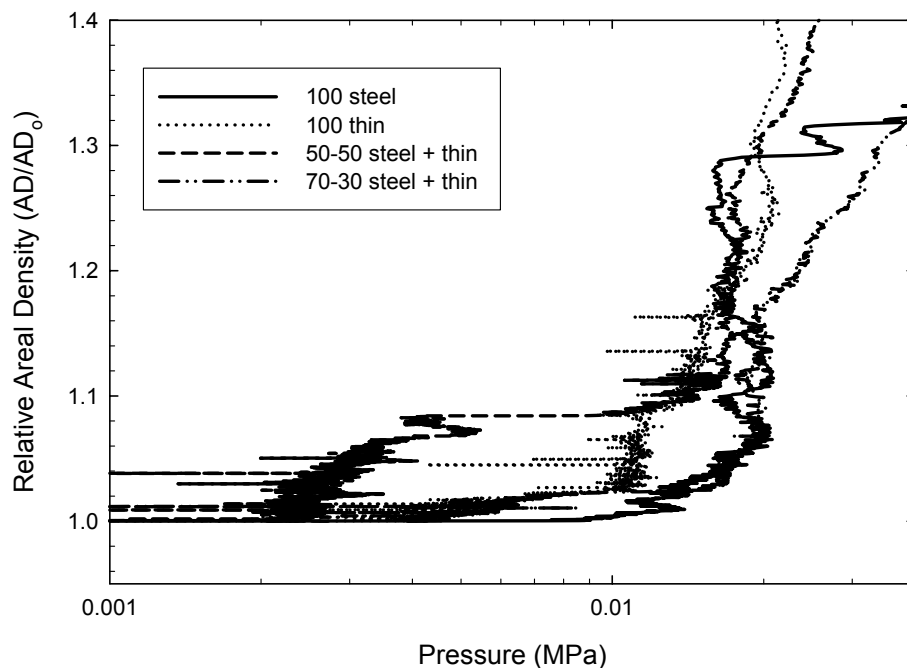


Figure 7-7. “Compaction diagrams” generated using thin o-rings and steel washers to represent soft and hard granulate. A shift in P1 is observed due to blending of the “granulate.” The areal density is reported as the projected area of each component, the steel washers are considered to be solid while the o-rings are considered hollow for the calculation.

Table 7-II. Suspension and Granulate Properties from the Batches Used to Prepare Granulate in this Study.

Batch	Viscosity (centipoises)	Specific Gravity of suspension	Mean Diameter (estimated) (micrometers)	Fill Density (g/cm <sup>3</sup> )	Flow Rate for 50 grams (sec.)
pPVA	800	1.662	270	0.930	24.27
Ligno	450	1.668	260	0.935	34.68
PEG	50	1.675	245	0.922	23.56
NB	200	1.683	240	0.958	54.78

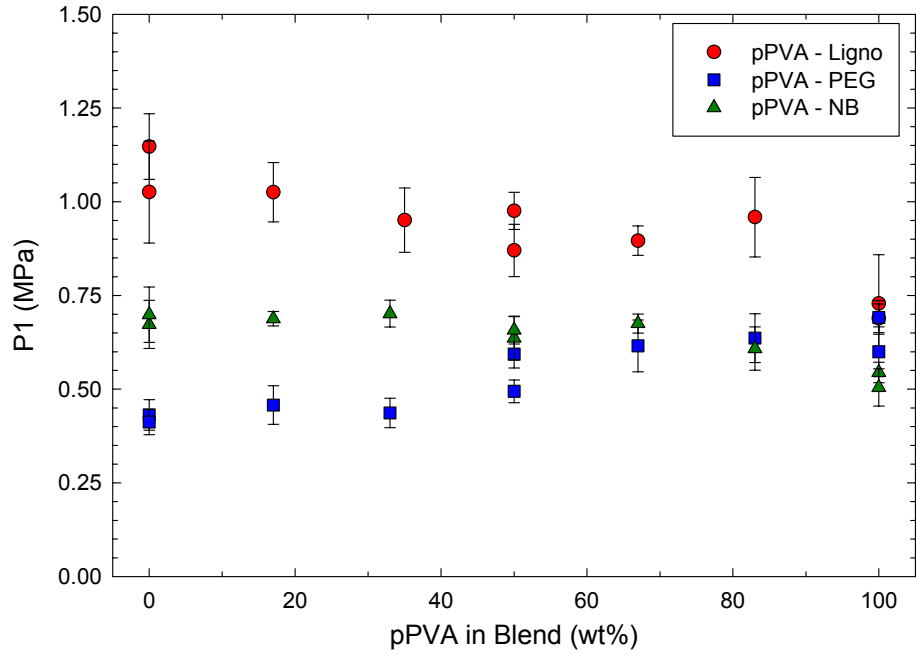


Figure 7-8. Comparison plot of the P1 values obtained from the blending study. A shift in P1 is observed as the concentration of pPVA granulate in the blend increases.

The compact density for the blending study is plotted in Figure 7-9. For each blend of granulate analyzed the pPVA-Ligno blends overall have a significantly lower compact density. This is a result of poor compaction due to a high P1 value. Blends that were prepared using softer granulate, i.e., those prepared with PEG or NB granulate, were observed to have a higher compact density.

The green strength of the compacts from the blending study is plotted in Figure 7-10. Statistically there was no difference in the measured green strength of the compacts in this study.

The roughness results from the interferometer for the samples prepared on the horizontal semi-isostatic press initially indicated a poor surface finish. The roughness from the pPVA samples, Buffalo China's standard dry-pressing body, prepared at Alfred University had a RMS roughness of  $10.06 \pm 1.14 \mu\text{m}$  compared to the industrially prepared samples which had a RMS roughness of  $8.54 \pm 0.61 \mu\text{m}$ , measured during the initial study. The initial results show not only a higher

roughness, but significantly more scatter in the data; as indicated by the error in the measured RMS roughness. The ware prepared on the horizontal semi-isostatic press at Alfred University was observed to have texture in the pressed surface that was apparent to the unaided eye.

Furthermore, it was believed that the error range in the measured roughness of the industrially prepared ware was partially an artifact of orientation of the ware in the die. Roughness at the “top” of the sample was higher compared to the “bottom” of the ware; the ware was pressed on edge. Since no orientation was indicated on the samples supplied by Buffalo China, this is merely a hypothesis. Samples from the industrial trials, discussed in Appendix E, support this hypothesis since pressing defects could be used to determine the orientation of the ware. No effort was made to correlate the orientation of the ware to the roughness as this data was not available for all samples; therefore the orientation was selected at random.

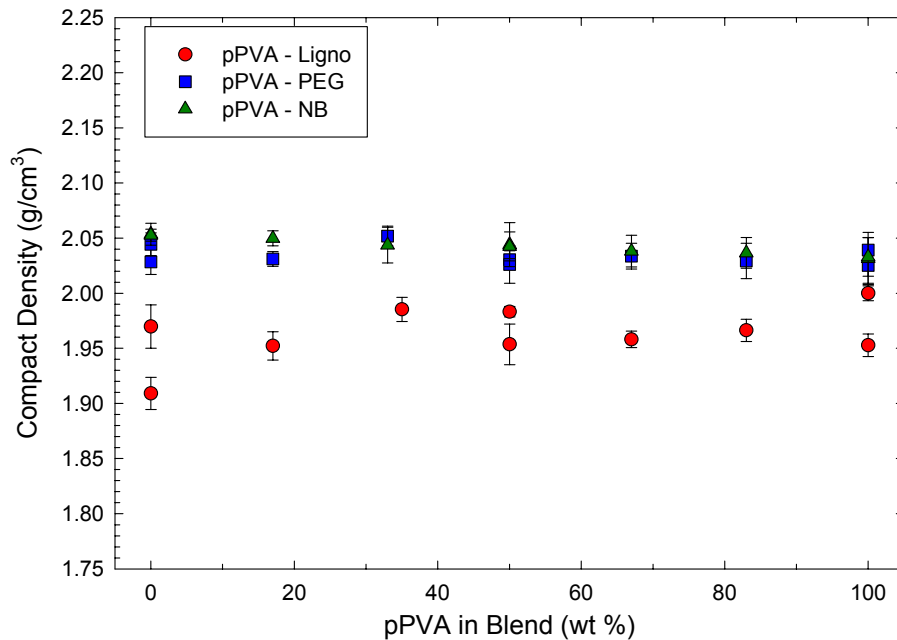


Figure 7-9. Comparison plot of the compact density obtained from the blending study. The density of the pPVA - Ligno blends is observed to be significantly lower than the other samples due to the higher P1 value.

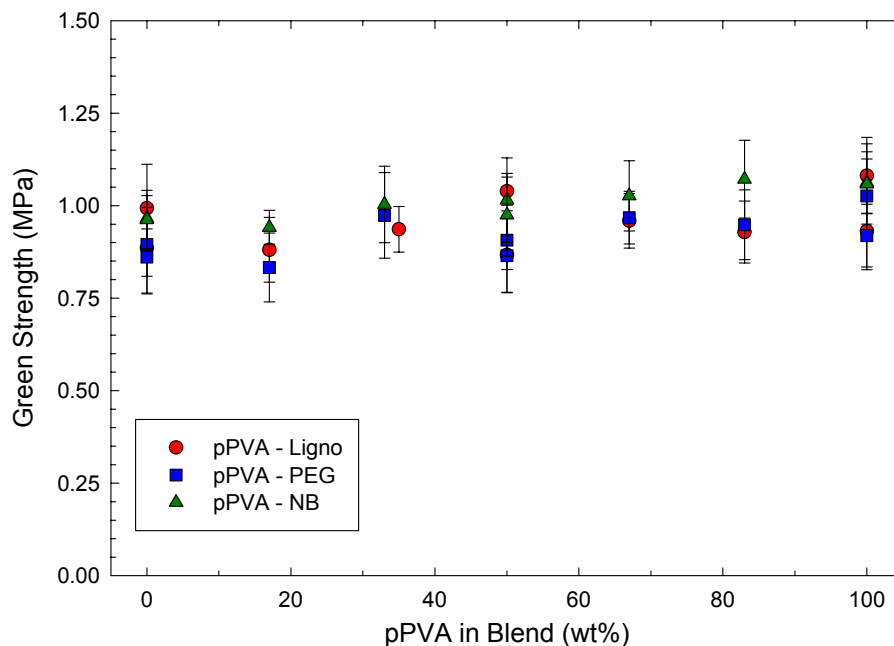


Figure 7-10. Comparison plot of the green strength from the blending study. No significant difference is observed in the green strength of the samples.

Based upon these observations the stitched roughness results from the interferometer were divided back into the original images using the masking function in the software, i.e., the results from the industrially prepared ware was divided into 48 images and the results from the ware prepared at Alfred University were divided into 25 images, all of which were 1.44 mm by 1.08 mm in size. By breaking down the data in this manner it was possible to evaluate the roughness on each individual image rather than the compiled data from the stitched image. The RMS roughness from each image was plotted as a function of position in a contour plot. Representative contour plots are shown in Figure 7-11 for the industrially prepared ware and Figure 7-12 for the samples prepared at Alfred University; the pPVA binder system is shown in both figures. The plots show that there was significantly higher variation in the RMS roughness from the ware prepared at Alfred University on the horizontal press. Buffalo China uses a vertical press to manufacture their dry-pressed ware. In a vertical press the granulate is filled by a gravity-assisted vacuum system; a schematic of the difference in the die design is shown in Figure 7-13. This design difference plays

a crucial role in the uniformity of the die fill. The gravity-assisted system, the vertical press, had a more uniform die fill resulting in better compaction of the granulate. There were fewer voids which needed to be filled by granule rearrangement, the initial stage of compaction, when the die fill was more uniform.

Since an uncontrolled variable, i.e., the die fill, was artificially inflating the measured surface roughness of the ware, the roughness results from only the individual images was considered. Three roughness results were calculated, 1) the roughness of the individual images, i.e., the average of 350 (14 samples and 25 images per sample) images, 2) the three lowest roughness readings from each sample, i.e., 42 out of 350 images were considered for the roughness reading, 2) the overall lowest reading from each sample, i.e., 14 out of 350 roughness results.

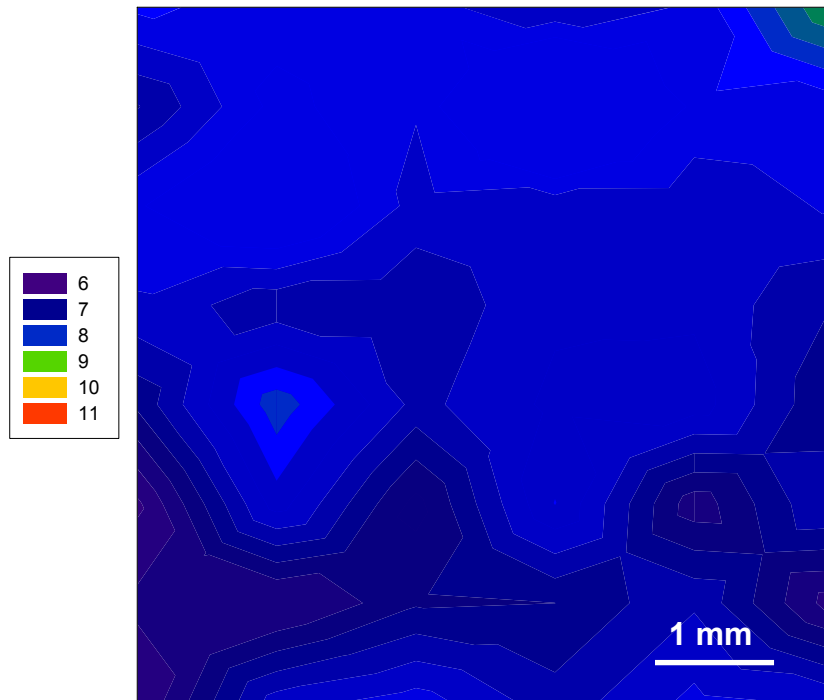


Figure 7-11. Contour plot of the RMS roughness, measured in micrometers, as a function of position on the pPVA sample prepared by Buffalo China in the vertical press. Little variation is observed in the RMS roughness of the surface as a function of position.

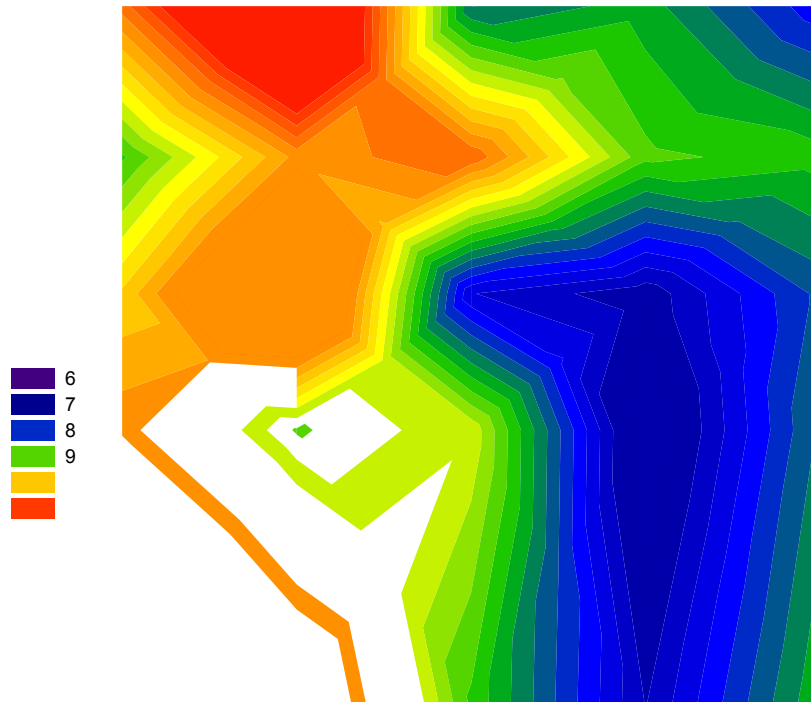


Figure 7-12. Contour plot of the RMS roughness, measured in micrometers, as a function of position on the pPVA sample prepared at Alfred University in the horizontal press. Large variations are observed in the RMS roughness of the surface as a function of position.

The roughness results are shown in Figure 7-14 (pPVA-Ligno blends), Figure 7-15 (pPVA-PEG blends), and Figure 7-16 (pPVA-NB blends). In each figure the three sets of data which were previously described are plotted. A comparison of the roughness results obtained when only considering the lowest roughness reading from each surface is shown in Figure 7-17. Similar to the P1 values a sigmoidal type of behavior was observed where the roughness initially has a plateau, followed by a sharp change in the roughness, and a secondary plateau. In the case of the pPVA-NB blends the roughness decreased as NB granulate was substituted for the pPVA. This was contrary to the prediction from the P1 results, where P1 increased as NB granulate was substituted for pPVA. It is proposed that while the NB granulate was “harder” than the pPVA granulate, once the P1 value was reached the NB granulate returned to the primary particles that make up the porcelain batch, i.e., it was a friable system.

Furthermore the P1 values were measured on dried samples of granulate while the samples were pressed using the as-received granulate from Buffalo China; as mentioned earlier physical water in the granulate serves to reduce P1.

To determine if the measured P1 value could be used to predict surface roughness of the dry-pressed ware from the Dorst press a correlation plot was prepared considering P1 as a function of the RMS roughness, Figure 7-18. A strong correlation as observed for the pPVA-Ligno and pPVA-PEG blends where the roughness increased as the P1 value increased. A different behavior was observed for the pPVA-NB blends. An increase was measured in the RMS roughness as the P1 value decreased. This inverse relationship was most likely the result of the friable nature of the NB granulate.

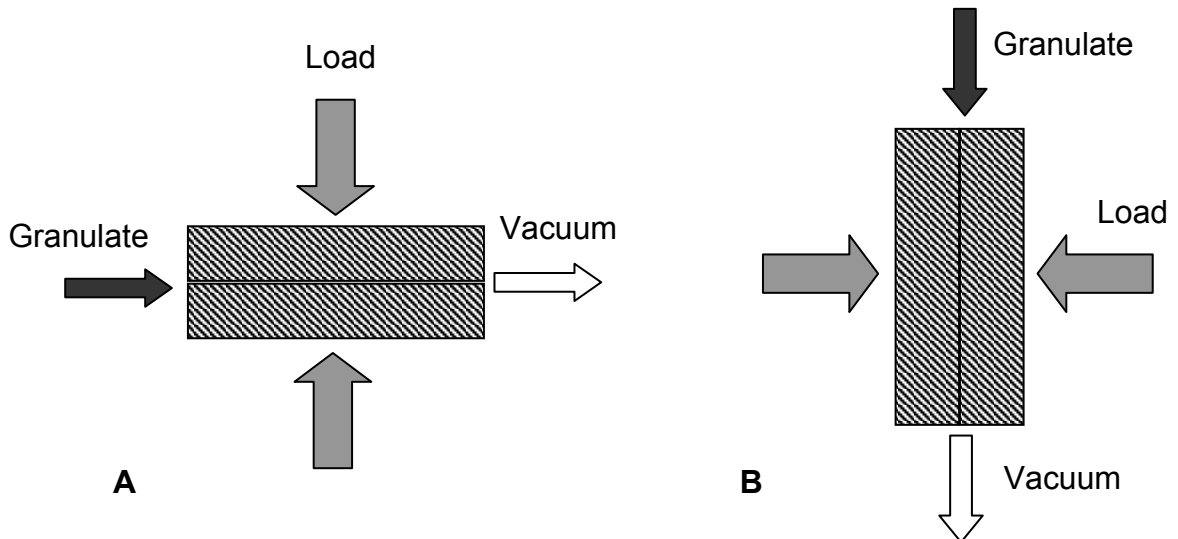


Figure 7-13. Schematic of the dies installed in the industrial presses used for this study, (A) horizontal press and (B) vertical press. The dies are shown as the cross-hatched boxes with the load applied as indicated by the gray arrows. The granulate is fed as illustrated by the black arrows and facilitated by a vacuum system (white arrow). In the case of the vertical press (B) the vacuum system is assisted by gravity to fill the die.

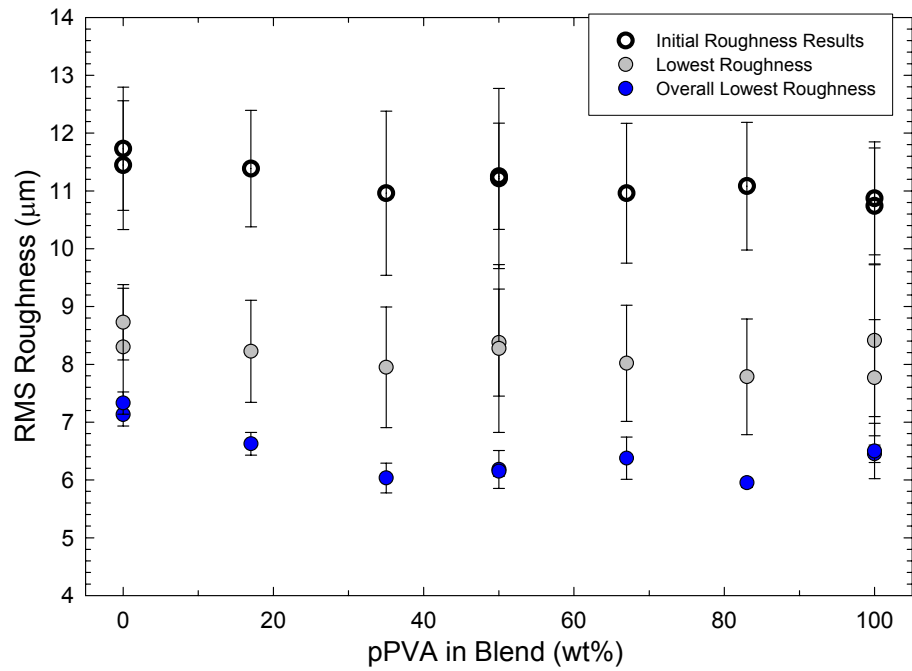


Figure 7-14. Plot of the roughness results for the pPVA – Ligno blends. Three results are plotted due to the poor die fill artificially inflating the roughness measurement; the lowest values (in blue) were used for comparison purposes.

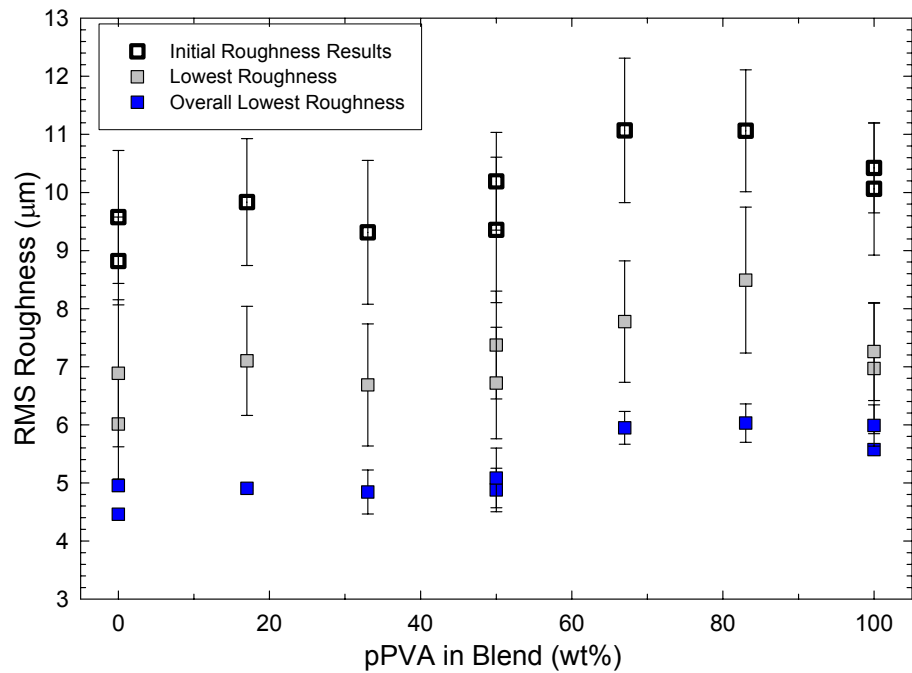


Figure 7-15. Plot of the roughness results for the pPVA – PEG blends. Three results are plotted due to the poor die fill artificially inflating the roughness measurement; the lowest values (in blue) were used for comparison purposes.

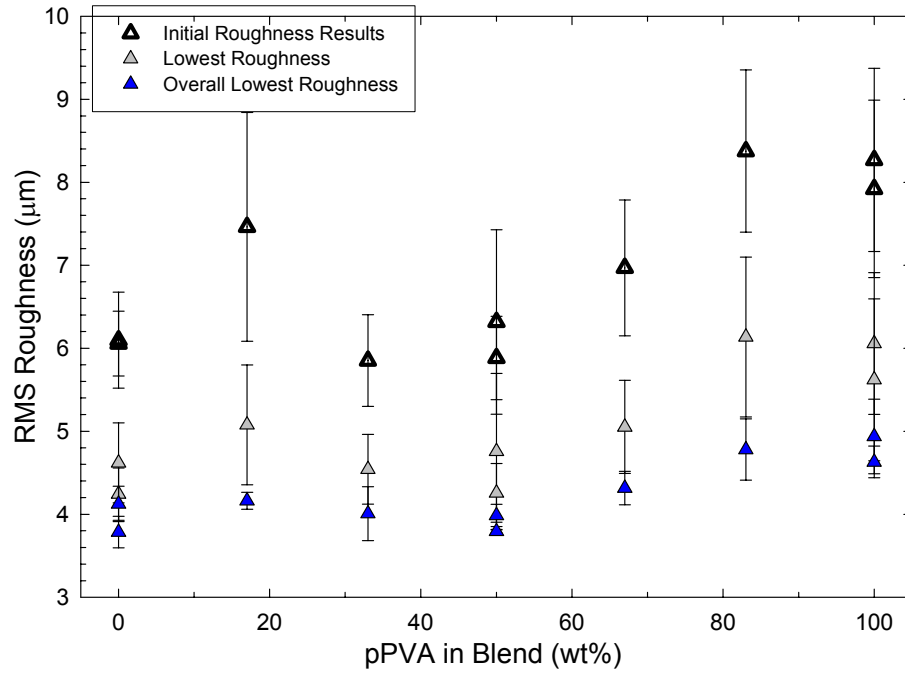


Figure 7-16. Plot of the roughness results for the pPVA – NB blends. Three results are plotted due to the poor die fill artificially inflating the roughness measurement; the lowest values (in blue) were used for comparison purposes.

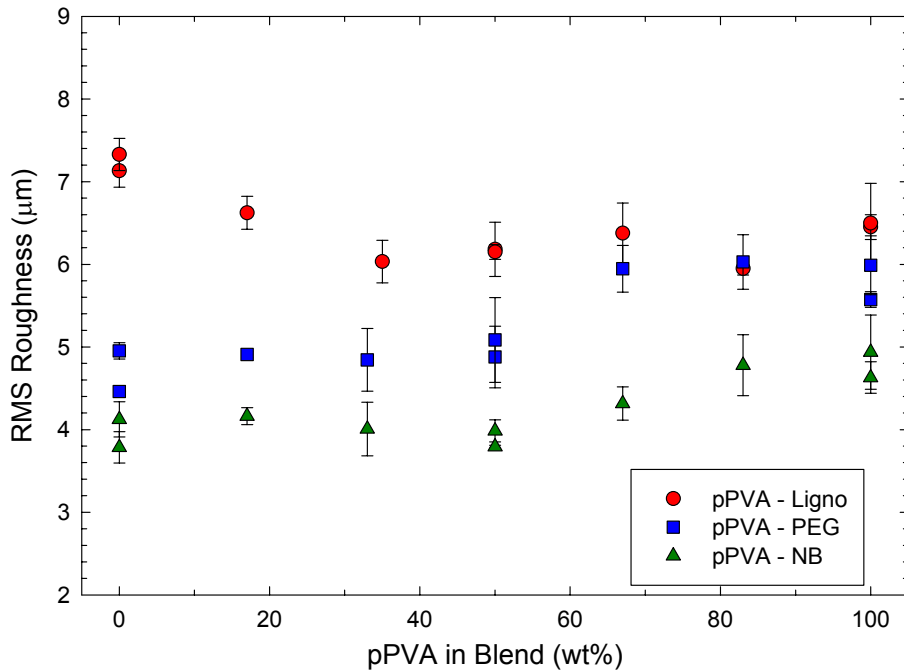


Figure 7-17. Comparison plot of the lowest RMS roughness reading for each sample as a function of the amount of pPVA granulate in the blend. The data reported is the average of fourteen roughness readings for each blend. Addition of Ligno granulate to the pPVA is observed to increase the RMS roughness while PEG and NB granulate are observed to reduce the RMS roughness.

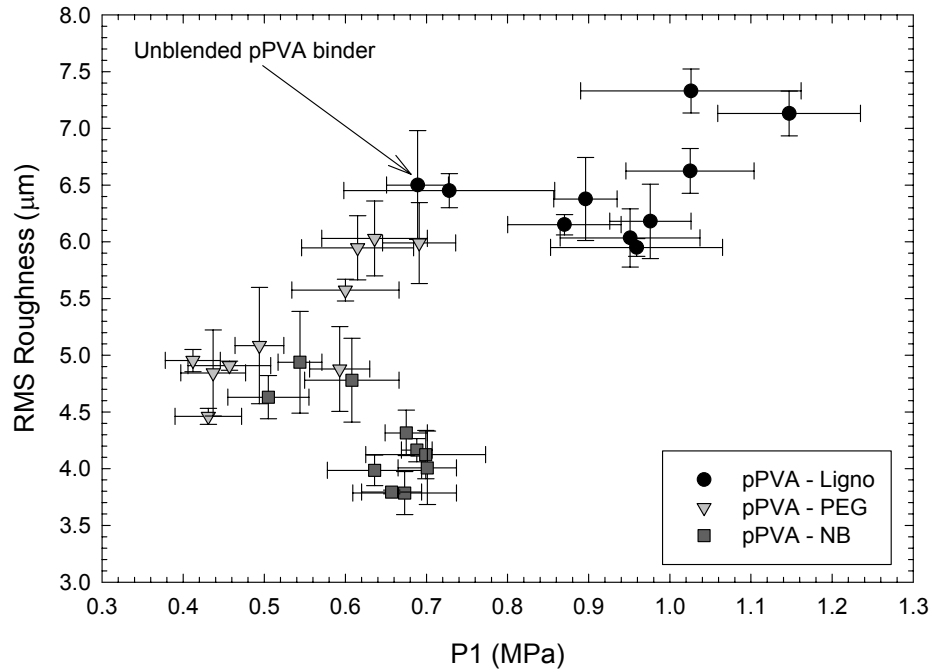


Figure 7-18. Correlation plot for the measured P1 value from the blended granulate and the measured RMS roughness from the optical interferometer. A correlation is observed for the pPVA-Ligno and pPVA-PEG blends while an inverse correlation is observed for the pPVA-NB blends.

As further evidence that the die fill was artificially inflating the measured RMS roughness, images of the surface from a 100% PEG sample were taken using an optical microscope, Figure 7-19. The light source was nearly parallel to the sample surface to create shadows, which are a semi-quantitative indication of the surface finish. Two images, only a few millimeters apart, were taken from the surface of the same sample. The first image shows a relatively smooth surface, Figure 7-19 (left), the second image shows a much rougher finish, Figure 7-19 (right).

Based upon the P1 and roughness results an industrial trial using blended granulate was arranged. In the industrial trial three sets of blended granulate were proposed and the unblended pPVA was used as a reference. Alfred University supplied the unblended pPVA granulate since storage at the dry-pressing facility may have changed the properties of the granulate due to fluctuations in moisture content and the possible growth of secondary organics,

i.e., fungal growth, within the granulate. The results from the industrial trial are discussed in Appendix E.

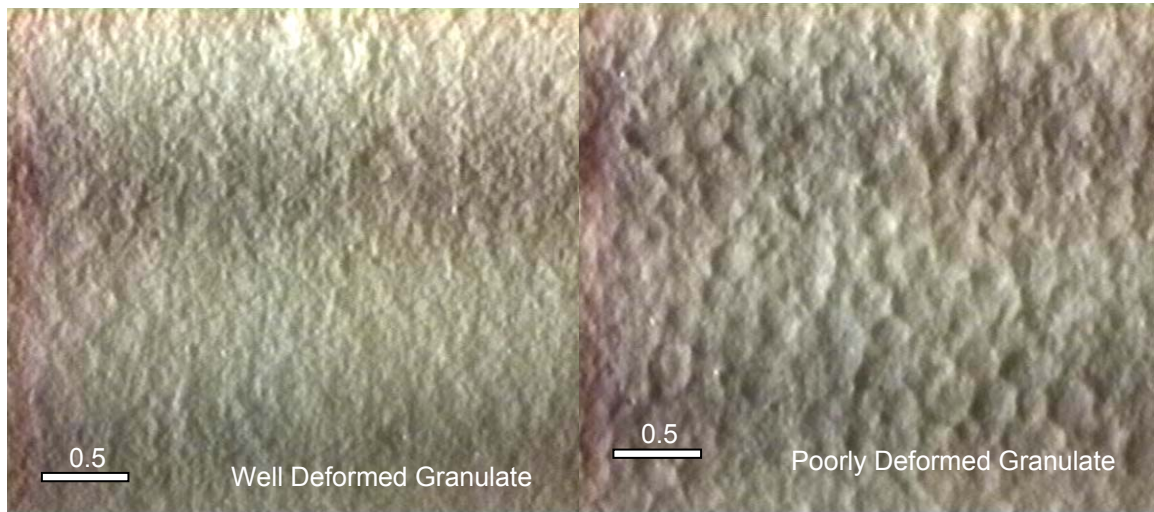


Figure 7-19. Images from the optical microscope of the surface from a 100% PEG sample pressed on the horizontal press at Alfred University. The image on the left shows well deformed granulate while the image on the right shows poorly deformed granulate. Both images were taken from the same sample only a few millimeters apart.

The roughness results from the samples prepared on the Aeonic press are shown in Figure 7-20. The roughness of the samples all fall below that of the jiggered ware, the smoothest surface evaluated in Chapter 6. Relics of the granulate were still observable in the images from the optical interferometer, not shown. Even at higher loads using a non-compliant, hardened steel, pressing surface the granulate was still observable in the pressed surface. The peak-to-valley distance, i.e., the worst-case statistic, was significantly lower for the samples prepared using the hardened steel die compared to the samples from the semi-isostatic press.

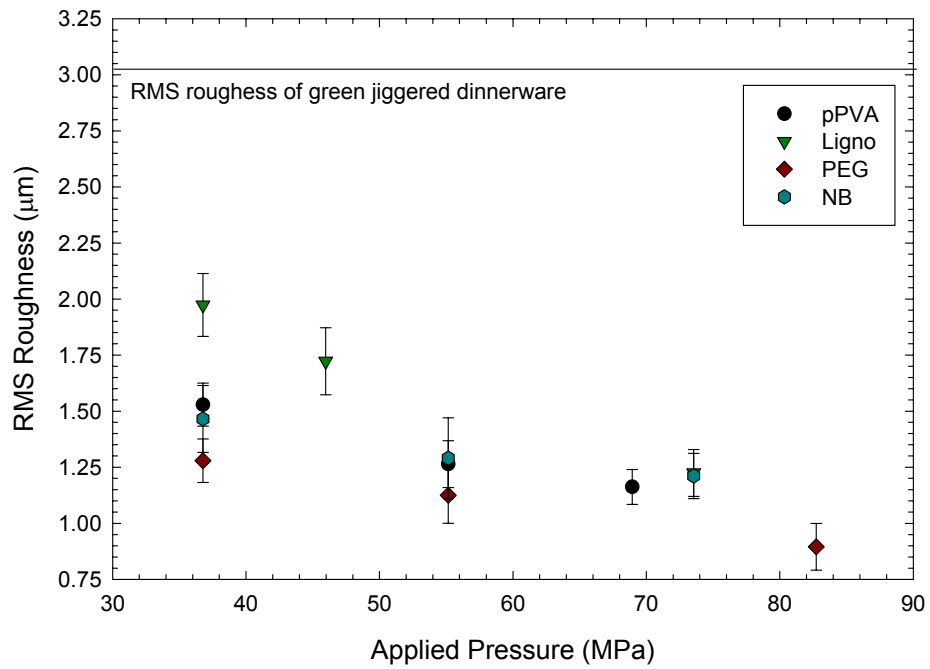


Figure 7-20. RMS roughness as a function of forming pressure for the samples prepared on the Aeonix press using a hardened steel die. Roughness is observed to decrease with increasing pressure, all roughness results are significantly below the roughness for the jiggered ware.

#### *7.2.4 Summary and Conclusions*

Blending of dried granulate systems with different P1 values was observed to result in a hybrid system where the P1 value was that of the majority constituent. No significant changes were observed in the compact density or green strength of the compacts prepared using the blended granule systems. The proposed model for compaction of binary blends of granulate, i.e., mixtures of hard and soft granules, was validated using steel washers and o-rings to simulate the granules.

Surface finish of dinnerware prepared in a semi-isostatic die was observed to be strongly dependent on the die fill prior to compaction. Die fill was an uncontrolled variable in the study that was observed to interfere with compaction. Texture was apparent to the unaided eye in the surface finish of the dinnerware prepared with the horizontal press.

RMS roughness was observed to be correlated to the P1 value determined by uniaxial compaction in a hardened steel die. Compaction in a hardened steel die was observed to significantly reduce the measured surface roughness of the pressed ware. Tiles prepared in a hardened steel die were observed to have a lower RMS roughness than that of the plastic-formed ware tested in Chapter 6.

## **7.3 Mechanics of Granule Deformation**

### *7.3.1 Introduction*

To understand the mechanics of granule deformation two studies were performed using the unblended granulate. The first involved understanding the effects of moisture content on P1. Samples of granulate were stored for a period of three weeks at 50°C in desiccators with various salt solutions. The presence of the salt solutions in the desiccators regulated the relative humidity within the chamber. The other study involved sieving granulate into a series of size fractions to determine the effect of granule size on compaction. In both studies the P1 value, the pressure at the onset of granule deformation, compact density, and green strength of the compacts was determined.

### *7.3.2 Relative Humidity Effects*

#### *7.3.2.1 Experimental Procedure*

For this study the industrial granulate, supplied by Buffalo China, with different binder systems was used. Approximately two grams of granulate were weighed into porcelain crucibles and the moisture content of each sample was determined by drying at 110°C for 16 hours. The crucibles were then stored for three weeks at 50°C in desiccators above saturated salt solutions that controlled the relative humidity within the chamber. The higher the solubility of the salt on a mole-fraction basis, the lower the relative humidity within the chamber. The various treatments for the granulate in this study are listed in Table 7-III; the relative humidity in the desiccator was measured using a hygrometer. The dried samples were not subjected to any treatment during the three weeks; the samples were stored in sealed plastic bags until they were tested. The samples that were designated “humidity uncontrolled” were stored at 50°C and ambient humidity during the three weeks of storage, i.e., the humidity was unregulated. After three weeks the samples were cooled to room temperature and the change in weight due to the absorption of water was measured. The samples were sealed in plastic bags for an additional two weeks prior to determining the pressure at the onset of granule deformation, P1. Samples were characterized

to determine P1, the pressed compact density, and green strength. Experimental procedures used for this study have been reported in Chapter 7.2.

Table 7-III. Storage Conditions Used to Regulate the Relative Humidity.

Storage Condition	Storage Temperature	Relative Humidity	Solubility
	(°C)	(%)	(g/100 g H <sub>2</sub> O)
As Dried	~18	0	N/A
Humidity Unregulated	50	5-10	N/A
LiCl	50	18	90
NaNO <sub>3</sub>	50	60	95
KCl	50	90	85
H <sub>2</sub> O	50	100	N/A
As Received	~18	N/A	N/A

### 7.3.2.2 Results

Storing granulate in humid surroundings allows physical water to condense in the pore structure of the granulate. A plot of the pore radius filled as a function of the relative humidity, calculated from thermodynamics,<sup>130</sup> is shown in Figure 7-21. Also shown in Figure 7-21 is the moisture content of the granulate after three weeks storage at 50°C over the salt solutions used in this study. A similar trend is observed in the data indicating that the neck region between particles in the granulate has become filled with physical water as a function of the relative humidity. During the two weeks that the hydrated granulate was stored at ambient conditions, prior to determining the onset of granule deformation, there was a change in the moisture content as the granulate gradually loses moisture to the surrounding environment. The moisture content of the granulate after generating the compaction diagrams is plotted in each figure.

Predictions for the amount of physical moisture condensed in a packed powder bed as a function of particle size can be determined by making some assumptions. Spherical particles were assumed to be in a dense face-centered-

cubic packing arrangement. The volume formed by a meniscus of water at the contact between two neighboring particles was calculated from liquid-phase sintering theory<sup>131</sup> and the radius of curvature for the meniscus was assumed to be equivalent to the radius of a pore that would be saturated at a given relative humidity.<sup>130</sup> The resulting plot is shown in Figure 7-22. For a set particle radius the moisture content of the compact increases with increasing relative humidity. Stated in another way the moisture content increases with decreasing particle size for a given relative humidity.

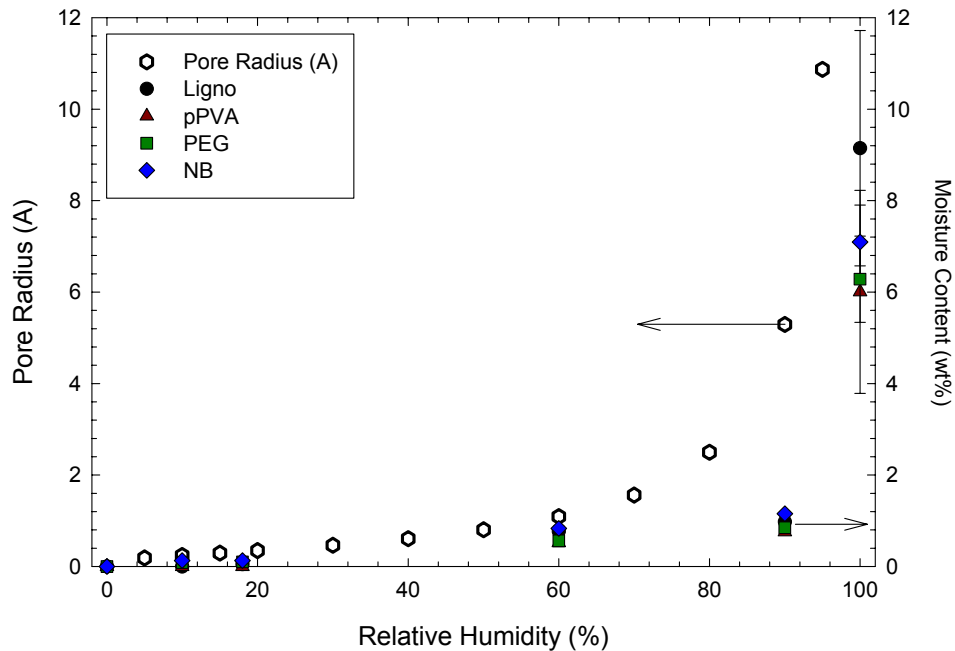


Figure 7-21. Plot of the pore radius filled as a function of relative humidity of the surrounding environment and the moisture content of the granule samples after three weeks in a humidity controlled environment.

The results for the hydrated granulate are compared in Figure 7-23 (P1), Figure 7-24 (compact density), and Figure 7-25 (green strength) as a function of the relative humidity at which the granulate were stored. The P1 value for the lignosulphonate granulate was observed to be significantly higher than the other binder systems until a relative humidity of 90%. Little difference was observed in the pressed density and the green strength between the granulate.

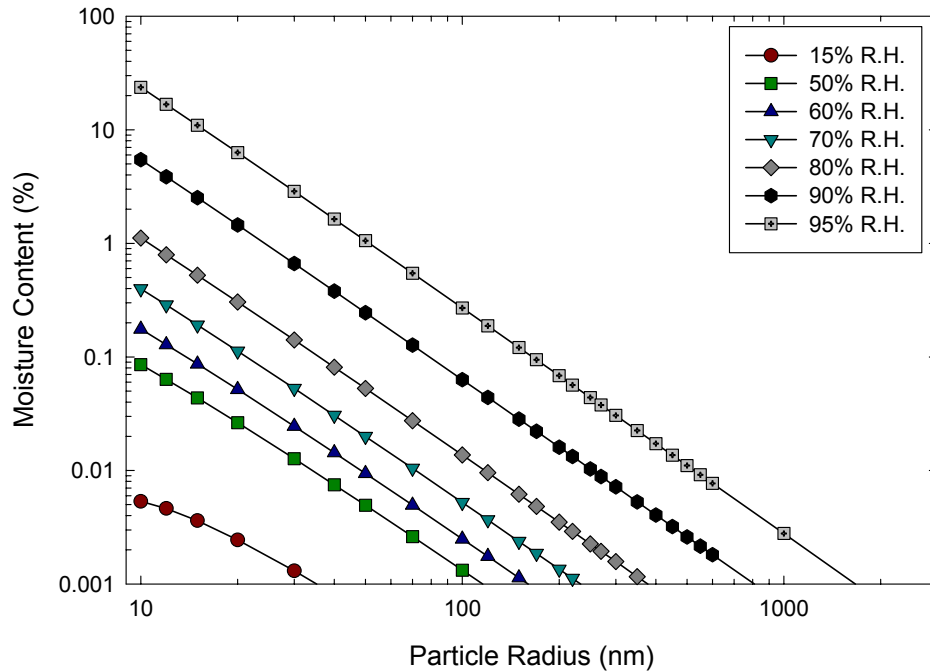


Figure 7-22. Prediction for the moisture content of a compact of assumed spherical particles in a face-centered cubic packing arrangement as a function of particle radius and relative humidity. Moisture content was calculated for an assumed FCC packing arrangement of spherical particles using sintering theory.

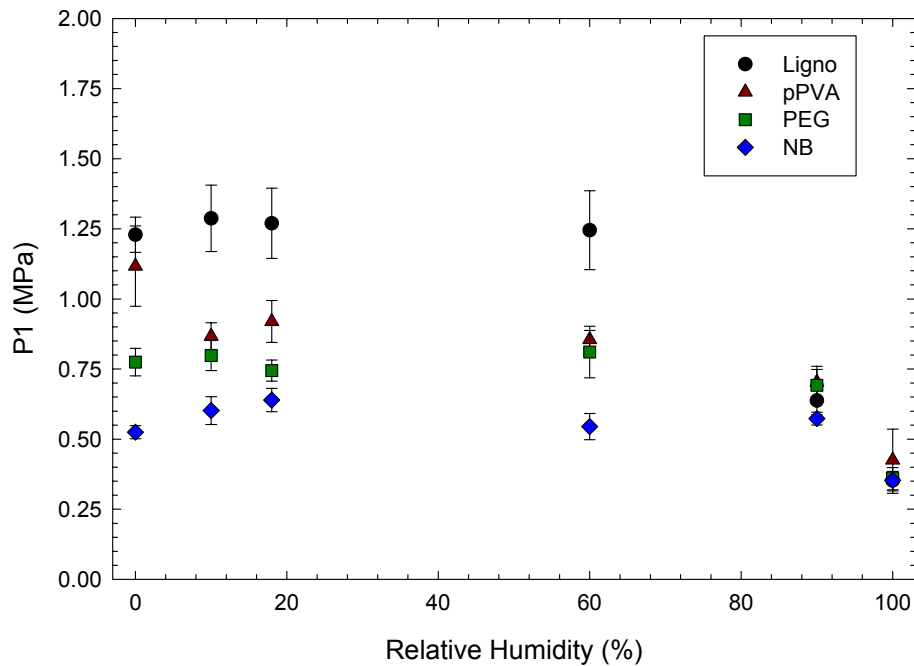


Figure 7-23. Plot of the pressure at the onset of granule deformation ( $P_1$ ) as a function of relative humidity for the hydrate granulate. In all of the binder systems studied there is a decrease in the measure  $P_1$  with increasing relative humidity.

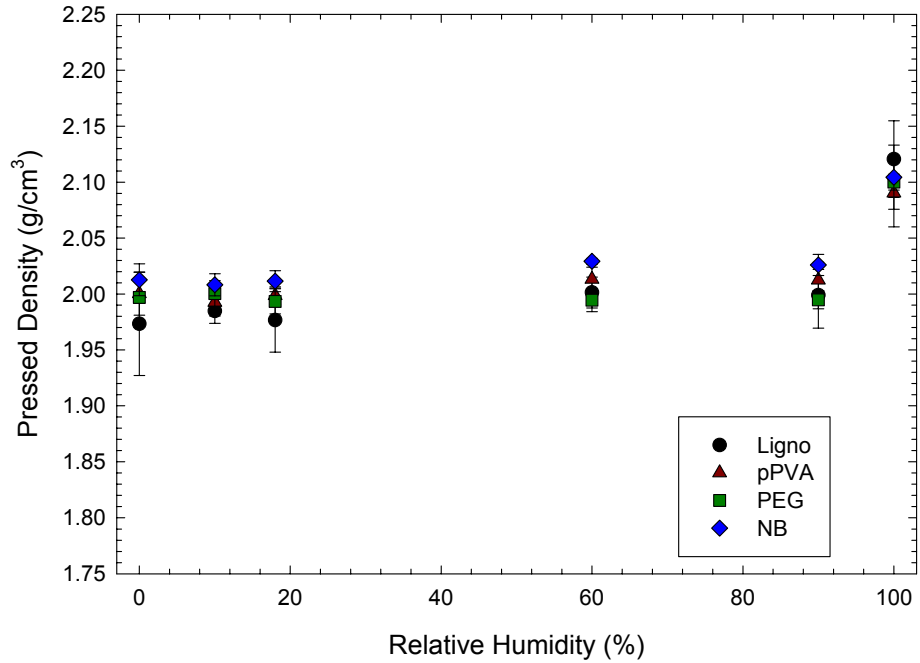


Figure 7-24. Plot of the pressed density as a function of relative humidity for the hydrated granulate. No significant difference is observed in the pressed density between the binder systems studied. There is a significant increase in the compact density above 90% relative humidity.

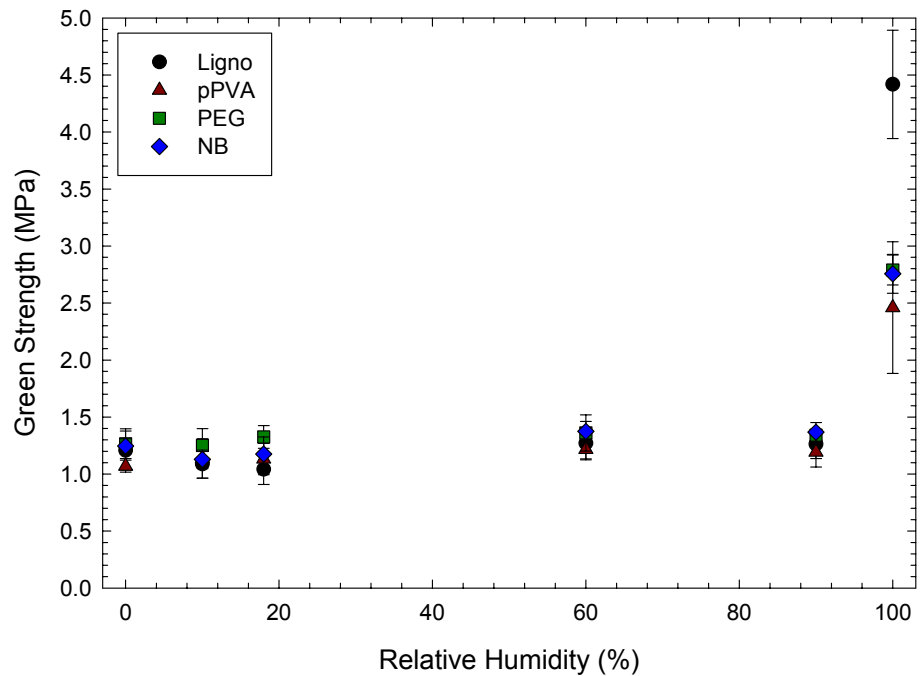


Figure 7-25. Plot of the green strength, measured by diametric compression, as a function of relative humidity for the hydrated granulate. No significant difference in strength is observed until 100% relative humidity.

### 7.3.2.3 Discussion

Moisture content had a significant effect on the deformation of the granulate in the binder systems tested. Moisture acts as a plasticizer for many organics reducing the glass-transition temperature, making the organic more deformable (or softer). When moisture is removed from the granulate P1 was observed to increase and when the granulate was re-hydrated at high relative humidity it was possible to re-introduce sufficient physical water into the granulate to again serve as a plasticizer, i.e., the P1 value was reduced to the as-received value.

No significant variation was observed in the compact density or green strength of the compacts that were stored at less than 90% relative humidity. Samples that were stored at 100% relative humidity were observed to have a significantly higher compact density and green strength. Furthermore the Ligno granulate that was stored at 100% relative humidity was observed to have a significantly higher green strength compared to the other binder systems studied.

The results indicate that when all water was removed (at 110°C) prior to re-hydration the granulate must be stored at greater than 90% relative humidity to reintroduce sufficient water to make the granulate deform like the as-received material. In the case of pPVA granulate there was an effect at lower relative humidity as observed by the drop in P1 at 10% relative humidity; this was due to the moisture plasticizing the PVA; water is known to be an effective plasticizer for PVA.<sup>39</sup>

When the samples were stored at 100% relative humidity the measured attributes, i.e., the P1 value, compact density, and green strength, of the re-hydrated granulate were observed to exceed those of the as-received material. There was a problem with storing the granulate at 100% humidity and that was the growth of secondary organics (i.e., fungal growth) within the granulate.

### 7.3.3 Effect of Granule Size on Compaction – moisture content distribution argument

#### 7.3.3.1 Experimental Procedure

Samples of granulate were sieved into size fractions ranging from 600 micrometers (30 mesh) to 45 micrometers (sub-270 mesh). Each size fraction was tested for moisture content by heating the sample to 110°C and measuring the weight loss. The remaining granulate from each size fraction was used to generate compaction diagrams to determine P1. The resulting pellets were tested for compact density and green strength; procedures were outlined in Chapter 7.2.

A two-dimensional computer model was developed to investigate the drying of a virtual droplet in the spray dryer. This model allowed the operator to control the size of the droplet, the particle size, solids loading (taken as an area fraction), and the parameters associated with the operation of the spray dryer. The model used mathematical formulas to simulate the changes during the drying process.<sup>132-139</sup> The model assumed that the particles are all uniformly dragged toward the center of the droplet as water was removed from the system. The spray dryer was assumed to be in a steady state and the difference in the inlet and outlet temperatures was assumed to be lost to evaporation of water, a cooling process, in the droplet.

Equations were derived to explain the change in the radius of the droplet as a function of the drying rate, gas flow rate, and the pump rate of the suspension. The derived equations are shown below:

$$\text{NumDroplet} = \frac{\text{Pumprate} \cdot 10^8}{\pi \cdot r_d} \quad (17)$$

$$\text{DryingRate} = \frac{\rho_{\text{gas}} \cdot \text{flowrate} \cdot C_{p(\text{gas})} \cdot (T_{\text{in}} - T_{\text{out}}) - \rho_{\text{powder}} \cdot \text{af} \cdot \text{Pumprate} \cdot C_{p(\text{powder})} \cdot (T_{\text{out}} - T_{\text{sus}})}{C_{p(\text{water})} (100 - T_{\text{sus}}) + H_{v(\text{water})} + C_{p(\text{steam})} (T_{\text{out}} - 100)} \cdot \text{NumDroplet} \quad (18)$$

$$dr_d = \frac{\text{DryingRate} \cdot \text{time} \cdot 10^8}{(1 - \text{af}) \cdot 2\pi \cdot r_d} \quad (19)$$

The Mathematica™ notebook, the system of mathematical equations to run the model, is shown in Appendix F. The full list of variables used in generating the virtual droplet is shown in Appendix F, section 1.0. The parameters used to study the drying time of an atomized droplet are listed in Table 7-IV.

Table 7-IV. Parameters Used to Model a Drying Droplet in a Spray Dryer.

Gas Inlet Temperature	300°C
Spray Dryer Outlet Temperature	120°C
Suspension Temperature	30°C
Gas Flow Rate	0.5167 m <sup>3</sup> /sec.
Suspension Pump Rate	2 mL/sec.

### 7.3.3.2 Results

The plots of the granule size distribution can be observed in Figure 7-26 (Ligno), Figure 7-27 (pPVA), Figure 7-28 (PEG), and Figure 7-29 (NB). The average moisture content in each size fraction is shown in the figures for each of the samples. There was a significant moisture content distribution in the granulate samples with the exception of the PEG granulate. The moisture content of each sample was tested at the time that the super-sacks were prepared by Buffalo China. The average moisture content for the as-received granulate, measured at the time that the granulate was prepared and during this study, are listed in Table 7-V. There was a significant decrease in the average moisture content of the granulate after it was stored at the dry-press facility, a facility that does not have any type of environmental controls other than heat. A sample of the stored pPVA granulate was returned to Buffalo China in January, 2003 and subjected to their standard tests, the results indicate that there was no measurable moisture content in the sample (according to their standard practice).<sup>140</sup>

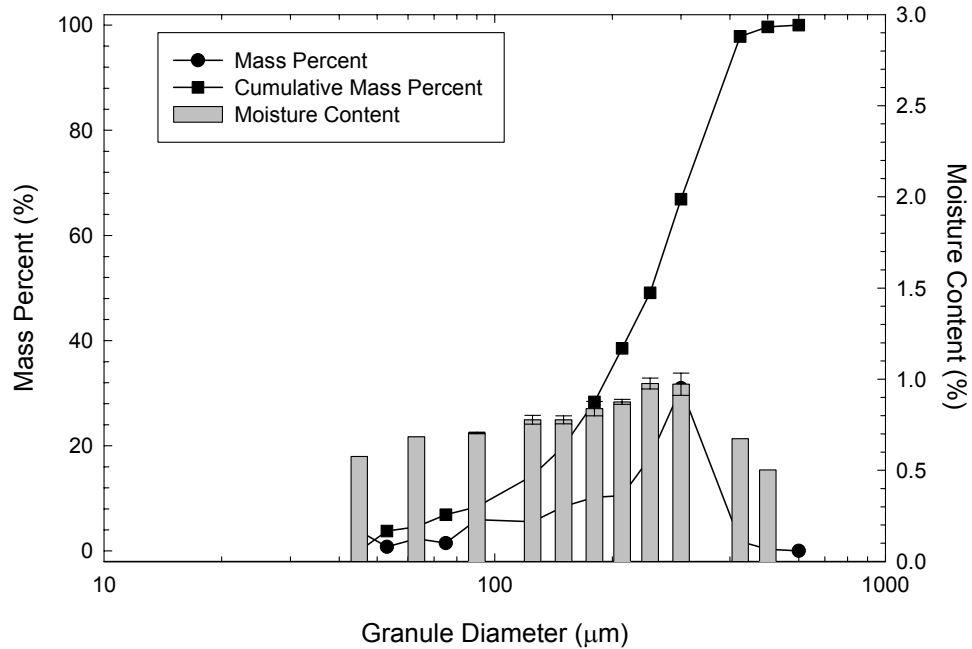


Figure 7-26. Granule size distribution and moisture content distribution for the Ligno granulate. A moisture content distribution is observed in the granulate with high moisture content in the larger granules.

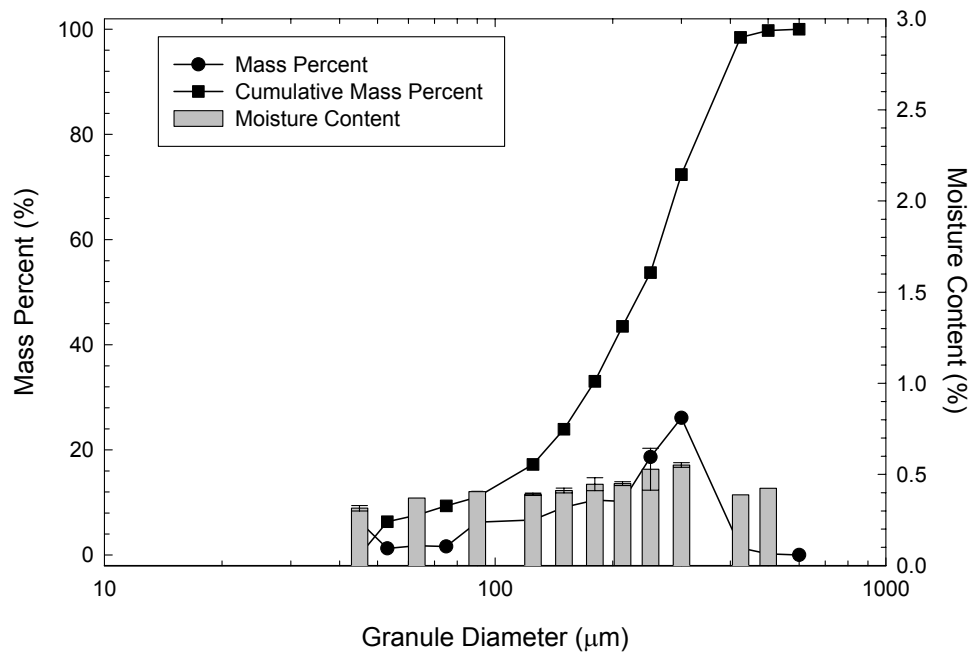


Figure 7-27. Granule size distribution and moisture content distribution for the pPVA granulate. A moisture content distribution is observed in the sieved granulate with the larger granules retaining more moisture.

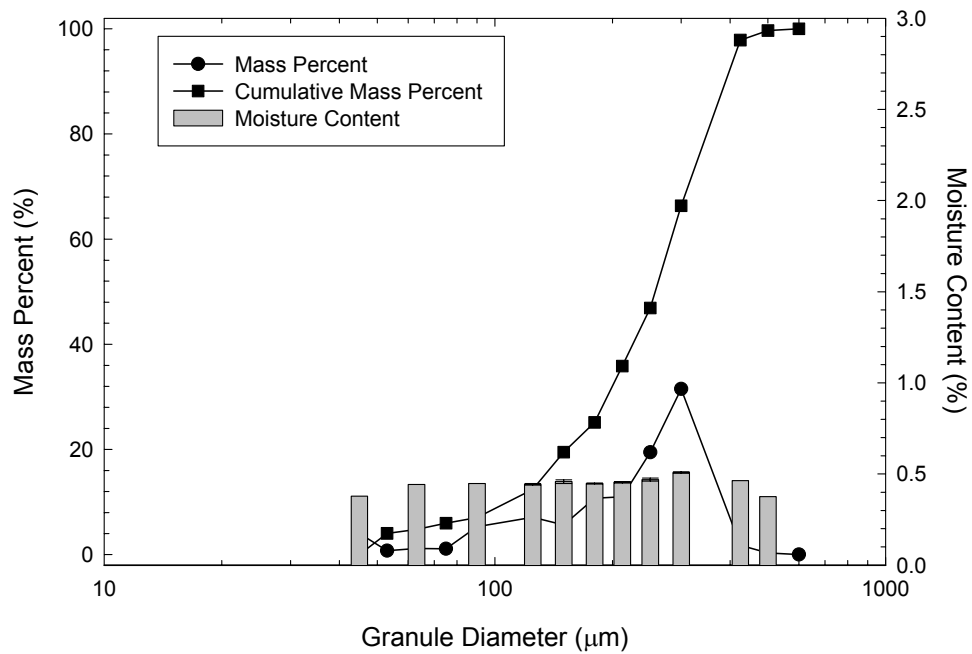


Figure 7-28. Granule size distribution and moisture content distribution for the PEG granulate. No significant moisture content distribution is observed in the granulate.

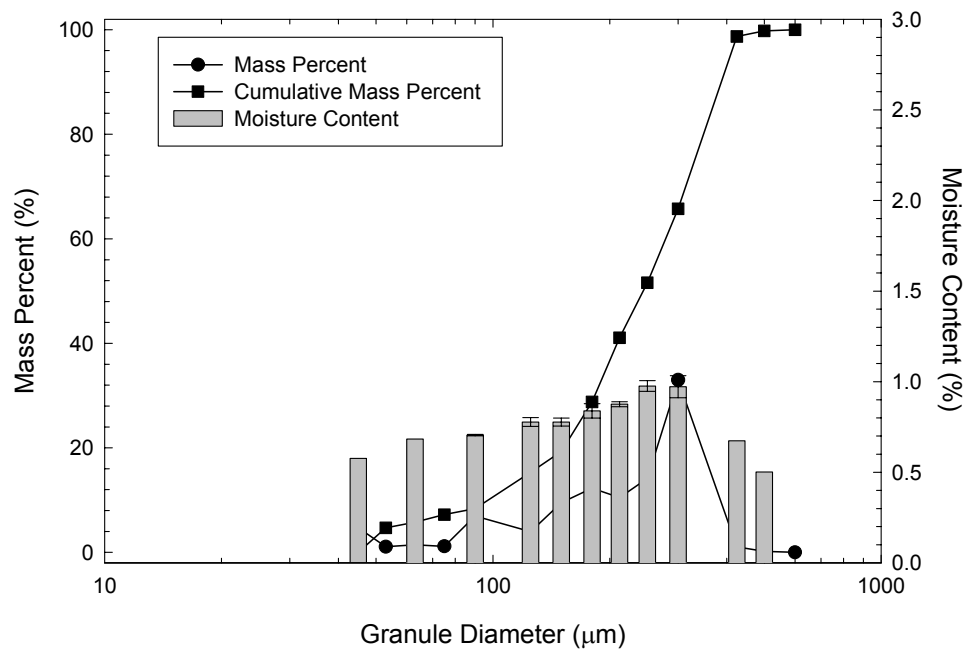


Figure 7-29. Granule size distribution and moisture content distribution for the no organic binder (NB) granulate. A small moisture content distribution is observed in the granulate.

Table 7-V. Moisture Content of the Granulate at the Time That it was Prepared by Buffalo China and at the Time of Analysis in This Study.

Binder System	Moisture Content when spray dried	Moisture Content at time of analysis*
	(wt%)	(wt%)
<b>Ligno</b>	2.50 ± 0.56	1.04 ± 0.05
<b>pPVA</b>	2.47 ± 0.68	0.66 ± 0.04
<b>PEG</b>	2.36 ± 0.27	0.66 ± 0.04
<b>No Binder (NB)</b>	2.06 ± 0.51	0.79 ± 0.02

\* Granulate was stored in sealed containers 6 months

A comparison of the results can be observed in Figure 7-30 (P1), Figure 7-31 (compact density), and Figure 7-32 (green strength) as a function of the granule diameter for each binder system in this study. The P1 value for lignosulphonate granulate was overall much higher (neglecting the P1 value for the sub-230 mesh material) than the other three binder systems; little difference in P1 was observed for the other systems studied. No difference in compact density was observed between the binder systems in this study. The green strength of pPVA granulate was higher than the other three binder systems. The pPVA granulate had a lower P1 value than the lignosulphonate granulate allowing the granules to deform under pressure (i.e., it was a softer binder system). The PEG granulate was a very soft binder system that was not effective as a dry-pressing binder; during the industrial trial the samples prepared with PEG failed upon ejection from the dry press. Finally the NB system had no organic binder to provide green strength; the pellets return to a powder under the applied load.

The data generated with the <50 µm granulate were observed to have significantly lower properties compared to the rest of the samples. This was an artifact of the internal friction between the particles during compaction. The <50 µm particles were approaching the size of the materials; the quartz used in this study was a sub-325 mesh powder. A 325-mesh sieve has an opening of 45

micrometers, i.e., all of the powder in the 325-mesh quartz had a particle size of less than 45 micrometers.

The Mathematica™ model was used to determine the drying time necessary for a spray-dried droplet as a function of solids loading, reported as an area fraction (af) and initial droplet radius, Figure 7-33. The change in the appearance of a drying droplet as a function of time is shown in Figure 7-34 for a 25 v/o alumina suspension with an initial radius of 200 micrometers.

#### *7.3.3.3 Discussion*

Only a small moisture content distribution was observed in the granulate samples tested. This was due to the storage conditions at the dry-press facility. The granulate used in this portion of the study was stored for a period of twelve months under ambient conditions in unsealed super-sacks. This resulted in the constant fluctuation of the moisture content within the granulate in an effort to equilibrate with the surrounding environment. At the time that the granulate samples were taken the relative humidity was high (greater than 80% in June, 2002) and during the six months of storage in sealed polypropylene containers the samples have still not reached an equilibrium moisture content in all size fractions.

The observed moisture-content distribution was a consequence of the spray-drying process. The finer granules dried earlier in the spray dryer and were subject to a thermal treatment that made the polymer more hydrophobic in nature (e.g., hydroxyl groups were removed from the PVA structure resulting in a carbon-to-carbon double bond; see Appendix G for the proposed decomposition reaction). Larger granules retained moisture longer in the spray drying process and therefore remained cooler allowing the polymer to remain more hydrophilic; there was less thermal degradation of the organic in the larger granules. The change in the nature of the polymer binder and the moisture content in each size fraction can be correlated to the change in the pressure at the onset of granule deformation. The PEG granulate was observed not to have a moisture content distribution. PEG is known to readily decompose to lower-molecular weight, volatile species rather than degrade to form a hydrophobic species.

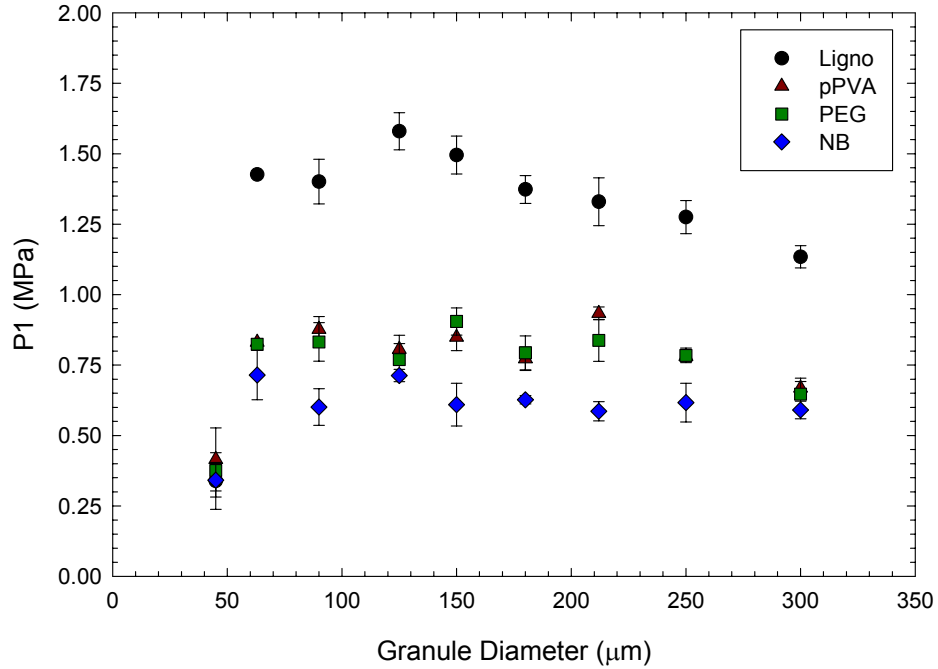


Figure 7-30. Comparison plot of the pressure at the onset of granule deformation (P1) for each binder system as a function of the granule diameter. The measured value for the lignosulphonate granulate is observed to be significantly higher than the other binder systems in this study.

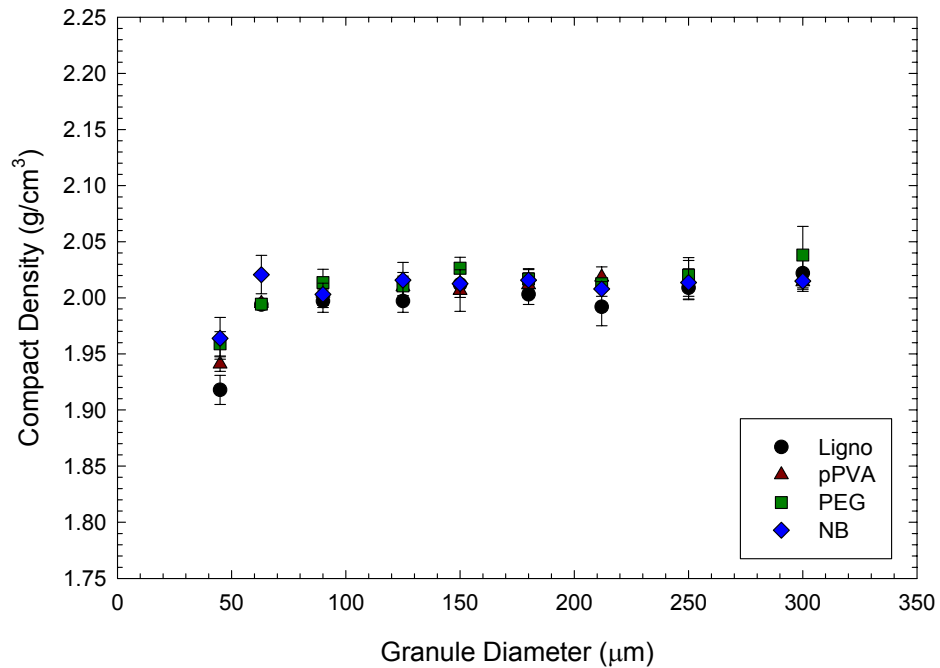


Figure 7-31. Comparison plot of the pressed density of the pellets prepared for each binder system in this study as a function of granule diameter. Little difference is observed in the compact density of the pellets prepared in this study.

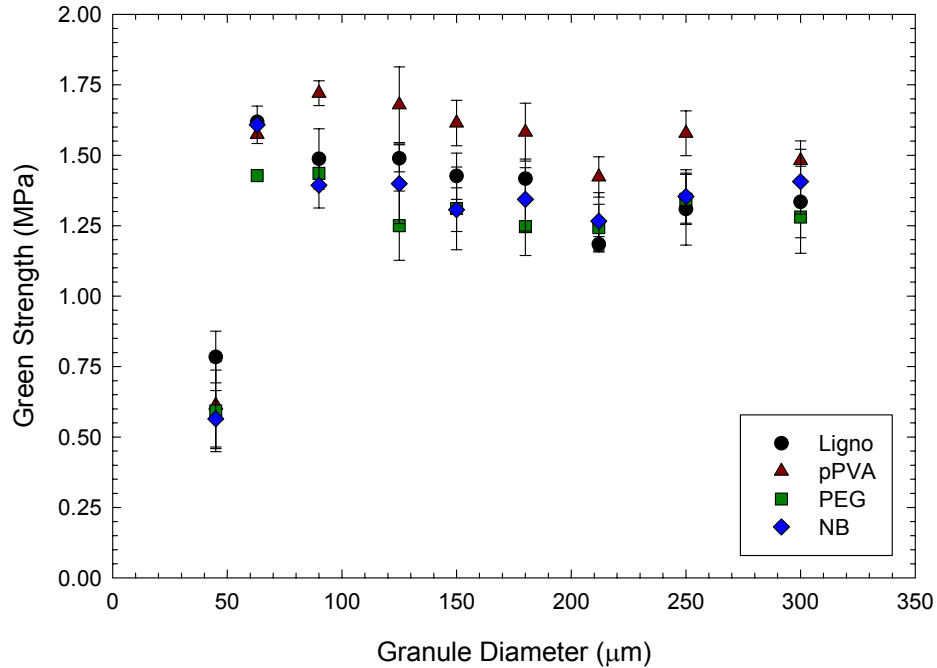


Figure 7-32. Comparison plot of the green strength, measured by diametric compression, for each binder system in this study as a function of granule diameter. pPVA granulate is observed to provide the highest green strength followed by lignosulphonate granulate. The PEG and NB granulate have lower green strengths due to the poor performance of these “additives.”

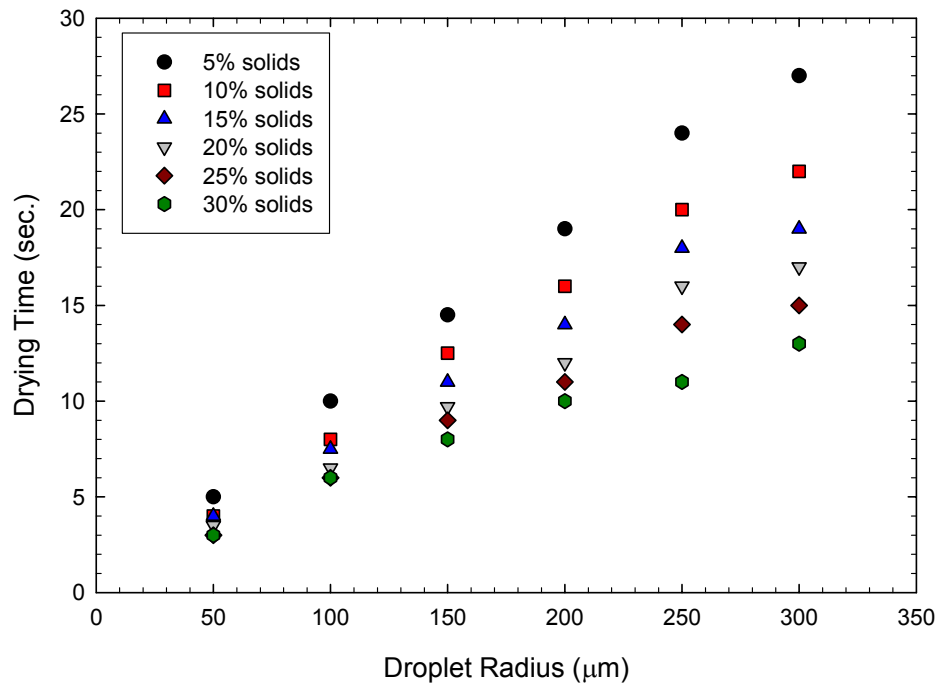


Figure 7-33. Drying time of a virtual droplet as a function of initial droplet radius and solids loading (reported as an area fraction, af).

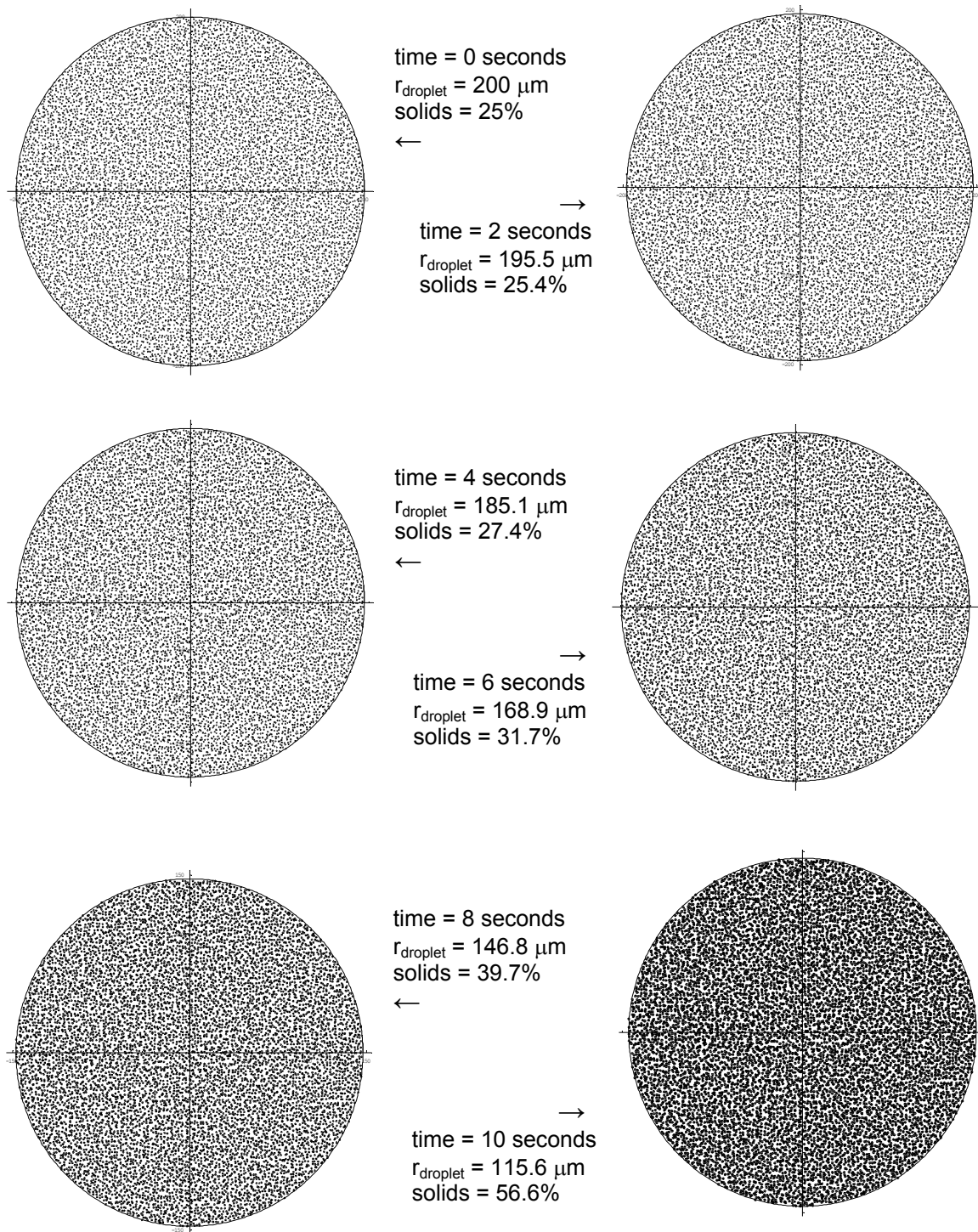


Figure 7-34: Results from the mathematical model to investigate the spray drying process. The virtual droplet has an initial radius of 200 micrometers and a solid loading of 25 volume percent.

While all size fractions (with the exception of the fines) were statistically pressed to the same density there was a significant difference in the green strength of the samples as a function of granule diameter. Larger granules were observed to have a lower green strength due to the larger flaw size (the porosity remaining between deformed granules). All binder systems passed through a maximum green strength as the granule diameter decreased; this maximum was observed between 60 and 90 micrometers in this study depending on the binder system. The smaller granule sizes resulted in a smaller flaw size within the pressed compact. The extreme fines, granules <50  $\mu\text{m}$  in diameter, were observed to have very low compact density and green strength. This fine fraction of the granule size distribution was approaching the size of the primary particles used to prepare the granule. Therefore the internal friction between the granules, or the primary particles, hindered particle rearrangement and compaction resulting in a sharp decrease in the compact density with a corresponding decrease in the green strength.

### *7.3.4 Summary and Conclusions*

Moisture content was confirmed as a crucial parameter in the deformation of granule systems. By initially drying samples of granulate and subsequently storing the granulate in a controlled humidity environment it was possible to rehumidify and restore the properties of the as-received granulate. Sample stored at 90% relative humidity performed as well as the as-received granulate. Samples stored at 100% relative humidity performed better than the as-received material in uniaxial compaction. The samples at 100% relative humidity were observed to have a fungal growth, indicated by the smell of the samples.

A moisture-content distribution was observed in the granulate samples, with the exception of the PEG binder system. Despite storage of the granulate in a sealed container for six months the moisture content was not observed to equilibrate. This moisture-content distribution could play a role in the deformation of the granulate since the finer fractions will have a lower moisture content than the larger size fractions. Compaction was not observed to be dependent on granule size with the exception of the extreme fines, the sub-230-mesh granulate. This fraction was approaching the size of the primary particles in the whiteware batch; the quartz is a sub-325 mesh grade. Compact density was observed to not be dependent on the granule size. Green strength passed through a maximum at an intermediate granule size (between 60 and 90 micrometers); larger granules have large residual pores after compaction which served as a critical flaw for failure.

## **7.4. Alternative Binder Systems for Dry Pressing**

### *7.4.1 Introduction*

Kim found that a negative interaction occurs between PAA (or PMAA) and PVA resulting in the phase separation of the organics into distinct domains.<sup>46</sup> The negative interaction results in case-hardened granules that do not easily deform during compaction. Alternative binders to replace PVA in the spray-drying process were investigated to reduce the P1 value of the resulting granulate. The resulting granulate was evaluated to determine the P1 value, compact density, and green strength. Dinnerware and tile samples were prepared to evaluate the surface finish of the pressed ware.

### *7.4.2 Experimental Procedure*

The alternative binder systems selected as possible replacements for pPVA in this study are listed in Table 7-VI; a discussion on the binder selection will follow the experimental procedure. The concentration of binder in the spray-dried granulate was varied to study the effects of binder concentration on the deformation of granulate and the properties of the resulting compacts.

Suspensions were prepared using the granulate supplied by Buffalo China without an organic binder system at 30 v/o solids; this is lower than typically used in industry to minimize problems in pumping the suspensions prepared with high concentrations of binder. The rheology of the samples with high binder concentration was tested to predict problems in pumping the suspension in the spray dryer. Granulate was prepared using the laboratory-scale spray dryer at Alfred University [BE985, Bowen Engineering Inc., North Branch, NJ]. The inlet temperature was set between 290 and 300°C and the outlet temperature was uncontrolled; evaporation of water determined the outlet temperature of the spray dryer. The pump speed was adjusted with viscosity of the suspension; higher-viscosity suspensions were pumped at higher rates. A 1.5-mm-diameter nozzle was used with the atomizer pressure set between 13 and 14 psig. Data on the control of the spray dryer can be found in Appendix G.

Table 7-VI. Binder Systems Investigated as Possible Replacements for pPVA Binder Systems in Dry Pressing.

Binder	Binder Concentration (wt%, dwb)**
pPVA	0, 0.25, 0.50, 1, 2, 5
Ligno	0.25, 0.50, 1, 2, 5
pPVA / Veegum™ T	0, 0.25, 0.50, 1, 2, 5
Agar	0, 0.25, 0.50, 1, 2, 5
Acrylic Latex	0, 0.25, 0.50, 1, 2, 5
Starch	0.25, 0.50, 1, 2, 5
Sugar	0.25, 0.50, 1, 2, 5
Veegum™ T	0.25, 0.50, 1, 2, 5
Methyl Cellulose	0, 0.1, 0.25, 0.5, 0.7
Carboxymethyl Cellulose	0, 0.1, 0.25, 0.5, 0.7
Veegum™ T / Vanzan™ D	0, 0.25, 0.50, 1, 2
Hydrolyzed Veegum™ T*	2

\* Plotted with the Veegum™ T data

\*\* dwb – dry weight basis

The resulting granulate was tested for granule size distribution, moisture content, P1, compact density, green strength by diametral compression, and fill density (determined from the compaction data). The granule size distribution was determined using the Horiba particle size analyzer [LA-920, Horiba Instruments, Inc., Irvine, CA] set up for dry samples. Moisture content, P1, compact density, and green strength were determined using the procedures outlined under Chapter 7.2. The fill density was determined using the measured dimensions of the die prior to compaction and the weight of granulate.

Samples were pressed for evaluation of the surface roughness using the Dorst industrial semi-isostatic dinnerware press and the Aeonic press with hardened steel dies. The samples were all pressed at approximately the same pressure, 300 bar or 30 MPa. The samples were characterized for surface roughness using the optical interferometer and an updated MetroPro software package [v.7.12.0, Zygo Corporation, Middlefield, CT] and the stitching method described in Chapter 6. The dinnerware samples from the Dorst press were characterized using a 5.77 mm by 4.33 mm area, corresponding to a 5 by 5 grid

of images and 1.23 million data points. The samples from the Aeonic press were characterized using a 3.61 mm by 2.70 mm area corresponding to a 3 by 3 grid of images and 480,000 data points. All images were filtered using a low-pass, median, 5 filter to remove noise.

It was demonstrated in Chapter 7.2 that blending of dried granulate could be used to reduce the measured P1 value. Based upon that conclusion it was hypothesized that by preparing blends of granulate with similar P1 values the surface finish could be further improved. This hypothesis was rationalized by the assumption that the slightly harder granule would initially deform the softer granule (once the P1 of the softer granule had been exceeded) followed by the subsequent deformation of the harder granule (once the P1 value had been exceeded). Therefore compaction would be a two-stage process allowing the softer granules for deform and fill the porosity followed by the deformation of the harder granules. Blends were selected so as to provide a range of  $\Delta P1$  values, where  $\Delta P1$  was the difference between the P1 values of the two constituent granulates. To normalize the data a factor was developed, using the equation:

$$P1_{\text{norm.}} = \Delta P1 * P1_{\text{avg.}} \quad (20)$$

The normalized P1,  $P1_{\text{norm.}}$ , has units of  $\text{MPa}^2$  and  $P1_{\text{avg.}}$  is the average P1 value of the two constituent granulates. It was proposed that the normalized P1 should scale with the hardness of the granulate blends and therefore with the P1 value. If there was a small value of  $\Delta P1$  and a high value of  $P1_{\text{avg.}}$  this would shift the normalized P1 to higher values. If  $P1_{\text{avg.}}$  was small and  $\Delta P1$  was large this would also shift the normalized P1 to higher values. Therefore, based upon this proposal, blends with a small normalized P1 should deform more easily and therefore have a superior surface finish. A list of the selected blends and the P1 values from the constituent granule samples are listed in Table 7-VII. Blends 1 through 23 were prepared as a 50-50 wt% blend of granulate while blends 24-26 were 25-75 wt% blends.

Table 7-VII. List of the Granule Blends Selected to Evaluate the Effects of Blending Granulate.

Blend #	Granulate 1*	Granulate 2*	Blend Conc.	P1 Component 1	P1 Component 2	P1 <sub>norm</sub>
			wt%	MPa	MPa	MPa <sup>2</sup>
1	2% Starch	1% PVA-V	50-50	0.27±0.02	0.27±0.09	0.000
2	1% Ligno	0.5% V-V	50-50	0.80±0.06	0.79±0.05	0.008
3	5% Latex	5% Agar	50-50	0.27±0.02	0.23±0.03	0.010
4	1% Sugar	5% Agar	50-50	0.17±0.02	0.23±0.03	0.012
5	0.5% Agar	5% Latex	50-50	0.30±0.02	0.27±0.02	0.021
6	2% Veegum™	2% Agar	50-50	0.29±0.08	0.36±0.02	0.025
7	5% Agar	5% Starch	50-50	0.23±0.03	0.33±0.60	0.028
8	2% Agar	1% PVA-V	50-50	0.36±0.02	0.27±0.09	0.028
9	2% V-V	2% Ligno	50-50	1.10±0.12	1.14±0.09	0.045
10	2% V-V	0.5% Starch	50-50	0.36±0.09	0.18±0.02	0.049
11	1% Sugar	1% Agar	50-50	0.17±0.02	0.32±0.02	0.054
12	5% Latex	5% sugar	50-50	0.27±0.02	0.44±0.2	0.060
13	1% Starch	0.5% CMC	50-50	0.21±0.03	0.45±0.04	0.079
14	1% Latex	1% Veegum™	50-50	0.47±0.06	0.18±0.02	0.094
15	0.5% MC	0.5% Latex	50-50	0.48±0.04	0.65±0.03	0.096
16	0.5% V-V	0.5% Ligno	50-50	0.79±0.05	0.64±0.05	0.107
17	0.5% Sugar	2% pPVA	50-50	0.44±0.04	1.08±0.16	0.486
18	2% Ligno	2% Sugar	50-50	1.14±0.09	0.55±0.06	0.490
19	2% Starch	2% V-V	50-50	0.27±0.02	1.10±0.12	0.569
20	1% PVA-V	1% V-V	50-50	0.27±0.09	1.09±0.04	0.578
21	5% pPVA	5% PVA-V	50-50	1.79±0.35	1.28±0.10	0.783
22	5% Ligno.	0.7% MC	50-50	1.92±0.36	0.56±0.11	1.686
23	5% Agar	5% Ligno	50-50	0.23±0.03	1.92±0.36	1.817
24	5% Agar	5% Veegum™	25-75	0.23±0.03	0.29±0.06	0.016
25	0.5% Agar	5% Veegum™	25-75	0.30±0.02	0.29±0.06	0.018
26	5% Agar	1% pPVA	25-75	0.23±0.03	0.88±0.09	0.361

\* Abbreviations for the granulate binders are: CMC= carboxymethyl cellulose, MC= methyl cellulose, pPVA= plasticized PVA, Ligno= Na-lignosulphonate, Latex= acrylic latex emulsion, PVA-V= plasticized PVA with Veegum™ T, V-V= Veegum™ T with Vanzan™ D

### 7.4.3 Organic Selection

Schematics of the structure from the organics used in this study can be found in Appendix H. All binder systems were added on a dry-weight-percent basis (dwb) of the granulate from Buffalo China except where noted.

#### 7.4.3.1 Plasticized PVA (*pPVA*)

Buffalo China's standard batch for dry pressing consists of a plasticized PVA binder system. This system was replicated at Alfred University for preparation in the Bowen laboratory spray dryer. Based upon data provided by Buffalo China an approximate ratio of plasticizer to PVA was calculated and used in this study, approximately 1 gram of plasticizer to 1.75 grams of PVA; the exact ratio used by Buffalo China is considered proprietary. The PVA was supplied as a 24-weight-percent solution of PVA in water [Celvol 24-203, Celanese Chemicals, Dallas, TX]. The plasticizer used by Buffalo China was Nalco 93QC215 [Nalco 93QC215, Ondeo Nalco, Bedford park, IL]; this organic was indicated to be a PEG-like molecule by Buffalo China. The concentration of binder added to the system was based upon the weight of PVA, i.e., for a 5% binder concentration 5% PVA was added to the suspension and the plasticizer was added to make the total concentration of organic additives approximately 7.85%. The plasticizer was not considered a binder for the purposes of this study; plasticizer was added to prevent hydrogen bonding between the polymer chains of PVA thus reducing the glass-transition temperature of the PVA. The concentration of PVA was varied between 0 and 5 wt%. The 1 wt% suspension was "over-plasticized" at a ratio of 1 gram of plasticizer to 0.77 g of PVA., i.e., too much plasticizer was added to the binder system.

#### 7.4.3.2 Na-Lignosulphonate (*Ligno*)

Lignosulphonate is a byproduct of the paper industry. It is generated during the treatment of wood pulp using sulfuric acid. The sulfuric acid breaks down the lignite into a soluble form (lignosulphonate) which is then separated from the cellulose which used to manufacture paper.<sup>141</sup> Doran (1995) demonstrated that lignosulphonate binders have a lower P1 value compared to

plasticized PVA.<sup>129</sup> Recent work on this binder system has indicated that Na-lignosulphonate is not significantly better, in some cases it is worse, than plasticized PVA. As mentioned, lignosulphonate is an effective dispersant for clay particles. Lignosulphonate was tested as a comparison to the data previously collected in this research. The concentration of binder was varied between 0.25 and 5 wt%. Storage of the binder at 110°C was observed to liquefy the lignosulphonate which was accompanied by a significant weight loss,  $7.43 \pm 0.12$  wt%, after storage for 16 hours.

#### *7.4.3.3 pPVA / Veegum™ T*

To determine the effects of replacing pPVA in a binder system a 50-50 weight percent blend of pPVA and Veegum™ T [Veegum™ T, R.T. Vanderbilt, Inc. Norwalk, CT] was prepared, i.e., 50% of the PVA in the binder system was replaced by Veegum™ T. The attributes of Veegum™ T will be discussed in the next section. The concept of replacing pPVA with a softer binder system is similar to the concept of blending hard and soft granulates. Veegum™ T was selected for this purpose since it will not migrate during the evaporation process in the spray dryer. Again, the total concentration of additives in this binder system exceeded the “target” level since the plasticizer was not considered a component in the binder system. The concentration of PVA / Veegum™ T was varied between 0 and 5 wt%.

#### *7.4.3.4 Veegum™ T*

Veegum™ T is Hectorite, a swellable 2:1-layer silicate. Veegum™ T does induce a significant increase in the viscosity with increasing “binder” concentration due to the hydrolysis, swelling, of the Hectorite. Veegum™ T also has the benefit of not migrating during evaporation in the spray-drying process. This has the possibility of decreasing P1, making the granulate more deformable. The concentration of binder was varied between 0.25 and 5 wt%. To study the effects of hydrolyzing the Veegum™ T, a suspension was prepared at 2 wt% Veegum™ T by first adding the Veegum™ T to distilled water. The suspension was allowed to rest for five days to fully hydrolyze the Veegum™; it was hypothesized that the hydrolysis of the Veegum™ T might induce a significant

change in the granulate properties.<sup>142</sup> The granulate from Buffalo China was then added to prepare the suspension at 30 v/o solids.

#### *7.4.3.5 Agar*

Agar [Agar, Aldrich Chemical Company, Milwaukee, WI] is a derivative from seaweed. While agar is not conventionally considered a binder for dry pressing it does possess several unique attributes. The material is nearly insoluble in water at room temperature, but at elevated temperatures, above 80°C, the material readily dissolves in water and forms a gelatin film upon cooling. The gelatin traps physical water in the structure allowing for high moisture contents in the resulting granulate. The samples prepared for measurement of the rheology were not heated prior to measurement. It was observed that the agar binder in the solid state interacted with the clay surface and the growth of secondary organics, indicated by the growth of a black substance which was assumed to be bacteria or a fungus, was observed at the higher binder levels over the summer months. The concentration of agar was varied between 0 and 5 wt%. Suspensions were prepared within 24 hours of spray drying to minimize the fungal growth prior to spray drying.

#### *7.4.3.6 Acrylic Latex Emulsion*

B-1080 [Duramax B-1080, Rohm and Haas, Philadelphia, PA], approximately 45 wt% solids, was used as an acrylic latex emulsion binder. Latex is a water-insoluble organic, therefore the acrylic latex used in this study was supplied as an emulsion.<sup>143</sup> An emulsion is a colloidal suspension of a hydrophobic species suspended in water, or vice versa. To facilitate making the emulsion the supplier adds a surfactant which orients at the interface between the hydrophobic and the hydrophilic liquids. A surfactant, or a surface-active agent, is an organic molecule with a hydrophobic group on one end of the polymer and hydrophilic group on the other end. The addition of a surfactant will therefore aid in the wetting at the interface between the hydrophobic and hydrophilic liquids. When dried, acrylic latex emulsions form an acrylic film at the particle contacts binding the particles together. The concentration of acrylic latex

was varied between 0 and 5 wt% solids; the batch was adjusted to compensate for the water present in the emulsion.

#### 7.4.3.7 Starch

Starch [Starch, soluble, reagent ACS, ACROS Organics, Morris Plains, NJ] is very similar to cellulose in structure; the exception is the orientation of the oxygen bridge between the two aromatic rings that comprise the repeating structure of the organic and the orientation of a functional group next to the oxygen bridge, see Appendix H for a schematic of the starch structure.<sup>144</sup> It has been stated that these two differences can have a pronounced effect on the properties of the organic in solution.<sup>145</sup> This was confirmed by the data collected in this study. The starch “binder” was not observed to affect the rheology of the suspension to the same extent as the cellulose binders studied, there was only a minor increase in viscosity with binder concentration, data not shown. The suspensions prepared with high concentrations of starch were observed to degrade in the clay-based suspension during storage for 6 weeks at room temperature over the summer months; it is assumed that similar reactions occurred in the lower-binder-concentration samples. The degradation was indicated by the formation of a black substance, assumed to be bacteria or a fungus, within the polypropylene container for the 2 and 5 wt% binder samples. It is assumed that the clay surface served as a catalyst for the degradation of the starch. Suspensions for spray drying were prepared within 24 hours of spray drying to minimize degradation of the starch binder. The concentration of binder was varied between 0.25 and 5 wt%. Solutions prepared to determine the surface tension of liquids, Chapter 5, indicated that the starch used in this study is not highly soluble in water. Solutions that were prepared above 0.25 wt%, 0.25 g of starch dissolved in 100 g of water, were observed to be opaque and settled when left to rest.

#### 7.4.3.8 Sugar (*Alpha-D(+)-Glucose*)

Sugar [*Alpha-D(+)-Glucose*, anhydrous 99+%, ACROS Organics, Morris Plains, NJ] is the “low-molecular-weight form” of starch.<sup>144</sup> Both have a similar chemical composition, but starch has one less oxygen that allows the structure to

repeat. Sugar is the basic building block for polysaccharides, a group which includes starch, cellulose, and other organic materials which are not involved in this study. The suspensions prepared for rheology characterization also exhibited a change with time during storage for 6 weeks over the summer months. The polypropylene containers were observed to swell as the sugar fermented in the presence of clay surface. Suspensions were prepared within 24 hours of spray drying to minimize degradation of the sugar. During the spray drying process the smell of burning sugar was apparent; it was more apparent at the higher binder concentrations. The concentration of binder was varied between 0.25 and 5 wt%.

#### *7.4.3.9 Methyl Cellulose*

Methyl cellulose [Methocel 20-214 Cellulose ether, Dow Chemical Company, Midland, MI] is known to significantly affect the suspension viscosity; traditionally cellulose is used as a thickener to control viscosity.<sup>144,146</sup> Methyl cellulose is also known to gel with temperature at higher binder concentrations. These two factors reduced the useful binder concentration range for this study. Therefore suspensions were prepared between 0 and 0.7 wt% binder. During the process of spray drying the 0.25 wt% sample it was necessary to stop spray drying to clean the nozzle due to thermal gelling of the cellulose. Subsequent samples were pumped at higher speeds to prevent clogging of the nozzle.

#### *7.4.3.10 Carboxymethyl Cellulose*

Carboxymethyl cellulose [Carboxymethyl Cellulose, sodium salt, Aldrich Chemical Company, Milwaukee, WI] is also known to significantly affect the viscosity of aqueous suspensions.<sup>144,146</sup> The grade used in this study was reported to have a viscosity between 3000 and 6000 centipoise for a 1 wt% solution of the binder, the viscosity of water is approximately 1 centipoise at room temperature. Carboxymethyl cellulose is also known to gel with temperature at higher binder concentrations. Suspensions were prepared between 0 and 0.7 wt% binder. At 0.7 wt% binder the suspension gelled in the nozzle of the spray dryer, pumping the suspension at higher speeds did not overcome the gelling problem.

#### *7.4.3.11 Veegum™ T / Vanzan™ D*

A binder system consisting of a 80-20 mix of Veegum™ T and xanthan gum [Vanzan™ D, R.T. Vanderbilt, Norwalk, CT] has been demonstrated to be relatively soft.<sup>142</sup> The Veegum™ T was dispersed in distilled water and allowed to hydrolyze (swell) for a period of five days. The granulate was then added and mixed until homogeneous followed by addition of the Vanzan™ D. Vanzan™ D is engineered to slowly dissolve in neutral and slightly acidic aqueous solutions. Since xanthan gum is a thickener this property of the Vanzan™ D allows for a more homogenous distribution of the xanthan gum particles prior to thickening the suspension. Due to the thickening properties of the hydrolyzed Veegum™ T and the Vanzan™ D additives the binder concentration was varied between 0 and 2 weight percent.

#### *7.4.4 Results*

##### *7.4.4.1 Granule Size Distribution*

To assure that the Horiba with the dry powder feeder was giving accurate data, the size distribution of the Buffalo China granulate collected from the sieve analysis, reported in Chapter 7.3.3, was compared to the data from the Horiba particle size analyzer. The results from the two methods are shown in Figure 7-35 for each of the binder systems prepared by Buffalo China. Little difference was observed between the two methods of measuring granule size distribution. The Horiba was observed to generate smoother granule size distribution curves as well as data at the finer granule sizes. This shifts the mean granule diameter to smaller sizes when compared to the sieve analysis.

The mean and standard deviation results reported by the Horiba for the granule size distribution analysis are shown in Table 7-VIII. The mean particle size reported is based upon the frequency (number) data. The standard deviation of the particle size distribution represents a 95% confidence level, i.e., 95% of the particle size distribution is within the mean particle size plus or minus the reported standard deviation. The granulate prepared at Alfred University is observed to be significantly finer than that prepared at Buffalo China in an

industrial spray dryer. It was reported under Chapter 7.3.3 that granule size had little effect on the deformation (i.e., P1) provided that the fine (sub-230-mesh) granulate was not being tested.

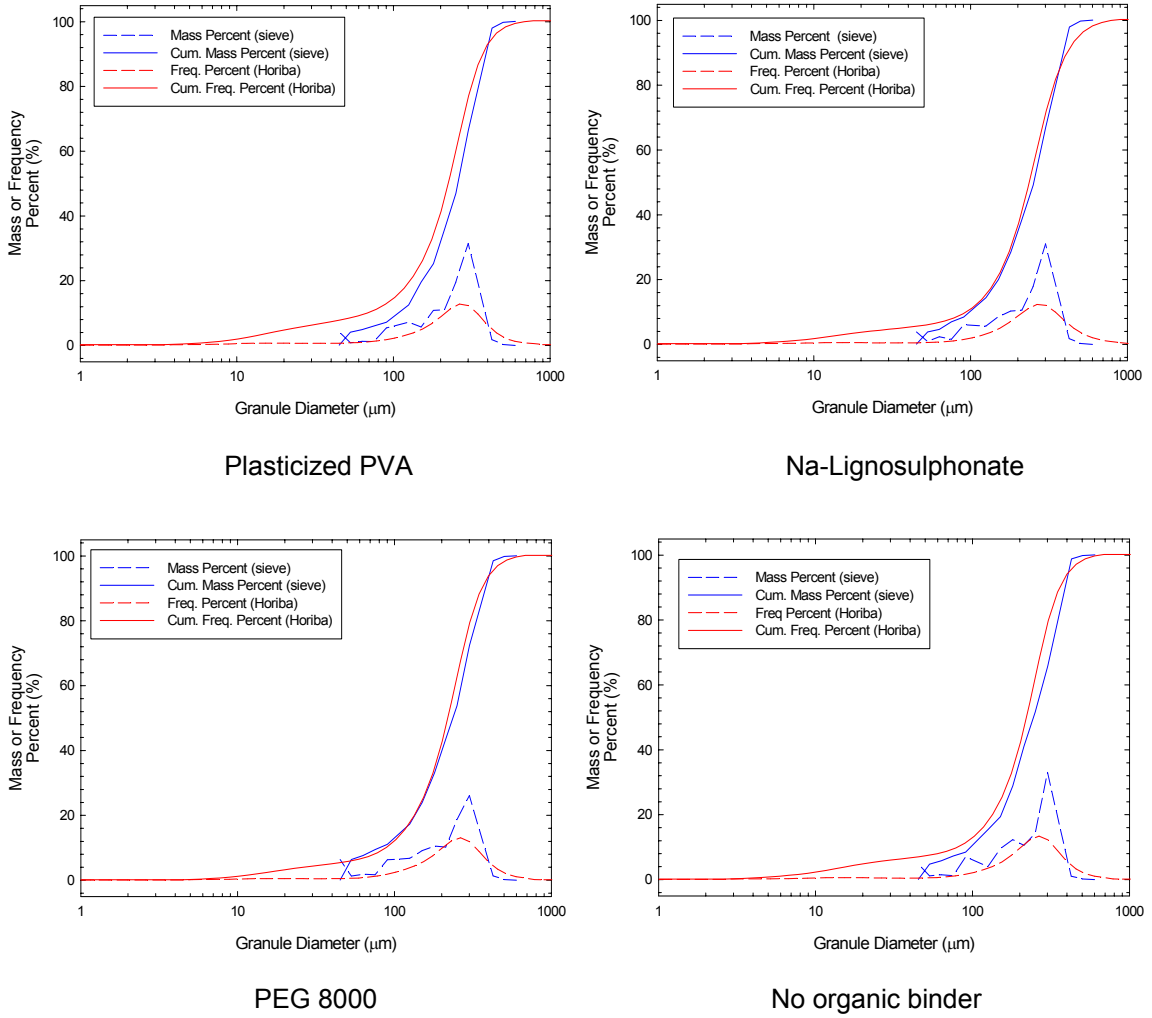


Figure 7-35. Comparison of the granule size distribution obtained from the sieve analysis (blue) and the Horiba particle size analyzer (red) for each of the granulate systems supplied by Buffalo China.

Table 7-VIII. Mean Particle Size and Standard Distribution from the Granulate Binder Systems in This Study.

<b>Buffalo China Granulate</b>						
<b>Binder System</b>		<b>Mean Particle Size (<math>\mu\text{m}</math>)</b>				
pPVA		226.2 $\pm$ 119.9				
Ligno		247.3 $\pm$ 132.6				
PEG		223.1 $\pm$ 110.1				
No Binder System		221.3 $\pm$ 111.3				
<b>Binder System</b>	<b>Binder Concentration (wt%)</b>					
	<b>0</b>	<b>0.25</b>	<b>0.5</b>	<b>1</b>	<b>2</b>	<b>5</b>
	<b>Mean Particle Size (<math>\mu\text{m}</math>)</b>					
pPVA	94.8 $\pm$ 60.7	100.4 $\pm$ 66.5	102.1 $\pm$ 68.9	100.5 $\pm$ 70.9	112.3 $\pm$ 86.0	125.3 $\pm$ 90.4
Ligno.	N/A*	114.1 $\pm$ 70.2	121.4 $\pm$ 81.4	120.3 $\pm$ 81.6	116.6 $\pm$ 76.1	112.1 $\pm$ 72.4
pPVA / Veegum™ T	105.2 $\pm$ 75.1	105.2 $\pm$ 68.8	111.9 $\pm$ 75.9	120.8 $\pm$ 80.4	115.3 $\pm$ 81.9	132.1 $\pm$ 87.1
Veegum™ T	N/A*	118.8 $\pm$ 85.1	118.9 $\pm$ 75.1	116.1 $\pm$ 72.3	119.2 $\pm$ 74.8	108.7 $\pm$ 64.7
Agar	132.5 $\pm$ 90.8	141.2 $\pm$ 104.6	150.2 $\pm$ 110.5	N/A**	N/A**	N/A**
Acrylic Latex	89.2 $\pm$ 56.0	112.7 $\pm$ 61.5	107.1 $\pm$ 59.3	128.8 $\pm$ 78.3	130.2 $\pm$ 76.6	136.6 $\pm$ 71.8
Starch	N/A*	109.3 $\pm$ 79.7	110.1 $\pm$ 72.8	100.2 $\pm$ 69.2	101.4 $\pm$ 7.30	102.6 $\pm$ 71.9
Sugar	N/A*	N/A**	96.1 $\pm$ 69.7	90.1 $\pm$ 66.2	101.9 $\pm$ 68.9	96.9 $\pm$ 71.8
Veegum™ T / Vanzan™ D	104.1 $\pm$ 75.2	116.2 $\pm$ 75.4	128.7 $\pm$ 82.1	132.6 $\pm$ 80.1	136.3 $\pm$ 83.5	NA*
Veegum™ T- hydrolyzed	NA*	NA*	NA*	NA*	118.8 $\pm$ 75.8	NA*
<b>Binder System</b>	<b>Binder Concentration (wt%)</b>					
	<b>0</b>	<b>0.1</b>	<b>0.25</b>	<b>0.5</b>	<b>0.7</b>	
	<b>Mean Particle Size (<math>\mu\text{m}</math>)</b>					
Methyl Cellulose	111.7 $\pm$ 73.0	115.9 $\pm$ 88.0	111.8 $\pm$ 68.8	136.0 $\pm$ 93.4	125.3 $\pm$ 75.3	
Carboxymethyl Cellulose	102.8 $\pm$ 63.5	115.6 $\pm$ 71.7	95.5 $\pm$ 65.9	122.4 $\pm$ 73.9	139.1 $\pm$ 81.6	

\* Experimental condition was not evaluated in this study

\*\* Sample clogged the Horiba particle size analyzer during the test.

#### 7.4.4.2 pPVA

The results from the pPVA system can be observed in Figure 7-36 (P1), Figure 7-37 (compact density), Figure 7-38 (green strength), and Figure 7-39 (RMS roughness). The moisture content is plotted in each figure as a reference. The moisture content was observed to be nearly constant until 5 wt% binder at which point there was a dramatic increase in the measured moisture content. During the process of drying the samples for the moisture content analysis the binder system was observed to degrade. This was evidenced by a change in the coloration of the samples after drying at 110°C for 16 hours. The samples with 0.25 to 2 wt% binder were observed to have a gray color, relative to the 0 wt% samples. At 5 wt% the samples were observed to have a pale yellow color. The P1 of the pPVA system was observed to significantly increase with increasing binder concentration. The 1 wt% dried sample showed an anomalous behavior that may be due to the excessive amount of plasticizer added to the system. The dried samples showed a plateau at higher concentrations of binder while the P1 values of the as-prepared samples continue to increase within the range tested. The compact density was observed to decrease with increasing binder concentration. The samples that were dried have a higher compact density than the samples that were tested in the as-prepared condition. The green strength of the samples was observed to increase with increasing binder concentration. The measured strengths for the dried samples was observed to be higher than that of the as-prepared granulate. The tiles pressed using the hardened steel die were observed to have a significantly lower surface roughness relative to the dinnerware samples prepared in the semi-isostatic die due to better deformation against the non-compliant die face. The roughness of both sets of samples was observed to initially decrease followed by an increase. Little variation was observed between the stitched and the averaged RMS roughness data with the exception of the dinnerware samples prepared with 2 and 5 wt% binder. This variation was due to the waviness, the long-range roughness, of the samples which created surface texture; this effect was also evident in the larger error in the averaged RMS roughness at 2 and 5 wt% binder.

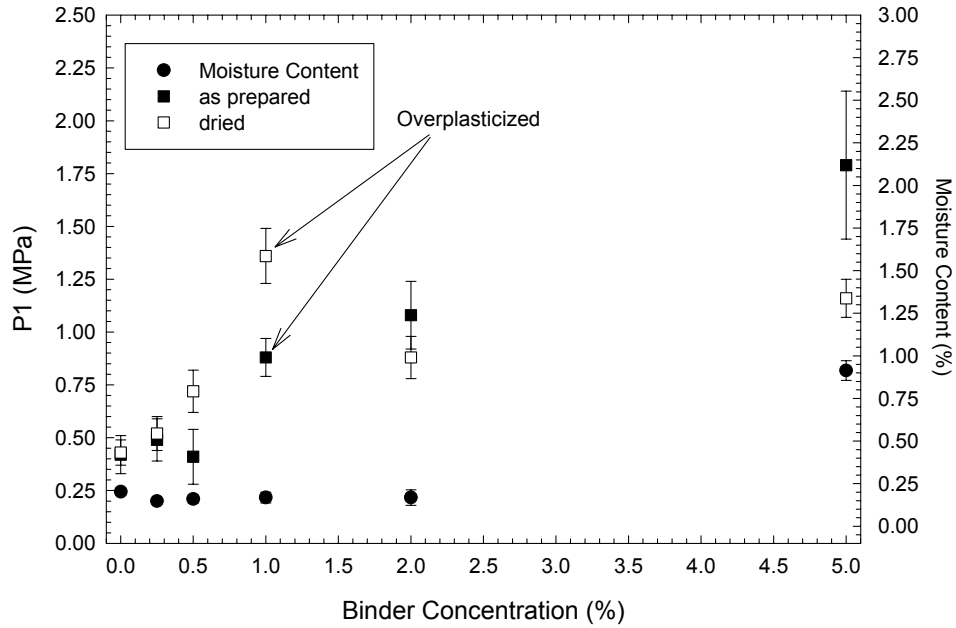


Figure 7-36. Plot of the pressure at the onset of granule deformation (P1) as a function of binder concentration for the as-prepared and dried samples with pPVA as a binder. Also plotted is the moisture content as a function of the binder concentration. The samples prepared at 1.0 wt% binder were overplasticized at a PVA:plasticizer ratio of 0.77:1 compared to the standard binder system which has a PVA:plasticizer ratio of 1.75:1.

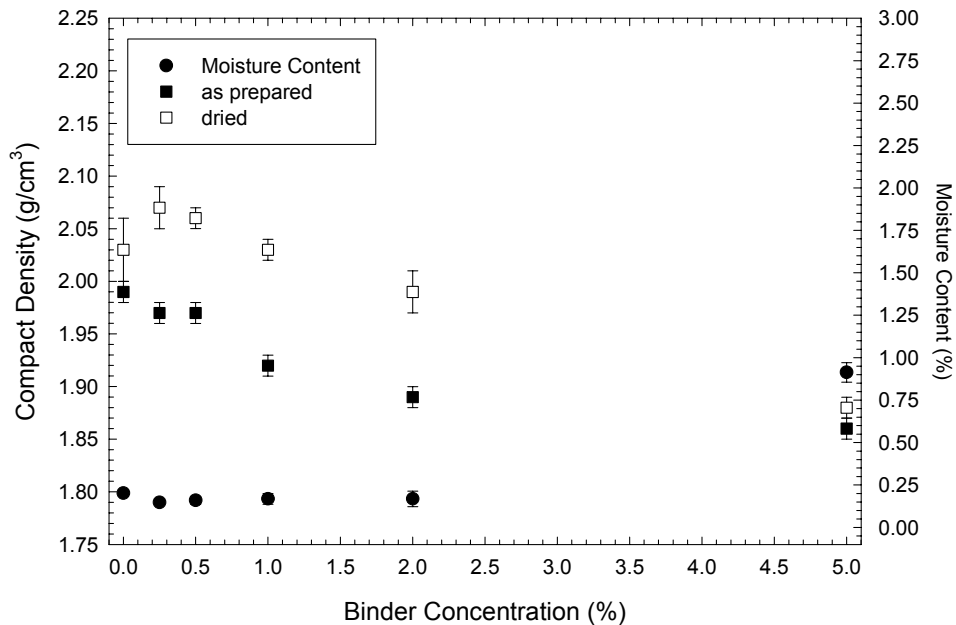


Figure 7-37. Plot of the compact density as a function of binder concentration for the as-prepared and dried samples with pPVA as a binder. Also plotted is the moisture content as a function of the binder concentration.

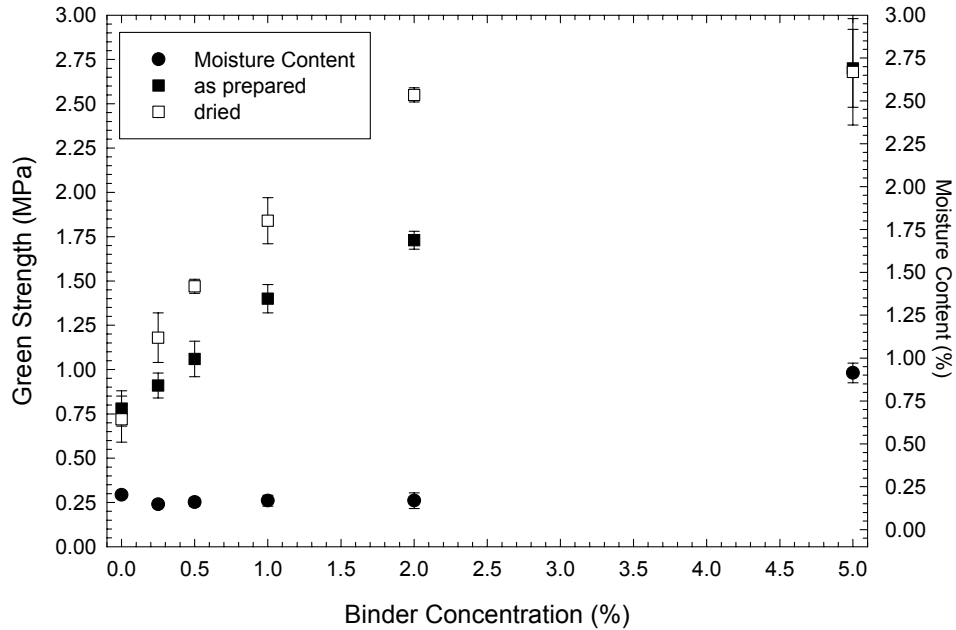


Figure 7-38. Plot of green strength as a function of binder concentration for the as-prepared and dried samples with pPVA as a binder. Also plotted is the moisture content as a function of the binder concentration.

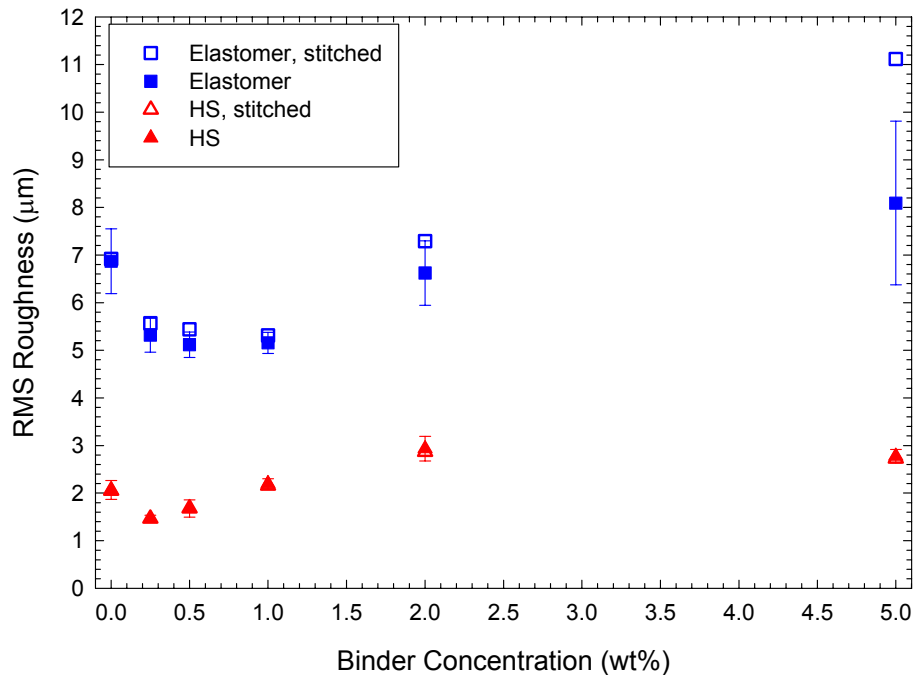


Figure 7-39. Plot of the RMS roughness as a function of binder concentration for samples prepared with pPVA as the binder. Samples were only pressed using the as-prepared granulate on the semi-isostatic (blue) and hardened steel (red) dies. RMS roughness is plotted for the stitched surface (open symbols) and the averaged data from the individual images (closed symbols) used to create the stitched image.

#### *7.4.4.3 Na-Lignosulphonate*

The results from the lignosulphonate granulate can be observed in Figure 7-40 (P1), Figure 7-41 (compact density), Figure 7-42 (green strength), and Figure 7-43 (RMS roughness). The moisture content of the granulate was observed to decrease until a plateau value was reached at 1 wt% binder. P1 was observed to increase for both sets of samples. The as-prepared samples showed a nearly linear increasing trend throughout the range tested in this study. Initially the dried samples exhibited a plateau until 1 wt% after which the values overlay the as-prepared granulate. The compact density of the dried samples was observed to slightly increase until a binder concentration of 1 wt%. Conversely, the compact density of the as-prepared samples was observed to slightly decrease over the range of binder concentrations tested in this study. The green strength of the compacts made from the as-prepared granulate showed an increasing trend over the range of binder concentration tested. The dried samples showed a minimum value at 1 wt% binder followed by an increase in the compact strength. The roughness of both sets of samples, tiles and dinnerware, was observed to increase with increasing binder concentration. The roughness of the dinnerware samples was observed to be significantly higher than that of the tile samples due to the compliant membrane surface. No significant variation was observed between the stitched and the averaged RMS roughness.

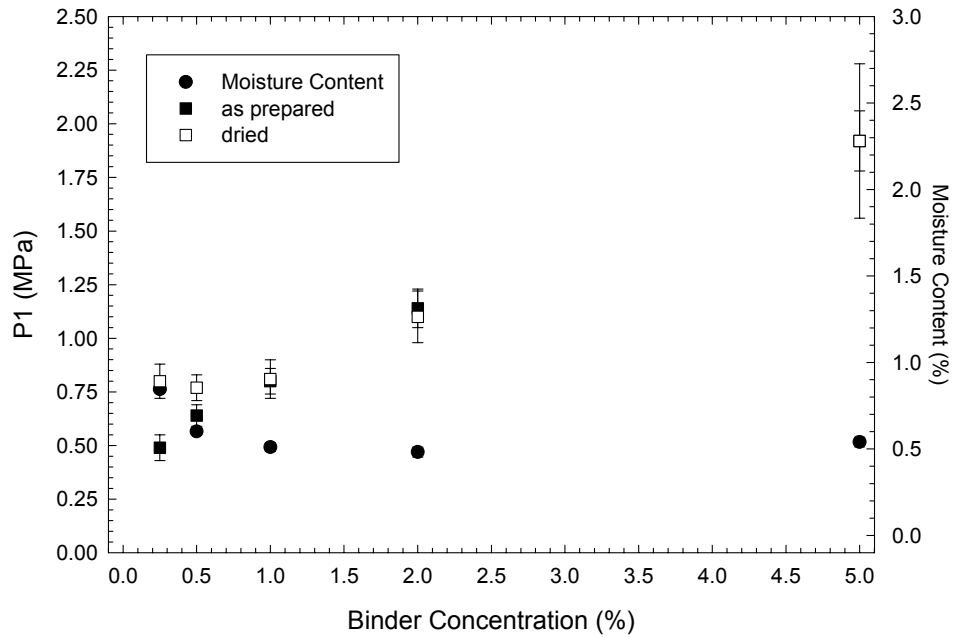


Figure 7-40. Plot of the pressure at the onset of granule deformation (P1) as a function of binder concentration for the as-prepared and dried samples with Na-lignosulphonate as a binder. Also plotted is the moisture content as a function of the binder concentration.

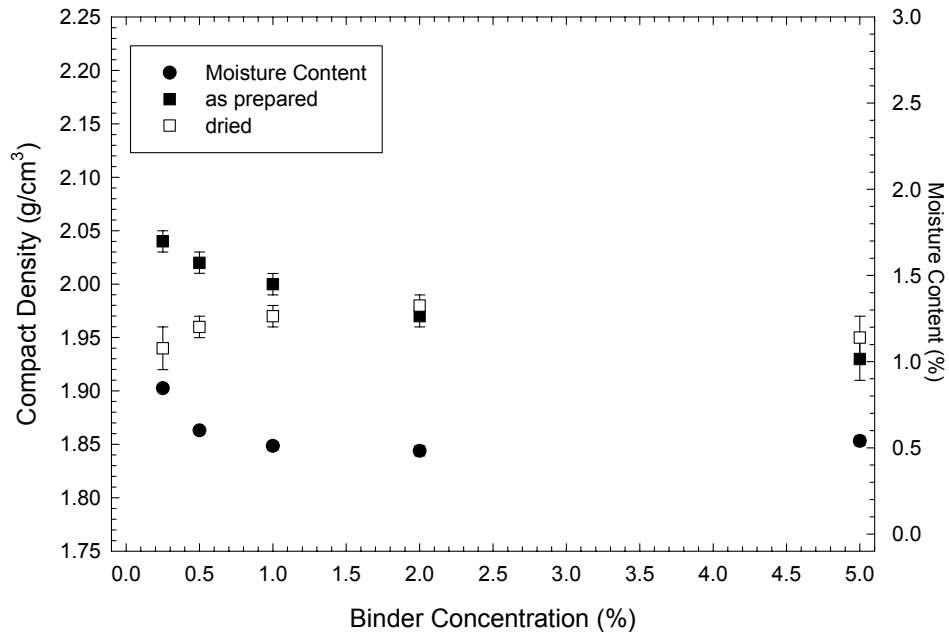


Figure 7-41. Plot of the compact density as a function of binder concentration for the as-prepared and dried samples with Na-lignosulphonate as a binder. Also plotted is the moisture content as a function of the binder concentration.

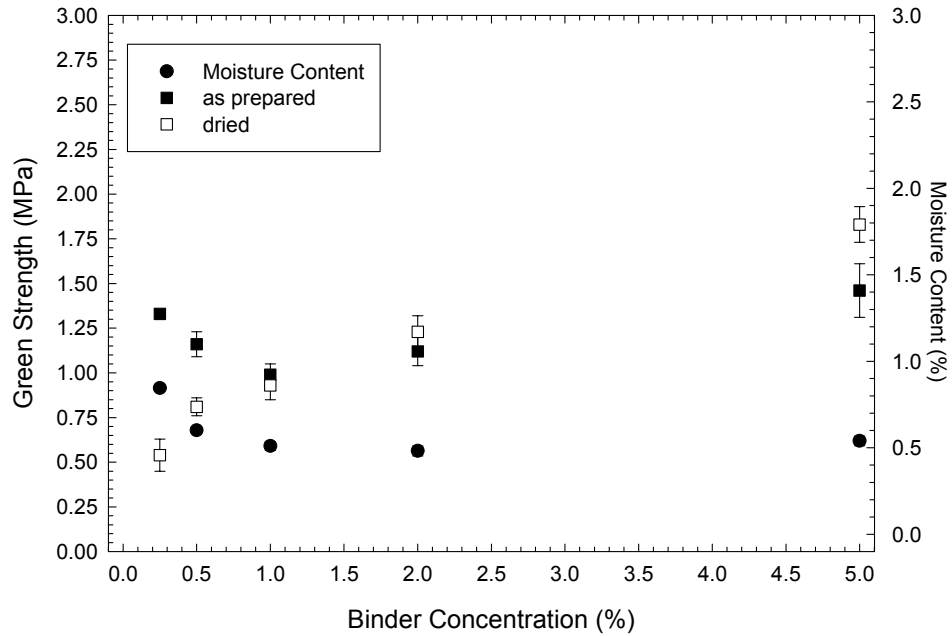


Figure 7-42. Plot of green strength as a function of binder concentration for the as-prepared and dried samples with Na-lignosulphonate as a binder. Also plotted is the moisture content as a function of the binder concentration.

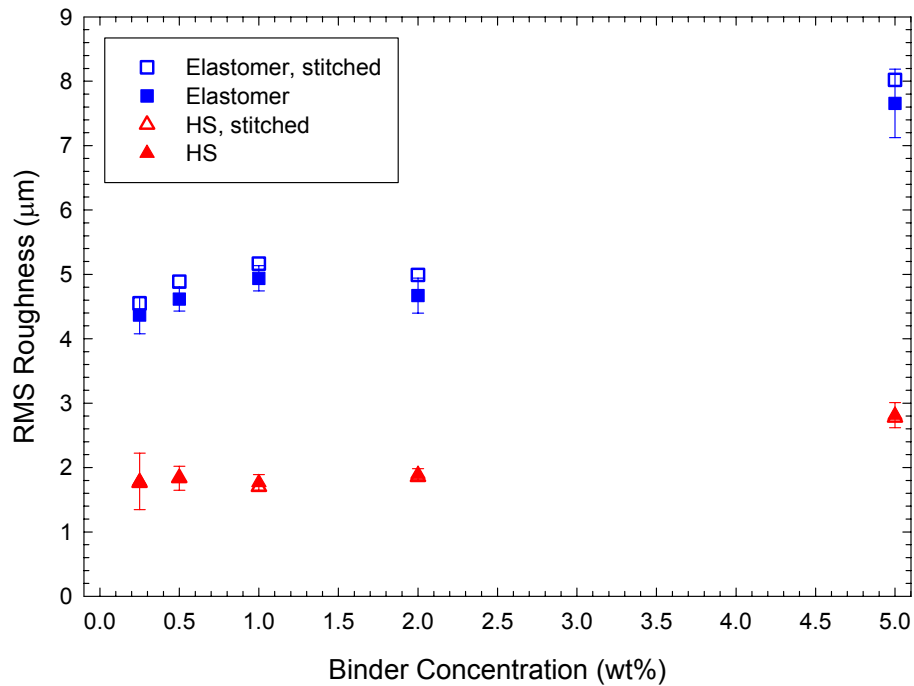


Figure 7-43. Plot of the RMS roughness as a function of binder concentration for samples prepared with Na-lignosulphonate as the binder. Samples were only pressed using the as-prepared granulate on the semi-isostatic (squares) and hardened steel (triangles) dies. RMS roughness is plotted for the stitched surface (open symbols) and the averaged data from the individual images (closed symbols) used to create the stitched image.

#### 7.4.4.4 pPVA / Veegum™ T

The results for the pPVA / Veegum™ T binder system are shown in Figure 7-44 (P1), Figure 7-45 (compact density), Figure 7-46 (green strength), and Figure 7-47 (RMS roughness). The moisture content of the pPVA / Veegum™ T granulate was observed to decrease with increasing binder concentration. Degradation of the binder system was again indicated by a change in the coloration of the granulate after storage at 110°C for 16 hours. The P1 value of the as-prepared granulate was observed to have an initial plateau until a binder concentration of 2 wt% followed by a significant increase in the P1 value at 5 wt% binder. The P1 value of the dried granulate was observed to initially decrease followed by an increase in P1 above 1 wt% binder. The compact density from the as-prepared granulate was observed to linearly increase with increasing binder concentration. The values for the dried granulate nearly overlay the as-prepared granulate samples except at the very low binder concentrations where the dried samples were observed to have a lower compact density. Both the as-prepared and dried samples showed an increase in green strength with increasing binder concentration. Statistically there was no significant difference in the green strength between the as-prepared and dried samples. The roughness of both sets of samples, dinnerware and tiles, was observed to increase with increasing binder concentration. The roughness of dinnerware samples was higher than that of the tiles samples due to the compliant membrane surface. A plateau was observed in the RMS roughness of the dinnerware samples above 2 wt% binder.

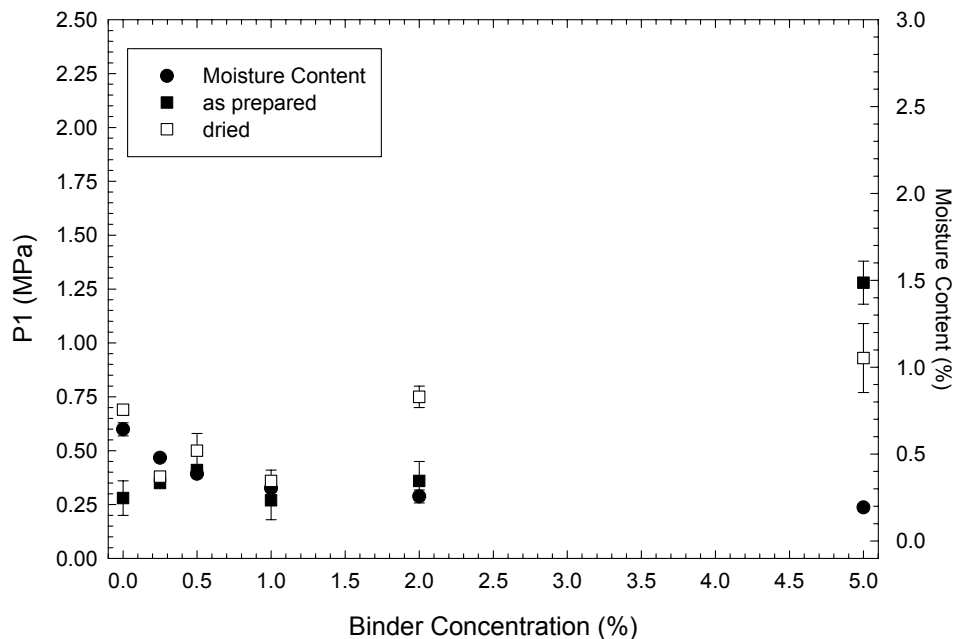


Figure 7-44. Plot of the pressure at the onset of granule deformation (P1) as a function of binder concentration for the as-prepared and dried samples with a 50-50 mix of pPVA and Veegum™ T as a binder. Also plotted is the moisture content as a function of the binder concentration.

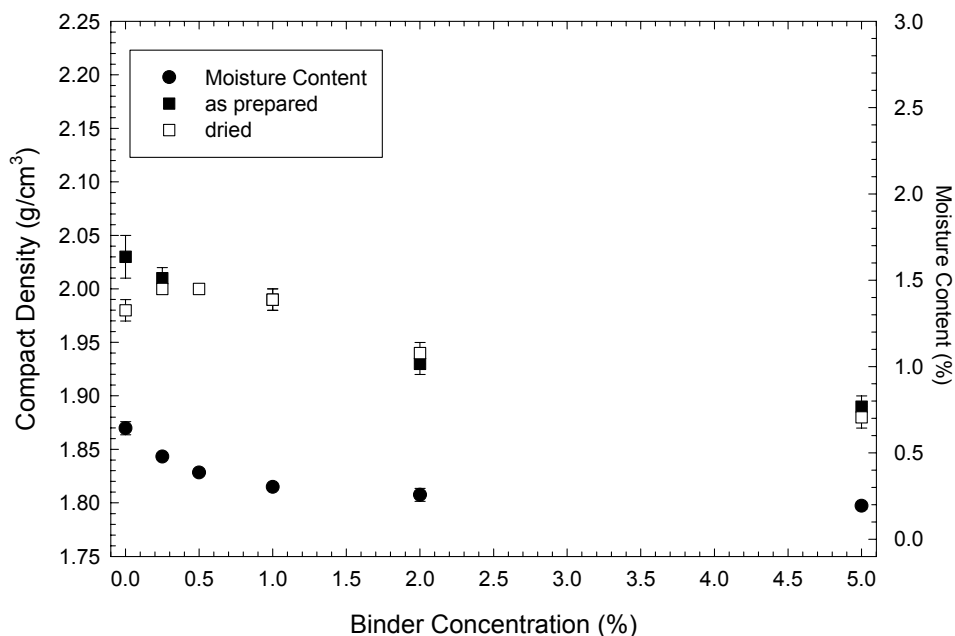


Figure 7-45. Plot of the compact density as a function of binder concentration for the as-prepared and dried samples with a 50-50 mix of pPVA and Veegum™ T as a binder. Also plotted is the moisture content as a function of the binder concentration.

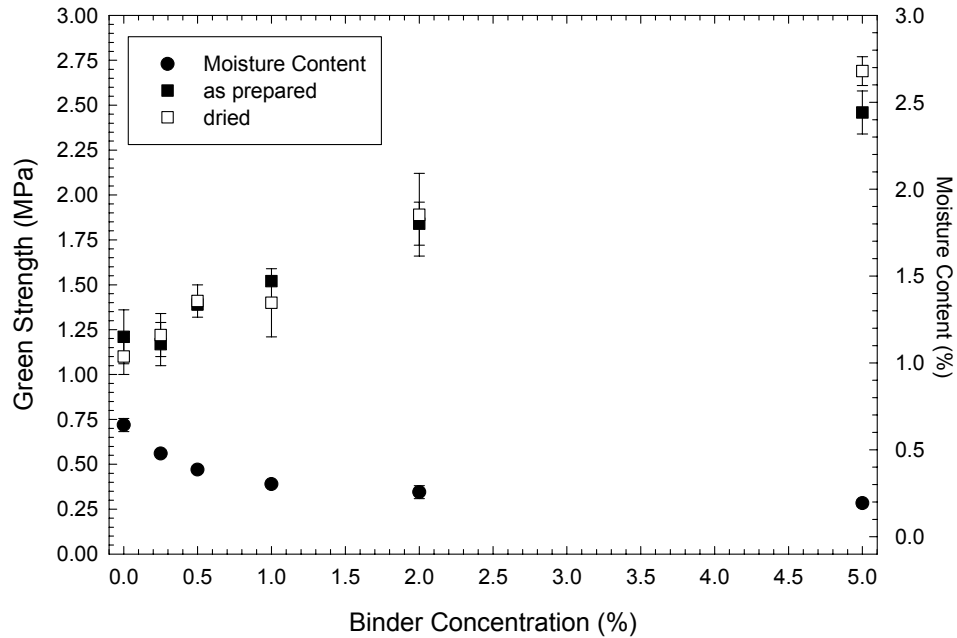


Figure 7-46. Plot of green strength as a function of binder concentration for the as-prepared and dried samples with a 50-50 mix of pPVA and Veegum™ T as a binder. Also plotted is the moisture content as a function of the binder concentration.

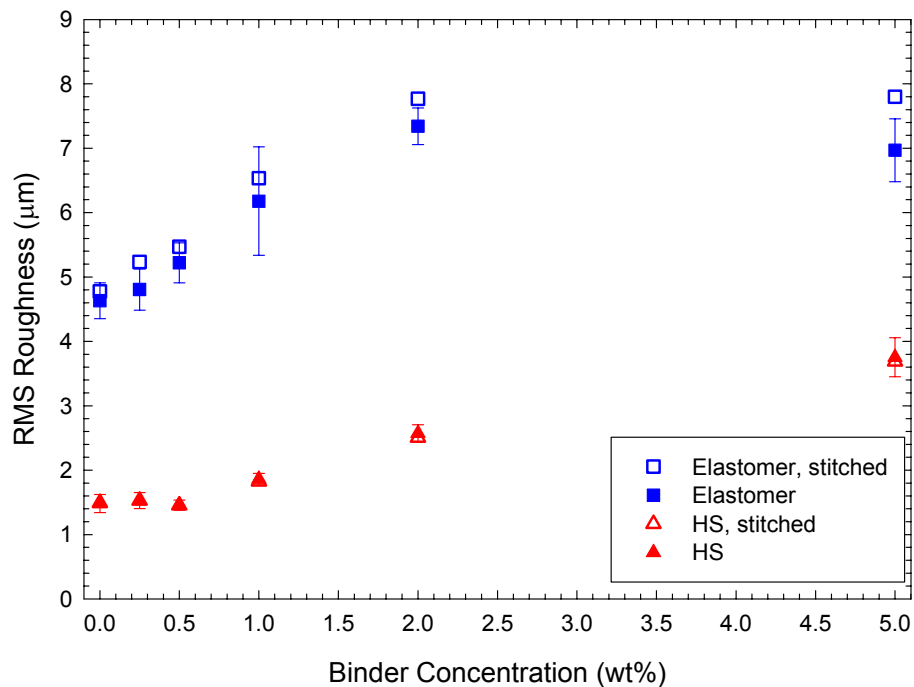


Figure 7-47. Plot of the RMS roughness as a function of binder concentration for samples prepared with a 50-50 mix of pPVA and Veegum™ T as the binder. Samples were only pressed using the as-prepared granulate on the semi-isostatic (squares) and hardened steel (triangles) dies. RMS roughness is plotted for the stitched surface (open symbols) and the averaged data from the individual images (closed symbols) used to create the stitched image.

#### 7.4.4.5 Veegum™ T

The results from the Veegum™ T granulate can be observed in Figure 7-48 (P1), Figure 7-49 (compact density), Figure 7-50 (green strength), and Figure 7-51 (RMS roughness). The results from the 2 wt% hydrolyzed Veegum™ T is plotted in for comparison. The moisture content of the granulate was observed to decrease with increasing binder concentration. P1 was observed to pass through a minimum value at 0.5 wt% binder for the dried samples of granulate and 1 wt% binder for the as-prepared granulate. The P1 values of the dried granulate were observed to exceed those of the as-prepared granulate at high binder concentration, but there was a cross over at approximately 0.5 wt% binder, i.e., the dried granulate was softer at low binder concentrations (below 0.5 wt%). No significant difference was observed in the compact density as a function of binder concentration or between the dried and as-prepared samples of granulate. The green strength of the dried granulate was observed to be significantly higher. The green strength of the as-prepared granulate was observed to be nearly independent of binder concentration, while the dried granulate exhibited a small increase with increasing binder concentration. Overall hydrolyzing the Veegum™ T was not observed to significantly effect the properties of the granulate; the one notable exception was the P1 value for the dried granulate. This indicated that the results obtained for the Veegum™ T granulate were independent of the preparation sequence. It can be deduced from these results that the Veegum™ T was able to fully hydrolyze in the suspension prepared at 30 v/o solids. A small increase was observed in the roughness of both the dinnerware and tile samples with increasing binder concentration. The roughness of the dinnerware samples was significantly higher than that of the tile samples due to the compliant membrane surface. No significant difference was observed in the roughness between the samples that were initially hydrolyzed and those that were not allowed to hydrolyze prior to adding the granulate.

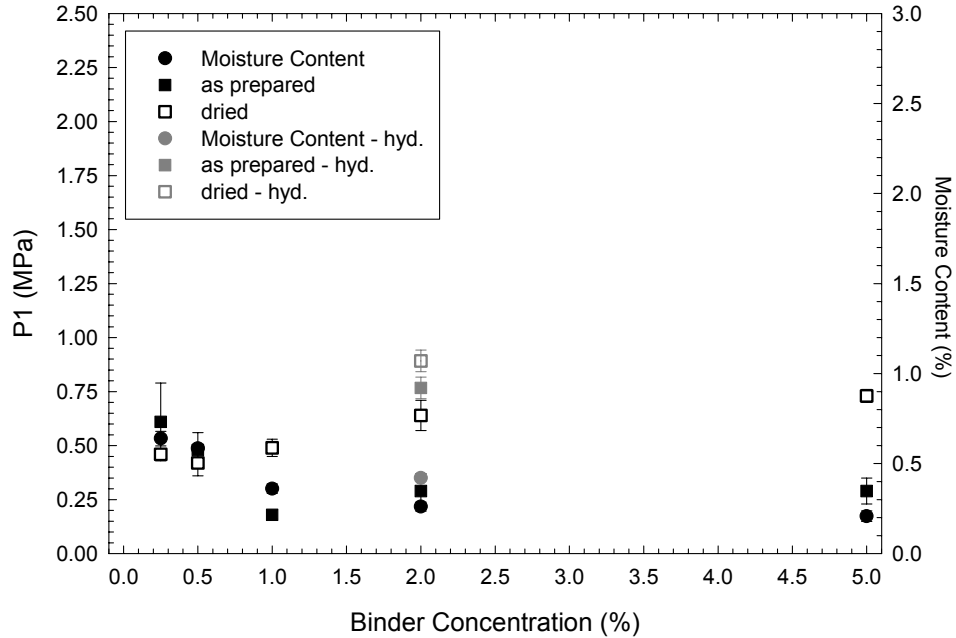


Figure 7-48. Plot of the pressure at the onset of granule deformation (P1) as a function of binder concentration for the as-prepared and dried samples with Veegum™ T as a binder. Plotted in gray are the results for the hydrolyzed Veegum™ T. Also plotted is the moisture content as a function of the binder concentration.

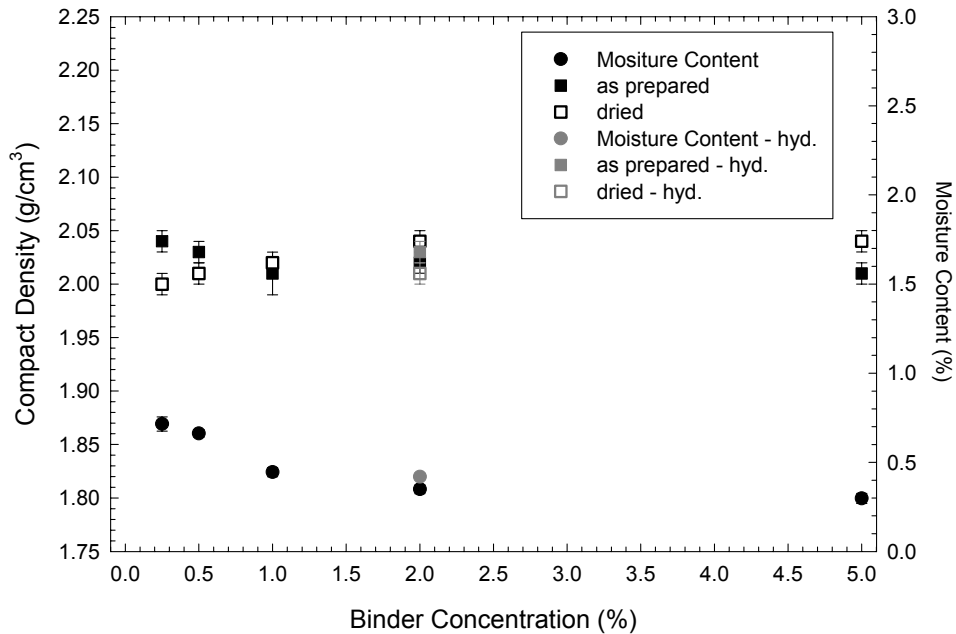


Figure 7-49. Plot of the compact density as a function of binder concentration for the as-prepared and dried samples with Veegum™ T as a binder. Plotted in gray are the results for the hydrolyzed Veegum™ T. Also plotted is the moisture content as a function of the binder concentration.

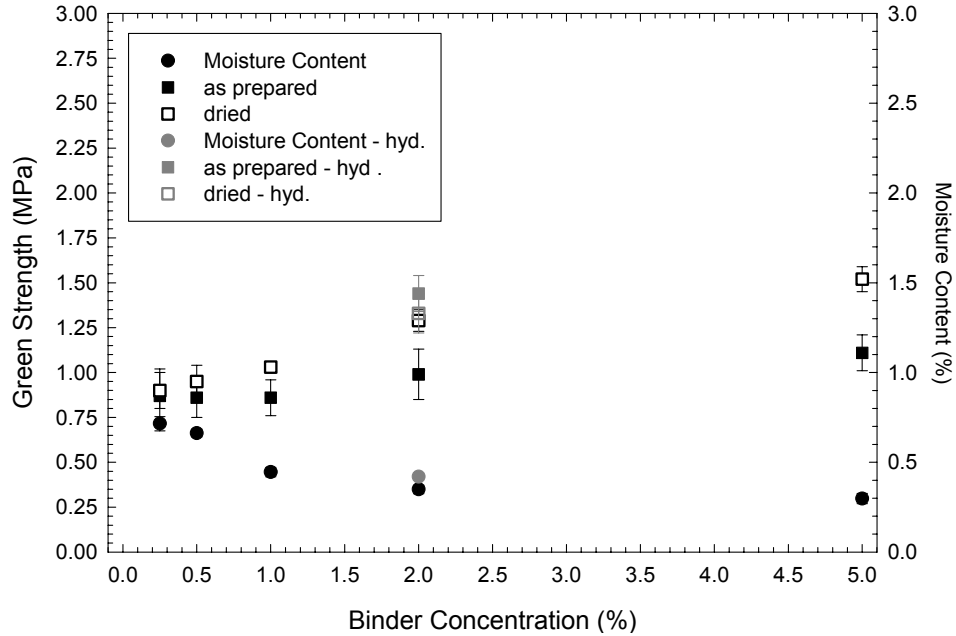


Figure 7-50. Plot of green strength as a function of binder concentration for the as-prepared and dried samples with Veegum™ T as a binder. Plotted in gray are the results for the hydrolyzed Veegum™ T. Also plotted is the moisture content as a function of the binder concentration.

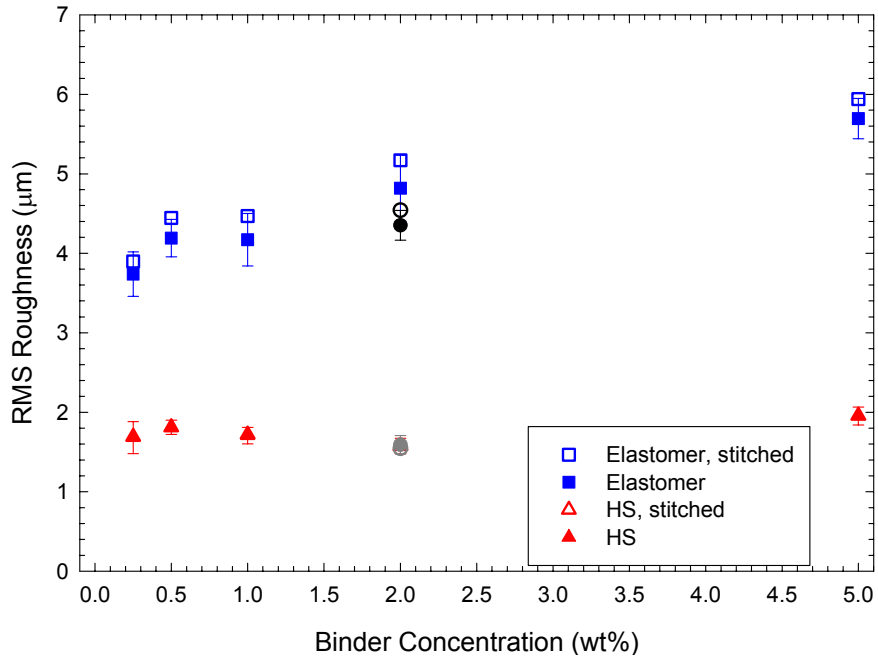


Figure 7-51. Plot of the RMS roughness as a function of binder concentration for samples prepared with Veegum™ T as the binder. Samples were only pressed using the as-prepared granulate on the semi-isostatic (squares) and hardened steel (triangles) dies. RMS roughness is plotted for the stitched surface (open symbols) and the averaged data from the individual images (closed symbols) used to create the stitched image. The results from the hydrolyzed Veegum T are shown in gray and black.

#### 7.4.4.6 Agar

The results from the agar binder system can be observed in Figure 7-52 (P1), Figure 7-53 (compact density), Figure 7-54 (green strength), and Figure 7-55 (RMS roughness). The moisture content of the granulate was observed to increase with higher concentrations of organic, with the maximum value  $18.05 \pm 2.14\%$  at five-weight-percent binder. During compaction of the as-prepared granulate with 5 wt% binder the compact stuck to the steel die despite the use of oleic acid as a lubricant. A drop in P1 was observed between 0.25 and 0.50 wt% binder for both the dried and as-prepared samples. Above 0.50 wt% agar no significant difference was observed in the P1 value. The dried samples were observed to consistently have a higher P1 value when compared to the as-prepared granulate. There was a significant difference in the compact density between the as-prepared and the dried samples below 5 wt% binder. At 5 wt% binder the agar was not completely dissolved during the spray drying process thus affecting the density of the compact; the loss of material that stuck on the die face also reduced the compact density since the samples were no longer perfectly cylindrical. An initial drop was observed in the green strength of the compact between 0.25 and 0.50 wt% agar. The dried samples were observed to plateau in green strength above 0.50 wt% binder while the as-prepared samples were observed to pass through a maximum value of  $2.15 \pm 0.29$  MPa at 2 wt% binder. This maximum value was due the physical water allowing rearrangement of the particles and the agar gel drying to form a binder film surrounding the particle network. Above 2 wt% binder the green strength was observed to decrease due to the undissolved agar. The roughness of the dinnerware samples was initially higher than that of the tile samples due to the compliant membrane surface. At 2 and 5 wt% binder the surface roughness of the tile samples was higher than that of the dinnerware samples. Undissolved agar was apparent to the unaided eye in the surface of both sets of samples. The non-compliant steel surface initially compressed the undissolved agar and upon releasing the load springback caused the agar grains to protrude from the surface. The surface finish of the tile samples between the agar grains was

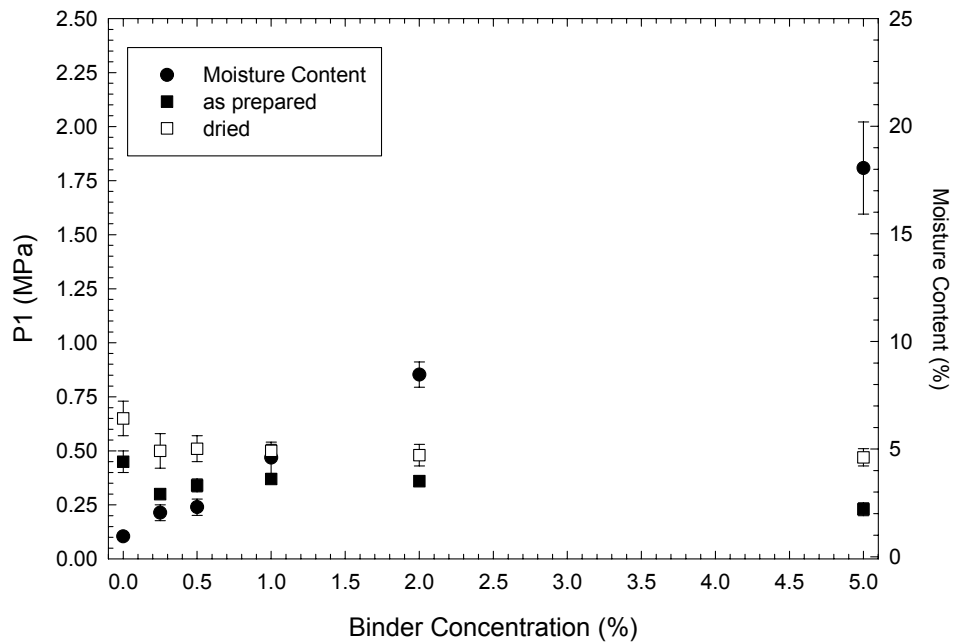


Figure 7-52. Plot of the pressure at the onset of granule deformation (P1) as a function of binder concentration for the as-prepared and dried samples with agar as a binder. Also plotted is the moisture content as a function of the binder concentration.

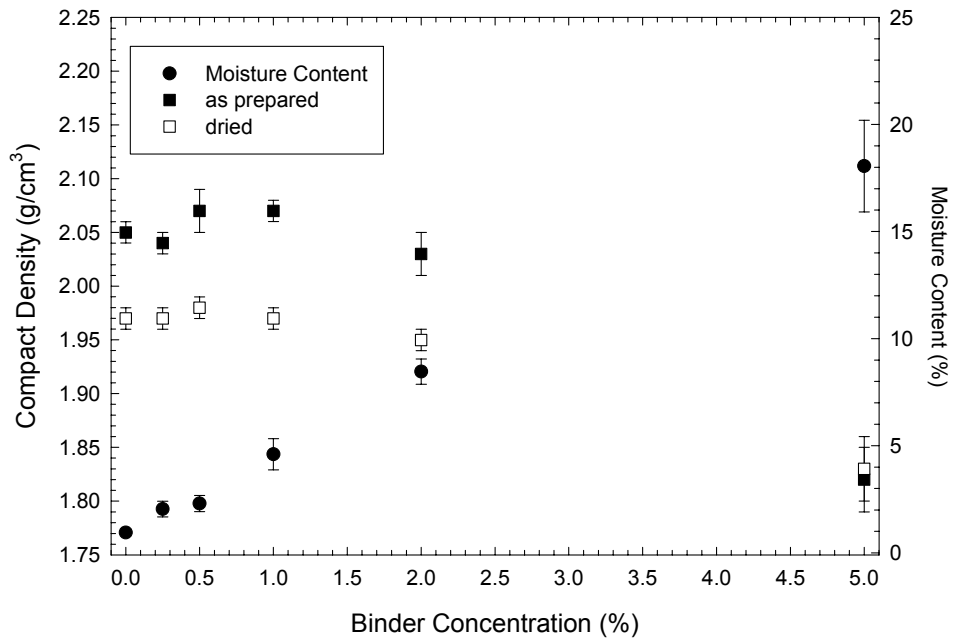


Figure 7-53. Plot of the compact density as a function of binder concentration for the as-prepared and dried samples with agar as a binder. Also plotted is the moisture content as a function of the binder concentration.

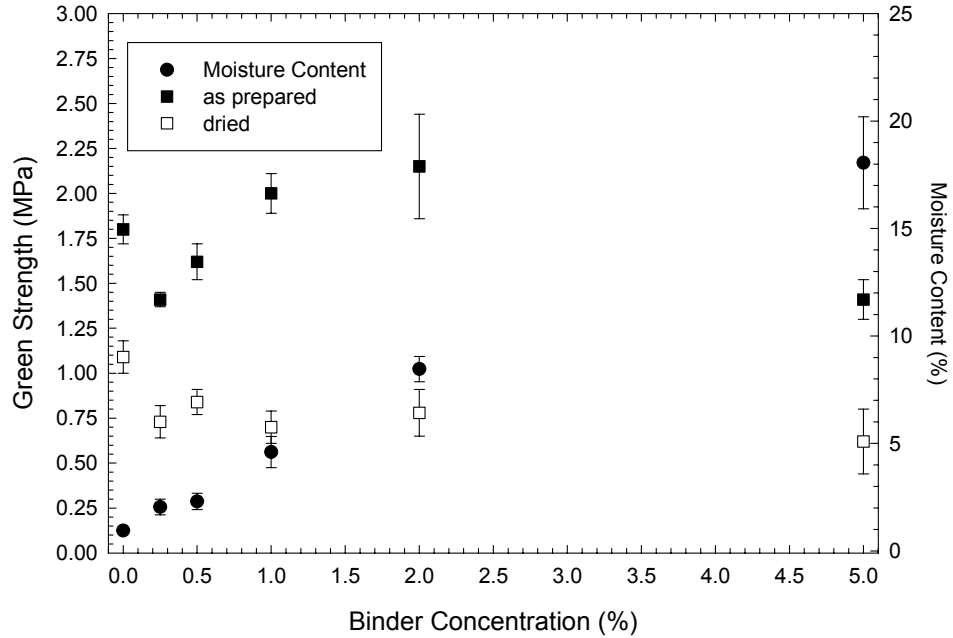


Figure 7-54. Plot of green strength as a function of binder concentration for the as-prepared and dried samples with agar as a binder. Also plotted is the moisture content as a function of the binder concentration.

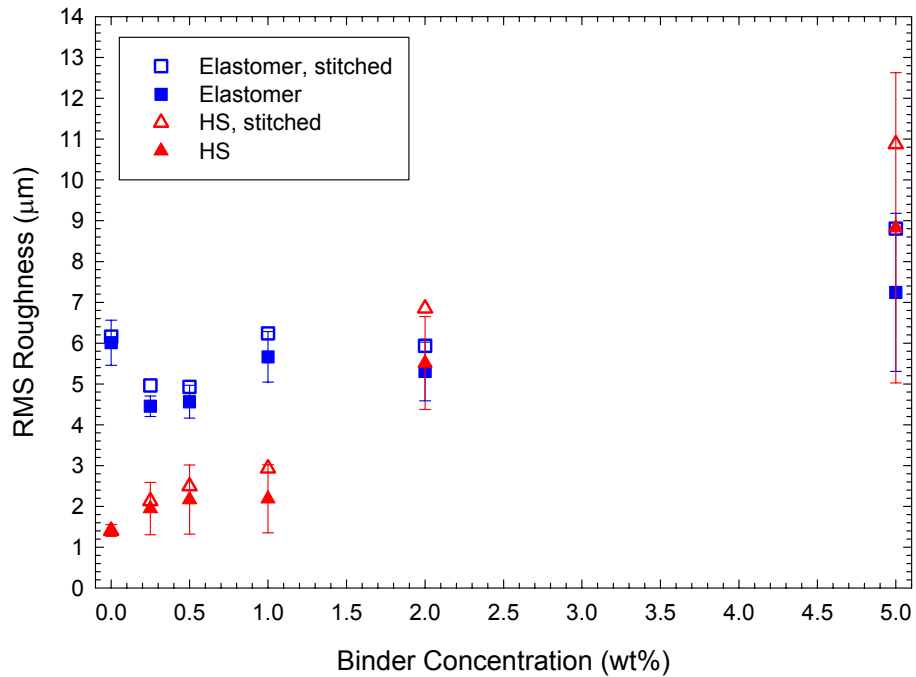


Figure 7-55. Plot of the RMS roughness as a function of binder concentration for samples prepared with agar as the binder. Samples were only pressed using the as-prepared granulate on the semi-isostatic (squares) and hardened steel (triangles) dies. RMS roughness is plotted for the stitched surface (open symbols) and the averaged data from the individual images (closed symbols) used to create the stitched image.

observed to be smooth. The roughness of the dinnerware samples was observed to initially decrease, as deformation of the granulate was assisted by the physical water trapped in the binder gel, followed by an increase in the measured roughness. Higher error was observed in the averaged RMS roughness at 2 and 5 wt% binder for both the dinnerware and tile samples. Little difference was observed between the stitched and the averaged RMS roughness for both the dinnerware and tile samples at the lower binder concentrations. A significant difference was observed at 2 and 5 wt% binder due to the presence of the undissolved agar at the surface. The spray-dried agar granulate appeared to be stable during storage for four months in a sealed container; all material was used within four months of preparing the granulate. There was no indication of the growth of a secondary organic in the spray-dried granulate despite the trapped physical water in the organic gelatin.

#### *7.4.4.7 Acrylic Latex Emulsion*

The results from the B-1080 granulate can be observed in Figure 7-56 (P1), Figure 7-57 (compact density), Figure 7-58 (green strength), and Figure 7-59 (RMS roughness). The moisture content of the granulate was observed to increase with higher binder concentrations with a significant increase between 2 and 5 wt% binder. P1 of the dried samples was observed to increase with increasing binder concentration; there was an anomaly at 0.50 wt% binder where P1 was observed to be significantly higher. P1 of the as-prepared granulate was observed to pass through a maximum at 2 wt% binder. The drop in the P1 value at 5 wt% binder was due to physical moisture in the sample plasticizing the binder; also the latex had not dried to a film prior to compaction in these samples. No significant difference was observed in the compact density as a function of binder concentration and no significant difference was observed between the as-prepared samples and the dried granulate. The green strength of the samples was observed to increase with increasing binder concentration. Above 2 wt% binder the as-prepared samples showed a decrease in strength while the dried samples appeared to reach a plateau value. The roughness of the dinnerware samples was observed to be significantly higher than that of the tile samples due

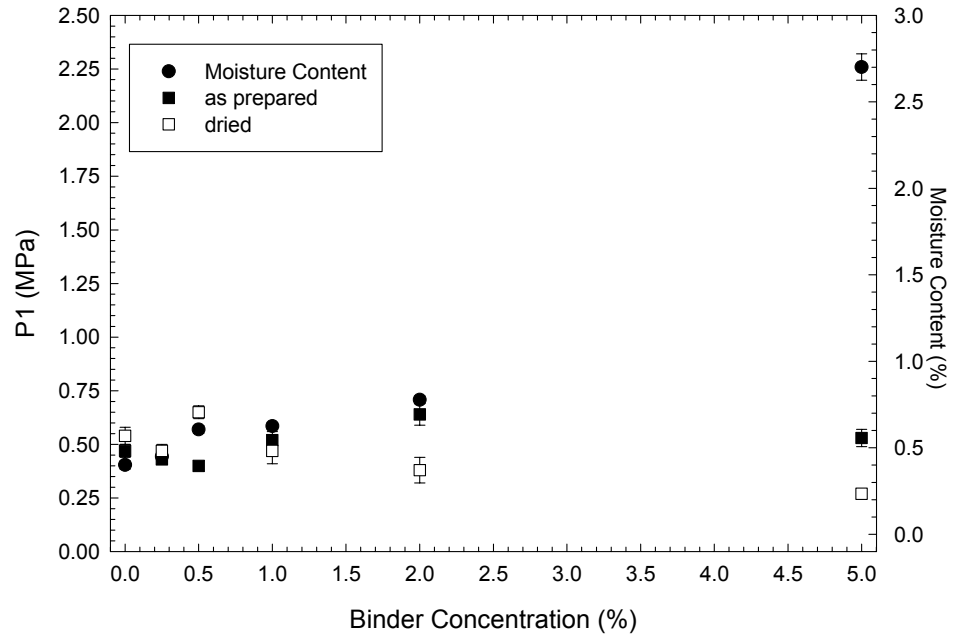


Figure 7-56. Plot of the pressure at the onset of granule deformation (P1) as a function of binder concentration for the as-prepared and dried samples with acrylic latex as a binder. Also plotted is the moisture content as a function of the binder concentration.

Figure 7-57. Plot of the compact density as a function of binder concentration for the as-prepared and dried samples with acrylic latex as a binder. Also plotted is the moisture content as a function of the binder concentration.

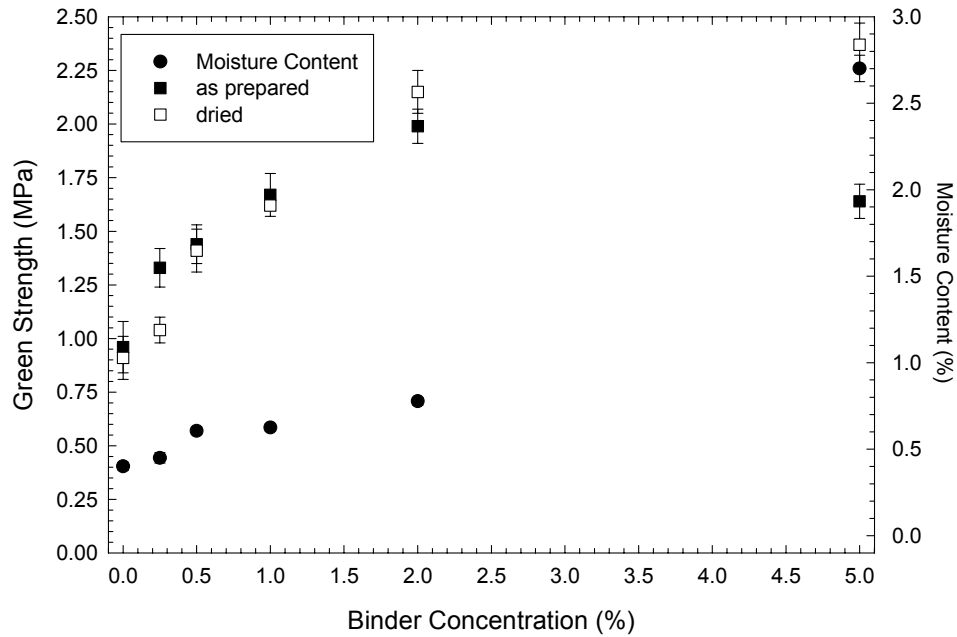


Figure 7-58. Plot of green strength as a function of binder concentration for the as-prepared and dried samples with acrylic latex as a binder. Also plotted is the moisture content as a function of the binder concentration.

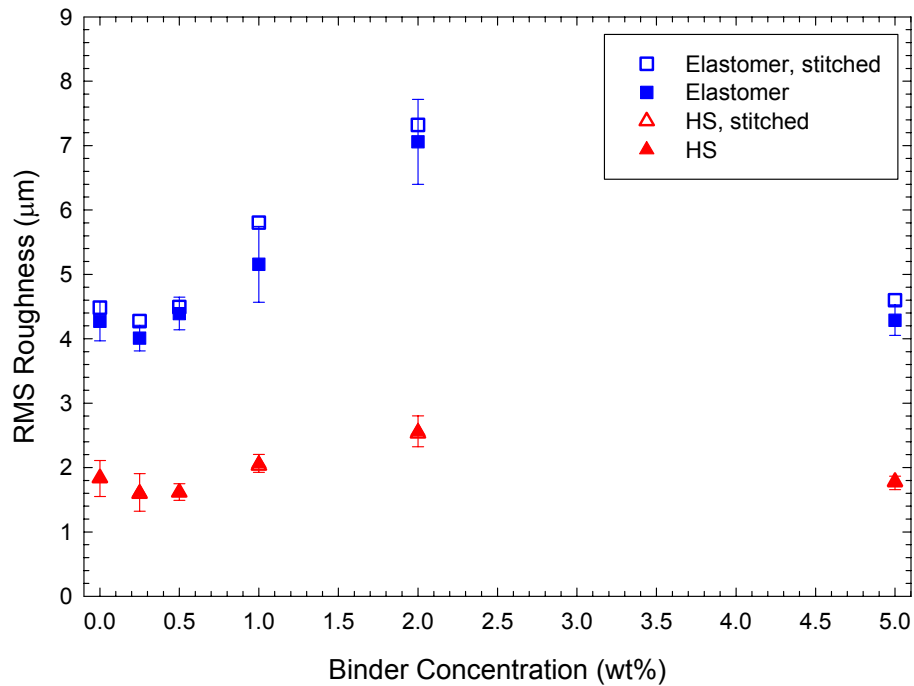


Figure 7-59. Plot of the RMS roughness as a function of binder concentration for samples prepared with acrylic latex as the binder. Samples were only pressed using the as-prepared granulate on the semi-isostatic (squares) and hardened steel (triangles) dies. RMS roughness is plotted for the stitched surface (open symbols) and the averaged data from the individual images (closed symbols) used to create the stitched image.

to the compliant membrane surface. The roughness of both the dinnerware and tile samples was observed to increase up to 2 wt% binder. Above 2 wt% there was a significant decrease in the measured roughness due to the higher moisture content of the granulate which aided the deformation. Little difference was observed between the stitched and the averaged RMS roughness for both the dinnerware and tile samples.

#### *7.4.4.8 Starch*

The results for the starch granulate can be observed in Figure 7-60 (P1), Figure 7-61 (compact density), Figure 7-62 (green strength), and Figure 7-63 (RMS roughness). The moisture content of the granulate was observed to be low and moisture content decreased with increasing binder concentration. P1 of the as-prepared samples was observed to decrease slightly followed by an increase above 0.50 wt% binder. There was more scatter in the dried sample data, but a minimum was observed around 2 wt% binder for the samples that were dried prior to compaction. No significant difference was observed in compact density between the dried and as-prepared samples. There was a decreasing trend in the compact density with increasing binder concentration for both sets of samples. There was no significant difference in the green strength between the as-prepared and dried samples. There was a slight decrease in the green strength of the as-prepared samples with increasing binder concentration. The roughness of the dinnerware samples was observed to be significantly higher than that of the tile samples due to the compliant membrane surface. No significant variation was observed in the measured roughness with increasing binder concentration.

#### *7.4.4.9 Sugar (Alpha-D(+)-Glucose)*

The results from the granulate prepared with sugar as a binder system can be observed in Figure 7-64 (P1), Figure 7-65 (compact density), Figure 7-66 (green strength), and Figure 7-67 (RMS roughness). The moisture content of the granulate was observed to increase slightly with increasing binder concentration. It was unknown to what extent the sugar decomposed during the spray-drying process. The P1 values for the as-prepared granulate contained significant

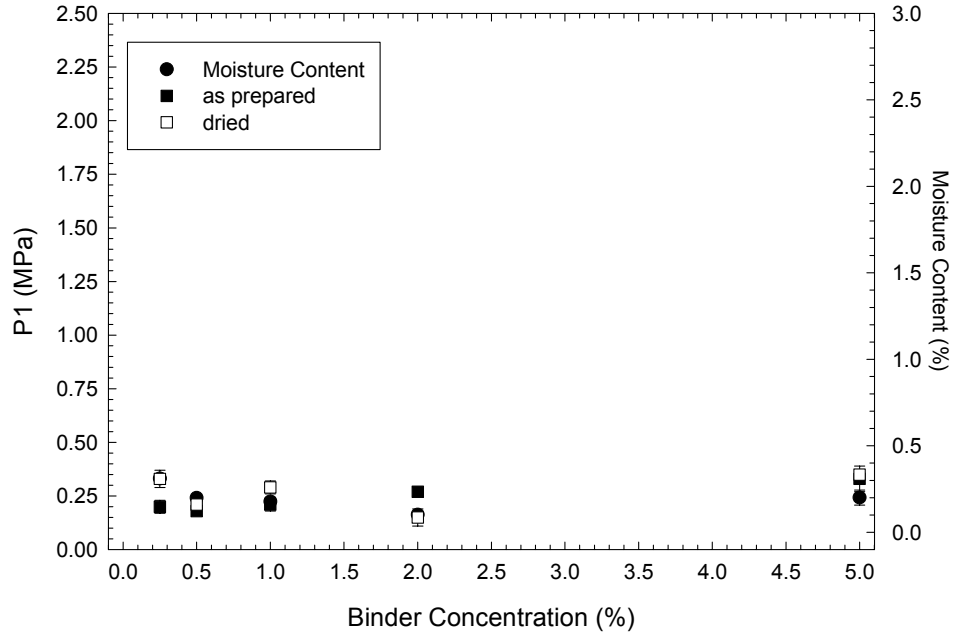


Figure 7-60. Plot of the pressure at the onset of granule deformation (P1) as a function of binder concentration for the as-prepared and dried samples with starch as a binder. Also plotted is the moisture content as a function of the binder concentration.

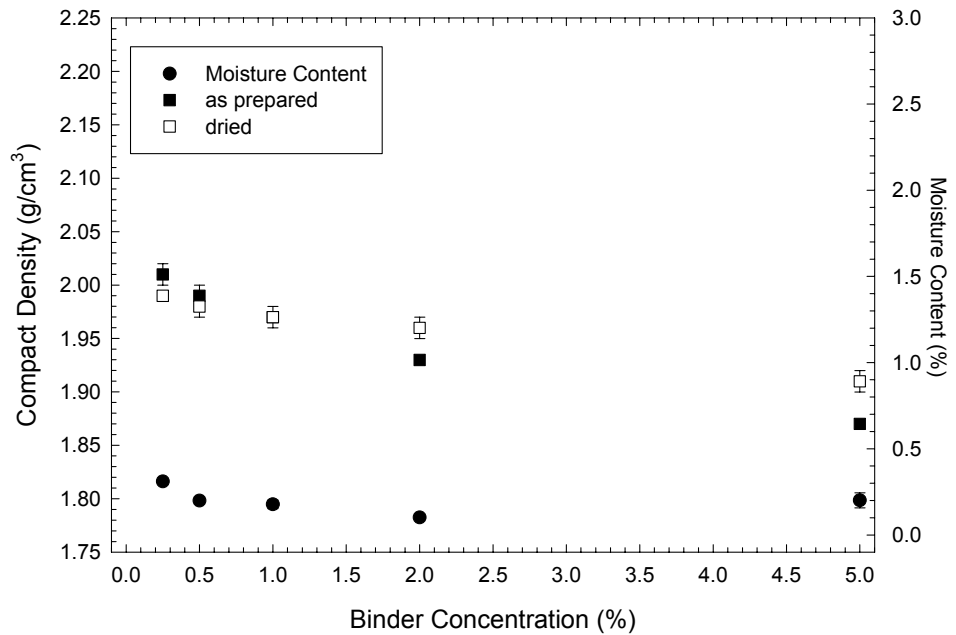


Figure 7-61. Plot of the compact density as a function of binder concentration for the as-prepared and dried samples with starch as a binder. Also plotted is the moisture content as a function of the binder concentration.

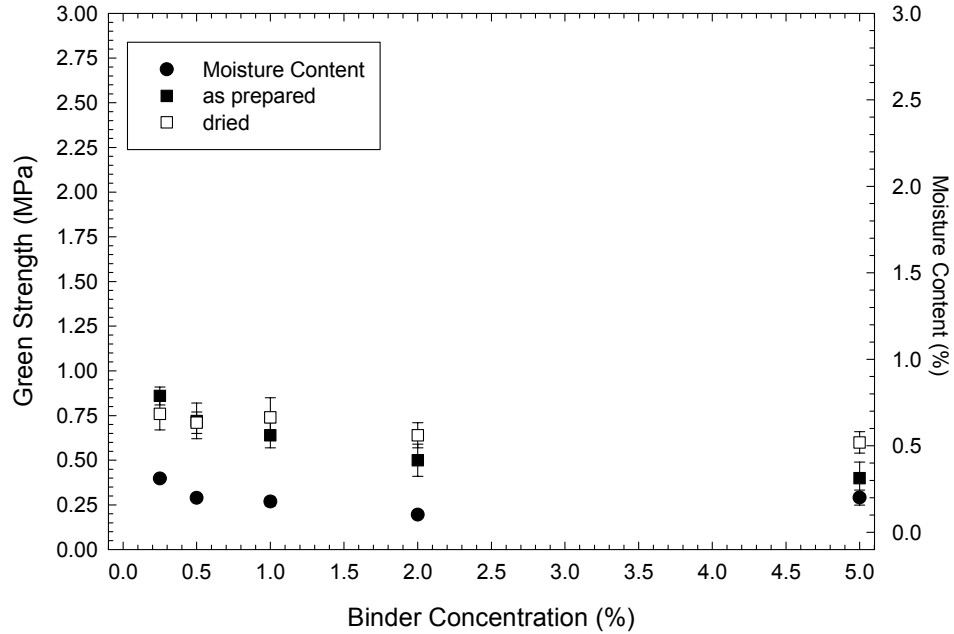


Figure 7-62. Plot of green strength as a function of binder concentration for the as-prepared and dried samples with starch as a binder. Also plotted is the moisture content as a function of the binder concentration.

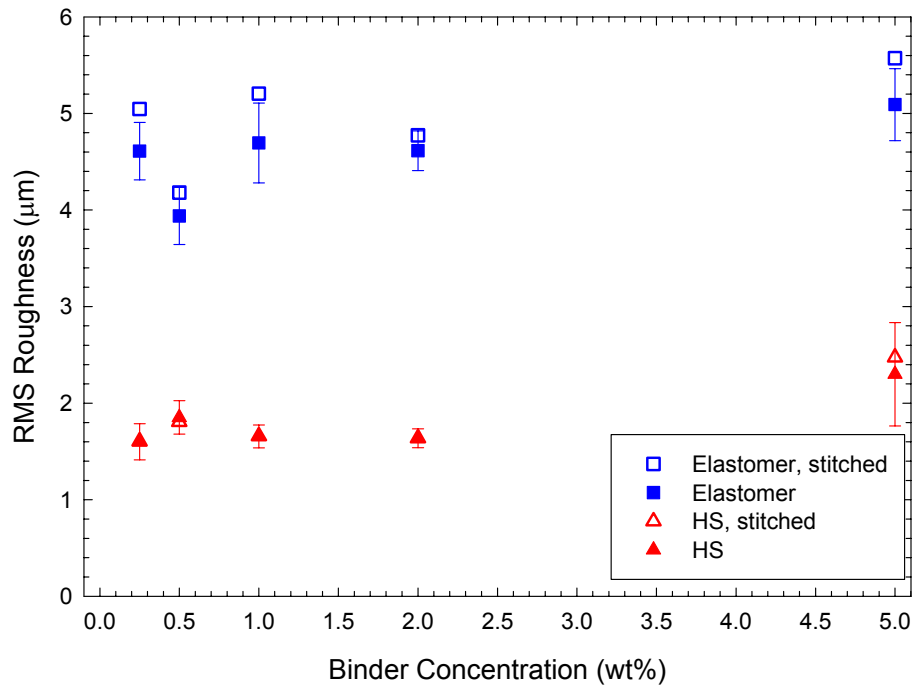


Figure 7-63. Plot of the RMS roughness as a function of binder concentration for samples prepared with starch as the binder. Samples were only pressed using the as-prepared granulate on the semi-isostatic (squares) and hardened steel (triangles) dies. RMS roughness is plotted for the stitched surface (open symbols) and the averaged data from the individual images (closed symbols) used to create the stitched image.

amounts of scatter. No P1 value could be determined at 5 wt% binder for the as-prepared samples; no peak was observed in the second derivative of the curve. The dried samples passed through a minimum value at 0.5 wt% binder followed by an increase to a plateau value at 1 wt% binder. The compact density was observed to remain nearly constant for the dried samples with increasing binder concentration. The compact density of the as-prepared samples was observed to decrease slightly with increasing binder concentration. This might have been due to the degradation of the sugar to form a caramel-like substance. The green strength of the compacts prepared with sugar increased with increasing binder concentration. The strength of the samples prepared with granulate that was dried prior to compaction overall exhibited higher strengths than those made with the as-prepared granulate. The roughness of the dinnerware samples was observed to be higher than that of the tile samples due to the compliant membrane surface. Roughness was observed to increase with increasing binder concentration. No significant difference was observed between the stitched and the averaged RMS roughness for the dinnerware or tile samples.

#### *7.4.4.10 Methyl Cellulose*

The results from the methyl cellulose granulate are shown in Figure 7-68 (P1), Figure 7-69 (compact density), Figure 7-70 (green strength), and Figure 7-71 (RMS roughness). The moisture content of the granulate was again observed to decrease with increasing binder concentration, this was likely due to the porous structure of the granulate and the thermal gelling of the cellulose. The outlet temperature was observed to increase during the spray-drying process due to the thermal gelling of the binder, see Appendix G. P1 of the dried samples was observed to be nearly independent of binder concentration. The P1 of the as-prepared granulate was observed to slightly decrease with increasing binder concentration. There was no significant change in the compact density with binder concentration and no significant difference was observed between the as-prepared and the dried granulate. The green strength of the dried granulate was observed to increase almost linearly with increasing binder concentration. The green strength of the as-prepared granulate was also observed to increase with

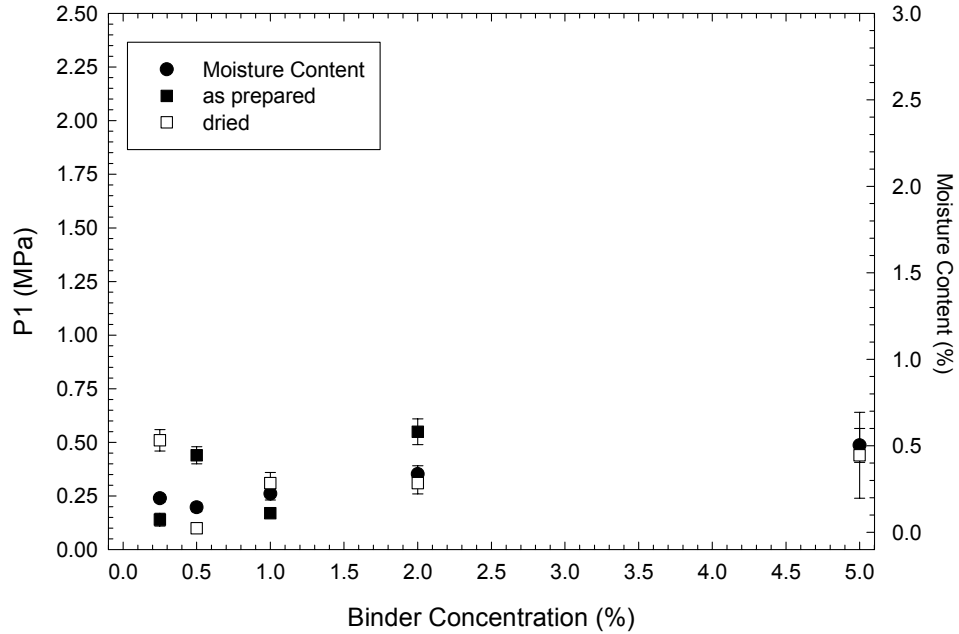


Figure 7-64. Plot of the pressure at the onset of granule deformation (P1) as a function of binder concentration for the as-prepared and dried samples with sugar as a binder. Also plotted is the moisture content as a function of the binder concentration.

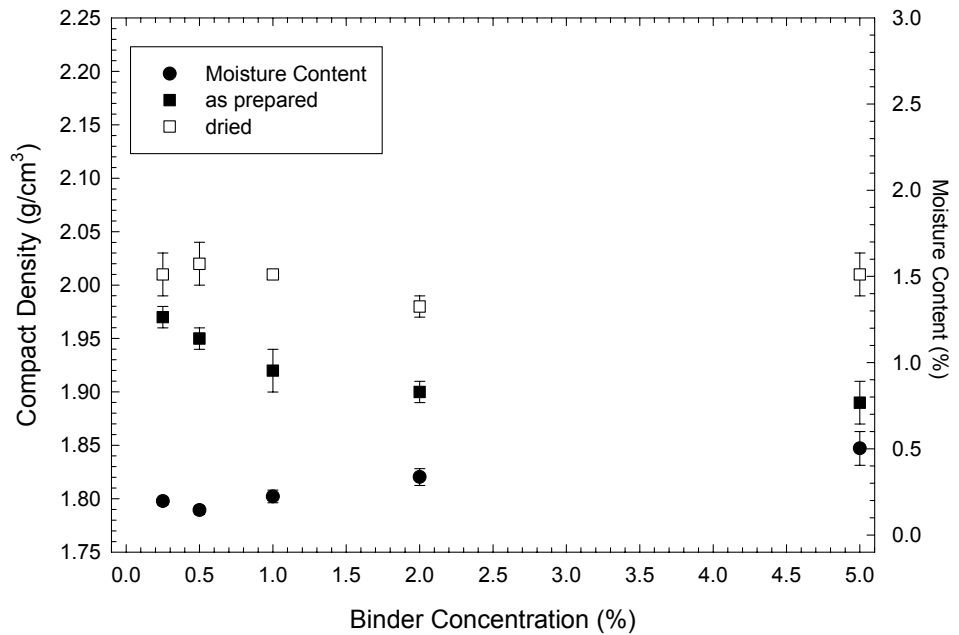


Figure 7-65. Plot of the compact density as a function of binder concentration for the as-prepared and dried samples with sugar as a binder. Also plotted is the moisture content as a function of the binder concentration.

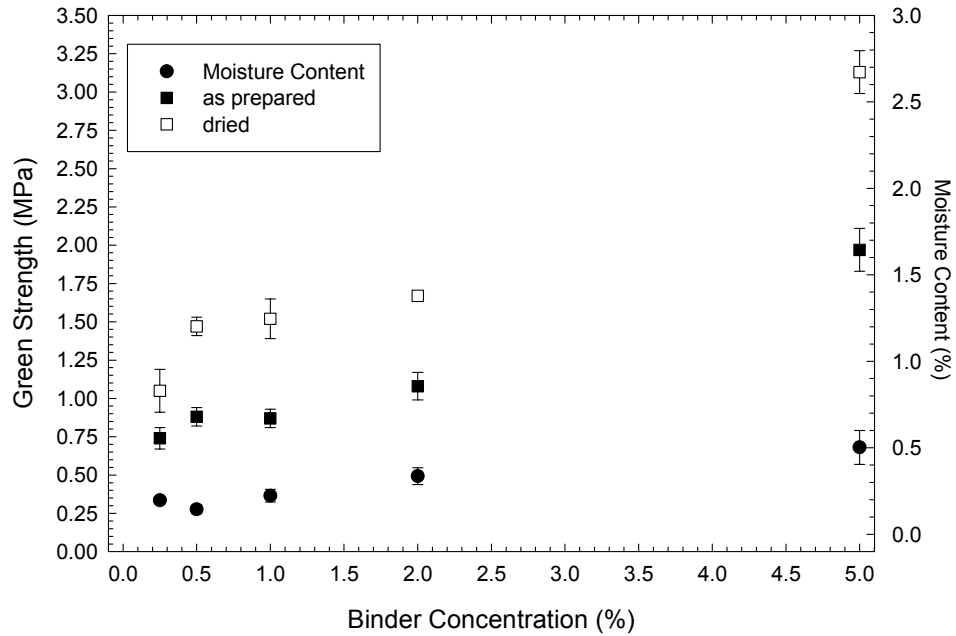


Figure 7-66. Plot of green strength as a function of binder concentration for the as-prepared and dried samples with sugar as a binder. Also plotted is the moisture content as a function of the binder concentration.

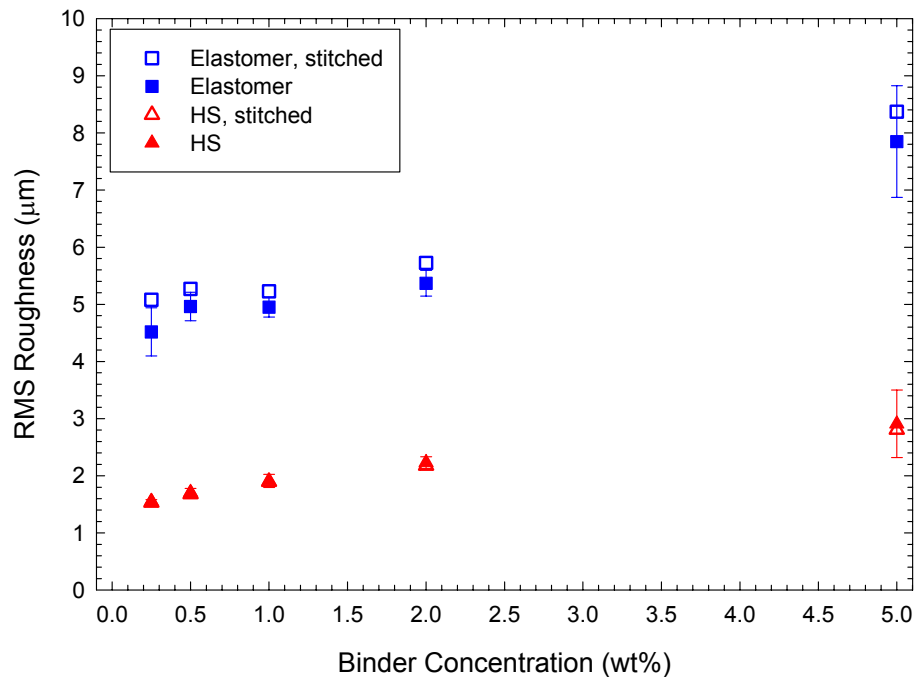


Figure 7-67. Plot of the RMS roughness as a function of binder concentration for samples prepared with sugar as the binder. Samples were only pressed using the as-prepared granulate on the semi-isostatic (squares) and hardened steel (triangles) dies. RMS roughness is plotted for the stitched surface (open symbols) and the averaged data from the individual images (closed symbols) used to create the stitched image.

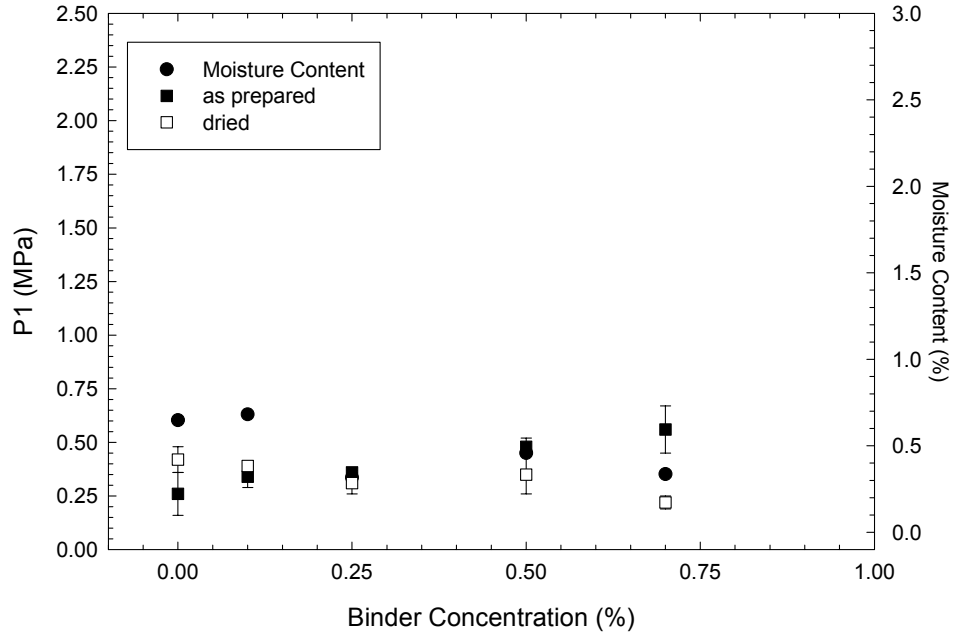


Figure 7-68. Plot of the pressure at the onset of granule deformation (P1) as a function of binder concentration for the as-prepared and dried samples with methyl cellulose as a binder. Also plotted is the moisture content as a function of the binder concentration.

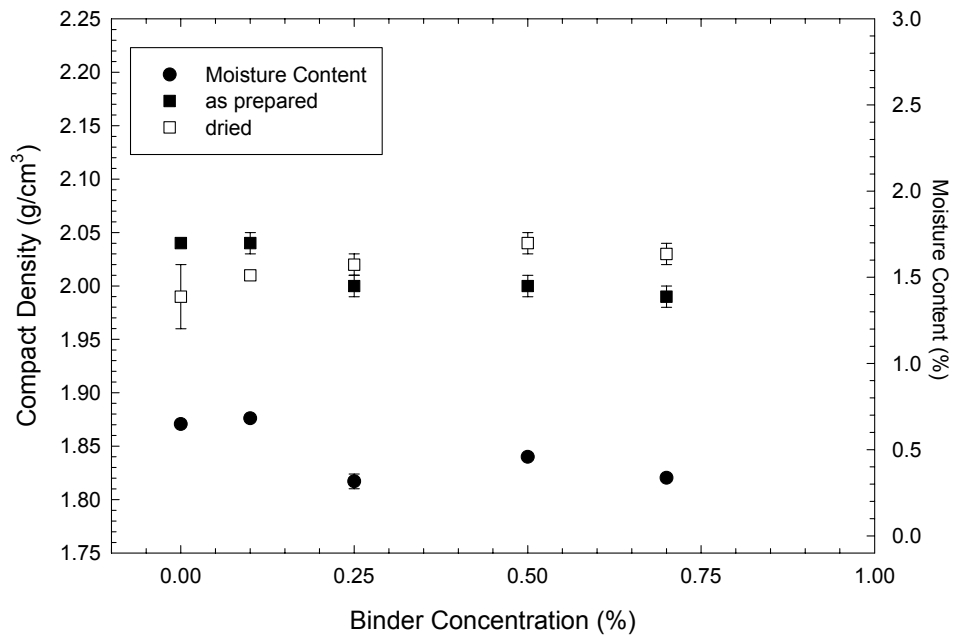


Figure 7-69. Plot of the compact density as a function of binder concentration for the as-prepared and dried samples with methyl cellulose as a binder. Also plotted is the moisture content as a function of the binder concentration.

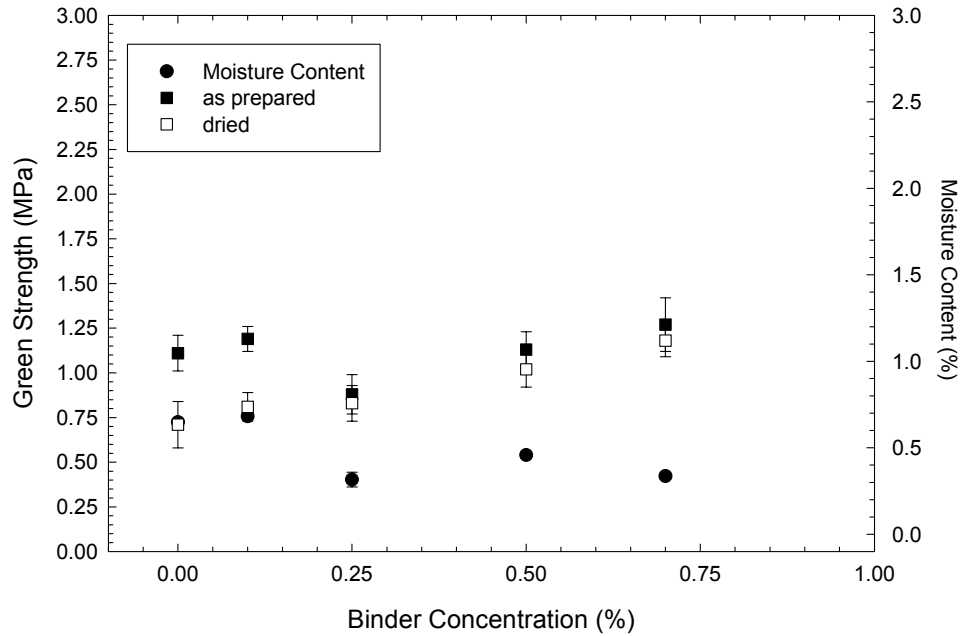


Figure 7-70. Plot of green strength as a function of binder concentration for the as-prepared and dried samples with methyl cellulose as a binder. Also plotted is the moisture content as a function of the binder concentration.

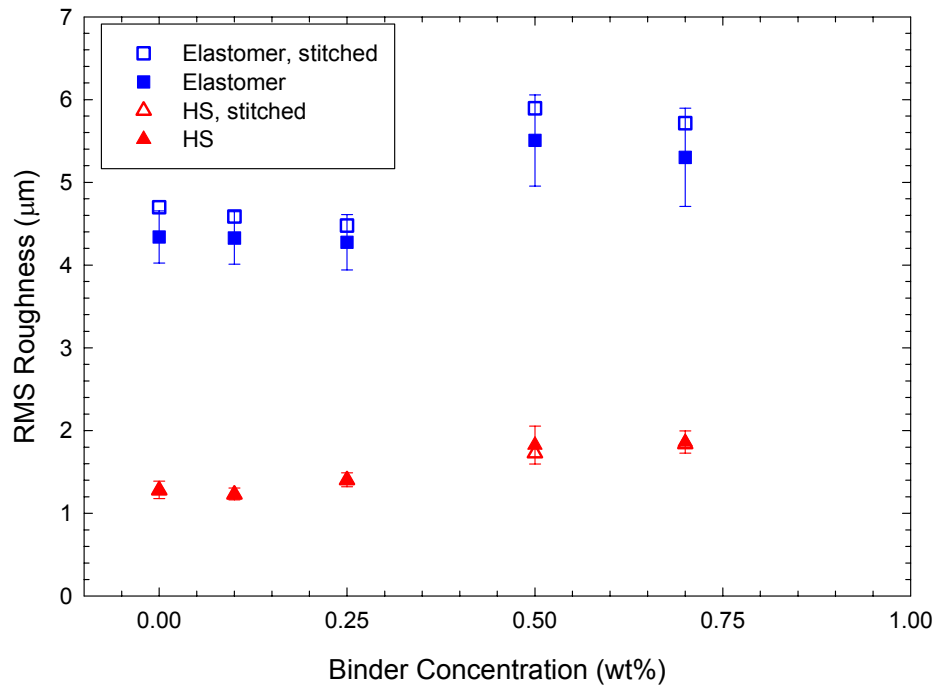


Figure 7-71. Plot of the RMS roughness as a function of binder concentration for samples prepared with methyl cellulose as the binder. Samples were only pressed using the as-prepared granulate on the semi-isostatic (squares) and hardened steel (triangles) dies. RMS roughness is plotted for the stitched surface (open symbols) and the averaged data from the individual images (closed symbols) used to create the stitched image.

binder concentration, but there was a decrease between 0.1 and 0.25 wt% binder; this was likely to be due to the decrease in the moisture content of the granulate. Above 0.25 wt% binder the green strength of the two sets of data were observed to nearly overlap. The roughness of the dinnerware samples was observed to be significantly higher than that of the tile samples due to the compliant membrane surface. A small increase was observed in the measured roughness with increasing binder concentration.

#### *7.4.4.11 Carboxymethyl Cellulose*

The results from the carboxymethyl cellulose binder system can be observed in Figure 7-72 (P1), Figure 7-73 (compact density), Figure 7-74 (green strength), and Figure 7-75 (RMS roughness). The moisture content of the samples was observed to decrease with increasing binder concentration due to the thermal gelling of the binder in the spray dryer; the thermal gelling resulted in more porous granulate which dried faster. The outlet temperature was also observed to increase with increasing binder concentration due to the increase in viscosity of the suspension due to thermal gelling. P1 was observed to increase with higher binder concentrations. There were again anomalous points in the data. The dried samples were also observed to have an overall higher P1 value compared to the as-prepared granulate. A decrease in compact density was observed with increasing binder concentration. This was due to the porous structure of the granulate as indicated by the low fill density; this data will be reported in the summary discussion. The green strength of the compacts was observed to increase with binder concentration and the dried samples were observed to be slightly stronger than the as-prepared samples. The roughness of the dinnerware samples was significantly higher than that of the tile samples due to the compliant membrane surface. A dinnerware sample was not pressed at 0.7 wt% binder due to a lack of granulate, a result of the thermal gelation of the suspension during the spray drying process. A maximum was observed in the RMS roughness of the dinnerware samples at 0.25 wt% binder, a similar trend was observed in the P1 value of the dried granulate. Little variation was

observed in the roughness of the tile samples with increasing binder concentration.

#### 7.4.4.12 *Veegum™ T / Vanzan™ D*

The results for the *Veegum™ T/Vanzan™ D* granulate are shown in Figure 7-76 (P1), Figure 7-77 (compact density), Figure 7-78 (green strength), and Figure 7-79 (RMS roughness). The moisture content of the granulate was observed to slightly increase with increasing binder concentration. The P1 value of the *Veegum™ T/Vanzan™ D* binder system was observed to increase with increasing binder concentration for both the as-prepared and the dried granulate. The dried granulate was observed to have a slightly higher P1 value compared to the as-prepared granulate. The compact density of the as-prepared samples was observed to slightly increase with increasing binder concentration. The density of the dried samples was independent of the binder concentration. Overall the green strength of the *Veegum™ T/Vanzan™ D* samples increased with increasing binder concentration, within the range studied. The dried samples showed a plateau in the green strength above 1 wt% binder. The as-prepared samples showed an initial decrease in the green strength followed by a significant increase in the green strength above 0.25 wt% binder. The roughness of the dinnerware samples was significantly higher than that of the tiles samples due to the compliant membrane surface. The stitched RMS roughness of the dinnerware samples was observed to plateau above 0.5 wt% binder while the averaged RMS roughness was observed to pass through a maximum. This difference in behavior was the result of long-range roughness, the waviness, which was taken into consideration in the stitched roughness. A small increase was observed in the roughness of the tile samples with increasing binder concentration.

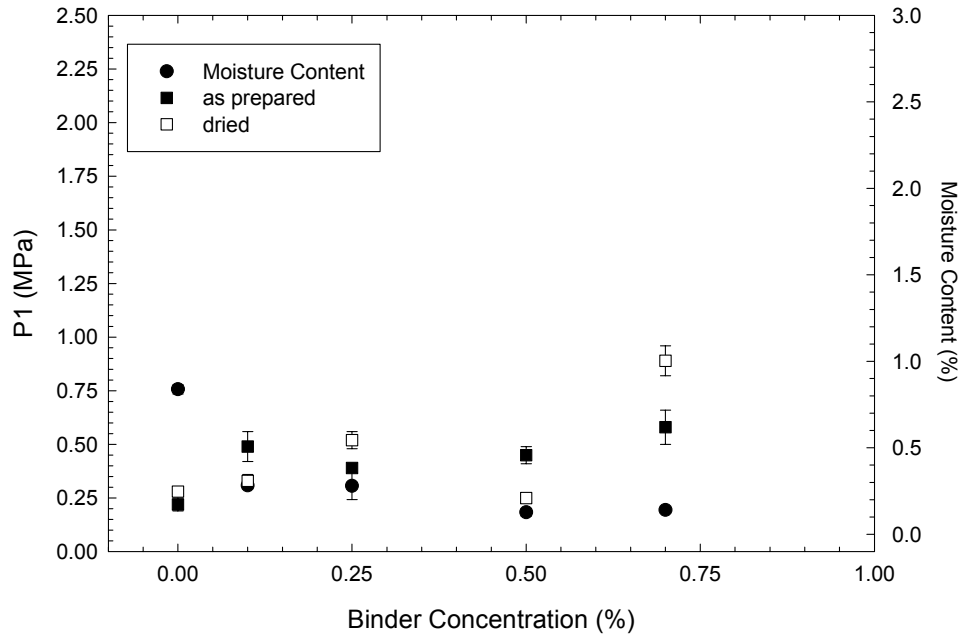


Figure 7-72. Plot of the pressure at the onset of granule deformation (P1) as a function of binder concentration for the as-prepared and dried samples with carboxymethyl cellulose as a binder. Also plotted is the moisture content as a function of the binder concentration.

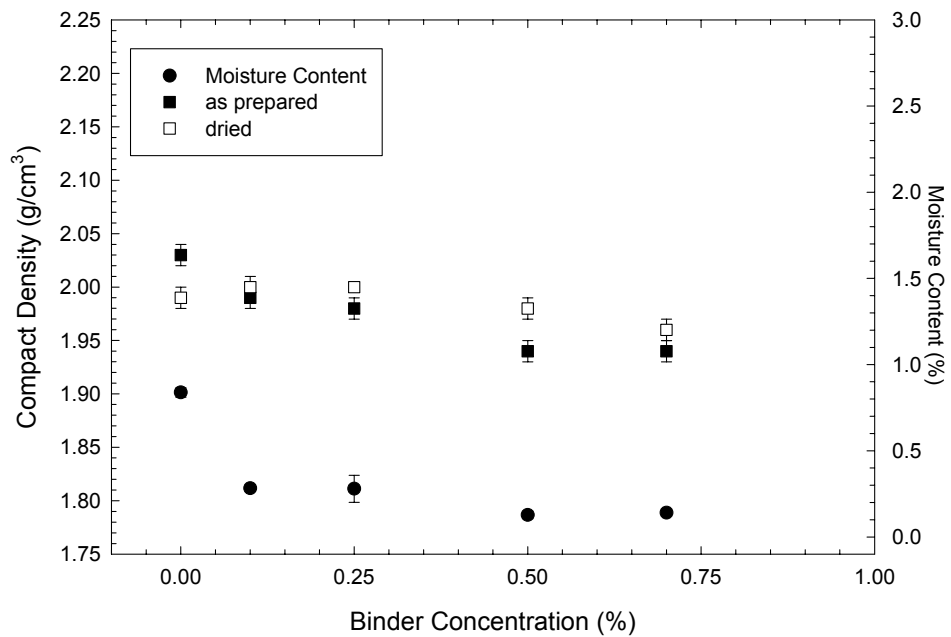


Figure 7-73. Plot of the compact density as a function of binder concentration for the as-prepared and dried samples with carboxymethyl cellulose as a binder. Also plotted is the moisture content as a function of the binder concentration.

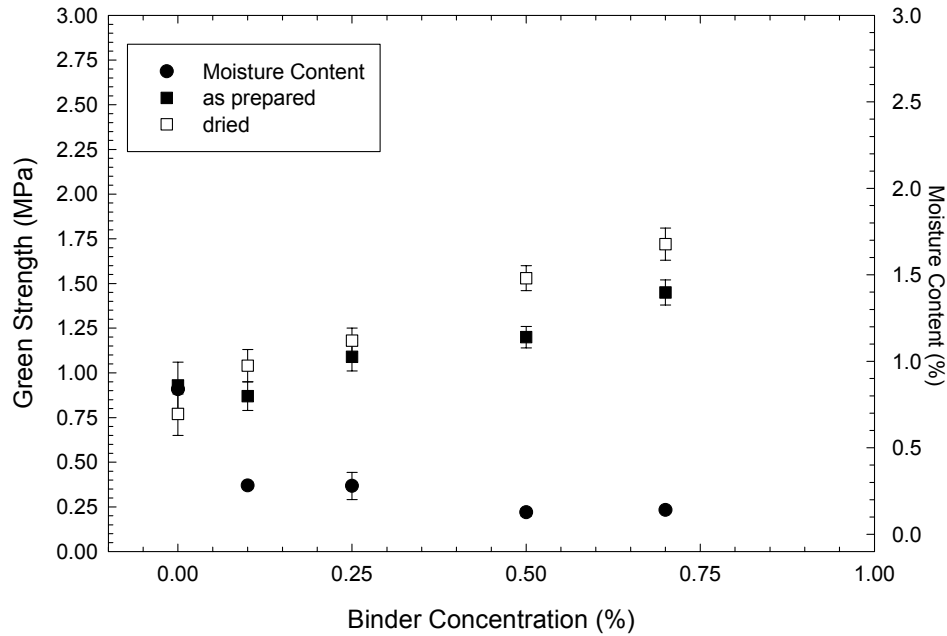


Figure 7-74. Plot of green strength as a function of binder concentration for the as-prepared and dried samples with carboxymethyl cellulose as a binder. Also plotted is the moisture content as a function of the binder concentration.

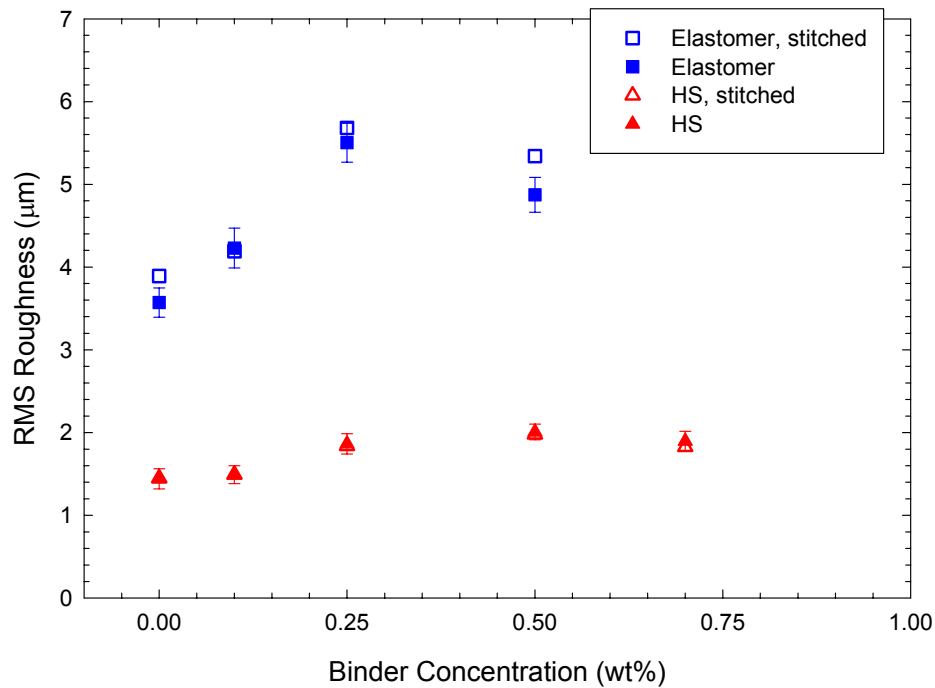


Figure 7-75. Plot of the RMS roughness as a function of binder concentration for samples prepared with carboxymethyl cellulose as the binder. Samples were only pressed using the as-prepared granulate on the semi-isostatic (squares) and hardened steel (triangles) dies. RMS roughness is plotted for the stitched surface (open symbols) and the averaged data from the individual images (closed symbols) used to create the stitched image.

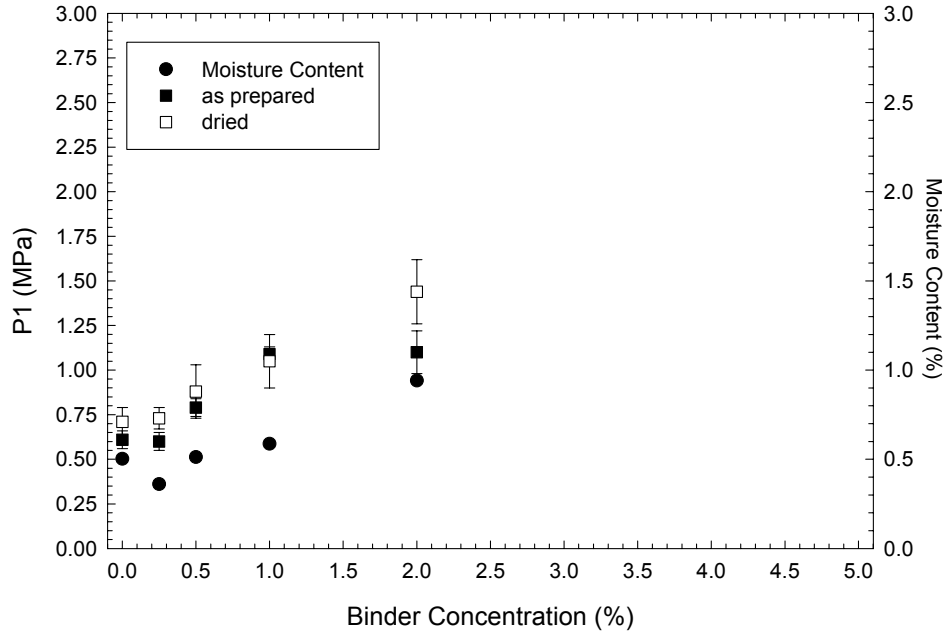


Figure 7-76. Plot of the pressure at the onset of granule deformation (P1) as a function of binder concentration for the as-prepared and dried samples with Veegum™ T and Vanzan™ D as a binder system. Also plotted is the moisture content as a function of the binder concentration.

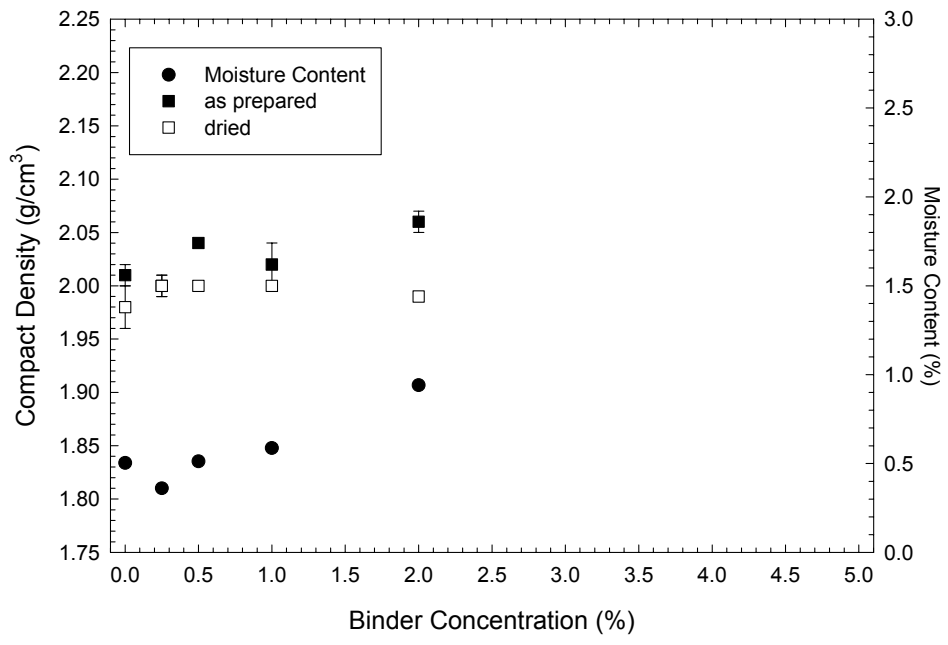


Figure 7-77. Plot of the compact density as a function of binder concentration for the as-prepared and dried samples with Veegum™ T and Vanzan™ D as a binder. Also plotted is the moisture content as a function of the binder concentration.

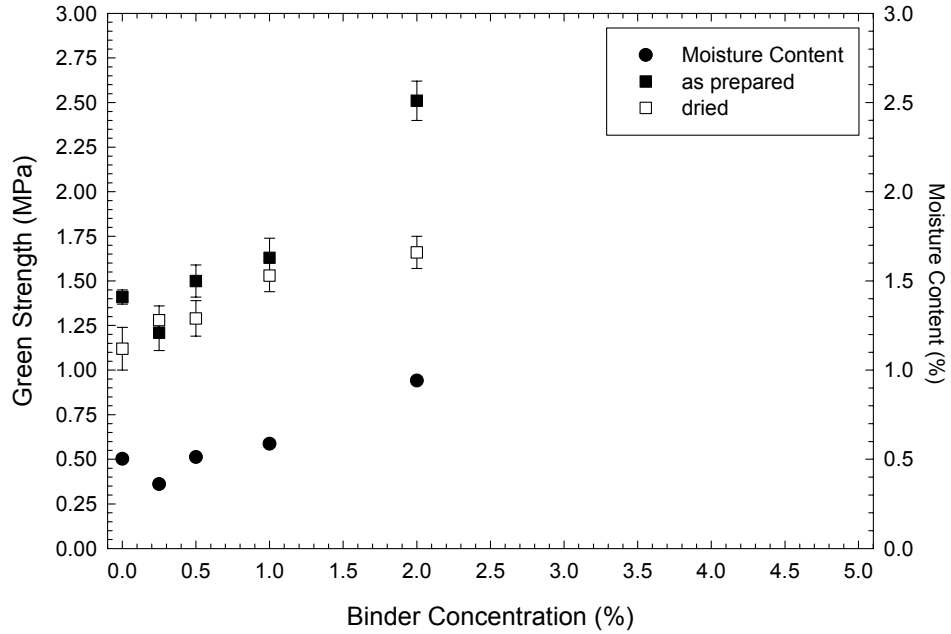


Figure 7-78. Plot of green strength as a function of binder concentration for the as-prepared and dried samples with Veegum™ T and Vanzan™ D as a binder. Also plotted is the moisture content as a function of the binder concentration.

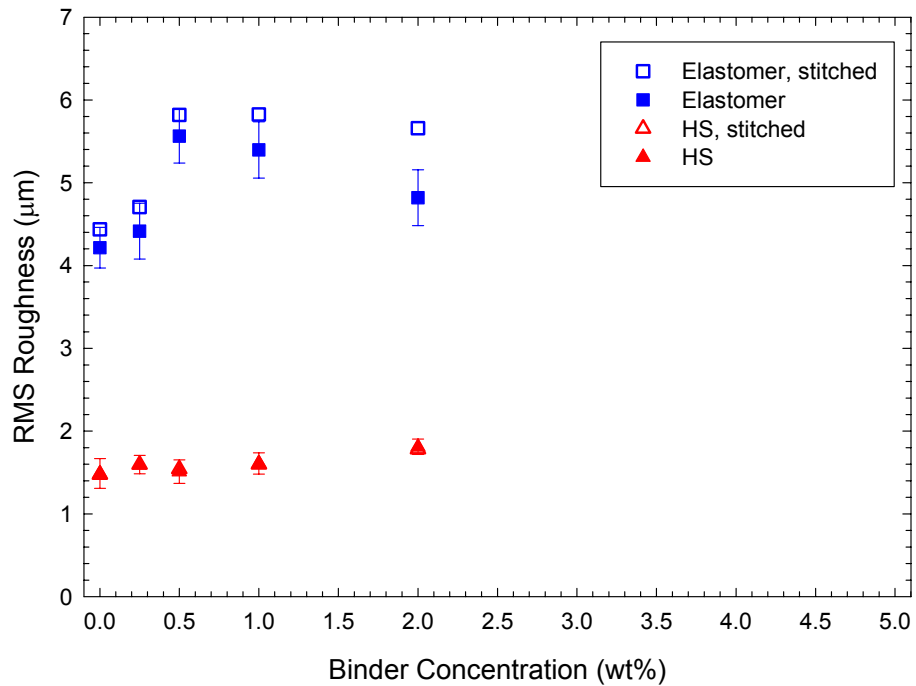


Figure 7-79. Plot of the RMS roughness as a function of binder concentration for samples prepared with Veegum™ T and Vanzan™ D as the binder. Samples were only pressed using the as-prepared granulate on the semi-isostatic (squares) and hardened steel (triangles) dies. RMS roughness is plotted for the stitched surface (open symbols) and the averaged data from the individual images (closed symbols) used to create the stitched image.

#### *7.4.4.13 Effects of Replacing pPVA with Veegum™ T*

The effects of replacing pPVA with Veegum™ T for the as-prepared granulate are plotted in Figure 7-80 (P1), Figure 7-81 (compact density), Figure 7-82 (green strength), and Figure 7-83 (RMS roughness). Replacing the pPVA in the binder system with Veegum™ T was observed to reduce the P1 value of the granulate. Initially the P1 value was near that of the unblended Veegum™ T granulate; above 1 wt% binder the P1 value was observed to fall between that of the unblended pPVA system and the unblended Veegum™ T binder systems. The compact density of the pPVA/Veegum™ T granulate was observed to fall between that of the unblended binder systems. Initially the green strength of the pPVA/Veegum™ T binder system was observed to exceed that of the unblended binder systems. Above 2 wt% binder the pPVA binder system was observed to have a slightly higher green strength than that of the pPVA/Veegum™ T system. Overall, replacement of pPVA with Veegum™ T was observed to have beneficial effects for each of the properties measured in this study. The dinnerware samples were observed to have a higher surface roughness relative to the tile samples. Little variation was observed in the RMS roughness of the tile samples due to deformation against the hardened steel surface. The dinnerware samples with Veegum™ T were observed to have the lowest RMS roughness of three binder systems. At intermediate binder concentrations, between 0.5 and 2 wt% binder, the pPVA binder system was observed to have a lower RMS roughness than the blended binder system, the pPVA/Veegum™ T binder system. The difference in the measured RMS roughness at these binder concentrations was small and therefore was not significant; the difference in the averaged RMS roughness fell within the experimental error (data not shown). At 5 wt% binder the pPVA binder system was observed to have the highest RMS roughness, followed by the blended pPVA/Veegum™ T binder system, and the unblended Veegum™ T binder system was observed to have the lowest RMS roughness.

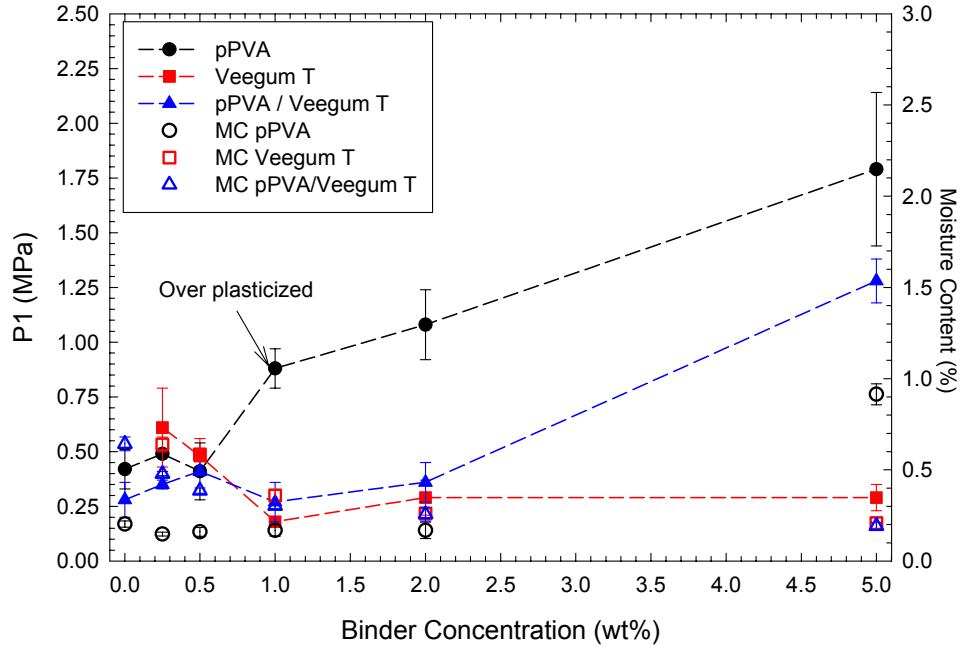


Figure 7-80. Comparison plot of the pressure at the onset of granule deformation (P1) as a function of binder concentration for the as-prepared samples where pPVA was replaced with Veegum™ T in the binder system. Also plotted is the moisture content (MC) as a function of the binder concentration. Lines are purely to help guide the eye.

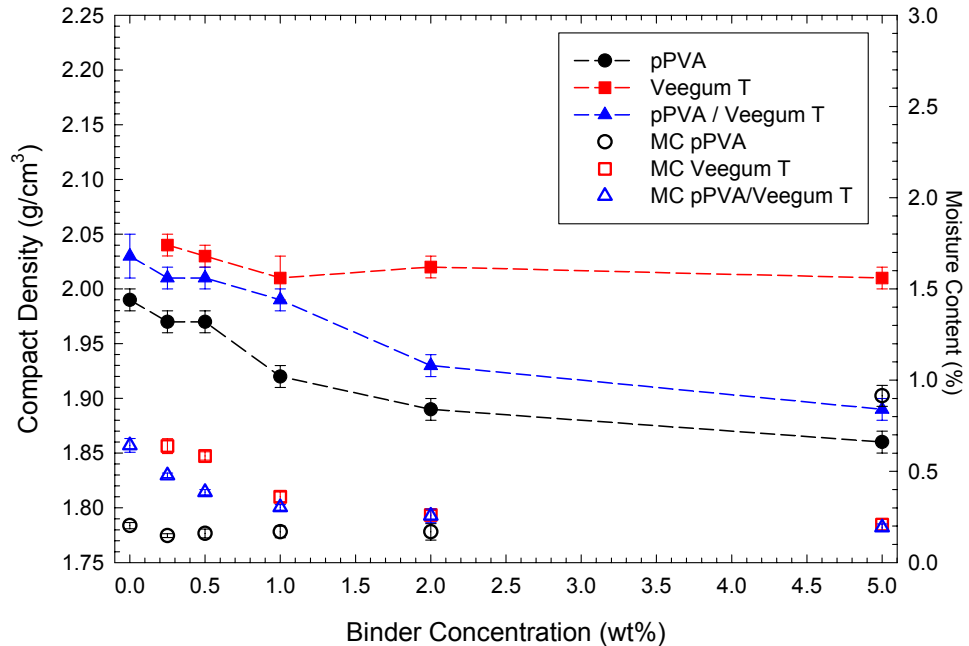


Figure 7-81. Comparison plot of the compact density as a function of binder concentration for the as-prepared samples where pPVA was replaced with Veegum™ T in the binder system. Also plotted is the moisture content (MC) as a function of the binder concentration. Lines are purely to help guide the eye.

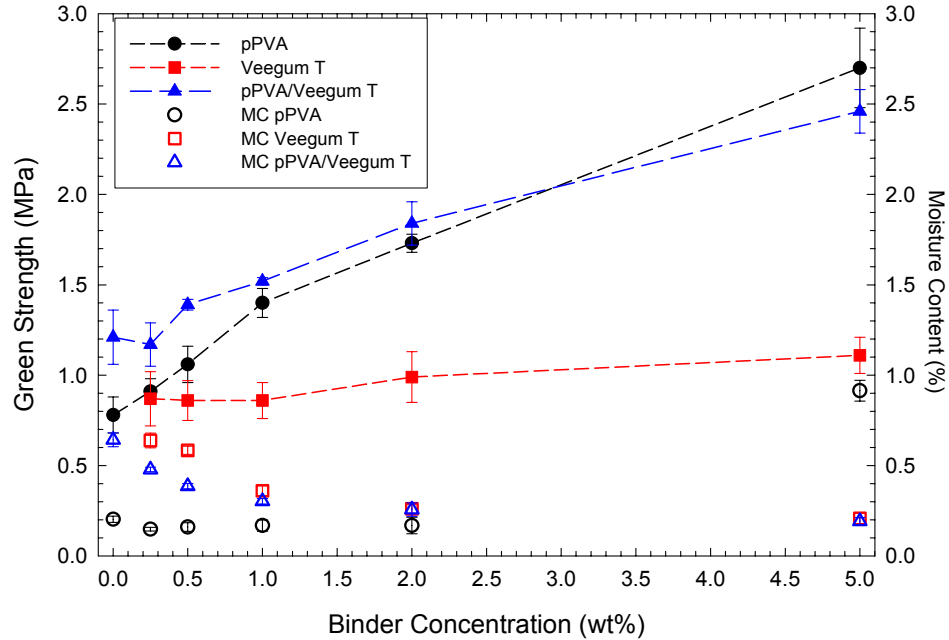


Figure 7-82. Comparison plot of green strength as a function of binder concentration for the as-prepared samples where pPVA was replaced with Veegum™ T in the binder system. Also plotted is the moisture content (MC) as a function of the binder concentration. Lines are purely to help guide the eye.

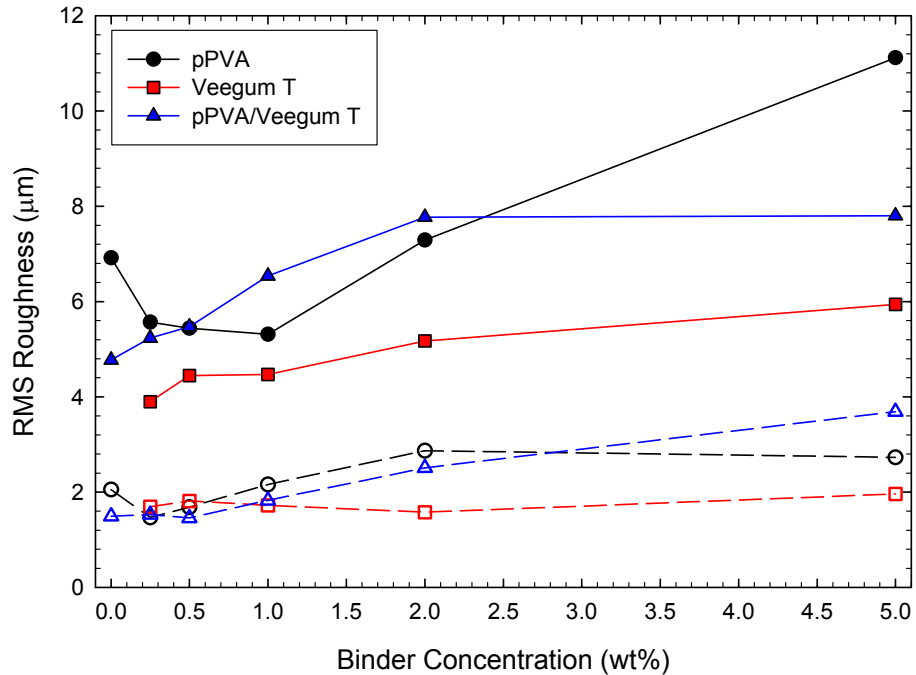


Figure 7-83. Comparison plot of the RMS roughness as a function of binder concentration for the as-prepared samples where pPVA was replaced with Veegum™ T in the binder system. Samples were only pressed using the as-prepared granulate on the semi-isostatic (closed symbols) and the hardened steel (open symbols) dies. RMS roughness is plotted for the stitched surface. Lines are purely to help guide the eye.

#### *7.4.4.14 Effects of Vanzan™ D on Veegum™ T Granulate*

The effects of replacing Veegum™ T with Vanzan™ D in the as-prepared granulate can be observed in Figure 7-84 (P1), Figure 7-85 (compact density), Figure 7-86 (green strength), and Figure 7-87 (RMS roughness). Overall the replacement of Veegum™ T with Vanzan™ D was observed to have detrimental effects. There was a significant increase in the measured P1 value. The compact density was observed to decrease with higher additions of the Veegum™ T/Vanzan™ D binder system. There was a significant increase in the green strength with addition of Vanzan™ D to the binder system. No significant difference was observed between the RMS roughness of the tile samples within the binder concentration range tested. The RMS roughness of the dinnerware samples prepared with the blended Veegum™ T/Vanzan™ D binder system was higher than that of the unblended Veegum™ T binder system.

#### *7.4.4.15 Comparison of the Binder Systems*

The data from the dried granulate has been plotted together to compare fill density (Figure 7-88), P1 (Figure 7-89), compact density (Figure 7-90), green strength (Figure 7-91), RMS roughness from the semi-isostatic die (Figure 7-92), and RMS roughness from the hardened steel die (Figure 7-93). The fill density prior to compaction helps assure that the part will be compacted to the appropriate green density and dimensions. The fill density of the two cellulose binders, i.e., carboxymethyl cellulose and methyl cellulose, was observed to significantly decrease with increasing binder concentration. As mentioned previously, this was due to the thermal gelling of the binder during the spray-drying process. The acrylic latex binder also showed a slight decrease in fill density with increasing binder concentration. The remainder of the binder systems tested showed either an increase in fill density or nearly constant fill density within the range of binder concentrations tested. The fill density of the samples was not corrected for the concentration of binder present in the granulate. Considering the concentration of binder present in the compact would decrease the density with increasing binder concentration; the binder occupied volume within the compact.

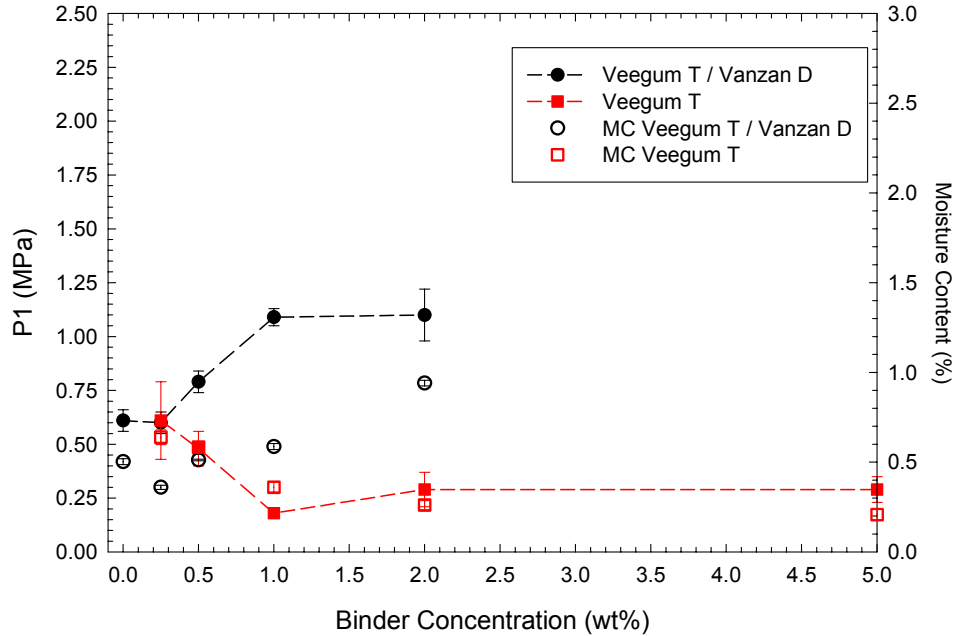


Figure 7-84. Comparison plot of the pressure at the onset of granule deformation (P1) as a function of binder concentration for the as-prepared samples with Veegum™ T or Veegum™ T / Vanzan™ D in the binder system. Also plotted is the moisture content (MC) as a function of the binder concentration. Lines are purely to help guide the eye.

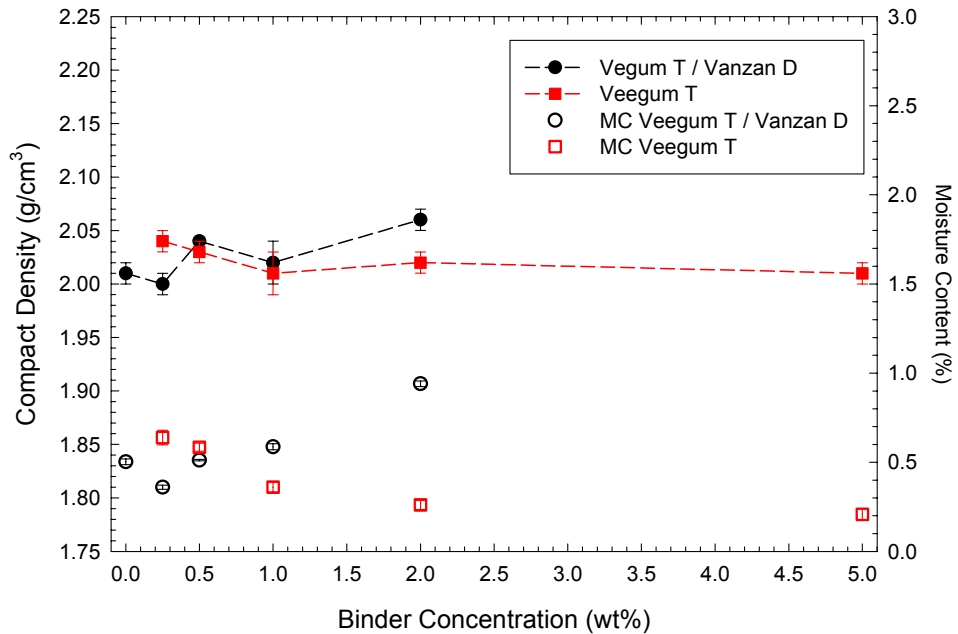


Figure 7-85. Comparison plot of the compact density as a function of binder concentration for the as-prepared samples with Veegum™ T or Veegum™ T / Vanzan™ D in the binder system. Also plotted is the moisture content (MC) as a function of the binder concentration. Lines are purely to help guide the eye.

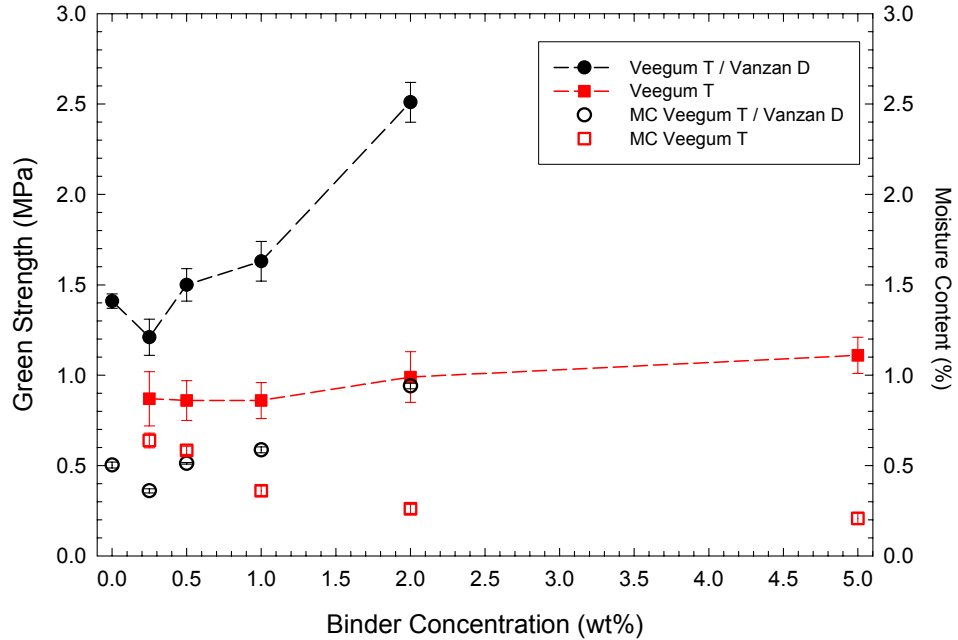


Figure 7-86. Comparison plot of green strength as a function of binder concentration for the as-prepared samples with Veegum™ T or Veegum™ T / Vanzan™ D in the binder system. Also plotted is the moisture content (MC) as a function of the binder concentration. Lines are purely to help guide the eye.

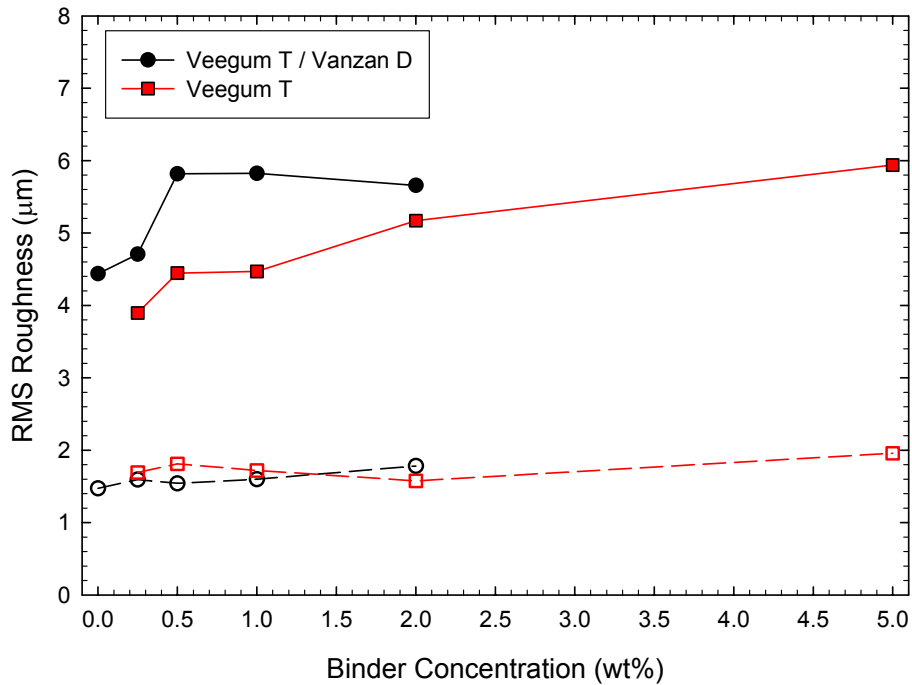


Figure 7-87. Comparison plot of stitched RMS roughness as a function of binder concentration for the as-prepared samples with Veegum™ T or Veegum™ T / Vanzan™ D. Samples were only pressed using the as-prepared granulate on the semi-isostatic (closed symbols) and the hardened steel (open symbols) dies. Lines are purely to help guide the eye.

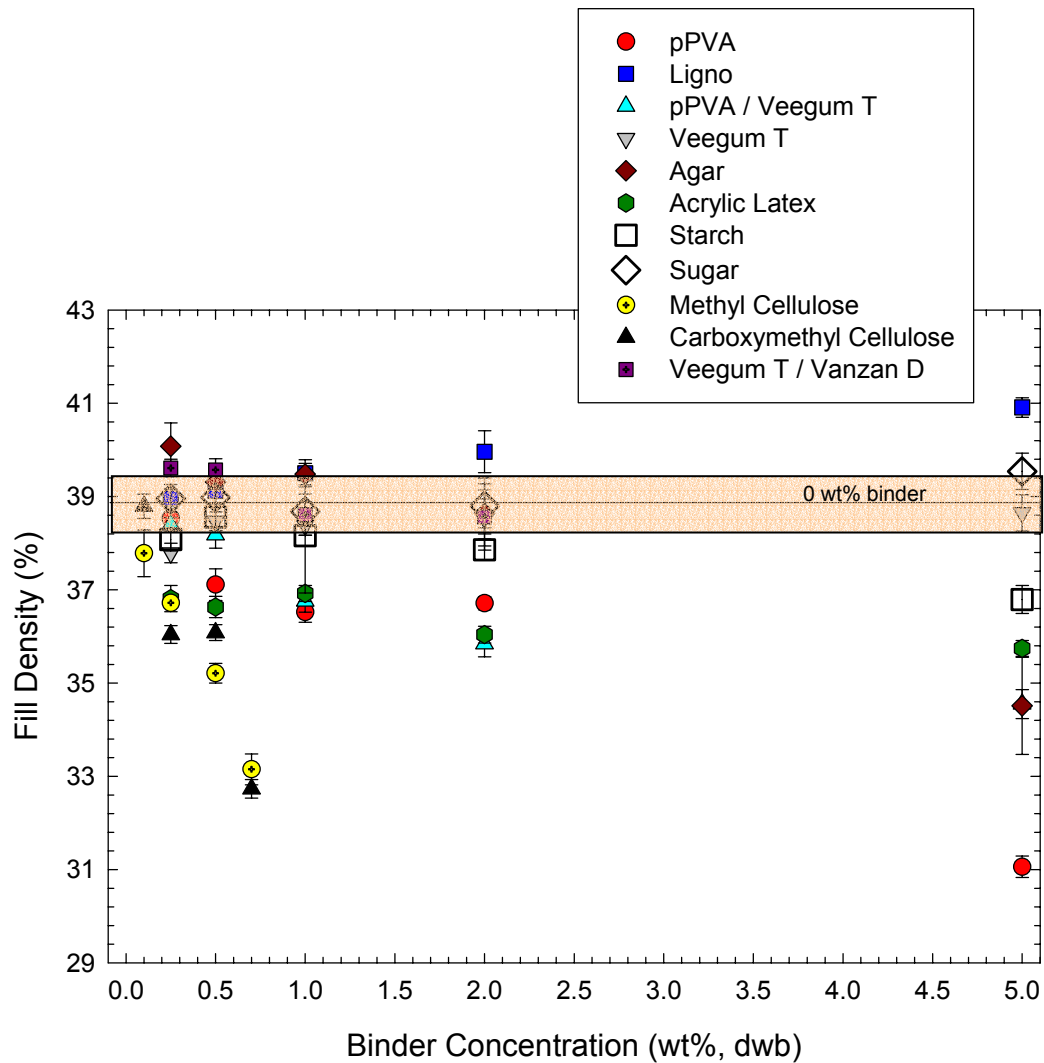


Figure 7-88. Summary plot of the fill density from the dried samples of granulate. Fill density was determined from the compaction diagrams. Binder concentration is observed to have little effect on fill density with the exception of binder systems that foam, e.g., cellulose systems and acrylic latex. Agar is observed to have a low fill density at 5wt% due to undissolved binder in the spray-dried granulate. The average measured fill density of the granulate prepared with 0 wt% binder is illustrated by the band in the figure.

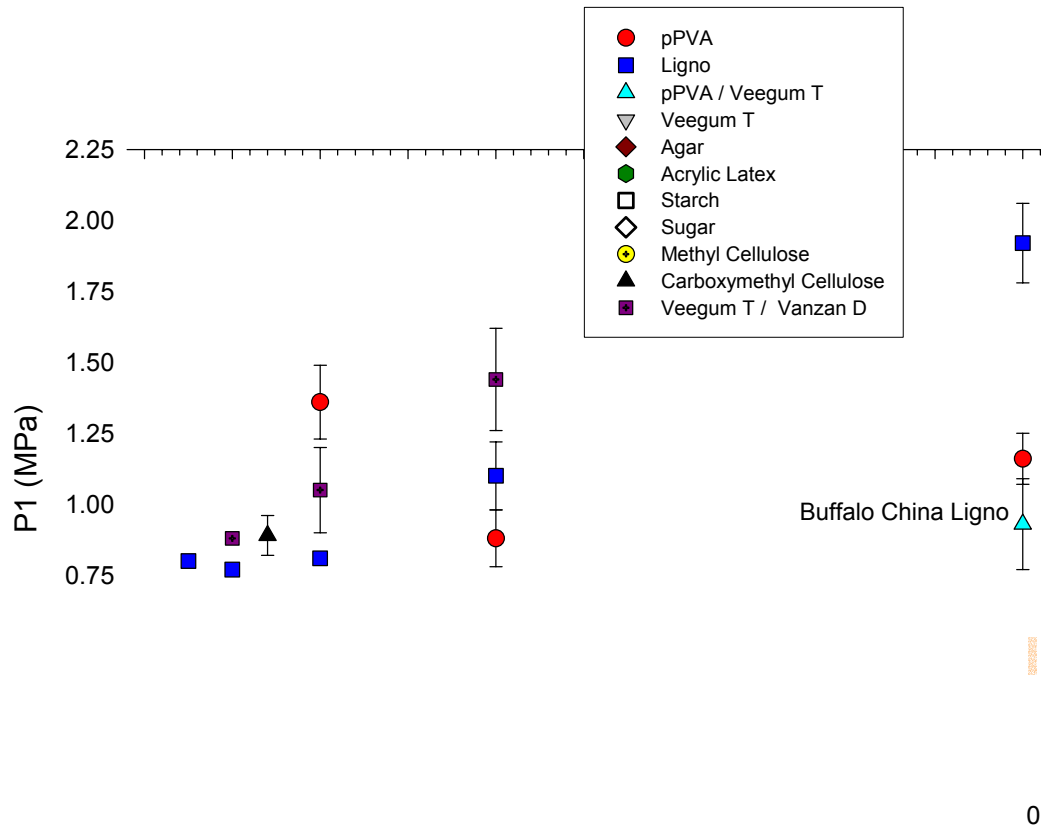


Figure 7-89. Summary plot of the pressure at the onset of granule deformation (P1) for the dried samples. Most systems do not show a significant change in P1 with increasing binder concentration. The lignosulphonate and Veegum™ T / Vanzan™ D samples are both observed to have a significant increase in P1 with increasing binder concentration. The cellulose systems are observed to have a decrease in P1 with increasing binder concentration. Starch and sugar have been eliminated as possible binders due to decomposition of the organic in the presence of the clay surface. The average measured P1 value of the granulate prepared with 0 wt% binder is illustrated by the band in the figure. Also shown are the P1 values from the industrial pPVA and Ligno granulate supplied by Buffalo China.

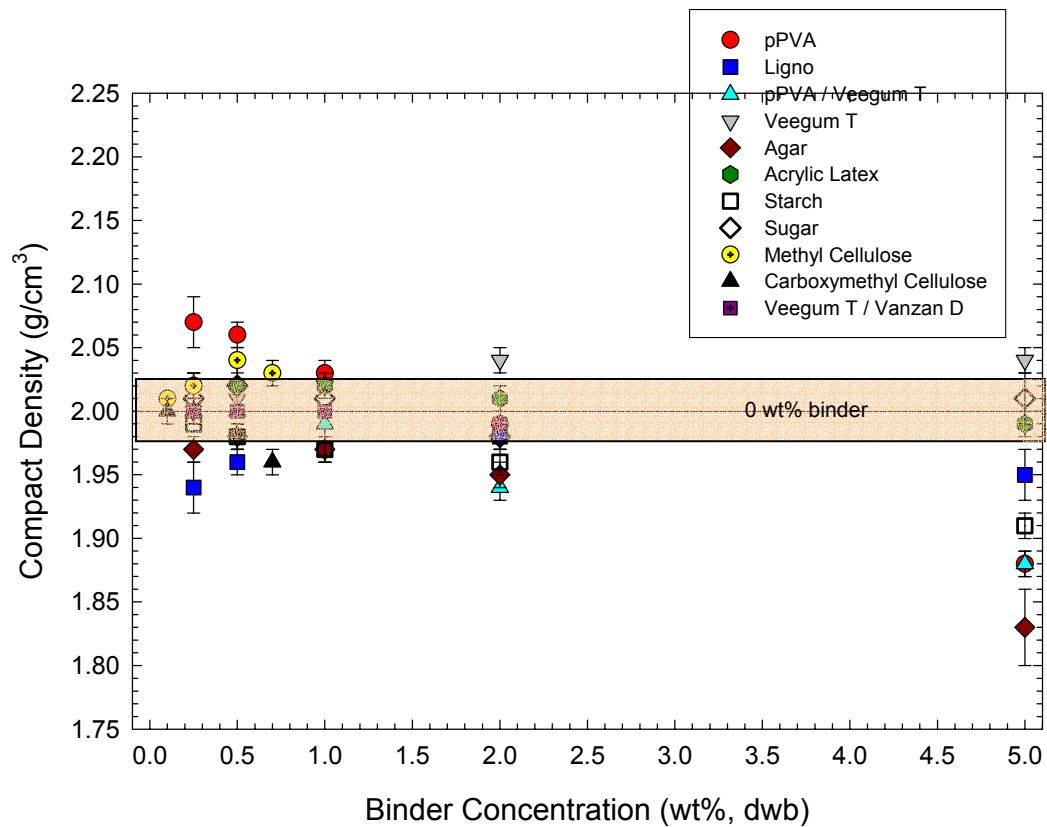


Figure 7-90. Plot of the compact density for the dried samples. Compact density is observed to predominately fall within the 1.95 to 2.02 g/cm<sup>3</sup> range for the samples. A significant decrease in density is observed in the 5 wt% samples. Densities were not adjusted for the concentration of binder present in the compact. The average measured compact density of the granulate prepared with 0 wt% binder is illustrated by the band in the figure.

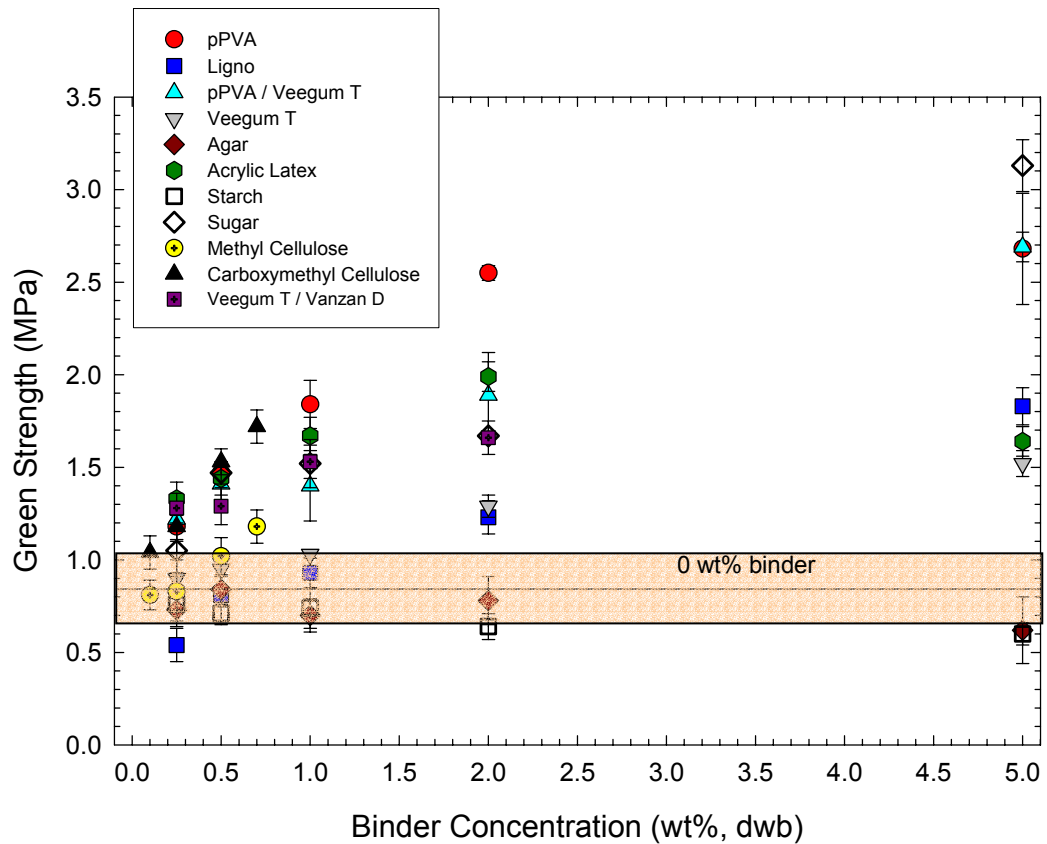


Figure 7-91. Plot of the green strength of the dried samples. Generally increases in green strength are observed with increasing binder. Agar and starch systems show a small decrease in strength with increasing binder concentration. The average measured green strength of the granulate prepared with 0 wt% binder is illustrated by the band in the figure.

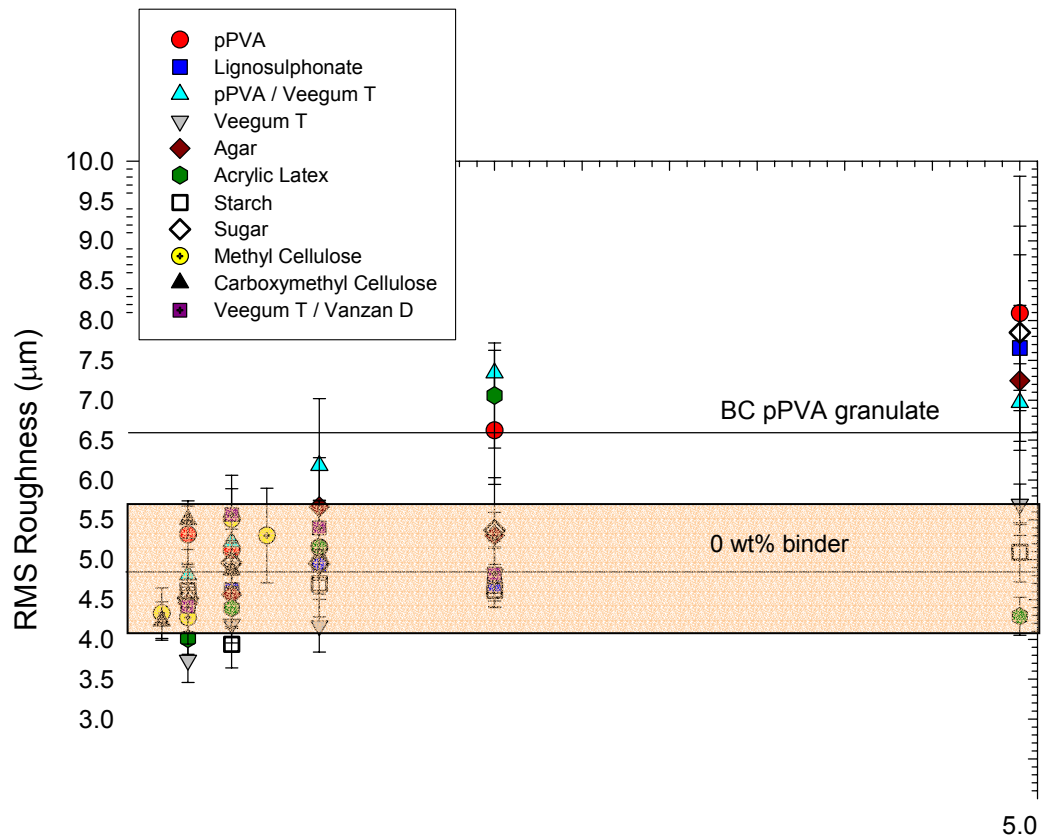
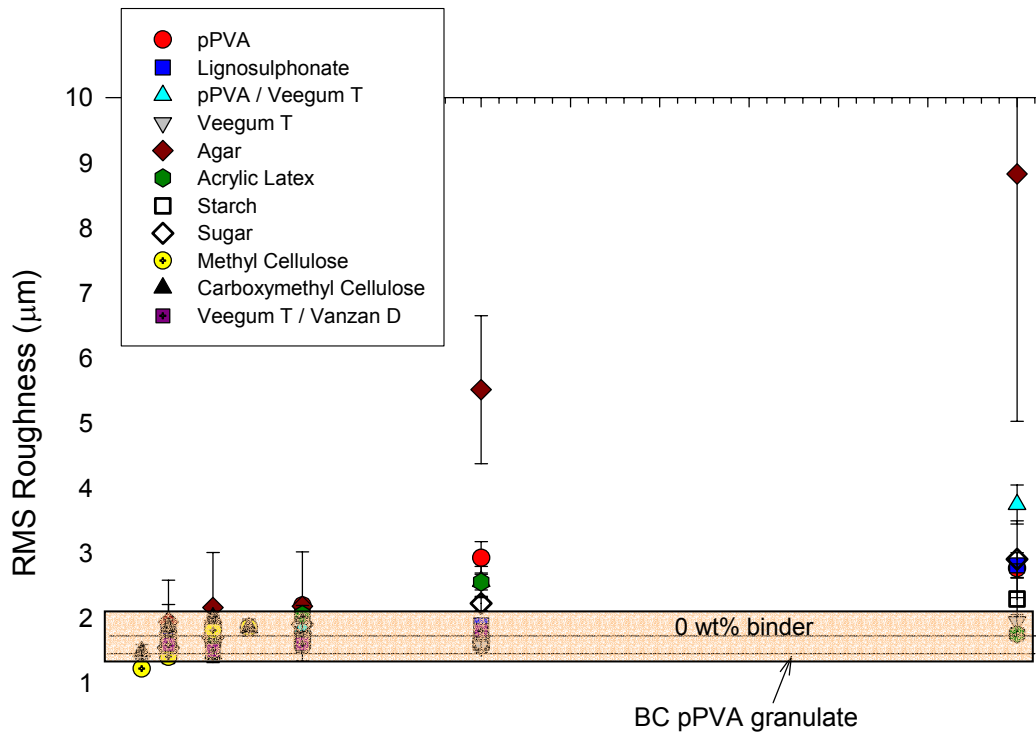


Figure 7-92. Plot of the RMS roughness of the dinnerware samples prepared with a semi-isostatic die on the Dorst press. Primarily an increase is observed in the RMS roughness with increasing binder concentration. Some binder systems exhibit a slight decrease in the measured roughness at low binder concentrations. The average measured RMS roughness of the dinnerware samples prepared with 0 wt% binder granulate is illustrated by the band in the figure. Also shown in the RMS roughness of a dinnerware sample prepared with the industrial pPVA granulate supplied by Buffalo China.



5.0

Figure 7-93. Plot of the RMS roughness of the tiles prepared with a hardened steel die on the Aeonic press. Primarily an increase is observed in the RMS roughness with increasing binder concentration. Softer binder systems have little to no change in the RMS roughness with increasing binder concentration due to good deformation at the hardened steel surface. The agar binder system has a significant increase in roughness with increasing binder concentration due to undissolved agar protruding from the surface. The average measured RMS roughness of the tiles samples prepared with 0 wt% binder granulate is illustrated by the band in the figure. Also shown in the RMS roughness of the tile sample prepared with the industrial pPVA granulate supplied by Buffalo China.

P1 is considered to be a good indication of the ability to compact granulate. A wide range of P1 values were measured for the binder systems tested. Higher values were observed to result from the lignosulphonate, pPVA, and Veegum™ T/Vanzan™ D binder systems. The lowest values were observed in the starch and sugar binder systems; regrettably these systems were not stable due to degradation of the organic additives in the presence of the clay surface and the formation of secondary organics, i.e., a fungus or bacterial growth, in suspension as well as thermal degradation during spray drying. The next lowest values were observed in the methyl cellulose system. The remainder of the samples tested fall within a band of P1 values between approximately 0.3 and 0.6 MPa. As previously stated, P1 has been demonstrated to be independent of granule size provided that the extreme fines (sub-230 mesh granules) were not being tested.

The compact density was observed to primarily range between 1.95 and 2.02 g/cm<sup>3</sup> for the majority of the samples prepared. Significant deviations were observed at the higher binder concentrations where the compact density was observed to decrease significantly in the case of the agar and lignosulphonate binder systems. The dried weight of the samples was not adjusted to compensate for the concentration of binder; making this adjustment would decrease the density of the compact with increasing binder concentration.

Green strength was observed to increase with increasing binder concentration in nearly all of the samples tested. Notable exceptions were starch and agar; in the case of agar incomplete dissolution of the organic affected the strength of the compacts. Significant increases in strength were observed in the sugar and acrylic latex binder systems. Green strength of the compact was necessary in an industrial setting to successfully remove the pressed ware from the die.

The RMS roughness of the dinnerware samples prepared on the Dorst press is illustrated in Figure 7-92; the RMS roughness of a dinnerware sample prepared using the pPVA Buffalo China granulate on the Dorst press by a line in the figure. The RMS roughness of the dinnerware samples prepared using the

Alfred University granulate was observed to increase with increasing binder concentration. The Veegum™ T, starch, methyl cellulose, and carboxymethyl cellulose binder systems did not have a RMS roughness that significantly varies from the samples pressed without a binder, i.e., the 0 wt% samples. The roughness of these samples all fall within the error associated with the samples prepared with 0 wt% binder. The samples prepared with acrylic latex passed through a maximum at 2 wt% binder that fell outside the error associated with the samples prepared with 0 wt% binder. The remaining binder systems have roughness values that exceed the error associated with the 0 wt% samples; these roughness values were observed at the higher binder concentrations.

The RMS roughness of the tile samples is shown in Figure 7-93; the RMS roughness of a sample prepared using the pPVA granulate supplied by Buffalo China on the Aeonic press is illustrated as a line in the figure. The RMS roughness of the tile samples was primarily observed to increase with increasing binder concentration. The RMS roughness of the Veegum™ T, methyl cellulose, and carboxymethyl cellulose binder systems was not observed to significantly vary from that of the samples prepared with 0 wt% binder. The roughness of the acrylic latex samples was observed to pass through a maximum at 2 wt% binder which falls outside of the error associated with the 0 wt% binder samples. The remainder of the binder systems were observed to have RMS roughness values that exceed the error associated with the 0 wt% binder samples. The most significant increase in the RMS roughness was observed in the agar binder system, which had tile sample RMS roughness values that exceeded the RMS roughness values of the dinnerware samples. The increase in RMS roughness of the agar samples was the results of undissolved agar grains that protruded from the pressed surface. Between the agar grains the RMS roughness of the samples was observed to approach that of the plastic formed ware in characterized in Chapter 6; an image of the pressed dinnerware surface from the interferometer at 5 wt% agar is shown in Figure 7-94. The RMS roughness for the 1.04 mm by 0.62 mm area between the undissolved agar grains is 4.704 micrometers which is approaching the surface roughness of the pressure-cast ware selected as a benchmark for the surface finish in Chapter 6.

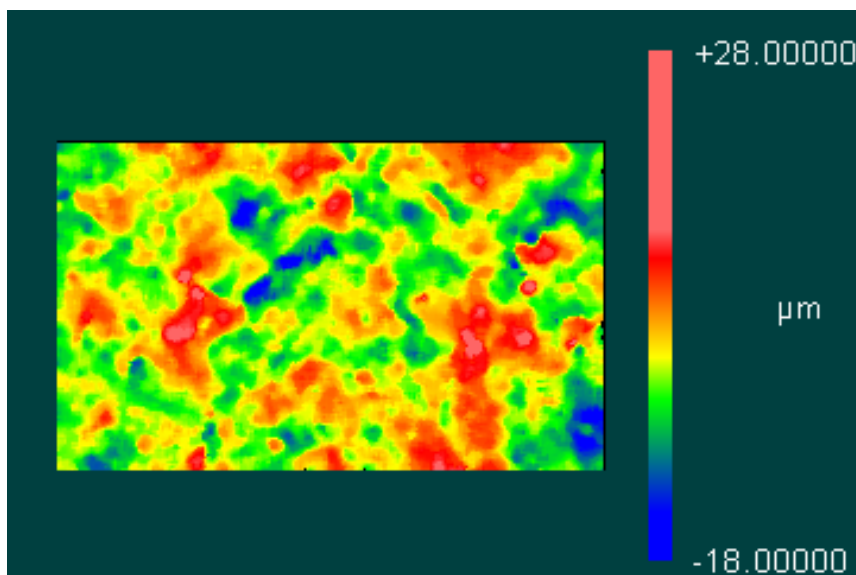


Figure 7-94. Image of the dinnerware surface pressed using the 5 wt% agar granulate in the Dorst semi-isostatic die. Image is from between the agar grains which protrude from the sample surface. RMS roughness of the surface is 4.704 micrometers for the 1.04 mm by 0.62 mm area.

Representative images of the surface finish from the optical interferometer are shown in Figure 7-95 (agar binder system) and Figure 7-96 (plasticized PVA binder system). Images are shown for both the dinnerware and tile samples. The agar binder system was selected to clearly illustrate the change in the surface finish with increasing binder concentration. The dinnerware samples from the Dorst press have a gradual change in appearance with undissolved agar protruding from the surface at high concentrations. Texture from the granules was visible in all of the images from the dinnerware samples due to the compliant nature of the membrane surface. The samples prepared with higher concentrations of binder on the Aeonic press had grains of undissolved agar which protruded from the surface. These undissolved grains significantly increased the RMS roughness. Between the grains of agar the surface appeared relatively smooth due to the good deformation of the granulate which had a high moisture content. The pPVA samples prepared on the Dorst press showed a gradual increase in the RMS roughness as more texture was apparent in the image of the surface. The initial decrease in the RMS roughness was due to

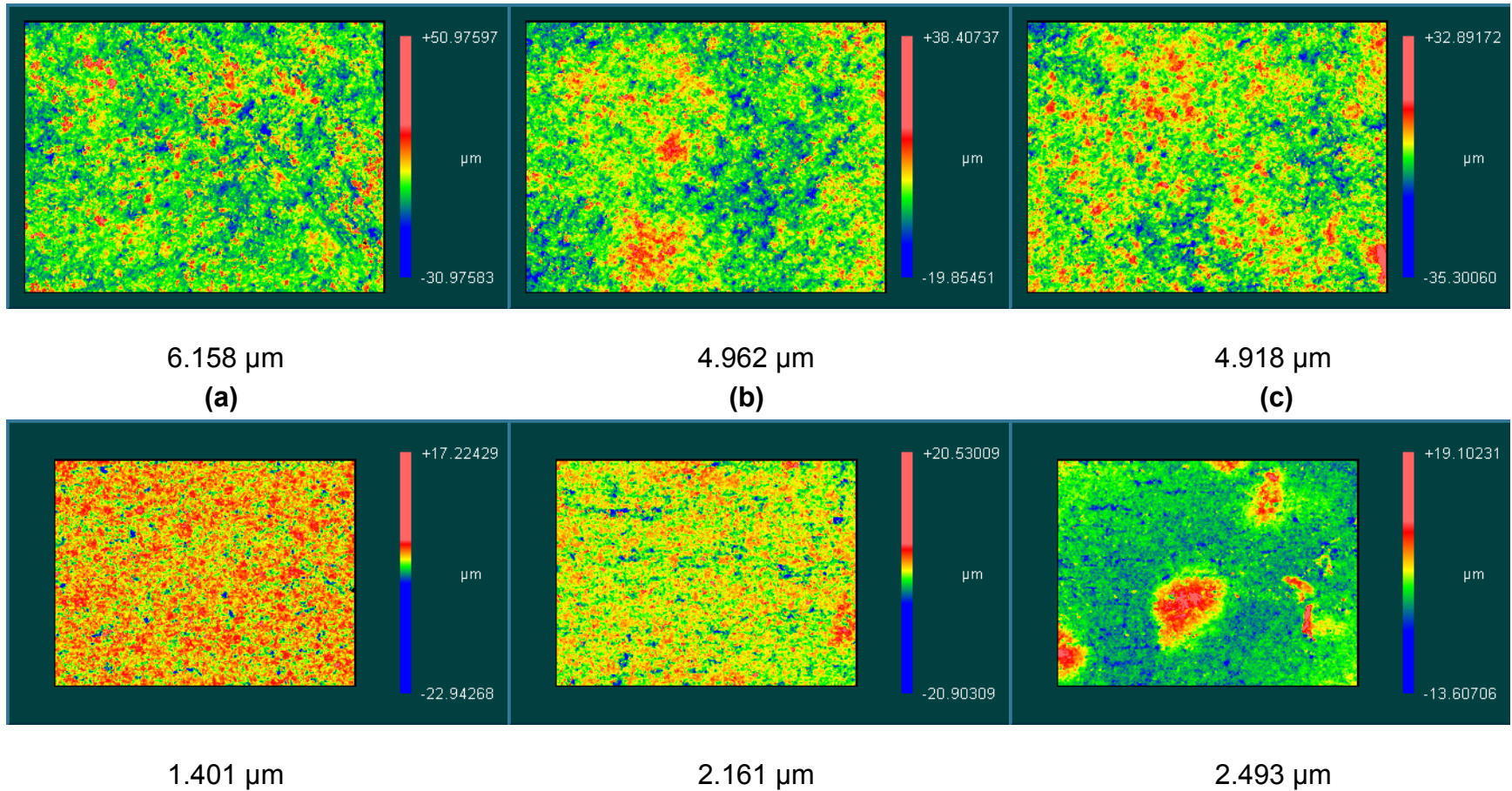


Figure 7-95. Images from the optical interferometer of the surface finish of samples prepared with agar as-prepared binder system. Images from the dinnerware samples prepared on the Dorst press (top) and on the Aeonic press (bottom) are shown. Binder concentration increases from left to right: a) 0 wt%, b) 0.25 wt%, and c) 0.50 wt%; higher concentration are shown on the next page. The RMS roughness from the stitched area has been listed below each image.

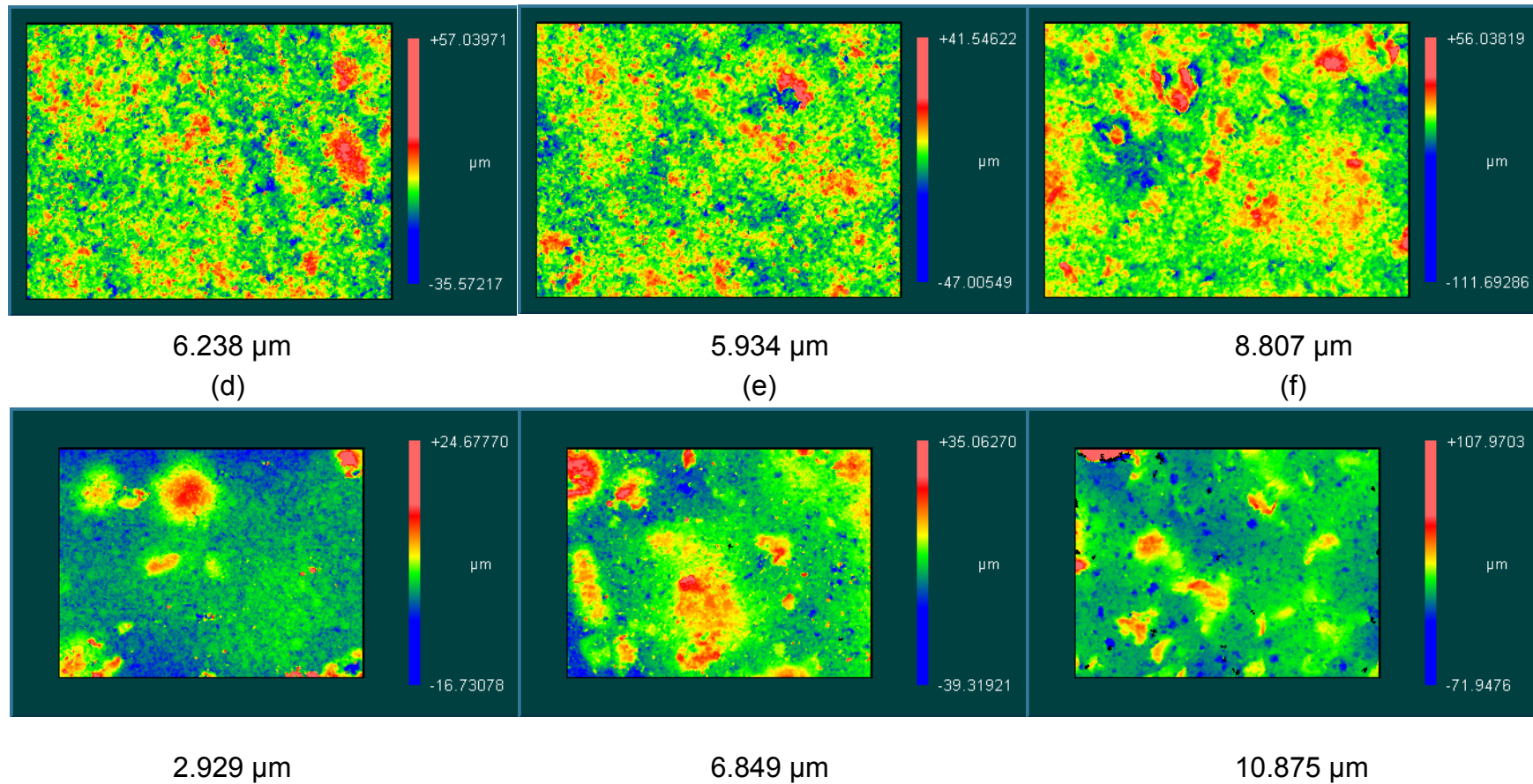
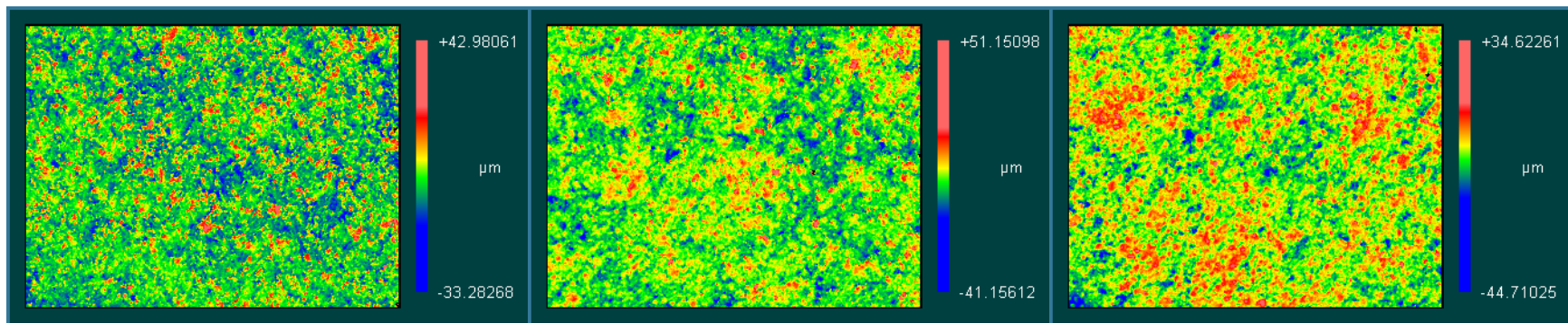


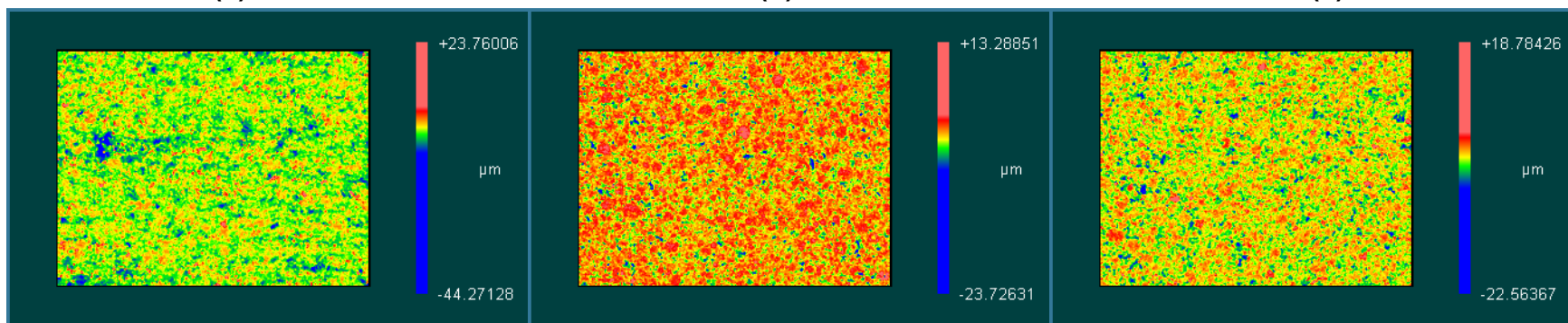
Figure 7-95 (cont.). Images from the optical interferometer of the surface finish of samples prepared with agar as-prepared binder system. Images from the dinnerware samples prepared on the Dorst press (top) and on the Aeonic press (bottom) are shown. Binder concentration increases from left to right: d) 1.00 wt%, e) 2.00 wt%, and f) 5.00 wt. The RMS roughness from the stitched area has been listed below each image.



6.916  $\mu\text{m}$   
**(a)**

5.568  $\mu\text{m}$   
**(b)**

5.438  $\mu\text{m}$   
**(c)**



2.052  $\mu\text{m}$

1.467  $\mu\text{m}$

1.681  $\mu\text{m}$

Figure 7-96. Images from the optical interferometer of the surface finish of samples prepared with plasticized PVA as a binder system. Images from the dinnerware samples prepared on the Dorst press (top) and on the Aeonix press (bottom) are shown. Binder concentration increases from left to right: a) 0 wt%, b) 0.25 wt%, and c) 0.50 wt%; higher concentration are shown on the next page. The RMS roughness from the stitched area has been listed below each image.

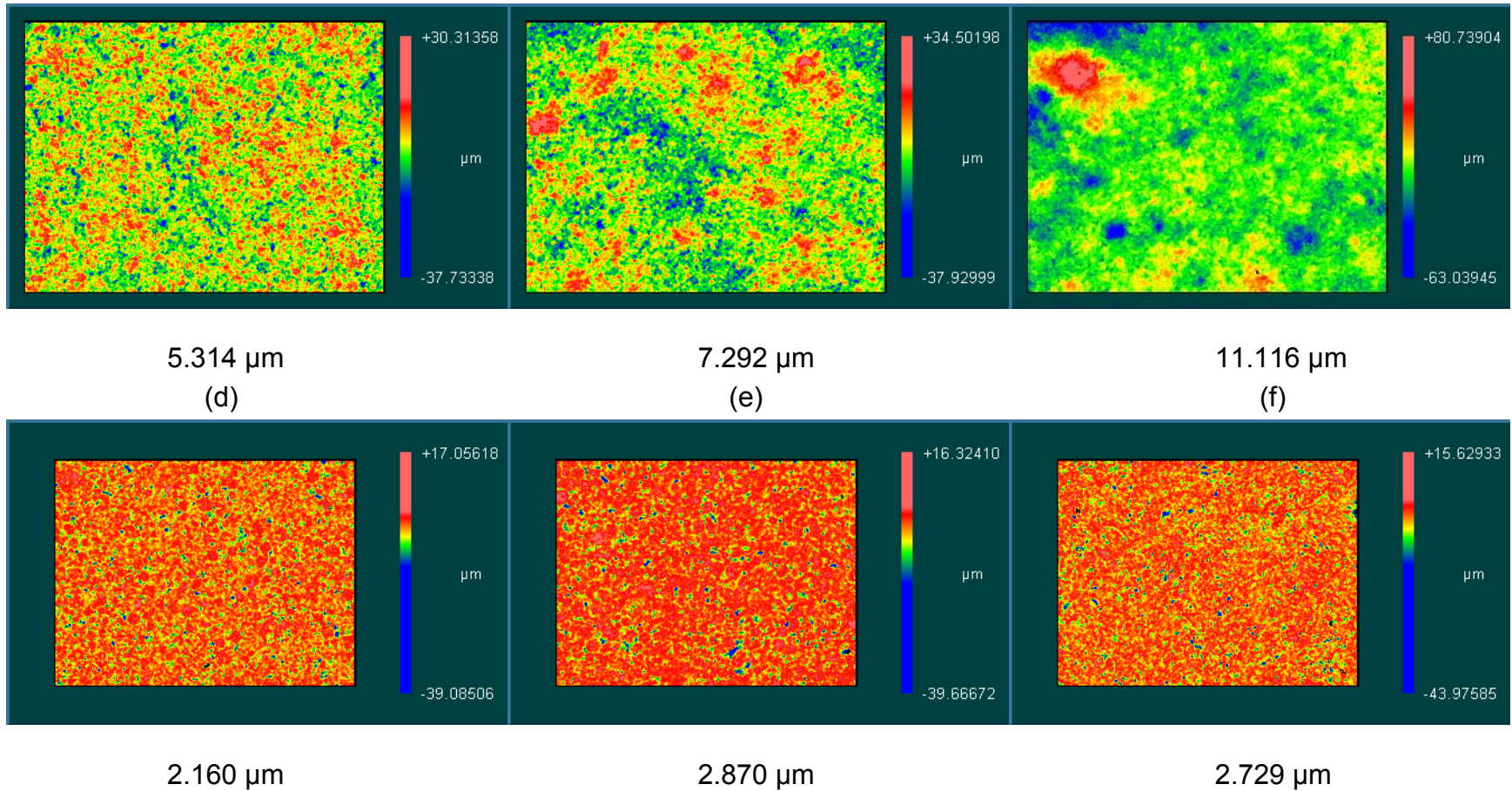


Figure 7-96 (cont.). Images from the optical interferometer of the surface finish of samples prepared with plasticized PVA as a binder system. Images from the dinnerware samples prepared on the Dorst press (top) and on the Aeonic press (bottom) are shown. Binder concentration increases from left to right: d) 1.00 wt%, e) 2.00 wt%, and f) 5.00 wt. The RMS roughness from the stitched area has been listed below each image.

dust or loose granules that were on the surface of the sample prepared with 0 wt% binder. The samples prepared on the Aeonic press showed a small increase in the RMS roughness. This gradual change in the surface finish was due to the poor deformation of the granulate and residual crevices that penetrate into the surface between the granules. With increasing binder concentration the crevices penetrated further into the surface increasing the RMS roughness of the sample. Images of the surfaces from all of the samples can be observed in Appendix I.

#### *7.4.4.16 Blending of Granulate with Alternative Binder Systems*

The P1 results from the blending of the granulate prepared at Alfred University can be observed in Figure 7-97. No clear trend was apparent in the data, although blending granulate with similar P1 values was observed to result in a small reduction in the P1 value. To determine if this benefit was significant correlation plots of P1 as a function of the normalizing factor (Figure 7-98) and P1 as a function of the moisture content (Figure 7-99) were prepared. No clear trend was apparent in the plot of P1 versus the normalizing factor,  $P1_{norm.}$ . A very clear trend was apparent in the plot of P1 versus moisture content. Therefore moisture content plays a more significant role in the deformation of the granulate in blended systems.

The roughness of the samples prepared by blending the granulate spray dried at Alfred University is shown in Figure 7-100. The roughness of the blends was observed to be significantly lower than that measured in the preliminary study, Chapter 6. As a comparison the roughness of a tile pressed using the pPVA granulate from Buffalo China is illustrated by a line in Figure 7-100. The roughness of the blended systems was primarily observed to be lower than that of the sample prepared using the industrial granulate. There was an increase in the roughness of the samples with an increase in the normalizing factor. A correlation plot of the RMS roughness and moisture content is shown in Figure 7-101; the roughness was observed to be a function of the moisture content of the granulate. An increase in the moisture content of the granulate was observed to result in a decrease in the measured RMS roughness. Surface images from the

interferometer of the samples prepared with blended granulate that was spray dried at Alfred University are shown in Appendix J.

The blended systems prepared with agar granulate show a significant reduction in the P1 value of the granulate. The physical water trapped within the agar gelatin served to plasticize the second binder allowing good deformation during compaction. The RMS roughness of these systems was inflated due to the presence of undissolved agar grains protruding from the surface of the pressed part. The dried green strength of the blends prepared with the agar granulate was observed to be significantly higher than that of the other blends in the study, Figure 7-102.

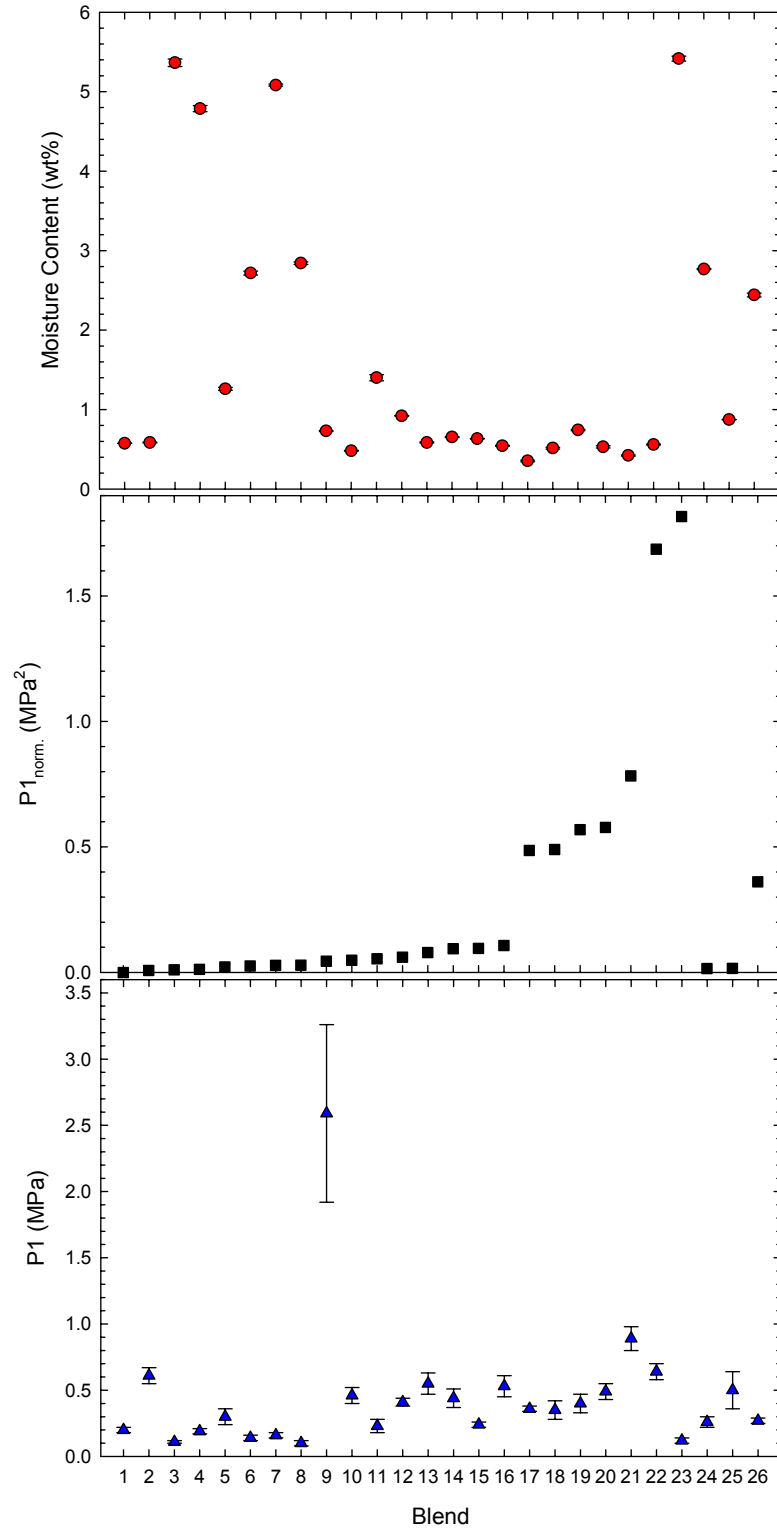


Figure 7-97. Results from blending granule systems with similar P1 values. No clear trend is apparent in the P1 data although there may be a small benefit to blending granulate with similar P1 values.

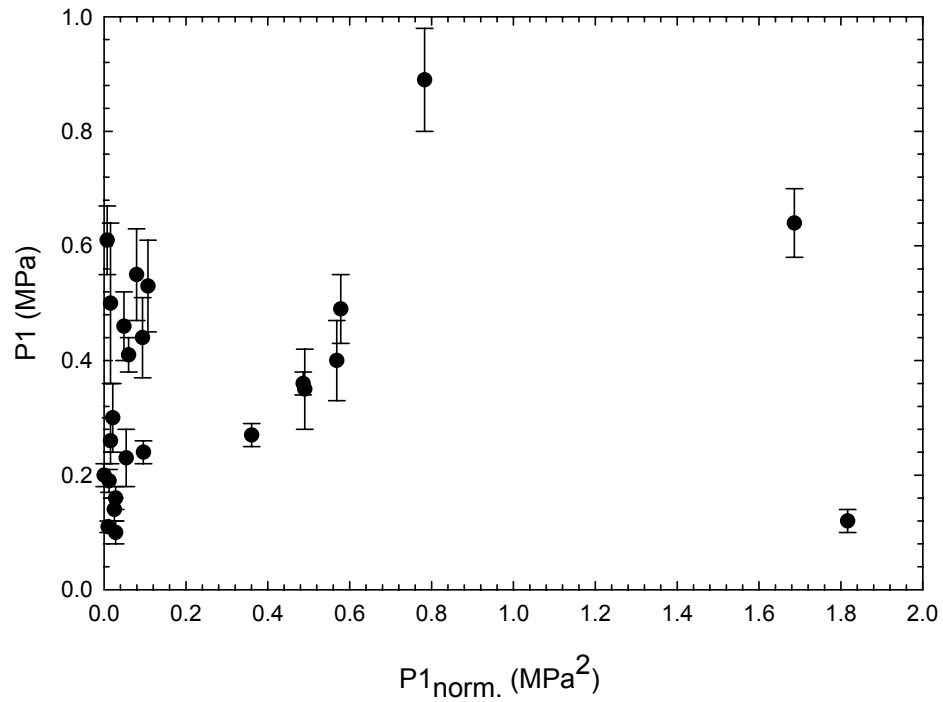


Figure 7-98. Correlation plot of the P1 value from the blended granulate systems versus the normalized P1 value. No correlation is observed.

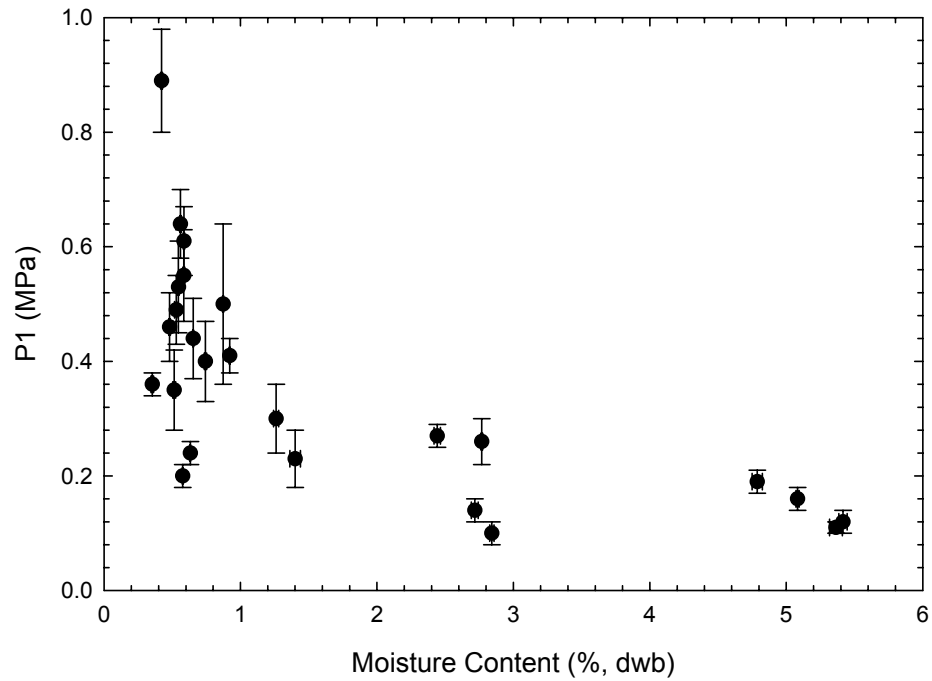


Figure 7-99. Correlation plot of the P1 value from the blended granule systems versus moisture content in the granulate. A strong correlation is observed where an increase in the moisture content results in a lower P1 value.

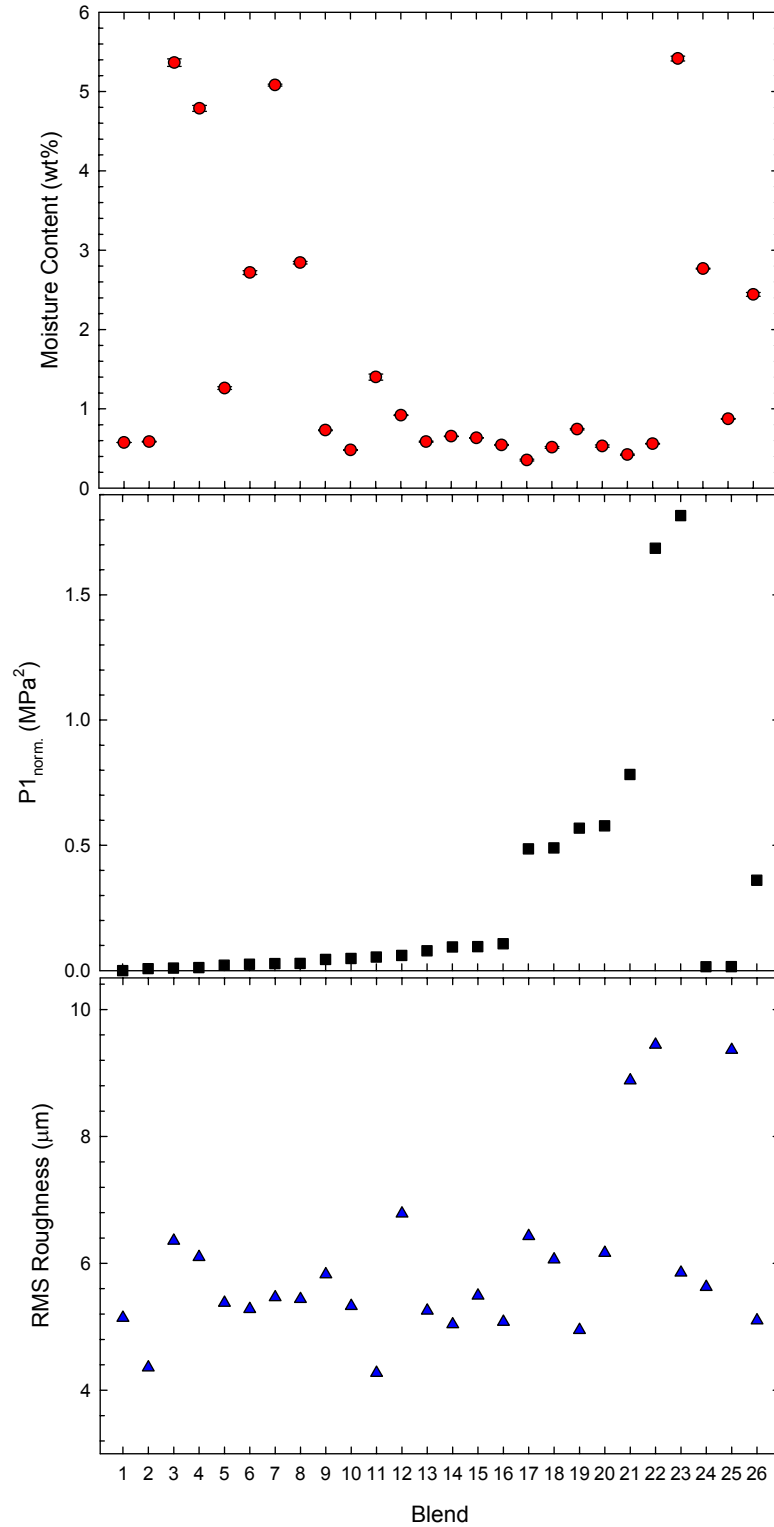


Figure 7-100. Plot of the RMS roughness as a function of the normalizing factor  $P1_{norm.}$ . An increase in the RMS roughness is observed with an increase in the normalizing factor. RMS roughness of the pPVA reference prepared using the industrial granulate is approximately 11 micrometers.

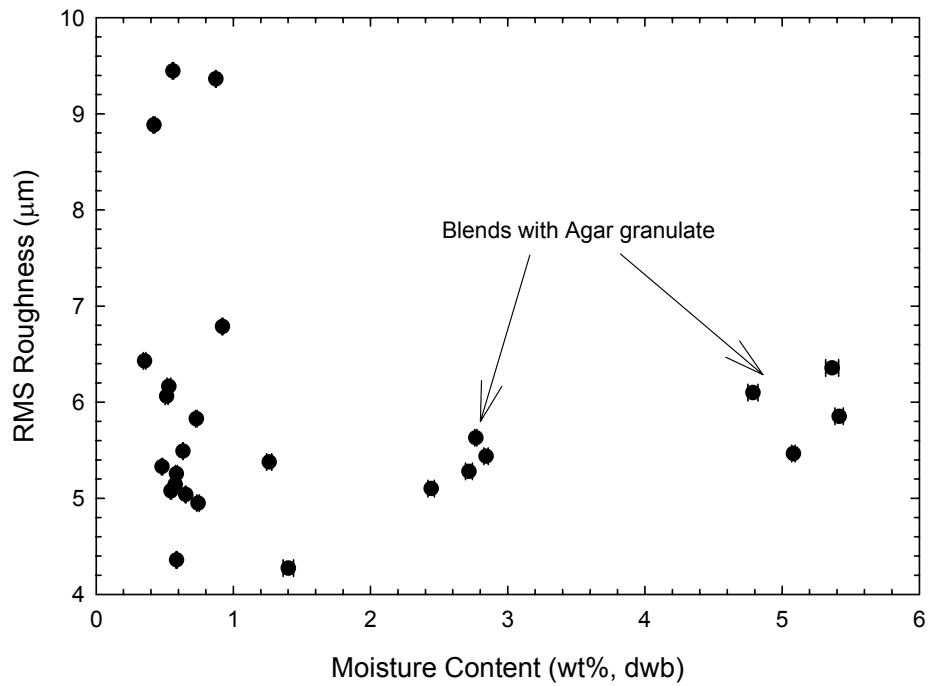


Figure 7-101. Correlation plot of the RMS roughness as a function of the moisture content in the blended granulate. A decrease is observed in the measured RMS roughness with an increase in moisture content. A slight increase is observed at high moisture contents due to the presence of undissolved Agar protruding from the samples surface

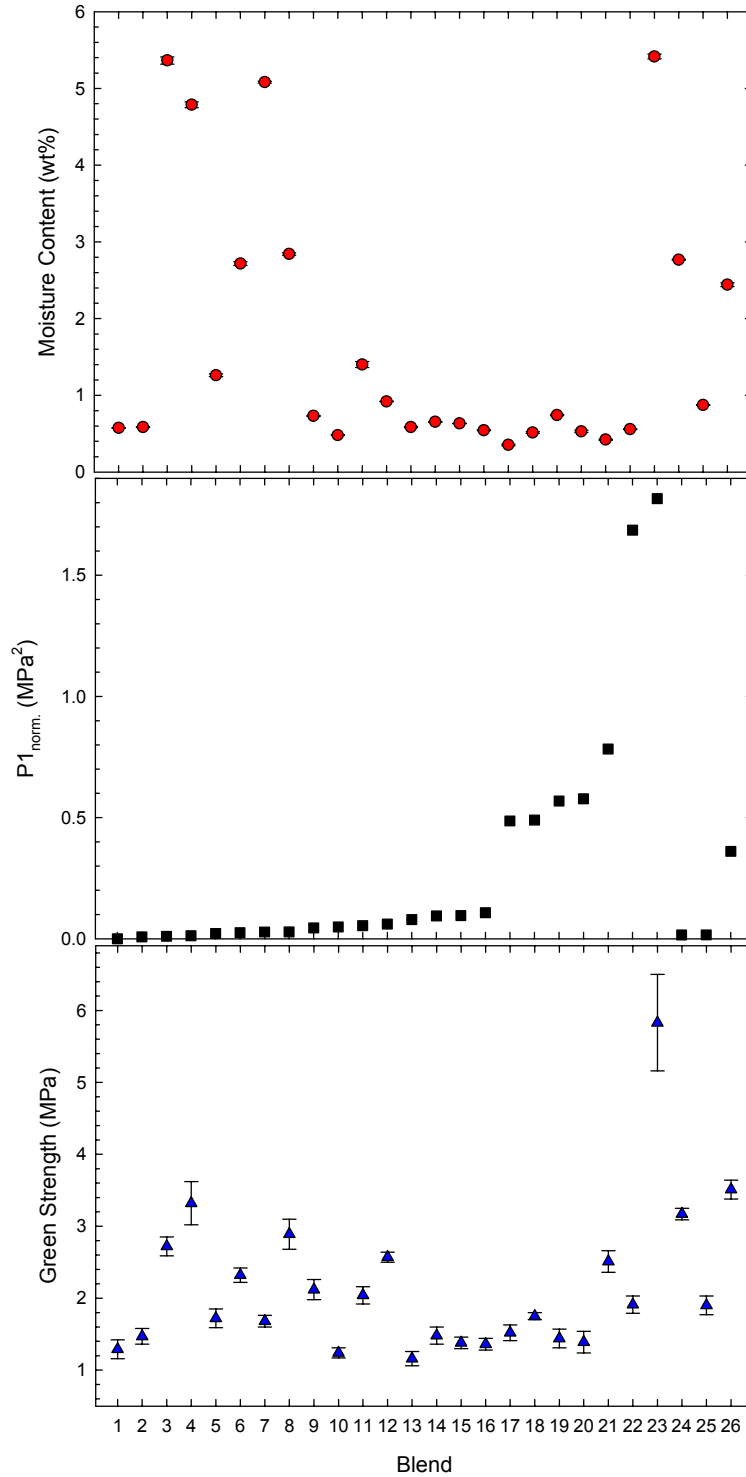


Figure 7-102. Plot of the green strength of the dried compacts prepared using blended-granule systems. Blends that were observed to have a higher moisture content, i.e., those blends prepared with agar granulate as one of the constituents, are observed to have a higher green strength, see blend #23.

#### *7.4.5 Summary and Conclusions*

Alternative binders are available to replace a pPVA binder system in dry pressing. Thermal gelling of cellulose type binders and thermal degradation of some organics, e.g., sugar, make some selections studied impractical for an industrial process. Other binder systems, starch and agar, were observed to degrade in the presence of the clay surface resulting in the growth of secondary organics while in suspension. The degradation of the organics was indicated by the formation of a black fungal growth within the polypropylene container or the swelling of the polypropylene container during storage. Agar has the ability to trap significant amounts of physical water into the gelatin structure which was available to facilitate compaction although undissolved agar was apparent in the surface of the pressed samples. Reduction of the particle size of the purchased organic may have helped in dissolving the agar. Partially replacing pPVA with an inorganic additive (Veegum™ T) was observed to maintain the green strength and the density of the compact while significantly reducing the measured P1 value.

Physical moisture within the granulate was more important for good compaction compared to blending binder systems. While there was some benefit to blending granulate, proper selection of the constituent binder systems is time consuming and difficult. Tighter process control on the moisture content of granulate prior to the dry-pressing process would facilitate compaction resulting in ware with a higher green strength, a higher compact density, and a superior surface finish.

Blending of agar granulate and granulate prepared with another binder system was observed to result in regions of good surface finish. The presence of undissolved agar grains at the surface of the sample served to inflate the measured RMS roughness of the samples. The physical water that is trapped within the agar gelatin served to plasticize the second binder resulting in good deformation and a high green strength for the pressed samples. The highest green strength was observed using a blend of agar and lignosulphonate granulate.

## 7.5 References

1. J.S. Reed, *Principles of Ceramic Processing*, 2<sup>nd</sup> ed.; Ch. 20. Wiley Interscience, New York, New York, 1995.
2. G. Ghorra, "Wet vs Dry Processing: Granulation of Ceramic Powders," *Ceram. Eng. Sci. Proc.*, **8** [11-12] 1211-9 (1987).
3. T. Busch, D. Schweizer, and C. Sorg, "Spray Granulation of Alumina with Organic Binders," *Ceram. Forum. Int.*, **68** [10-11] 527-9 (1991).
4. K. Masters, *Spray Drying Handbook*, 5<sup>th</sup> ed. Wiley Interscience, New York, New York, 1991.
5. K. Masters, "Applying Spray Drying to Ceramics," *Am. Ceram. Soc. Bull.*, **73** [1] 63-72 (1994).
6. S.J. Lukasiewicz, "Spray-Drying Ceramic Powders," *J. Am. Ceram. Soc.*, **72** [4] 617-24 (1989).
7. R.W. Matz and J. Nemeth, "Process Control Standards for Spray Drying," *Ceram. Eng. Sci. Proc.*, **4** [11-12] 999-1001 (1983).
8. J.S. Reed, "Spray Drying and Implications for Compactibility of Product Granules," *Ceram, Eng. Sci. Proc.*, **18** [2] 343-58 (1997).
9. S. Mager and H. Niffka, "Spray Drying," *Ceram. Forum Int.*, **73** [2] 92-4 (1996).
10. J.M. Phelps and O. Ratsep, "Spray Drying Ceramics," *Ceram. Eng. Sci. Proc.*, **5** [11-12] 1004-11 (1984).
11. D.E. Walton and C.J. Mumford, "Spray Dried Products – Characterization of Particle Morphology," *Trans. Inst. Chem. Eng. A*, **77** [1] 21-38 (1999).
12. J.A. Duffie and W.R. Marshall, "Factors Influencing the Properties of Spray-Dried Materials, Part I," *Chem. Eng. Prog.*, **49** [8] 417-23 (1953).
13. J.A. Duffie and W.R. Marshall, "Factors Influencing the Properties of Spray Dried Materials, Part II," *Chem. Eng. Prog.*, **49** [9] 480-6 (1953).
14. E.J. Crosby and W.R. Marshall, "Effects of Drying Conditions on the Properties of Spray-Dried Particles," *Chem. Eng. Prog.*, **54** [7] 56-63 (1958).
15. S.S. Moor and C.J. Judson, "Visualization of Spray Dynamics in a Pilot Spray Dryer by Laser-Initiated Fluorescence," *Ind. Eng. Chem. Res.* **37** [2] 561-8 (1998).
16. D.D. Frey and C.J. Frey, "Effects of Surfactants on Mass Transfer During Spray Drying," *J. Am. Inst. Chem. Eng.*, **32** [3] 437-43 (1986).
17. T.G. Kieckbusch and C.J. King, "Volatiles Loss During Atomization in Spray Drying," *J. Am. Inst. Chem. Eng.*, **26** [5] 718-25 (1980).
18. E.R. Hoffman, "Importance of Binders in Spray Dried Pressbodies," *Am. Ceram. Soc. Bull.*, **51** [3] 240-2, (1972).

19. J. Mazabek, U.V. Gizycki, and Z. Khwaja, "Control of the Properties of Spray Dried Granulates using Organic Additives," *Ceram. Forum, Int.*, **70** [6] 272-4 (1993).
20. A.G. Pincus and L. Shipley, "The Role of Organic Binders in Ceramic Processing," *Ceram. Ind.*, **92** [1] 106-9,146 (1969).
21. D.W. Whitman, X.K. Wu, and W.C. Finch, "Control of Dry Pressing Performance via Binder Optimization," pp. 225-32 in *Science, Technology, and Commercialization of Powder Synthesis and Shape Forming Processes*. American Ceramic Society, Westerville, Ohio, 1995.
22. S. Baklouti, T. Chartier and J.F. Baumard, "Mechanical Properties of Dry-Pressed Ceramic Green Products: The Effect of the Binder," *J. Am. Ceram. Soc.*, **80** [8] 1992-6 (1997).
23. C.R. Perry and W.M. Carty, "Effect of Plasticizer on Compaction Behavior and Springback Defects," *Ceram. Eng. Sci. Proc.*, **20** [2] 51-63 (1999).
24. K.J. Moeggenborg, "Springback in Dry Pressing: Time, Additive, and Processing Effects," pp. 217-24 in *Science, Technology, and Commercialization of Powder Synthesis and Shape Forming Processes*. American Ceramic Society, Westerville, Ohio, 1995.
25. G.Y. Onoda, "Theoretical Strength of Dried Green Bodies with Organic Binders," *J. Am. Ceram. Soc.*, **59** [5-6] 236-9 (1976).
26. C.W. Nies and G.L. Messing, "Effect of Glass - Transition Temperature of Polyethylene Glycol - Plasticized Polyvinyl Alcohol on Granule Compaction," *J. Am. Ceram. Soc.*, **67** [4] 301-4 (1984).
27. R.A. DiMilia and J.S. Reed, "Dependence of Compaction on the Glass-transition temperature of the Binder Phase," *Am. Ceram. Soc. Bull.*, **62** [4] 484-8 (1983).
28. C.W. Nies and G.L. Messing, "Binder Hardness, and Plasticity in Granule Compaction," pp. 58-66 in *Advances in Ceramics*, Vol. 9. American Ceramic Society, Columbus, Ohio, (1984).
29. F. Ebba, P. Piccerelle, P. Prinderre, D. Opota, and J. Joachim, "Stress Relaxation Studies of Granules as a Function of Different Lubricant," *Eur. J. Pharm. Biopharm.*, **52** [2] 211-20 (2001).
30. R. Bast, "On the Use of Dispersants and Deflocculants," *Ceram. Forum Int.*, **67** [9] 395-8 (1990).
31. W.J. Walker and J.S. Reed, "Polyethylene Glycol Binders for Advanced Ceramics," *Ceram. Eng. Sci. Proc.*, **14** [11-12] 58-79 (1993).
32. A.S. Barnes, J.S. Reed, and A.M. Anderson, "Using Cobinders to Improve Manufacturability," *Am. Ceram. Soc. Bull.*, **76** [7] 77-82 (1997).
33. D.W. Whitman, X. Tang, D.I. Cumbers, and S.A. Ibbitson, "Using Polymer Blends to Fine-Tune Binder Performance," pp. 193-200 in *Science*,

*Technology, and Commercialization of Powder Synthesis and Shape Forming Processes.* American Ceramic Society, Westerville, Ohio, 1995.

34. N. Sarkar and G.K. Greminger, "Methylcellulose Polymers as Multifunctional Processing Aids in Ceramics," *Am. Ceram. Soc. Bull.*, **62** [11] 1280-4,8 (1983).
35. X.K. Wu, D.W. Whitman, W.L. Kaufell, W.C. Finch, and D.I. Cumbers, "Acrylic Binders for Dry Pressing Ceramics," *Am. Ceram. Soc. Bull.*, **76** [1] 49-52 (1997).
36. X.K. Wu, D.W. Whitman, W.L. Kaufell, W.C. Finch, and D.I. Cumbers, "Acrylic Binders for Dry Pressing Ceramics," *Ceram. Eng. Sci. Proc.*, **18** [2] 422-38 (1997).
37. F. Andreola, P. Pozzi, M. Romagnoli, A. Bresciani, and G. Pasquali, "Additives Used in the Pressing of Tableware," *Am. Ceram. Soc. Bull.*, **75** [8] 57-60 (1996).
38. S.L. Bassner and E.H. Klingenberg, "Using Poly(Vinyl Alcohol) as a Binder," *Am. Ceram. Soc. Bull.*, **77** [6] 71-5 (1998).
39. E. Klingenberg, "Poly(vinyl alcohol): Important Properties Related to Its Use as a Temporary Binder in Ceramic Processing," pp. 43-56 in *Science of Whitewares II*. Edited by W.M. Carty and C.W. Sinton. American Ceramic Society, Westerville, Ohio, 2000.
40. J.W. Gilman, D.L. van der Hart, and T. Kashiwagi, "Thermal Decomposition Chemistry of Poly(vinyl alcohol)," Ch. 11 in *Fire and Polymers II: Materials and Test for Hazard Prevention*. American Chemical Society, Washington, D.C., 1994.
41. S. Baklouti, T. Chartier, C. Gault, and J.F. Baumard, "Young's Modulus of Dry-pressed Ceramics: The Effect of the Binder," *J. Eur. Ceram. Soc.*, **19** [8] 1569-74 (1999).
42. S. Baklouti, T. Chartier, C. Gault, and J.F. Baumard, "The Effect of Binders on the Strength and Young's Modulus of Dry-pressed Alumina," *J. Eur. Ceram. Soc.*, **18** [4] 323-8 (1998).
43. N.G. Stanley-Wood and M.S. Shubair, "The Variation of the Surface Topography of Granules under Compression with Degree of Binder Addition," *Powder Technol.*, **25** [1] 57-64 (1980).
44. N. Shinohara, S. Katori, M. Okumiya, T. Hotta, K. Nakahira, M. Naito, Y. Cho, and K. Uematsu, "Effect of Heat Treatment of Alumina Granules on the Compaction Behavior and Properties of Green and Sintered Bodies," *J. Eur. Ceram. Soc.*, **22** [16] 2841, 8 (2002).
45. U. Kim, "The Role of Polymer Compatibility in Ceramic Processing"; Ph.D. Thesis. Alfred University, Alfred, New York, 2002.

46. Y. Zhang, T. Suga, M. Kawasaki, X. Tang, N. Uchida, and K. Uematsu, "Effect of Poly(vinyl alcohol) Adsorption on Binder Segregation during Drying," *J. Am. Ceram. Soc.*, **79** [2] 435-40 (1996).
47. A.E. Nesterov and Y.S. Lipatov, "Compatibilizing Effect of a Filler in Binary Polymer Mixtures," *Polymer*, **40** [5] 1347-9 (1999).
48. M.L. Corrin and W.D. Harkins, "Determination of the Critical Concentration for Micelle Formation in Solutions of Colloidal Electrolytes by the Spectral Change of a Dye," *J. Am. Chem. Soc.*, **69** [3] 679-83 (1947).
49. M.L. Corrin and W.D. Harkins, "The Effect of Salts on the Critical Concentration for the Formation of Micelles in Colloidal Electrolytes," *J. Am. Chem. Soc.*, **69** [3] 683-8 (1947).
50. F. Negre and E. Sanchez, "Advances in Spray-Dried Powder Processing for Tile Manufacture," pp. 169-81 in *Science of Whitewares*. Edited by V.E. Henkes, G.Y. Onoda, and W.M. Carty. American Ceramic Society, Westerville, Ohio, 1996.
51. D. Doshi and J.S. Reed, "Critical Flaws in Sintered Compacts of Alumina Granules," *Ceram. Eng. Sci. Proc.*, **16** [9-10] 939-48 (1995).
52. U.B. Agbarakwe, J.S. Banda, and P.F. Messer, "Non-uniformities and Pore Formation," *Mater. Sci. Eng. A*, **109** [1-2] 9-16 (1989).
53. S.J. Lukasiewicz and J.S. Reed, "Character and Compaction Response of Spray-Dried Agglomerates," *Am. Ceram. Soc. Bull.*, **57** [9] 798-801 (1978).
54. J. Zheng and J.S. Reed, "Particle and Granule Parameters Affecting Compaction Efficiency in Dry Pressing," *J. Am. Ceram. Soc.*, **71** [11] C456-8 (1988).
55. R.G. Frey and J.W. Halloran, "Compaction Behavior of Spray-Dried Alumina," *J. Am. Ceram. Soc.*, **67** [3] 199-203 (1984).
56. T. Kennedy, S. Hampshire and Y. Yaginuma, "A Study of the Compaction Mechanism of Granulate Material," *J. Eur. Ceram. Soc.*, **17** [2/3] 133-9 (1997).
57. R. Topolevsky and R.E. Caligaris, "Compaction Behavior of Ceramic Powders. Correlation Functions Between Processing Variables and Fired Properties," *Powder Technol.*, **46** [2-3] 215-8 (1986).
58. W.J. Walker and J.S. Reed, "Granule Fracture During Dry Pressing," *Am. Ceram. Soc. Bull.*, **78** [6] 53-7 (1999).
59. H. Abe, T. Hotta, M. Naito, N. Shinohara, M. Okumiya, H. Kamiya, and K. Uematsu, "Origin of Strength Variation of Silicon Nitride Ceramics with CIP Condition in a Powder Compaction Process," *Powder Technol.*, **119** [2-3] 194-200 (2001).
60. M. Wikberg and G. Alderborn, "Compression Characteristics of Granulated Materials: II. Evaluation of Granule Fragmentation during Compressions

- by Tablet Permeability and Porosity Measurements," *Int. J. Pharm.*, **62** [2-3] 229-41 (1990).
61. M. Wikberg and G. Alderborn, "Compression Characteristics of Granulated Materials: III. The Relationship Between Air Permeability and mechanical Strength of Tablets of Some Lactose Granulations," *Int. J. Pharm.*, **63** [1] 23-7 (1990).
  62. M. Wikberg and G. Alderborn, "Compression Characteristics of Granulated Materials: IV. The Effect of Granule Porosity on the Fragmentation Propensity and the Compactibility of Some Granulations," *Int. J. Pharm.*, **69** [3] 239-53 (1991).
  63. M. Wikberg and G. Alderborn, "Compression Characteristics of Granulated Materials: VI. Pore Size Distribution, Assessed by Mercury Penetration, of Compacts of Two Lactose Granulations with Different Fragmentation Propensities," *Int. J. Pharm.*, **84** [2] 191-5 (1992).
  64. S.M. Wolfrum, "Dry Pressing Surface-Modified Powders," *J. Mater. Sci. Lett.*, **7** [10] 1130-2 (1988).
  65. M. Otani, H. Minoshima, W. Hino, and K. Shimohara, "Wall Friction Characteristics of Differently Shaped Particles," *J. Ceram. Soc. Jpn.*, **105** [12] 1099-102 (1997).
  66. D.T. Gethin, V.D. Tran, R.W. Lewis, and A.K. Ariffin, "An Investigation of Powder Compaction Processes," *Int. J. Powder Metall.*, **30** [4] 385-98 (1994).
  67. U. Klemm, D. Sobek, B. Schone, and J. Stockmann, "Friction Measurements during Dry Compaction of Silicon Carbide," *J. Eur. Ceram. Soc.*, **17** [2-3] 141-5 (2000).
  68. W.A. Lewis, "Variables Encountered in Dry Pressing Technical Ceramics," *Ceram. Eng. Sci. Proc.*, **17** [1] 137-43 (1996).
  69. B. Frisch, W.R. Thiele, and W. Berwanger, "Cyclical Dry Pressing and Its Effects on the Green and Sintered Properties of Stabilized and Unstabilized Clay-base and Oxide Ceramics," *Ceram. Forum, Int.*, **63** [6] 263-71 (1986).
  70. W. Chen, A. Pechenik, S.J. Dapkunas, G.J. Piermarini, and S.G. Malghan, "Novel Equipment for the Study of the Compaction of Fine Powders," *J. Am. Ceram. Soc.*, **77** [4] 1005-10 (1994).
  71. M. Ciftcioglu, M. Akinc, and L. Burkhart, "Measurement of Agglomerate Strength Distributions in Agglomerated Powders," *Am. Ceram. Soc. Bull.*, **65** [12] 1591-6, (1986).
  72. D.E. Niesz, R.B. Bennett, and M.J. Snyder, "Strength Characterization of Powder Aggregates," *Am. Ceram. Soc. Bull.*, **51** [9] 677-80, (1972).

73. R.A. Thompson, "Mechanics of Powder Processing: III, Model for the Green Strength of Pressed Powders," *Am. Ceram. Soc. Bull.*, **60** [2] 248-51 (1981).
74. F.S. Ortega, R.G. Pileggi, P. Sepulveda, and V.C. Pandolfelli, "Optimizing the Particle Packing in Powder Consolidation," *Am. Ceram. Soc. Bull.*, **78** [8] 106-11 (1999).
75. W. Pyda and M.S.J. Gani, "Microstructure and Mechanical Properties of Spherical Zirconia-Yttria Granules," *J. Mater. Sci.*, **30** [8] 2121-9 (1995).
76. B.J. Briscoe and N. Ozkan, "Compaction Behavior of Agglomerated Alumina Powders," *Powder Technol.*, **90** [3] 195-203 (1997).
77. D.C.C. Lam, "Effects of Binder and Compaction Pressure on Strength and Fracture Origins in Bodies Pressed from Granules," *J. Ceram. Soc. Jpn.*, **102** [11] 1010-5 (1994).
78. G.L. Messing, C.J. Markhoff, and L.G. McCoy, "Characterization of Ceramic Powder Compaction," *Am. Ceram. Soc. Bull.*, **61** [8] 857-60 (1982).
79. J.W. Halloran, "Role of Powder Agglomerates in Ceramic Processing," pp. 67-75 in *Advances in Ceramics*, Vol. 9. American Ceramic Society, Columbus, Ohio, (1984).
80. H. Kuno and J. Okada, "The Compaction Process and Deformability of Granules," *Powder Technol.*, **33** [1] 73-9 (1982).
81. A.R. Cooper and L.E. Eaton, "Compaction Behavior of Several Ceramic Powders," *J. Am. Ceram. Soc.*, **45** [3] 97-101 (1962).
82. D.B. Leiser and O.J. Whittemore, "Compaction Behavior of Ceramic Particles," *Am. Ceram. Soc. Bull.*, **49** [8] 714-7 (1970).
83. R.A. Youshaw and J.W. Halloran, "Compaction of Spray-Dried Powders," *Am. Ceram. Soc. Bull.*, **61** [2] 227-30 (1982).
84. J. van der Zwan and C.A.M. Siskens, "The Compaction and Mechanical Properties of Agglomerated Materials," *Powder Technol.*, **33** [1] 43-54 (1982).
85. V.M. Kenkre, M.R. Endicott, S.J. Glass, and A.J. Hurd, "A Theoretical Model for Compaction of Granular Materials," *J. Am. Ceram. Soc.*, **79** [12] 3045-54 (1996).
86. P.R. Mort, R. Sabia, D.E. Niesz and R.E. Riman, "Automated Generation and Analysis of Powder Compaction Diagrams," *Powder Technol.*, **79** [2] 111-9 (1994).
87. R.L.K. Matsumoto, "Analysis of Powder Compaction Using a Compaction Rate Diagram," *J. Am. Ceram. Soc.*, **73** [2] 465-8 (1990).
88. R.D. Carneim, G.L. Messing, "Response of Granular Powders to Uniaxial Loading and Unloading," *Powder Technol.*, **115** [2] 131-8 (2001).

89. M. Taha, J. Paletto, Y. Jorand, G. Fantozzi, A. Samdi, M. Jebrouni, and B. Durand, "Compaction and Sintering Behavior of Zirconia Powders," *J. Eur. Ceram. Soc.*, **15** [8] 759-68 (1995).
90. S.J. Glass and C. Newton, "A Comparison of Pressure Compaction and Diametral Compression Tests for Determining Granule Strengths," pp. 203-15 in *Science, Technology, and Commercialization of Powder Synthesis and Shape Forming Processes*. American Ceramic Society, Westerville, Ohio, 1995.
91. S. Labisch, C. Weber, and H. Werner, "Investigation of the Stiffness of Individual and Agglomerated Granules by the Finite Element Method," *Ceram. Forum, Int.*, **72** [9] 541-5 (1995).
92. H. Zipse, "Finite-Element Simulation of the Die Pressing and Sintering of a Ceramic Component," *J. Eur. Ceram. Soc.*, **17** [14] 1707-13 (2000).
93. A. Geigle, K. Hauswurz, and S. Mager, "Optimization of Spray-Dried Granulates for Isostatic Pressing of Tableware," *Interceram.*, **42** [1] 16-9 (1993).
94. W. Schulle, R. Bartusch, and R. Lucke, "New Findings on the Compaction and Evaluation of Isostatically Pressed Whiteware Compacts," *Ceram. Forum, Int.*, **67** [12] 560-5 (1990).
95. E.L.J. Papen, H.D.B. Raes, and G. Deplace, "Development and Application of the Isostatic Pressing Process in the Refractories, Ceramic, and Electrical Porcelain Industrials," *Interceram*, **23** [3] 204-11 (1974).
96. R.J. Henderson, H.W. Chandler, A.R. Akisanya, H. Barber, and B. Moriarty, "Finite Element Modelling of Cold Isostatic Pressing," *J. Eur. Ceram. Soc.*, **20** [8] 1121-8 (2000).
97. L.T. Kuhn, R.M. McMeeking, and F.F. Lange, "A Model for Power Consolidation," *J. Am. Ceram. Soc.*, **74** [3] 682-5 (1991).
98. H. Takahashi, N. Shinohara, M. Okumiya, K. Uematsu, T. Junlchiro, Y. Iwamoto, and H. Kamiya, "Influence of Slurry Flocculation on the Character and Compaction of Spray-Dried Silicon Nitride Granules," *J. Am. Ceram. Soc.*, **78** [4] 903-8 (1995).
99. H. Takahashi, N. Shinohara, and K. Uematsu, "Influence of Spray-Dry Slurry Flocculation on the Structure of Sintered Silicon Nitride," *J. Ceram. Soc. Jpn.*, **104** [1] 59-61 (1996).
100. G.E. Fair and F.F. Lange, "Effect of Interparticle Potential on Forming Solid, Spherical Agglomerates During Drying," *J. Am. Ceram. Soc.*, **87** [1] 4-9 (2004).
101. S.J. Lukasiewicz, "Compaction of Agglomerated and Bulky Ceramic Powders"; M.S. Thesis. Alfred University, Alfred, New York, 1976.
102. J.A. Brewer, "Compaction Response of Agglomerated Powder During Isostatic Pressing"; M.S. Thesis. Alfred University, Alfred, New York, 1979.

103. R.H. Moore, "The Dependence of Compaction in a Metal Die on the Character of Agglomerated Feed Powder"; M.S. Thesis. Alfred University, Alfred, New York, 1979.
104. W.J. Walker, "Polyethylene Glycol Binders for Advanced Ceramic Processing"; M.S. Thesis. Alfred University, Alfred, New York, 1992.
105. W.J. Walker, "Powder Compaction: Processing to Optimize the Granule Characteristics for Advanced Ceramics"; Ph.D. Thesis. Alfred University, Alfred, New York, 1996.
106. A.S. Barnes, "Evaluation of the Effects of Organic Binder System, Alumina Types, and Firing Schedule on the Spray Drying, Granule, and Compaction Properties of Advances Alumina Ceramics"; M.S. Thesis. Alfred University, Alfred, New York 1996.
107. O. Abe, S. Kanzaki, and H. Tabata, "Structural Homogeneity of CIP Formed Green Compacts (Part 2), Influence of Applying Pressure," *J. Ceram. Soc. Jpn.*, **97** [1] 32-7 (1989).
108. D. Bortzmeyer, "Modelling Ceramic Powder Compaction," *Powder Technol.*, **70** [2] 131-9 (1992).
109. B.J. Briscoe and S.K. Sinha, "Density Distribution Characteristics of Green Ceramic Compacts Using Scratch Hardness," *Tribol. Int.*, **30** [7] 475-82 (1990).
110. J.J. Lannutti, T.A. Deis, M. Kong, and D.H. Phillips, "Density Gradient Evolution during Dry Pressing," *Am. Ceram. Soc. Bull.*, **76** [1] 53-8 (1997).
111. B.J. Briscoe and P.D. Evans, "Wall Friction in the Compaction of Agglomerated Ceramic Powders," *Powder Technol.*, **65** [1-3] 7-20 (1991).
112. P.K. Lu and J.J. Lannutti, "Effect of Density Gradients on Dimensional Tolerance during Binder Removal," *J. Am. Ceram. Soc.*, **83** [10] 2536-42 (2000).
113. C.M. Kong and JJ. Lannutti, "Localized Densification during the Compaction of Alumina Granules: The Stage I-II Transition," *J. Am. Ceram. Soc.*, **83** [4] 685-90 (2000).
114. A.B. van Groenou and R.C.D. Lissenburg, "Inhomogeneous Density in Die Compaction: Experiments and Finite Element Calculations," *J. Am. Ceram. Soc.*, **66** [9] C156-8 (1983).
115. N. Ozkan and B.J. Briscoe, "Characterization of Die-Pressed Green Compacts," *J. Eur. Ceram. Soc.*, **17** [5] 697-711 (1997).
116. A.B. van Groenou, "Compaction of Ceramic Powders," *Powder Technol*, **28** [2] 221-8 (1981).
117. "Standard Test Method for Splitting Tensile Strength of Intact Rock Core Specimens," ASTM Test Designation D3967-95a. American Society for Testing and Materials, West Conshohocken, Pennsylvania.

118. D.K. Shetty, A.R. Rosenfield, P. McGuire, G.K. Bansal, and W.H. Duckworth, "Biaxial Flexure Tests for Ceramics," *Am. Ceram. Soc. Bull.*, **59** [12] 1193-7 (1980).
119. A. Rudnick, A.R. Hunter, and F.C. Holden, "An Analysis of the Diametral-Compression Test," *Mater. Res. Stand.*, **3** [4] 283-9 (1963).
120. M. Radeka, J. Ranogajec, R. Marinkovic-Neducin, and B. Zivanovic, "Compaction Mechanism as the Function of Atomized Powder Particle Size," *Ceram. Ind.*, **21** [4] 249-55 (1995).
121. B.D. Mosser, J.S. Reed, and J.R. Varner, "Strength and Weibull Modulus of Sintered Compacts of Spray Dried Alumina," *Am. Ceram. Soc. Bull.*, **71** [1] 105-9 (1992).
122. J. Zheng, W.B. Carlson, and J.S. Reed, "Dependence of Compaction Efficiency in Dry Pressing on the Particle Size Distribution," *J. Am. Ceram. Soc.*, **78** [9] 2527-33 (1995).
123. W.J. Walker and J.S. Reed, "Influence of Granule Character on Strength and Weibull Modulus of Sintered Alumina," *J. Am. Ceram. Soc.*, **82** [1] 50-6 (1999).
124. A. Meurk, J. Yanez, and L. Bergström. "Silicon Nitride Granule Friction Measurements with an Atomic Force Microscope: Effect of Humidity and Binder Concentration," *Powder Technol.*, **119** [2-3] 241-9 (2001).
125. D.W. Whitman, D.I. Cumbers, and X.K. Wu, "Humidity Sensitivity of Dry Press Binders," *Am. Ceram. Soc. Bull.*, **74** [8] 76-9 (1995).
126. R.A. DiMilia and J.S. Reed, "Effect of Humidity on the Pressing Characteristics of Spray-Dried Alumina," pp. 38-46 in *Advances in Ceramics*, Vol. 9. American Ceramic Society, Columbus, Ohio, (1984).
127. H. Tanaka, S. Fukai, N. Uchida, K. Uematsu, A. Sakamoto, and Y. Nagao, "Effect of Moisture on the Structure and Fracture Strength of Ceramic Green Bodies," *J. Am. Ceram. Soc.*, **77** [12] 3077-80 (1994).
128. W.M. Carty, New York State College of Ceramics, Alfred University, Alfred, New York, October, 2001, Private Communication.
129. J. Doran, New York State College of Ceramics, Alfred University, Alfred, New York, 1995 (unpublished).
130. J.E. Funk, "Psychrometric Drying," pp. 77-95 in *Technical Innovations in Whitewares*. Edited by J.S. Reed, J.E. Funk, P.E. Johnson, and J.R. Varner. Alfred University Press, Alfred, New York, 1982.
131. R.M. German, "Liquid Phase Sintering," Ch. 6 in *Sintering Theory and Practice*. Wiley Interscience Publication, New York, New York, 1996.
132. M. Radeka, M. Djuric, J. Ranogajec, B. Zivanovic, and L. Petrasinovic-Stojkanovic, "Transport Characteristics of Ceramic Particles During Compaction," *Ceram. Forum Int.*, **77** [4] 24-9 (2000).

133. B.R. Pai, S. Michelfelder, and D.P. Spalding, "Prediction of Furnace Heat Transfer with a Three-Dimensional Mathematical Model," *Int. J. Heat Mass Transfer*, **22** [5] 571-80 (1978).
134. B. Gal-Or, G.E. Klinzing, and L.L. Tavlarides, "Bubble and Drop Phenomena," *Ind. Eng., Chem.*, **61** [2] 21-31 (1969).
135. W.E. Ranz and W.R. Marshall, "Evaporation from Drops," *Chem. Eng. Prog.*, **48** [3] 141-6 (1952).
136. A. Negiz, E.S. Lagergren, and A. Cinar, "Mathematical Modeling of Cocurrent Spray Drying," *Ind. Eng. Chem. Res.* **34** [10] 3289-302 (1995).
137. D.E. Oakley and R.E. Bahu, "Computational Modelling of Spray Dryers," *Comput. Chem. Eng.*, **17** [1] 493-8 (1993).
138. I. Zbicinski, S. Grabowski, C. Strumillo, L. Kiraly, and W. Krzanowski, "Mathematica Modelling of Spray Drying," *Comput. Chem, Eng.*, **12** [2-3] 209-14 (1988).
139. J.P. Hecht and C.J. King, "Spray Drying: Influence of Developing Drop Morphology on Drying Rates and Retention of Volatile Substances. 2. Modeling," *Ind. Eng. Chem. Res.*, **39** [6] 1766-74 (2000).
140. N.J. Ninos, Oneida Dinnerware, Buffalo, New York, January, 2002, Private Communication.
141. "Lignin," pp. 233-72 in *Encyclopedia of Polymer Science and Technology: Plastics, Resins, Rubbers, Fibers*, Vol. 8. Edited by H.F. Mark, N.G. Gaylord, and N.M. Bikales. Wiley Interscience Publishers, New York, New York, 1968.
142. K. Rieger, R.T. Vanderbilt, Inc., Norwalk, Connecticut, October, 2003, Private Communication.
143. "Latexes," pp. 164-94 in *Encyclopedia of Polymer Science and Technology: Plastics, Resins, Rubbers, Fibers*, Vol. 8. Edited by H.F. Mark, N.G. Gaylord, and N.M. Bikales. Wiley Interscience Publishers, New York, New York, 1968.
144. "Polysaccharides," pp. 396-424 in *Encyclopedia of Polymer Science and Technology: Plastics, Resins, Rubbers, Fibers*, Vol. 11. Edited by H.F. Mark, N.G. Gaylord, and N.M. Bikales. Wiley Interscience Publishers, New York, New York, 1969.
145. P. Scheiner, Simpson, Gumperta, & Heger, Inc., October, 2003, Private Communication.
146. "Cellulose," pp. 131-219 in *Encyclopedia of Polymer Science and Technology: Plastics, Resins, Rubbers, Fibers*, Vol. 3. Edited by H.F. Mark, N.G. Gaylord, and N.M. Bikales. Wiley Interscience Publishers, New York, New York, 1965.

## **8. Compaction versus Shear Compaction**

### **8.1 Introduction**

Based upon the previous work the P1 value of granulate can be reduced by proper selection of a binder system and control of the moisture content of the granulate. Previous unpublished work indicates that the combination of compaction and shear further facilitates the deformation of the granulate resulting in superior compaction.<sup>1</sup> Failure of granular materials has been determined using a Jenike-type shear cell where a linear relationship was observed between the normal stress and the shear stress.<sup>2</sup> The loads used in the study were insufficient to cause deformation of the granular materials. Therefore a study was performed to compare uniaxial compaction diagrams, via the Instron testing machine, and shear compaction diagrams, generated in the HPASC, as a function of moisture content. In the process of generating shear compaction diagrams the plasticity of the granulate was also characterized.

### **8.2 Experimental Procedure**

Approximately 250 grams of the granulate supplied by Buffalo China, each binder system was evaluated separately, were tumbled in a steam chamber constructed at Alfred University. The chamber, shown in Figure 8-1, consisted of a Lexan box which was set over a steam humidifier. A thermostat and an infrared bulb were used to control the temperature within the chamber. A small fan was used to circulate the air within the box and a cell, consisting of perforated PVC lined with a 270-mesh stainless steel cloth, was tumbled at approximately 12 rpm within the chamber. Early attempts to control the humidity and temperature within the chamber proved difficult due to variations in the temperature and humidity within a 24-hour period. It was decided therefore to maintain the temperature above 35°C and the relative humidity at 100%. The temperature and humidity in the chamber were monitored using a traceable hygrometer [Fisher Scientific, Pittsburgh, PA] with a memory recall for the highest and lowest values of temperature (in °C and °F) and relative humidity.

Samples were tumbled for various periods of time to increase the moisture content of the granulate. Due to the high relative humidity in the chamber

physical moisture was condensed within the pores of the granulate, see Chapter 7.3.2 for a discussion of re-hydrating granulate. Once the granulate had been humidified the samples were stored in sealed polypropylene containers until they were tested.

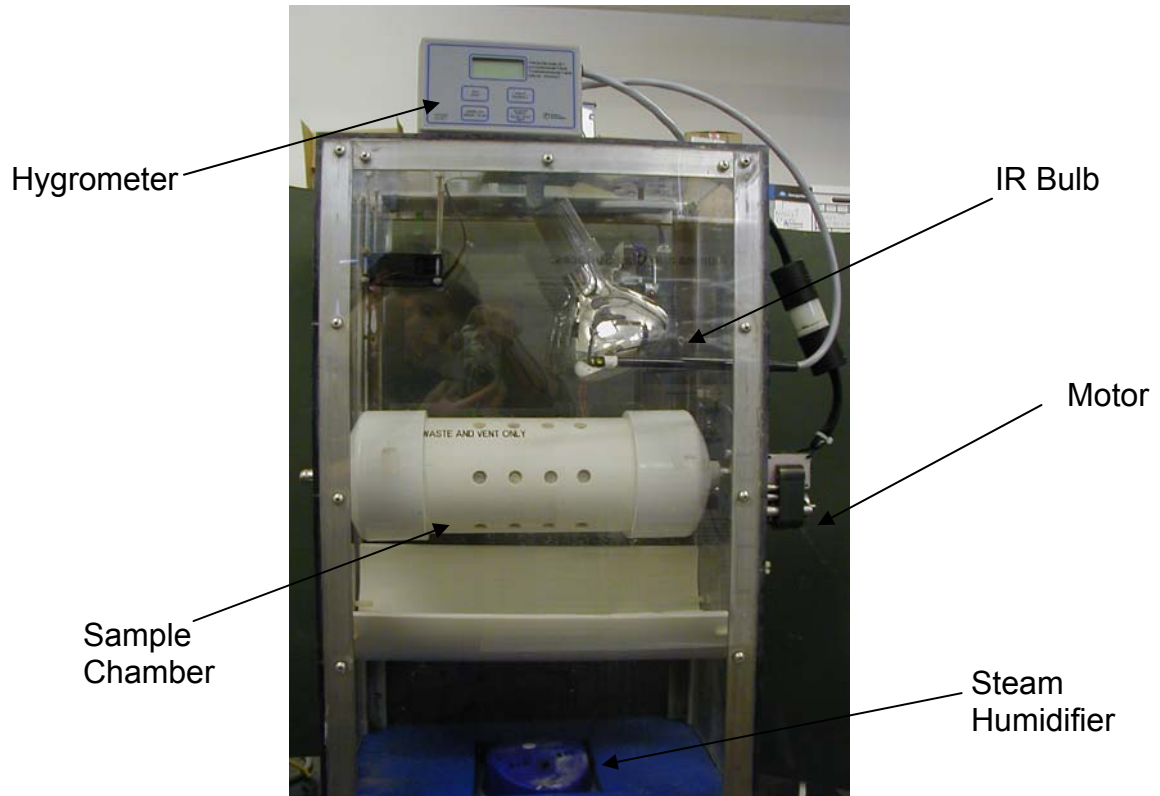


Figure 8-1. Digital image of the steam chamber constructed at Alfred University.

Samples were tested in uniaxial compression and in shear to determine a uniaxial P1 and a shear P1 value. The uniaxial P1 value was determined by a standard compaction test. The resulting compacts from the uniaxial compaction were tested for density and green strength. Procedures to determine P1, the compact density, and green strength were reported in Chapter 7.2.

The shear P1 was determined using the HPASC. The design of the sample cell for the HPASC was discussed in Chapter 5. The sample in the cell was placed in shear by rotating the bottom portion of the cell at 0.53 rpm while holding the top portion stationary. The vertical position of the top portion of the

cell was monitored by a height gage clamped to the frame of the HPASC. To obtain the low loads necessary to measure P1 the arm of the dead-weight system was counter balanced with 117.5 pounds. The load on the dead-weight system was ranged from 12.5 to 250 pounds in small increments. The sample was allowed to equilibrate at each load for two minutes, corresponding to one revolution of the lower portion of the cell. The test was ended when either the maximum load was reached, water was observed to be expressed from the sample, or when frictional effects were observed to interfere with the test. Samples that were compacted in shear were not available to test the density and the green strength.

Samples were prepared at higher moisture content using the Brabender prep-mixer as described in Chapter 5. These samples were prepared so that the moisture content would overlap that from the steam chamber. Samples were prepared with increasing moisture content until it appeared that the samples were oversaturated with water, i.e.,  $DPS > 1$ .

The lignosulphonate and pPVA granulate from the steam chamber was used to press samples for measurement of the surface roughness. Samples were pressed on the Aeonic press using an elastomer insert, cut from an elastomer membrane for the Dorst press, to replicate a semi-isostatic pressing process. Samples that appeared to be aggregated due to the moisture in the steam chamber were not pressed.

### *8.2.1 Regression Analysis to Determine Shear P1*

While it was possible to obtain low normal pressures to consolidate the samples in shear, no inflection point, i.e., a P1 value, was observed. Therefore a linear regression was taken for the shear compaction data using Excel. A second regression was taken for the low-pressure region of the uniaxial compaction data, see Figure 8-2. The intersection of the two lines was calculated and taken as the P1 value in shear; it was assumed that the fill density of the samples was independent of the test method. For a further discussion of this method and a sample calculation see Appendix K.

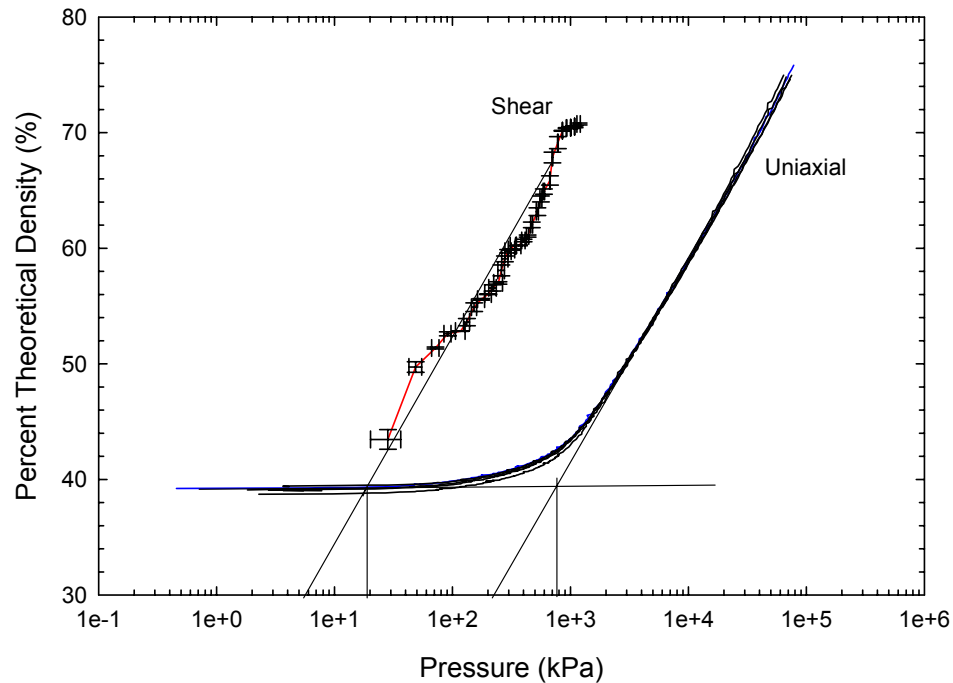


Figure 8-2. Comparison of uniaxial compaction curves to a shear compaction curve for a sample of dried pPVA granulate.

### 8.2.2 Plasticity of a Granulated Porcelain Body with Organic Binders

During shear compaction of the re-humidified granulate data was collected to study the plasticity of the granulated porcelain body as function of moisture content using the procedure reported in Chapter 5. Each normal pressure/shear stress pair corresponded to a single Mohr's stress circle where the normal pressure was the center, plotted along the x-axis, and the shear stress corresponded to the circle radius (this was based upon the assumption that the maximum shear stress was measured). A linear regression was taken through the data, using Excel, where the slope was taken as the pressure dependence (a measure of the internal friction) and the y-intercept was the cohesion. The raw data from the HPASC was used to perform the regression analysis so that there were 40 repeat points for each normal load tested.

### 8.3 Results

The P1 results from uniaxial compaction and shear compaction are shown in Figure 8-3. As the moisture content of the granulate increased the measured uniaxial P1 value undergoes an initial rapid decrease followed by a plateau above 3% moisture. The P1 value measured in shear was nearly independent of the moisture content. While the P1 measured in shear was low it is important to note that the dried samples were not fully consolidated prior to the frictional effects stopping the test. The dried samples were observed to be consolidated in the shear region, but unconsolidated outside of the shear region.

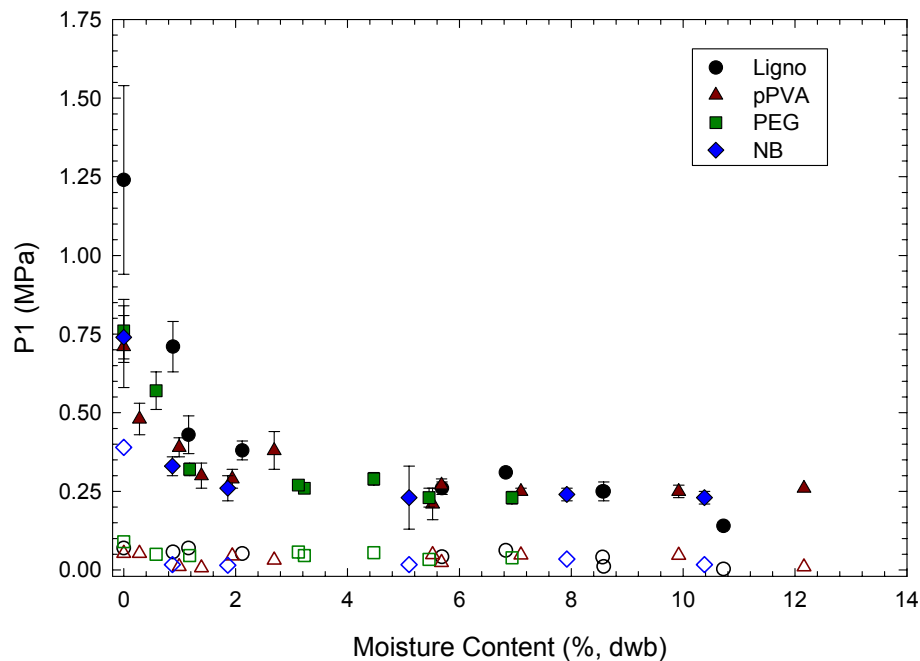


Figure 8-3. Comparison of the P1 measured in uniaxial (solid symbols) and shear (open symbols) compaction as a function of moisture content. P1 in uniaxial compaction is observed to decrease until a plateau value is reached at approximately 3% moisture. Shear during compaction process is observed to reduce the measured P1 value by approximately 1 order of magnitude.

The compact density is plotted in Figure 8-4 for each of the binder systems studied in uniaxial compaction. The compact density was observed to significantly increase with increasing moisture content. Above 3% moisture the density was observed to plateau. The green strength of the compacts prepared

in uniaxial compaction is plotted in Figure 8-5. The green strength increases with increasing moisture content up to approximately 3% at which point the green strength reached a plateau.

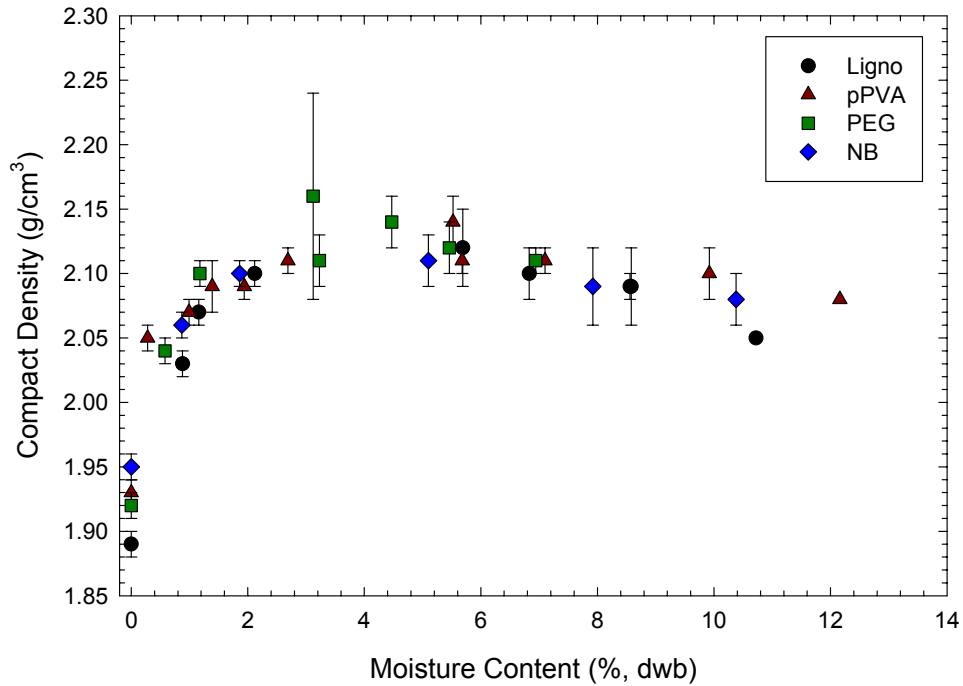


Figure 8-4. Compact density of the samples prepared by uniaxial compaction. Compact density is observed to increase up to approximately 3% moisture at which point the density reaches a plateau value.

The roughness results are plotted in Figure 8-6 for the pPVA and Ligno binder systems. The roughness of the tiles decreases with increasing moisture content. Above 3% moisture the roughness values reached a plateau. The roughness measured in this study was significantly higher than those that were initially measured on Buffalo China’s dry pressed ware, Chapter 6. This was an artifact of the forming process, i.e., compaction in a hardened steel die with an elastomer insert. A strong correlation was again observed between P1 and the measured RMS roughness, Figure 8-7. Images of the surface finish from the optical interferometer are shown in Appendix L.

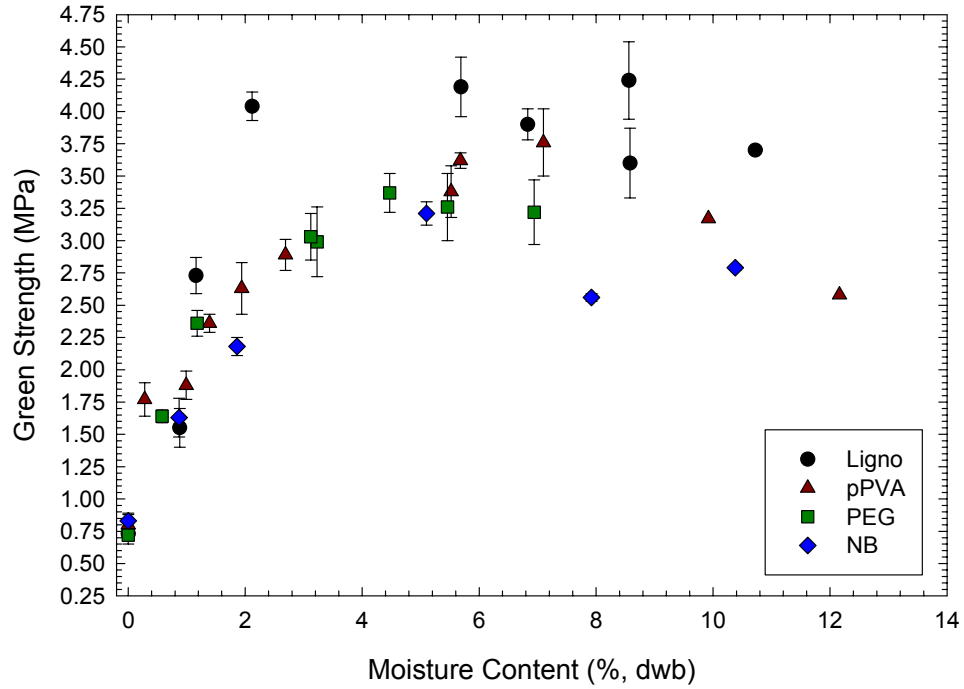


Figure 8-5. Plot of the green strength of the compacts from uniaxial compaction. The green strength is observed to increase until a plateau value is reached at approximately 3% moisture.

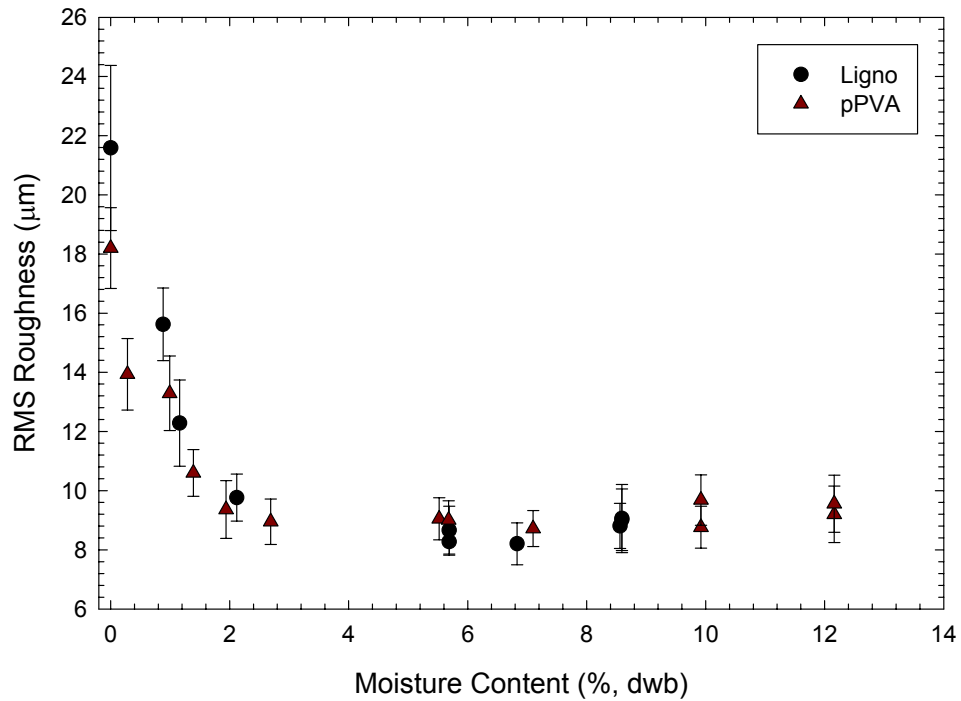


Figure 8-6. Plot of the RMS roughness as a function of moisture content for the Ligno and pPVA granulate. RMS roughness is observed to rapidly decrease with increasing moisture content until a plateau is reached at approximately 3% moisture.

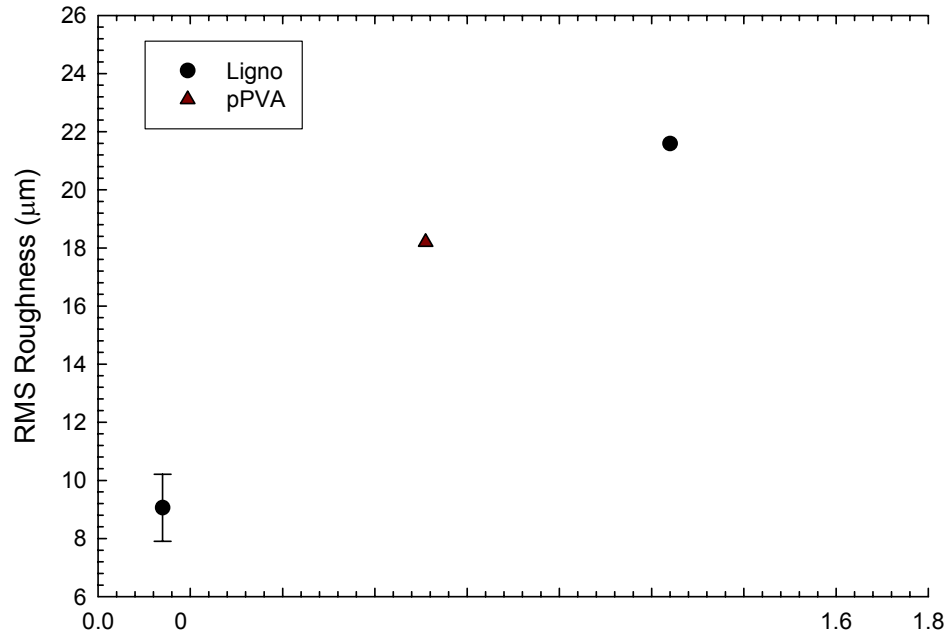


Figure 8-7. Correlation plot for the RMS roughness and uniaxial P1 value for the Ligno and pPVA granulate samples. Uniaxial P1 and RMS roughness are observed to be correlated.

Negre and Sanchez indicate that moisture content of granulate can reduce the flowability.<sup>3</sup> Moisture contents above 3% were observed to significantly reduce the flowability of the granulate in their work. Plateau values in this study were observed at approximately 3% moisture. At 3% moisture the P1 and RMS roughness reach a minimum value while the density and green strength reach a maximum.

### 9.3.1 Plasticity of a Granulated Porcelain Body with Organic Binders

The results from the characterization of the plasticity on the granulated porcelain body prepared with organic binders are shown in Figure 8-8 (cohesion) and Figure 8-9 (pressure dependence). All systems show similar trends; there was an initial decrease in cohesion, resulting in a negative cohesion value, followed by an increase to a maximum value and finally a decrease in the cohesion of the sample at high moisture content. In all cases the pressure dependence of the samples initially increased followed by a decrease with

increasing moisture content. The samples that were prepared with the Brabender mixer were observed to overlap the samples humidified in the steam box. The data from the HPASC was used to construct a shear rheology map, cohesion as a function of pressure dependence, for each binder system. The shear rheology maps are shown in Figure 8-10 (Ligno), Figure 8-11 (pPVA), Figure 8-12 (PEG 8000), and Figure 8-13 (NB). The peak cohesion values for each binder system are listed in Table 8-I.

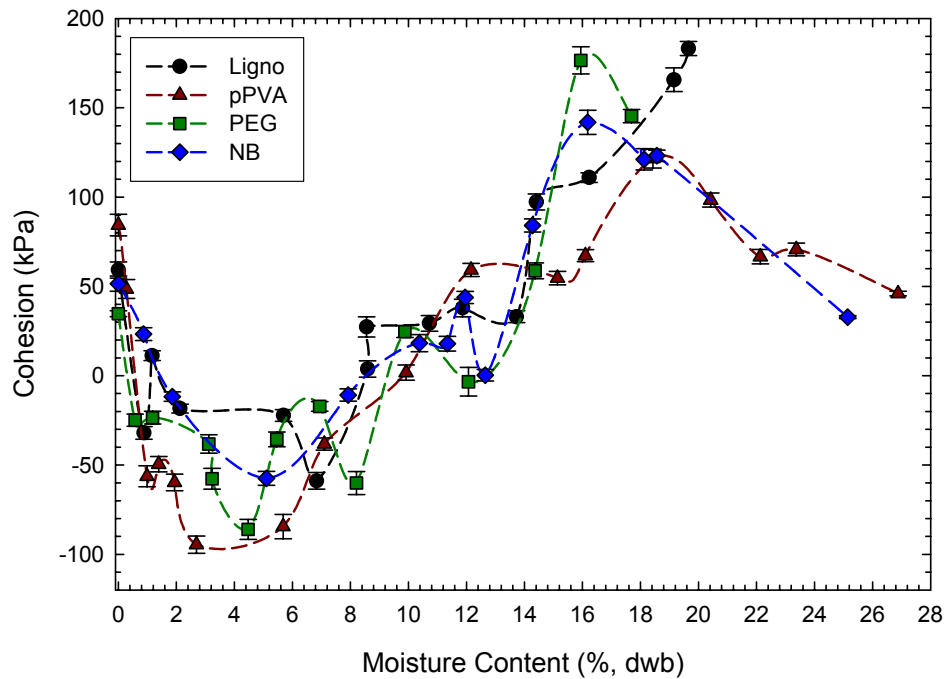


Figure 8-8. Plot of the measured cohesion as a function of moisture content for the binder systems in this study. Little variation is observed between the NB and the PEG system. The pPVA system is shifted to slightly down and to the right, i.e., the peak occurs at higher moisture content, but with a lower maximum value. The Ligno curve is shifted up and to the right; a peak is not observed within the moisture content range used in this study. Lines have been added to help guide the eye.

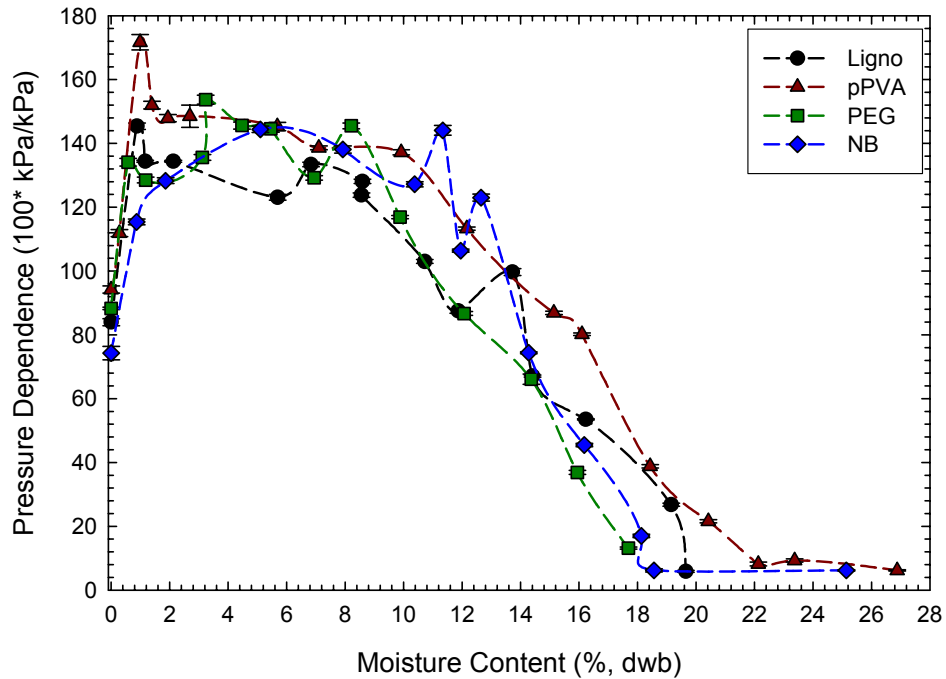


Figure 8-9. Plot of the pressure dependence measure using the HPASC for each of the binder systems in this study. Little variation is observed in the pressure dependence. Lines have been added to help guide the eye.

Table 8-I. Peak Cohesion Values Determined on the HPASC for Each Binder System in This Study.

Binder System	Peak Cohesion	Pressure Dependence	Moisture Content
	kPa	100*kPa/kPa	wt%, dwb
Lignosulphonate*	183.24±3.94	5.90±0.30	19.62
pPVA	121.60±5.30	38.80±0.50	18.43
PEG 8000	176.59±7.60	36.90±0.60	15.94
NB	123.19±3.21	6.20±0.50	18.56

\* Peak cohesion was not observed within the moisture content range tested

The change in the shear rheology of the granulated feed material will be discussed in reference to the system prepared with no organic binder. The NB granulate was observed to have a relatively low peak cohesion value and a low

pressure dependence. The addition of PEG 8000 to the granulate material was observed to increase the peak cohesion value and the pressure dependence. The moisture content at the peak cohesion value for the PEG 8000 granulate was observed to be significantly lower than that of the NB system. The pPVA granulate was observed to have no significant change in the peak cohesion value, but there was a significant increase in the pressure dependence of the plastic material. The addition of lignosulphonate was observed to significantly increase the peak cohesion value; no peak was actually observed within the range of moisture contents tested, but the highest value observed exceeded that of the NB system. The pressure dependence of the lignosulphonate system was observed to be low near the peak cohesion value. Furthermore the moisture content of required to achieve the peak cohesion was the highest observed for the binder systems studied.

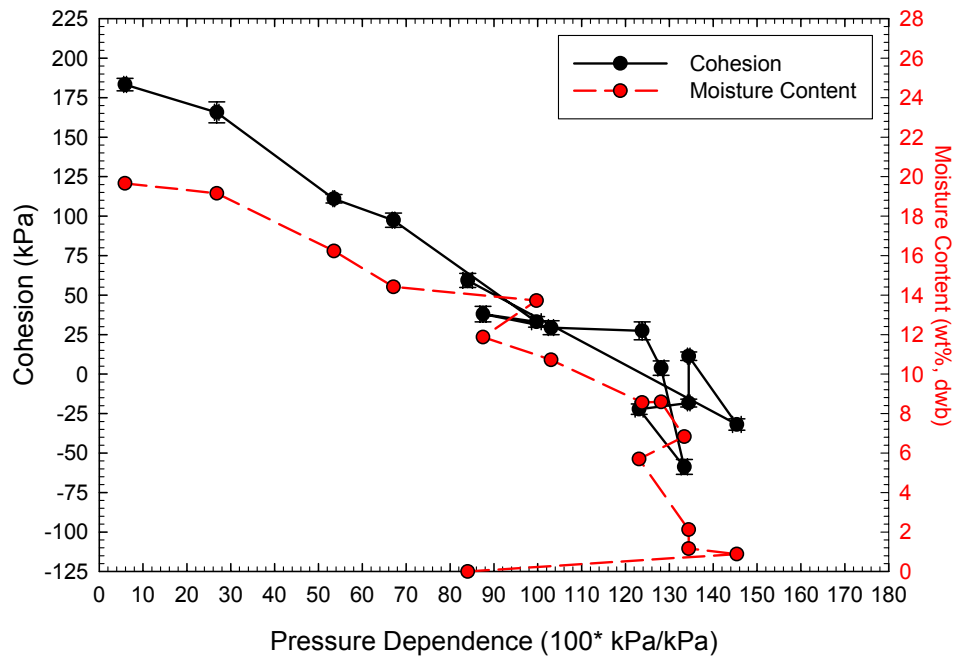


Figure 8-10. Cohesion and moisture content as a function of pressure dependence for the granulate with the lignosulphonate binder system. Cohesion is initially observed to decrease with increasing pressure dependence and moisture content. Significant scatter is observed at high pressure dependence. At high moisture content the cohesion is observed to increase with a decrease in pressure dependence. A maximum is not observed in the cohesion for the lignosulphonate binder system. Lines are purely to help guide the eye.

The plasticity results can be related back to the surface tension results reported in Chapter 5 and the adsorption of the organics on the particle surface. The addition of PEG 8000 or pPVA in solution was observed to reduce the surface tension of water due to their hydrophobic nature. The addition of lignosulphonate was also observed to decrease the surface tension of water. Since PEG and PVA do not significantly adsorb onto the surface on clay these additives remained in the bulk solution and had detrimental effects on the plasticity of the TK6 clay. The adsorption of lignosulphonate on the surface of the clay removed these species from the bulk solution and created an electrosteric barrier to particle-particle interactions. This resulted in a reduction in the pressure dependence of the clay with a corresponding increase in the cohesion.

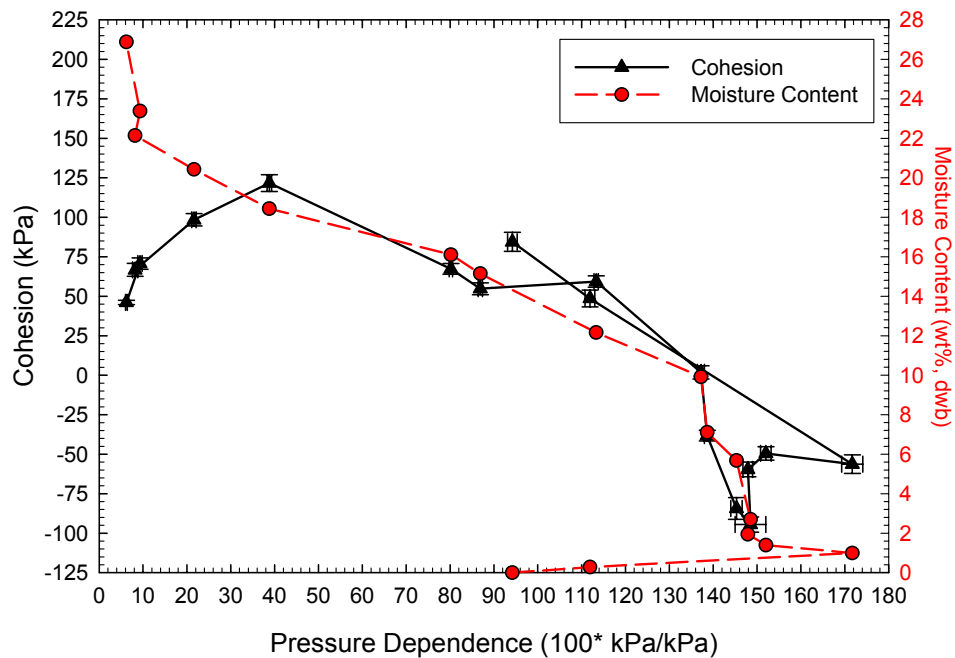


Figure 8-11. Cohesion and moisture content as a function of pressure dependence for the granulate with the pPVA binder system. Cohesion is initially observed to decrease with increasing pressure dependence and moisture content. Significant scatter is observed at high pressure dependence. At high moisture content the cohesion is observed to increase with a decrease in pressure dependence. A peak in the cohesion is observed at a pressure dependence of approximately 38. Lines are purely to help guide the eye.

For the purposes of this research plasticity has been defined as a high cohesion with low pressure dependence. Based upon this definition the addition of lignosulphonate was observed to improve the plasticity of the granulate relative to the system with no organic binder. Plasticized PVA and PEG 8000 were both observed to be detrimental to the plasticity.

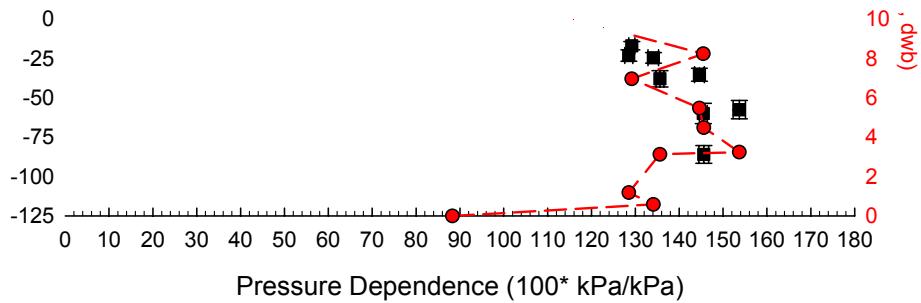


Figure 8-12. Cohesion and moisture content as a function of pressure dependence for the granulate with the PEG binder system. Cohesion is initially observed to decrease with increasing pressure dependence and moisture content. Significant scatter is observed at high pressure dependence. At high moisture content the cohesion is observed to increase with a decrease in pressure dependence. A peak in the cohesion is observed at a pressure dependence of approximately 37. Lines are purely to help guide the eye.

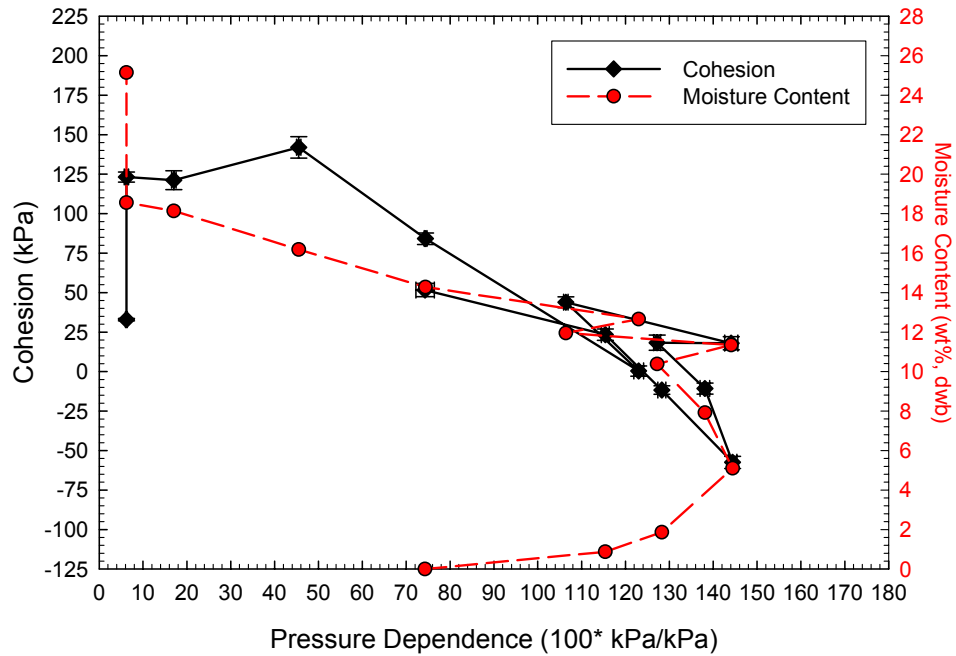


Figure 8-13. Cohesion and moisture content as a function of pressure dependence for the granulate with the NB binder system. Cohesion is initially observed to decrease with increasing pressure dependence and moisture content. Significant scatter is observed at high pressure dependence. At high moisture content the cohesion is observed to increase with a decrease in pressure dependence. The cohesion is observed to peak at a pressure dependence of approximately 45. Lines are purely to help guide the eye.

#### **8.4 Summary and Conclusions**

Moisture content was again observed to have an important role in the deformation of the granulate. By increasing the moisture content of the granulate the P1 value was reduced resulting in higher compact densities and green strengths as well as a better surface finish on the pressed ware. The measured properties of the granulate and compacts prepared by uniaxial compaction reached a plateau value at approximately 3% moisture. The addition of shear during the compaction process was observed to significantly reduce the measured P1 value. The process used to apply shear to the granule bed in this study was observed to make the shear P1 value independent of the moisture content in the powder. The samples that were tested in the dried state were not fully consolidated prior to frictional effects interfering with the test.

Addition of lignosulphonate as a binder to the granulated porcelain body was observed to improve the plasticity relative to the system with no organic binder. PVA and PEG 8000 were both observed to reduce the plasticity of the porcelain batch.

### **8.5 References**

1. J. Doran, New York State College of Ceramics, Alfred University, Alfred, New York, 1995 (unpublished).
2. H. Tsunakawa and R. Aoki, "Measurements of the Failure Properties of Granular Materials and Cohesive Powders," *Powder Technol.* **33** [2] 249-56 (1982).
3. F. Negre and E. Sanchez, "Advances in Spray-Dried Powder Processing for Tile Manufacture"; pp.169-182 in *Science of Whitewares*. Edited by V.E. Henkes, G.Y. Onoda, and W.M. Carty. The American Ceramic Society, Westerville, Ohio, 1996.

## **9. Plasticizers for PVA**

### **9.1 Introduction**

The plasticizer (Nalco 93QC215) for PVA that was used in this study was supplied by Buffalo China. As a final study in this research the concentration of Nalco 93QC215 necessary to fully plasticize, i.e., shift the glass transition temperature ( $T_g$ ) of the PVA to its minimum value, was characterized by dynamic mechanical analysis.

### **9.2 Literature Review**

Plasticizers are used with organic additives (binders) to reduce the glass-transition temperature ( $T_g$ ). Below  $T_g$  the binder is said to be hard and brittle. Above  $T_g$  the binder is referred to as “soft and rubbery.” For good compaction the binder should be above  $T_g$  so that the organic is easily deformed under a load, i.e.,  $T_g$  should be below room temperature.<sup>1-10</sup>

Plasticizers form an associated complex with the PVA molecule by hydrogen bonding with the hydroxyl groups in the PVA chain. Without a plasticizer the PVA chains can hydrogen bond creating a repeating, oriented structure in the dried film; this structure is referred to as the crystallinity of the organic. The oriented structure in the PVA film increases the measured  $T_g$  of the polymer film. Addition of the plasticizer disrupts the crystallinity of a dried PVA film by hydrogen bonding with the PVA molecule, thus reducing the  $T_g$  of the PVA. The associated complex formed between the PVA and plasticizer results in a new, “hybrid” molecule with a  $T_g$  between that of the plasticizer and PVA. In cases where there is either no interaction between the organic additives or phase separation two transition temperatures are measured, one for each organic additive.<sup>10</sup>

### **9.3 Experimental Procedure**

Mixtures of organic additives were prepared by mixing approximately 20 grams of PVA solution (at 24 weight percent PVA) with the appropriate amount of plasticizer to create the desired ratio of PVA:plasticizer. Both the PVA solution and the plasticizer were supplied by Buffalo China and are the materials used in

their industrial process. After thorough mixing a glass fiber cloth was immersed in the solution. A vacuum was used to assure complete saturation of the glass fiber cloth with the organic solution. Attempts to cast a film of organic were unsuccessful so the glass fiber cloth was used as a support for the organic film.

While specific adsorption of the organic additives on the glass fiber will result in a shift in the transition temperature, two factors minimize this error: 1) while PVA does adsorb on silica surfaces the concentration of PVA adsorbed is low ( $\sim 0.25 \text{ mg/m}^2$  at pH 5.3 which was close to the measured pH of the PVA solution used in this study)<sup>11</sup> and 2) the glass fiber cloth has a low surface area ( $0.12 \text{ m}^2/\text{g}$  by nitrogen adsorption). Therefore only a small quantity of PVA will adsorb onto the glass fiber cloth used as a support to determine  $T_g$ .

The saturated glass cloth was dried at  $50^\circ\text{C}$  overnight prior testing the samples. The samples were tested using a controlled-strain method in a dynamic mechanical analyzer (DMA) [DMA 800, TA Instruments, New Castle, DE] using a dual cantilever clamp. The samples were initially heated at  $5\text{K} / \text{minute}$  to  $130^\circ\text{C}$  and held for 5 minutes to remove moisture. The samples were then cooled to  $-100^\circ\text{C}$  using a gas-cooling accessory filled with liquid nitrogen and stabilized for 5 minutes. The samples were heated at  $3\text{K} / \text{minute}$  to  $130^\circ\text{C}$  under a nitrogen atmosphere evaporated from the liquid nitrogen cooling accessory, i.e., the atmosphere in the furnace was completely dry (0% relative humidity). During the heating cycle the sample was strained in an oscillatory manner and the storage modulus, a measure of the elastic properties, and the loss modulus, a measure of the viscous properties of the samples, were monitored.  $\text{Tan } \delta$  was then calculated as the ratio of the loss modulus to the storage modulus. A peak in the  $\text{Tan } \delta$  curve corresponded to a transition from an elastic state to a viscous state, i.e., a glass-transition temperature.<sup>4</sup> The peak in the  $\text{Tan } \delta$  curve was determined using the DMA software [Universal Analysis 2000 v.3.8B, TA Instruments, New Castle, DE]

#### **9.4 Results**

The results from some of the samples tested in the DMA are plotted in Figure 9-1. The plasticizer used throughout this study, supplied by Buffalo

China, has a  $T_g$  at approximately  $-34^\circ\text{C}$ . The dried PVA was observed to have a  $T_g$  at approximately  $82^\circ\text{C}$ ; this was found to be near the manufacturer's reported  $T_g$  of  $75\text{-}85^\circ\text{C}$ . As the concentration of plasticizer in the polymer mixture increased the PVA peak was observed to shift slightly, but there was no significant shift to lower temperatures. At high concentrations of plasticizer a peak was observed at  $-34^\circ\text{C}$  in addition to the peak for the PVA at approximately  $82^\circ\text{C}$ . These results indicated that the plasticizer used in this study was in fact not a plasticizer for PVA. For comparison the results from a PVA and glycerin sample, prepared at a PVA:glycerin ratio of 1.2:1, are also shown in Figure 9-1 (top curve). The addition of excess glycerin to the PVA resulted in two glass-transition temperatures; one for the glycerin at approximately  $-45^\circ\text{C}$  and a second peak for the associated complex at approximately  $28^\circ\text{C}$ . The addition of glycerin to PVA resulted in a shift in the  $T_g$  of the PVA due to the formation of an associated complex.

The  $T_g$  of the PVA when mixed with glycerin was observed to shift by 54K. While the measured  $T_g$  of the PVA and glycerin mixture remained above room temperature there was still a significant shift to a lower glass-transition temperature. Data reported by Klingenburg for Airvol 205, the commercial name for Celvol 205 when it was sold by Air Products and Chemicals, Inc., indicated that measuring the glass-transition temperature of PVA at 50% relative humidity further shifted the  $T_g$  to lower temperatures.<sup>10</sup> Therefore the thermal cycle that was performed prior to testing the glass-transition temperature, i.e., the heating of the sample to  $130^\circ\text{C}$ , served to completely dry the PVA film thus shifting the  $T_g$  to a temperature slightly above room temperature.

The organic solutions that were prepared to make the samples for the DMA were allowed to rest undisturbed for seven days. After a period of seven days the solutions were photographed. The solutions that were prepared with low concentrations of "plasticizer" appeared homogeneous, but at higher concentrations of "plasticizer" phase separation into two distinct domains occurred, Figure 9-2. The PVA:glycerin sample was observed to remain homogeneous. Based upon the data supplied with the pPVA granulate in this

study it was calculated that the ratio of PVA:plasticizer was approximately 1.75:1 on a weight basis. This ratio of PVA:plasticizer falls within the phase separation region. During the spray-drying process the PVA and plasticizer will phase separate to form two distinct domains as water is evaporated from the droplet, thus increasing the relative concentration of PVA and plasticizer.

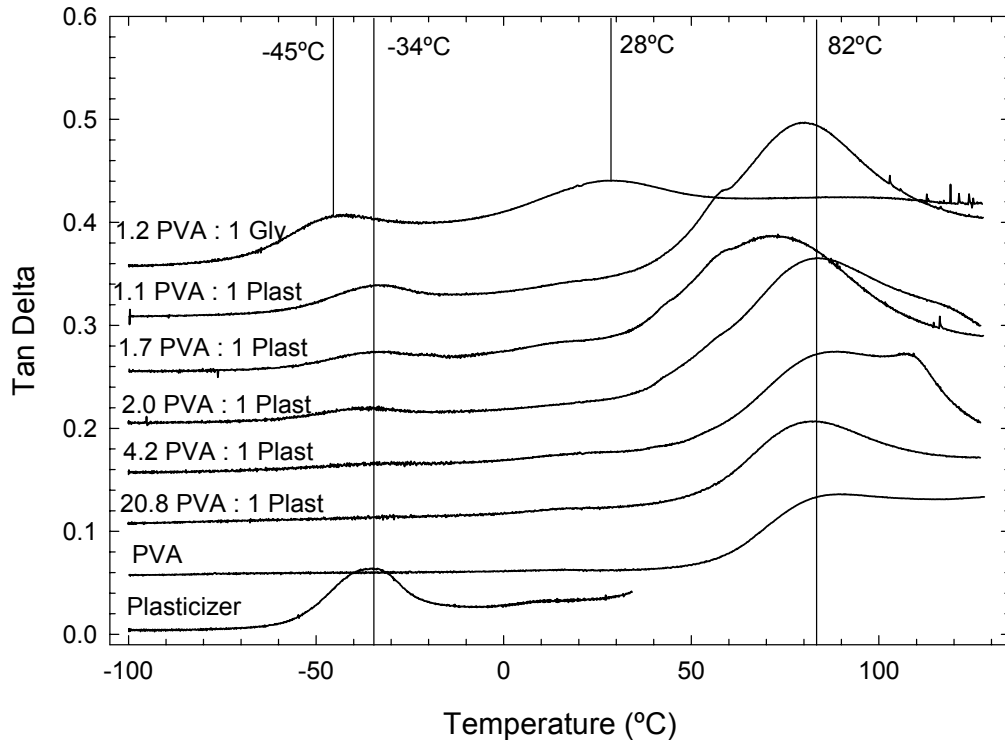


Figure 9-1. Results from the DMA for the PVA binder system. The unmixed plasticizer and PVA results are shown at the bottom. As the relative concentration of plasticizer in the mix increases a peak for the plasticizer is observed. No shift in the  $T_g$  of the PVA is observed in the DMA results. Mixing PVA with glycerin is observed to result in two  $T_g$  values, one corresponding to the glycerin ( $-45^\circ\text{C}$ ) and another for the PVA-glycerin associated complex at  $28^\circ\text{C}$ .

This could further aggravate the interactions between the dispersant and PVA binder systems which were demonstrated to phase separate by Kim.<sup>12</sup> The result is a granule with a high concentration of PVA on the surface, i.e., a case-hardened granule. The granulate prepared in this study was dispersed prior to spray drying using a poly[acrylic acid]. The addition of PVA and an incompatible

plasticizer will result in an organic solution that will further aggravate the phase separation since the dispersant is strongly adsorbed to the particle surface. Furthermore the presence of naturally-occurring organics in solution or adsorbed at the particle surface will also enhance the phase separation of the binder system.<sup>13-15</sup>

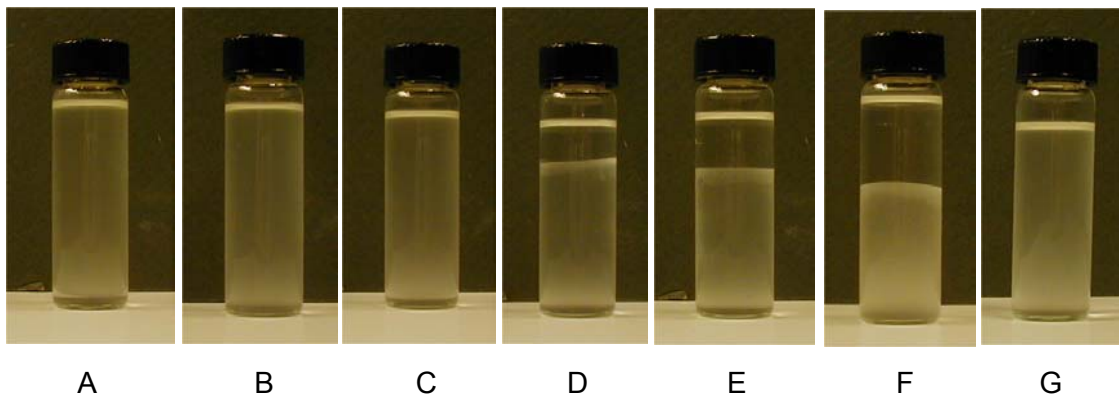


Figure 9-2. Digital images of the organic solutions used to determine  $T_g$ . (A) unmixed PVA, (B) 20.8 PVA: 1 plasticizer, (C) 4.2 PVA: 1 plasticizer, (D) 2.0 PVA: 1 plasticizer, (E) 1.7 PVA: 1 plasticizer, (F) 1.1 PVA: 1 plasticizer, and (G) 1.2 PVA: 1 Glycerin. Phase separation of the organic additives is observed in mixes D, E, and F. Homogeneous solutions are observed in A, B, and C. Based upon the DMA results a homogeneous solution of glycerin and the associated complex formed between PVA and glycerin is observed in G.

The data from the DMA and the observed phase separation can be used to explain data plotted in Figures 9-3, data from Chapter 7.4 for the pPVA system (Figure 7-36). During the preparation of the suspension for spray drying the 1 wt% pPVA was over plasticized, at a PVA:plasticizer ratio of 0.77:1, relative to the standard procedure, at a PVA:plasticizer ratio of 1.75:1, used by Buffalo China. No effort was made to correct the situation at that time. During the testing of the resulting granulate it was determined that the P1 value in the dried state was significantly higher than that measured for the 2- and 5-weight-percent granulate. Less of an effect was observed for the as-prepared granulate. Since moisture is a well-known plasticizer for PVA the samples in the as-prepared state were deformed more easily due to the small quantity of moisture, 0.168 wt%, in

the granulate. When that moisture was removed prior to compaction, the measured P1 value was significantly higher since the binder system had phase separated and the PVA was no longer plasticized.

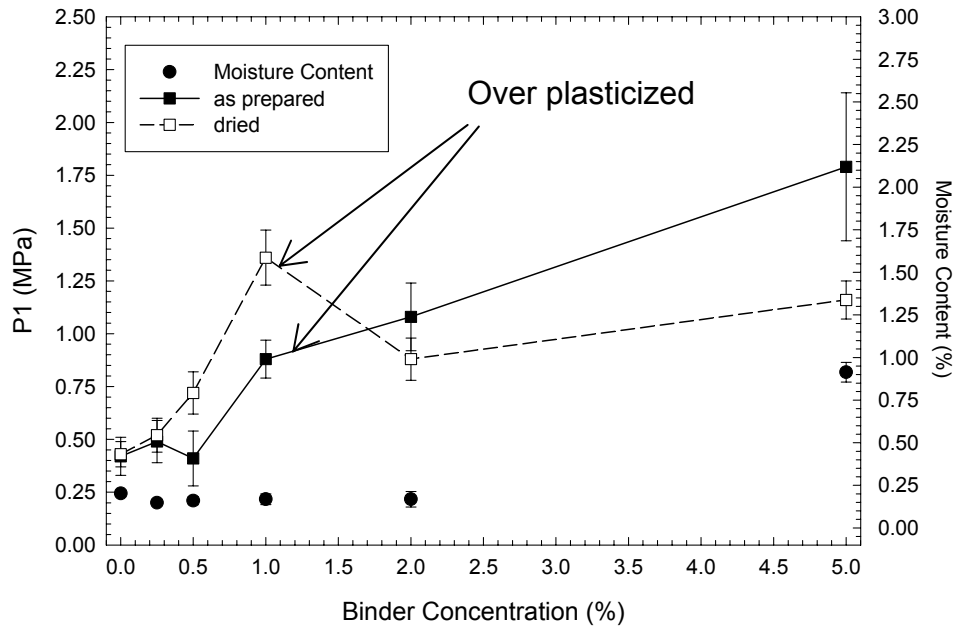


Figure 9-3. Plot from Chapter 7.4 showing the effect of pPVA concentration on the measured P1 value in uniaxial compaction. The 1 wt% sample was “over plasticized,” at a PVA:plasticizer ratio of 0.77:1, while preparing the suspension for spray drying. All other samples were prepared at an approximate PVA:plasticizer ratio of 1.75:1. Upon drying the organics phase separated into distinct domains resulting in the high P1 value at 1 wt% in the dried granulate. The as-prepared granulate has sufficient physical water remaining in the granulate to plasticize the PVA and no discontinuities are observed in the P1 value. Lines have been added to help guide the eye.

## **9.5 Summary and Conclusions**

The combination of PVA and plasticizer used in the majority of this study has been determined to be incompatible and at higher concentrations to undergo phase separation into a “plasticizer”-rich domain and a PVA-rich domain. Since the organic additive used as a plasticizer has no plasticizing effect on the PVA there was no reduction in the measured  $T_g$  of the PVA. The PVA remained hard and brittle making it more difficult to deform the granule during compaction. While the presence of physical water in the granulate served to plasticize the PVA, the addition of the plasticizer had no beneficial effect. Furthermore the presence of high concentrations of the “plasticizer,” even the concentration used in preparing the granulate for this study, will result in phase separation and case hardening of the granules during spray drying. Glycerin was demonstrated to have a positive interaction with PVA, reducing the  $T_g$  of the PVA molecule.

## 9.6 References

1. J.S. Reed, *Principles of Ceramics Processing*, 2<sup>nd</sup> ed.; Ch. 12. Wiley Interscience Publishers, New York, New York, 1995.
2. R.A. DiMilia and J.S. Reed, "Dependence of Compaction on the Glass-transition temperature on the Binder Phase," *Am. Ceram. Soc. Bull.*, **62** [4] 484-8 (1983).
3. C.W. Nies and G.L. Messing, "Effect of Glass-transition temperature of Polyethylene Glycol – Plasticized Polyvinyl Alcohol on Granule Compaction," *J. Am. Ceram. Soc.*, **64** [4] 301-4 (1984).
4. L.H. Sperling, "Theories of the Glass Transition"; pp. 334-52 in *Introduction to Physical Polymer Science*, 2<sup>nd</sup> ed. Wiley Interscience Publishers, New York, New York, 1992.
5. L.H. Sperling, "Effect of Molecular Weight on  $T_g$ "; pp. 352-5 in *Introduction to Physical Polymer Science*, 2<sup>nd</sup> ed. Wiley Interscience Publishers, New York, New York, 1992.
6. L.H. Sperling, "Effect of Copolymerization on  $T_g$ "; pp. 355-60 in *Introduction to Physical Polymer Science*, 2<sup>nd</sup> ed. Wiley Interscience Publishers, New York, New York, 1992.
7. L.H. Sperling, "Effect of Crystallinity on  $T_g$ "; pp. 360-3 in *Introduction to Physical Polymer Science*, 2<sup>nd</sup> ed. Wiley Interscience Publishers, New York, New York, 1992.
8. H.R. Allcock and F.W. Lampe, "The Glass-transition temperature"; pp. 425-7 in *Contemporary Polymer Chemistry*, 2<sup>nd</sup> ed. Prentice-Hall International Editors, New York, New York, 1992.
9. I.M. Campbell, "Glass-transition Temperatures ( $T_g$ )"; pp. 45-50 in *Introduction to Synthetic Polymers*. Oxford Science Publications, New York, New York, 1994.
10. E. Klingenberg, "Poly(vinyl alcohol): Important Properties Related to Its Use as a Temporary Binder in Ceramic Processing"; pp. 43-56 in *Science of Whitewares II*. Edited by W.M. Carty and C.W. Sinton. The American Ceramic Society, Westerville, Ohio, 2000.
11. I. Rachas, Th.F. Tadros, and P. Taylor, "The Displacement of Adsorbed Polymer from Silica Surfaces by the Addition of a Nonionic Surfactant," *Colloids Surf., A*, **161** [2] 307-19 (2000).
12. U. Kim, "Role of Polymer Compatibility in Ceramic Processing"; Ph.D. Thesis. Alfred University, Alfred, New York, 2002.
13. A.G. Zavarzina, V.V. Demin, T.I. Nifant'eva, V.M. Shkinev, T.V. Danilova, and B.Y. Spivakov, "Extraction of Humic Acids and Their Fractions in Poly(ethylene glycol)-based Aqueous Biphasic Systems," *Anal. Chim. Acta*, **452** [1] 95-103 (2002).

14. J.F. Kadla and S. Kubo, "Lignin-based Polymer Blends: Analysis of Intermolecular Interactions in Lignin-Synthetic Polymer Blends," *Composites, Part A*, **35** [3] 395-400 (2004).
15. A.E. Nesterov and Y.S. Lipatov, "Compatibilizing Effect of a Filler in Binary Polymer Mixtures," *Polymer*, **40** [5] 1347-9 (1999).

## **10. Summary and Conclusions**

The adsorption of Na-PAA on the surface of alumina was observed to approach the values reported in the literature; no effect of polymer molecular weight was observed. Adsorption of Na-PAA on the surface of commercial kaolinitic clays showed a significant deviation from the predicted values based upon a model of the mineralogy of kaolinite. The proposed adsorption model was confirmed using source clay minerals, specifically a poorly crystallized kaolinite, a non-swelling Ca-montmorillonite, and a swelling Na-montmorillonite. The adsorption plateau for the kaolinite source clay confirmed the proposed model for adsorption on the alumina-like basal plane of the kaolinite platelet. Adsorption on the montmorillonite minerals was determined to be either negligible or negative due to the mineralogy of montmorillonite, i.e., a 2:1-layer silicate.

The low adsorption levels that were measured for the commercial kaolinitic clays were determined to be the result of naturally-occurring organics and impurity minerals which were present in the as-received clay. A washing and beneficiation process to remove the organic and inorganic impurities, i.e., minerals which were not kaolinite, was observed to increase the measured adsorption levels for the commercial clays. The naturally-occurring organics that were present in clays, as well as additives that are doped into commercial clays by suppliers, were observed to be pH active. These species, when present in the supernatant of the suspension, interfered with the titration technique selected to determine the concentration of organics present in solution.

The organics present in TK6, a commercial kaolin clay, and Huntingdon, a commercial ball clay with added digested lignite, were observed to compete with the dispersant, Darvan™ 811, for the surface of the clay minerals. This competitive adsorption resulted in the organics present in the clay desorbing from the clay surface and being replaced by the PAA polymer. The results from the GPC indicated that there was no significant difference in the molecular weight of the species desorbing from the Huntingdon clay surface upon addition of PAA.

No precipitate was formed during the titration of the TK6 samples; the precipitate was used to prepare the GPC polymer solutions.

The supplier of the Huntingdon clay adds digested lignite, prepared by heating the organic lignite in a 1N solution of NaOH, to the clay to improve the plasticity of the clay. The addition of fractioned lignite or fractioned-digested lignite, fractioned by the solubility as a function of pH, was observed to have an effect on the viscosity of 30 v/o suspensions of TK6. The viscosity was initially observed to decrease with organic addition, but with higher additions (or additions with a high sodium concentration) the viscosity was observed to increase due to coagulation of the suspension. The fractioned organics were not observed to significantly affect the shear rheology of the suspension as determined by the HPASC. Therefore it was concluded that the added organics do not affect the plasticity, instead the addition of salt was observed to reduce the cohesion of the plastic clay. A transition was observed in the pressure dependence of the plastic samples with increasing salt concentration. Above the CCC of the salt the pressure dependence of the samples was observed to decrease due to a change in the particle-particle interactions. The high surface charge on the kaolin platelets results in a non-DLVO, or extended DLVO interaction between the particles which results in a short-range repulsion.

The addition of Na-lignosulphonate was observed to increase the cohesion of TK6 with a corresponding decrease in the pressure dependence at a target moisture content of 22%. Lignosulphonate is a known dispersant for clays and the creation of an electrosteric barrier on the clay surface reduced the particle-particle interactions thus reducing the internal friction (pressure dependence). The addition of lignosulphonate, in sufficient quantities to saturate the clay surface, was observed to increase the cohesion of the clay sample by approximately 20% with a corresponding 300% decrease in the pressure dependence.

Based upon the results from the initial study the dry-pressed surface finish was significantly worse than that of the other forming processes. The quantitative and semi-quantitative measurements performed in this study

indicated that a minimum acceptable RMS roughness of 4.60  $\mu\text{m}$ , equivalent to that of the pressure-cast ware, was necessary for a dry-pressing operation to replace the plastic-forming methods currently used by Buffalo China. At this roughness value it was observed that the granule features were nearly unidentifiable in the image of the surface.

Dried blends of hard and soft granulate were observed to significantly reduce the measured roughness of the dry-pressed ware when compared to the unblended pPVA binder system. Blending of granulate below the percolation threshold of the hard granulate reduced the measured RMS roughness by approximately 0.8  $\mu\text{m}$ . Above the percolation threshold, approximately 50% hard granulate, no benefits were observed in blending since the hard granulate created a network to support the applied load. Samples pressed in an industrial setting using blends of dried granulate were considerably weaker and, in the case of the pPVA - NB system, could not survive the industrial forming process.

Moisture content had a significant role in compaction. Moisture, physical water in the granulate, acted as a plasticizer for many organic systems. Plasticizers made the organic softer and more deformable under an applied load. Samples of granulate that were dried prior to re-humidification could be returned to the as-received condition through storage at elevated relative humidity. Storage for an extended period of time at 100% relative humidity and 50°C was observed to result in the growth of secondary organics within the granulate. Storage at 100% relative humidity did result in a significantly stronger compact, although significant drying shrinkage and sticking of the part were problems.

Granule size did not have a significant role in compaction, provided that the extreme fines (sub-230 mesh) were not considered. A maximum in the green strength was observed in the small size fractions, between 60 and 90 micrometers, due to the reduction in the flaw size within the compact; larger granules resulted in larger interstices which needed to be filled during compaction.

Die fill was demonstrated to play a crucial role in the surface finish of the pressed ware. Variations in the measured surface roughness from the horizontal

press were determined to be the result of poor die fill, a consequence of the design of the press loaned to Alfred University. Proper design of the dry press, i.e., vertical versus horizontal, determined the uniformity of the die fill. Artifacts of die fill were still observed in the pressed ware prepared by Buffalo China for this study, but these artifacts resulted in a much smaller variation in the roughness compared to the semi-isostatic press at Alfred University.

Alternative binders to replace pPVA in dry pressing are available. Systems that have shown promise include methyl cellulose and Veegum™ T. Replacing pPVA with a 50-50 wt% blend of pPVA and Veegum™ T was demonstrated to significantly reduce the P1 value of the granulate without decreasing the green strength or density of the compact. Blends of granulate, selected based upon a normalized P1 value, which were spray dried at Alfred University did not significantly change the measured P1 value of the granulate. Instead a stronger correlation was observed with the moisture content of the granulate. Agar was shown to be an effective additive for dry pressing since the organic gelatin retained significant amounts of physical water which was available to aid in the deformation of the granulate. Undissolved agar was apparent in the pressed surface which was observed to inflate the measured roughness; reduction in the particle size of the agar would aid in the dissolution of the agar at elevated temperatures.

The most significant improvement in the surface finish is realized by using a harder elastomer membrane in the semi-isostatic press. The use of the proper membrane in a semi-isostatic press can reduce the surface roughness of the dry-pressed ware to a value less than that of the jiggered ware.

A reduction in the surface roughness of the dry pressed ware was realized by reducing the mean diameter of the spray-dried granulate. The granulate prepared at Alfred University has a significantly smaller mean diameter compared to the industrially prepared granulate. This resulted in a reduction of the measured surface roughness since the depth crevices between the granules in the compacted surface was reduced.

Under uniaxial compaction there was no shear applied to the granulate once the P1 value was exceeded. The granulate settled into a tight packing arrangement and only normal loads were transmitted between the granules. The combination of shear and compaction was observed to significantly reduce the P1 value of the granulate. Moisture content was observed to significantly reduce the measured P1 value and increase the measured compact density and green strength of samples prepared by uniaxial compaction. A plateau in the measured attributes of the compacts was observed above 3 wt% moisture for all binder systems tested in uniaxial compaction. Moisture content was not observed to be significant to shear compaction although it was observed that the dried granulate was not fully consolidated prior to frictional effects interfering with the test. The material under shear was observed to be compacted, but outside of the shear region the granulate remained undeformed.

The roughness of the samples prepared with pPVA or lignosulphonate was observed to decrease with increasing moisture content; a plateau was observed above 3 wt% moisture. A strong correlation was observed between the measured P1 value and the RMS roughness of the surface.

The plasticity of the spray-dried granulate with various binder systems was determined at moisture contents ranging from 0 to 20 wt%. For all binder systems an increase in the pressure dependence and a decrease in cohesion was observed with small additions of water. This was due to the water wetting the particle surfaces and increasing the particle-particle interactions, i.e., higher friction. With higher additions of water the cohesion was observed to pass through a maximum while the pressure dependence was observed to decrease. The addition of pPVA or PEG 8000 was observed to reduce the plasticity of the granulate relative to the system with no organic binder. The addition of lignosulphonate was observed to increase the plasticity of the porcelain batch. While no peak cohesion was observed for the lignosulphonate binder within the moisture-content range tested, the highest cohesion observed exceeded that of the other three systems at a lower pressure dependence. The changes in

plasticity were related back to the adsorption of organics and the change in the surface tension of water with dissolved organics.

The plasticizer, Nalco 93QC215, which was used throughout this study was supplied by Buffalo China from their production line. It was determined that the material supplied as a plasticizer did not form an associated complex with the PVA molecule and there was no significant change in the measured  $T_g$  of the PVA with addition of the plasticizer. Furthermore evidence was found that the PVA and plasticizer phase separate into distinct domains at the ratio used by Buffalo China in their industrial process. Data collected indicated that the presence of moisture within the granulate will compensate for the phase separation and the PVA molecule will be plasticized, resulting in a softer granule. Upon drying the granulate the P1 value was observed to increase significantly. Samples prepared with excess plasticizer were observed to be significantly harder, i.e., a higher P1 value, compared to samples prepared with the ratio used by Buffalo China. A sample of PVA mixed with glycerin, a known plasticizer for PVA, at the same ratio was observed to significantly reduce the  $T_g$  of the PVA with the excess plasticizer in the mixture having a second peak in the  $\text{Tan } \delta$  curve.

The results from the plasticity study have implications for the dry pressing of granulated materials. Typical moisture content for dry pressing of granulate materials is between 1 and 3 wt% to maintain flowability while having good deformation. A plateau was observed in this study for the roughness, P1, compact density, and green strength above 3% moisture. Seasonal variations, from a cold, dry winter to a hot, humid summer, will cause the moisture content of the granulate to fluctuate, thus changing the compaction of the granulate. Between 1 and 3 wt% moisture a significant decrease in the cohesion was observed, this was likely due to frictional effects under high normal pressures. Furthermore between 1 and 3 wt% moisture there was a significant increase in the pressure dependence of the sample. These two factors will interfere with the deformation of the granulate during consolidation.

Storage of granulate in a controlled environment, i.e., regulated humidity and temperature, will aid in controlling the moisture content of the granulate and prevent complications that arise from seasonal fluctuations in temperature and relative humidity. Proper selection of the organic additives, i.e., selection of a compatible binder system, is crucial to achieving good deformation of the granulate. While physical moisture within the granulate can serve as a plasticizer, thus reducing the hardness of the organic, small fluctuations in the moisture content can have drastic implications for the compaction of an incompatible binder system. Using an elastomer membrane with a higher shore hardness for isostatic compaction will provide a slight improvement in the surface finish of the dry pressed ware, but the compliant nature of the elastomer will result in texture, i.e., relics from the granulate, that remain visible in the pressed surface. Hardened steel dies will further improve the surface finish, but problems associated with cleaning the dies to prevent powder from flowing between the punches and die walls are prohibitive in an industrial process.

The use of organics which trap physical moisture into a gelatin, e.g., agar, result in an improved surface finish provided that complete dissolution of the organic is achieved during the spray-drying process. The growth of secondary organics needs to be considered in using these systems, agar is primarily used to grow bacterial cultures in a laboratory. Blending of agar granulate with a second binder system has beneficial effects since the water trapped in the gelatin is available to plasticize the organic binder during compaction. The spray-dried-agar granulate in this study was observed to be stable, i.e., no degradation was indicated, for a period of at least four months. Furthermore these systems were observed to have a significantly higher green strength in the dried state.

Based upon these results a blended granule system in which one of the constituents is a gelatin-type binder is recommended. These systems are observed to have a significantly better surface finish and a lower P1 value relative to the other blended systems studied. It is not recommended that an excessive amount of gelatin-type binder should be used as this will effect the flowability of the granulate.

## ***Appendix A. Calibration Curves to Determine the Concentration of Polymer in Solution by Potentiometric Titration***

### ***1.0 Creation of the Calibration Curve***

The titration technique selected to determine the concentration of organic remaining in solution involved converting the volume of titrant, 0.25 N HCl, to a concentration of organic in solution. To affect this conversion a calibration curve was needed for each poly[acrylic acid] (PAA) used in this research. The process of generating the calibration curve for Acumer™ 1510 is reported in this Appendix.

Solutions with a known concentration of polymer were prepared by mixing Acumer™ 1510, 27 wt% PAA, with distilled water to make 85 mL of solution. Care was taken to account for the water present in the organic solution. The pH of the solutions was adjusted to above 10.5 using 6 N NaOH. The samples were titrated using 0.25 N HCl to a pH of 2. The volume of titrant necessary to saturate, i.e., fully protonate, the functional groups of the polymer chain was determined as the volume between the two inflection points; Figure A-1 is a plot of some titration curves used to prepare the calibration curve.

The results were plotted as the milligrams of PAA versus the milliliters of titrant as shown in Figure A-2. A linear regression of the results, forcing the y-intercept to zero, was determined using Excel. The slope of the regression was used as a conversion from the milliliters of titrant to the milligrams of polymer in solution. The calculation to determine the concentration of polymer present in the supernatant of an unknown sample is detailed below.

### ***2.0 Sample Calculation to Determine the Concentration of Polymer in an Unknown Solution***

The titration curve for a supernatant solution from a 15 volume percent alumina sample prepared with approximately 0.90 mg/m<sup>2</sup> Acumer™ 1510 is shown in Figure A-3. The supernatant was collected by centrifuging the alumina suspension. The supernatant was diluted with distilled water; 40 mL of supernatant was diluted to a total volume of 85 mL. The volume of titrant between the inflection points was determined to be 2.5725 mL of 0.25 N HCl.

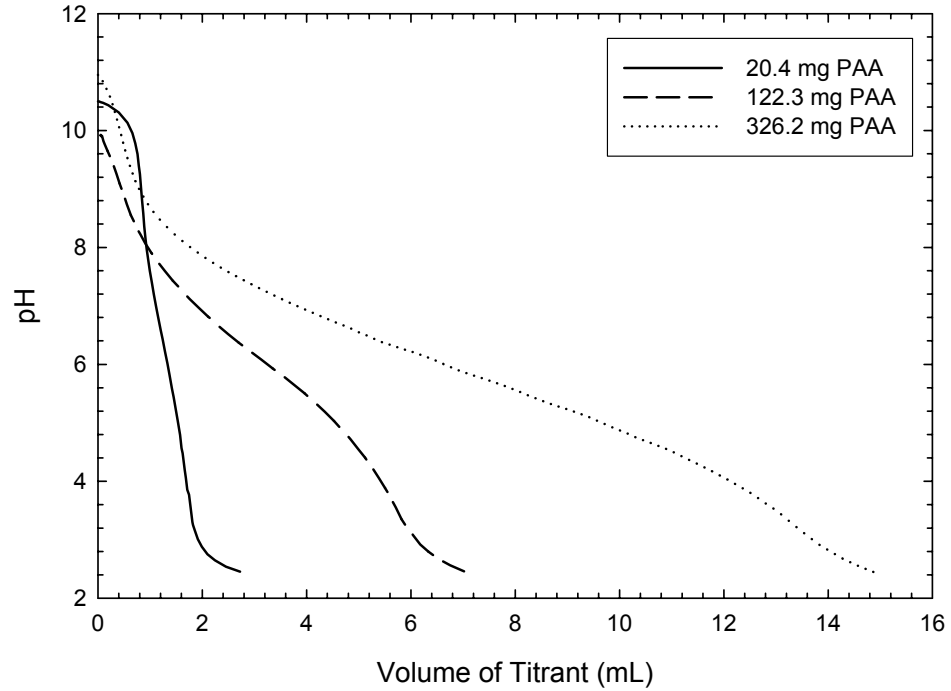


Figure A-1. Titration curves for Acumer™ 1510 that were used to generate a calibration curve. The volume of titrant between the inflections points was determined by the first derivative of the curve, not shown.

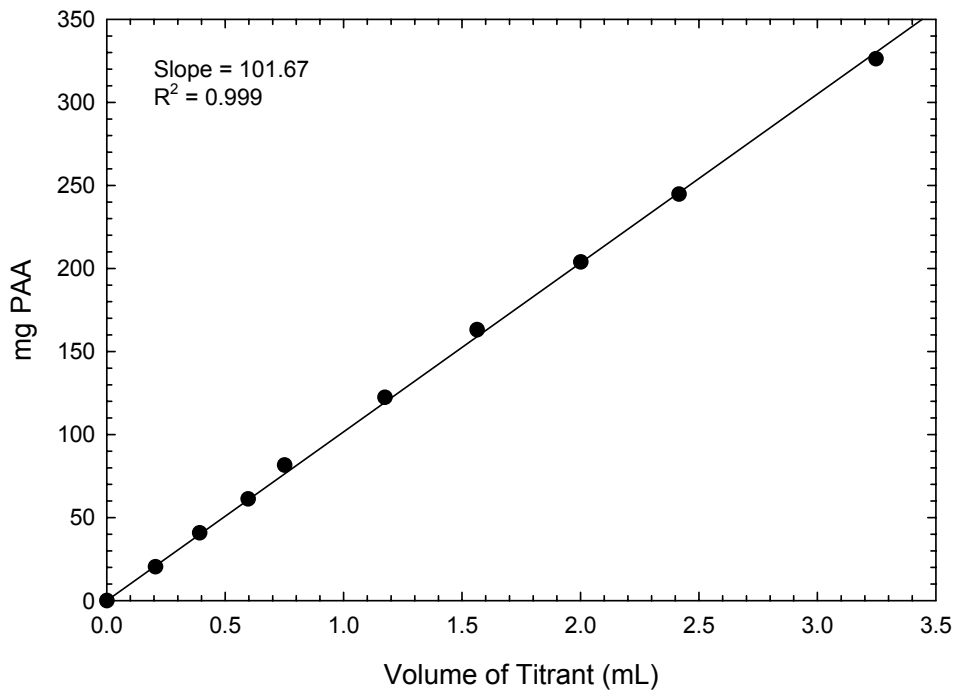


Figure A-2. Calibration curve for Acumer™ 1510. The slope of the regression, forced through a y-intercept of zero, was used to convert the mL of titrant to the mg of PAA present in the supernatant of the unknown polymer solutions.

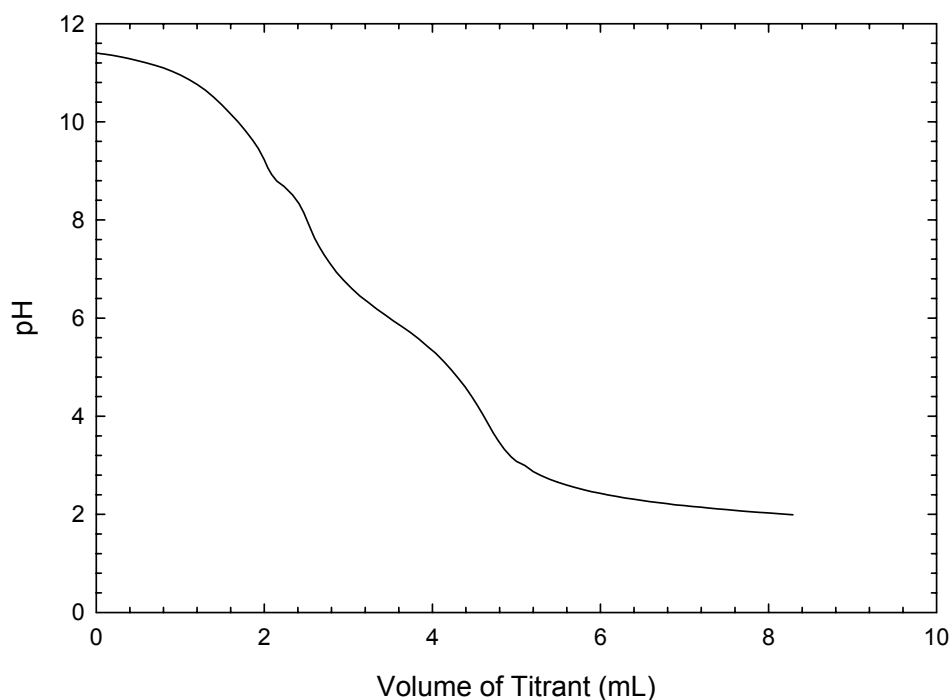


Figure A-3. Titration curve from the alumina sample prepared with approximately 0.90 mg/m<sup>2</sup> of PAA used for the sample calculation.

The volume of titrant was converted to the millimoles of H<sup>+</sup> necessary to saturate the polymer chain.

$$2.5725 * 0.25 \frac{\text{mmoles}}{\text{mL}} = 0.6431 \text{mmole H}^+ \quad (21)$$

The mg of PAA in the solution was calculated using the slope from the calibration curve, for Acumer™ 1510 the slope was calculated to be 101.67 mg PAA/mmole H<sup>+</sup>.

$$0.6431 * 101.67 \frac{\text{mg}}{\text{mmole}} = 65.39 \text{mg PAA} \quad (22)$$

Since the supernatant was diluted prior to titration it was necessary to compensate for the dilution.

$$65.39 * \frac{85}{40} = 138.95 \text{ mg PAA} \quad (23)$$

The amount of Acumer™ 1510 added to the initial suspension was 1.5400 g, or 1540.0 mg. The Acumer™ 1510 solution was a 27 wt% solution of PAA in water therefore the weight of PAA added to the suspension was 415.8 mg. The amount of PAA adsorbed on the surface for the powder is the difference between the amount added and the amount detected in the supernatant.

$$415.8 - 138.95 = 276.85 \text{ mg PAA adsorbed} \quad (24)$$

Based upon the specific surface area of the alumina, 7.7 m<sup>2</sup>/g, the amount of PAA adsorbed was converted to a surface coverage in mg/m<sup>2</sup>. Since 59.7 g of alumina was added to the initial suspension the surface coverage was:

$$\frac{276.85}{59.7 \text{ g Alumina} * 7.7 \text{ m}^2/\text{g}} = 0.602 \frac{\text{mg}}{\text{m}^2} \quad (25)$$

Therefore the surface coverage of the alumina powder with 0.904 mg/m<sup>2</sup> of added PAA was 0.602 mg/m<sup>2</sup>.

## **Appendix B. Calculation of the Free Quartz in a Commercial Clay**

### **1.0 Chemical Analysis of TK6**

The chemical analysis of TK6 is shown in Table B-I. Two sets of data are shown, the left column is the data reported by Acme Analytical Laboratories where the sum of the oxides is less than 100%, this is due to the LOI of the clay. The right column is normalized such that the total of the oxides equals 100%. The LOI of TK6, determined by thermal analysis, is 12.55%. There are two methods of calculating the amount of free quartz present in a clay: 1) from the LOI and 2) from the chemical analysis.

Table B-1. Chemical Analysis of TK6 Reported by Acme Analytical Laboratories.

<b>Oxide</b>	<b>Weight Percent (wt %)</b>		<b>Oxide</b>	<b>Weight Percent (%)</b>
SiO <sub>2</sub>	45.78		SiO <sub>2</sub>	54.55
TiO <sub>2</sub>	1.38		TiO <sub>2</sub>	1.62
Al <sub>2</sub> O <sub>3</sub>	35.54		Al <sub>2</sub> O <sub>3</sub>	43.35
Fe <sub>2</sub> O <sub>3</sub>	0.43		Fe <sub>2</sub> O <sub>3</sub>	0.51
MgO	0.44		MgO	0.52
CaO	0.24		CaO	0.29
Na <sub>2</sub> O	0.00		Na <sub>2</sub> O	0.00
K <sub>2</sub> O	0.13		K <sub>2</sub> O	0.15
<b>Total</b>	<b>83.92</b>		<b>Total</b>	<b>100.00</b>

### **2.0 Free Quartz from the LOI (Sample Calculation)**

The free quartz determined from the LOI is calculated using two equations and two unknowns. The equations used were:

$$f_{\text{quartz}} + f_{\text{kaolinite}} = 1 \quad (26)$$

$$f_{\text{quartz}} * \text{LOI}_{\text{quartz}} + f_{\text{kaolinite}} * \text{LOI}_{\text{kaolinite}} = \text{LOI}_{\text{meas.}} \quad (27)$$

where  $f_{\text{quartz}}$  and  $f_{\text{kaolinite}}$  are the fraction of quartz and kaolinite respectively and  $\text{LOI}_{\text{meas.}}$  is the measured LOI of the clay sample. Since the theoretical LOI of kaolinite is 13.94% and the LOI of quartz is 0%, rearranging and combining these two equations to solve for the fraction of quartz yields the equation:

$$f_{\text{quartz}} = 1 - \left( \frac{\text{LOI}_{\text{meas.}}}{13.94} \right) \quad (28)$$

Using the data for TK6, the free quartz from the LOI is:

$$f_{\text{quartz}} = 1 - \left( \frac{12.55}{13.94} \right) \quad (29)$$

Therefore the amount of free quartz from the LOI is 9.97%.

### **3.0 Free Quartz from the Chemical Analysis (Sample Calculation)**

To calculate the amount of free quartz present in TK6 from the chemical analysis one must assume that only quartz and kaolinite are present in the clay sample. Based upon the chemical analysis listed in Table B-I this assumption is not valid, no alkali or alkaline earth oxides are present in wither kaolinite or quartz. When the chemical water in the crystal lattice is removed the resulting material is metakaolin, the formula of metakaolin is  $\text{Al}_2\text{O}_3 \cdot 2\text{SiO}_2$ . Assuming that 100 g of metakaolin are tested the weight percent listed in Table B-I is equivalent to the grams of oxide present.

The first step is to convert the weight percent of the oxides present to moles. The molar mass of quartz is 60.08 and the molar mass of alumina is 101.96. The moles of alumina and silica present are:

$$\frac{54.55 \text{ g}}{60.08 \frac{\text{g}}{\text{mole}}} = 0.908 \text{ moles SiO}_2 \quad (30)$$

and

$$\frac{43.35 \text{ g}}{101.96 \frac{\text{g}}{\text{mole}}} = 0.425 \text{ moles Al}_2\text{O}_3 \quad (31)$$

For each mole of alumina there are two moles of silica present in metakaolin. Therefore the number of moles of silica in metakaolin is:

$$2 * 0.425 \text{ moles Al}_2\text{O}_3 = 0.850 \text{ moles SiO}_2 \quad (32)$$

The remainder of the silica in the chemical analysis is present as free quartz. Therefore the number of moles of free quartz is:

$$0.908 - 0.850 = 0.058 \text{ moles free quartz} \quad (33)$$

The grams of free quartz is:

$$0.058 \text{ moles} * 60.8 \frac{\text{grams}}{\text{mole}} = 3.48 \text{ g free quartz} \quad (34)$$

Since 100 grams of dehydroxylated clay was assumed there is 3.48 wt% free quartz in TK6.

#### **4.0 Summary**

There is a large discrepancy between the amount of free quartz calculated from the LOI, 9.97 wt%, and the chemical analysis, 3.48 wt%. In both calculations it was assumed that only quartz and kaolinite were present in the clay sample. As mentioned previously this assumption is not valid. The presence of 2:1-layer silicates in the commercial clay will change the LOI of the clay. 2:1-layer silicates have a variable LOI depending on their thermal history and processing. Swellable 2:1 silicates can have a large quantity of physical water trapped in the interlayer structure that may not be vaporized below temperatures of 300°C. Non-swelling 2:1-layer silicates can have a LOI of 0%. This error will change the measured LOI. The presence of 2:1-layer silicates in the clay invalidate the assumption for the allocation of the silica measured by ICP.

**Appendix C. Chemical Analysis of Organics Used to Affect Plasticity in Clays**

**1.0 ICP-AES Rock Analysis**

The complete chemical analysis of the organic samples tested by ICP-AES rock analysis are listed in Table C-I.

Table C-I. Chemical Analysis for the Samples that were Tested by ICP-AES Rock Analysis.

Organic	SiO <sub>2</sub>	Al <sub>2</sub> O <sub>3</sub>	Fe <sub>2</sub> O <sub>3</sub>	MgO	CaO	Na <sub>2</sub> O	K <sub>2</sub> O	TiO <sub>2</sub>
	%	%	%	%	%	%	%	%
Lignite	31.01	10.62	1.38	0.25	0.58	0.09	0.34	1.42
Lignite IN	46.12	9.36	1.07	0.18	0.35	1.12	0.32	1.56
Lignite AI	5.35	3.86	1.44	0.13	0.41	1.45	0.08	0.91
Dig. Lig.	15.08	8.88	1.06	0.23	0.55	10.54	0.27	1.13
Dig. Lig. IN	35.54	15.8	0.76	0.17	0.08	3.02	0.46	1.95
Dig. Lig. AI	1.1	0.81	0.55	0.03	0.13	6.77	0.02	0.63
	P <sub>2</sub> O <sub>5</sub>	MnO	Cr <sub>2</sub> O <sub>3</sub>	Ba	Ni	Sr	Zr	Y
	%	%	%	ppm	ppm	ppm	ppm	ppm
Lignite	0.04	0.01	0.005	372	< 20	145	268	60
Lignite IN	0.05	0.01	0.006	416	< 20	118	375	53
Lignite AI	0.05	< .01	0.01	185	23	118	154	61
Dig. Lig.	0.04	0.01	0.005	345	21	138	148	57
Dig. Lig. IN	0.05	< .01	0.005	480	22	137	238	35
Dig. Lig. AI	0.04	< .01	0.003	141	< 20	73	104	32
	Nb	Sc	LOI	TOT/C	TOT/S	ORG/C	GRA/C	
	ppm	ppm	%	%	%	%	%	
Lignite	43	12	54	31.53	0.66	31.49	0.02	
Lignite IN	37	10	39.3	23.69	0.45	23.63	0.04	
Lignite AI	58	14	86	48.65	0.83	48.61	0.03	
Dig. Lig.	40	10	62	32.21	0.54	15.68	15.87	
Dig. Lig. IN	47	12	41.6	22.71	0.37	22.63	0.02	
Dig. Lig. AI	39	9	95	49.24	0.58	49.22	< .02	

IN = insoluble fraction, AI= Acid-insoluble fraction

TOT/C = total carbon, TOT/s = total sulfur, ORG/C = organic carbon, GRA/C = graphitic carbon

## 2.0 ICP-AES Water Analysis

The complete chemical analysis of the organic samples tested by ICP-AES water analysis is listed in Table B-II.

Table C-II. Chemical Analysis for the Samples that were Tested by ICP-AES Water Analysis.

Organic	Ag	Al	As	Au	B	Ba	Be	Bi
	Atom%							
L.S.	3.33E-05	2.40	5.52E-04	2.28E-05	8.05E-03	6.56E-04	7.13E-03	1.01E-06
DLS	2.28E-05	3.01	5.52E-04	1.41E-05	3.27E-03	1.51E-03	3.13E-03	5.11E-06
Ligno.	1.02E-05	6.82E-02	2.53E-04	2.59E-05	4.77E-03	4.50E-03	2.08E-07	6.65E-06
	Br	Ca	Cd	Ce	Cl	Co	Cr	Cs
	Atom%							
L.S.	4.71E-03	9.22	1.29E-04	1.06E-02	1.46E-01	1.34E-02	1.05E-03	8.89E-05
DLS	5.31E-03	3.91	7.78E-05	1.10E-02	1.58E-01	3.63E-03	5.03E-03	8.70E-05
Ligno.	1.10E-02	7.67	3.11E-05	2.36E-05	3.85E-03	2.29E-04	4.11E-03	6.07E-05
	Cu	Dy	Er	Eu	Fe	Ga	Gd	Ge
	Atom%							
L.S.	2.37E-03	4.33E-03	2.78E-03	5.15E-04	3.76	8.17E-04	3.86E-03	2.66E-04
DLS	1.87E-03	3.77E-03	2.40E-03	5.41E-04	3.47	2.52E-03	3.76E-03	5.04E-05
Ligno.	1.74E-03	6.53E-06	3.58E-06	1.66E-07	1.38	4.40E-05	7.36E-06	6.74E-06
	Hf	Hg	Ho	In	Ir	K	La	Li
	Atom%							
L.S.	9.52E-07	4.89E-05	1.01E-03	8.06E-05	2.65E-07	8.03E-02	4.03E-03	2.57E-04
DLS	4.76E-06	4.95E-05	8.37E-04	5.76E-05	1.33E-07	5.60E-02	3.86E-03	4.57E-04
Ligno.	1.25E-06	7.36E-05	7.07E-07	2.49E-07	1.20E-04	2.56	1.00E-05	1.80E-04
	Lu	Mg	Mn	Mo	Na	Nb	Nd	Ni
	Atom%							
L.S.	3.18E-04	2.87	2.46E-01	5.29E-06	80.6	8.20E-07	8.35E-03	1.21E-02
DLS	2.85E-04	9.98E-01	8.42E-02	7.19E-06	88.1	7.51E-06	9.14E-03	4.39E-03
Ligno.	6.65E-07	8.61E-01	4.60E-01	1.11E-04	86.4	3.96E-05	1.47E-05	8.32E-07

Table C-II (cont.).

Organic	Os	P	Pb	Pd	Pr	Pt	Rb	Re
	Atom%							
L.S.	1.32E-07	5.29E-05	3.21E-03	1.06E-06	1.55E-03	2.65E-08	1.27E-03	1.38E-06
DLS	1.33E-07	6.28E-04	2.49E-03	7.98E-07	1.65E-03	1.86E-07	7.62E-04	4.52E-07
Ligno.	2.08E-07	1.13E-01	1.45E-04	5.82E-06	2.16E-06	4.16E-08	5.27E-03	2.08E-07
	Rh	Ru	S	Sb	Sc	Se	Si	Sm
	Atom%							
L.S.	2.65E-08	1.32E-07	3.45E-03	1.01E-06	2.59E-04	3.49E-05	1.68E-02	2.18E-03
DLS	2.66E-08	1.33E-07	8.44E-04	2.85E-06	4.44E-04	1.86E-05	5.37E-02	2.49E-03
Ligno.	5.03E-06	2.08E-07	8.75E-02	1.68E-05	2.54E-04	1.22E-04	2.10E-01	2.95E-06
	Sn	Sr	Ta	Tb	Te	Th	Ti	Tl
	Atom%							
L.S.	2.01E-06	8.23E-02	1.40E-06	6.34E-04	2.01E-06	5.74E-06	7.14E-05	1.53E-04
DLS	1.94E-06	4.05E-02	5.32E-08	5.78E-04	9.58E-07	1.58E-05	1.09E-04	6.98E-05
Ligno.	1.78E-04	8.30E-02	7.19E-06	9.15E-07	1.58E-06	4.27E-05	6.70E-03	9.69E-06
	Tm	U	V	W	Y	Yb	Zn	Zr
	Atom%							
L.S.	3.74E-04	1.06E-04	9.44E-04	3.31E-06	4.05E-02	2.06E-03	4.73E-02	6.44E-05
DLS	3.14E-04	3.73E-05	1.34E-02	5.32E-08	3.00E-02	1.81E-03	2.12E-02	1.31E-04
Ligno.	2.91E-07	2.49E-05	4.64E-04	3.16E-04	4.88E-05	2.87E-06	9.38E-03	5.42E-05

## **Appendix D. Calculation to Determine the Surface Tension of Organic Solutions**

### **1.0 Sessile Drop Method**

The sessile drop method of determining surface tension involves placing a droplet of the liquid on a non-wetting pedestal. Gravity causes the droplet to flatten and the shape of the droplet can be used to calculate the surface tension of the liquid. The higher the surface tension of the liquid the less the droplet will flatten.

### **2.0 Other Methods of Determining the Surface Tension of Liquids**

Paddy lists a series of alternative methods to determine the surface tension of a liquid. These alternative methods are listed in Table D-I. The sessile drop method was selected for this study since it was easy to obtain the necessary equipment and it suffered the fewest complications from factors such as drafts or aging of the test solutions.

Table D-I. List of the Methods Available to Determine the Surface Tension of Liquids.

<b>Method</b>	<b>Remarks on Suitability*</b>	
	Pure liquids	Solutions
Sessile drop profile	Very satisfactory	Very suitable when aging occurs
Pendant drop profile	Very satisfactory but limited experimentally	
Capillary Height	Very satisfactory	Not suitable if contact angle altered from 0°
The Wilhelmy plate	Very quick and easy to operate; susceptible to atmospheric contamination	Accuracy good; suitable when aging occurs
The Du Noüy ring	Satisfactory	Not suitable
Drop weight	Very suitable when atmospheric contamination suspected	Poor when aging effects suspected
Maximum bubble pressure	Somewhat difficult to operate successfully	Poor when aging effects suspected

\* Remarks are taken from J.F. Paddy, "Theory of Surface Tension," pp 101-149 in *Surface Colloid Sci.*, ed. E Mitjevic, Wiley Interscience, New York, New York, 1969.

### **3.0 Surface Tension of Liquids**

Pure water has a high surface tension due to van der Waals interactions orienting the water molecules at the surface of the droplet. The addition of salts is known to slightly increase the surface tension of water since the ions will increase the polarity of the water. This aids in the orientation of the water molecules and increases the surface tension. The effect of organic additives can be classified in two groups. The addition of a hydrophilic additive, i.e., a “water-liking” organic, will not significantly effect the surface tension of water. The hydrophilic molecule will remain uniformly distributed throughout the solution thus having little effect of the surface tension of the droplet. The addition of a hydrophobic additive, i.e., a “water-hating” organic, will cause the surface tension to decrease since the organic will migrate to the surface of the droplet. At the surface of the droplet the organic molecule will disrupt the orientation of the water molecules thus affecting a decrease in the surface tension. It was observed in this research that the smallest addition of a hydrophobic organic resulted in a significant decrease in the surface tension of the solution. Higher additions of the organic were not observed to result in a further decrease in the surface tension of the solution.

### **4.0 Sample Calculation to Determine the Surface Tension from a Sessile Droplet**

The equations used to determine the surface tension of the sessile drop were:

$$f = \frac{(r_{45} - h_{45})}{r_{90}} - 0.4142 \quad (35)$$

which calculates the “flatness” of the droplet. This factor is then used to calculate the surface tension using the equation:

$$\gamma = g(\rho_{\text{lig}} - \rho_{\text{air}})r_{90}^2 \left[ \frac{0.05200}{f} - 0.12268 + 0.0481 * f \right] \quad (36)$$

where  $\gamma$  is the surface tension of the solution,  $\rho_{\text{lig}}$  is the density of the solution, and  $\rho_{\text{air}}$  is the density of air. The term “g” is the acceleration due to gravity, 9.8 m/sec<sup>2</sup>. Evaporation of the liquid will slightly alter the measured surface tension since evaporation will alter the structure of the water at the surface of the droplet.

For this sample calculation a 3 wt% solution of plasticized PVA was selected. The image of the sessile drop used to determine the surface tension is shown in Figure D-1. The image was taken on a day when the ambient temperature was 20°C and the ambient relative humidity was 22%. From psychrometric charts the amount of water in the air at that temperature and relative humidity is 0.0034 kg water per kilogram of dry air. At 22°C the density of dry air is 1.1413 g/L and the density of water is 0.9982 g/cm<sup>3</sup>.

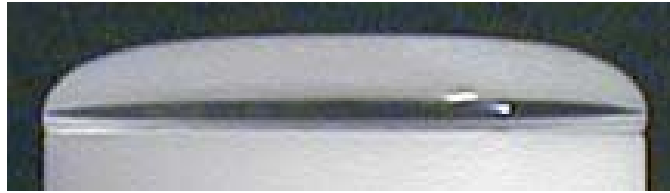


Figure D-1. Image of the sessile drop used to calculate the surface tension of the 3 wt% plasticized PVA solution

The dimensions of the projected droplet were measured to be:

$$r_{90} = 13.9 \text{ cm} \quad (37)$$

$$r_{45} = 13.25 \text{ cm} \quad (38)$$

$$h_{45} = 1.85 \text{ cm} \quad (39)$$

$$\text{diamter}_{\text{base}} = 27.55 \text{ cm} \quad (40)$$

Based upon the measured dimensions of the droplet the factor (f) is:

$$f = \frac{(13.25 - 1.85)}{13.90} - 0.4142 = 0.4059 \quad (41)$$

The magnification of the image was determined using the actual diameter of the Teflon pedestal. The actual diameter of the base was 2.86 cm, therefore the magnification of the image was:

$$\frac{27.55}{2.86} = 9.63 \quad (42)$$

The actual radius of the droplet at the vertical tangent,  $r_{90}$ , was therefore 1.44 cm.

The density of plasticized PVA was determine to be 1.1965 g/cm<sup>3</sup> by weighting a 25 wt% solution of plasticized PVA and distilled water. Using the rule of mixtures the density of the 3 wt% solution is:

$$1.1965 * 0.03 + (1 - 0.03) * 0.9982 = 1.0042 \frac{\text{grams}}{\text{cm}^3} \quad (43).$$

The density of the air is also calculated by the rule of mixtures:

$$0.0034 * 0.9982 + (1 - 0.0034) * \frac{1.1413}{1000} = 0.0045 \frac{\text{grams}}{\text{cm}^3} \quad (44)$$

The surface tension of the solution is therefore:

$$980 * (1.0042 - 0.0045) * 1.44^2 * \left( \frac{0.052}{0.4059} - 0.12268 + 0.0481 * 0.4059 \right) = 50.9 \frac{\text{dynes}}{\text{cm}} \quad (45)$$

## ***Appendix E. Determine the Performance of Blended Granulate in Production at Buffalo China.***

### ***1.0 Introduction***

Two industrial trials were performed at Buffalo China using blended granulate as a feed material in an attempt to improve the surface finish of the dry-pressed ware. In addition to these trials, samples were supplied by Buffalo China for evaluation over the course of the project. These samples were supplied at times when Buffalo China thought there was a significant improvement in the roughness of their dry-pressed ware.

### ***2.0 Experimental Procedure***

The first industrial trial involved three blends of granulate: 1) a 50-50 blend of pPVA and PEG, 2) a 33-67 blend of pPVA and PEG, and 3) a 50-50 blend of pPVA and NB. As a control two other sets of samples were prepared: 1) using the aged pPVA granulate that had been stored at the dry-press facility at Alfred University and 2) using fresh pPVA granulate from the production line at Buffalo China.

The roughness of the samples was determined using the optical interferometer and the procedure outlined in Chapter 6.

A second trial in a region that shown promise for a further reduction in the surface roughness. An intermediate blend of 41-59 weight percent blend of pPVA and PEG granulate would be evaluated. Furthermore the 50-50 weight percent blend of pPVA and PEG granulate was repeated to verify the preliminary results as this blend performed well in an industrial environment. Samples were also prepared using the unblended pPVA granulate stored at the dry-press facility as a reference. Also, at the time of the second trial Buffalo China submitted the pPVA granulate stored at Alfred University to their standard tests.

### ***3.0 Results***

The roughness results from the various samples provided by Buffalo China are shown in Figure E-1. Samples were supplied by Buffalo China for evaluation of the surface roughness throughout this project. These samples are

listed in Table E-I with an approximate date of delivery. Not included in this list are the samples initially provided by Buffalo China to set a baseline for the surface roughness, Chapter 6.

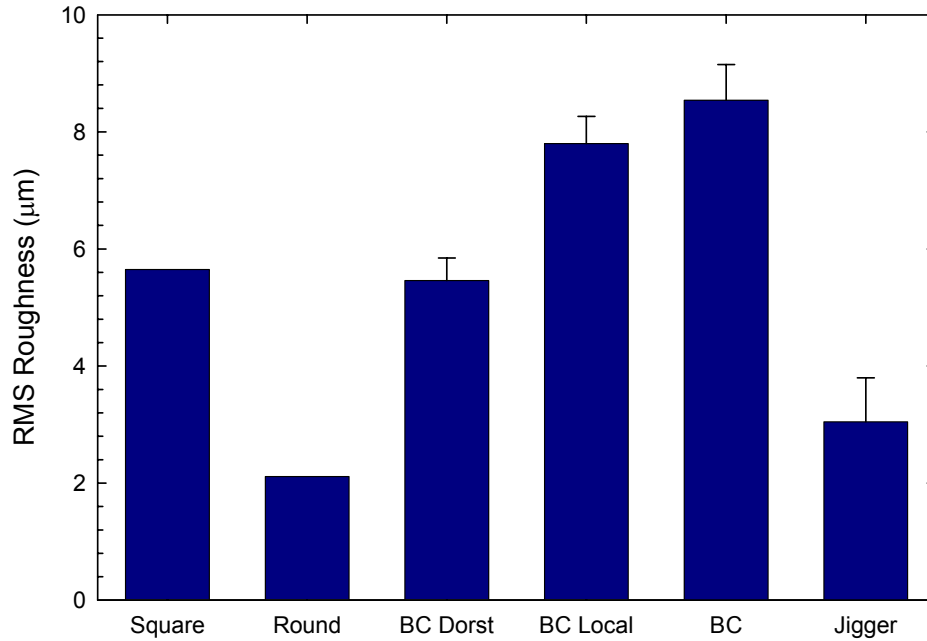


Figure E-1. RMS roughness results of the samples provided by Buffalo China for evaluation throughout this project. All samples, except the jiggered ware, were prepared using pPVA granulate supplied by Buffalo China and evaluated in the green state. Samples studied were the Dorst square sample (Square), Dorst round sample (Round), samples prepared using the Dorst membrane at Buffalo China (BC Dorst), samples prepared using the Local Vendor's version of the Dorst membrane (BC Local), the initial roughness results for the Buffalo China samples that were dry pressed (BC) and jiggered (Jigger).

No details were provided with the samples as to their processing or forming conditions and only one sample was provided for evaluation of the surface finish. Therefore only a cursory evaluation and qualitative remarks will be made. The roughness of the “square” sample in the green state was significantly lower than that of the ware typically manufactured by Buffalo China. The RMS roughness was 5.65 µm for a 6.85 mm by 6.76 mm area compared to 8.54±0.61 µm which was the baseline roughness determined in Chapter 6. The second sample provided by Dorst was a round sample. The measured RMS

roughness of this sample was 2.11  $\mu\text{m}$  which was superior to the surface finish from the jiggering process, RMS roughness of  $3.04 \pm 0.75 \mu\text{m}$ .

Table E-I. List of the Samples Provided by Buffalo China for Evaluation of the Surface Finish.

Sample	Approximate Delivery Date	RMS roughness
Dorst, square (green)	December, 2001	5.65*
Dorst, square (bisque)	December, 2001	8.35* <sup>†</sup>
Dorst, round (green)	December, 2001	2.11*
Dorst, round (bisque)	December, 2001	3.78* <sup>†</sup>
Dorst, hard membrane (green)	February, 2002	$5.46 \pm 0.39$
Local Vendor, hard membrane (green)	December, 2002	$7.79 \pm 0.49$
Buffalo, "sig. improvement" (green)	January, 2003	$8.00 \pm 0.64$

\* Only one sample was provided for evaluation

<sup>†</sup> Roughness in the bisque fired state was demonstrated to be higher due to noise, Chapter 6

Following the evaluation of these samples Dorst supplied to Buffalo China a die manufactured using the harder membrane material for evaluation in Buffalo China's facility. Samples prepared using this harder membrane and the pPVA granulate were supplied for evaluation of the surface finish. The measured RMS roughness of these samples, for a 6.85 mm by 6.76 mm area, was  $5.46 \pm 0.39 \mu\text{m}$ . While the roughness was higher than that of the jiggering process, the use of the harder membrane resulted in a significant improvement in the surface finish. Due to the excessively high costs of shipping membranes from Germany, Buffalo China turned to their local supplier for an equivalent product.

Samples prepared using the local supplier's membrane were evaluated for surface finish. The RMS roughness of the samples was measured at  $7.80 \pm 0.46 \mu\text{m}$  for a 6.85 mm by 6.76 mm area, which represents a significant increase in the roughness compared to the samples prepared using Dorst's membrane. The causes for this change are unknown as Buffalo China has indicated that both elastomers have the same shore hardness.<sup>1</sup>

Finally, Buffalo China provided a set of samples that were termed to have “the best surface finish” they had ever observed.<sup>1</sup> Buffalo China measures surface roughness using a stylus-type profilometer which mechanically drags a tip across the surface and determines a roughness based upon the deflection of the tip. This type of measurement can result in tip artifacts similar to those observed in atomic force microscopy. These samples were evaluated using the interferometer at Alfred University using a 6.85 mm by 6.76 mm area and the RMS roughness was determined to be  $8.00 \pm 0.64 \mu\text{m}$ .

The samples prepared from the 50-50 blend of the pPVA and NB did not have sufficient green strength to survive the ejection and finishing steps in the industrial process. While the experimental results generated at Alfred University from this blend showed promise, this granulate system was abandoned since it cannot survive in an industrial setting. Focus was therefore placed on the pPVA and PEG blends.

The results from the industrial trial are shown in Figure E-2. A comparison between the roughness results from this trial and the previous results show that there is an improvement in the surface finish of the dinnerware prepared using the blended granulate. The slight decrease in the measured roughness of the pPVA granulate relative to the preliminary data, used to set the baseline, is the result of a change in Buffalo China’s production process to the harder membrane.

Statistical analysis (ANOVA: Single Variable, Excel v.2000) showed that there is a significant difference in the roughness results from this industrial trial. Based upon the statistical analysis there is a 99.96% confidence level that there is a significant difference in the roughness of the samples in the current study. Duncan’s Multiple Range Test was used to determine which samples in the analysis were significantly different.<sup>2</sup> The results indicate that there is no significant difference in surface finish between the two blended granulate systems and that the samples prepared using granulate pPVA had statistically equivalent roughness, i.e., storing the granulate at the dry-press facility did not effect the measured surface roughness. A significant difference in roughness

was found between the samples prepared using the blended granulate and the samples prepared with the unblended pPVA granulate. Therefore blending pPVA and PEG granulate, within the ranges studied, resulted in a significant decrease in the measured RMS roughness compared to the unblended pPVA granulate.

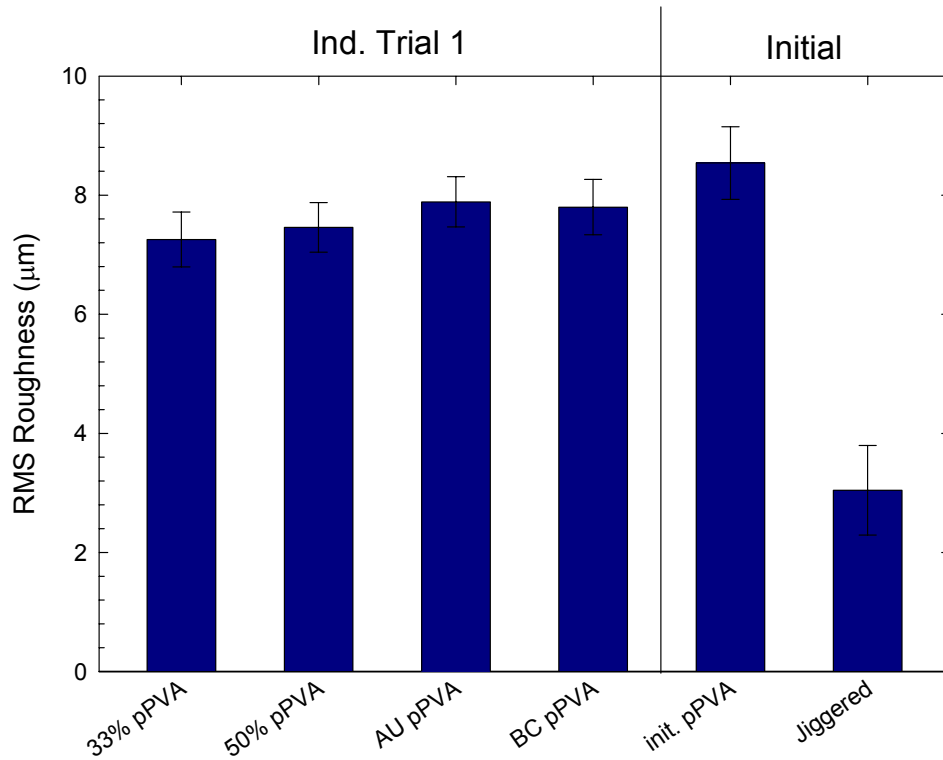


Figure E-2. Plot of the measured RMS surface roughness from the various blends studied in the first industrial trial. The results from the first industrial trial are on the left and previous results are plotted on the right, the fraction of pPVA granulate in each blend increases from left to right in the current study. The AU pPVA was stored at the dry pres facility prior to pressing samples while the BC pPVA samples were prepared using fresh pPVA granulate from Buffalo China process. There is a significant difference in surface roughness between the samples prepared using blended granulate and unblended granulate in the current study. Using a harder membrane for pressing pPVA granulate has a significant effect on the measured roughness, compare Init. pPVA to BC pPVA results. Compared to the jiggered surface the dry-pressed samples have a significantly higher measured roughness. Sample prepared using a 50-50 blend of pPVA and NB were not strong enough to survive an industrial dry-pressing process and no roughness results could be obtained.

The results from the second industrial trial are shown in Figure E-3, also plotted are the results from the first industrial trial for comparison. No further improvement is observed in the measured RMS roughness. The roughness values from the second trial are observed to be slightly higher than those from the first trial. This may be an artifact of the change in weather, i.e., the ambient humidity, between the two tests or a change in the operational parameters of the press; data on the operation of the press has not been provided.

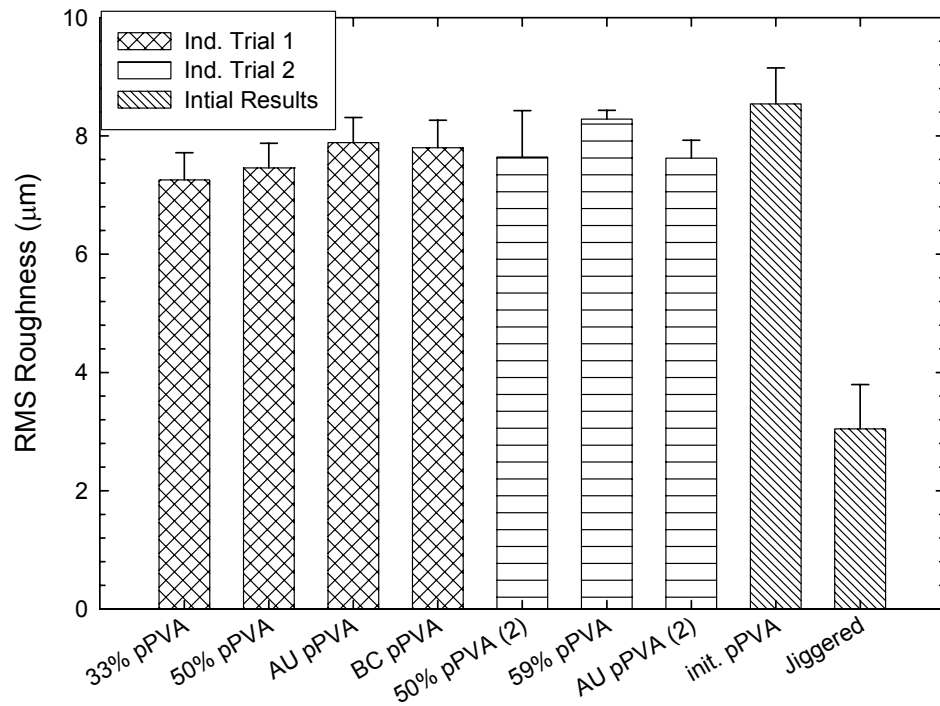


Figure E-3. Summarized results from the two industrial trials at Buffalo China. Also plotted are the initial roughness results from the pPVA granulate and the jiggered ware. No significant improvement in the RMS roughness is observed compared to the first industrial trail. All the measured roughness values continue to be significantly higher than that of the jiggered ware ( $3.04 \pm 0.753 \mu\text{m}$ ). See the text for details on the composition of the blends.

#### **4.0 Summary and Conclusions**

The samples provided by Buffalo China for evaluation of the surface roughness were observed to be inconsistent. Ware that was reportedly manufactured using a die with the same shore hardness was observed to have significantly different roughness values. Uncontrolled variables in the industrial setting interfered with understanding the change in the measured roughness. Samples provided by Dorst, prepared in Germany, were observed to have a lower roughness than that of the jigged and ram pressed ware. Samples prepared using a membrane surface provided by Dorst in Germany observed to have a low surface roughness ( $5.46 \pm 0.39 \mu\text{m RMS}$ ) using the standard binder system. Based upon the images from the optical interferometer and discussions with Buffalo China it was determined that the low roughness from the Dorst membrane would be sufficient for an aesthetically pleasing decoration. Subsequent samples prepared using the same binder system had a significantly higher roughness of approximately  $7.79 \pm 0.49 \mu\text{m RMS}$ .

Blending of pPVA and PEG granulate resulted in a small but significant decrease in the measured roughness of the dinnerware samples prepared at Buffalo China. More significant was the change to a membrane elastomer with a higher shore hardness.

Based upon these results it was decided to investigate the plasticized PVA binder system used by Buffalo China. The results of this study are reported in Chapter 9.

## **5.0 References**

1. N.J. Ninos, Oneida Dinnerware, Buffalo, New York, January, 2002, Private Communication.
2. D.C. Montgomery, *Design and Analysis of Experiments*; pp 100-3. John Wiley & Sons, New York, New York, 1997.

## ***Appendix F. Mathematica™ program written to Simulate a Droplet Drying in a Spray Dryer***

### ***1.0 List of Variables in the Notebook***

rd::usage="Radius of the droplet";

rp::usage="Radius of the particle";

af::usage="area fraction of the powder in suspension";

n::usage="number of particles in the suspension";

ri::usage="dimension of the area for each particle in the initial droplet";

p::usage="list of the position and radius of each particle in the droplet";

q::usage="modified form of p to include the head 'disk' in the list of  
position vectors";

theta::usage= "list of random vectors to create a random distribution of  
particles in the droplet";

dx::usage="x component of the random vectors normalized to the distance 'ri'";

dy::usage="y component of the random vectors normalized to the distance 'ri'";

deltax::usage="total x displacement of the particle due to the random vectors";

deltay::usage="total y displacement of the particle due to the random vectors";

x::usage="x coordinate of the particle in the rigid array";

y::usage="y coordinate of the particle in the rigid array";

s::usage="x component of the conditional statement to check if the particles  
overlap after applying the random vector";

t::usage="y component of the conditional statement to check if the particles  
overlap after applying the random vector";

a::usage="x coordinate position in the list 'p' of the particles in the  
initial droplet";

b::usage="y coordinate position in the list 'p' of the particles in the initial droplet";

xcoord::usage="list of the x coordinates for each particle in the initial droplet";

ycoord::usage="list of the y coordinates for each particle in the initial droplet";

tempin::usage="inlet temperature of the spray dryer";

tempout::usage="outlet temperature of the spray dryer";

tempsus::usage="temperature of the suspension being spray dried";

ductarea::usage="area of the inlet duct for the heated air in the spray dryer";

flowrate::usage="rate that the heated air is moved through the dryer";

dryingrate::usage="calculated variable to determine the rate at which water is removed from the droplet";

drd::usage="rate of change of the radius of the droplet during drying";

time::usage="variable to represent time in the drying process";

a::usage="list of images to represent the change droplet as water is removed from the system";

waste::usage="list of waste data generated by a conditional statement that limits the number of images generated by the model";

kappa::usage="list of the angles opposite to the position vector defined by 'angle' to each particle in the droplet for a given 'time'";

count1::usage="iterator for determining if the particles in the virtual droplet overlap";

count2::usage="iterator for appending the particles to list 'e' during the drying process";

e::usage="list of the particle positions in the droplet as it is drying";

density::usage="density of the powder in the suspension";

distance::usage=distance from the center of the droplet to each particle,  
 used to prorate the rate of shrinkage of each particle in the droplet";

changex::usage="x component of the vector from the center of the droplet  
 to each particle, used to shrink the droplet";

changey::usage="y component of the vector from the center of the droplet  
 to each particle, used to shrink the droplet";

## ***2.0 Series of Equations to Create a “Droplet” with “Particles”***

```
rd=50.;
(*droplet radius in micrometers*)

rp=1.;
(*particle radius in micrometers*)

af=.15;
(*area fraction (volume fraction) for the powder in suspension*)

n=af(rd/rp)^2;

ri=(\[Pi] rd^2/n)^0.5;

p={};

xcoord={};

ycoord={};

Do[theta={};
  Do[AppendTo[theta, Random[Real, {0,2\[Pi]}]], {2}];

  dx=Cos[theta] rp;
  dy=Sin[theta] rp;
```

```
deltax=dx[[1]]+dx[[2]];
```

```
deltay=dy[[1]]+dy[[2]];
```

```
If[(x^2+y^2)^0.5\LessEqual] rd,
```

```
If[((x+deltax)^2+(y+deltay)^2)^0.5\LessEqual] (rd-rp),
```

```
For[s\LessEqual]( x+deltax±2 rp);
```

```
t\LessEqual] (y+deltay±2 rp),
```

```
MemberQ[p,{{s,t},rp}},
```

```
count1++,
```

```
deltax=deltax+dx[[1]];
```

```
deltay=deltay+dy[[1]];
```

```
s\LessEqual] (x+deltax±2 rp);
```

```
t\LessEqual] (y+deltay±2 rp)];
```

```
a=(x+deltax);
```

```
b=(y+deltay);
```

```
AppendTo[p,{{a, b}, rp)];
```

```
AppendTo[xcoord, a];
```

```
AppendTo[ycoord, b],
```

```
For[s\LessEqual]( x-deltax± 2 rp);
```

```
t\LessEqual] (y-deltay±2 rp),
```

```
MemberQ[p,{{s,t},rp}},
```

```
count1++,
```

```
deltax=deltax+dx[[1]];
```

```

deltay=deltay+dy[[1]];
s\[LessEqual] (x-deltax±2 rp);
t\[LessEqual] (y-deltay±2 rp)
];
a=(x-deltax);
b=(y-deltay);
AppendTo[p,{{a, b}, rp}];
AppendTo[xcoord, a];
AppendTo[ycoord, b]
],
Null
],
{y, -rd+rp/2, rd-rp/2, ri},{x, -rd+rp/2, rd-rp/2, ri}];
q=Apply[Disk,p,1];
Show[Graphics[Circle[{0,0}, rd]], Graphics[q], AspectRatio\[Rule]Automatic,
Axes\[Rule]True, PlotRange\[Rule] {-50, 50}]

```

### **3.0 Series of Equations to Simulate “Drying” of the “Droplet”**

```

tempin=300;
(*spray dryer inlet gas temperature in degrees Celcius*)
tempout=120;
(*spray dryer outlet gas temperature in degrees Celcius*)
tempsus=30;
(*suspension temperature in degrees Celcius*)
flowrate=.5167;
(*blower gas flow rate in m^3/s*)

```

```

density=3.98;
(*density of the particles in the suspension*)
pumprate=2;
(*pump rate for the suspension into the spray dryer in ml/sec*)
numdrop=pumprate 10^8/[Pi] rd^2;

dryingrate=
  ((637 flowrate (tempin-tempout)
    -((tempout-tempsus) af pumprate density .8209))
    /(4.18 (100-tempsus)+2257+1.87(tempout-100)))/numdrop;

time=0;a={};
waste={};
kappa={};
waste={};
wastell={};
kappa =ArcTan[xcoord, ycoord];

For[time=0, af[LessEqual] .75, time++,
  e={};
  drd= dryingrate time 10^8/(1-af)^2 \[Pi] rd;
  AppendTo[waste,drd];
  AppendTo[wastell, af];
  distance=(xcoord^2+ycoord^2)^0.5;
  changex=drd Cos[kappa] distance/rd;

```

```

changey=drd Sin[kappa] distance/rd;
xcoord=xcoord-changex;
ycoord=ycoord-changeey;

Do[
  For[s\[LessEqual](xcoord+changex±2 rp);
    t\[LessEqual] (ycoord+changeey±2 rp),
    MemberQ[e,Disk[{s,t},rp]],
    count3++,
    changex=0;
    changeey=0];
  AppendTo[e, Disk[{xcoord[[count2]], ycoord[[count2]]}, rp]],
  {count2, 1, Length[q]};
rd=rd-drd;
af= n rp^2/rd^2;

```

#### **4.0 Equations to Plot the “Droplet” While “Drying”**

```

Show[Graphics[e],Graphics[Circle[{0,0}, rd]],
  AspectRatio[Rule]Automatic, Axes\[Rule]True,
  PlotRange[Rule] {-50, 50}
];
ListPlot[waste];
ListPlot[wastell];
Print[time]
TableForm[waste]
TableForm[wastell]

```

**Appendix G. Parameters Associated with the Control of the BE985 Spray Dryer at Alfred University**

**1.0 Operational Parameters for the Spray Drier**

The following Tables list the recorded inlet and outlet temperatures from the BE 985 spray dryer that was used to prepared the granulate in this study. Also reported is the pump speed, in arbitrary units, used to atomize the suspension. The atomizer pressure was maintained between 13 and 14 psig for each of the runs.

Table G-I. Parameters from the Spray Dryer While Preparing the pPVA Granulate for this Study.

Binder Conc. (wt%,dwb)	Initial Temperature (°C)		Final Temperature (°C)		Pump Speed
	Inlet	Outlet	Inlet	Outlet	
0	289	126	290	129	2.5
0.25	290	125	292	132	2.5
0.5	291	122	291	134	2.5
1	291	125	291	137*	2.5
2	291	124	291	141	2.5
5	291	129	291	144	2.5

\* Temperature reached 160 °C during spray drying

Table G-II. Parameters from the Spray Dryer While Preparing the Na-Lignosulphonate Granulate for this Study.

Binder Conc. (wt%,dwb)	Initial Temperature (°C)		Final Temperature (°C)		Pump Speed
	Inlet	Outlet	Inlet	Outlet	
0.25	291	126	291	120	3
0.5	291	127	291	126	2.8
1	291	127	291	125	2.8
2	291	126	291	129	2.8
5	291	126	291	125	2.8

Table G-III. Parameters from the Spray Dryer While Preparing the pPVA / Veegum™ T Granulate for this Study.

Binder Conc. (wt%,dwb)	Initial Temperature (°C)		Final Temperature (°C)		Pump Speed
	Inlet	Outlet	Inlet	Outlet	
0	290	131	290	131	2.8
0.25	290	129	290	137	2.8
0.5	290	130	290	134	2.8
1	290	131	290	129	3
2	290	127	291	135	3.25
5	290	141	291	125	3.5

Table G-IV. Parameters from the Spray Dryer While Preparing the Veegum™ T Granulate for this Study.

Binder Conc. (wt%,dwb)	Initial Temperature (°C)		Final Temperature (°C)		Pump Speed
	Inlet	Outlet	Inlet	Outlet	
0.25	290	125	288	127	2
0.5	285	120	289	127	2
1	290	117	292	132	2.5
2	290	120	293	140	3
5	290	125	295	137	4

Table G-V. Parameters from the Spray Dryer While Preparing the Agar Granulate for this Study.

Binder Conc. (wt%,dwb)	Initial Temperature (°C)		Final Temperature (°C)		Pump Speed
	Inlet	Outlet	Inlet	Outlet	
0	291	126	290	124	3
0.25	291	120	290	126	3
0.5	290	125	290	125	3
1	290	127	290	125	3
2	290	127	290	120	3
5	291	125	291	132	3

Table G-VI. Parameters from the Spray Dryer While Preparing the Acrylic Latex Granulate for this Study.

Binder Conc. (wt%,dwb)	Initial Temperature (°C)		Final Temperature (°C)		Pump Speed
	Inlet	Outlet	Inlet	Outlet	
0	290	135	300	135	2.5
0.25	295	154	290	135	2.5
0.5	290	102	290	125	2.5
1	290	105	290	130	2.5
2	290	110	290	125	2.8
5	290	105	295	105	3

Table G-VII. Parameters from the Spray Dryer While Preparing the Starch Granulate for this Study.

Binder Conc. (wt%,dwb)	Initial Temperature (°C)		Final Temperature (°C)		Pump Speed
	Inlet	Outlet	Inlet	Outlet	
0.25	291	136	290	141	2.5
0.5	291	132	290	133	2.5
1	289	121	290	139	2.5
2	290	124	290	140	2.5
5	290	125	291	139	2.5

Table G-VIII. Parameters from the Spray Dryer While Preparing the Sugar Granulate for this Study.

Binder Conc. (wt%,dwb)	Initial Temperature (°C)		Final Temperature (°C)		Pump Speed
	Inlet	Outlet	Inlet	Outlet	
0.25	289	131	289	145	2.5
0.5	289	130	290	142	2.5
1	289	128	290	145	2.5
2	289	135	290	150	2.5
5	291	127	290	145	2.5

Table G-IX. Parameters from the Spray Dryer While Preparing the Methyl Cellulose Granulate for this Study.

Binder Conc. (wt%,dwb)	Initial Temperature (°C)		Final Temperature (°C)		Pump Speed
	Inlet	Outlet	Inlet	Outlet	
0	295	128	295	126	2.5
0.1	295	115	295	110	2.75
0.25*	290	113	295	135	3
0.5	292	103	294	111	3
0.7**	292	120	295	111	4

\* Suspension clogged nozzle due to thermal gelling of cellulose

\*\* 5 drops of Bubble Breaker 748 [Bubble Breaker 748, Witco Corporation, New York, New York] added to minimize foaming during suspension preparation

Table G-X. Parameters from the Spray Dryer While Preparing the Carboxymethyl Cellulose Granulate for this Study.

Binder Conc. (wt%,dwb)	Initial Temperature (°C)		Final Temperature (°C)		Pump Speed
	Inlet	Outlet	Inlet	Outlet	
0	292	132	290	135	2.5
0.1	290	126	290	140	2.5
0.25	290	123	290	138	2.8
0.5	290	123	291	159	2.8
0.7*	290	140	290	170	5

\* Suspension clogged nozzle due to thermal gelling of cellulose

Table G-XI. Parameters from the Spray Dryer While Preparing the Veegum™ T / Vanzan™ D Granulate for this Study.

Binder Conc. (wt%,dwb)	Initial Temperature (°C)		Final Temperature (°C)		Pump Speed
	Inlet	Outlet	Inlet	Outlet	
0	290	125	290	135	2.5
0.25	291	125	291	140	2.5
0.5	290	123	291	128	3
1	291	120	291	135	3
2	291	115	291	132	3.5
2 - hyd.	290	127	291	139	2.5

## Appendix H. Structure of the Organics Used in This Study

### 1.0 Organic Structures

Schematics of the structure of the organics used in this study are presented in this Appendix. The structure of the plasticizer used in this research is unknown as only the trade name is known. It has been reported that the plasticizer is a “small, PEG-like” molecule. The structure of agar could not be found. The structure of humic acid and fulvic acid were presented Chapter 2.

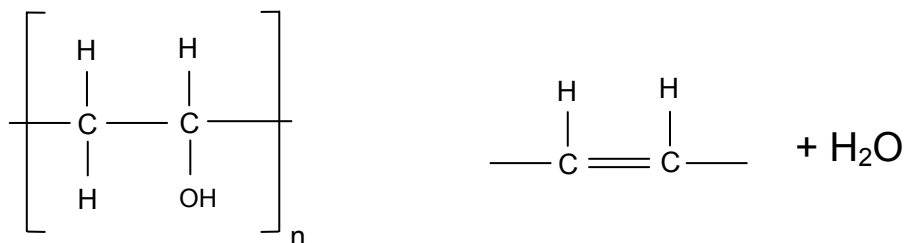


Figure H-1. Schematic of a fully hydrolyzed poly[vinyl alcohol] (left) where “n” represents the degree of polymerization.<sup>1</sup> The proposed mechanism for the thermal degradation of PVA (right) is presented to understand the transition from a slightly hydrophilic molecule to a hydrophobic molecule.

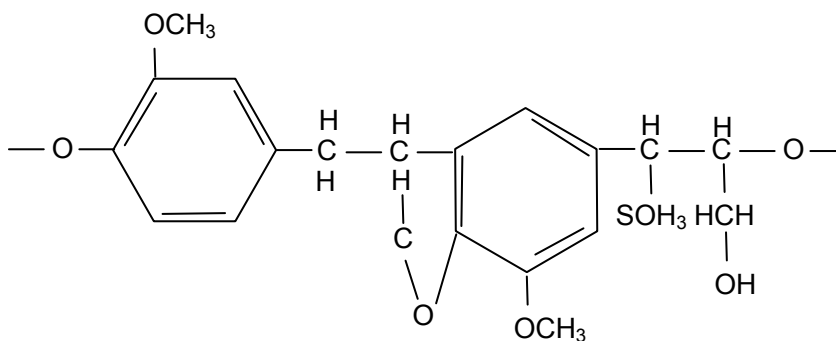


Figure H-2. Schematic of a simplified lignosulphonate molecule.<sup>2</sup>

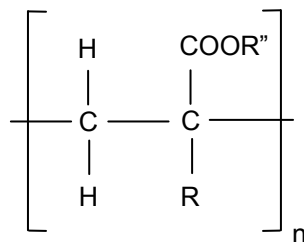


Figure H-3. Schematic of the structure of an acrylic latex. The functional group R can represent H or CH<sub>3</sub> and R' can represent H, CH<sub>3</sub>, or CH<sub>2</sub>CH<sub>3</sub>.<sup>3</sup>

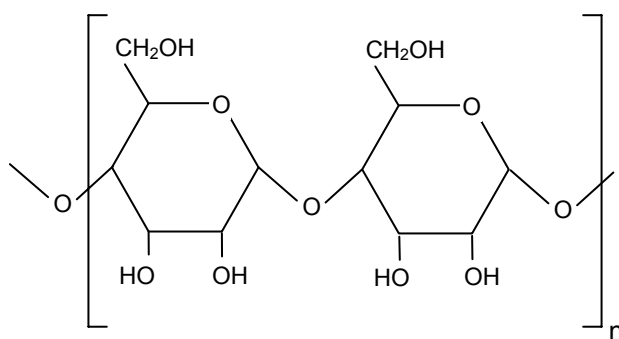


Figure H-4. Schematic of the structure of a mer of starch. Starch is a polysaccharide, i.e., a polymerized form of glucose. Not shown in the schematic are the carbon atoms in the ring structure or the hydrogen atoms that surround those carbon atoms. The structure of starch has ringed structures that are all oriented in the same direction, i.e., an isotactic structure.<sup>1,2,4</sup>

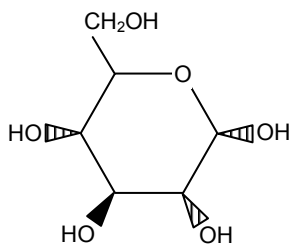


Figure H-5. Schematic of the structure of sugar (glucose) the building block for polysaccharides. The crosshatched triangles represent bonds that are above the plane of the paper and the solid triangle represents a bond that is below the plane of the paper.<sup>5</sup>

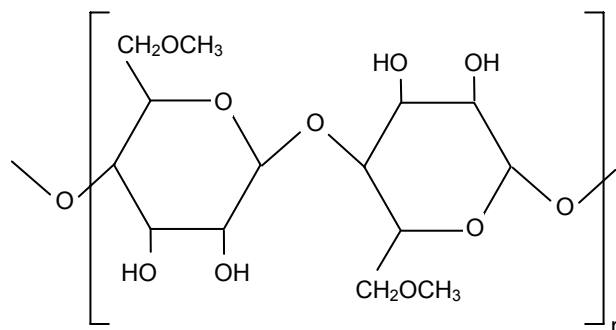


Figure H-6. Schematic of the structure of a mer of methyl cellulose. Methyl cellulose is a polysaccharide, i.e., a polymerized form of glucose. Not shown in the schematic are the carbon atoms in the ring structure or the hydrogen atoms that surround those carbon atoms. The cellulose structure has ringed structures that alternate, i.e., an atactic structure.<sup>1,2,4</sup>

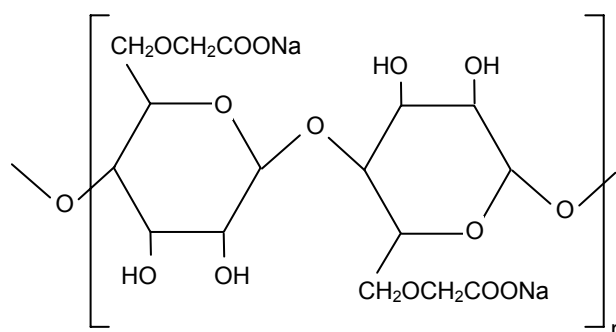


Figure H-7. Schematic of the structure of a mer of sodium carboxymethyl cellulose. Carboxymethyl cellulose is a polysaccharide, i.e., a polymerized form of glucose. Not shown in the schematic are the carbon atoms in the ring structure or the hydrogen atoms that surround those carbon atoms. The cellulose structure has ringed structures that alternate, i.e., an atactic structure.<sup>1,2,4</sup>

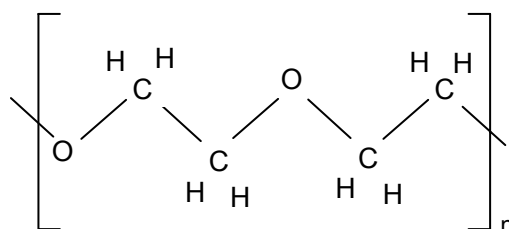


Figure H-8. Schematic of the structure of poly[ethylene glycol]. Shown are two mers of ethylene glycol that demonstrates how the structure alters ion the polymer. For PEG 8000 the degree of polymerization (n) for the shown structure is 91.<sup>5</sup>

## 2.0 References

1. J.S. Reed, *Principles of Ceramic Processing*, 2<sup>nd</sup> ed.; Ch. 11. John Wiley & Sons, New York, New York, 1995.
2. D.J. Shanefield, *Organic Additives and Ceramic Processing*, 2<sup>nd</sup> ed.: with *Applications in Powder Metallurgy, Ink, and Paint*; Ch. 3. Kluwer Academic Publishers, Boston, Massachusetts, 1996.
3. A.S. Barnes, "Evaluation of the Effects of Organic Binder System, Alumina Type, and Firing Schedule on Spray Drying, Granule, and Compaction Properties of Advanced Alumina Ceramics"; M.S. Thesis. Alfred University, Alfred, New York, 1996.
4. I.M. Campbell, *Introduction to Synthetic Polymers*; Ch. 1. Oxford Science Publications, New York, New York, 1994.
5. Alpha-D(+)-Glucose, Anhydrous 99+%, ACROS Organics, Morris Plains, NJ.
6. W.M. Carty, "Processing of Ceramic Fibers from Particle Suspensions"; Ph.D. Thesis. University of Washington, Seattle, Washington, 1992

## ***Appendix I. Images from the Interferometer of the Surface Finish from the Samples Prepared with Alternative Binder Systems***

### ***1.0 Surface Evaluation***

The images from the optical interferometer for the samples prepared with alternative binder systems are shown. The RMS roughness, reported by the interferometer, is shown below each image. The images from the dinnerware and tile samples are shown.

The images from each binder system will be shown on two pages. The binder systems are listed in the following order:

Figure I-1. plasticized PVA

Figure I-2. Na- lignosulphonate

Figure I-3. plasticized PVA / Veegum™ T (50-50 wt% mixture)

Figure I-4. Veegum™ T

Figure I-5. Agar

Figure I-6. Acrylic latex emulsion

Figure I-7. Starch

Figure I-8. Sugar

Figure I-9. Methyl cellulose

Figure I-10. Carboxymethyl cellulose

Figure I-11. Veegum™ T / Vanzan™ D (80-20 wt% mixture)

Figure I-12. plasticized PVA reference (Buffalo China granulate)

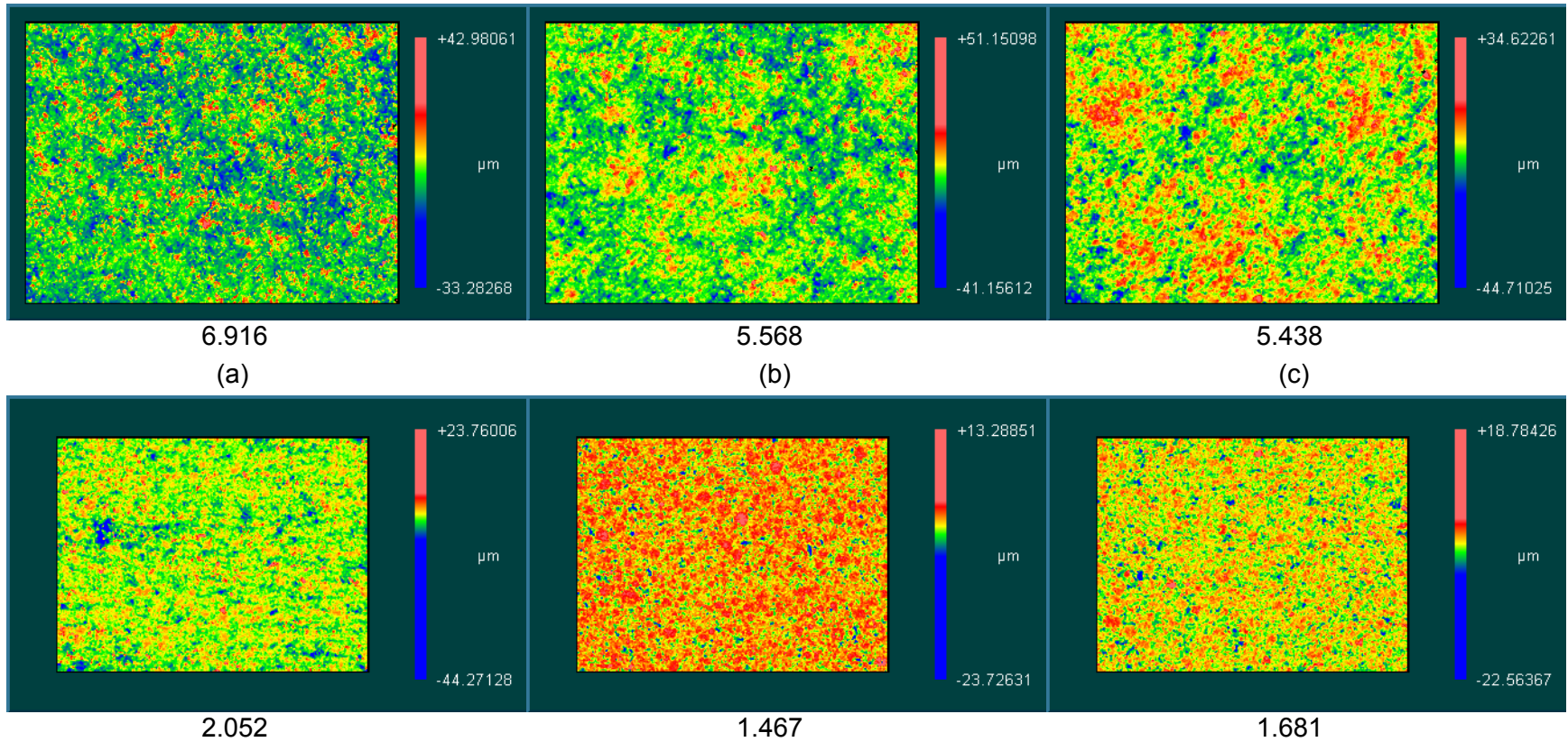


Figure I-1. Images of the surface finish of the samples prepared using the granulate spray dried using pPVA as a binder system. The images from the dinnerware samples are shown above and the images from the tile samples are shown below. Shown are the images prepared with (a) 0 wt%, (b) 0.25 wt%, and (c) 0.50 wt%. The RMS roughness is listed below each image.

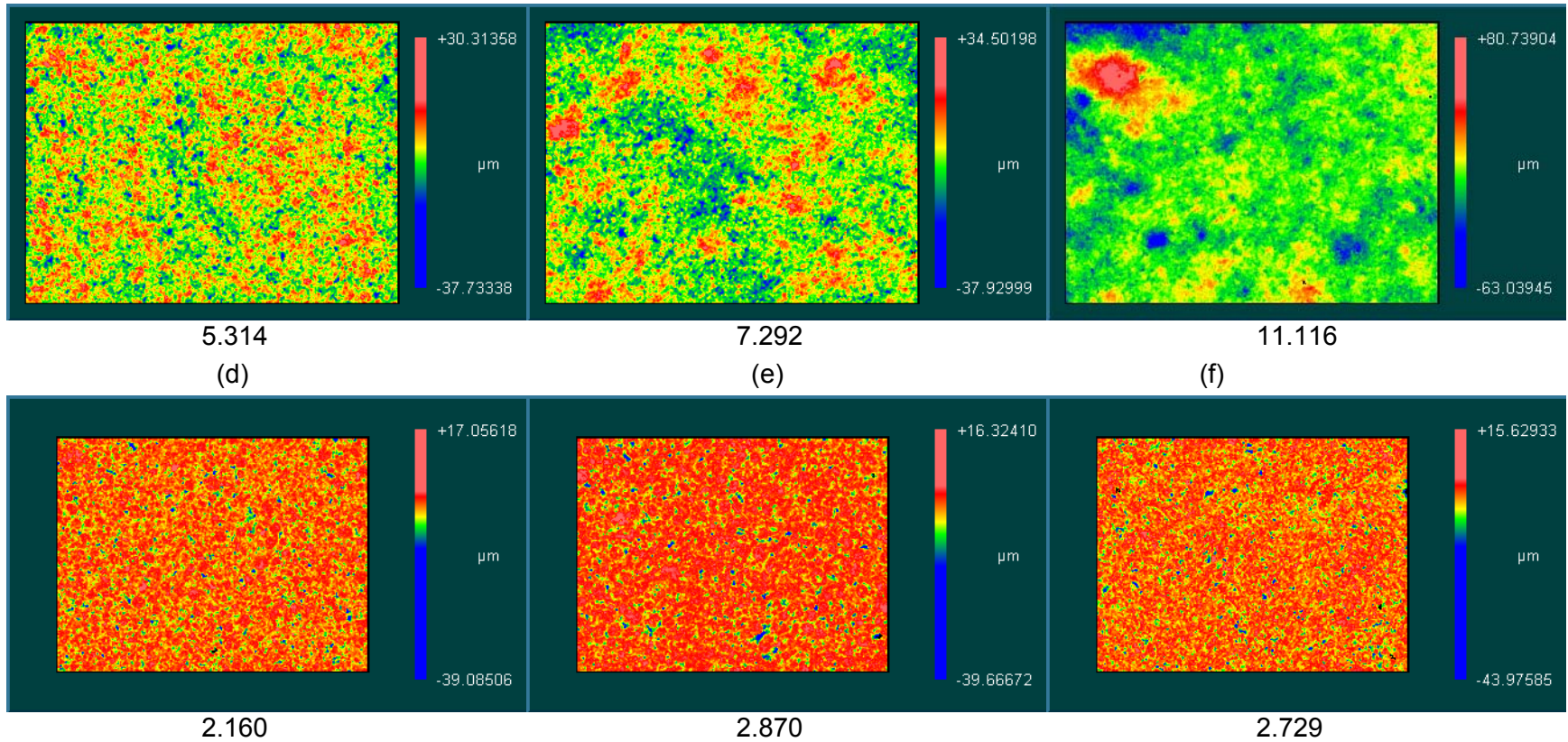


Figure I-1 (cont.). Images of the surface finish of the samples prepared using the granulate spray dried using pVA as a binder system. The images from the dinnerware samples are shown above and the images from the tile samples are shown below. Shown are the images prepared with (d) 1 wt%, (e) 2 wt%, and (f) 5 wt%. The RMS roughness is listed below each image.

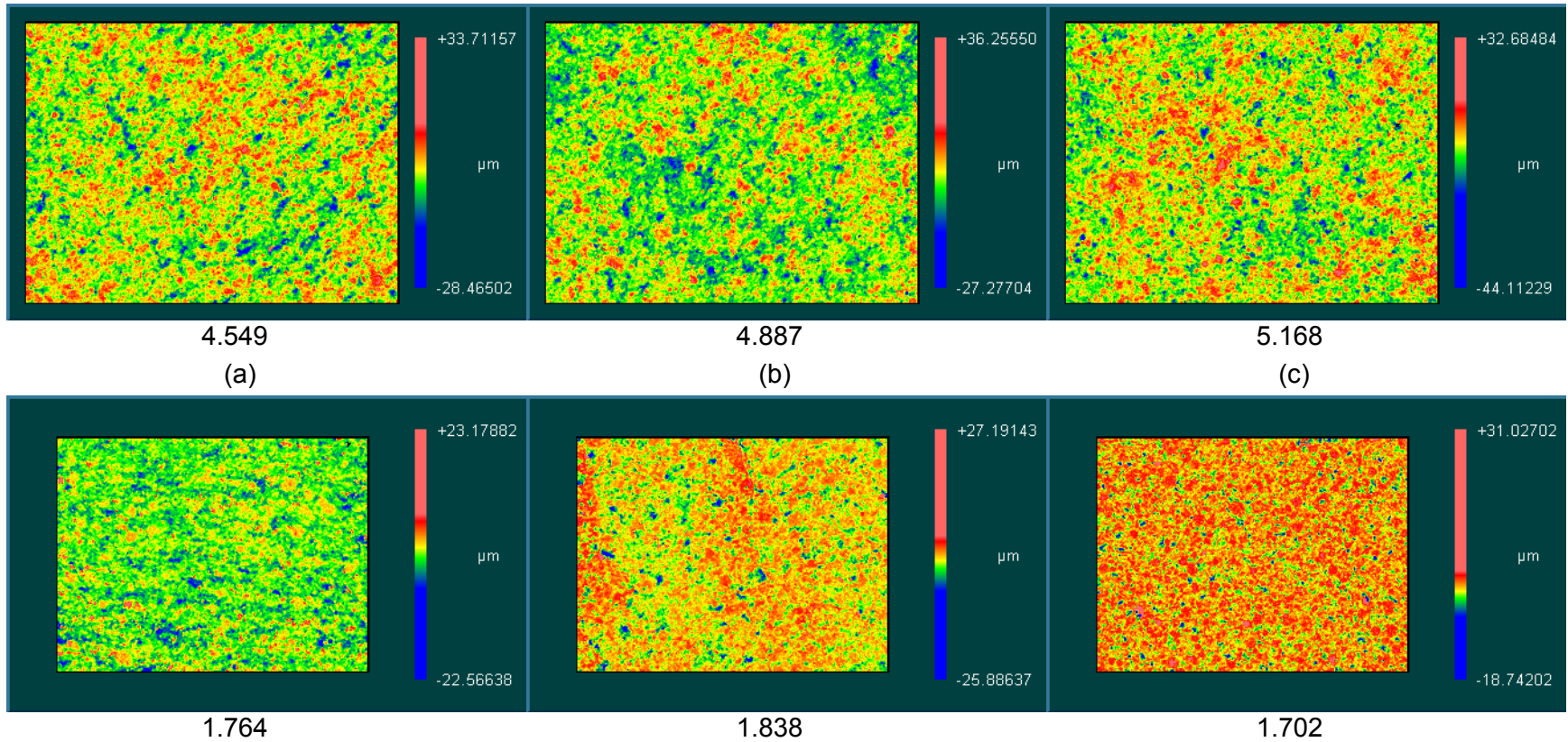


Figure I-2. Images of the surface finish of the samples prepared using the granulate spray dried using Na-lignosulphonate as a binder system. The images from the dinnerware samples are shown above and the images from the tile samples are shown below. Shown are the images prepared with (a) 0.25 wt%, (b) 0.50 wt%, and (c) 1 wt%. The RMS roughness is listed below each image.

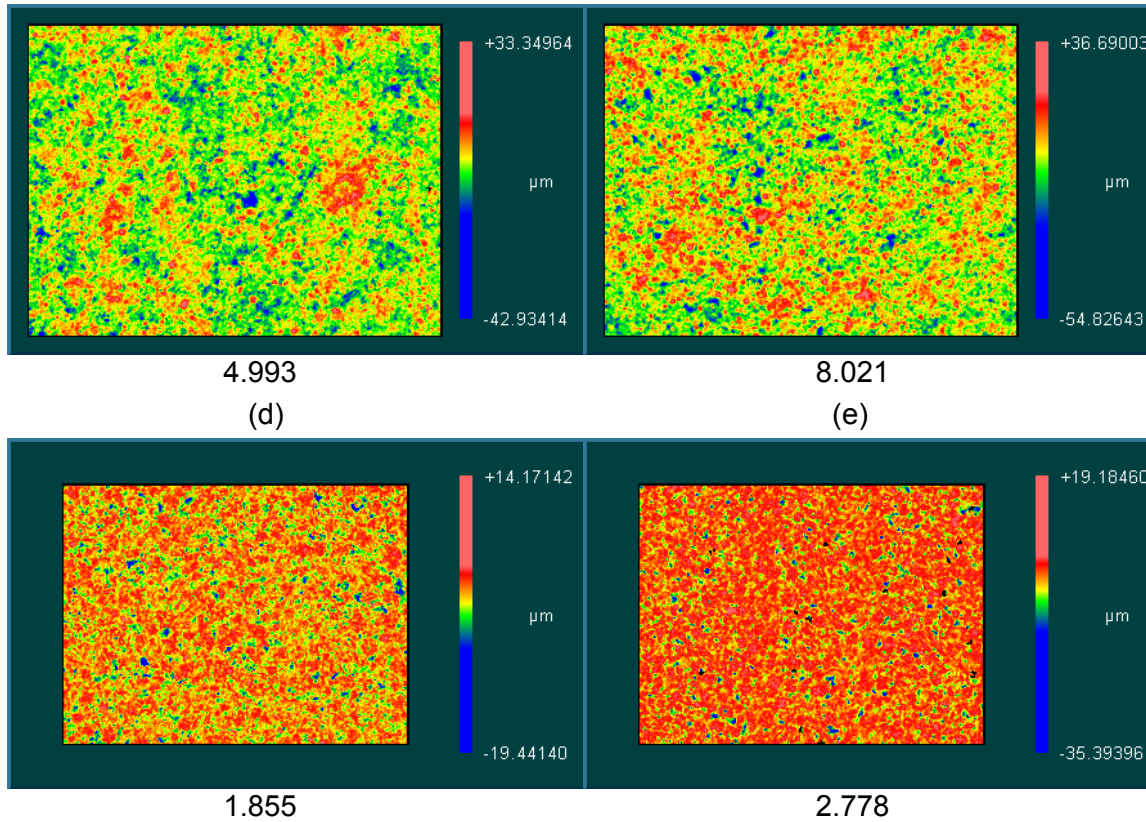


Figure I-2 (cont.). Images of the surface finish of the samples prepared using the granulate spray dried using Na-lignosulphonate as a binder system. The images from the dinnerware samples are shown above and the images from the tile samples are shown below. Shown are the images prepared with (d) 2 wt% and (e) 5 wt%. The RMS roughness is listed below each image.

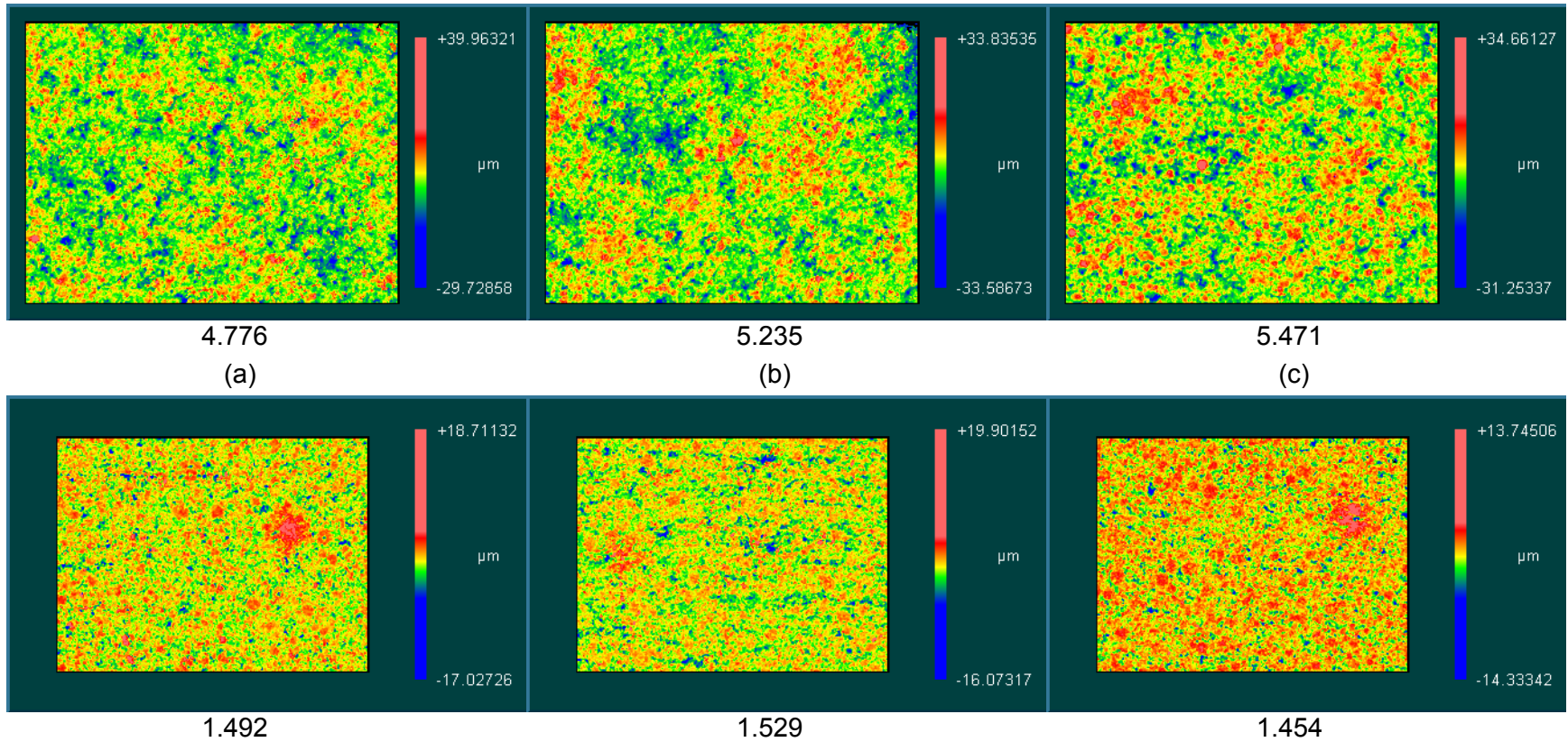


Figure I-3. Images of the surface finish of the samples prepared using the granulate spray dried using pPVA / Veegum™ T (50-50 wt% mixture) as a binder system. The images from the dinnerware samples are shown above and the images from the tile samples are shown below. Shown are the images prepared with (a) 0 wt%, (b) 0.25 wt%, and (c) 0.50 wt%. The RMS roughness is listed below each image.

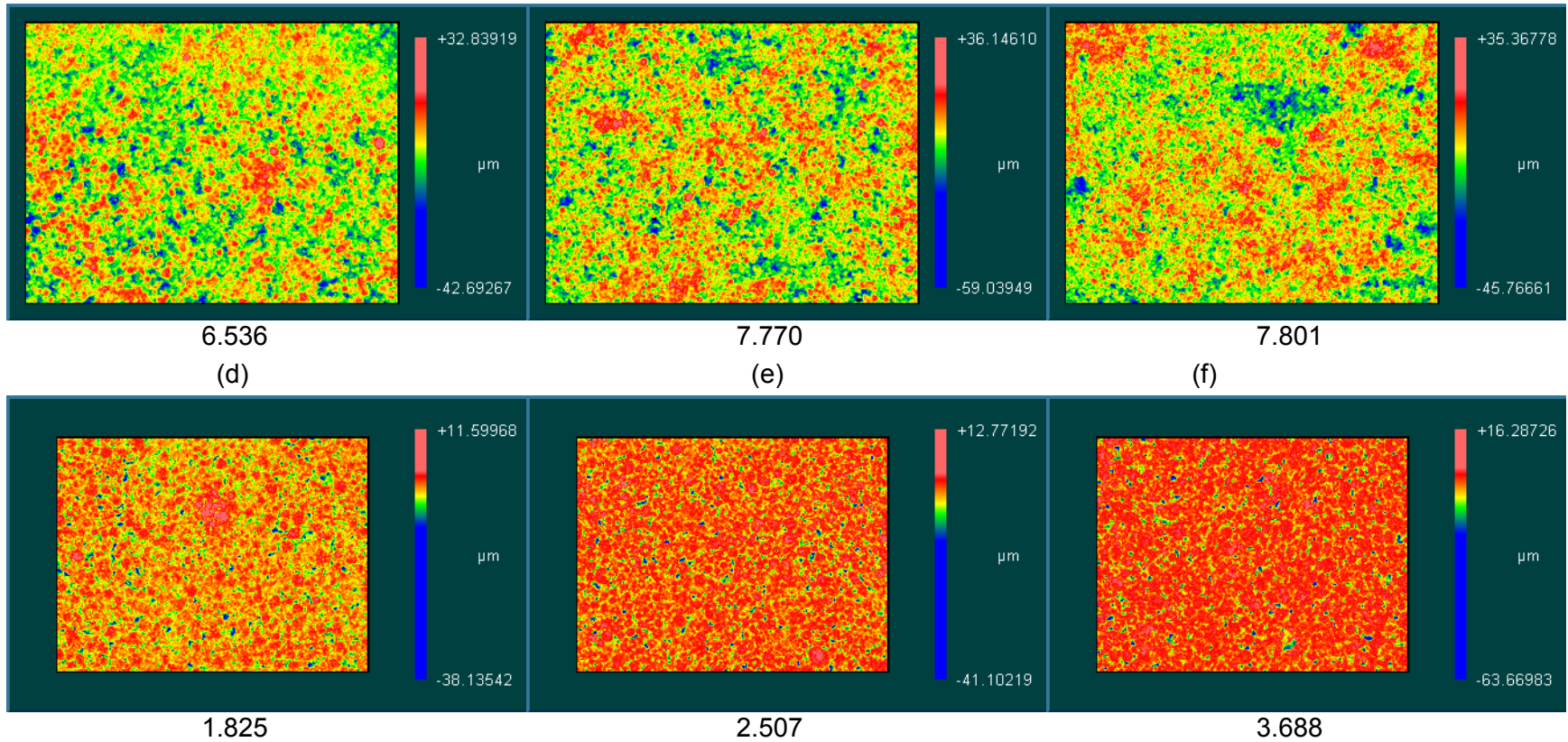


Figure I-3 (cont.). Images of the surface finish of the samples prepared using the granulate spray dried using pPVA / Veegum™ T (50-50 wt% mixture) as a binder system. The images from the dinnerware samples are shown above and the images from the tile samples are shown below. Shown are the images prepared with (d) 1 wt%, (e) 2 wt%, and (f) 5 wt%. The RMS roughness is listed below each image.

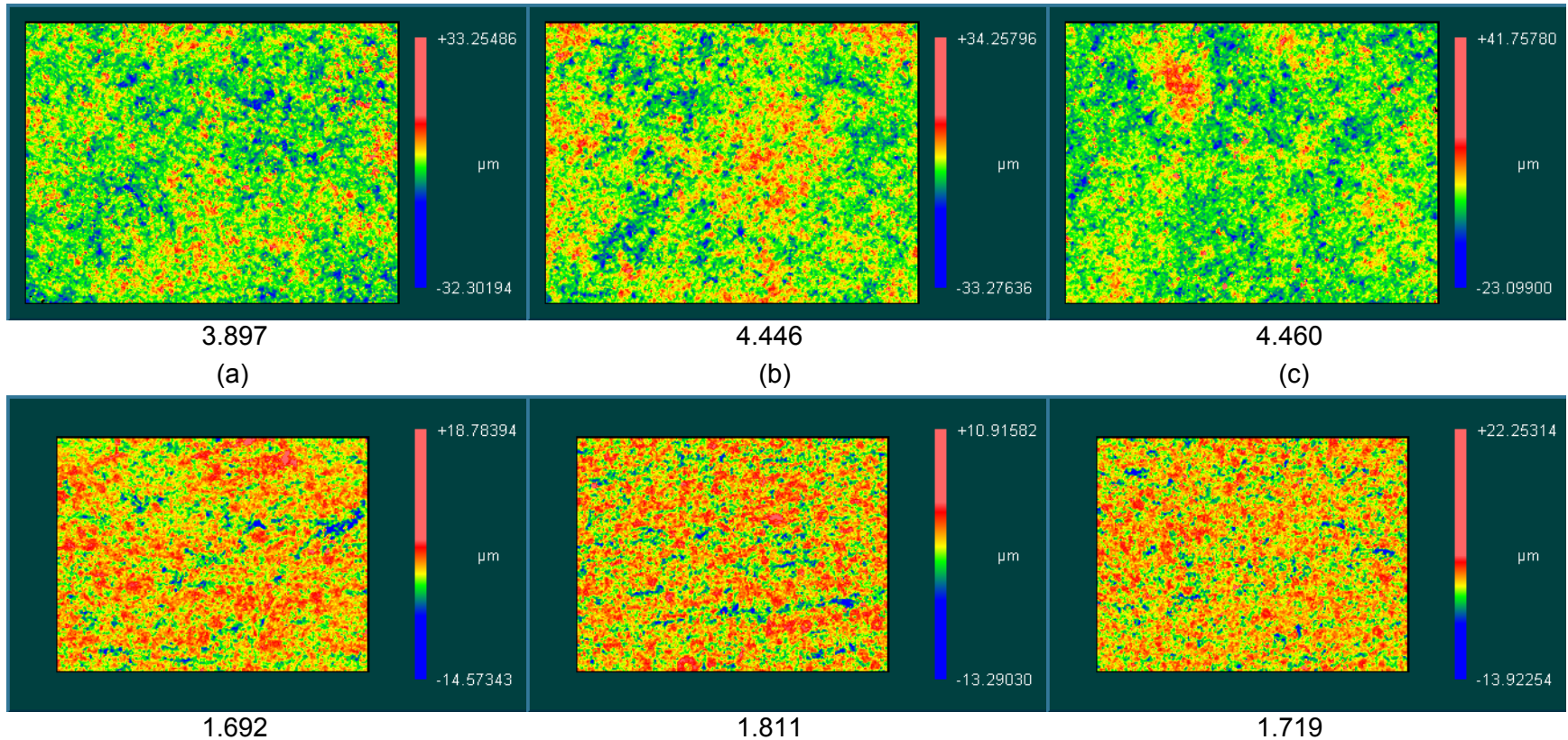


Figure I-4. Images of the surface finish of the samples prepared using the granulate spray dried using Veegum™ T as a binder system. The images from the dinnerware samples are shown above and the images from the tile samples are shown below. Shown are the images prepared with (a) 0.25 wt%, (b) 0.50 wt%, and (c) 1 wt%. The RMS roughness is listed below each image.

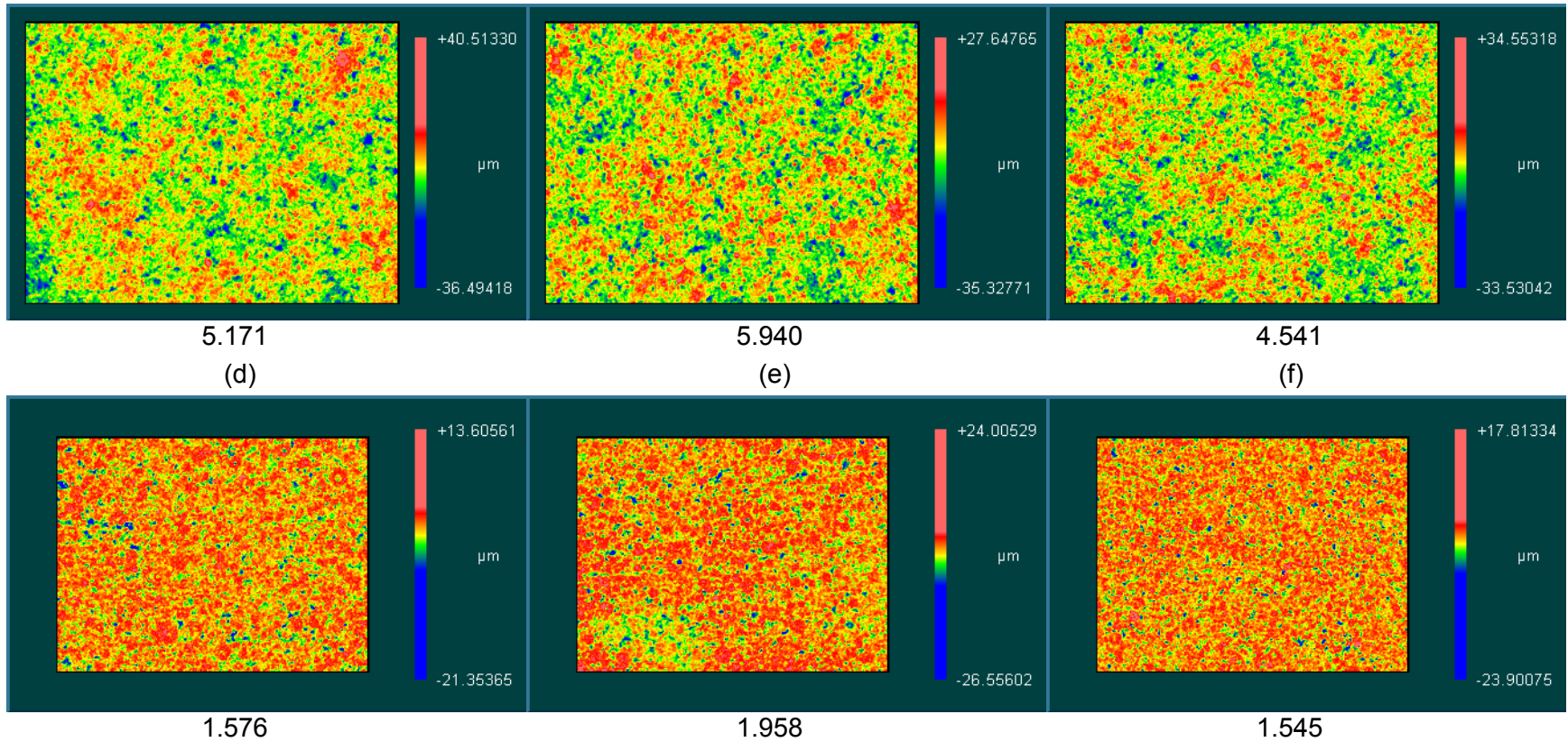


Figure I-4 (cont.). Images of the surface finish of the samples prepared using the granulate spray dried using Veegum™ T as a binder system. The images from the dinnerware samples are shown above and the images from the tile samples are shown below. Shown are the images prepared with (d) 2 wt%, (e) 5 wt%, and (f) 2 wt% hydrolyzed. The RMS roughness is listed below each image.

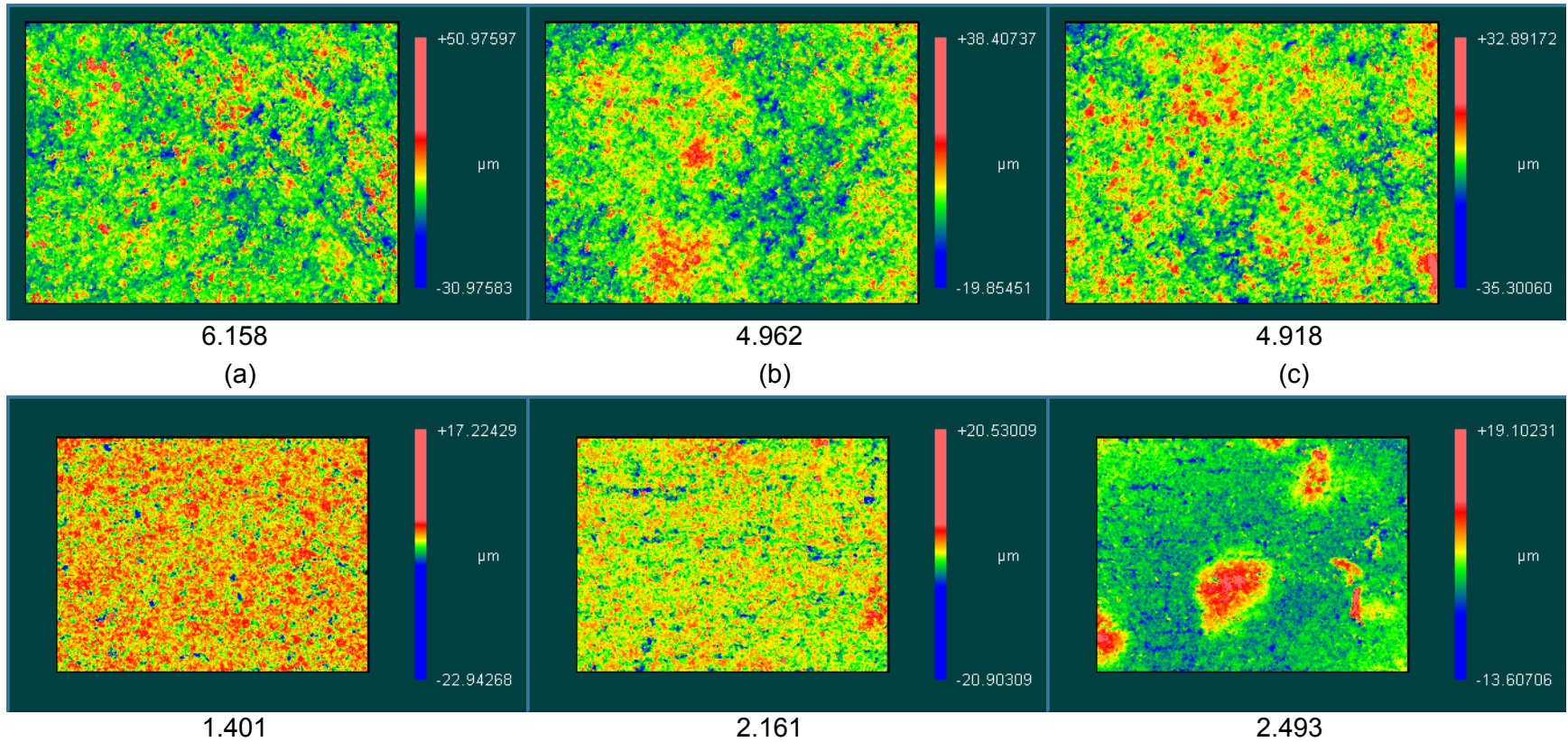


Figure I-5. Images of the surface finish of the samples prepared using the granulate spray dried using agar as a binder system. The images from the dinnerware samples are shown above and the images from the tile samples are shown below. Shown are the images prepared with (a) 0 wt%, (b) 0.25 wt%, and (c) 0.50 wt%. The RMS roughness is listed below each image.

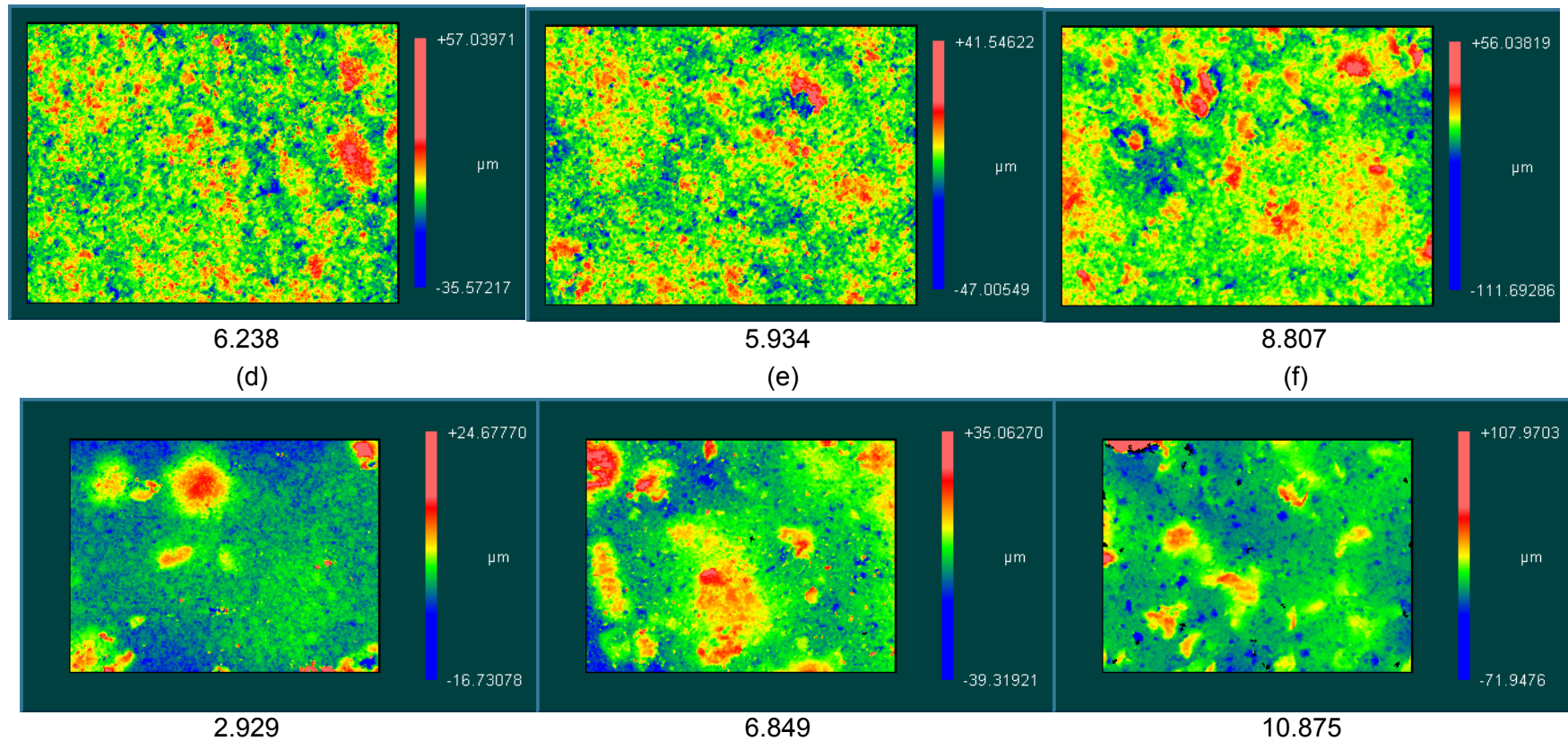


Figure I-5 (cont.). Images of the surface finish of the samples prepared using the granulate spray dried using agar as a binder system. The images from the dinnerware samples are shown above and the images from the tile samples are shown below. Shown are the images prepared with (d) 1 wt%, (e) 2 wt%, and (f) 5 wt%. The RMS roughness is listed below each image.

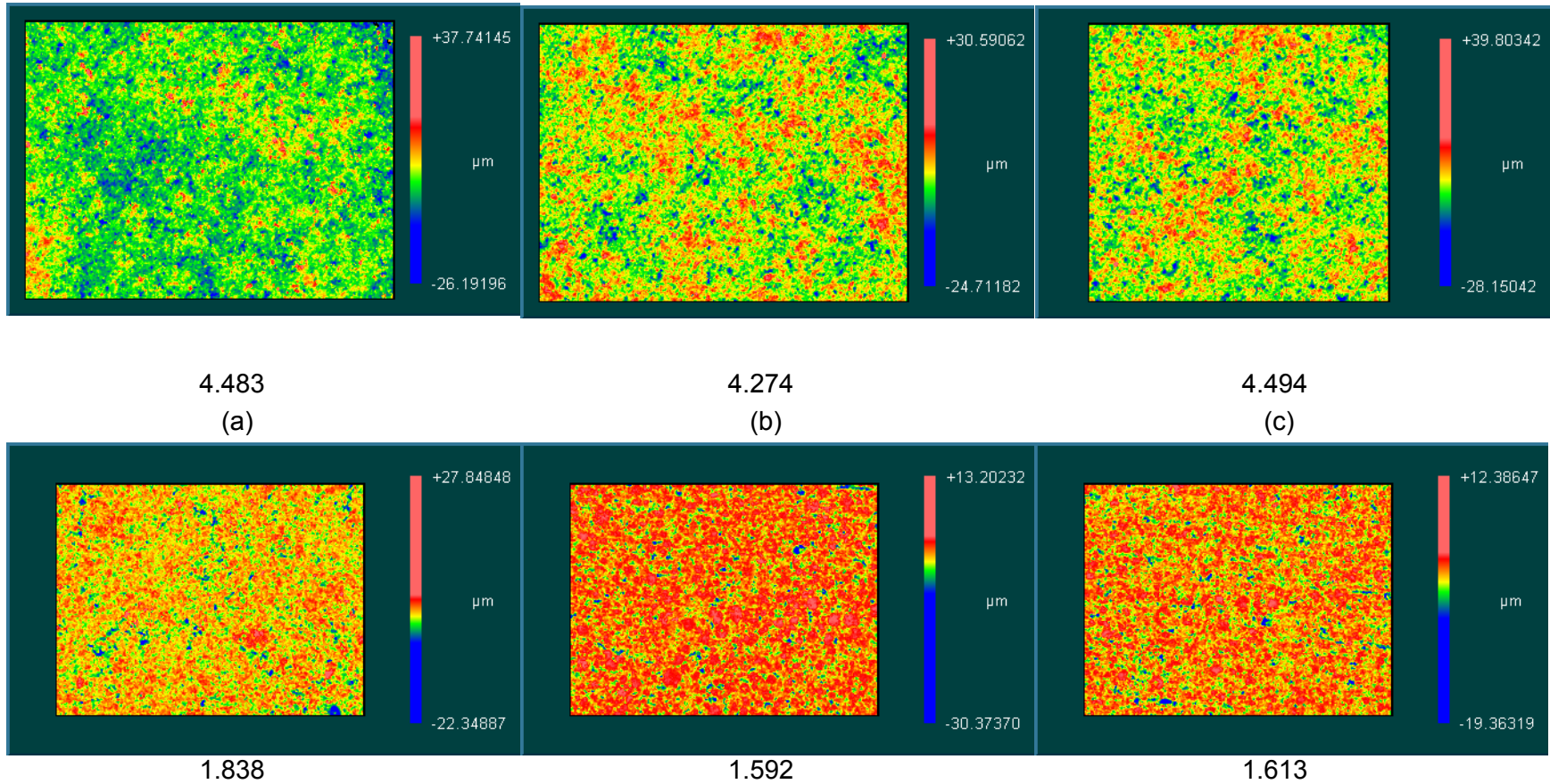


Figure I-6. Images of the surface finish of the samples prepared using the granulate spray dried using an acrylic latex emulsion as a binder system. The images from the dinnerware samples are shown above and the images from the tile samples are shown below. Shown are the images prepared with (a) 0 wt%, (b) 0.25 wt%, and (c) 0.50 wt%. The RMS roughness is listed below each image.

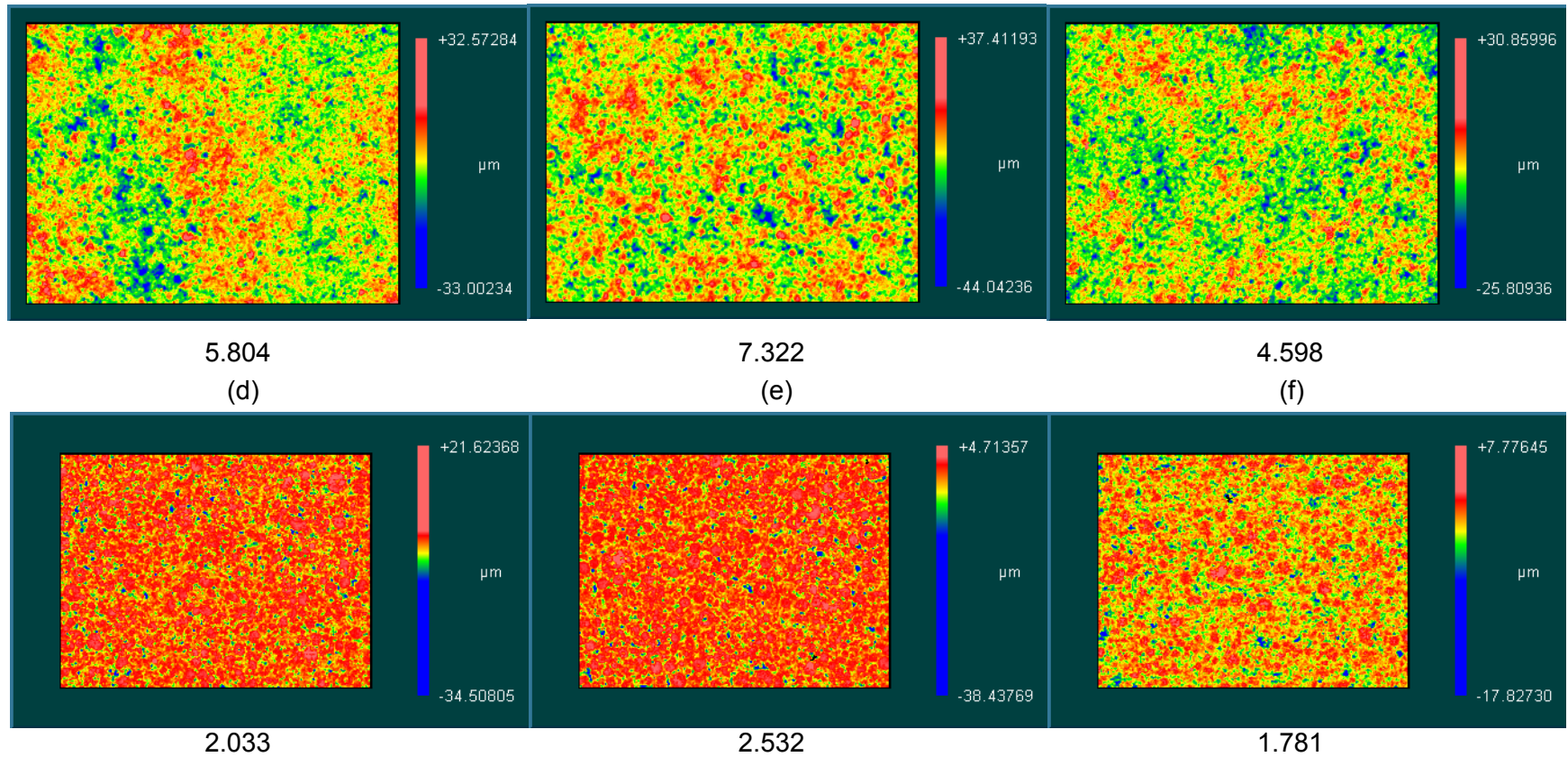


Figure I-6 (cont.). Images of the surface finish of the samples prepared using the granulate spray dried using an acrylic latex emulsion as a binder system. The images from the dinnerware samples are shown above and the images from the tile samples are shown below. Shown are the images prepared with (d) 1 wt%, (e) 2 wt%, and (f) 5 wt%. The RMS roughness is listed below each image.

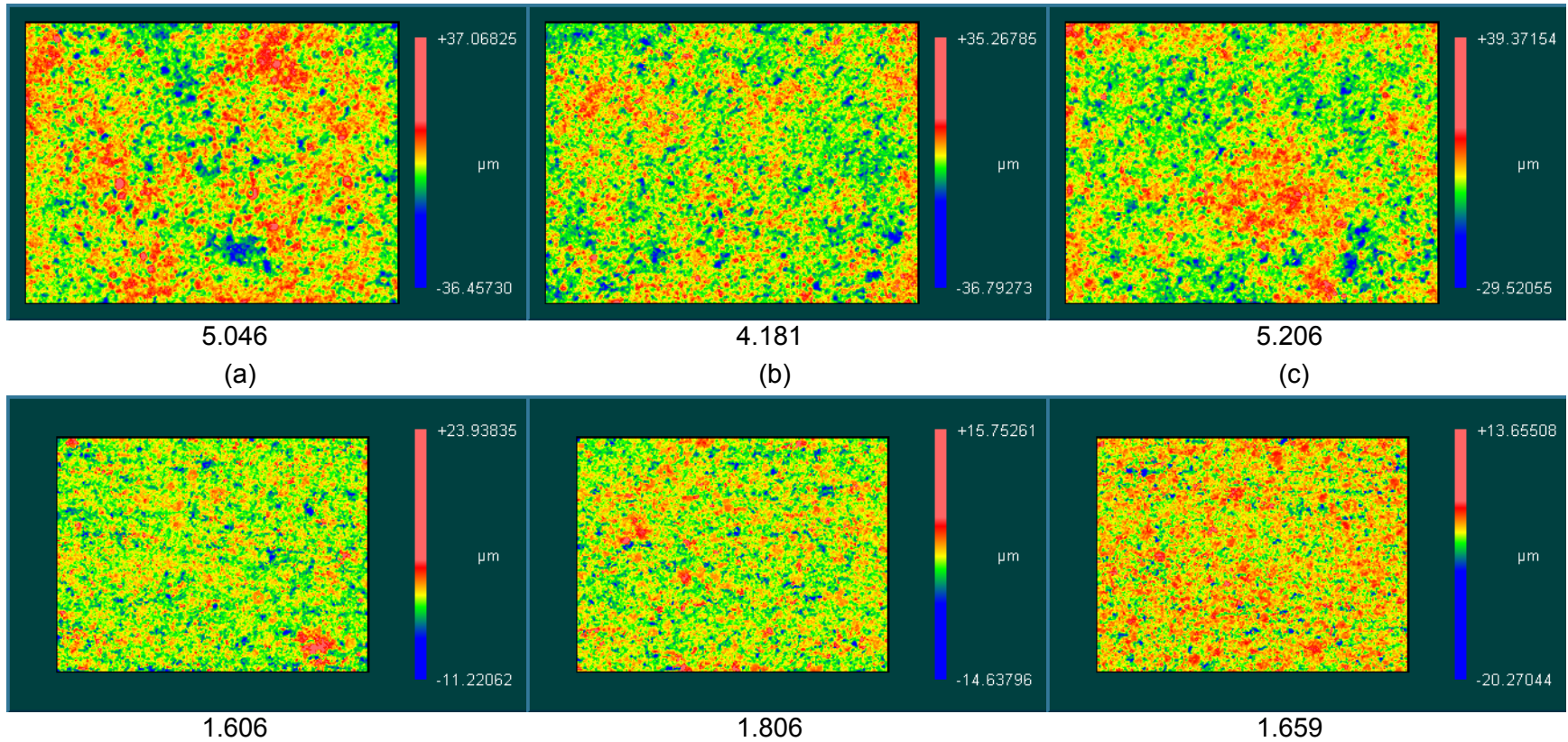


Figure I-7. Images of the surface finish of the samples prepared using the granulate spray dried using starch as a binder system. The images from the dinnerware samples are shown above and the images from the tile samples are shown below. Shown are the images prepared with (a) 0.25 wt%, (b) 0.50 wt%, and (c) 1 wt%. The RMS roughness is listed below each image.

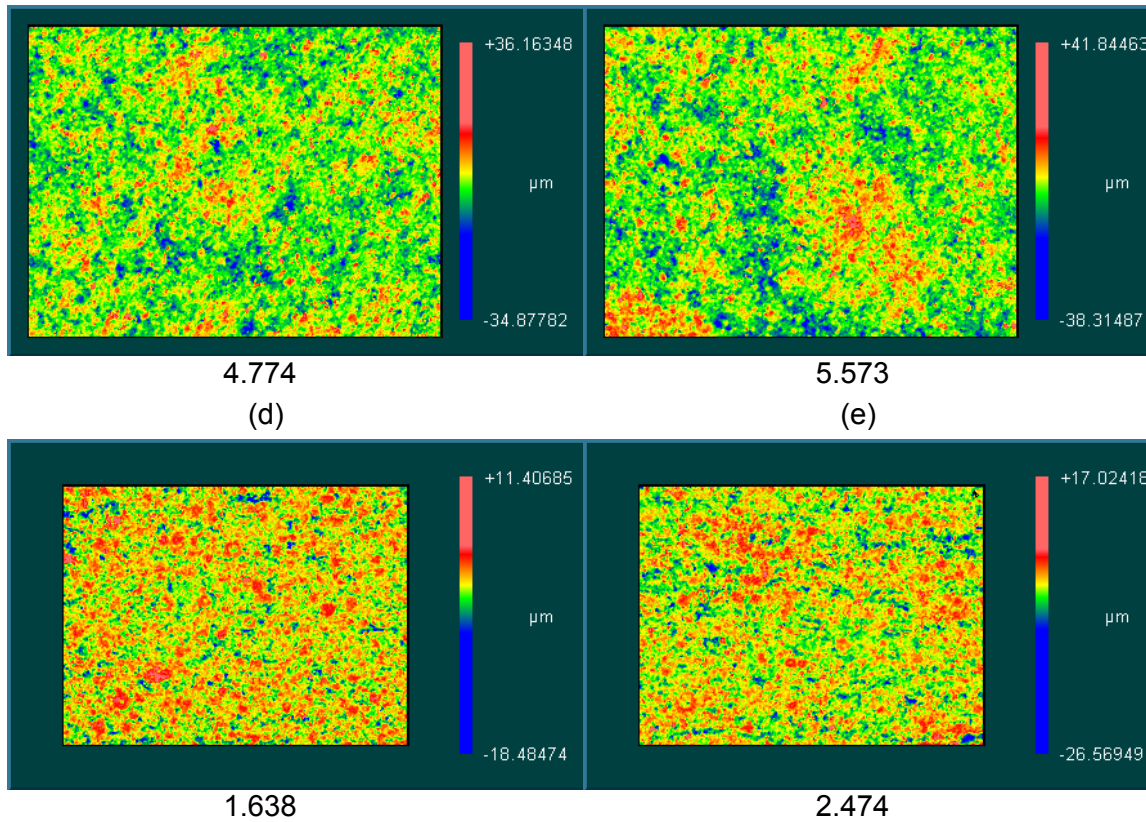


Figure I-7 (cont.). Images of the surface finish of the samples prepared using the granulate spray dried using starch as a binder system. The images from the dinnerware samples are shown above and the images from the tile samples are shown below. Shown are the images prepared with (d) 2 wt% and (e) 5 wt%. The RMS roughness is listed below each image.

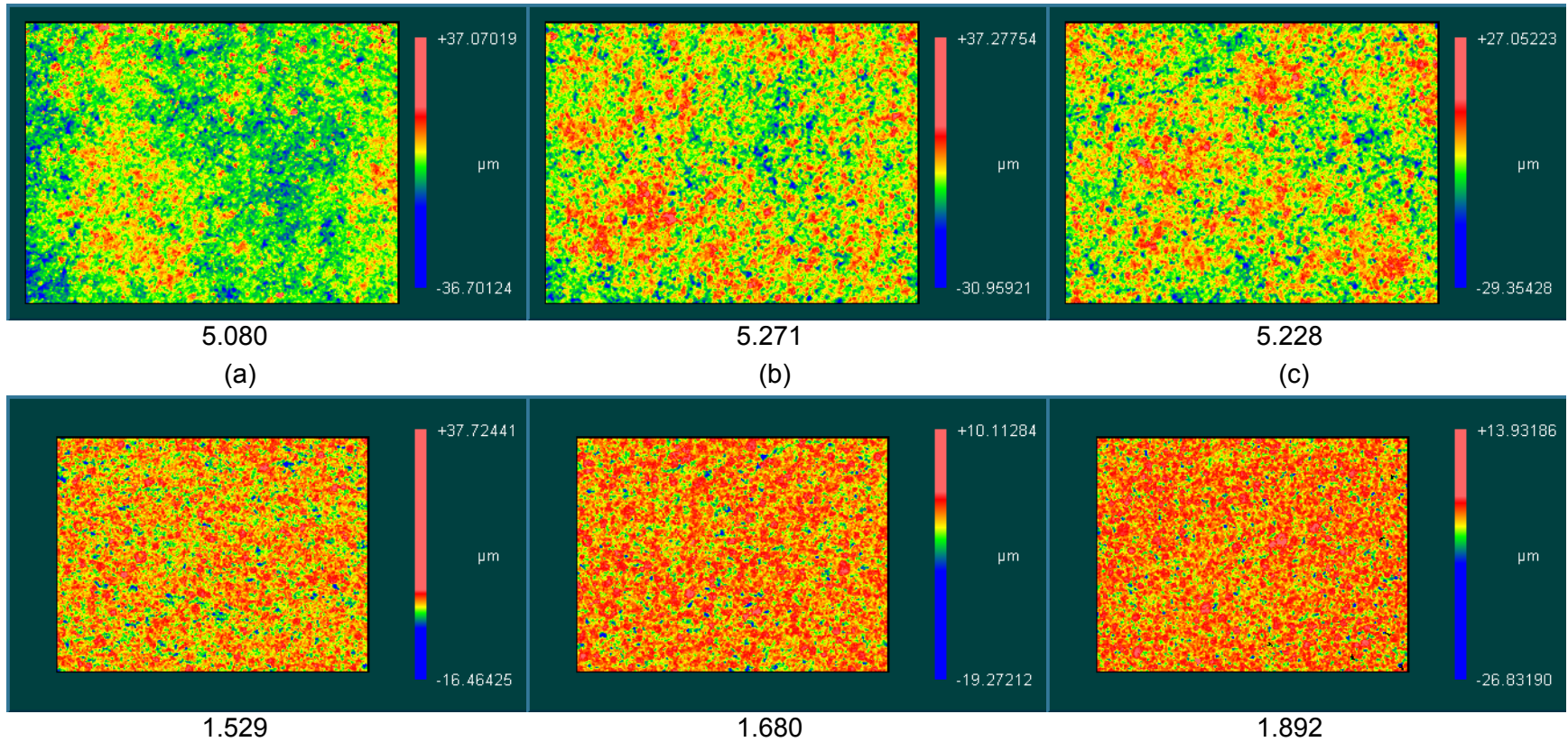


Figure I-8. Images of the surface finish of the samples prepared using the granulate spray dried using sugar as a binder system. The images from the dinnerware samples are shown above and the images from the tile samples are shown below. Shown are the images prepared with (a) 0.25 wt%, (b) 0.50 wt%, and (c) 1 wt%. The RMS roughness is listed below each image.

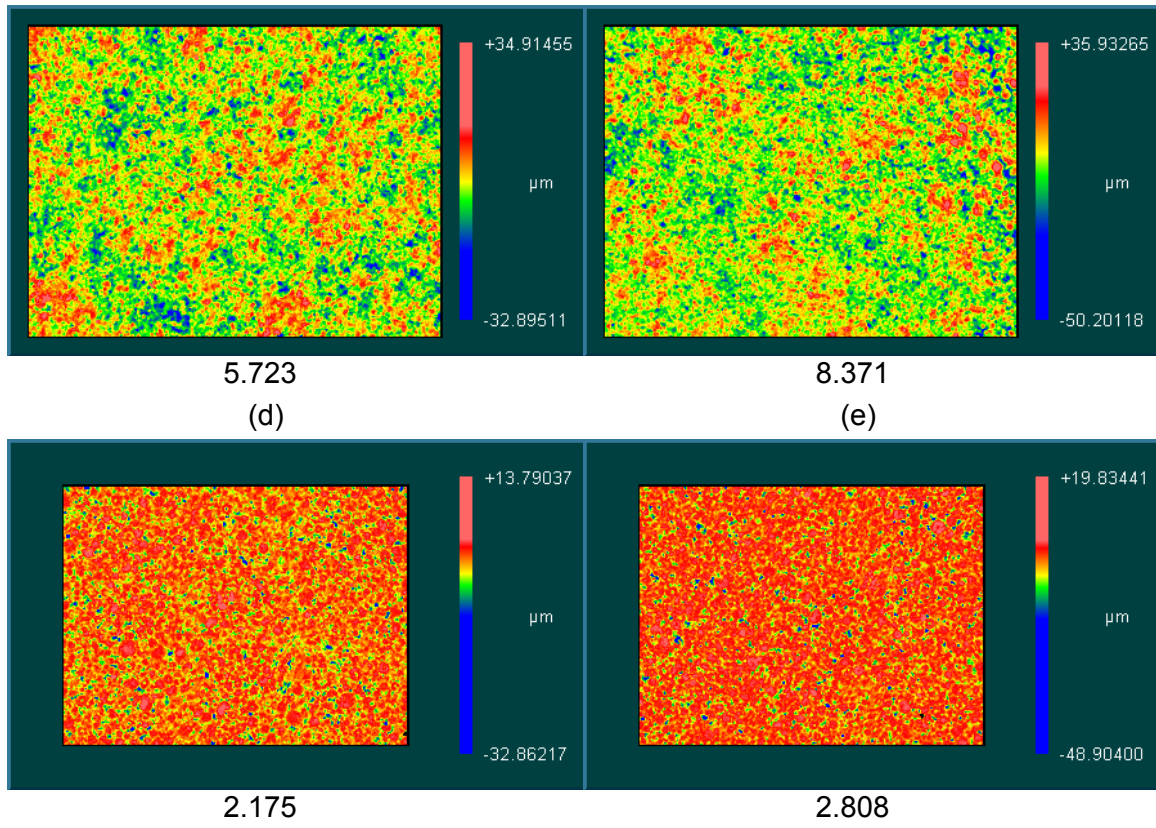


Figure I-8 (cont.). Sugar Images of the surface finish of the samples prepared using the granulate spray dried using sugar as a binder system. The images from the dinnerware samples are shown above and the images from the tile samples are shown below. Shown are the images prepared with (d) 2 wt% and (e) 5 wt%. The RMS roughness is listed below each image.

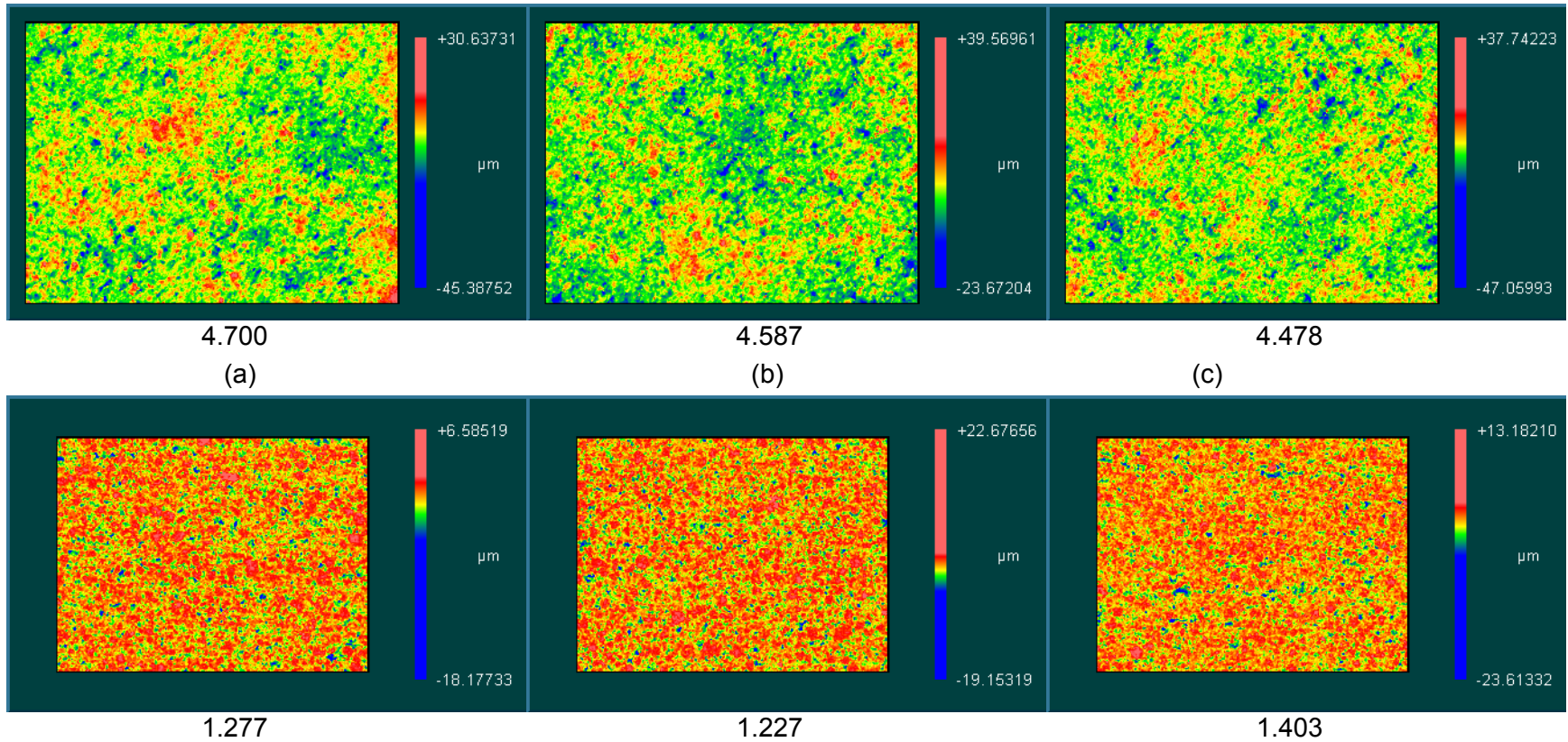


Figure I-9. Images of the surface finish of the samples prepared using the granulate spray dried using methyl cellulose as a binder system. The images from the dinnerware samples are shown above and the images from the tile samples are shown below. Shown are the images prepared with (a) 0 wt%, (b) 0.10 wt%, and (c) 0.25 wt%. The RMS roughness is listed below each image.

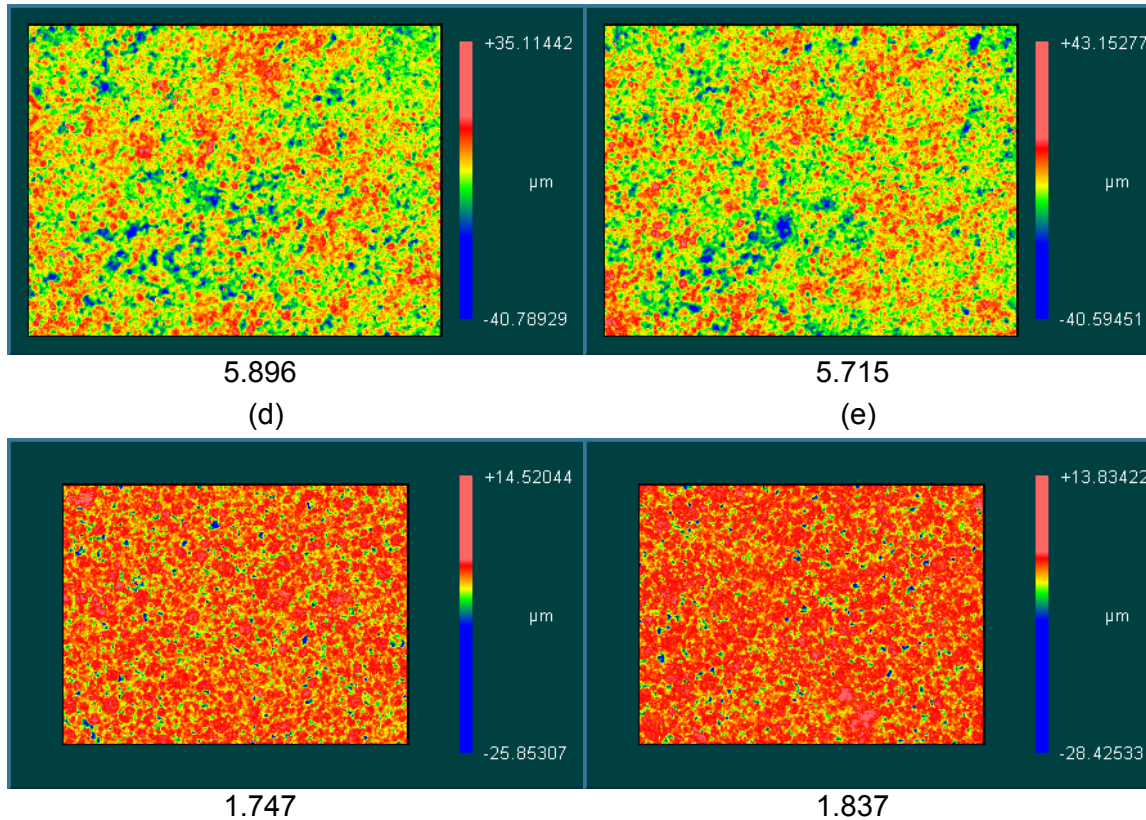


Figure I-9 (cont.). Images of the surface finish of the samples prepared using the granulate spray dried using methyl cellulose as a binder system. The images from the dinnerware samples are shown above and the images from the tile samples are shown below. Shown are the images prepared with (d) 0.50 wt% and (e) 0.70 wt%. The RMS roughness is listed below each image.

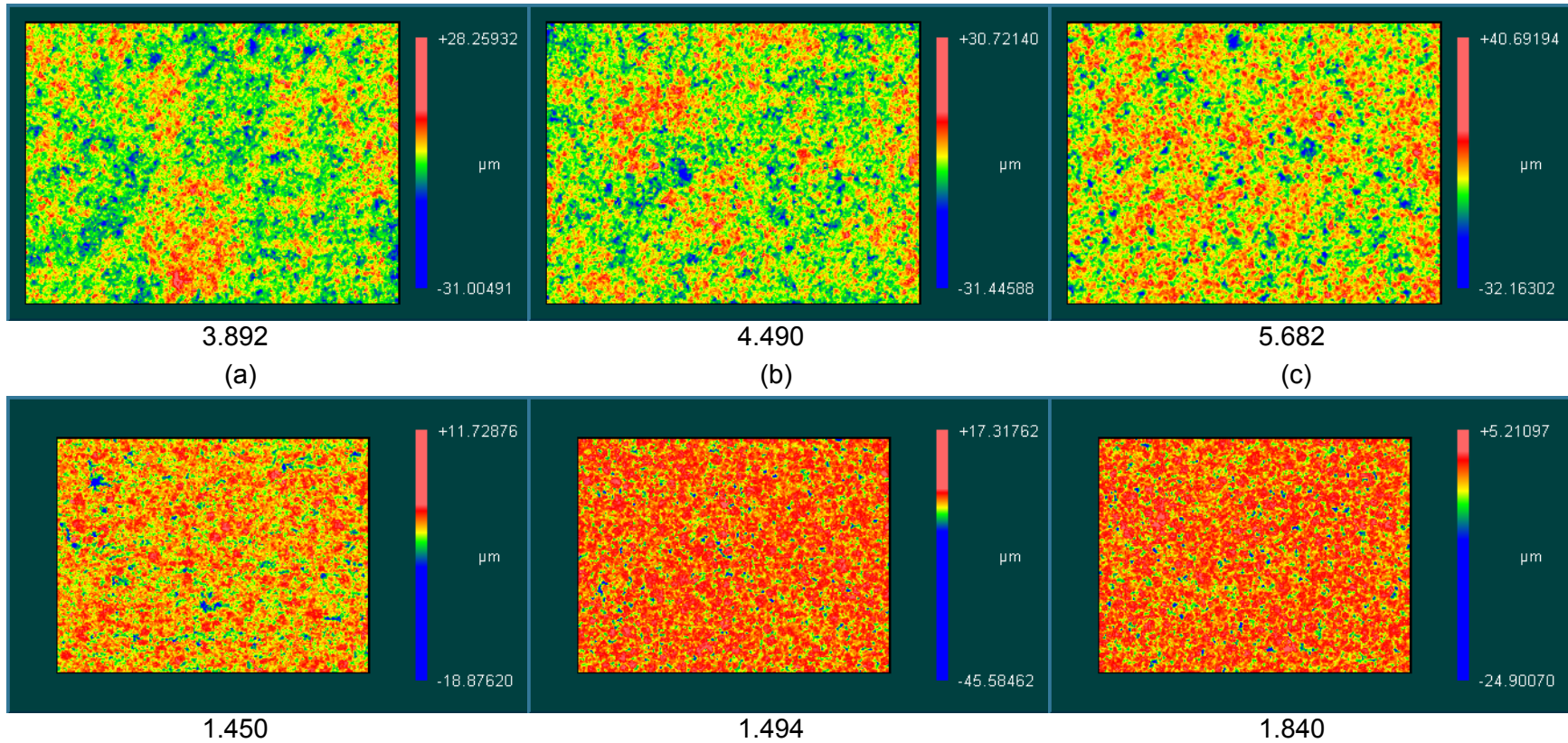


Figure I-10. Images of the surface finish of the samples prepared using the granulate spray dried using carboxymethyl cellulose as a binder system. The images from the dinnerware samples are shown above and the images from the tile samples are shown below. Shown are the images prepared with (a) 0 wt%, (b) 0.10 wt%, and (c) 0.25 wt%. The RMS roughness is listed below each image.

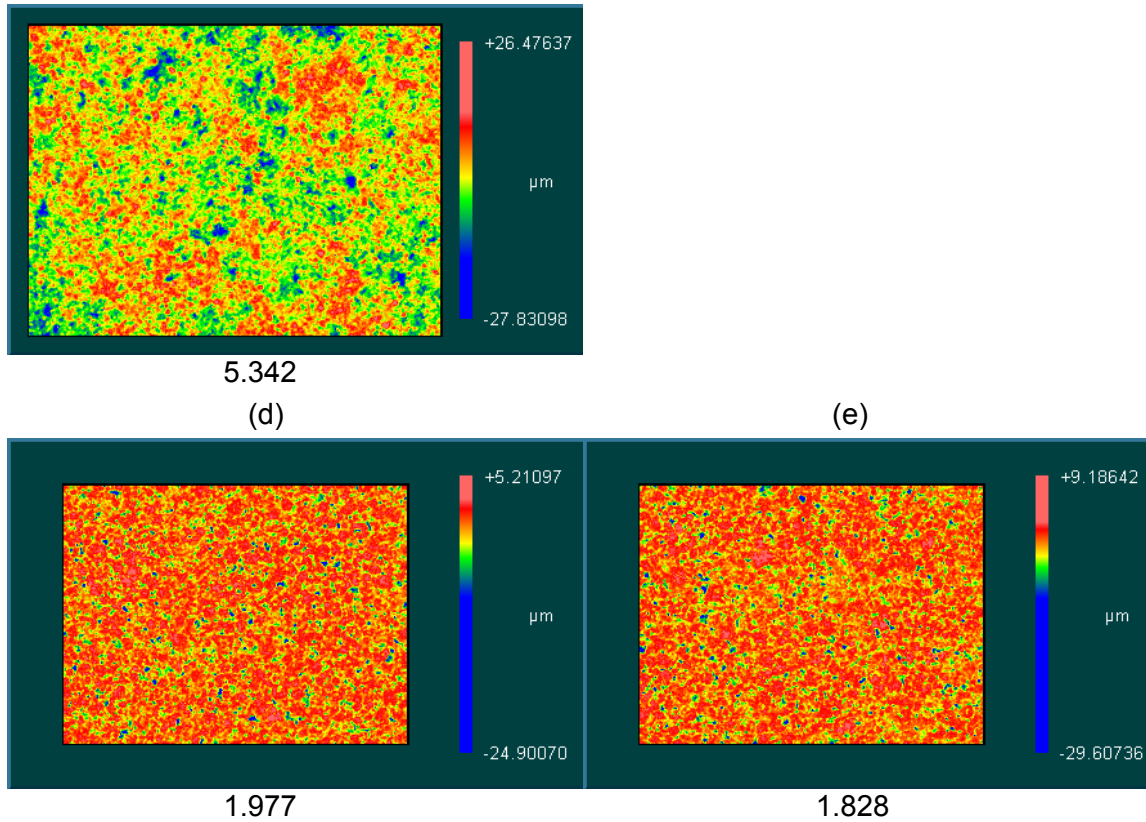


Figure I-10 (cont.). Images of the surface finish of the samples prepared using the granulate spray dried using carboxymethyl cellulose as a binder system. The images from the dinnerware samples are shown above and the images from the tile samples are shown below. Shown are the images prepared with (d) 0.50 wt% and (e) 0.70 wt%. The RMS roughness is listed below each image.

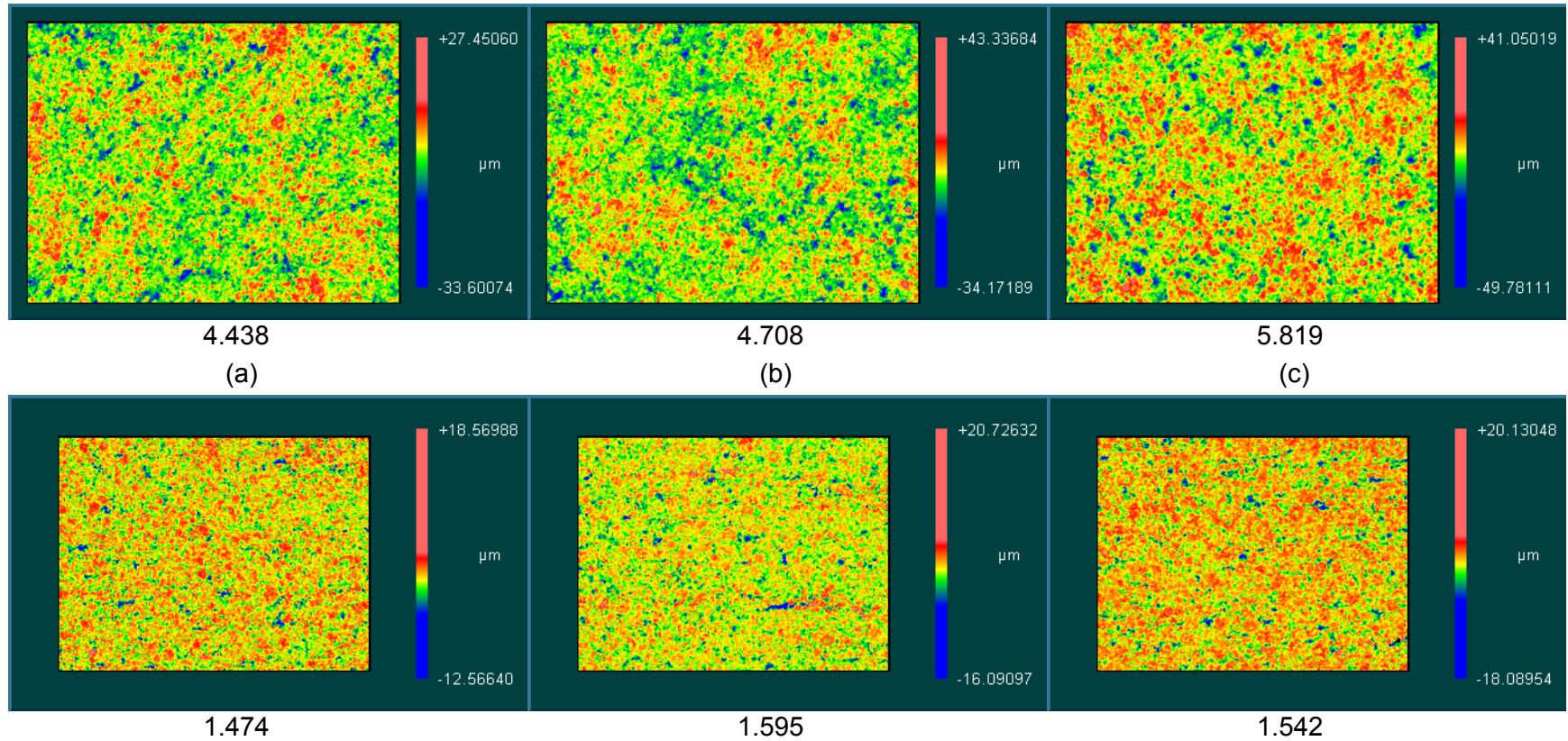


Figure I-11. Images of the surface finish of the samples prepared using the granulate spray dried using Veegum™ T / Vanzan™ D (80-20 wt% mixture) as a binder system. The images from the dinnerware samples are shown above and the images from the tile samples are shown below. Shown are the images prepared with (a) 0 wt%, (b) 0.25 wt%, and (c) 0.50 wt%. The RMS roughness is listed below each image.

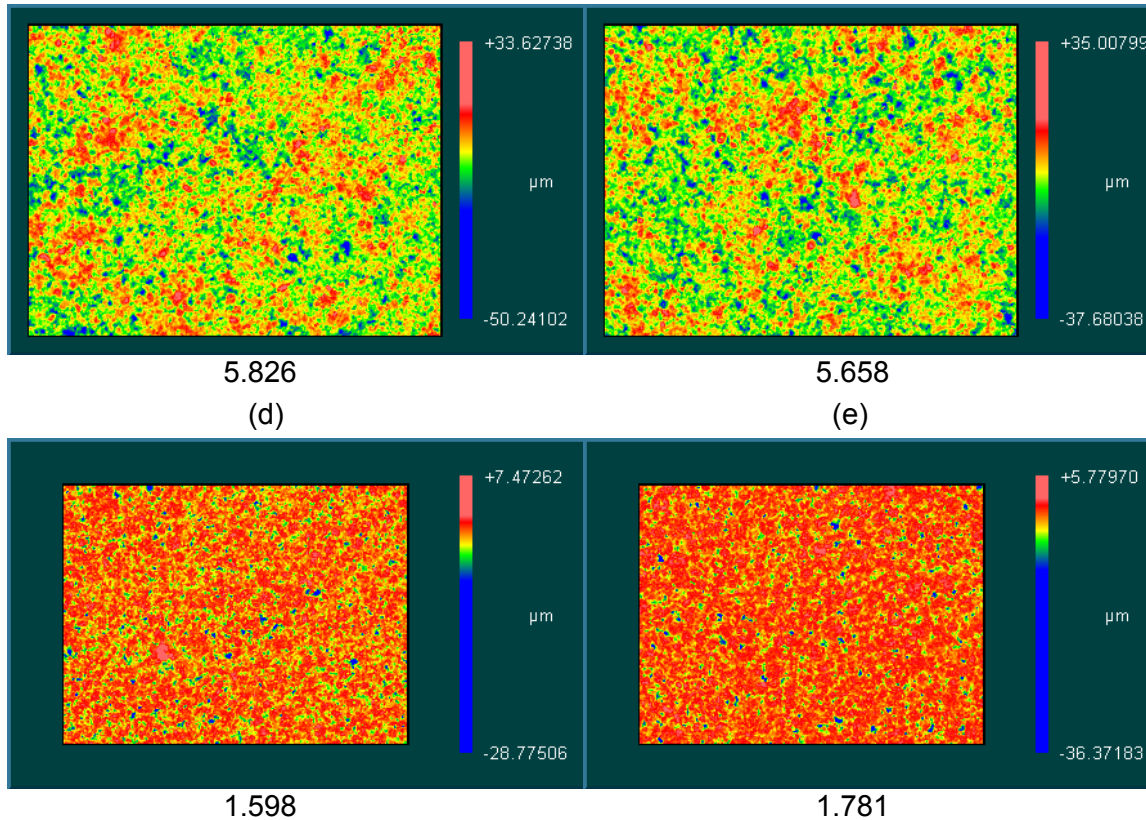


Figure I-11 (cont.). Images of the surface finish of the samples prepared using the granulate spray dried using Veegum™ T / Vanzan™ D (80-20 wt% mixture) as a binder system. The images from the dinnerware samples are shown above and the images from the tile samples are shown below. Shown are the images prepared with (d) 1 wt% and (e) 2 wt%. The RMS roughness is listed below each image.

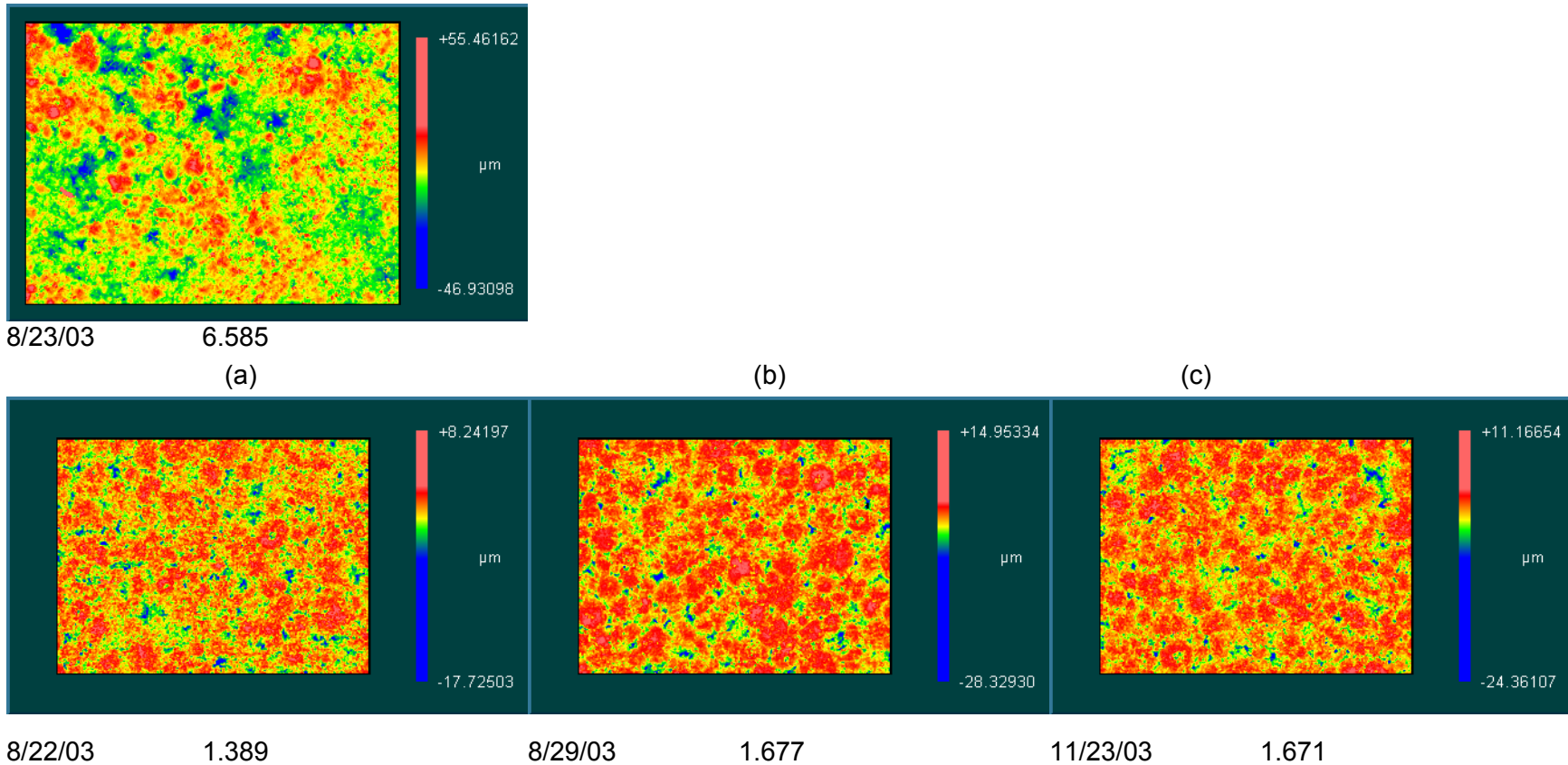


Figure I-12. Images of the surface finish of the samples prepared using the granulate spray dried using pPVA as a binder system at Buffalo China. The images from the dinnerware samples are shown above and the images from the tile samples are shown below, the dates when the reference samples were pressed are listed below each image. The RMS roughness is listed below each image.

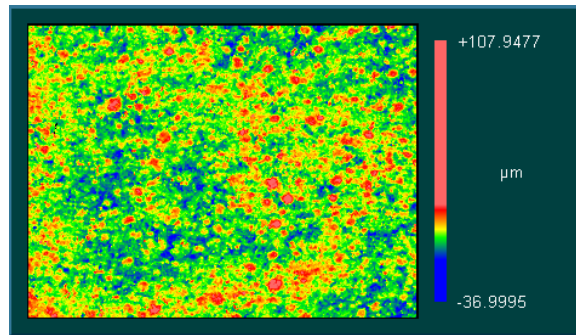
**Appendix J. Images from the Interferometer of the Surface Finish from the Samples Prepared Using Blends of Granulate Spray Dried at Alfred University**

**1.0 Surface Evaluation**

The images from the optical interferometer to evaluate the surface finish of the blends prepared using alternative binder systems are listed in Table I-I. Also listed are the RMS roughness values measured by the optical interferometer.

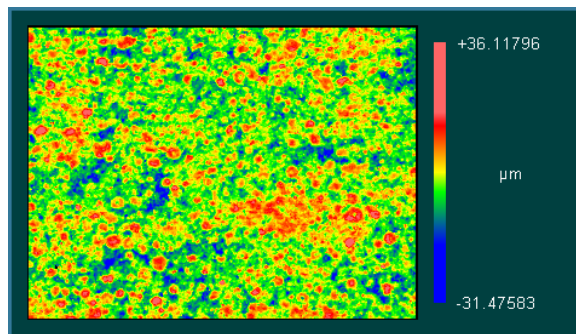
Table J-I. List of the Granule Blends Selected to Evaluate the effects of Blending Samples with Similar P1 Values.

Blend # Figure #	Granulate 1*	Granulate 2*	Blend Conc.	RMS roughness	P1 <sub>nom.</sub>
1	2% Starch	1% PVA-V	50-50	5.142	0.000
2	1% Ligno	0.5% V-V	50-50	4.36	0.008
3	5% Latex	5% Agar	50-50	6.356	0.010
4	1% Sugar	5% Agar	50-50	6.1	0.012
5	0.5% Agar	5% Latex	50-50	5.377	0.021
6	2% V	2% Agar	50-50	5.28	0.025
7	5% Agar	5% Starch	50-50	5.465	0.028
8	2% Agar	1% PVA-V	50-50	5.437	0.028
9	2% V-V	2% Ligno	50-50	5.828	0.045
10	2% V-V	0.5% Starch	50-50	5.329	0.049
11	1% Sugar	1% Agar	50-50	4.274	0.054
12	5% Latex	5% sugar	50-50	6.786	0.060
13	1% Starch	0.5% CMC	50-50	5.255	0.079
14	1% Latex	1% V	50-50	5.039	0.094
15	0.5% MC	0.5% Latex	50-50	5.491	0.096
16	0.5% V-V	0.5% Ligno	50-50	5.077	0.107
17	0.5% Sugar	2% pPVA	50-50	6.429	0.486
18	2% Ligno	2% Sugar	50-50	6.062	0.490
19	2% Starch	2% V-V	50-50	4.949	0.569
20	1% PVA-V	1% V-V	50-50	6.165	0.578
21	5% pPVA	5% PVA-V	50-50	8.884	0.783
22	5% Ligno.	0.7% MC	50-50	9.445	1.686
23	5% Agar	5% Ligno	50-50	5.853	1.817
24	5% Agar	5% V	25-75	5.629	0.016
25	0.5% Agar	5% V	25-75	9.363	0.018
26	5% Agar	1% pPVA	25-75	5.102	0.361



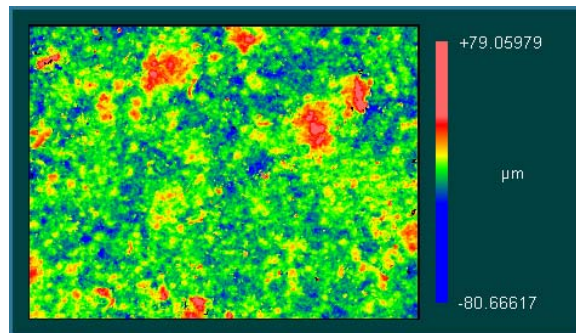
RMS = 5.142

Figure J-1. Image from the optical interferometer of the surface finish of the sample dry-pressed in a hardened steel die with an elastomer insert prepared using a 50-50 blend 2 wt% starch and 1 wt% pPVA- Veegum™ T of granulate.



RMS = 4.36

Figure J-2. Image from the optical interferometer of the surface finish of the sample dry-pressed in a hardened steel die with an elastomer insert prepared using a 50-50 blend of 1 wt% Ligno and 0.50 wt% Veegum™ T - Vanzan™ D granulate.



RMS = 6.356

Figure J-3. Image from the optical interferometer of the surface finish of the sample dry-pressed in a hardened steel die with an elastomer insert prepared using a 50-50 blend of 5 wt% acrylic latex and 5 wt % agar granulate.

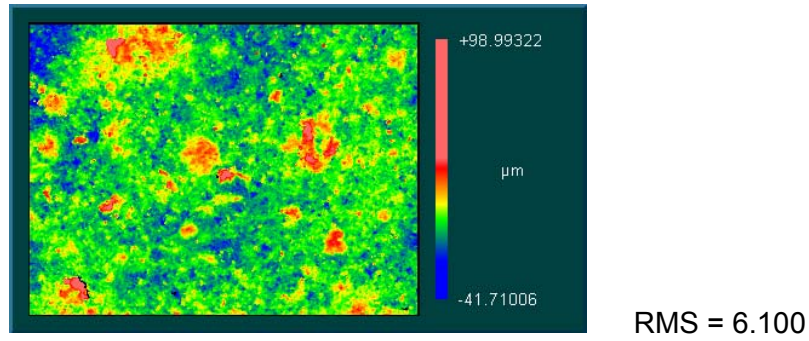


Figure J-4. Image from the optical interferometer of the surface finish of the sample dry-pressed in a hardened steel die with an elastomer insert prepared using a 50-50 blend of 1 wt% sugar and 5 wt% agar granulate.

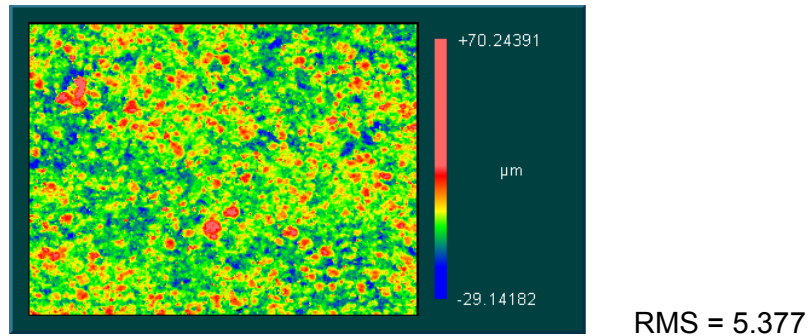


Figure J-5. Image from the optical interferometer of the surface finish of the sample dry-pressed in a hardened steel die with an elastomer insert prepared using a 50-50 blend of 0.50 wt% agar and 5 wt% acrylic latex granulate.

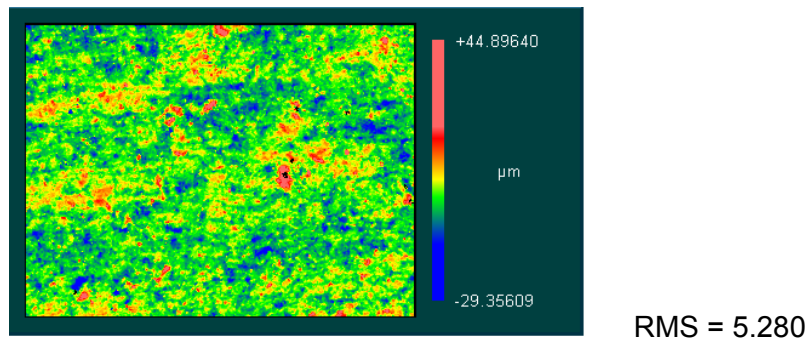


Figure J-6. Image from the optical interferometer of the surface finish of the sample dry-pressed in a hardened steel die with an elastomer insert prepared using a 50-50 blend of 2 wt% Veegum™ T and 2 wt% agar granulate.

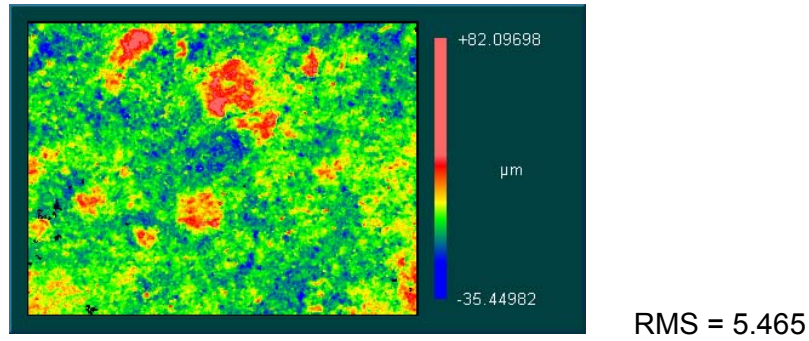


Figure J-7. Image from the optical interferometer of the surface finish of the sample dry-pressed in a hardened steel die with an elastomer insert prepared using a 50-50 blend of 5 wt% agar and 5 wt% starch granulate. The black regions in the lower left corner are missing data that was outside the scan length.

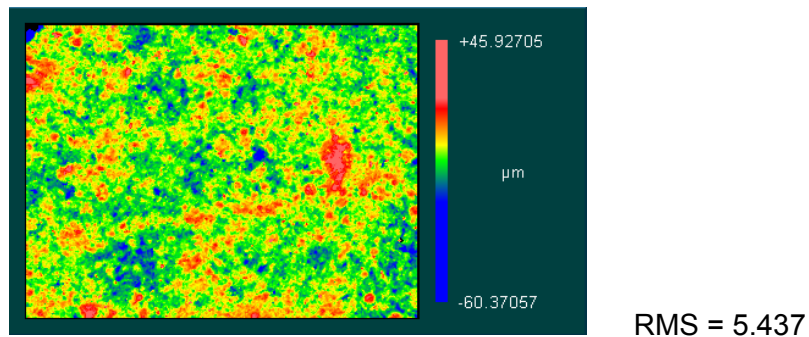


Figure J-8. Image from the optical interferometer of the surface finish of the sample dry-pressed in a hardened steel die with an elastomer insert prepared using a 50-50 blend of 2 wt% agar and 1 wt% pPVA-Veegum™ T granulate.

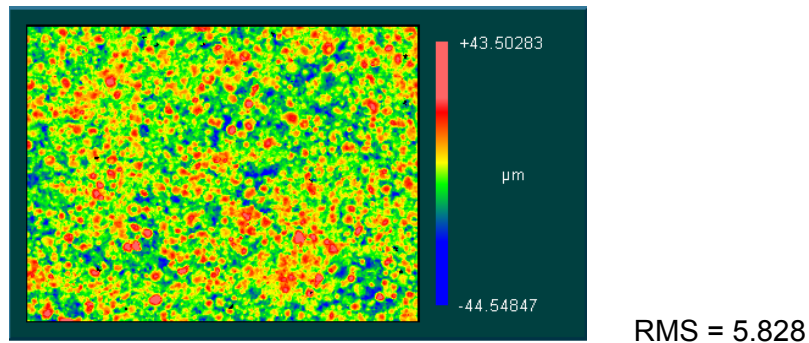


Figure J-9. Image from the optical interferometer of the surface finish of the sample dry-pressed in a hardened steel die with an elastomer insert prepared using a 50-50 blend of 2 wt% Veegum™ T-Vanzan™ D and 2 wt% Ligno granulate.

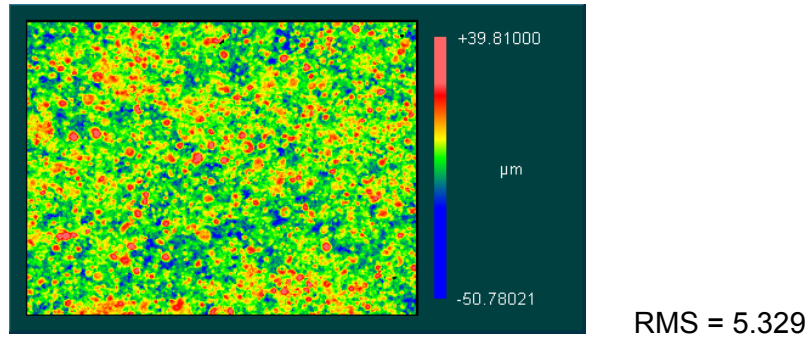


Figure J-10. Image from the optical interferometer of the surface finish of the sample dry-pressed in a hardened steel die with an elastomer insert prepared using a 50-50 blend of 2 wt% Veegum™ T-Vanzan™ D and 0.50 wt% starch granulate.

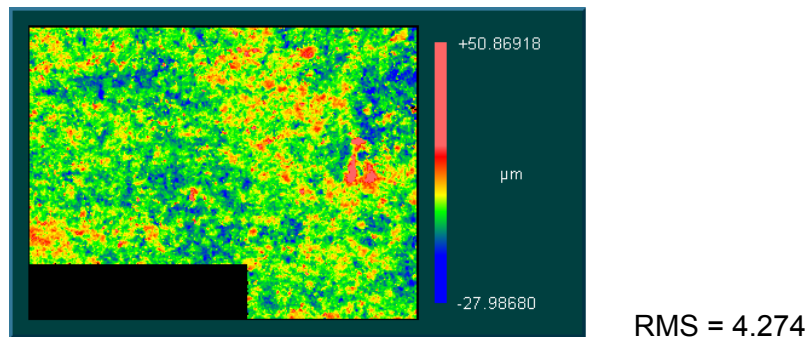


Figure J-11. Image from the optical interferometer of the surface finish of the sample dry-pressed in a hardened steel die with an elastomer insert prepared using a 50-50 blend of 1 wt% sugar and 1 wt% agar granulate. The black region in the lower left corner is missing data that was outside the scan length.

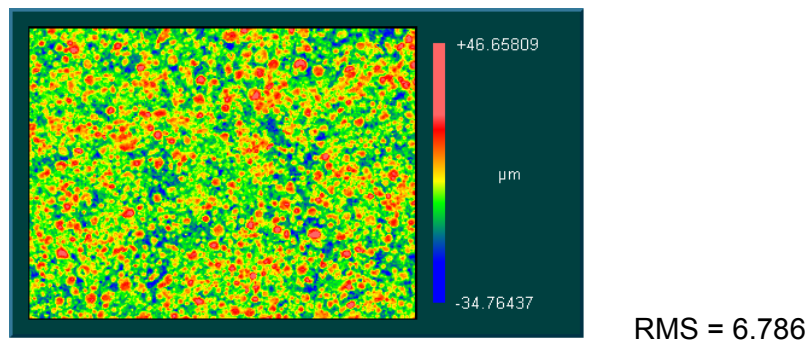


Figure J-12. Image from the optical interferometer of the surface finish of the sample dry-pressed in a hardened steel die with an elastomer insert prepared using a 50-50 blend of 5 wt% acrylic latex and 5 wt% sugar granulate.

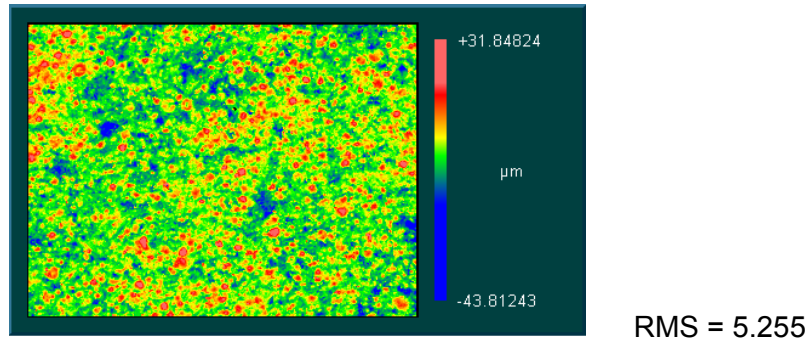


Figure J-13. Image from the optical interferometer of the surface finish of the sample dry-pressed in a hardened steel die with an elastomer insert prepared using a 50-50 blend of 1 wt% starch and 0.50 wt% carboxymethyl cellulose granulate.

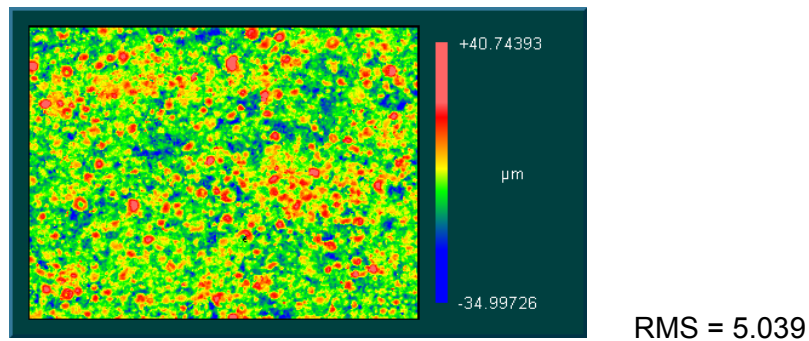


Figure J-14. Image from the optical interferometer of the surface finish of the sample dry-pressed in a hardened steel die with an elastomer insert prepared using a 50-50 blend of 1 wt% acrylic latex and 1 wt% Veegum™ T granulate.

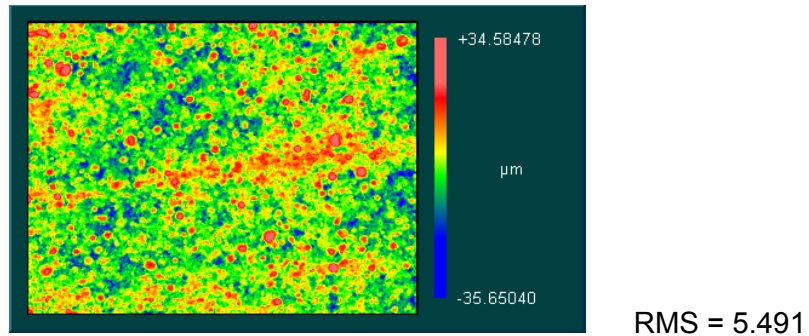


Figure J-15. Image from the optical interferometer of the surface finish of the sample dry-pressed in a hardened steel die with an elastomer insert prepared using a 50-50 blend of 0.50 wt% methyl cellulose and 0.50 wt% acrylic latex granulate.

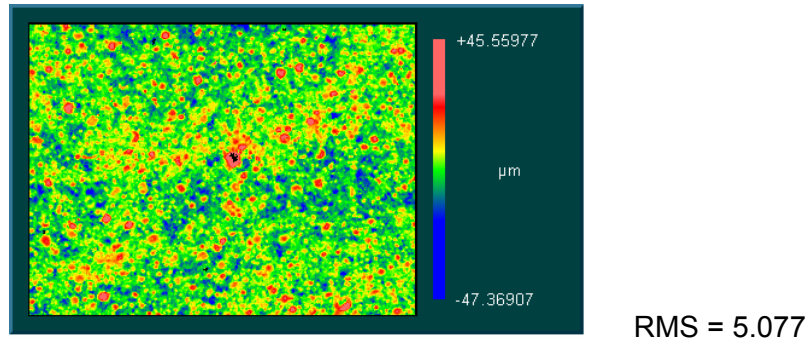


Figure J-16. Image from the optical interferometer of the surface finish of the sample dry-pressed in a hardened steel die with an elastomer insert prepared using a 50-50 blend of 0.50 wt% Veegum™ T-Vanzan™ D and 0.50 wt% Ligno granulate.

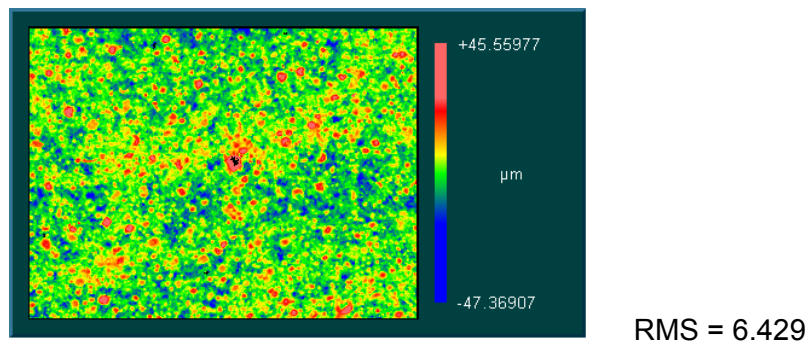


Figure J-17. Image from the optical interferometer of the surface finish of the sample dry-pressed in a hardened steel die with an elastomer insert prepared using a 50-50 blend of 0.50 wt% sugar and 2 wt% pPVA granulate.

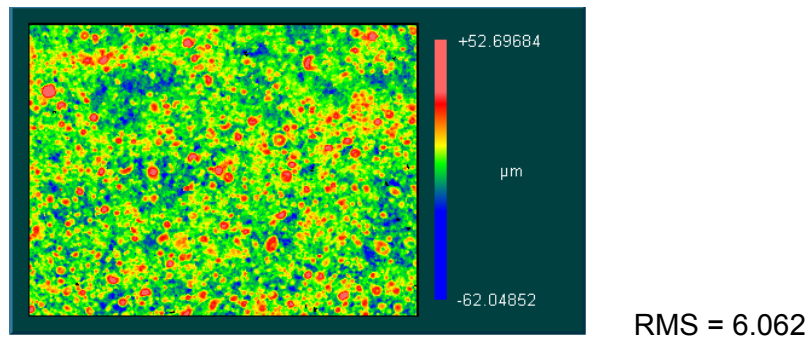


Figure J-18. Image from the optical interferometer of the surface finish of the sample dry-pressed in a hardened steel die with an elastomer insert prepared using a 50-50 blend of 2 wt% Ligno and 2 wt% sugar granulate.

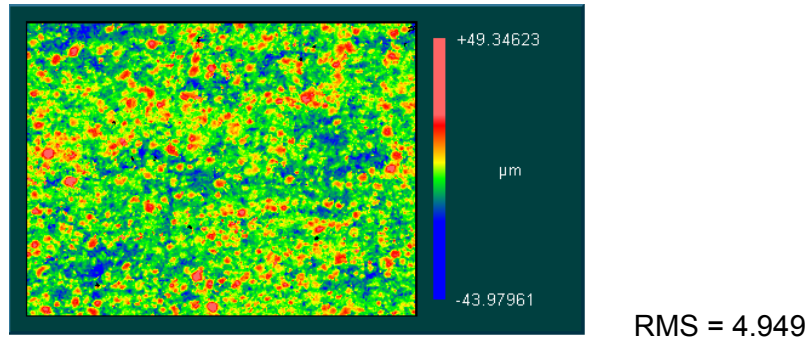


Figure J-19. Image from the optical interferometer of the surface finish of the sample dry-pressed in a hardened steel die with an elastomer insert prepared using a 50-50 blend of 2 wt% starch and 2 wt% Veegum™ T-Vanzan™ D granulate.

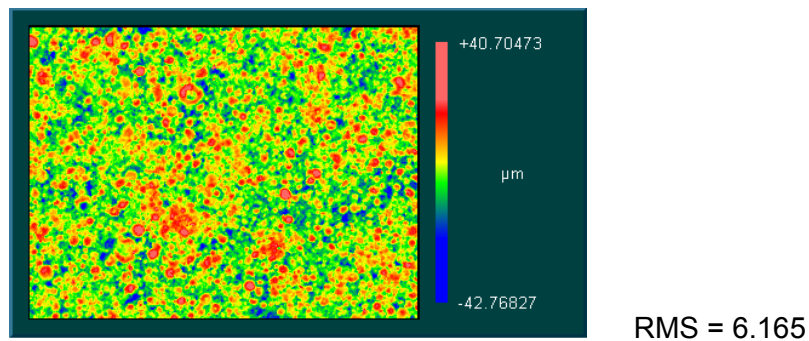


Figure J-20. Image from the optical interferometer of the surface finish of the sample dry-pressed in a hardened steel die with an elastomer insert prepared using a 50-50 blend of 1 wt% pPVA-Veegum™ T and 1 wt% Veegum™ T-Vanzan™ D granulate.

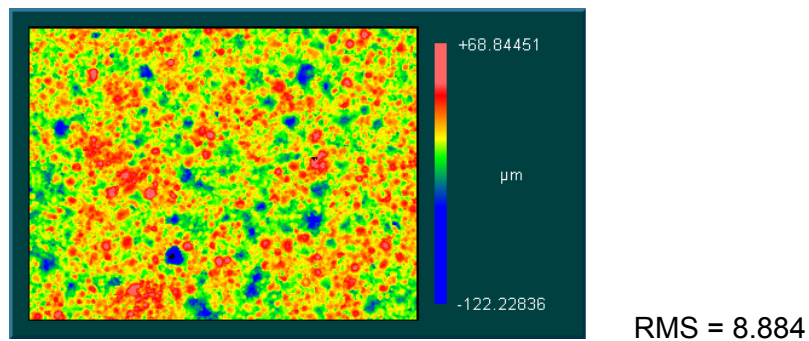


Figure J-21. Image from the optical interferometer of the surface finish of the sample dry-pressed in a hardened steel die with an elastomer insert prepared using a 50-50 blend of 5 wt% pPVA and 5 wt% pPVA-Veegum™ T granulate.

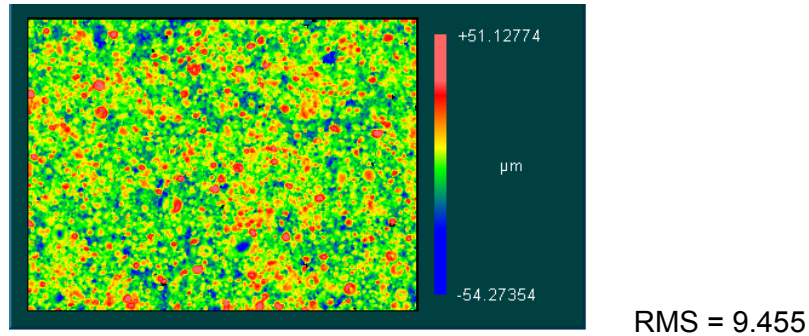


Figure J-22. Image from the optical interferometer of the surface finish of the sample dry-pressed in a hardened steel die with an elastomer insert prepared using a 50-50 blend of 5 wt% Ligno and 0.70 wt% methyl cellulose granulate.

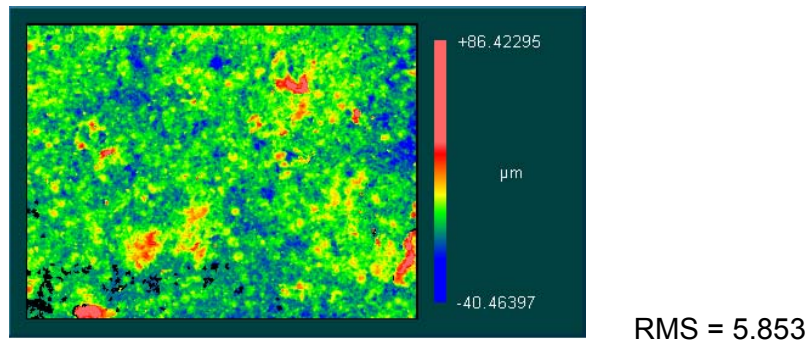


Figure J-23. Image from the optical interferometer of the surface finish of the sample dry-pressed in a hardened steel die with an elastomer insert prepared using a 50-50 blend of 5 wt% agar and 5 wt% Ligno granulate. The black regions in the lower left corner are missing data that was outside the scan length. The black regions in the lower left corner are missing data that was outside the scan length.

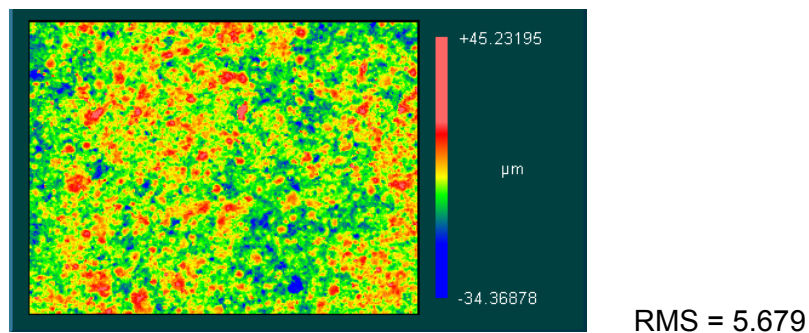
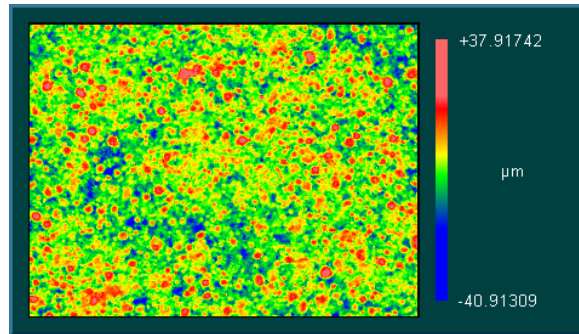
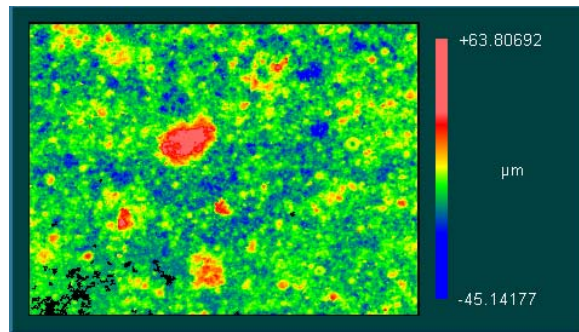


Figure J-24. Image from the optical interferometer of the surface finish of the sample dry-pressed in a hardened steel die with an elastomer insert prepared using a 25-75 blend of 5 wt% agar and 5 wt% Veegum™ T granulate.



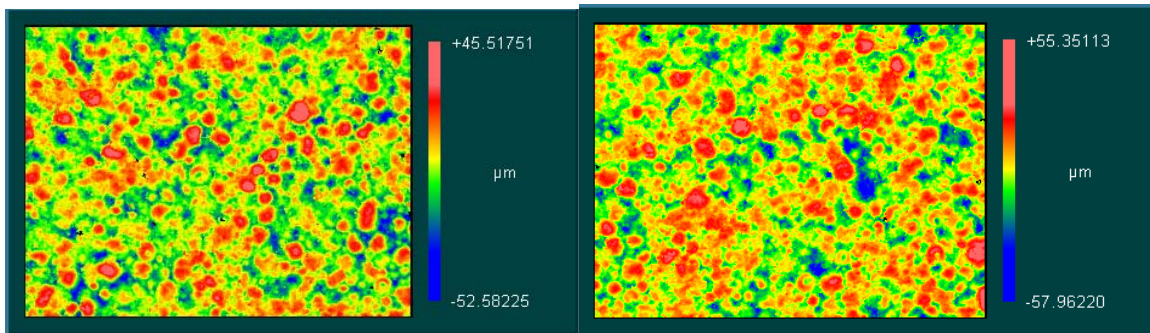
RMS = 9.363

Figure J-25. Image from the optical interferometer of the surface finish of the sample dry-pressed in a hardened steel die with an elastomer insert prepared using a 25-75 blend of 0.50 wt% agar and 5 wt% Veegum™ T granulate.



RMS = 5.102

Figure J-26. Image from the optical interferometer of the surface finish of the sample dry-pressed in a hardened steel die with an elastomer insert prepared using a 25-75 blend of 5 wt% agar and 1 wt% pPVA granulate. The black regions in the lower left corner are missing data that was outside the scan length.



RMS = 11.866

RMS = 10.668

Figure J-27. Image from the optical interferometer of the surface finish of the samples dry-pressed in a hardened steel die with an elastomer insert prepared using pPVA granulate spray dried at Buffalo China.

## **Appendix K. Regression Method to Determine the Shear P1 Value of the Granulated Porcelain Body**

### **1.0 Introduction**

The dead weight system was counter balanced to achieve very low normal loads on the sample cell. Unfortunately, it was impossible to reach a low enough load to measure the P1 value in shear. Therefore a regression method was used to determine a shear P1 value.

### **2.0 Compaction and Shear Compaction Diagrams**

A plot of the uniaxial and shear compaction diagrams from a sample of dried pPVA granulate supplied by Buffalo China is shown in Figure K-1. A linear regression is shown through the data from the HPASC. No apparent break is observed in the shear compaction diagram. Therefore it was assumed that the fill density prior to compaction in uniaxial and shear was the same.

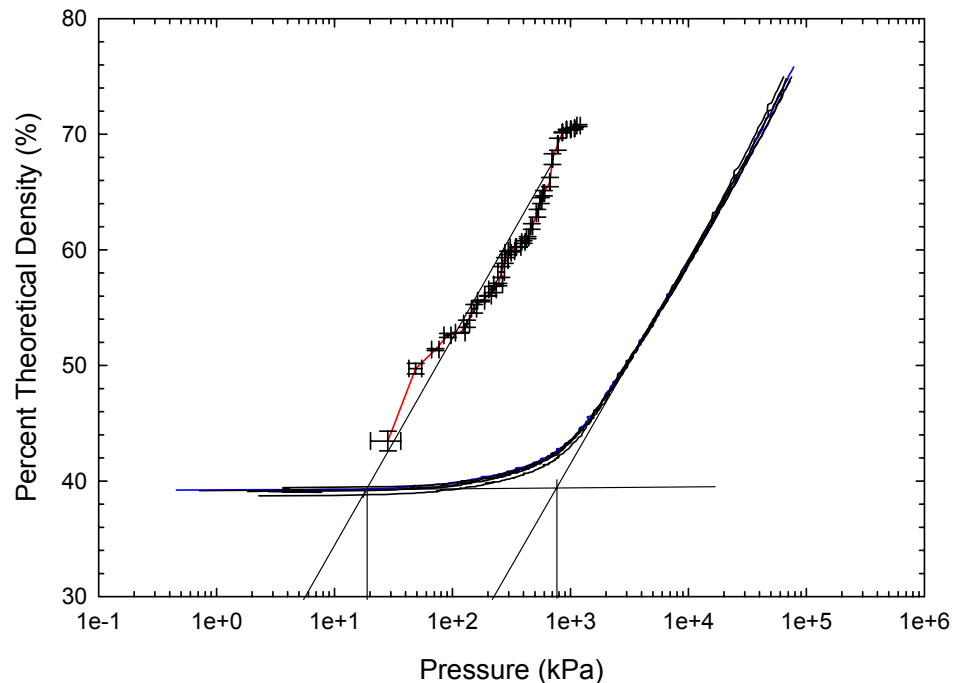


Figure K-1. Compaction diagrams from the Instron (uniaxial compaction) and the HPASC (shear compaction) for a sample of dried pPVA granulate.

### **3.0 Regression Method to Determine the Shear P1**

To determine the shear P1 value a linear regression for the data from the HPASC was determined using Excel. A second linear regression for the low pressure uniaxial data, below the uniaxial P1 pressure, was determined. The intersection between the two linear regressions was calculated, only the value along the x-axis was important since that would correspond to the logarithm of the pressure at the onset of granule deformation in shear.

### **4.0 Sample Calculation to Determine the Shear P1**

For this sample calculation the results from a dried sample of pPVA, supplied by Buffalo China, will be used. The linear regression from the low pressure region in uniaxial compaction yielded the equation:

$$y = 0.2115x + 39.7886 \quad (46)$$

where x is the logarithm of the pressure. The linear regression from the HPASC data yielded the equation:

$$y = 12.413x + 55.248 \quad (47)$$

At the intersection both lines share the same (x,y) coordinates. The resulting equation to solve for x, the pressure at the onset of granulate deformation in shear is:

$$0.2115x + 39.7886 = 12.413x + 55.248 \quad (48)$$

Solving for x leads to the equation:

$$x = \frac{(39.7886 - 55.248)}{(12.412 - 0.2115)} \quad (49)$$

and therefore:

$$x = -1.2671 \quad (50)$$

The pressure at the onset of granulate deformation in shear is:

$$P1 = 0.054\text{MPa} \quad (51)$$

**Appendix L. Images from the Interferometer of the Surface Finish from the Samples Prepared with Increasing Moisture Content.**

**1.0 Surface Evaluation**

The images of the surface from the optical interferometer are listed in Table L-I. A decrease is observed in the measured roughness with increasing moisture content. A significant change in the appearance of the surface finish is observed with increasing moisture content. The high moisture content in the granulate decreases the flowability and results in the sample sticking to the die during the pressing operation. Above 3% moisture significant problems with flowability and die fill were observed.

Table L-I. List of the Images from the Interferometer and the Measured Roughness and Moisture Content from the Tile Samples.

<b>Na-Lignosulphonate</b>			<b>pPVA</b>		
Figure	Roughness (µm)	Moisture Content (wt%)	Figure	Roughness (µm)	Moisture Content (wt%)
L-1	21.585	0.00	L-9	18.199	0.00
L-2	15.621	0.88	L-10	13.932	0.28
L-3	12.283	1.16	L-11	13.290	0.99
L-4	9.763	2.12	L-12	10.599	1.39
L-5	8.272	5.69	L-13	9.363	1.94
L-6	8.202	6.86	L-14	8.951	2.69
L-7	8.805	8.58	L-15	9.047	5.52
L-8	9.014	8.59	L-16	9.008	5.68
			L-17	8.720	7.10
			L-18	8.763	9.92
			L-19	9.197	12.16

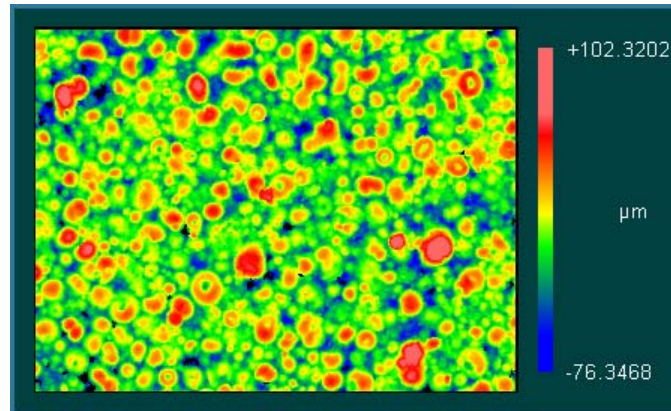


Figure L-1. Image of the surface finish of the dry-pressed sample prepared in a hardened steel die with an elastomer insert using the lignosulphonate binder at a moisture content of 0.00%, dried sample. The RMS roughness of the sample is 21.585  $\mu\text{m}$ .

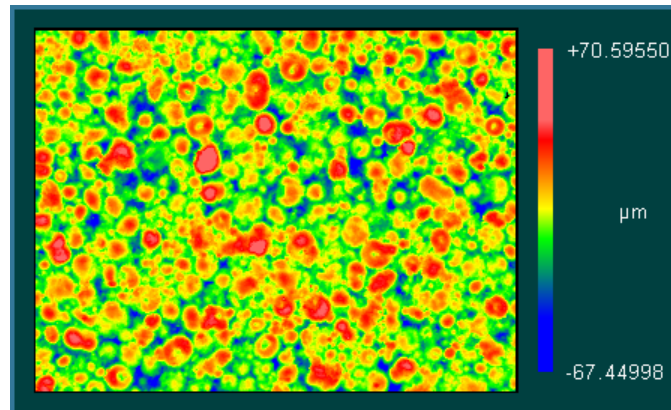


Figure L-2. Image of the surface finish of the dry-pressed sample prepared in a hardened steel die with an elastomer insert using the lignosulphonate binder at a moisture content of 0.88%. The RMS roughness of the sample is 15.621  $\mu\text{m}$ .

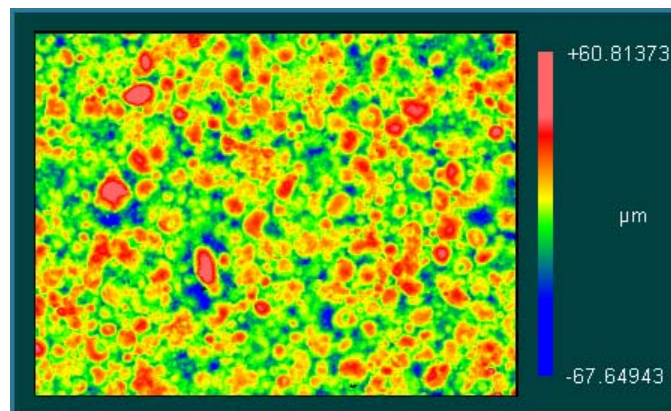


Figure L-3. Image of the surface finish of the dry-pressed sample prepared in a hardened steel die with an elastomer insert using the lignosulphonate binder at a moisture content of 1.16%. The RMS roughness of the sample is 12.283  $\mu\text{m}$ .

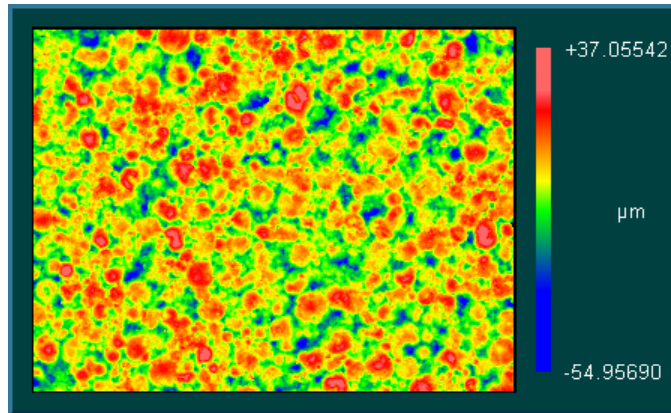


Figure L-4. Image of the surface finish of the dry-pressed sample prepared in a hardened steel die with an elastomer insert using the lignosulphonate binder at a moisture content of 2.12%. The RMS roughness of the sample is 9.763  $\mu\text{m}$ .

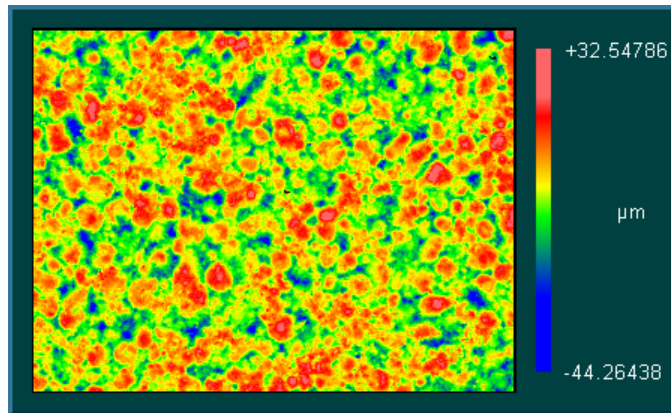


Figure L-5. Image of the surface finish of the dry-pressed sample prepared in a hardened steel die with an elastomer insert using the lignosulphonate binder at a moisture content of 5.69%. The RMS roughness of the sample is 8.272  $\mu\text{m}$ .

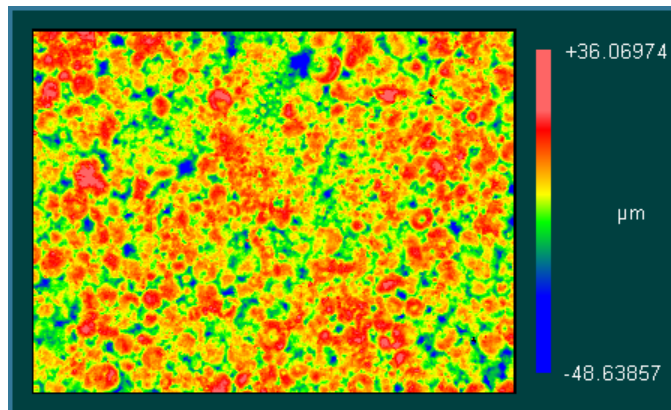


Figure L-6. Image of the surface finish of the dry-pressed sample prepared in a hardened steel die with an elastomer insert using the lignosulphonate binder at a moisture content of 6.86%. The RMS roughness of the sample is 8.202  $\mu\text{m}$ .

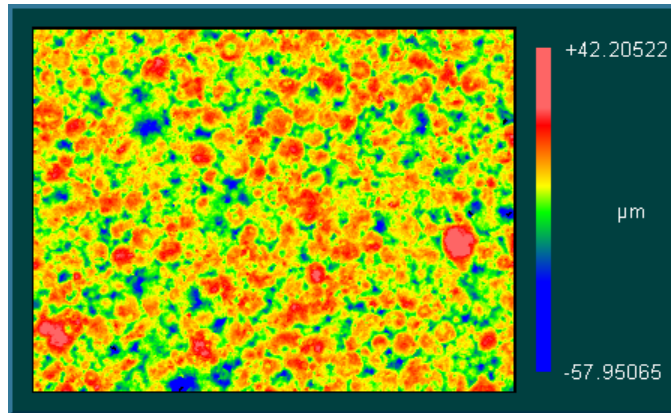


Figure L-7. Image of the surface finish of the dry-pressed sample prepared in a hardened steel die with an elastomer insert using the lignosulphonate binder at a moisture content of 8.56%. The RMS roughness of the sample is 8.805 μm.

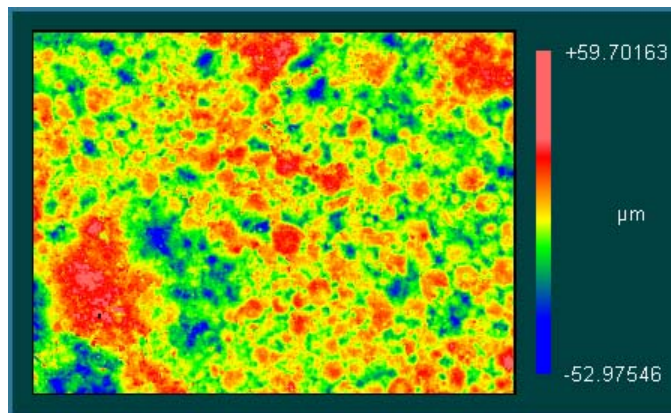


Figure L-8. Image of the surface finish of the dry-pressed sample prepared in a hardened steel die with an elastomer insert using the lignosulphonate binder at a moisture content of 8.59%. The RMS roughness of the sample is 9.014 μm.

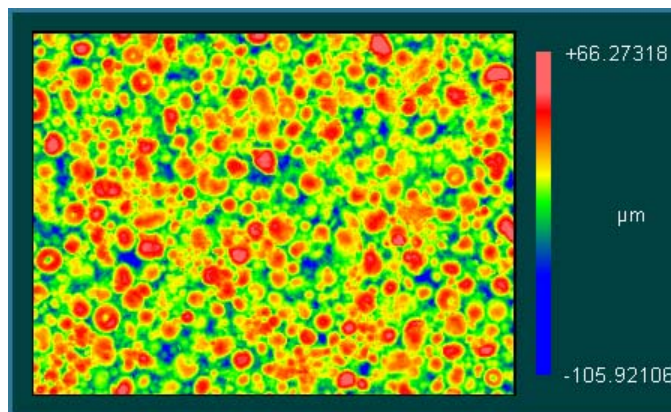


Figure L-9. Image of the surface finish of the dry-pressed sample prepared in a hardened steel die with an elastomer insert using the pPVA binder at a moisture content of 0.00%. The RMS roughness of the sample is 18.199 μm.

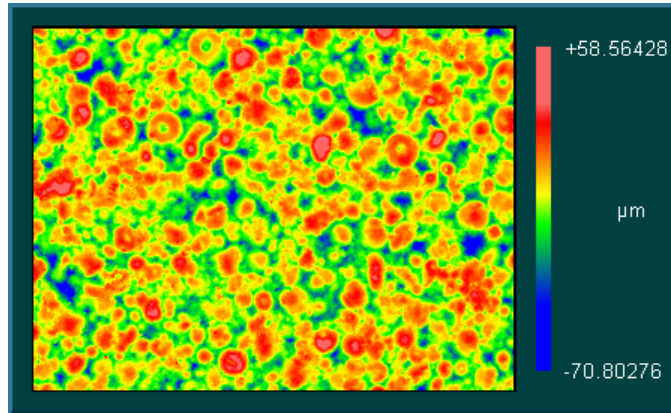


Figure L-10. Image of the surface finish of the dry-pressed sample prepared in a hardened steel die with an elastomer insert using the pPVA binder at a moisture content of 0.28%. The RMS roughness of the sample is 13.932  $\mu\text{m}$ .

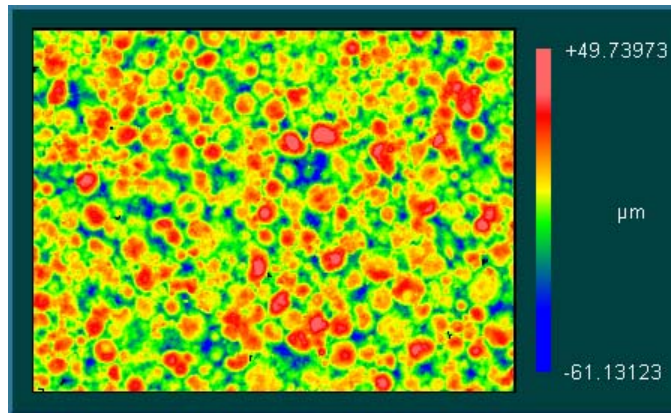


Figure L-11. Image of the surface finish of the dry-pressed sample prepared in a hardened steel die with an elastomer insert using the pPVA binder at a moisture content of 0.99%. The RMS roughness of the sample is 13.290  $\mu\text{m}$ .

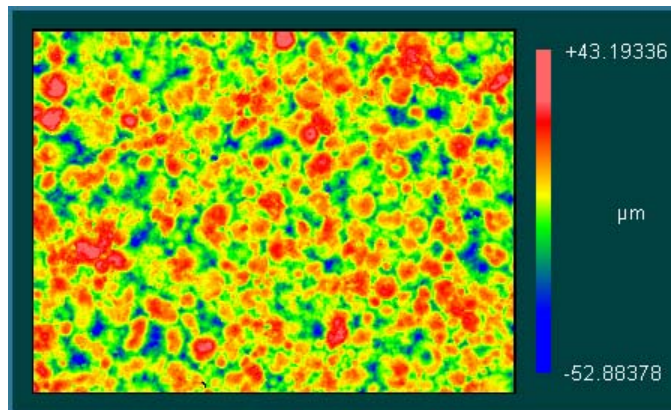


Figure L-12. Image of the surface finish of the dry-pressed sample prepared in a hardened steel die with an elastomer insert using the pPVA binder at a moisture content of 1.39%. The RMS roughness of the sample is 10.599  $\mu\text{m}$ .

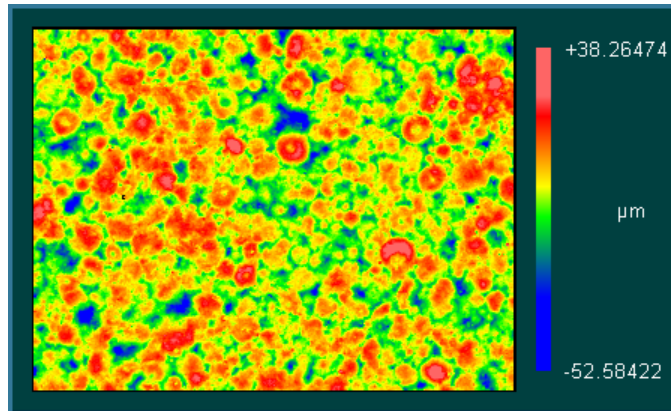


Figure L-13. Image of the surface finish of the dry-pressed sample prepared in a hardened steel die with an elastomer insert using the pPVA binder at a moisture content of 1.94%. The RMS roughness of the sample is 9.363  $\mu\text{m}$ .

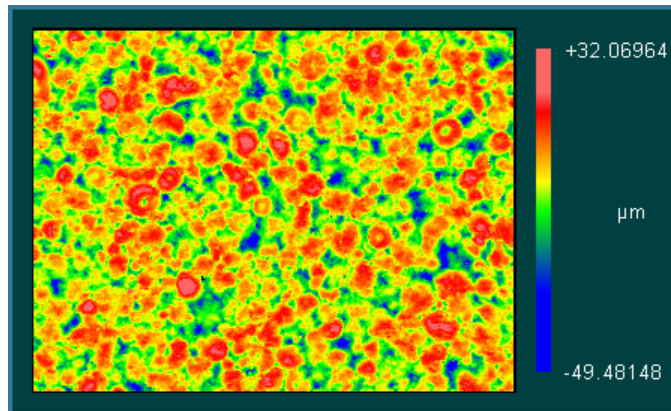


Figure L-14. Image of the surface finish of the dry-pressed sample prepared in a hardened steel die with an elastomer insert using the pPVA binder at a moisture content of 2.69%. The RMS roughness of the sample is 8.951  $\mu\text{m}$ .

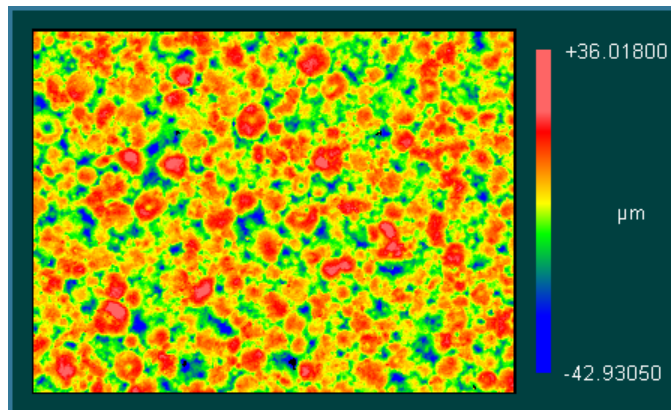


Figure L-15. Image of the surface finish of the dry-pressed sample prepared in a hardened steel die with an elastomer insert using the pPVA binder at a moisture content of 5.52%. The RMS roughness of the sample is 9.047  $\mu\text{m}$ .

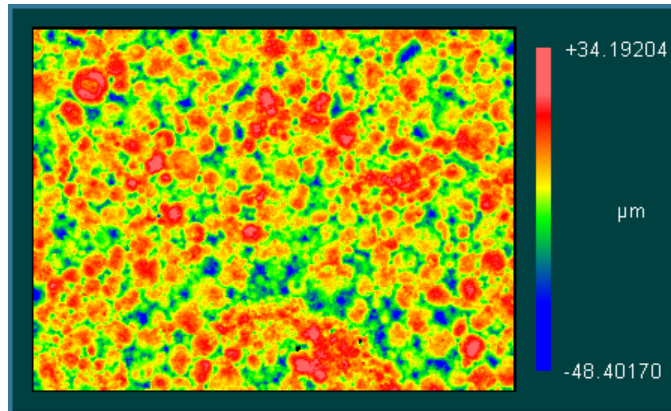


Figure L-16. Image of the surface finish of the dry-pressed sample prepared in a hardened steel die with an elastomer insert using the pPVA binder at a moisture content of 5.68%. The RMS roughness of the sample is 9.008  $\mu\text{m}$ .

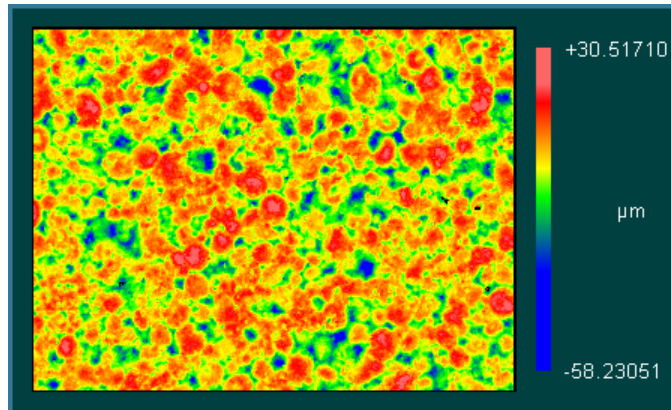


Figure L-17. Image of the surface finish of the dry-pressed sample prepared in a hardened steel die with an elastomer insert using the pPVA binder at a moisture content of 7.10%. The RMS roughness of the sample is 8.720  $\mu\text{m}$ .

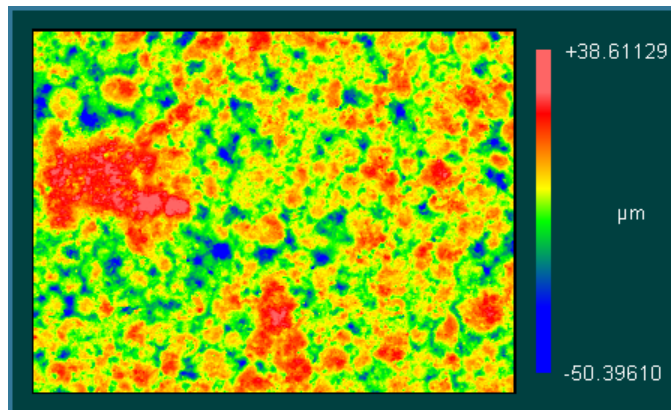


Figure L-18. Image of the surface finish of the dry-pressed sample prepared in a hardened steel die with an elastomer insert using the pPVA binder at a moisture content of 9.92%. The RMS roughness of the sample is 8.763  $\mu\text{m}$ .

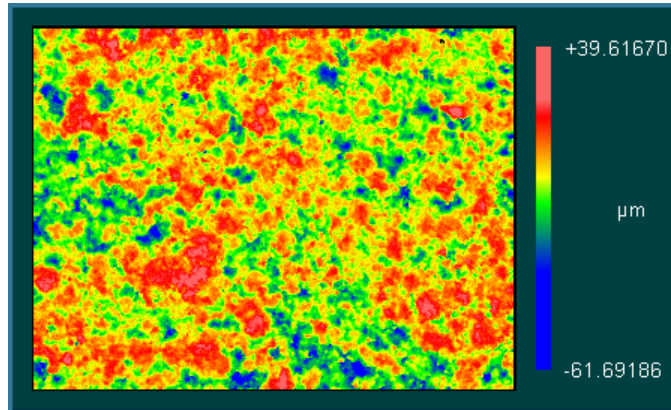


Figure L-19. Image of the surface finish of the dry-pressed sample prepared in a hardened steel die with an elastomer insert using the pPVA binder at a moisture content of 12.16%. The RMS roughness of the sample is 9.197  $\mu\text{m}$ .